INDIAN NATIONAL SCIENCE ACADEMY

INDIAN NATIONAL REPORT FOR IUGG 2023

28th IUGG GENERAL ASSEMBLY

11 – 20 JULY, 2023

BERLIN, GERMANY

NATIONAL COMMITTEE FOR
INTERNATIONAL UNION OF GEODESY AND GEOPHYSICS (IUGG)
AND
INTERNAIONAL GEOGRAPHICAL UNION (IGU)

Professor Archana Bhattacharyya, FNA, IIG, Navi Mumbai - Chairman

Professor Virendra Mani Tiwari, FNA, NGRI, Hyderabad – Member

Professor Ashok P. Dimri, IIG, Navi Mumbai – Member

Dr. Baldev Raj Arora, Dehradun – Member

Dr. G. Parthasarathy, FNA, NIAS, Bengaluru – Member

Dr. Ajay Manglik, NGRI, Hyderabad – Member

Professor K. S. Krishna, FNA, University of Hyderabad, Hyderabad – Member

Professor S. C. Rai, University of Delhi, Delhi – Member

Professor N. Nagabhushanam, S. V. Univsersity, Tirupati - Member

Executive Summary

This is a report on some of the scientific activities carried out in India in the domains of each of the eight associations, which comprise the International Union of Geodesy and Geophysics (IUGG), during the period August 2019 to March 2023. The report is prepared on behalf of the Indian National Science Academy (INSA), which is the adhering body for IUGG, and provides a glimpse of some of the work done by Indian scientists on topics related to various aspects of Earth and its space environment, which fall within the domains of the eight associations of IUGG: the International Association of Cryospheric Sciences (IACS), International Association of Geodesy (IAG); International Association of Geomagnetism and Aeronomy (IAGA); International Association of Hydrological Sciences (IAHS); International Association of Meteorology and Atmospheric Sciences (IAMAS); International Association for the Physical Sciences of the Oceans (IAPSO) ; International Association of Seismology and Physics of the Earth's Interior (IASPEI); and International Association of Volcanology and Chemistry of the Earth's Interior (IAVCEI).

The summary of research carried out in India in Cryospheric Sciences, by A. P. Dimri, Thamban Meloth, and Gulab Singh, provides a glimpse into some of the important areas covered by this research, such as understanding the critical role played by the cryosphere in a warming world, and its response to global warming; and major components of the global cryosphere like the Antarctica and Himalayas. These include studies of the impact of climate change on Himalayan glaciers, and various paleo-atmospheric and biogeochemical studies of ice and snow from East Antarctica to understand its linkage to climatic variations during the past, over decadal to millennial time scales.

The IAG report written by Virendra M. Tiwari and Ravi Kumar Muppidi, summarises the important contributions from India in areas covered by the objectives of the IAG, Significant developments have been made for upgrading the Spatial Reference frame infrastructure in India; in the establishment of the Indian Regional Navigation Satellite System (IRNSS) and GPS Aided GEO Augmented Navigation (GAGAN), and a network of GNSS observations for studying plate movement, earthquake cycle, isostatic adjustments, etc. An important process that is being studied is the deformation of Earth's surface caused by hydrological loads. Satellite gravity data has yielded information about the spatio-temporal variability of Terrestrial Water Storage and spatio-temporal patterns of mass changes in the Himalayan glaciated region.

A report on IAGA activities in India was compiled by Kusumita Arora.One of the highlights of these activities during this quadrennial was the hosting of the IAGA- IASPEI Joint Scientific Assembly virtually during August, 2021, by CSIR-NGRI and INSA. The areas of research conducted in India include planetary magnetic fields of internal origin, aeronomic phenomena in the ionosphere-thermosphere coupled system, magnetospheric phenomena such as the interplanetary medium-magnetosphere connection, radiation belts, and ionosphere-magnetosphere interactions. Activity in the area of Geomagnetic Observatories encompasses surveys and analysis of data and indigenous development of proton precession magnetometers. Under 'Electromagnetic Induction in Earth and Planetary Bodies', magnetotelluric studies have been taken up at different locations in India.

Indian scientists working in the field of hydrology have actively pursued research on various important topics related to both the quantity and quality of surface water and ground water. These research activities, summarized by V.M. Tiwari and N. Srinivas, have contributed significantly to deepening the understanding of surface hydrological processes, aquifer mapping, water quality monitoring, water resources management, and climate change impacts. Detailed hydro-geological studies have been carried out using Earth Observation data, ground based Ground Penetrating Radar observations, and detailed well inventory, to understand the sea water intrusion scenario in different seasons. Combined

in situ and satellite-based datasets have been used along with meteorological model simulations, to study the impact of irrigation on extreme moist heat in South Asia.

During the period covered by this report, Indian scientists have carried out extensive research in some of the areas covered by IAMAS, summarized by A. P. Dimri. Research pertaining to the lower atmosphere and meteorology include various aspects of atmospheric aerosols, impacts of COVID-19 lockdown on various atmospheric pollutants, and on the Indian summer monsoon, impacts of tropical volcanic eruptions on Indian droughts, the impact of recent changes in Asian anthropogenic emissions of SO_2 on sulphate loading in the atmosphere and the associated radiative changes; link between dust-Induced ice cloud modification and strengthened Indian Summer Monsoon Precipitation susceptibility; and Paleo-climatic studies over India.

The report for IAPSO, prepared by T. Srinivasa Kumar, on some of the research conducted by Indian scientists during the quadrennial, includes a brief description of important projects undertaken and the outcome of these investigations. To make operational a high-resolution ocean circulation model for the Indian Ocean, a Local Ensemble Transform Kalman Filter has been developed for interfacing with the present basin-wide operational Regional Ocean Modeling System to enable data assimilation. Effects of Cyclones on the Biogeochemical Processes in the Bay of Bengal, and the upper oceanic thermal response have been studied under different prevailing upper ocean structures.

For IASPEI, a comprehensive report is presented by Ajay Manglik. During the quadrennial, several new results were obtained on the crustal and upper mantle structure of the Indian shield, both at regional and geological province scale. The Himalayas continue to receive major attention in seismological research in many Indian Institutes who operated broadband seismological networks along the Himalayan arc, to further our understanding of the structure of the Main Himalayan Thrust, crustal and upper mantle structure as well as the dip of the under-thrusting Indian plate; and for estimation of attenuation. Other studies have focused on borehole seismology for near-field investigations of anthropogenic seismicity in the Koyna - Warna region.

Progress made during the period 2019 – 2023 by Indian studies on volcanic materials and Chemistry of the Earth's Interior, is succinctly described in the IAVCEI report prepared by N.V. Chalapathi Rao and G. Parthasarathy. The report is mainly confined to the rock types of basalts and mafic dykes, kimberlites, lamproites, lamprophyres, and carbonatites with a focus on their regional representation from the various domains of the Indian shield in a chronological sequence.

I am thankful to all my colleagues who have prepared the reports for the different associations under IUGG, and other scientists who have contributed summaries of the research carried out by their groups during the quadrennial. I take this opportunity to congratulate, on behalf of the National Committee for IUGG-IGU, the two winners from India, of the IUGG Early Career Scientist award this year: Mohd Farooq Azam (Glaciology/ Hydrlogy) and Jayashree Bulusu (Geomagnetism).

Archana Bhattacharyya, FNA
Chairman, National Committee for IUGG-IGU,
Indian National Science Academy, New Delhi

Table of Contents

1. **Cryosphere Research Work Summary (2019 to 2023)** **1**

   A. P. Dimri, Thamban Meloth, and Gulab Singh

2. **Indian National Report on IAG activities (2019-2023): Salient Features** **49**

   Virendra M. Tiwari and Ravi Kumar Muppidi

3. **Indian National Report for IAGA (2019 - 2023)** **78**

   Kusumita Arora

4. **Glimpses of Surface and Ground Water Studies in India During 2019-2022** **143**

   Virendra M. Tiwari and N. Srinivas

5. **Indian National Report on IAMAS activities (2019 -2023)** **164**

   A. P. Dimri

6. **Quadrennial Report on some Indian contributions to IAPSO science** **198**

   T. Srinivasa Kumar

7. **National Report on Seismological Research in India: 2019 – 2022** **260**

   Ajay Manglik

8. **Recent studies on volcanic materials and Chemistry of the Earth's Interior - An Indian Perspective: Progress made during the period 2019 - 2023** **323**

   N.V.Chalapathi Rao and G. Parthasarathy

Cryosphere Research Work Summary (2019 to 2023)

A. P. Dimri[1], Thamban Meloth[2], and Gulab Singh[3]

[1]Indian Institute of Geomagnetism, New Panvel, Navi Mumbai
[2]National Centre for Polar and Ocean Research, Vasco-da-Gama, Goa
[3]Indian Institute of Technology, Powai, Mumbai

Climate Change Impact on Himalayan Glaciers

The research aimed to answer three scientific questions. First, how the glacier dynamics and mass change in the current scenario. Second, how the glaciers in Himalaya respond to the changing temperature conditions as global warming continues. Third, apart from the glaciers' retreat and mass loss, how the neighbouring high-altitude vegetation responds to the changing climate. This helped define three concrete objectives, which led to three main research contributions, enumerated as follows:

1. Mass balance: Spatially detailed large-scale mass balance is estimated using the high-resolution and freely disseminated SAR data.
2. Climate feedback: The mass balance is influenced by the climate (especially under increasing temperature conditions), but owing to the warming climate, there are meltwater-influx spots that have been generated on a regional scale. For the first time, such meltwater-influx spots named 'anomalous points' across Himalaya have been identified. These are prominent features as there exists a strong tributary system in the glaciers of Himalaya.
3. Vegetation line shift: In response to the retreating glacier and the changing climatic conditions, the sparse vegetation is shifting to a higher altitude in Himalaya. A model has been developed using sparse linear regression, which can predict vegetation expansion by selectively using climate parameters and glacier variables.

Elevation change and mass budget in Uttarakhand (catchment scale) using geodetic method (30m SRTM-C and TanDEM-X DEM)

Quantification of surface elevation change for a part of central Himalayan glaciers (Uttarakhand) is done for the decade 2000-2014. It is observed that the mean elevation change rate for the 1950 glaciers in the region is -0.68 ± 0.01 m yr^{-1}. There was a dearth of information on the central Himalayan glaciers as previous studies mainly focused on the western Himalayan region, especially Lahaul-Spiti or the Karakoram (Gardelle et al., 2013; Rankl and Braun, 2016; Vijay and Braun, 2018). Kääb et al. (2012), were one of the first to publish large-scale elevation change over Pan-Himalaya, comparing ICESat and SRTM-X band elevation data. However, inconsistency in results has been found for the Lahaul-Spiti region. With the release of TanDEM-X data, it was possible to attain elevation change estimates using complete bi-static data. Since X- band and C- band have differential penetration properties, SRTM-C and TanDEM-X are used to estimate the mean elevation change for part of the Central Himalayan region of India after the bias correction. This region served as a test bed for the TanDEM-X data. The total mean elevation change is calculated on a catchment scale. The entire state of Uttarakhand in central Himalaya is divided into eight catchments and the mean glacier

elevation change is found to be -9.56 ± 0.2 m from 2000-2014. Table 1 shows that Bhagirathi holds the maximum catchment area and glaciated area (791 km^2) but the mean elevation change (-0.41 m) is much lower with respect to other catchments. It might seem that the maximum elevation change is in Pindar (-0.89 m); however, the glaciated area in this catchment is one of the lowest (75.97 km^2) with respect to other catchments. Hence the contribution of Pindar towards the total mass budget is significantly low. The mass budget for the entire central Himalayan glaciers of India for the period 2000-2014 is -0.61 ± 0.04 m.w.eq. yr^{-1} (Bandyopadhyay et al., 2019).

Table 1. details Catchment wise elevation change, mass budget, and glaciated area during 2000-2014.

Catchment	**Glaciated area (km^2)**	**Rate of mean Elevation Change (m yr^{-1})**	**Mass Balance (m.w.eq. yr^{-1})**
Yamunotri	107.13	-0.84 ± 0.06	-0.08 ± 0.02
Upper Bhagirathi	791.16	-0.41 ± 0.06	-0.28 ± 0.02
Mandakini	37.40	-0.34 ± 0.07	-0.01 ± 0.01
Upper Alaknanda	403.82	-0.37 ± 0.06	-0.13 ± 0.01
Dhauliganga	492.96	-0.86 ± 0.08	-0.36 ± 0.03
Pindar	75.97	-1.07 ± 0.08	-0.07 ± 0.01
Goriganga	247.49	-0.66 ± 0.09	-0.14 ± 0.01
Upper Kali/Sarda	198.03	-0.89 ± 0.08	-0.15 ± 0.01

Elevation change and mass budget in Himalaya (state wise) using geodetic method (90 m SRTM-C and TanDEM-X DEM)

Region-wise glacier elevation change on pan-Himalaya scale is estimated. The trend of glacier elevation change shows that in the far west near Karakoram, there is an overall positive mass change which has been reported previously as well (Gardelle et al., 2012; Rankl and Braun, 2016; Vijay and Braun, 2016, 2018) as seen in Fig. 1. The spatial distribution of the mean elevation change indicates a high elevation change in Jammu West as compared to Jammu East. This could be due to the surging glaciers in the Karakoram Range near Jammu East (Gardelle et al., 2013; Rankl and Braun, 2016; Vijay and Braun, 2018). Further, as we move towards the East of the Pan-Himalayan range, the percentage of the glaciated area significantly decreases, which also impacts the elevation change rate of the glacier. The elevation change is more for smaller glaciers, which is reflected in the spatial distribution pattern. Himachal Pradesh shows a maximum change in ice-thickness, whereas Uttarakhand and Nepal have a moderate elevation change. This could be attributed to the local topographic factors (like slope, aspect or debris cover) or the transition from one atmospheric circulation pattern to another in these regions. However, there is a clear trend of increasing elevation change in the Eastern Himalaya as we move from Sikkim to Arunachal Pradesh. This could be because region with larger glaciated area responds to the warming climate slower than regions with lesser glaciated area.

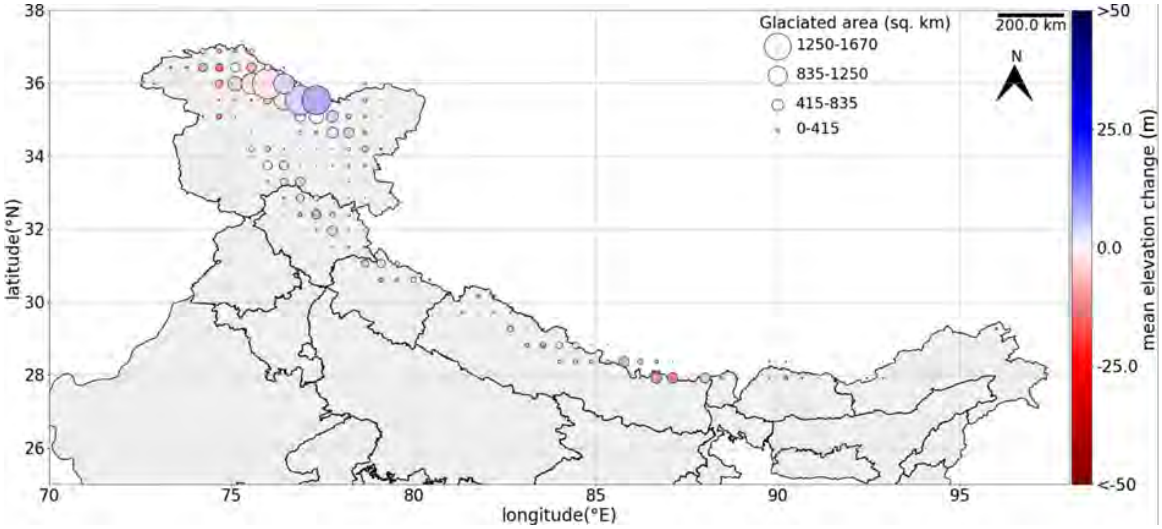

Fig. 1. Mean elevation change for the entire Himalayan range with the red colour denoting high negative elevation change and blue colour representing a positive mass change from 2000-2014. The map is made on a 50 km x 50 km grid showing glaciated area by the size of the circle and the colour of the circle by the mean elevation change.

Table 2. Glacier elevation and mass budget for Indian Himalaya during 2000-2014

Region	**Glacier area (km^2)**	**Rate of elevation change (m yr^{-1})**	**Mass budget (Gt yr^{-1})**	**Normalised mass budget (Gt yr^{-1} km^{-2}) x 10^{-4}**
Jammu and Kashmir	25328.40	-0.22 ± 0.10	-4.74 ± 0.50	-1.83
Himachal Pradesh	3504.71	-0.59 ± 0.21	-1.76 ± 0.59	-5.03
Uttarakhand	2422.72	-0.52 ± 0.25	-1.06 ± 0.55	-4.43
Nepal	6637.90	-0.47 ± 0.20	-1.64 ± 0.39	-3.18
Sikkim	494.71	-0.48 ± 0.19	- 0.20 ± 0.42	-4.13
Bhutan	702.22	-0.54 ± 0.26	-0.33 ± 0.26	-4.66
Arunachal Pradesh	350.61	-0.58 ± 0.25	-0.17 ± 0.12	-4.95

The result is slightly underestimated when compared with the values estimated by Kääb et al. (2012), with an elevation change of -0.51 ± 0.06 m yr^{-1} as opposed to our measurements of -0.22 ± 0.01 m yr^{-1}. The discrepancy in values reported could be due to the different data set being used. In addition, Kääb et al. (2012) interpolated ICESat data, which could result in an over-estimation of the mass balance. Further, the mass balance reported for Bhutan by Gardelle et al. (2013) is -0.22 ± 0.13 m w. eq. a^{-1} for 1999-2011, whereas this study shows -0.46 ± 0.01 m w. eq. yr^{-1} for 2000-2014. However, Brun et al. (2017) suggest a mass balance of -0.42 ± 0.20 m.w.eq. a^{-1} for the period 2000-2016. This slight variation could be using a different data set (ASTER DEM in their study as opposed to TanDEM-X DEM utilized in this study).

Climate effect on ice-thickness change in the Himalaya

The evidence of how rapid ice thinning is produced due to a warming climate feedback mechanism is given in Fig. 2(a). However, these melt-water injections are currently found to be discrete in the Himalayan region. Such anomalous points have been identified (from the interpretation of space-borne remote sensing data) over Pan-Himalaya, as seen in Fig. 2(b). The phenomenon of anomalous ice thinning and loss in the glaciers is correlated to the tributary glacier retreat and meltwater influx points (Fig. 2(b)), which were not reported before in detail at such a large scale.

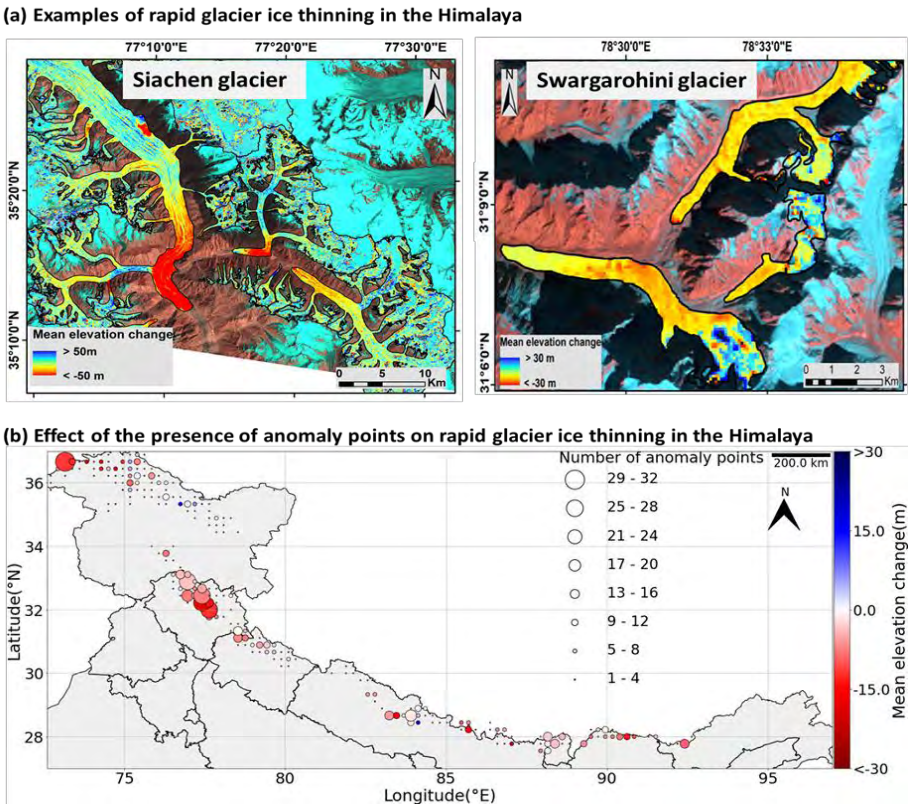

Fig. 2. (a) examples of regions showing water streams flowing (white dashed ellipses) from retreated tributary glacier resulting in sudden glacier ice thinning (shown in red colour) for Siachen glacier and its tributaries in Jammu-Kashmir and Swargarohini glacier in Uttarakhand (b) plot of mean elevation change indicated by colour range varying from red (depicting ice-thickness loss) to blue (signifying gain in ice-thickness) and size of the circles showing the density of such anomaly points in a 25 km × 25 km grid.

Vegetation line shift in high-altitude Himalaya

All the seven regions considered in the study show a visibly higher shift in vegetation line from 2000 to 2014. The hypsometry (Fig. 3) estimates the change in the percentage area covered by vegetation (expressed in terms of NDVI varying from -0.5 to 0.5) with the change in altitude (in meters). The bi-modal nature of the plot indicates a significant shift from a vegetated area to a glaciated area. The first mode represents the vegetated area, which is restricted to a lower elevation, with positive values of NDVI (0 to 0.5). As one moves to a higher altitude, it is observed that there is a sharp decline in the value of NDVI, highlighting that the vegetation is sparse as the glaciated terrain is approached. The percentage area shown in the second mode

represents the glaciated area having zero or negative NDVI values. Each hypsometry curve contains two lines, the orange line for the year 2000 and the blue line for 2014. In 14 years, the vegetated area has considerably shifted from a lower to a higher altitude, varying from 100 m in Uttarakhand to 400 m in Jammu and Kashmir (Table 3).

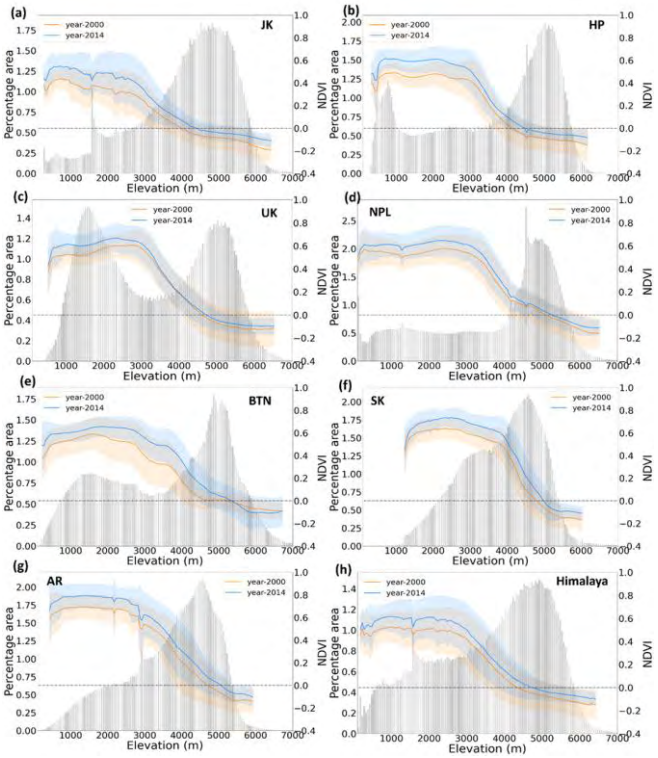

Fig. 3. The attitudinal distribution of the vegetated region and the glaciated area is shown as a bi-modal plot with the percentage area covered by each region is shown in the Y-axis. The secondary Y-axis plots the mean NDVI values at every 50m interval. The plots are for (a) Jammu and Kashmir (JK), (b) Himachal Pradesh (HP), (c) Uttarakhand (UK), (d) Nepal (NPL), (e) Bhutan (BTN), (f) Sikkim (SK), (g) Arunachal Pradesh (AR) and (h) Himalaya. The orange line shows the trend in NDVI for the year 2000, and the blue line depicts the year 2014.

Table 3. Altitude up to which the vegetation line shifted (Δ Veg line) in the study period (2000-2014) for each of the seven regions. Change in NDVI for the same study period in the next column, followed by the change of elevation (i.e. glacier ice-thickness change) over 2000-2014

Region	**Δ Veg line(± 21 m)**	**Δ NDVI**	**Δ glacier elevation (m)**
Jammu and Kashmir	400	0.05	- 3.08 ± 1.40
Himachal Pradesh	350	0.06	- 8.26 ± 2.94
Uttarakhand	100	0.02	- 7.28 ± 3.50
Nepal	150	0.04	- 6.58 ± 2.80
Bhutan	100	0.01	- 6.72 ± 2.66
Sikkim	180	0.05	-7.56 ± 3.64
Arunachal Pradesh	350	0.08	- 8.12 ± 3.50

Notably, the data pose uncertainty in vertical accuracy (±15 m for SRTM and ±2 m for TanDEM-X DEM) and horizontal inaccuracy (with a resolution of 30 m from Landsat images, SRTM DEM, and TanDEM-X DEM), which might add to the error in the estimates. The overall uncertainty estimated from these sources is ± 21 m. On comparing the influence of the change in glacier dynamics (glaciated area and ice thickness change) on the vegetation line shift as well as the change in the vegetation growth (through NDVI), maximum change can be seen over the two extreme regions, namely, Jammu and Kashmir (JK) and Arunachal Pradesh (AR). On the one hand, JK has the maximum glaciated area, so the slightest retreat or change in elevation (ice-thickness) in the glaciers allows a larger de-glaciated area to be covered by subnivial vegetation (i.e. the vegetation that grows below the snowline). That is precisely what has happened with the maximum ingress of vegetation line (400 m) and a relatively substantial NDVI change in the fourteen years of the study period. However, it is interesting to note that the growth of the vegetation is not significant, as the NDVI changes by 0.05 only. On the other hand, AR has the least glaciated area; however, a massive loss in ice-thickness has led to more water being released over a shorter period, resulting in such a high level of ingress of subnivial vegetation. The relatively high change in NDVI value corroborates the fact that glacier dynamics strongly influence the upward shift of vegetation and, to a certain extent, the growth of the vegetation. Moreover, Sikkim shows unusual behaviour at higher altitudes, where the NDVI shows a visibly reduced growth pattern. This anomalous behaviour could be due to other topographic parameters like slope and aspect or climate variables such as temperature and precipitation. Thus, all such parameters are introduced for a regression analysis (detailed in Table 4) to understand better the predictors of such high NDVI change and the ingress of vegetation line to higher altitudes. The positive signs show a direct correlation between ΔNDVI and the parameter. In contrast, the negative sign signifies an opposing effect on ΔNDVI. Spare linear regression based on the penalty function of maximising coefficient of determination and minimising parameters selectively determines seven parameters that influence the change in NDVI or vegetation change.

Table 4. Coefficients of least-square regression models of mean change in greenness (NDVI) within 70 x 70 km grids in relation to eleven climatic, glacial and topographic parameters). All explanatory variables were normalised prior to analysis.

	Parameter	**Linear regression**	**Sparse linear regression**
Ground	glacier area	-0.0035	-0.0032
	elevation change	-0.0044	-0.0022
	mass loss	+0.0057	-
	slope	-0.0187	-0.0130
	aspect	-0.0023	-0.0001
	elevation	-0.0066	-0.0059
Climate	Precipitation	+0.0042	-
	snow water equivalent	-0.0029	-
	daily maximum temperature	-0.0208	-0.0053
	run-off	+0.0128	+0.0011
	soil moisture	+0.0144	+0.0067

The remaining regions, namely Uttarakhand (UK), Nepal (NPL), and Bhutan (BTN), follow a moderate trend of a shift in vegetation line ranging from 100-180 m (Table 3) with reasonable change in NDVI values (range from 0.02 to 0.04) over 14 years.

Anomalous Glacier Dynamics

The spatial distribution of Chandra and Bhaga sub-basin glacier ice velocities are estimated using the most accurate remote sensing technique. Most of the glaciers in both Chandra and Bhaga sub-basin were found to be flowing with less than 2 cm/day velocity rate. Glacier velocities are mostly low and reduced as they get closer to the terminus because, in general, glacier velocity is controlled by thickness, steepness, density and ice mass. Besides this, it is also observed that large glaciers like Bara Shigri and Samudra Tapu in Chandra sub-basin are moving with the highest velocity among all the remaining glaciers in Chandra and Bhaga sub-basins (fig. 1).

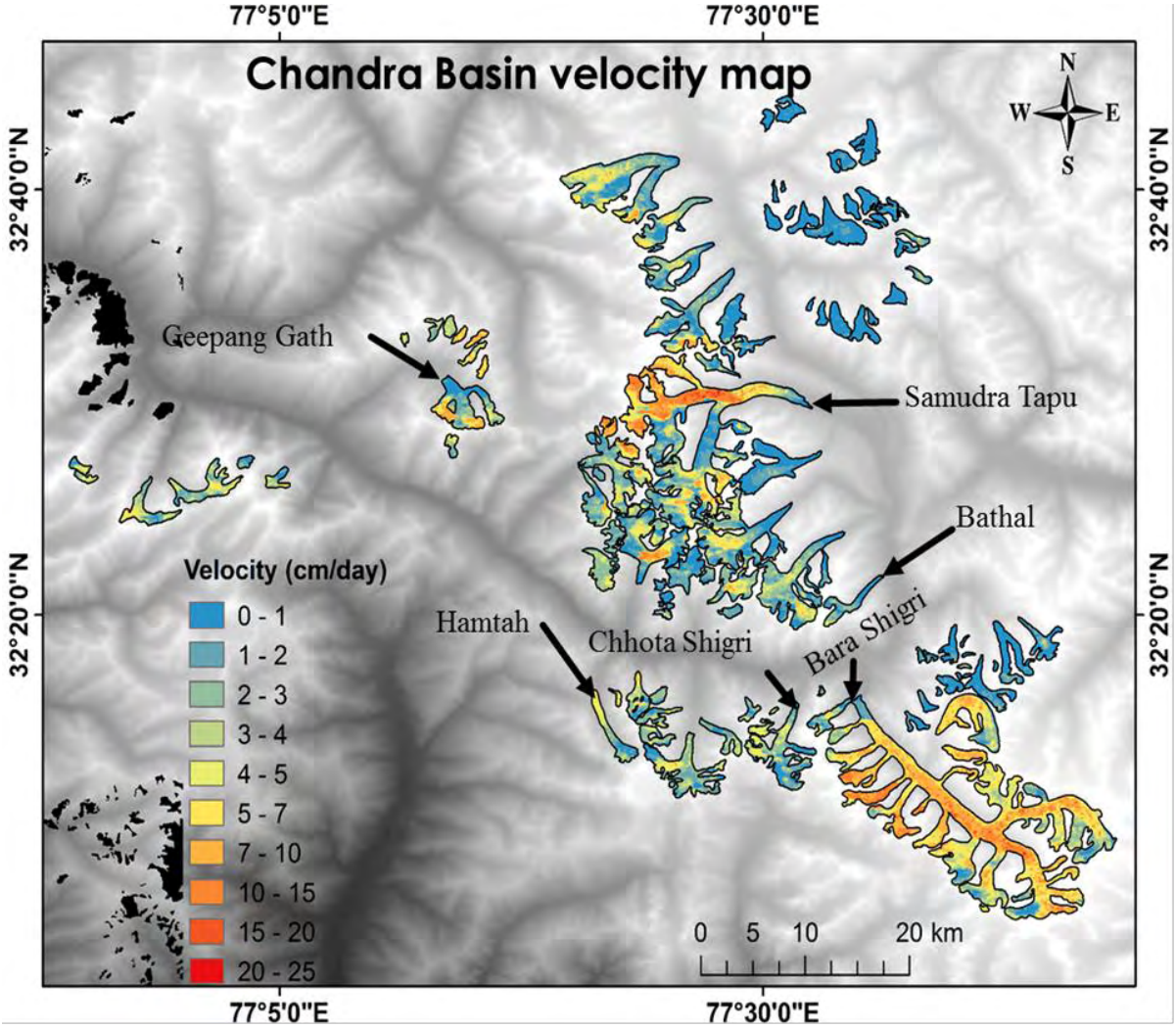

Fig. 4. Spatial distribution of Chandra sub-basin glacier ice velocities generated using the DInSAR technique (from Singh et al., 2020).

There are several interesting factors/reasons are existed behind the high flow rates of certain glaciers (fig. 2). In case of glacier 'A', high flow rate in frontal area was expected to be associated with a steep slope or abrupt changes in elevation, which also agrees well with high steepness of the terrain. The higher velocities in frontal areas of glaciers 'B' and 'C' are not correlated with slope. An interesting factor is discovered that influenced these glaciers' flow/velocity in the frontal area. The discharge from the adjacent glacier meltwater which falls from the detached glacier's tributaries to the main trunk of glacier contributes to the increase in flow rates in frontal areas. We also observed that the thinning rate gradually increases from accumulation to ablation region. High thinning rate in the frontal area of the three anomalous glaciers in Bhaga sub-basin is due to the steep slope and subglacial meltwater flow as compared to other glaciers in this region. The retreat of glaciers is not only their self-melting process, but also by the discharge of water from adjacent glaciers or its ex-tributaries. The process of melting and retreat forms these adjacent/tributary glaciers.

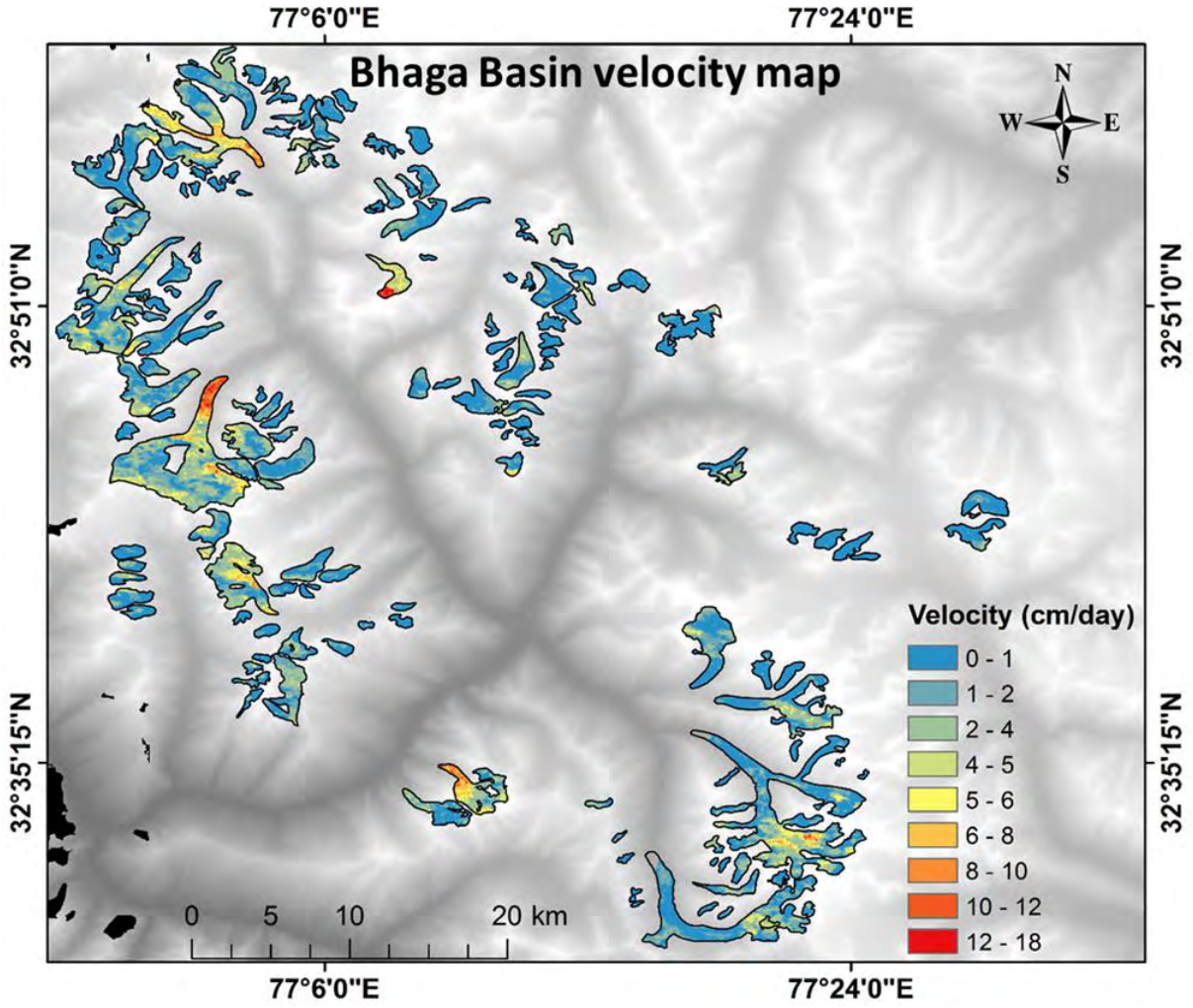

Fig. 5. Spatial distribution of Bhaga sub-basin glacier ice velocities generated using the DInSAR technique and observed fast-moving glacier in Bhaga sub-basin named as 'A', 'B' and 'C'. 'P' is the Patseo glacier (from Singh et al., 2020).

Consequently, this melting water helps to increase the glacier movement, which results in faster glacier ice melting and increased thinning rate (negative mass balance). This is one of the major effect as well as disadvantage in the glacier detaching process. However, the observations indicate high velocity and ice thinning rate can be also due to changes in the hydraulic system, formation of cavities, deformation of subglacial till caused by the discharge of melt. Further, the meltwater discharge can influence the performance of glacier dynamics models for ice flux and mass studies (Fig. 3). Thus subglacial drainage knowledge is important for developing relations between glacier hydrology and its movements.

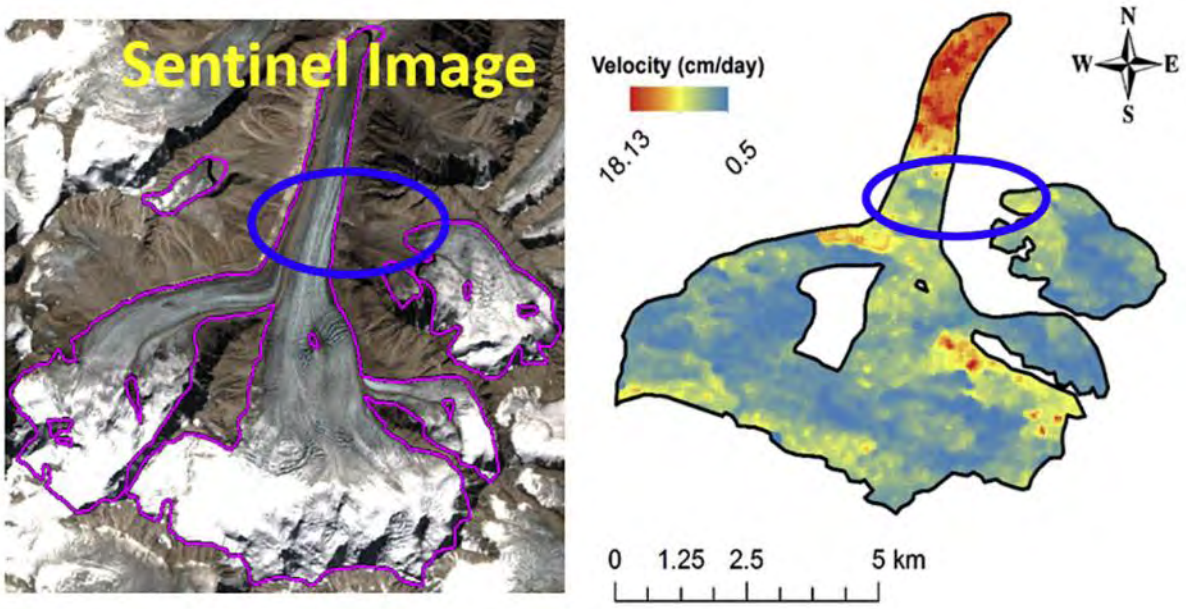

Fig. 6. The effect of meltwater influences on the glacier dynamics. The water stream (see blue circle area on optical Sentinel-2A image (acquired on October 2, 2016) and velocity map of Glacier ‘B') of adjacent glacier causing an increment in the flow of glacier ‘B' in the ablation region (from Singh et al., 2020).

In case of Severnaya Zemlya archipelago, we estimates the movement of the Severnaya Zemlya archipelago region using the DInSAR technique to understand the dynamics of this area. We observed a high movement rate (293 m/yr) for one of the marine-terminating glaciers (glacier ‘A’) in the Academy of Sciences Ice Cap in the year 2018 (Fig. 4b). The velocity observed in this study shows a four-fold increase as compared to the velocity (70 m/yr) reported in 1995. Climatic parameters shall not dictate such regional changes but the intrinsic properties of the ice cap itself might. The plausible reason has been identified as the presence of an inefficient sub-glacial hydraulic system which leads to a sudden increase in velocity. The existence of such a system is supported by the fact that a large portion of such glaciers is submerged in the sea and deformable sediments are common. This leads to the development of low-pressure conditions and fast basal movement, which is reflected at the surface. Owing to such high-velocity changes over the past 23 years, it is important that a time series analysis of glacier velocity be done for a better understanding of the glacier/ice cap dynamics and the effect of climatic changes. For other glaciers in this archipelago, namely, in the Karpinsky Ice Cap, for land-terminating glaciers, we observed a comparatively low movement rate with respect to the marine-terminating glaciers. Such information about the ice caps adds to the existing sparse database for the glacier movement in the Severnaya Zemlya archipelago, which could act as a useful input for modeling future glacier velocity.

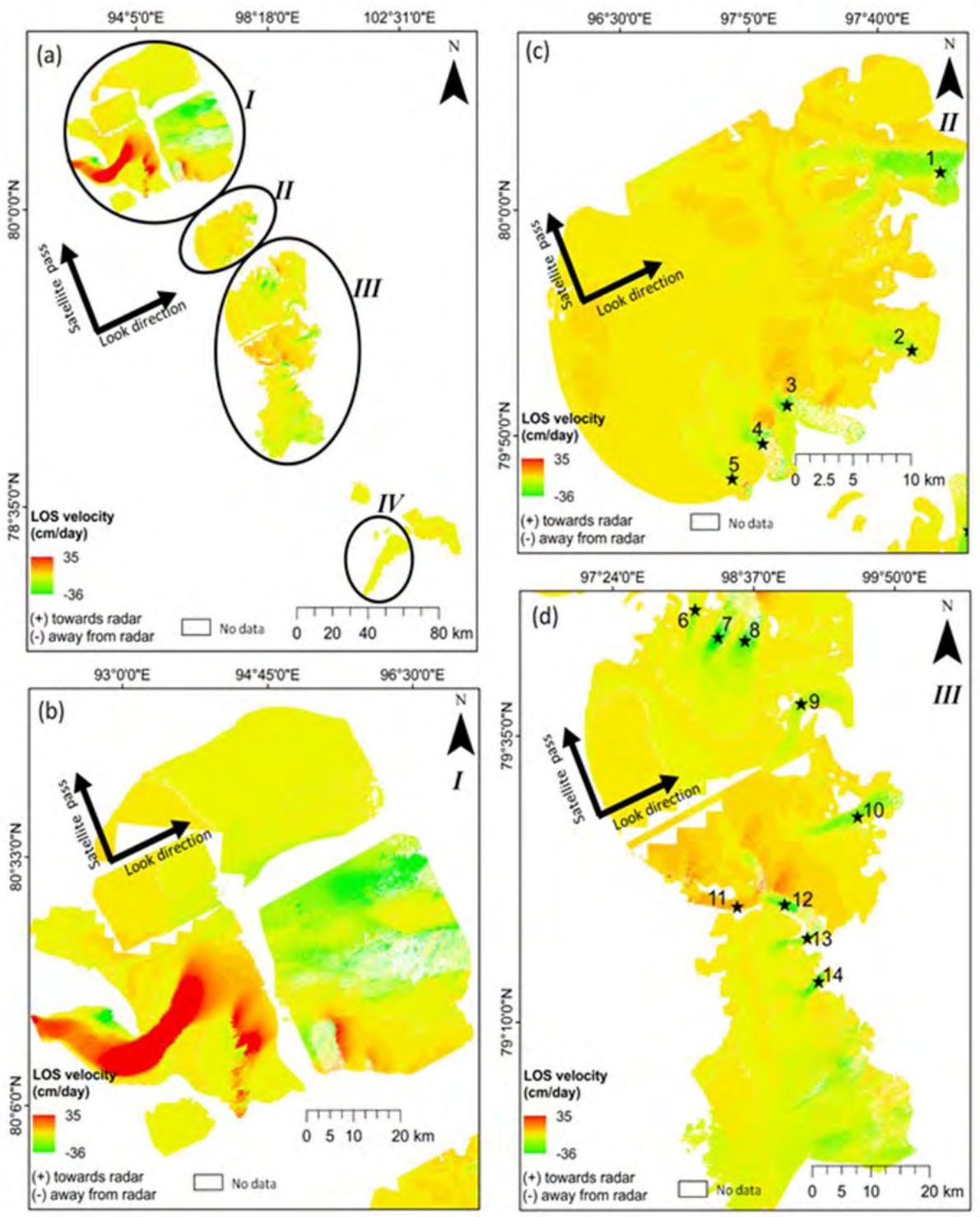

Fig. 7. Glacier movement in LOS direction of the Severnaya Zemlya archipelago using the two-pass DInSAR technique. (a) An enlarged section of Severnaya Zemlya; (b) Academy of Sciences Ice Cap; (c) Rusanov Ice Cap; (d) Karpinsky and University ice caps (white portion represents no movement/no data) (from Nela et al., 2019).

In case of the Svalbard archipelago, a 3-pass differential interferometry technique is tested efficiently for determining the glacier velocity using freely available spaceborne microwave satellite data from Sentinel 1A/1B sensors (Fig. 5). The assumption for this study is that the glacier movement is constant over the period of observation. This assumption is admissible

since the used datasets have a total temporal gap of 12 days only. The error due to topography, which is one of the major error sources in the 2-pass DInSAR process, is eliminated by adopting a 3-pass DInSAR technique as the external DEM is replaced by Double Difference Interferogram (DDI). Compared to the other DInSAR applications like earthquake monitoring and land subsidence/uplift studies, DEM errors significantly affect the accuracy levels of glacier movement due to the irregular structure of the glacier and continuously changing glacier surface elevation/ice thickness. However, the availability of DEMs with more accuracy and the near time of the acquired interferometry pair gives an insignificant change in 2-pass DInSAR velocity results with the 3-pass. Hence, the 3- pass DInSAR technique is effective in absence of accurate DEM availability. The 3-DInSAR technique also enables precise monitoring of the glacier flow dynamics along with providing an unprecedented level of information related to glaciers that were previously not obtained from traditional methods. Furthermore, the 3-pass DInSAR based movement studies are more suitable over the region of surge-type glacier as compared to 2-pass DinSAR. On the other hand, the same technique (DInSAR) can be used to generate the topography map using the double-difference interferogram, which cancels out the velocity component and leaves behind only the phase variations due to topography. Additionally, a double-difference interferogram also gives information to find the grounding line of ice sheets (i.e., a boundary line between grounded and floating ice).

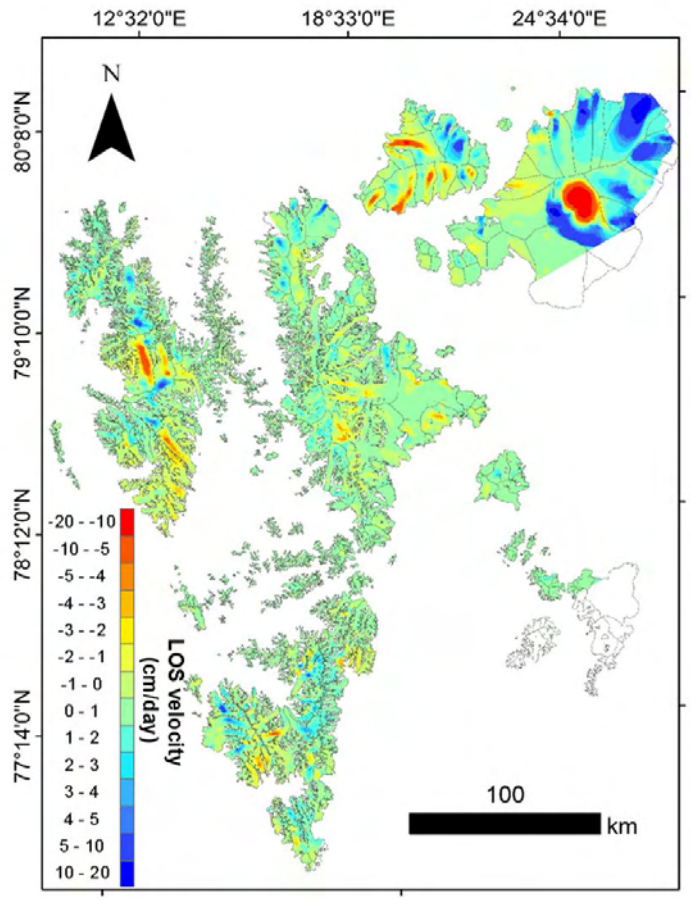

Fig. 8. The 3-pass DInSAR line-of-sight (LOS) velocity of the Svalbard region, generated with the Sentinel -1A/1B C- band data in the October month-2020 (from Nela et al., 2022).

Ice thickness distribution of Himalayan glaciers

The spatial distribution of ice thickness is derived from the surface velocity of the glaciers, which is actually inferred using the most accurate radar remote sensing technique (fig. 6). The optimum SAR data for the Himalayan region glaciers (ALOS-2/PALSAR-2), and TanDEM-X—DEM are used in the laminar flow law to derive the ice thickness. The accurate ice thickness measurements are important to the precise estimation of volume/glacier stored water, which is momentous for water resource and disaster management systems. The complete glacier ice thickness distribution of Himachal Pradesh, and partial distribution of Arunachal Pradesh, Bhutan, Sikkim, and Uttarakhand are presented in our study. Few large glaciers, namely Miyar, Bara Shigri, Samudra Tapu, and Gangotri, were exhibited more ice thickness. The results of our study show the laminar flow inversion-based ice thickness method is more sensitive to ice flow and slope factors. Hence, accurate DEMs are important to understand the glacier dynamics and its parameter changes. The validated analysis is performed on a few benchmark glaciers with the existing literature. However, this method is more suitable for the unchanging internal parameters of a glacier throughout its surface area. The study also addressed the problems concerning the glacier dynamics. The high-velocity rate due to the influx of melting water from adjacent glaciers causes an increment in the flow rate. Thus, the abnormal velocity gives erroneous ice thickness measurements (fig. 7). This is one of the major problems to be considered in the velocity-based thickness-derived procedures. Finally, our investigation suggests the inclusion of the velocity influencing parameters (other than the slope) in the physical-based models for estimating accurate ice thickness inversion.

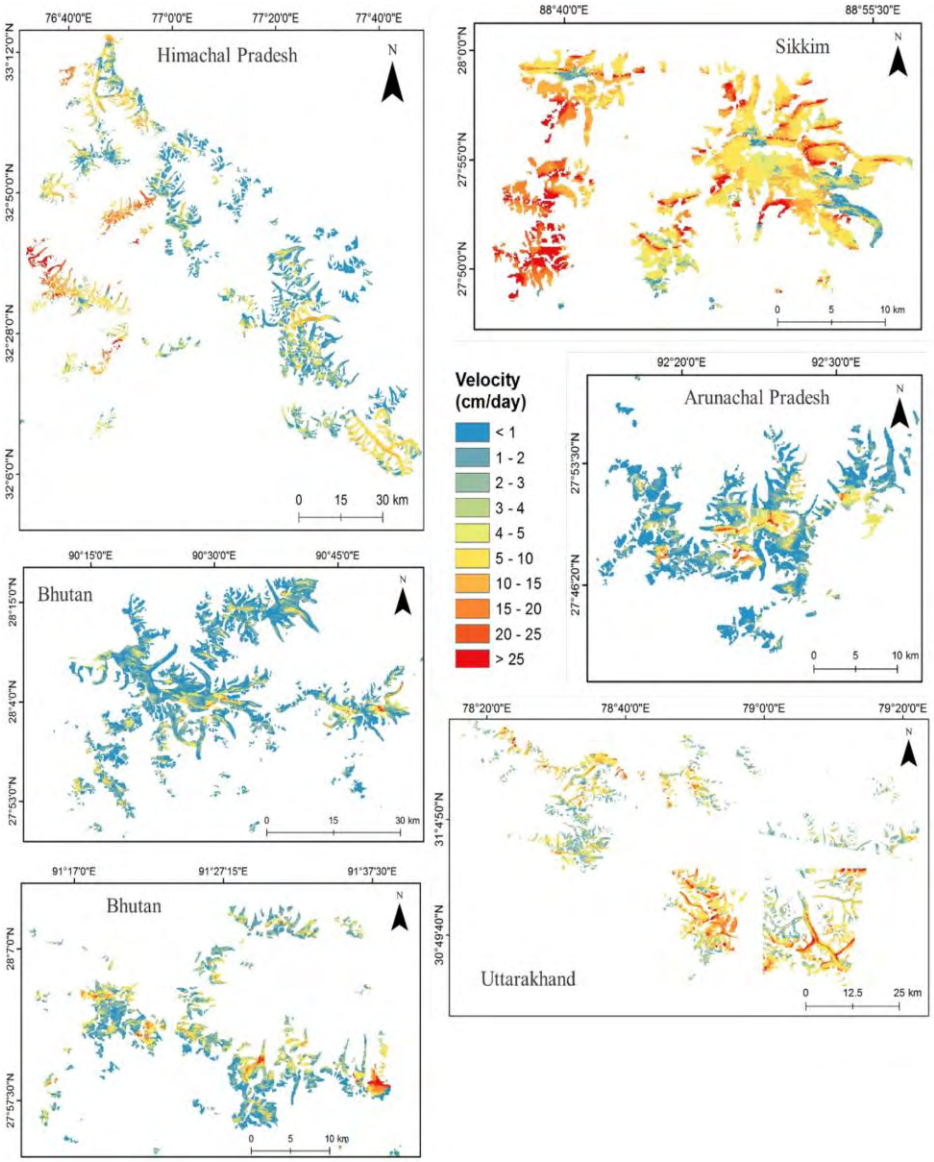

Fig. 9. The glacier surface velocity generated by the 2-pass DInSAR technique over the regions of Himachal Pradesh, Uttarakhand, Sikkim, Bhutan, and Arunachal Pradesh (from Nela et al., 2022).

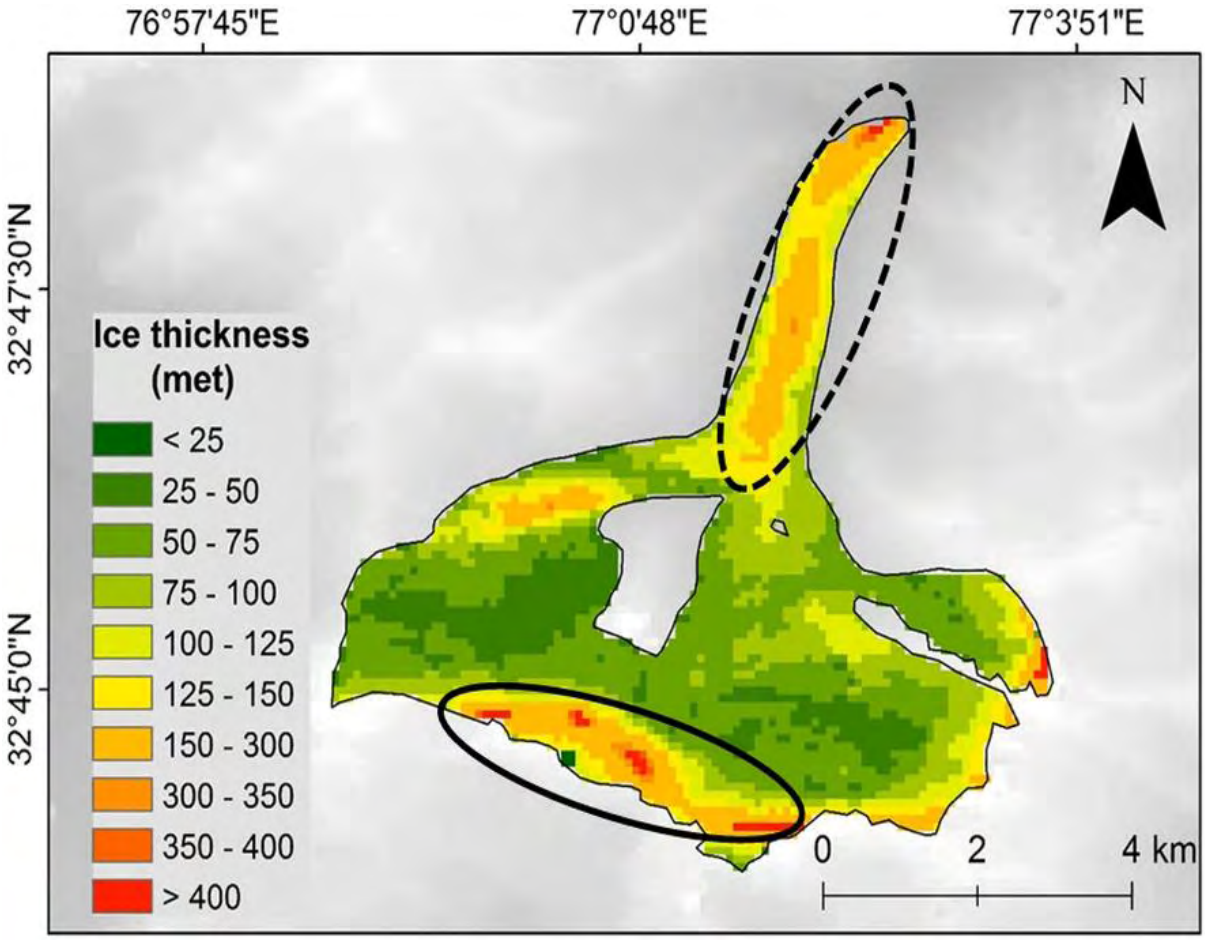

Fig. 10. The effect of low slope and high velocity on glacier ice thickness (dotted circle showing the velocity effect and continuous circle showing the slope effect) (from Nela et al.,2022).

Glaciated Terrain Classification/Glacier Facies Mapping

Glaciers have distinct features (snow, ice, and debris cover) and their identification and classification using satellite imagery is still a challenging task. Classification of different glacier features (zones) using remote sensing data is useful for numerous environmental and societal applications. Facies identification and their distribution over the terrain provides the relationship between the mass balance and the dynamics of the glacier which will aid monitoring of the glaciers. The foremost objective study is to classify different glaciers into different radar zones/facies in the Himalayan region with the development and implementation of different methodologies using polarimetric SAR datasets.

Development of full PolSAR GF-DNN for glacier facies mapping

Fully polarimetric SAR data from ALOS/PALSAR over the part of Siachen and ALOS-2/PALSAR-2 over Bara Shigri glacier for the identification of distinct glacier facies/zones have been utilized. The purpose of this study is to develop the fully polarimetric SAR (PolSAR) deep neural networks classification approach for the extraction of different features of the alpine glaciers. The developed approach was tested and classification results were compared with the support vector machines-based classification over the part of two glaciers: Siachen

glacier and Bara Shigri glacier. The high percolation facies were only found over the sub-part of Siachen Glacier due to the intense freezing conditions that the glacier is exposed to throughout the year. For the Bara Shigri glacier, the upper percolation zone does not exist in this location, due to the early summer melting of compact dry snow. As the seasons change from winter to summer, the temperature rises significantly, causing substantial melting and the disappearance of the lower percolation zone. The overall accuracy (OA) of GF-DNN classification is relatively high (91.17% for Siachen and 89% for Bara Shigri) with a good kappa coefficient (0.88 for Siachen and 0.85 for Bara Shigri) as compared to SVM for both the selected glaciers. An improvement of more than 10% is achieved in the OA of GF-DNN classification as compared to SVM for both the glaciers. The obtained classified results and accuracy demonstrates the potential of deep neural networks-based glacier features classification approach for glaciated terrain features.

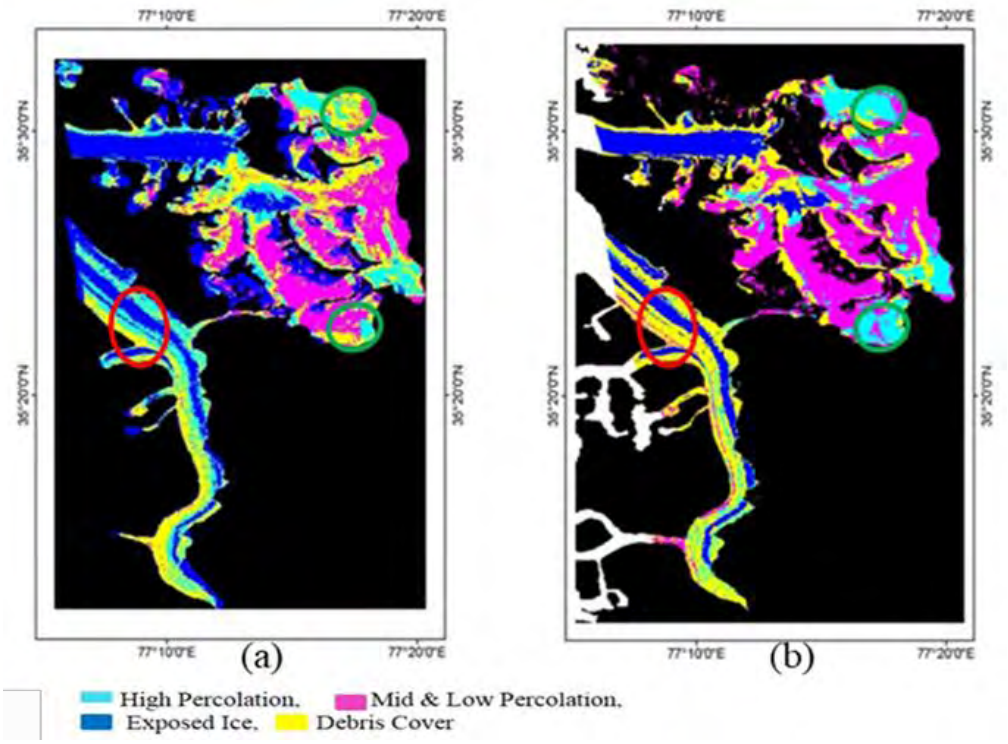

Fig. 11. Sub-part of Siachen glacier: (a) Classified map using SVM, area inside the red and green circle – shows the misclassification of debris cover class into percolation class and vice-versa (b) Classified map using GF-DNN, red and green circles – indicates correctly classified area (from Panwar et al., 2022).

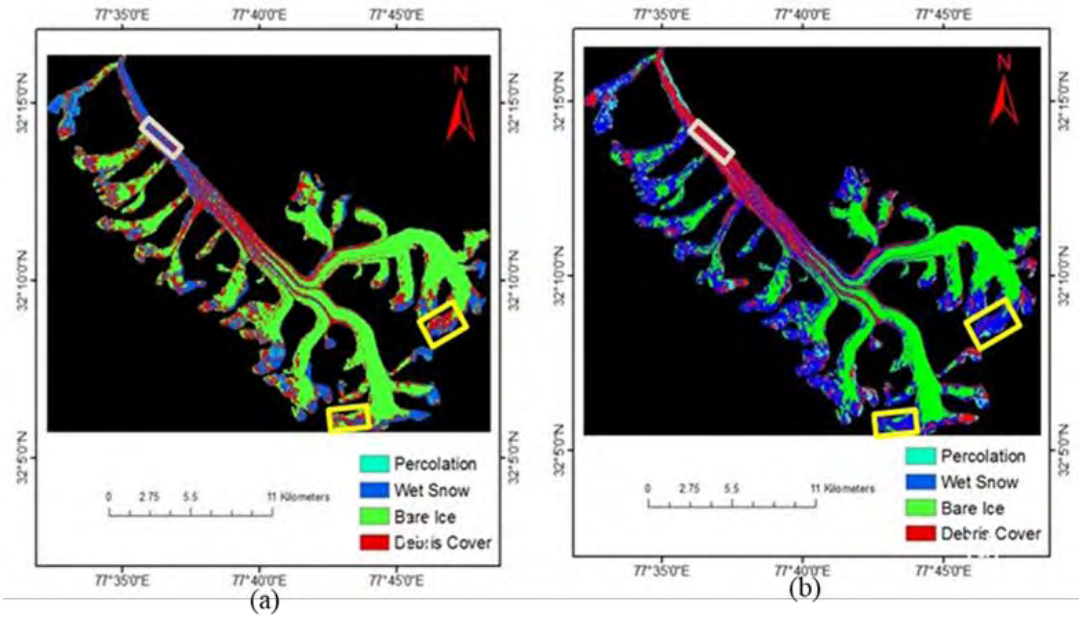

Fig. 12. Bara Shigri glacier: (a) SVM classified map, pixels inside the yellow boxes show wrongly classified as debris cover and bare ice at higher reaches (b) GF-DNN classified map, yellow boxes indicate the correctly classified pixels as debris cover and bare ice at higher reaches (from Panwar et al., 2022).

Quantification of Glacier Facies and ELA Delineation using Sentinel-1 SAR Data:

The potential of using freely available multi-temporal Sentinel-1 SAR images for glacier zone mapping in the Chandra basin of Himachal Pradesh is investigated. The images recorded in three different months (January, May and September) of the years 2015 and 2016 were used. The SVM algorithm was implemented on twenty-four glaciers to classify the different zones lying on the glaciated terrain. The classification of glacier zones was performed using Sentinel-1 datasets and a multi-temporal SAR-based method. Higher temperatures, along lower elevations, give rise to snow melting that causes variations in backscattering intensities of different glacier zones. As time proceeds from winter to early summer and the late summer, temperatures gradually increase giving rise to temporal variations along different glacier zones. The SAR datasets of three different seasons in each year were stacked to create RGB composite images. The glacier facies/ glacier surface features reveal different tonal variations, as the glacier liquid water content changes owing to the season. The classification was performed on two glaciers in the study area for a period of two years - 2015 and 2016.

Fig. 13. Multi-temporal classified maps using SVM for the years 2015 and 2016.

As the glacier is completely dynamic, there is inconsistency in the areal extent of resulting classes. The total area of accumulation zone is more in the year 2015 and lesser in 2016 collectively for all 24 glaciers. In Bara Shigri, the accumulation zone occupies roughly 41% in the year 2015 and about 32% in the year 2016. Rest is the ablation zone which is 59% in 2015 and 68% in the year 2016. From the classified maps, it can be seen that the debris cover is extensive over the Chota Shigri and Bara Shigri. Due to warmer temperatures, ELA moves upwards in elevation which makes the area covered by the accumulation zone reduced and the ablation area increases that indicate retreat of glacier health.

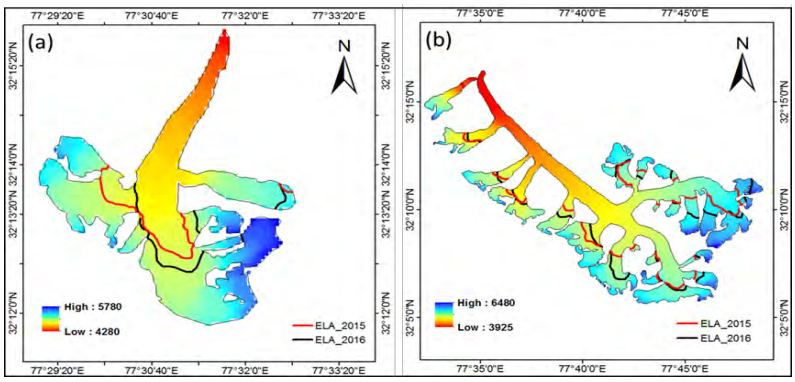

Fig. 14. Illustration of change in ELA positions over (a) Chota Shigri (b) Bara Shigri glacier in the year 2015 and 2016.

On the contrary, over cold conditions, ELA moves downwards in altitude representing the advancing health of the glacier and positive glacier mass balance. After the classification of glacier zones, the equilibrium line altitude for glaciers successfully delineated in consideration for the years 2015 and 2016. 2015 had ELA at the lowest for both the selected glaciers. ELA

is strongly influenced by surrounding climatic and temperate conditions. In this study, SAR based ELA technique has been adopted. SVM performs well with an accuracy of more than 90% for both years. This study gives an idea of how ELA and zones change in two different years. The accumulation area is more and ELA is at the lowest in the year 2015 for both Chota Shigri and Bara Shigri glaciers.

Glaciated terrain classification using SVM scattering based learning classifier:

The study focuses on the classification of different features of the glaciated terrain and understanding the different types of scattering mechanism that takes place at a different elevation. Using model-based decomposition with pre-processed ALOS-2/PALSAR-2 data, incorporating the knowledge of polarimetric microwave interactions the different glaciated terrain features were identified. In this, model-based scattering power decomposition i.e. 6SD in combination with SVM has been used for glaciated terrain classification.

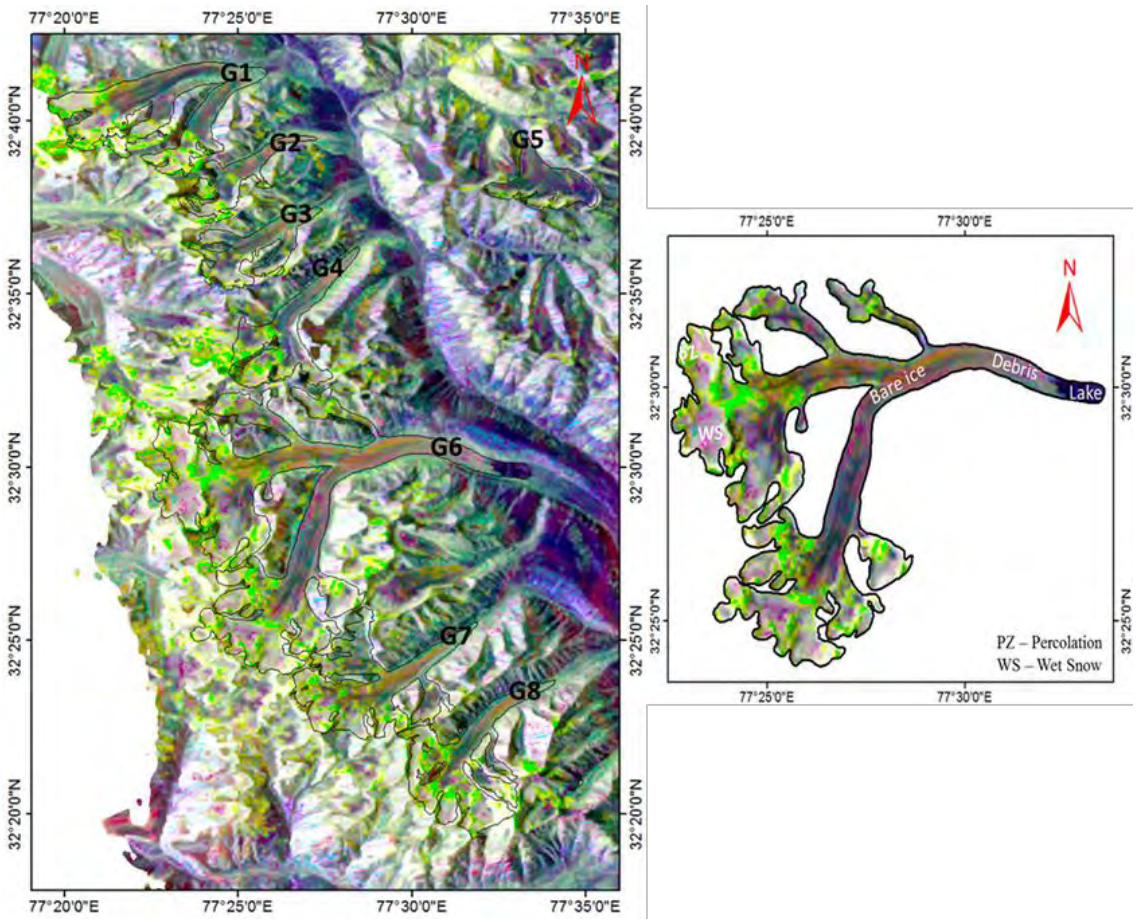

Fig. 15. 6SD RGB composite (image is colored by Pd (red), Pv (green), and Ps (blue)); Samudra Tapu (G6) marked with distinct glacier features.

There is a difference in the scattering mechanisms between debris cover, bare ice, wet snow, lake, and percolation that makes it possible to distinguish different features. The results from the six-component scattering model-based supervised classification allow us to analyse and identify the scattering mechanisms associated with different features of the glacier. In Fig. 5 of the G6 glacier, a bluish and greenish tinge at higher reaches of the glacier gives surface

scattering and volume scattering that depicts wet snow and percolation features. From the outcome of 6SD, we found that single-bounce/surface scattering and volume scattering are prominent for the glacier features. It has also been observed that scattering variations take place because of surface roughness. In the ablation zone, a dark green tinge shows volume scattering for the debris cover zone, and glacial ice and lake surface scattering takes over volume scattering shown in blue color. For better extraction of glacier radar features, the SVM approach is used for generating the classified maps displayed in Fig. 6.

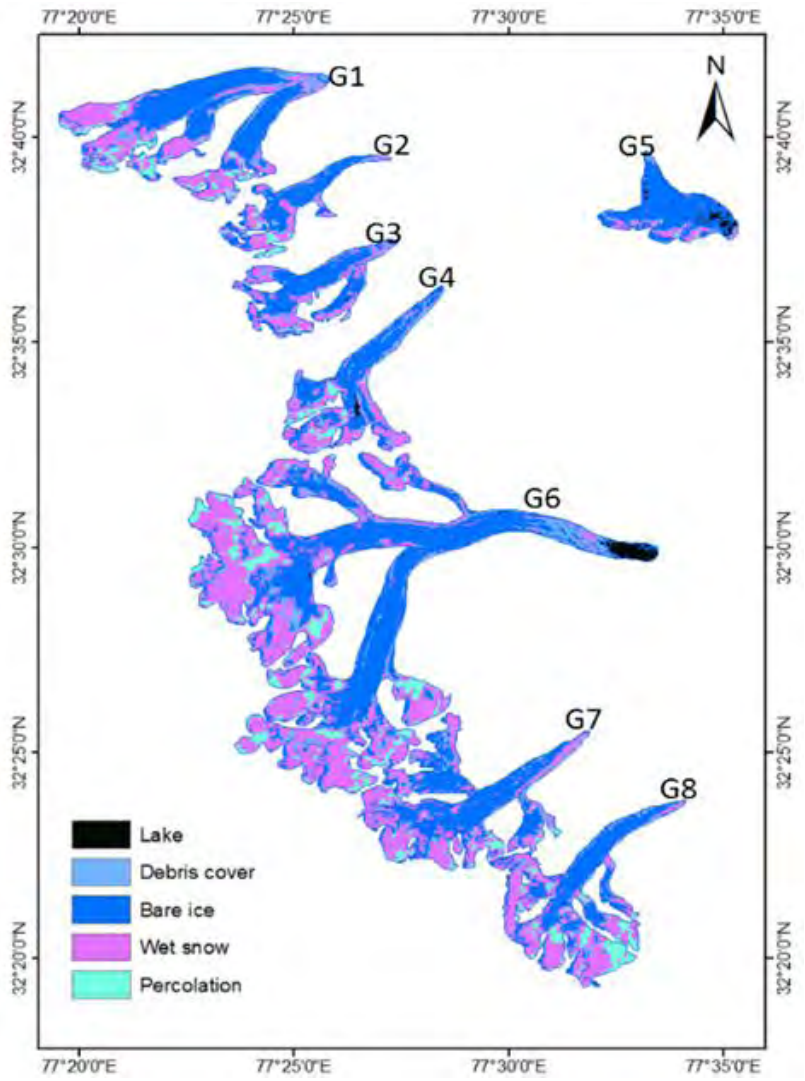

Fig. 16. Classification results exhibiting different glacier features.

Some pixels of debris cover are misclassified as wet snow owing to the confusion of scattering behavior between debris cover and wet snow. The user's accuracy ranged from 36% to 98% and the producer's accuracy ranged from 60% to 97%. The maximum user's accuracy was achieved in the lake and the lowest was in debris cover. The highest producer's accuracy was obtained in wet snow and the lowest was in debris cover. The misclassification of pixels occurred between the class debris cover and percolation. The user accuracies of percolation, wet snow, bare ice, debris cover, and lake are 54.26%, 95.67%, 95.62%, 36.29%, and 98.76%, respectively. And the total accuracy of the test data is 89.16% the kappa coefficient is about 0.82. The results indicate that a combination of physical scattering model-based decomposition

and support vector machine is a reliable and efficient method to detect glacier facies using SAR imagery.

Two stage 6SD based SVM classification scheme for improved glacier facies mapping:

The motive of this study is to utilize the scattering information for classification and how valuable the scattering model is for the classification of distinct glacier facies. In this work, fully polarimetric ALOS/PALSAR data over a part of Siachen glacier was analysed for classification in two ways: backscatter-based ([T]) SVM classification and 6SD based SVM classification.

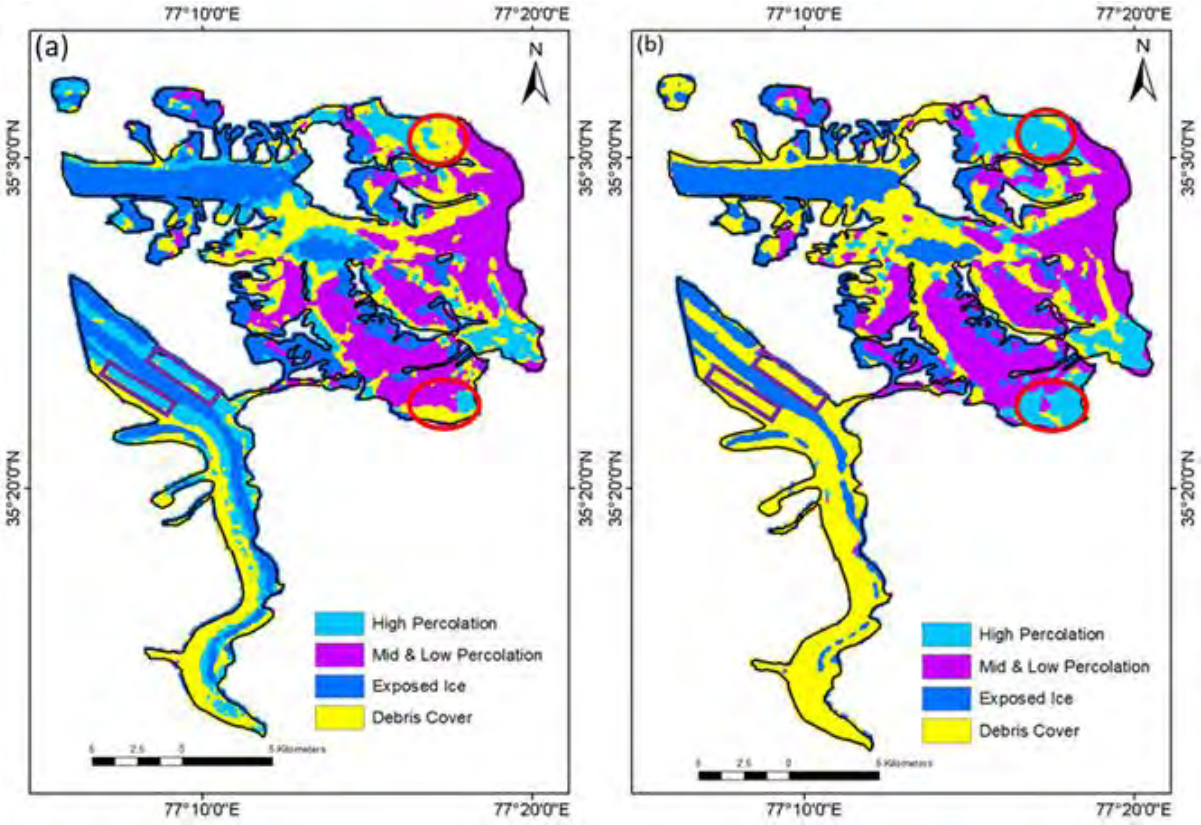

Fig. 17. (a) [T]-SVM-based classification (b) 6SD-SVM-based classification (In (a) pixels inside the red circle and purple rectangle – shows the misclassification of percolation class into debris cover class and vice-versa and (b) pixels inside the red circle and purple rectangle – indicates correctly classified pixels red circle as percolation class and purple rectangle as debris cover).

In Fig. 14(a), there is a lot of misclassification among percolation areas and debris cover using backscatter-based SVM classification, but it is improved to some extent using physical scattering model-based SVM classification in Fig. 14(b). It is because the 6SD-SVM gives an idea about the different sorts of scattering mechanisms existing on different glaciated terrain features. Although, the output of model-based classification i.e., 6SD-SVM is well compared to backscatter-based classification i.e. [T]-SVM classification but still there is ambiguity, especially between mid & low percolation and debris cover. So, the ambiguity can be resolved by taking the probability difference of surface scattering and volume scattering 6SD powers. Further, this probability difference image helps to find out the threshold that reduces the

uncertainty between the above-mentioned classes. The pixel values of probability difference, DP_{s-v} range between -1 to 1 and helps to determine the dominant scattering component from volume and surface in the 6SD image. For further improvement, the probability difference image of surface scattering and volume scattering (DP_{s-v}) has been utilized to discriminate debris cover and mid & low-percolation pixels. So, in this regard, the conditional approach provides better discrimination of high percolation, mid & low percolation, and debris cover (Fig. 18).

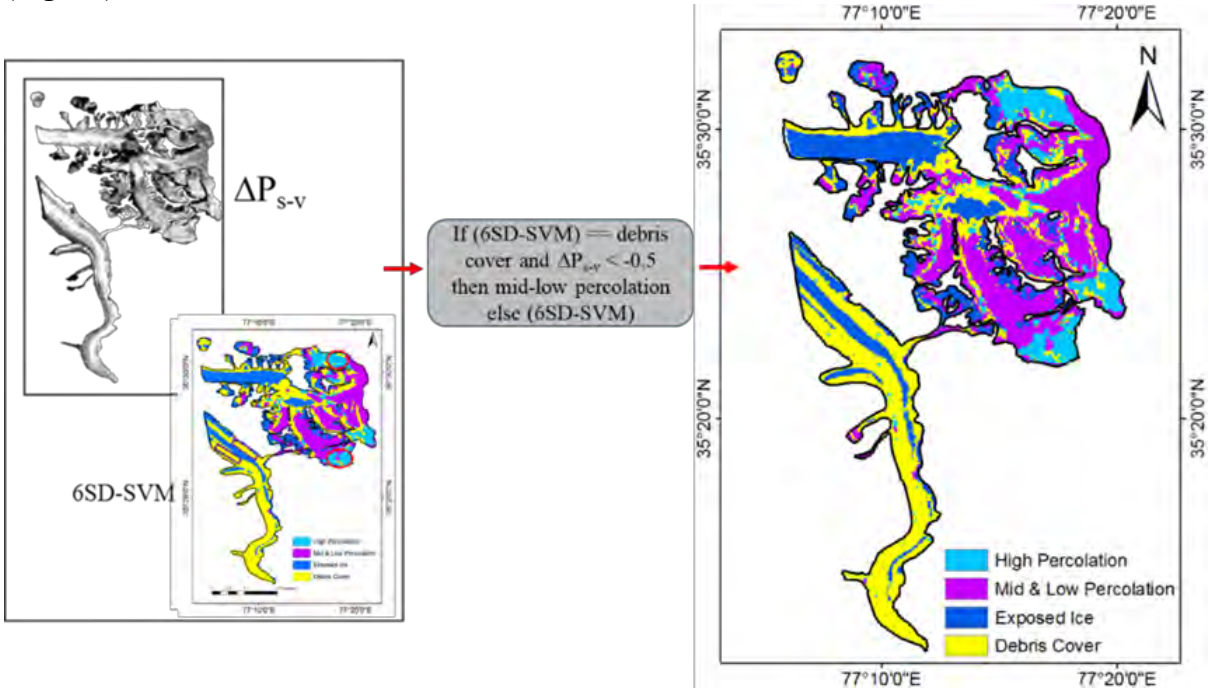

Fig. 18. Improved image separating debris cover and mid & low percolation using probability difference between surface scattering and volume scattering.

SAR full polarimetry allows discrimination of different types of scattering mechanisms. Classification based on the decomposed scattering powers can achieve a good performance. but there is some uncertainty in the classified image when attempting to distinguish between the debris cover and mid and low percolation. To clarify the differences between debris cover and mid- and low-percolation, the probability difference has been merged with the supervised classification process that enhanced the accuracy. After the probability difference using image classification, the performance of the adopted approach has been evaluated. The overall accuracy is 80.44% and the kappa coefficient is 0.73 for backscatter-based SVM classification, whereas for 6SD-based SVM classification the overall accuracy is 87.58% and the kappa coefficient is 0.82. The analysis of both these methods shows that 6SD-based supervised classification outperforms the [T]-SVM classification.

Retrieval of Snow Depth and Snow Water Equivalent Using Dual Polarization SAR Data

This paper deals with the retrieval of snow depth (SD) and snow water equivalent (SWE) using dual-polarization (HH-VV) synthetic aperture radar (SAR) data. The effect of different snowpack conditions on the SD and SWE inversion accuracy was demonstrated by using three TerraSAR-X acquisitions. The algorithm is based on the relationship between the SD, the co-polar phase difference (CPD), and particle anisotropy. The Dhundi observatory in the Indian

Himalaya was selected as a validation test site where a field campaign was conducted for ground truth measurements in January 2016. Using the field measured values of the snow parameters, the particle anisotropy has been optimized and provided as an input to the SD retrieval algorithm. A spatially variable snow density (ρs) was used for the estimation of the SWE, and a temporal resolution of 90 m was achieved in the inversion process. When the retrieval accuracy was tested for different snowpack conditions, it was found that the proposed algorithm shows good accuracy for recrystallized dry snowpack without distinct layering and low wetness (w). The statistical indices, namely, the root mean square error (RMSE), the mean absolute difference (MAD), and percentage error (PE), were used for the accuracy assessment. The algorithm was able to retrieve SD with an average MAE and RMSE of 6.83 cm and 7.88 cm, respectively. The average MAE and RMSE values for SWE were 17.32 mm and 21.41 mm, respectively. The best case PE in the SD and the SWE retrieval were 8.22 cm and 18.85 mm, respectively.

Dual-polarization SAR data at X-band was used for the retrieval of the SD and SWE. The algorithm used SAR-derived CPD, particle anisotropy, snow density, and the local incidence angle for the inversion of SD. The CPD model proposed by [8] was used to optimize the particle anisotropy for the prolate and oblate shapes. A spatially variable ρs calculated using an algorithm given by [11] was used for the SWE retrieval. In the process, a spatial resolution of 90 m was achieved for SD and SWE. The SD and SWE inversion accuracy was tested with three SAR acquisitions covering different characteristics (in terms of layering and wetness) of the snowpack, i.e., fresh snow on top of the old snow (8 January 2016), recrystallized snow (19 January 2016), and layered snowpack with high wetness (30 January 2016)). We have noticed that the algorithm performance is satisfactory for recrystallized snow with no hard crust. The SD inversion shows good accuracy on 8 and 19 January 2016 (average MAE = 6.5 cm, RMSE = 7.5 cm, and PE = 12.24%). Likewise, SWE retrieval on 19 January resulted in MAE = 17.32 mm, RMSE = 21.41 mm, and PE = 18.85%. However, the SWE retrieval shows underestimation on 8 January 2016 (due to low retrieved ρs values) and 30 January 2016 (due to low penetration), respectively. Hence, it is found that the inversion algorithm appears to have acceptable accuracy for SD and SWE in the case of the recrystallized snowpack. Also, good accuracy of SD inversion is noticed for the snowpack formed with fresh and old snow with low wetness. The ground-based experiments to measure CPD at high temporal resolution can add more information on the behaviour of CPD. In the future, we will focus on improving the retrieval of SD and SWE for complex snowpack.

Snow depth and snow water equivalent retrieval using X-band PolInSAR data

Monitoring the dynamics of snow and glaciers in the Indian Himalaya has always attracted the attention of the remote sensing community. The snow water equivalent (SWE) represents the amount of water contained in the snowpack, and it is a product of snow depth (SD) and snow density (ρs). The estimation of SD at high spatial and temporal resolution is still a challenge, especially in rugged mountainous terrain, like the Himalayas. In this paper, bistatic TerraSAR-X quad-polarization data is used to retrieve the SD using the Polarimetric SAR Interferometry (PolInSAR) coherences. The PolInSAR coherence at hv polarization shows a linear relationship with SD, which is verified with the field data. This relationship is utilized for the retrieval of SD using the proposed algorithm. Spatially variable ρs is used to retrieve the SWE. The coefficient of determination (R2) values of the retrieved SD on 8 January 2016 and 19

January 2016 are 0.62 and 0.80, respectively. Likewise, it is 0.61 and 0.72 for retrieved SWE. The root mean square error (RMSE) in SD on 8 January 2016 and 19 January 2016 are 7.00 cm and 5.48 cm, respectively; for SWE, it is 2.02 cm and 1.48 cm, respectively.

A Novel Approach for the Snow Water Equivalent Retrieval Using X-Band Polarimetric Synthetic Aperture Radar Data

An algorithm for snow depth (SD) and snow water equivalent (SWE) retrieval is proposed based on a polarimetric synthetic aperture radar (SAR) decomposition model and field measured snow data. The field campaigns were conducted at the Dhundi observatory (in the Indian Himalaya) in January 2016 and 2018. The field-measured data are used here to build a linear regression between wetness (w) and the imaginary part of the snow permittivity (ε''), and the validation of retrieved SD and SWE. The snow density (ρ_s) and w are calculated with a generalized volume parameter derived using a theoretical model and SAR data (coherency matrix). These snow parameters and the field-based regression relating w and ε'' are eventually used for the SD and SWE retrieval. Three TerraSAR-X scenes of the quad-polarization X-band data acquired in January 2016 are used to study the effect of the snow conditions on the accuracy of the proposed algorithm. The mean absolute error (MAE), root-mean-square error (RMSE), and index of agreement (IOA) for SD are 4.84 cm, 5.12 cm, and 0.71, respectively. On the other hand, for SWE, it is 1.42 cm, 1.53 cm, and 0.71, respectively.

Retrieval of Spatial and Temporal Variability in Snowpack Depth over Glaciers in Svalbard Using GPR and Spaceborne POLSAR Measurements

The highly dynamic nature of snow requires frequent observations to study its various properties. Keeping this in mind, the present investigation presents results from the analysis of fully polarimetric synthetic aperture radar (POLSAR) parameters for the development of a snow depth (SD) inversion model for SD retrieval. Snow depth retrieved using ground penetrating radar (GPR) at 500 MHz over Austre Grønfjordbreen in the Svalbard region was used to understand the behaviour of certain polarimetric parameters. A significant correlation was found between field-measured SD and POLSAR parameters, namely coherence and normalized volume scattering power (R^2 = 0.84 and R^2 = 0.73, respectively.) Using the POLSAR scattering powers obtained from the six-component model-based decomposition (6SD), the heterogeneity and anisotropic behaviour in the firn areas are also explained. Further, based on the analyses shown in this work, a polarimetric parameter-based SD inversion algorithm have been proposed and validated. The univariate model with co-polarization coherence has the highest correlation (R^2 = 0.84, Root Mean Square Error (RMSE) = 0.18). We have even tested several multivariate models for the same, to conclude that a combination of coherence, normalized volume and double-bounce scattering have a high correlation with SD (R^2 = 0.84, RMSE = 0.18). Additionally, temporal and spatial variability in SD was also observed from three polarimetric SAR images acquired between 4 April 2015 and 15 May 2015 over the Western Nordenskiöld Land region. Increase in snow depth corresponding to snow precipitation events were also detected using the POLSAR data.

A Novel Approach for The Retrieval Of Snow Water Equivalent Using SAR Data

Over the last decade, many snowpack parameter retrieval algorithms utilizing C- and X-band Synthetic Aperture Radar (SAR) data have been proposed. These algorithms are capable of retrieving snow density and snow wetness accurately, but not Snow Water Equivalent (SWE). In this paper, a novel approach of SWE estimation is proposed based on TerraSAR-X full-polarimetric data. A unique relationship between the extinction coefficient of the snowpack and snow wetness is built and verified with field data. This relationship enables the retrieval of Snow Depth (SD) and SWE using existing snow density algorithm and volume scattering power. The validation of SD and SWE is carried out with near-real-time ground truth measurements. The accuracy assessment for SD showed Mean Absolute (MAE) and Root Mean Squared (RMSE) Errors of 15 cm and 16 cm, respectively. On the other hand, SWE retrievals resulted in MAE and RMSE of 22.7 mm and 30 mm, respectively.

Cryosphere in a warming world - Indian scientific contributions

The cryosphere is the second largest component of the climate system with respect to the mass and heat capacity. On a regional scale, many glaciers and ice caps play a crucial role in freshwater availability. Presently, ice permanently covers 10% of the land surface, of which only a tiny fraction lies in ice caps and glaciers outside Antarctica and Greenland. Just as changes in the cryosphere can influence the climate, changes in climate can also dramatically alter the Earth's snow- and ice-covered areas. Unlike other substances found on the Earth, snow and ice exist relatively close to their melting points and can easily change back and forth between solid and liquid. With just slight variations in Earth's temperature, thousands of square miles of snow and ice can accumulate or melt, making the cryosphere one of the most powerful indicators of climate and climate change.
Considering the importance of understanding the role and response of cryosphere in warming world, Indian researchers have been carrying out scientific research in the major components of the global cryosphere like the Antarctica and Himalayas.

1. Antarctic Cryosphere Studies

The main focus of Antarctic cryosphere studies is to understand the current status its cryosphere and its interactions with the global climate system. NCPOR provide a state of the art ice/snow processing and analytical facilities for researchers to conduct various paleo-atmospheric and biogeochemical studies of ice and snow from East Antarctica to understand its linkage to climatic variations during the past. We use novel and traditional ice core proxies, observational records and model studies to reconstruct past surface temperature, snow accumulation, sea ice variability and atmospheric circulation over decadal to millennial time scales. We have conducted several Antarctic fieldwork and studies as a part of national and international collaborative projects, including the Indo-Norwegian project entitled “Mass balance, dynamics, and climate of the central Dronning Maud Land coast, East Antarctica” (MADICE). As part of this project, geophysical surveys and ice core drilling were undertaken for studying the ice shelf dynamics, current mass balance, microbial ecology and millennial-long evolution in coastal Antarctica.

1.1 Establishment of chronology of coastal Antarctic ice cores

The Antarctic ice core records offer critical insights into the millennial, centennial and decadal-scale climate variability in Antarctica and its tropical linkages. Ice rises scattered around coastal Dronning Maud Land, East Antarctica, preserves several centuries of climatic records. Ice-rise summits are ideal for obtaining deeper ice cores having longer climatic records, with their simple local ice-flow regime and large surface mass balance. A geophysical study was conducted on two ice rises, Kupol Verbljud (VER) and Kamelryggen (KAM), near the Lazarev Ice Shelf during 2021-22 (Fig. 19a). The shallow and deep-sounding radar profiling of more than 400 km found that the bed is relatively smooth, with an ice thickness of 560 m for VER and 525 m for KAM (Fig. 19 b). Englacial stratigraphy shows well-defined Raymond Arches for KAM (Fig. 19c), suggesting stable ice-divide positions. A preliminary age-depth estimate at KAM's summit accounting for internal stratigraphy suggests ~20 k-year-old ice 85 m above the bed (Fig. 19d) at three years per centimetre resolution, and it is the best-suited ice coring site over the survey area.

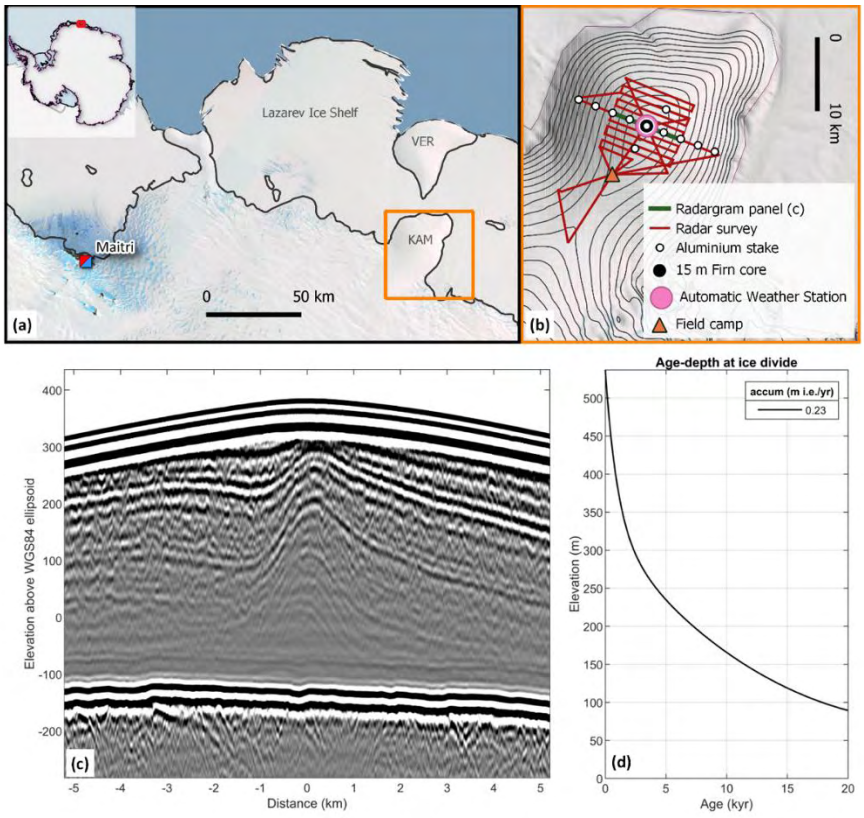

Fig. 19: (a) Ice rises Kupol Verbljud (VER) and Kamelryggen (KAM) near the Lazarev Ice Shelf; (b) Field survey over KAM; (c) Deep-sounding radar profile going across the summit of KAM and (d) Age-depth estimate obtained using a 1-D ice flow model.

Establishing an accurate chronology is crucial for interpreting ice-core-based climatic records. The visual stratigraphy (VS) is obtained from line scan images as a proxy for annual layer counting in the firn section (top 50 m) of an ice core (dated 1919–2016 C.E.) from the Djupranen ice rise in central Dronning Maud Land, East Antarctica. These images were used

to obtain melt history for the site, and it was found that traditional thickness-based quantification of melt proportion may result in significant overestimations (Fig. 20). The study revealed that melt layers do not significantly alter the VS records if masked out during pre-processing. The age-depth model based on the reconstructed VS profile revealed an excellent match with identified time markers within the uncertainty of ±2 years (Dey et al., 2022). In addition, stable isotopes of Antarctic ice cores are used extensively in accurately determining the chronology of the ice cores. The Spatio-temporal variations of snow accumulation and stable isotopic composition revealed that water isotope variations are dominantly influenced by snow accumulation in the Dronning Maud Land (DML) and temperature in the Princess Elizabeth Land (PEL), East Antarctica (Mahalinganathan et al., 2022). Further, the study revealed that while isotope diffusion exists even in high accumulation sites of coastal Antarctica, it does not significantly impact the dating and paleoclimate interpretation of isotope records, unlike in low accumulation areas (Mahalinganathan et al., 2022).

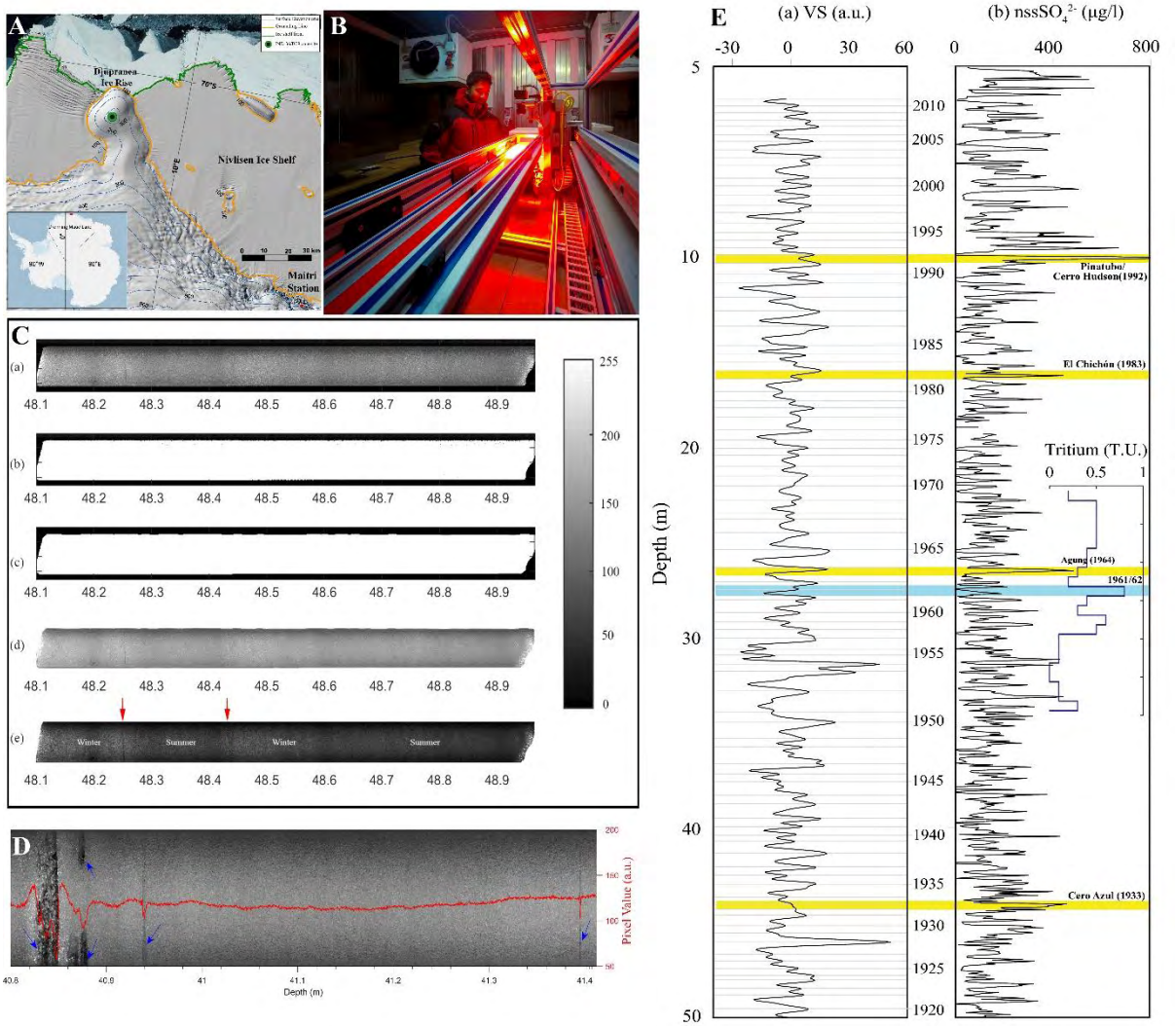

Fig. 20: The ice core site (green circle) at the summit of the Djupranen Ice Rise in coastal Dronning Maud Land (a). The Intermediate Layer Core Scanner (ILCS) setup at the Ice Core Lab of the National Centre for Polar and Ocean Research (b), line scan image processing steps from 48.1 to 48.97 m depth, line scan image profile of a core section melt layer (d). Comparison of age models using Visual Stratigraphy (VS) record and volcanic events (e).

1.2 Antarctic ice core proxies' records and their linkage to climate variability

The Antarctic climate system fluctuated through glacial–interglacial and millennial–centennial–decadal timescales in the past, closely coupled with other components of the global climate system (Thamban et al., 2020). As part of the Indian initiatives to obtain reliable climatic records beyond the instrumental period, several ice cores have been retrieved from the coastal Dronning Maud Land in East Antarctica. The oxygen isotope (δ18O) record from a coastal ice core in the Dronning Maud Land (DML), East Antarctica, is used to reconstruct the long-term Sea Ice Concentration (SIC) and reveals a significant decline during 1830–1884 CE with a rate of 0.58% ± 0.12% per decade followed by a moderate increase during 1927–1993 CE with a rate of 0.24% ± 0.11% per decade (Fig. 21). The study suggests that wind-driven sea-ice dynamics associated with positive phases of Southern Annular Mode and remote

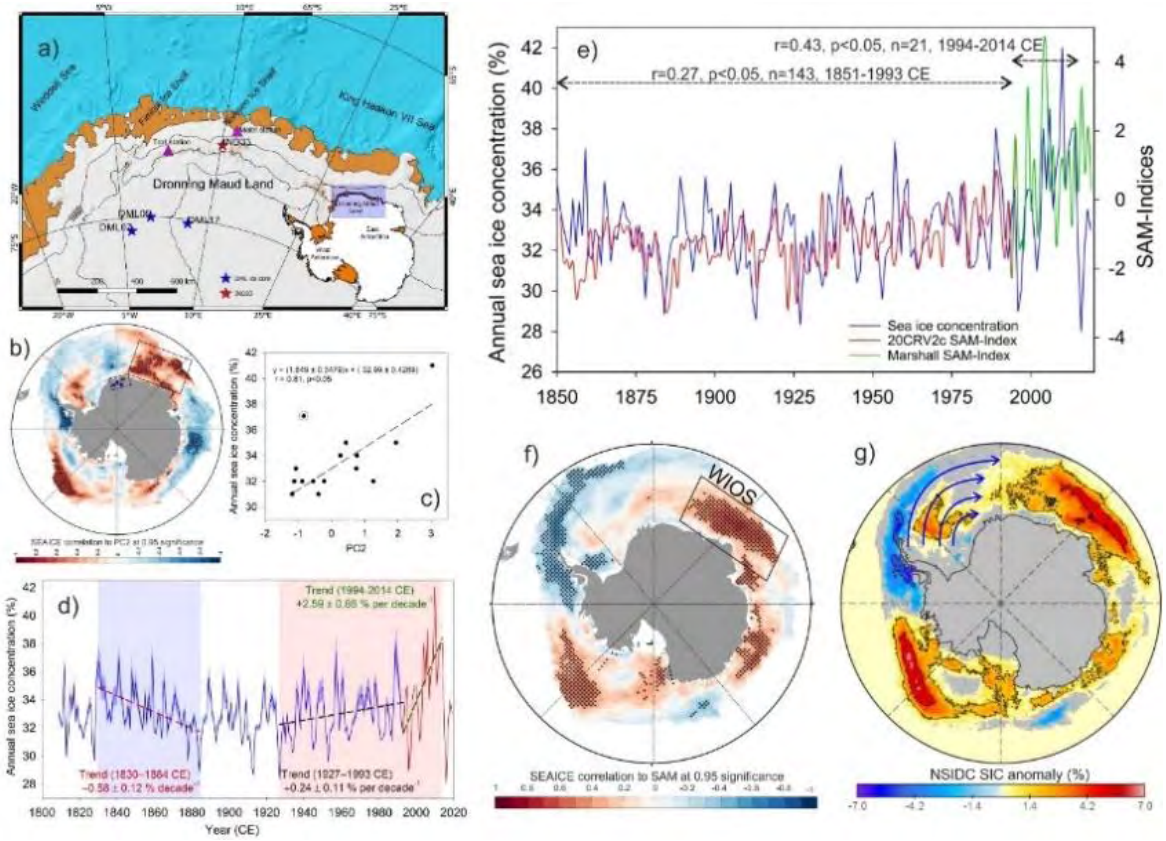

teleconnections of Pacific oscillations largely control this region's interannual to decadal sea-ice variability (Ejaz et al., 2021).

Fig. 21. (a) Location map of ice cores in Dronning Maud Land, East Antarctica. (b) The PC2 is correlated with NSIDC SIC for 1979□1993 CE (c) PC2 shows a significant correlation with NSIDC sea ice concentration. (d) Trend analysis of annual sea ice record of the Western Indian Ocean Sector of Antarctica derived from ice cores combined with recent NSIDC sea ice record. (e) Correlation between the reconstructed SIC record (PC2) (1809-1993 CE) and (f) NSIDC SIC record (1979-2013 CE) is correlated with Marshall SAM Index. (g) Composite anomaly maps of NSIDC SIC (%) for the positive SAM periods from 1979-2019.

Ice cores drilled deep into the Antarctic ice sheets have yielded highly resolved information on large numbers of climate variables over the past. A high-resolution ice core dust record (1905–2005 CE) from coastal Dronning Maud Land (East Antarctica) revealed dust flux variability in Southern Hemisphere is concomitant with the in-phase relationship between the El-Niño Southern Oscillation and Pacific Decadal Oscillations, which influenced the spatial distribution of the global wet-dry phase (precipitation pattern). Further, shifting Southern Annular Mode to a positive phase made wind conditions more conducive for long-range dust transport from SSA to the coastal Dronning Maud Land region. Our radiative forcing estimates corresponding to the enhanced dust flux yield nearly a 30% increase in aerosol forcing during the late 20th century (Fig. 4). This has resulted in a 40% decrease in atmospheric cooling rate, contributing to net atmospheric warming of nearly 1°C (Laluraj et al., 2020).

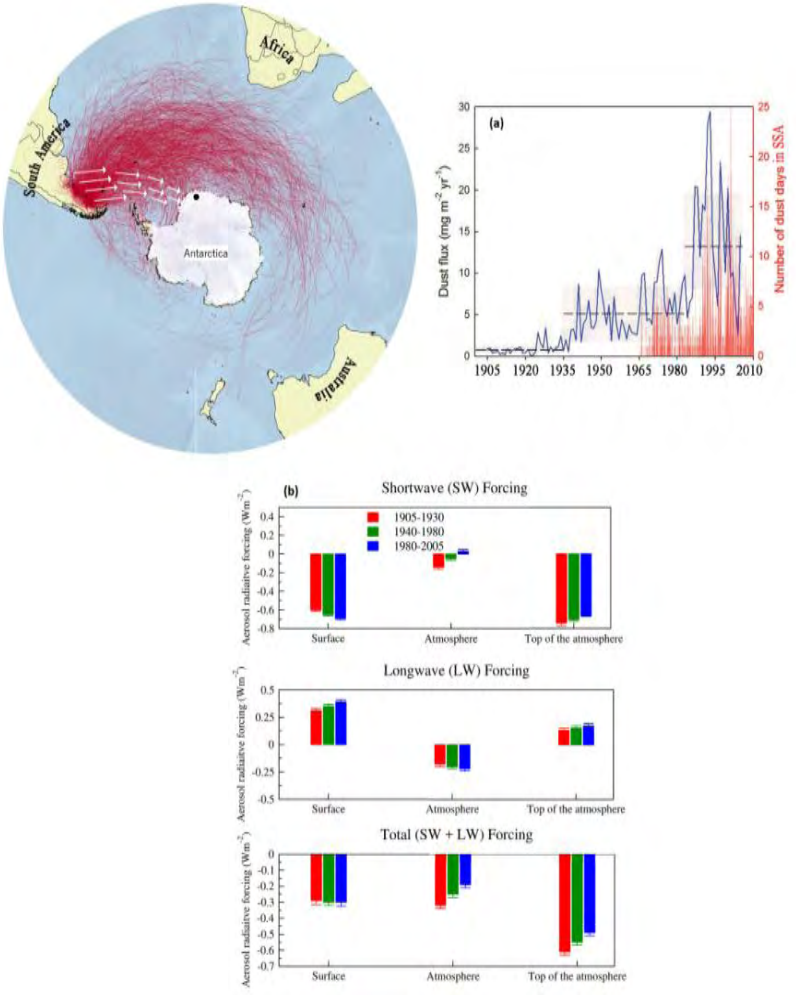

Fig. 22. Study area and ice core location in East Antarctica along with forward trajectory analysis showing dust path ways from Southern South America, (a) The stepwise increase in dust deposition during 20th century and (b) estimates of aerosol radiative forcing corresponding four-fold dust increase during three time periods.

The Antarctic climate system fluctuated through multiple timescales in the past, closely coupled with other components of the global climate system. The reconstructed DML temperature record of the past two centuries (1809-2019 CE) at an annual resolution based on

□18O ice core record (1809-1993 CE) combined with the recent ERA5 surface air temperature record (1994-2019 CE) reveals a significant cooling trend in the 19th century during 1809-1907 CE with a rate of -0.164 ± 0.045 °C decade -1 followed by a warming trend from the mid-20th to early 21st century (1942-2019 CE) with a rate of +0.452 ± 0.056 °C decade -1 (Ejaz et al., 2022). This long-term warming trend since the 1940s coincides with the increase in ENSO events and its strong anti-phase relation with SAM, suggesting an increasing influence of SAM-ENSO coupling in modulating the DML temperature in recent decades (Ejaz et al., 2022). Similarly, Antarctic surface air temperature reconstructed for the past five centuries reveals an increasing trend at ENSO frequencies since ~1850 CE. The investigation of greenhouse gas forced model simulation reveals that the ENSO activity and its influence on Antarctic temperature have increased in response to continuing greenhouse warming since the industrial era (Rahaman et al., 2019s). In addition, the Extreme precipitation events (EPEs) consisting of the largest 10% of daily totals are shown to contribute more than 40% of the total annual precipitation across much of the continent, with some areas receiving in excess of 60% of the total from these events. This has huge implications for reconstructing past climate records using data from ice cores (Turner et al., 2019).

1.3 Ice shelf dynamics and mass balance of coastal Dronning Maud land, East Antarctica

Numerous ice rises and rumples within the Antarctic ice shelves greatly influence their stability. The current knowledge of these features, also examining regional datasets and using satellite data to determine changes in calving front positions and map ice shelf morphology, was reviewed by Goel et al., 2020 and found that some ice shelves, such as the RoiBaudouin and Brunt Ice Shelves, may be more vulnerable than others to future unpinning of ice rumples at the calving front. Evidence from the ice rises showed that much of coastal Dronning Maud Land (DML) and Enderby Land has been undergoing changes over the past several millennia. Assimilating the results, it was found that four promising ice rises that have been stable for several millennia could be suitable for ice coring and several other ice rises are suitable for paleoclimate data over shorter timescales, particularly in central DML (Fig. 23).

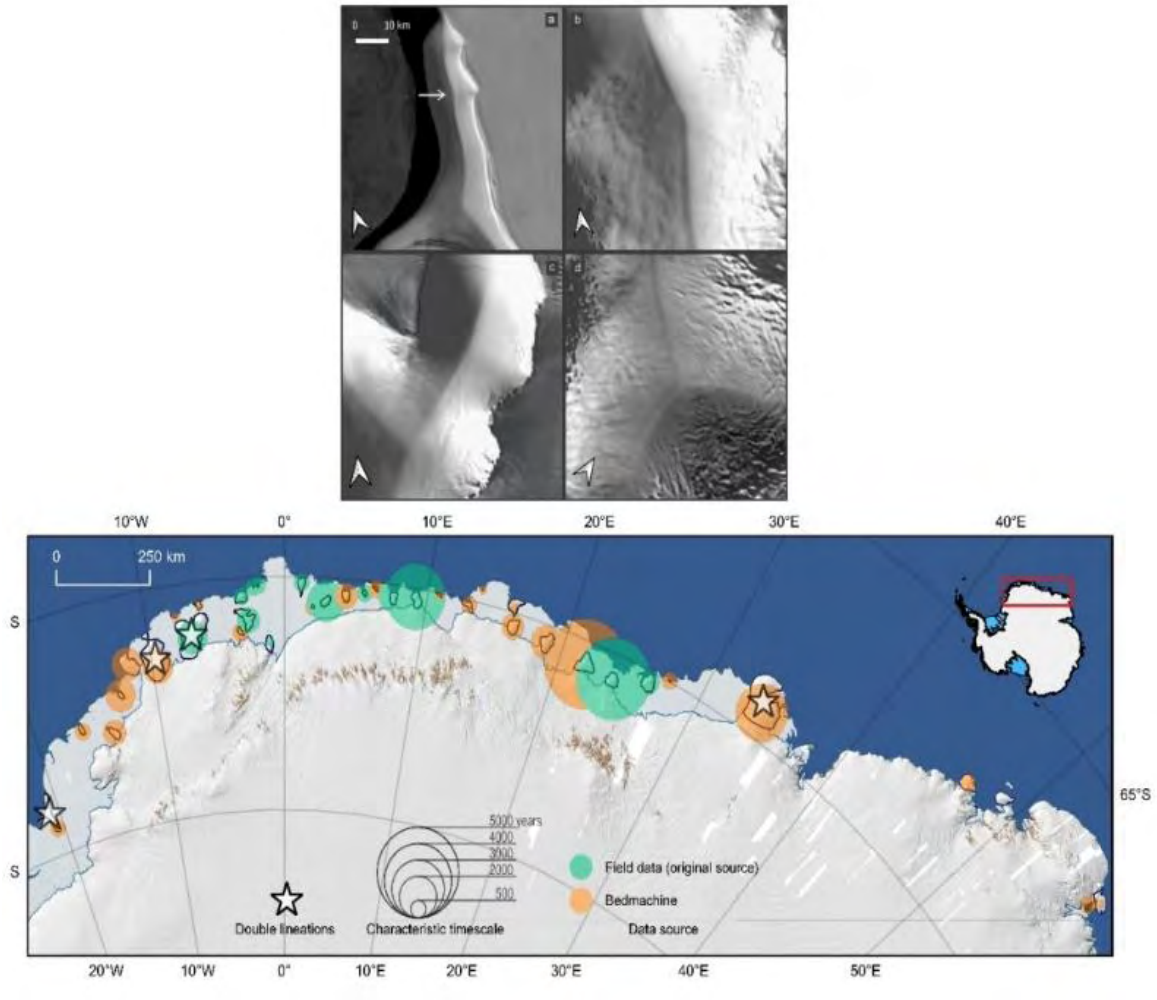

Fig. 23. MODIS satellite imagery showing double lineations, an indicator of long-term stability over ice rises; (a) Lyddan, (b) Søråsen, (c) Halvfarryggen and (d) Riiser-Larsenhalvøya. Characteristic timescale (T) of ice rises in Dronning Maud land. A circle's area shows T, its color shows the source of the ice thickness data. The stars indicate four ice rises with double lineations (an indicator of long-term stability over ice rises) visible in MODIS imagery.

The coastal Droning Maud Land in East Antarctica is characterized by small ice shelves with numbers of promontories and locally grounded isles called ice rises. These ice rises are typically dome-shaped, and their surface elevations are hundreds of meters above the surrounding ice shelves, which causes strong orographic effects on surface mass balance (SMB). A shallow ice-penetrating radar sounding was carried out to visualize firn stratigraphy in the top 35 m over ~400 km of profiles across the Nivlisen Ice Shelf and in a grid pattern over two adjacent ice rises (Djupranen and Leningradkollen). The overall SMB pattern across the ice shelf remained similar for all periods; however, the east-west contrast in SMB varies by a factor of 1.5–2 between the Leningradkollen and Djupranen grounding lines (Fig. 24). The SMB patterns over the ice rises are more varied owing to complex interactions between topography, snowfall and wind (Pratap et al., 2021).

Fig. 24: Study region with GPR profile locations (a), shallow radar profiles (b, c & d), and surface mass balance pattern (e) between Djupranen and Leningradkollen ice rises, East Antarctica.

Thinning rates of ice shelves vary widely around Antarctica, and basal melting is a major component of ice shelf mass loss. As part of the Indo-Norwegian MADICE project, basal melting in Nivlisen ice shelf (East Antarctica) were quantified using ApRES methods revealed that the annually averaged melt rates are moderate (□0.8 m yr□1), with highest melt rates (3.9 m yr□1) observed near the ice shelf front (Fig. 25). Further, the study highlights that although many of the ice shelves of East Antarctica have generally low melt rates, their seaward portions remain susceptible to higher rates of melting due to the influence of summer-warmed surface waters. Increase in basal melting will tend to thin the ice shelves and reduce the buttressing on the inland ice sheet. Long-term, high-resolution time-series data are important to understand the complex mechanisms involved in ice shelf ocean interactions, which in turn is important for ice sheet models (Lindbäck et al., 2019).

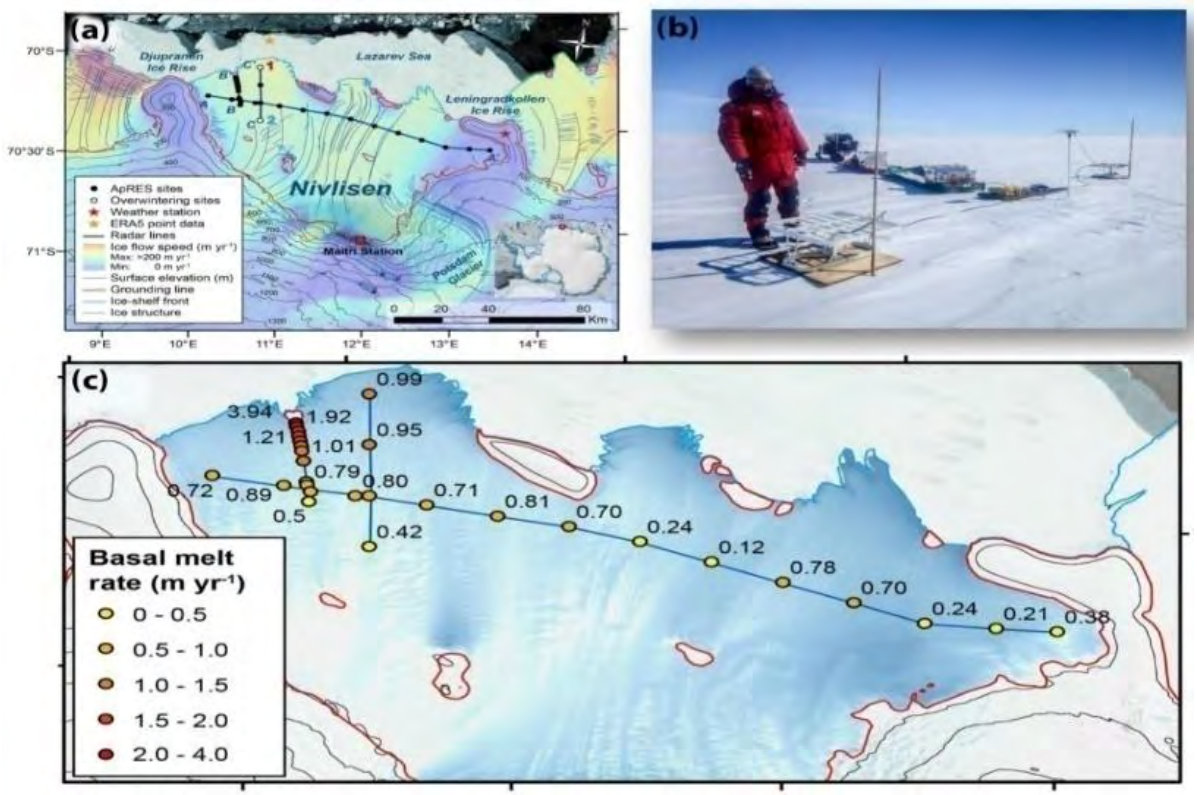

Fig. 25. Autonomous phase-sensitive radio-echo sounders (ApRES) measurements for basal melting (a) Nivlisen Ice Shelf, stakes profile and survey area (b) installation of phase-sensitive radar (c) ApRES-derived annual averaged basal melt rates for 2017.

1.4 Biogeochemical cycling and microbial ecology in Antarctic cryosphere

The cryobiology and biogeochemistry research in India have gained momentum not only on the diversity and physiology of cryospheric life forms but also on how cryospheric microbial communities might drive the biogeochemical cycles in polar regions. The mesocosm experiments and in situ measurements of dissolved organic carbon (DOC) shows how sunlight exposure, concomitant primary and bacterial production, viral activity, the initial nature and quantity of organic matter, exchange of atmospheric gases, sediment interaction and potential hydrological connectivity, control the transformation and fate of DOC on the glacier surface (Samui et al., 2020). This highlights the potential for continued shifts in DOC quality with shifts in the duration of solar exposure and microbial activity during the transitions from light to dark conditions. The continued warming enhance surface melt rates, increasing the proportion of nutrients and organic substrates available for bacterial activity, while photo-degradation of this organic matter could further stimulate bacterial processing (Fig. 8). These controls will determine the fate of DOC moving from the glacier surface to the surrounding oceans, through surface or subsurface drainage systems, with important implications for the downstream ecosystem processes (Samui et al., 2020).

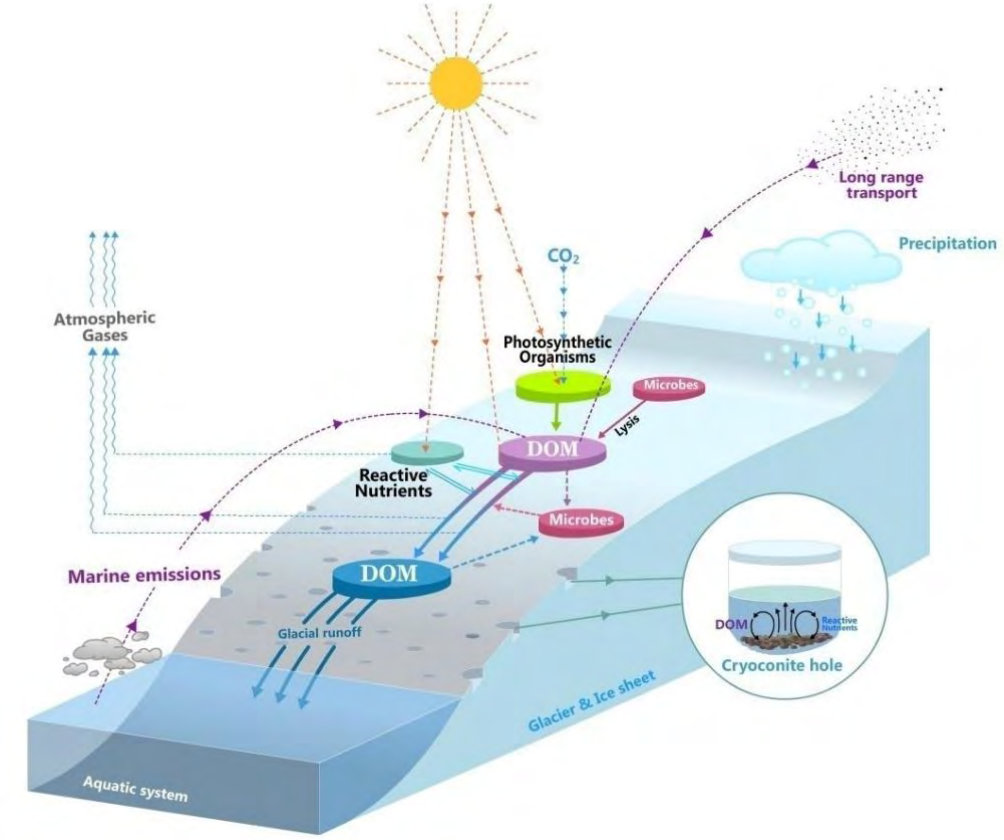

Fig. 26. Cycling of dissolved organic matter on the glacier surface.

The Antarctic continent comprises diverse ecosystems like snow, glacier ice, sea ice, melt pools, glacial soils, and supraglacial and subglacial lakes that accommodate numerous microbial and algal communities (Nagar et al., 2021). The diversity, metabolic capability, and extracellular enzyme profiles of yeasts from snow, blue ice and cryoconite hole environments from East Antarctica and cryoconite holes from a glacier in Western Himalaya were determined, in order to understand their contribution to essential ecological processes such as the mineralization of organic matter and rock minerals in these environments. A high abundance and diversity of yeasts were observed in cryoconite hole environments characterized by high organic carbon and nutrient concentrations, compared to the more oligotrophic snow and blue ice environments. Overall, the ability of yeasts to use diverse organic compounds prevalent on the glacier surface points to their ecological significance in the decomposition of organic matter, cycling of nutrients, and weathering minerals in supraglacial environments (Sanyal et al., 2020). Active microbial communities associated with snow and ice sheet surfaces have an important role in biogeochemical cycling in supraglacial systems.

Himalayan Cryosphere Studies

Understanding the behaviour of the Himalayan glaciers and their contribution to the sustainable supply of water is one of the grand challenges of Indian scientific community. Since the ongoing climate change is heterogeneous, the Himalayan glacier responses could also be heterogeneous. The NCPOR initiated glaciological studies on six benchmark glaciers of

Western Himalaya under the "Cryosphere and Climate" project in 2014. The project is continuing and has already made necessary infrastructure in Chandra basin, Lahaul-Spiti region in Western Himalaya and generated excellent quality of data required for mass, hydrological and energy budget in the basin.

2.1 Mass and Area changes in Chandra and adjoining basins

Our studies show that most of the glaciers of Chandra and adjoining basins under observations have been continuously losing a significant mass. In spite of having significant years (25%) of positive mass balance, Chandra basin glaciers have lost a huge mass of ice during last two decades. The mean annual mass wastage of Chandra basin glaciers was -0.21 m w.e. before 2000 which increased significantly to −0.56 m w.e. after 2000 (Sharma et al, 2019). Our studies have revealed that Chandra basin has lost 3.1 GT (Giga ton; 0.64m w.e a-1) of glacier mass with mean thing of 4.5 m during last 7 years. Annual mass loss of monitored glaciers in Chandra basin varies from +0.71 m w.e. a-1 to -1.65m w.e. a-1. One of our model based study revealed that the Chandra basin glaciers have been losing its mass with a mean annual mass balance of -0.59 ± 0.12 m w.e. a^{-1} during 2013-2019 (Patel et al., 2021).

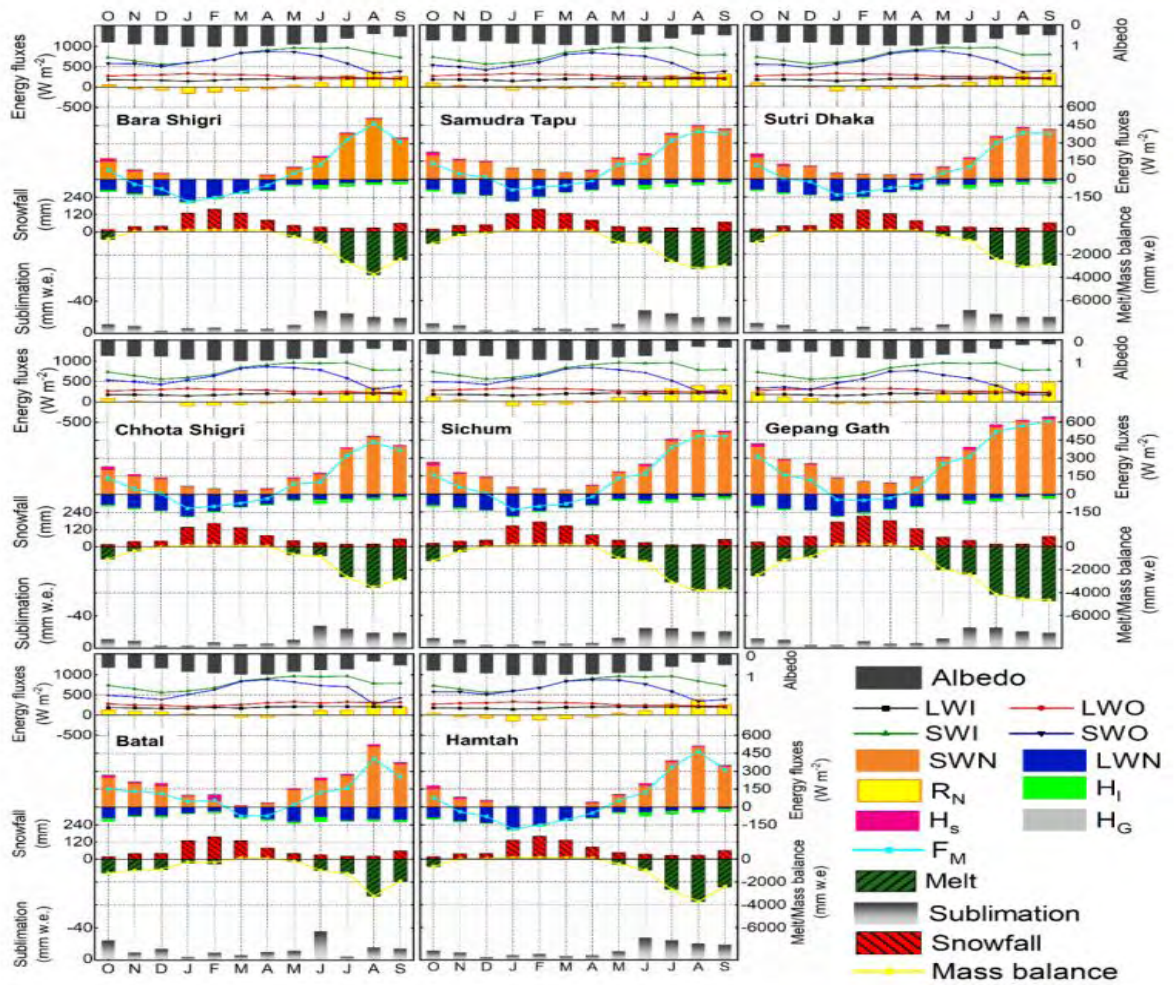

Fig. 27. Average monthly energy and mass fluxes of the selected glacier during the six hydrological years (2013 – 2019)

Similarly other adjoining basin Miyar, Bhaga and, Parvati has also been continuously losing a huge mass (0.85m w.e a-1). In Bhaga basin most of the glaciers have experienced critical thinning and lost huge ice mass in the range-6.07 m.w.e. to-9.06 m.w.e. during 2008-2018 (Nagajothi et al, 2021). Apart from mass loss our studies also highlighted glacier fragmentation and significant area loss (0.2 km2a-1) in four glacier basins (Chandra, Bhaga, Miyar, and Parvati) covering a large glacierised area of 1306 km2 during last two decades. Snow cover estimate showed no significant changes (a slight decrease in snow cover area) during 2000-2019. However, the ERA-Interim reanalysis data revealed a systematic increase in temperature, a decrease in precipitation, and an increase in liquid precipitation over the region during 1979-2018. The increased liquid precipitation could be a possibly contributor to the faster melting of the snow cover in these glacier basin (Patel et al, 2021). One of our studies on temporal dynamics of glaciers in Sind watershed of Jhelum basin in North-western Himalayas has similar results and shows a significant loss of 22.5% during last 28 years and number of glaciers have increased from 92(1990) to 116(2018). Majority of small glaciers are a result of defragmentation of larger ones, hence more vulnerable to melting. In Upper Jhelum basin, total glacier area has reduced by 20% at the rate of 0.56 km2 a−1 and the lower elevation zone (3800-4200 masl) has reduced by 35% (Ahmad et al, 2021). Mean Equilibrium Line Altitude (ELA) of glaciers (> 0.5 Km2) has shifted from 4336 to 4432 masl with an annual upward shift of 3.4 m. The results show that mass balance is found to be dependent mostly on solar radiation, local and regional precipitation, debris cover, slope and the shading effect of surrounding steep. The continued glacier recession in the region is largely due to decreasing solid precipitation in the winter months (November–March) and increasing mean annual temperatures (Ahmad et al, 2021). Further supraglacial debris is also one of the significant features which have critical control on surface melting in Chandra basin glaciers. Since 22% of the glacier area of Chandra basin are covered with debris with various thickness ranging from 5 to 200 cm, variation in thermal resistance of supraglacial debris pack have a great influence on downward energy propagation and eventually control the mass loss of underneath ice. Results show that high resistance (0.55 ± 0.09 m2 °C W-1) under thick debris has effectively retarded the energy transmission due to high thermal resistivity and help to reduce the glacier melting (Patel et al, 2021, frontiers in Earth Science). Geospatial data (GRACE) based our studies over the Karakoram and Himalayas (KH) region showed that the total mass change rate over the KH region was higher (– 55.0 ± 8.7 Gt yr–1) during 2002-2019. However, in contrast of positive mass balance anomaly of KH, the junction area between the western Himalaya (WH) and central Himalaya (CH) region observed an extreme negative mass change. The inter-annual mass change showed a higher correlation of mass change with total precipitation and snowfall over the spatiotemporal scale. However, the uncertainty and sensitivity test for mass change demonstrated that snowfall and temperature have a strong influence on the response of mass change (Patel et al, 2021).

Distributed energy balance over Chandra basin

Distributed energy balance over Chandra basin shows strong spatial and temporal variability in the energy fluxes. Our field based observations coupled with a physically based model studies highlighted that inward fluxes account for most of the total heat flux over the ablation zone, resulting in strong summertime melting in the Chandra basin. The study revealed that the

net radiation (RN) contributes ~75% in total energy (FM) during the melt season while sensible heat (HS), latent heat (Hl), and ground heat (HG) fluxes shared 15%, 8%, and 2%, respectively. Net short wave radiation progressively increases during ablation and decreases during winter but net long wave radiation worked as sink of energy throughout the year. Higher positive sensible and latent heat flux over the ablation zone during summer of the glacier surface enhance the ice ablation and contribute ~88% of total ice melt. A sensitivity analysis demonstrates that the mass balance of the glacier is affected by both air temperature (−0.21 m w.e. a−1 °C−1) and precipitation (0.19 m w.e. a−1 (10%)−1) changes but highly sensitive to albedo and surface radiation (Oulkar et al,2022;Patel et al, 2021; Pratap et al, 2019).

Hydrological studies

Water discharge and suspended sediment dynamics shows that temperature is the major governing factor of the river discharge and Suspended Sediment (SS) concentration. A significant positive correlation among temperature, discharge and SS shows an increase in mobilization of stored sediment by the glacier during winter in Chandra basin. It also increases the mobilization of sediment along the river due to increase in river discharge during summer (May-September) (Singh et al., 2020). A delayed response of discharge with respect to temperature showed a mean lag time of 6-8 hrs which could be due to delayed routing of melt-water from snow/ glaciers to the discharge site. Study suggests that 1oC rise in air temperature leading to 22 m3s-1 (15% of mean) increase in the river discharge during the ablation period (May-September). Hydrograph of Chandra River suggested that the groundwater (38.3 ± 5.6%) is a significant source of the river runoff followed by a direct contribution from glacier melt (30.9 ± 9%;) and seasonal snowmelt (30.6 ± 5.7%;), respectively, with negligible contribution from rainfall (Fig. 28).

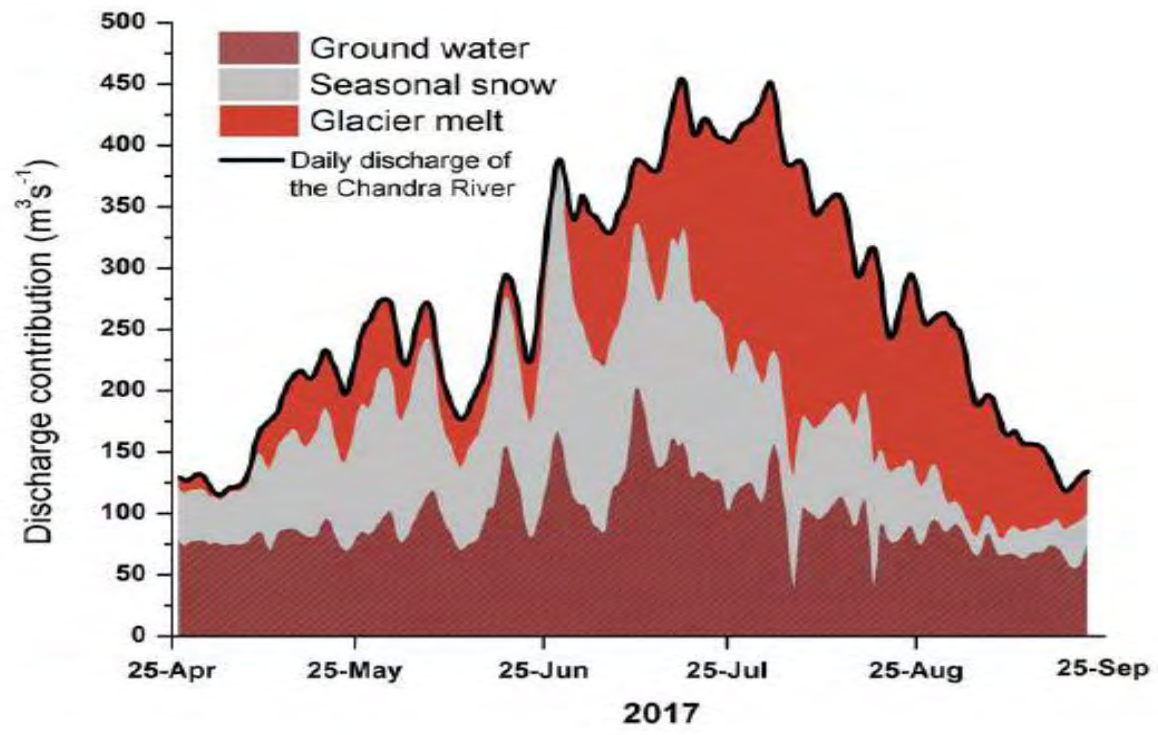

Fig. 28. Hydrograph depicting contributions from ground water, seasonal snow melt and glacier melt to the discharge in Chandra River

Although groundwater is a significant contributor to the river runoff, the infiltration of seasonal snowmelt (54%) and glacier melt (46%) mostly contribute to the groundwater recharge (Singh et al., 2021). Isotopic seasonality based observations suggested that glacier ice melt is the major source of proglacial discharge. Snowmelt is the predominant source during the early ablation season (June) and the peak ISM period (August and September), whereas ice melt reaches a maximum in the peak melt period (July). The monthly contribution of rain is on the lower side and shows a steady rise and decline with onset and retreat of the monsoon. Stable water isotope fingerprinting revealed that the major source of precipitation to Chandra basin, western Himalaya is derived from Mediterranean region. This study augments the significant role of the ISM in glacier mass balance up to the boundary of the central-western Himalayan glaciated region (Singh et al, 2019; Kumar et al, 2021). Hydrological model based our study highlighted that the runoff from the glacierised parts of the catchments is sensitive to temperature changes, but is insensitive to precipitation changes during summer however the behaviour of the summer runoff from the non-glacierised parts is exactly opposite. With shrinking glacier cover over the coming decades, the summer runoff from the glacierised catchments is expected become more sensitive to the precipitation forcing and less sensitive to the temperature forcing (Laha et al, 2023).

Surface velocity of Chandra basin glaciers

Our study highlighted the contrasting behaviour of lake-terminating and debris-covered glaciers for the surface velocity and also emphasize the additional control of the slope, supraglacial lake, debris thickness and convergence of glacier channels on the glacier surface velocity. Highest surface velocity prominent in a large and clean-type glacier and the lowest in a small and debris-covered glacier were observed. (Patel et al, 2021)

Glaciological studies in Arctic

The spatial and temporal variability in Snow Water Equivalent (SWE) and its impact over Vestre Broggerbreen and Feiringbreen glaciers situated across the Kongsfjorden around Ny-Ålesund in Svalbard, Arctic were investigated in early snow season for the period 2012-2017. The glaciers have experienced negative balance and lost a significant amount of ice (~4 m.w.e) since 2012. Similarly the mean annual mass waste of Svalbard glaciers has increased by 16–26% during 2000-2017 due to high melting rate of glaciers in this region. Increased liquid precipitation and temperature in early snow season have reduced SWE and enhanced the mass loss over both these valley glaciers. Further a model named “GlabTop2” has also applied to estimate ice thickness distribution and storage volume of these glaciers (Vestre Broggerbreen and Feiringbreen). This model has simple approach and requires only glacier extent and surface topography as inputs. The modelled results of ice thickness for both the glaciers (59 m and 92 m for VB and FB respectively) are found to be in good agreement with in-situ GPR data of ice thickness (Sharma et al., 2020: Patel et al, 2019, Kumari et al, 2021).

Expeditions are going on the Chhota Shigri glacier in western Himalaya, and in the year 2021, it started on the Durung Drung glacier in the Zanskar valley, Ladakh. Our research work also deals with remote sensing datasets and their applications in the field of glaciology. As a team, we are focusing on the reconstruction of long-term series of mass balance and runoff estimates

using different modelling approaches by incorporating field observations and remote sensing data.

Details of the work done by the IIT Indore team over 2019-2023 are given below:

Work categories:

1. Field expeditions
2. Glacio-hydrological modelling
3. Glacier training programs

1. Field observations

Field expeditions are carried out on two big glaciers: Chhota Shigri in Lahaul-Spiti Valley, Himachal Pradesh and Durung Drung in Zanskar Valley, Ladakh. Objectives of the field expeditions:

- To observe the microclimate of the glaciers,
- To estimate the annual and seasonal mass balances,
- To estimate the surface velocities and the dynamics,
- To estimate the point geodetic mass balance and
- To estimate the emergence velocity.

1.1 Chhota Shigri Glacier

- Meteorological condition: installation of 2 Automatic weather stations (AWS) (one at base camp ~3850 m a.s.l and one at the high camp ~4863 m a.s.l). The data is collected in June and end of September each year.
- Near surface temperature along the glacier length: 10 air temperature and relative humidity sensors were installed in June 2022 at 2-m height to observe the near surface temperature and humidity over the ablation area of Chhota Shigri Glacier.
- Annual and seasonal Mass balance measurements: Each year, two research expedition in early summer and post monsoon have been carried out for annual and seasonal mass balance estimation on Chhota Shigri glacier. A total of 23 stakes were installed over the ablation area and 7 snow pits/ cores were dug in the accumulation area for the point mass balance observations.
- Surface velocity: All the ablation stakes have been surveyed using a differential global positioning system (DGPS) relative to two fixed bases to observe the glacier surface velocity along the middle flow of the glacier.
- Discharge measurements: An automatic Water level Recorder was installed in June 2022 to measure the discharge from Chhota Shigri Glacier.
- Evaporation measurement: An evaporation pan was installed in June 2022 to measure the evaporation losses.

Based on the field observations we investigated the role of sublimation process in the total glacier wastage on Chhota Shigri Glacier (Mandal et al., 2022, Convey et al., 2022). The sublimation may account up to 42% of total winter snow fall on Chhota Shigri Glacier. Further a detailed analysis of the mass balance, meteorological conditions and discharge was conducted on Chhota Shigri Glacier (Mandal et al., 2020). The mean annual glacier-wide mass balance was negative with a value of -0.46 ± 0.40 m w.e. a^{-1} over 2002–2019 on Chhota Shigri

Glacier. The observed decreasing surface velocity suggests that the glacier is adjusting its flow in response to negative mass balance.

1.2 Durung Drung Glacier:

In-situ investigation on Durung Drung Glacier has been started in 2021 to fill the gap for a large glacier monitoring in the Himalayan region.

- Meteorological condition: installation of 2 AWS (one at base camp ~4100 m a.s.l and one at the high camp ~4950 m a.s.l). A new AWS was again installed at the base camp in collaboration with Space Application Centre (ISRO).
- Annual and seasonal Mass balance measurements: Each year, two research expedition in early summer and post monsoon have been carried out for annual and seasonal mass balance estimation on Durung Drung Glacier. A total of 40 stakes were installed over the ablation area and 2 snow pits were dug in the accumulation area for the point mass balance observations.
- Surface velocity: All the ablation stakes have been surveyed using a differential global positioning system (DGPS) relative to two fixed bases to observe the glacier surface velocity along the middle flow of the glacier.

2. Glacio-hydrological modelling

2.1 Mass balance and runoff estimates

Temperature-index modelling

Long-term glacier-wide mass balances and runoffs were reconstructed for two glacierized catchments in Monsoon and Alpine regimes. For this study, the Chhota Shigri glacier (CSG) catchment in western Himalaya and Dokriani Bamak glacier (DBG) catchment in central Himalaya were selected. The model was forced using in-situ observations as well as the ERA5 reanalysis precipitation and temperature datasets and calibrated using the observed mass balance and runoff estimates. In the CSG catchment, it was observed that the snow accumulation in winter and summer seasons together controls the glacier mass balances as well as catchment-wide runoff. In the CSG catchment snowmelt contributes the maximum to the total mean annual runoff of 63% while glacier melt and rain contribute 17% and 20%, respectively. Whereas in DBG catchment rain contributes the most to the total mean annual runoff with 44%, while snow and ice melt contribute 34% and 22%, respectively. Though the mass wastage patterns were roughly similar on both the glaciers, CSG showed consistently lower terminus retreat than that of the DBG because of the presence of thick debris cover and local steep topographic settings around the glacier snout.

Glacier-wide mass balances of the Gangotri, Chaturangi, Raktavaran, Meru, and Gangotri Glacier System were also reconstructed with a temperature-index (T-index) model. The model was forced with the bias-corrected ERA5 precipitation and temperature data. Gangotri Glacier's tongue is covered by thick debris having several supra-glacial lakes and ice cliffs (considered as melting hotspots); therefore, despite the presence of thick debris, we assume the

melting over this area as of a clean glacier. Gangotri, Meru glaciers, and Gangotri glacier system showed negative mean mass wastage whereas the mass budgets of fragmented tributary Chaturangi and Raktavaran glaciers were positive. The positive MBs of the Raktavaran and Chaturangi glaciers are due to their high area-elevation distribution and heavily debris-covered tongues. The positive MBs on these fragmented tributary glaciers are due to non-climatic topographic reasons and should not be misunderstood as climate change deniers or compared with Karakoram Anomaly.

Energy balance modelling

Mass and energy-balance models were used to simulate the glacier-wide mass balance on DBG and CSG. Sublimation/re-sublimation was calculated using the latent heat flux and the latent heat of vaporization. The losses through sublimation were around 22% on DBG and 20% on CSG to the total ablation with a strong spatial and temporal variability. Modelled mass balance is highly sensitive to snow albedo. This study provides insights into the regional variations in mass-wastage governing SEB fluxes at a glacier-wide scale, which is helpful for understanding the glacier–climate interactions in the Himalaya and stresses an inclusion of sublimation scheme in T-index models.

2.2 **Snowmelt runoff modeling**

In this study, the transferability of snowmelt runoff model parameters between the catchment and basin scales was systematically checked. The snowmelt runoff model was applied to a reference catchment of CSG in western Himalaya and the daily discharge from the catchment was reconstructed. The same calibrated model parameters at the catchment scale were applied for the basin scale snowmelt runoff modelling in Chandra-Bhaga Basin. Though the model parameters were calibrated at data plenty catchment, they were not transferable even in the same basin. Additionally, sensitivity analysis was also performed for the nine different model parameters. Among nine model parameters runoff coefficient for snow and degree day factor were the most sensitive parameters for catchment as well as basin-scale snowmelt runoff modelling. The daily discharge was reconstructed for the CSG catchment and Chandra-Bhaga Basin over 2003-2018 using the precipitation, temperature, and snow cover area (SCA). The reconstructed discharge was mainly controlled by summer temperature and summer SCA in the CSG Catchment and summer SCA and summer precipitation in the Chandra-Bhaga Basin. The decadal comparison showed an increase and early onset of maximum monthly discharge over 2011–2018 compared to 2003–2010 in both catchment and basin scales.

3. Capacity Building: Glacier training programs

Two field training programs have been conducted. A basic training program was organized with the collaboration of Goldsmiths University of London (England) and 3 trainees were trained about the basics of mountaineering and the in-situ investigations on Durung Drung Glacier. Another detailed training program was organized with the collaboration of Grenoble Alpes University, IRD (France), and 9 trainees from different parts of India were trained. There were 2 resource persons and 1 mountaineer with us to train the trainees about all aspects of mountaineering and about the field investigations such as stake installation, DGPS survey, sensors, etc.

Acknowledgement: Inputs from Dr. Parmanand Sharma, and Dr. C.M. Laluraj , National Centre for Polar and Ocean Research, Goa; and Dr. Mohd Farooq Azam, Indian Institute of Technology, Indore, are gratefully acknowledged.

References:

- Bandyopadhyay, D., Mukherjee, S., Singh, G., & Coomes, D. (2023). The rapid vegetation line shift in response to glacial dynamics and climate variability in Himalaya between 2000 and 2014. *Environmental Monitoring and Assessment*, *195*(1), 1-18. https://doi.org/10.1007/s10661-022-10577-9
- Singh, G., Bandyopadhyay, D., Nela B. R., Mohanty, S., Malik, R. and Kulkarni, A.V., (2021). Anomalous glacier thinning due to climate feedback mechanism in the Himalaya and evidences in other mountain ranges. *Remote Sensing Applications: Society and Environment*, 22, p.100512. https://doi.org/10.1016/j.rsase.2021.100512
- Singh, G., Nela, B.R., Bandyopadhyay, D., Mohanty, S. and Kulkarni, A.V., (2020). Discovering anomalous dynamics and disintegrating behaviour in glaciers of Chandra-Bhaga sub-basins, part of Western Himalaya using DInSAR. *Remote Sensing of Environment*, 246, p.111885. https://doi.org/10.1016/j.rse.2020.111885
- Bandyopadhyay, D., Singh, G., & Kulkarni, A. V. (2019). Spatial distribution of decadal ice-thickness change and glacier stored water loss in the Upper Ganga basin, India during 2000–2014. *Scientific Reports*, *9*(1), 16730. https://doi.org/10.1038/s41598-019-53055-y
- Nela, B.R., Bandyopadhyay, D., Singh, G., Glazovsky, A.F., Lavrentiev, I.I., Kromova, T.E. and Arigony-Neto, J., (2019). Glacier flow dynamics of the Severnaya Zemlya archipelago in Russian high arctic using the differential SAR interferometry (DInSAR) technique. *Water*, 11(12), p.2466. https://doi.org/10.3390/w11122466
- Nela, B. R., Singh, G., Kulkarni, A.V., (2022). Ice thickness distribution of Himalayan glaciers inferred from surface velocity. *Environmental Monitoring and Assessment.* https://doi.org/10.1007/s10661-022-10658-9
- Nela, B. R., Singh, G., Mohanty, S., Rajat., Arigony-Neto, J., and Glazovsky, A.F., (2022). Retrieval of Svalbard ice flow velocities using Sentinel 1A/1B three-pass Differential SAR Interferometry. *Geocarto International*, 1-19. https://doi.org/10.1080/10106049.2022.2032391
- R. Panwar, G. Singh, (2022). "Classification of Glacier with Supervised Approaches using PolSAR Data". *Environmental Monitoring and Assessment*. https://doi.org/10.1007/s10661-022-10582-y.
- Singh, G.; Lavrentiev, I.I.; Glazovsky, A.F.; Patil, A.; Mohanty, S.; Khromova, T.E.; Nosenko, G.; Sosnovskiy, A.; Arigony-Neto, J. Retrieval of Spatial and Temporal Variability in Snowpack Depth over Glaciers in Svalbard Using GPR and Spaceborne POLSAR Measurements. *Water* 2020, 12, 21. https://doi.org/10.3390/w12010021
- A. Patil, G. Singh, C. Rüdiger, S. Mohanty, S. Kumar and Snehmani, "A Novel Approach for the Snow Water Equivalent Retrieval Using X-Band Polarimetric Synthetic Aperture Radar Data," in *IEEE Transactions on Geoscience and Remote Sensing*, vol. 59, no. 5, pp. 3753-3763, May 2021, doi: 10.1109/TGRS.2020.3016527

- Akshay Patil, Shradha Mohanty & Gulab Singh (2020) Snow depth and snow water equivalent retrieval using X-band PolInSAR data, *Remote Sensing Letters*, 11:9, 817-826, DOI: 10.1080/2150704X.2020.1779373
- Patil, A.; Singh, G.; Rüdiger, C. Retrieval of Snow Depth and Snow Water Equivalent Using Dual Polarization SAR Data. *Remote Sensing*. 2020, 12, 1183. https://doi.org/10.3390/rs12071183
- Ahmad, S. T., Rayees Ahmed, Gowhar Farooq Wani, Parmanand Sharma, Pervez Ahmed (2021) Assessing the status of glaciers in upper Jhelum basin of Kashmir Himalayas using Sentinel-2 earth observation data" Earth Systems and Environment, doi.10.1007/s41748-021-00273-y
- Ahmad, S. T., Rayees Ahmed, Gowhar Farooq Wani, Parmanand Sharma, Pervez Ahmed (2021) Glacier changes in Sind basin (1990–2018) of North-western Himalayas using earth observation data, Modeling Earth Systems and Environment, doi.org/10.1007/s40808-021-01246-w
- Arun, B.S., Aswini, A.R., Gogoi, M. M., Hegde, P., Kompalli, S.K., Sharma, P., Babu, S. S. (2019). Physico-chemical and optical properties of aerosols at a background site (~4 km a.s.l.) in the western Himalayas, Atmospheric Environment, 218, 117017
- Dey R., Thamban M., Laluraj C.M., Mahalinganathan K., Redkar B.L., Kumar S., Matsuoka K. (2022). Application of visual stratigraphy from line-scan images to constrain chronology and melt features of a firn core from coastal Antarctica. Journal of Glaciology 1–12. https://doi.org/10.1017/jog.2022.59
- Ejaz T, Rahaman W, Laluraj C. M., Mahalinganathan K and Thamban MJFIES (2022). Rapid Warming Over East Antarctica Since the 1940s Caused by Increasing Influence of El Nino Southern Oscillation and Southern Annular Mode. Frontiers in Earth Science, 10. doi: doi.org/10.3389/feart.2022.799613
- Ejaz T, Rahaman W, Laluraj C.M, Mahalinganathan K and Thamban M (2021). Sea Ice Variability and Trends in the Western Indian Ocean Sector of Antarctica During the Past Two Centuries and Its Response to Climatic Modes. Journal of Geophysical Research-Atmospheres, 126(23). doi: 10.1029/2020jd033943
- Goel V and others (2020). Characteristics of ice rises and ice rumples in Dronning Maud Land and Enderby Land, Antarctica. Journal of Glaciology, 66(260): 1064-1078. doi: 10.1017/jog.2020.77
- Goel V, Morris A, Moholdt G and Matsuoka K (2022). Synthesis of field and satellite data to elucidate recent mass balance of five ice rises in Dronning Maud Land, Antarctica. Frontiers in Earth Science, 10. doi: 10.3389/feart.2022.975606
- Kulkarni, A. V., Shirsat, T. S., Kulkarni, A., Negi, H.S., Bahuguna, I.M., Thamban, M. (2021). State of Himalayan cryosphere and implications for water security. Water Security, 14: 100101, https://doi.org/10.1016/j.wasec.2021.100101
- Kulkarni, A. V., Shirsat, T. S., Kulkarni, A., Negi, H.S., Bahuguna, I.M., Thamban, M. (2021). State of Himalayan cryosphere and implications for water security. Water Security, 14: 100101, https://doi.org/10.1016/j.wasec.2021.100101
- Kumar, N., Ramanathan, A., Arora, A., Soheb, M., Mandal, A., Sharma, P., Ranjan, S. (2019): Study of Isotopic Seasonality to Assess the Water Source of Proglacial Stream in Chhota Shigri glaciated basin, Western Himalaya, Hydrological Processes, 34,1285-1300

- Kumar. A., Sanyal. P. and Agrawal (2019) S. Spatial distribution of d18O values of water in the Ganga river basin: Insight into the hydrological processes. Journal of Hydrology, 571, 225-234
- Kumari, S., Ankur Pandit, Lavkush Patel, RAAJ Ramsankaran, Parmanand Sharma, and Ramanathan AL. (2021): Modelling of ice thickness and storage volume of Svalbard Glaciers monitored through Indian Arctic Programme, Polar Science, 30, 100741

- Kumari, S., Ankur Pandit, Lavkush Patel, RAAJ Ramsankaran, Parmanand Sharma, and Ramanathan AL. (2021): Modelling of ice thickness and storage volume of Svalbard Glaciers monitored through Indian Arctic Programme, Polar Science, 30, 100741

- Laluraj C M, Rahaman W, Thamban M and Srivastava R (2020). Enhanced Dust Influx to South Atlantic Sector of Antarctica During the Late-20th Century: Causes and Contribution to Radiative Forcing. Journal of Geophysical Research: Atmospheres, 125(8). doi: 10.1029/2019jd030675
- Lindbäck, K., Moholdt, G., Nicholls, K. W., Hattermann, T., Pratap, B., Thamban, M., and Matsuoka, K. (2019). Spatial and temporal variations in basal melting at Nivlisen ice shelf, East Antarctica, derived from phase-sensitive radars. The Cryosphere, 13(10): 2579-2595. doi: 10.5194/tc-13-2579-2019
- Mahalinganathan K, Thamban M, Ejaz T, Srivastava R, Redkar B L and Laluraj C M (2022). Spatial variability and post-depositional diffusion of stable isotopes in high accumulation regions of East Antarctica. Frontiers in Earth Science, 10. doi: 10.3389/feart.2022.925447
- Matsuoka K. (2022). Application of visual stratigraphy from line-scan images to constrain chronology and melt features of a firn core from coastal Antarctica. Journal of Glaciology: 1-12. doi: 10.1017/jog.2022.59
- Morlighem, M., Rignot, E., Binder, T. et al. Deep glacial troughs and stabilizing ridges unveiled beneath the margins of the Antarctic ice sheet. Nat. Geosci. 13, 132–137 (2020). https://doi.org/10.1038/s41561-019-0510-8
- Nagajothi, V., M. Geetha Priya., P. Sharma , I.M.Bahuguna (2020) Mass balance of glaciers in Bhaga basin, Western Himalaya: a geospatial and temperature-weighted AAR based model approach, Current Science, 119(12):1961-1973
- Nagar S, Antony R and Thamban M (2021). Extracellular polymeric substances in Antarctic environments: A review of their ecological roles and impact on glacier biogeochemical cycles. Polar Science, 30: 100686. doi: 10.1016/j.polar.2021.100686
- Oulkar S.N., Thamban M., Sharma P., Pratap B., Singh A.T., Patel L.K., Pramanik A. and Ravichandran M. (2022). Energy fluxes, mass balance, and climate sensitivity of the Sutri Dhaka Glacier in the western Himalaya. Frontiers in Earth Science 10:949735. https://doi.org/10.3389/feart.2022.949735

- Oulkar S.N., Thamban M., Sharma P., Pratap B., Singh A.T., Patel L.K., Pramanik A. and Ravichandran M. (2022). Energy fluxes, mass balance, and climate sensitivity of the Sutri Dhaka Glacier in the western Himalaya. Frontiers in Earth Science 10:949735. https://doi.org/10.3389/feart.2022.949735

- Patel, A., Goswami, A., Dharpure, J.K., Sharma, P., Patel, L.K., Thamban, M. (2022). Monitoring glacier characteristics and their mass balance using a multi-dimensional approach over the glaciers of the Chandra basin, western Himalaya. Hydrological Sciences Journal, https://doi.org/10.1080/02626667.2022.2027950

- Patel, A., Goswami, A., Dharpure, J.K., Sharma, P., Patel, L.K., Thamban, M. (2022). Monitoring glacier characteristics and their mass balance using a multi-dimensional approach over the glaciers of the Chandra basin, western Himalaya. Hydrological Sciences Journal, https://doi.org/10.1080/02626667.2022.2027950
- Patel, A., Goswami, A., Dharpure, J.K., Thamban, M., Kulkarni, A.V., Sharma, P. (2021). Regional mass variations and its sensitivity to climate drivers over glaciers of Karakoram and Himalayas, GIScience & Remote Sensing, https://doi.org/10.1080/15481603.2021.1930730
- Patel, A., Goswami, A., Dharpure, J.K., Thamban, M., Kulkarni, A.V., Sharma, P. (2021). Regional mass variations and its sensitivity to climate drivers over glaciers of Karakoram and Himalayas, GIScience & Remote Sensing, https://doi.org/10.1080/15481603.2021.1930730
- Patel, A., Goswami, A., Dharpure, J.K., Thamban, M., Sharma, P., Kulkarni, A.V., Oulkar, S. (2021). Estimation of mass and energy balance of glaciers using a distributed energy balance model over the Chandra River basin (Western Himalaya), Hydrological Processes, https://doi.org/10.1002/hyp.14058
- Patel, A., Goswami, A., Dharpure, J.K., Thamban, M., Sharma, P., Kulkarni, A.V., Oulkar, S. (2021). Estimation of mass and energy balance of glaciers using a distributed energy balance model over the Chandra River basin (Western Himalaya), Hydrological Processes, https://doi.org/10.1002/hyp.14058
- Patel, L. K., Sharma, P. and Thamban, M. (2019) Spatio-temporal variability of snow water equivalent over the Vestre Broggerbreen and Feiringbreen glaciers, Ny-Ålesund, Svalbard. Journal of Earth System Science, 128: 183.
- Patel, L.K., Sharma, A., Sharma, P., Singh, A., Thamban, M. (2021). Glacier area changes and its relation to climatological trends over Western Himalaya between 1971 and 2018. Journal of Earth System Science 130, 217 (2021). https://doi.org/10.1007/s12040-021-01720-0.
- Patel, L.K., Sharma, A., Sharma, P., Singh, A., Thamban, M. (2021). Glacier area changes and its relation to climatological trends over Western Himalaya between 1971 and 2018. Journal of Earth System Science 130, 217 (2021). https://doi.org/10.1007/s12040-021-01720-0.
- Patel, L.K., Sharma, P., Singh, A. T., Pratap, B., Oulkar, S., Thamban, M. (2022). Spatial surface velocity pattern in the glaciers of Chandra Basin, western Himalaya. Geocarto International, https://doi.org/10.1080/10106049.2021.1920627
- Patel, L.K., Sharma, P., Singh, A. T., Pratap, B., Oulkar, S., Thamban, M. (2022). Spatial surface velocity pattern in the glaciers of Chandra Basin, western Himalaya. Geocarto International, https://doi.org/10.1080/10106049.2021.1920627
- Patel, L.K., Sharma, P., Singh, A., Oulkar, S., Pratap, B. Thamban, M. (2021) Influence of Supraglacial Debris Thickness on Thermal Resistance of the Glaciers of Chandra Basin, Western Himalaya. Frontiers in Earth Science, https://doi.org/10.3389/feart.2021.706312
- Patel, L.K., Sharma, P., Singh, A., Oulkar, S., Pratap, B. Thamban, M. (2021) Influence of Supraglacial Debris Thickness on Thermal Resistance of the Glaciers of Chandra Basin, Western Himalaya. Frontiers in Earth Science, https://doi.org/10.3389/feart.2021.706312
- Pratap B, Dey R, Matsuoka K, Moholdt G, Lindbäck K, Goel V, Laluraj CM, Thamban M. (2021). Three-decade spatial patterns in surface mass balance of the Nivlisen Ice Shelf,

central Dronning Maud Land, East Antarctica. Journal of Glaciology, 68(267): 174-186. doi: 10.1017/jog.2021.93

- Pratap, B., Sharma, P., Patel, L., Singh, A. T., Gaddam, V. K., Oulkar, S. and Thamban, M. (2019). Reconciling High Glacier Surface Melting in Summer with Air Temperature in the Semi-Arid Zone of Western Himalaya. Water, 11(8), 1561.
- Rahaman W, Chatterjee S, Ejaz T and Thamban M (2019). Increased influence of ENSO on Antarctic temperature since the Industrial Era. Sci Rep, 9(1): 6006. doi: 10.1038/s41598-019-42499-x
- Samui G, Antony R and Thamban M (2020). Fate of Dissolved Organic Carbon in Antarctic Surface Environments During Summer. Journal of Geophysical Research: Biogeosciences, 125(12): e2020JG005958. doi: 10.1029/2020JG005958
- Sanyal A, Antony R, Ganesan P and Thamban M (2020). Metabolic activity and bioweathering properties of yeasts isolated from different supraglacial environments of Antarctica and Himalaya. J Antonie van Leeuwenhoek, 113(12): 2243-2258. doi: 10.1007/s10482-020-01496-1
- Sharma P., Patel L.K., Singh A.T., Meloth T., Ravindra R. (2020) Glacier response to climate in Arctic and Himalaya during last seventeen years: A case study of Svalbard, Arctic and Chandra basin, Himalaya, In: Goel P., Ravindra R., Chattopadhyay S. (eds) Climate Change and the White World, Springer Cham ,139-156
- Singh, A. T., Laluraj, C.M., Sharma, P., Redkar, B.L., Patel, L.K., Pratap, B. Oulkar, S., Thamban, M. (2021). Hydrograph apportionment of the Chandra River draining from a semi-arid region of the Upper Indus Basin, western Himalaya, Science of The Total Environment, 780, https://doi.org/10.1016/j.scitotenv.2021.146500
- Singh, A. T., Laluraj, C.M., Sharma, P., Redkar, B.L., Patel, L.K., Pratap, B. Oulkar, S., Thamban, M. (2021). Hydrograph apportionment of the Chandra River draining from a semi-arid region of the Upper Indus Basin, western Himalaya, Science of The Total Environment, 780, https://doi.org/10.1016/j.scitotenv.2021.146500
- Singh, A. T., Rahaman, W., Sharma, P., Laluraj, C. M., Patel, L. K., Pratap, B., Gaddam, V. K. and Thamban, M. (2019). Moisture sources for precipitation and hydrograph component of the Sutri Dhaka Glacier Basin, western Himalaya. Water, 11 (11), 2242
- Singh, A. T., Sharma, P., Sharma, C., Laluraj, C. M., Patel, L. K., B. Pratap, Oulkar, S. and Thamban, M. (2020). Water discharge and Suspended Sediment dynamics in the Chandra River, western Himalaya. Journal of Earth System Science, 129, 206 https://doi.org/10.1007/s12040-020-01455-4
- Singh, A. T., Sharma, P., Sharma, C., Laluraj, C. M., Patel, L. K., B. Pratap, Oulkar, S. and Thamban, M. (2020). Water discharge and Suspended Sediment dynamics in the Chandra River, western Himalaya. Journal of Earth System Science, 129, 206 https://doi.org/10.1007/s12040-020-01455-4
- Thakur, R. C., Arun, B. S., Gogoi, M. M., Thamban, M., Thayyen, R. J., Redkar, B. L., & Babu, S. S. (2021). Multi-layer distribution of black carbon and inorganic ions in the snow-packs of western Himalayas and snow albedo forcing. Atmospheric Environment, https://doi.org/10.1016/j.atmosenv.2021.118564
- Thakur, R. C., Arun, B. S., Gogoi, M. M., Thamban, M., Thayyen, R. J., Redkar, B. L., & Babu, S. S. (2021). Multi-layer distribution of black carbon and inorganic ions in the snow-packs of western Himalayas and snow albedo forcing. Atmospheric Environment, https://doi.org/10.1016/j.atmosenv.2021.118564

- Thamban M, Rahaman W and Laluraj CM (2020). Millennial to Quasi-Decadal Variability in Antarctic Climate System as Evidenced from High-resolution Ice Core Records. Current Science, 119(2): 255-NA. doi: 10.18520/cs/v119/i2/255-264
- Turner, J., Phillips, T., Thamban, M., Rahaman, W. et al., (2019). The Dominant Role of Extreme Precipitation Events in Antarctic Snowfall Variability. Geophysical Research Letters, 46(6): 3502-3511. doi: 10.1029/2018gl081517
- Vinze P and Azam M F (2023). Transferability of Snowmelt Runoff Model parameters: Discharge simulation in the Chandra-Bhaga Basin (western Himalaya), Frontiers in Water, 4, https://doi.org/10.3389/frwa.2022.1086557.
- Hussain Md. A, Azam M F, Srivastava S and Vinze P (2022), Positive mass balance of high altitude and debris-covered fragmented Gangotri Glacier system, Himalaya, Frontiers in Earth Science, 10:978836. doi: 10.3389/feart.2022.978836 (IF = 3.66).
- Mandal A, Angchuk T, Azam M F, Ramanathan A, Wagnon P, Soheb M and Singh C, (2022) 11-year record of wintertime snow surface energy balance and sublimation at 4863 m asl on Chhota Shigri Glacier moraine (western Himalaya, India). The Cryosphere, 16, 3775-3799, doi: 10.5194/tc-16-3775-2022. (IF: 5.80)
- Conway, Jonathan P, Jakob Abermann, Liss M. Andreassen, Azam M F, Nicolas J Cullen, Noel Fitzpatrick, Rianne Giesen et al. (2022) Cloud forcing of surface energy balance from in-situ measurements in diverse mountain glacier environments. The Cryosphere, 1-35, doi: 10.5194/tc-2022-24 (IF = 5.80).
- Srivastava S and Azam M F (2022) Mass-, and energy-balance modelling and sublimation losses on Dokriani Bamak and Chhota Shigri glaciers in Himalaya since 1979. Frontiers in Water, 4:874240. doi:10.3389/frwa.2022.874240.
- Srivastava S and Azam M F (2022) Functioning of glacierized catchments in Monsoon and Alpine regimes of Himalaya. Journal of Hydrology, 609, 127671, doi:10.1016/j.jhydrol.2020.125432. (IF = 6.70).
- Srivastava S, Garg PK and Azam M F (2022). Seven Decades of Dimensional and Mass Balance Changes on Dokriani Bamak and Chhota Shigri Glaciers, Indian Himalaya, Using Satellite Data and Modelling. J Indian Soc Remote Sens, 50, 37-54 (2022). https://doi.org/10.1007/s12524-021-01455-x (IF = 1.89).
- Shugar DH, Jacquemart M, Shean D, Bhushan S, Upadhyay K, Sattar A, Schwangart W, McBride S, Van Wyk de Vries M, Mergili M, Emmer A, Deschamps-Berger C, McDonnell M, Bhambri R, Allen S, Berthier E, Carrivick J, Dokukin M, Dunning S, Frey H, Gascoin S, Haritashya UK, Huggel C, Kaab A, Kargel JS, Kavanaugh J, Lacroix P, Petley D, Rupper S, Azam M F, Clague JJ, Cook S, Dimri AP, Eriksson M, Farinotti D, Fiddes J, Gnyawali G, Koppes M, Kumar A, Majeed U, Mal S, Muhuri A, Noetzli J, Paul F, Rashid I, Sain K, Steiner J, Ugalde F, Watson CS, Westoby MJ. (2021) A massive rock-ice avalanche caused the 2021 hazard cascade at Chamoli, Indian Himalaya. SCIENCE, 373 (6552), 300-306. doi: 10.1126/science.abh 4455. (IF = 63.71).
- Haq A, Azam M F and Vincent C (2021). Efficiency of artificial neural networks for glacier ice-thickness estimation: a case study in Western Himalaya, India. Journal of Glaciology, 67(264), 671-684, doi:10.1017/jog.2021.19 (IF = 4.27).
- Farinotti D, Brinkerhoff D.J., Fürst J. J., Gantayat P, Gillet-Chaulet F, Huss M, Leclercq P.W., Maurer H, Morlighem M, Pandit A, Rabatel A, Ramsankaran R, Reerink T.J., Robo E, Rouges E, Ward JJ van P, Mauro A W, Azam M F, Huilin LI, Liss M A (2021). Results

from the Ice Thickness Models Intercomparison eXperiment phase 2 (ITMIX). Frontiers in Earth Sciences, doi: 10.3389/feart.2020.571923 (IF = 3.66)

- Azam M F and Srivastava S (2020). Mass balance and runoff modelling of partially debris-covered Dokriani Glacier in monsoon-dominated Himalaya using ERA5 data since 1979. Journal of Hydrology, 550, 125432, doi:10.1016/j.jhydrol.2020.125432 (IF = 6.70).
- Mandal A, Ramanathan AL, Azam M F, et al. (2020). Understanding the interrelationships among mass balance, meteorology, discharge and surface velocity on Chhota Shigri Glacier over 2002-2019 using in situ measurements. Journal of Glaciology 1-15, doi:10.1017/jog.2020.42 (IF = 4.27).
- Nizam S, Sen IS, Vinoj V, Galy V, Selby D, Azam M F et al. (2020). Biomass-Derived Provenance Dominates Glacial Surface Organic Carbon in the Western Himalaya. Environmental Science & Technology. 54 (14), 8612-8621, doi: 10.1021/acs.est.0c02710 (IF = 9.029).
- Kumar P, Saharwardi S, Banerjee A, Azam M F, Dubey AK and Murtugudde R (2019). "Snowfall Variability Dictates Glacier Mass Balance Variability in Himalaya-Karakoram." Scientific Reports. 9, doi: 10.1038/s41598-019-54553-9 (IF = 4.99).
- Azam M F, Wagnon P, Vincent C, Ramanathan AL, Kumar N, Srivastava S, Pottakkal JG, and Chevallier P (2019). "Snow and Ice melt contributions in a highly glacierized catchment of Chhota Shigri Glacier (India) over the last five decades." Journal of Hydrology, 574: 760-773, doi:10.1016/j.jhydrol.2019.04.075 (IF = 6.70).
- de Kok, Remco J, Jakob S F, Litt M, Wagnon P, Koch I, Azam M F, and Immerzeel WW (2019). "Measurements, models and drivers of incoming longwave radiation in the Himalaya." International Journal of Climatology, 40(2), 942-956.doi:10.1002/joc.6249 (IF = 3.65).

Indian National Report to IAG (2019-2023): Salient Features

Virendra M. Tiwari and Ravi Kumar Muppidi

CSIR-National Geophysical Research Institute, Hyderabad, India

There is an unceasingly growing and advancing progress in the knowledge of the Earth's geometry, shape and gravitational field due to the geodetic and gravity studies carried out in India. This report presents a brief sketch of work carried out and the list of articles published during the calendar years 2019-2023. A considerable progress is made in enhancing the terrestrial networks of GNSS, absolute and relative gravity observations and parallelly extensively utilizing these data along with satellite data for subsurface density modelling, deformation studies, hydrological and cryosphere studies.

1. Improvement and Maintaining of Geodetic Infrastructure

The geodetic infrastructure in India is well-developed and is constantly being updated and upgraded to meet the needs of science and society. The system of observational devices, analyses techniques to measure and monitor the shape, size, and position of the Earth's surface and services provided on the basis of the observations and analyses is referred as geodetic infrastructure. The GPS receivers, gravimeters, surveying equipment and the geodetic satellites are the main source geodetic and gravity observations. Survey of India (SOI), the national organization ~~of~~ for surveying and mapping maintains the major geodetic infrastructure and a network of Geodetic Control Points (GCPs), which are used to establish a common reference frame for all the surveying activities in the country. SOI has initiated to establish the Continuously Operated Receiver Station (CORS) network in India (Figure 1). Currently, SoI is in the process of upgrading its Spatial Reference frame infrastructure under which about 1000 CORS stations are being installed all over India, out of which about 820 stations have been installed. In addition to providing the reference frame, these CORS stations are also capable of generating Network RTK corrections.

ISRO, the space agency of India has introduced Indian Regional Navigation Satellite System (IRNSS) and GPS Aided GEO Augmented Navigation (GAGAN) which are providing positioning and navigation services for different operations. Several research institutes (e.g. CSIR-NGRI, CSIR-4PI, WIHG, IIG and ISR) engaged in solid earth and atmospheric studies have also established ~ another 200 GNSS CORS and campaign based GNSS observations to study plate movement, earthquake cycle, isostatic adjustments, etc. CSIR- National Geophysical Research Institute (CSIR-NGRI), a leading Centre of solid earth research has established and is maintaining about hundred fifty permanent GNSS measurement stations, including an IGS station (HYDE). Recently, under a project Assessment of Regional Hydrological System using Space Borne Gravity Observations ", CSIR-NGRI installed fifteen CORS GPS stations including six collocated soil Moisture Instruments to understand ground water variability in the Ganga Basin, India. Indian Institute of Geomagnetism (IIG), is operating a good number of permanent GNSS stations and campaign GNSS stations in the different seismically active regions of Indian plate.

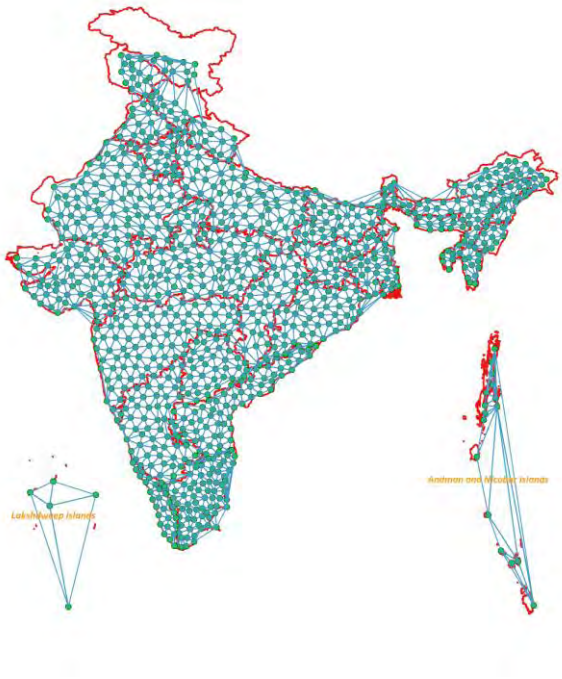

Figure 1: Operational and Proposed CORS Network, modified after (Singh & Kumar, 2019)

At present, Tidal observations are primarily carried out by Survey of India (30 active tidal observatories) and INCOIS (21 active tidal observatories and a proposal to ~~be~~ expand them to 36). In addition to above, a number of ports also operate their own tidal observatories for managing their maritime navigation work. SOI is in process of upgrading its Tidal Infrastructure in line with recommendation of GLOSS Implementation Plan 2012. Under this plan, in phase I, during 2023-24, 6 tidal observatories will be upgraded to install Radar Type Tide gauges and GNSS sensor. In Phase II, 30 more observatories will be upgraded during 2024-25.

Department of Science and Technology, GoI has supported to establish a new Centre for Geodesy (NCG) at IIT Kanpur, which is engaged in development of gravimetric geoid (Goyal et al., 2021; Goyal, 2022), calibration and validation activities for the upcoming NASA-ISRO the NISAR mission, and training courses on Geodesy for capacity building in the country. Centre has also established a permanent IGS-GNSS station at Kanpur and proposes to set-up VLBI for improving celestial frame of reference due to the necessity demonstrated through simulation (Dhar et al, 2021).

Most important transformation that happened recently, is announcement of the National Geospatial Policy 2022, which will provide a framework for the development and management (https://dst.gov.in/sites/default/files/National%20Geospatial%20Policy.pdf) of geospatial data in the country. The Indian Geodetic Datum (IGD), as the reference frame is the basic requirement for all geospatial data cataloging, including maps, satellite images, and survey data. The horizontal and vertical datums and reference frames in India are well-defined and are constantly being updated and refined (Sing et al., 2018). Realizing the need to redefine the Indian geodetic datums, collectively being called Indian Geodetic Reference Frame (InGReF), a series of measurements and computations are being carried out like pan India levelling network (Figure. 2). Dikshit et al. (2022) have assessed all the SoI-established the

CORS stations in the state of Uttar Pradesh. Initially, more stable CORS stations (from the ~1000 CORS stations) established by the SoI are chosen to be included in InGReF. In 2009, SoI has started Redefinition of Indian Vertical Datum and about 1,80,000 Line Km of dense leveling work has been completed to support development of Geoid Model for India. The three new approaches viz. the Stokes-Helmert method, the Least squares modification of the Stokes formula with additive correction, and the so-called Curtin University's approach (Goyal et al., 2021; Goyal, 2022) tested to develop the Indian gravimetric geoid models with the available gravity and terrain datasets. The vertical deflections have also been digitized over India to be used in the geoid slope validations (Featherstone and Goyal, 2022). Goyal et al. (2020a) have also developed an efficient spatial-spectral combined method to calculate the planar terrain correction. SOI has recorded ~ 12,000 gravity observations at an interval of 10 Km, and Geoid Model of states of Punjab, Haryana, Goa and Telangana have been prepared, and Geoid model of Kerala is under Progress.

Figure 2: Levelling Network for Redefinition of Indian Vertical Datum

2. Crustal Deformation

Tectonic geodesy is the study of the deformation of the Earth's crust caused by tectonic processes using geodetic techniques such as GPS, satellite radar interferometry, and precise levelling. In India, there are several institutions and organizations that focus on tectonic geodesy and related research areas and play a crucial role in advancing the knowledge of tectonic geodesy in India and contribute to developing the earthquake hazard scenarios. Some recent contributions to tectonic geodesy are discussed here.

CSIR-NGRI is operating about 150 permanent GPS sites in India including the IGS station at Hyderabad (HYDE), which is operational for past >30 years. Most of these sites are located in the tectonically active regions, e.g., Kashmir, Ladakh, Spiti, and Garhwal Kumaun in the Himalayan arc region, Indo-Burmese arc and Andaman-Nicobar region in the Sumatra-Andaman-Indo-Burmese arc, Shillong plateau, Godavari filed rift and Koyna Warna regions of intraplate region of India plate. CSIR-NGRI is also maintaining a permanent GPS site at

Maitri, the permanent base of India in Antarctica. Primary objective of establishing these sites is to understand the tectonics and geodynamics of the region, but these data have extensively been used for water vapour estimation during the extreme events and total electron content during solar eclipse. During the 26 December 2019 annular solar eclipse, a significant depletion in TEC of ~6–8 TECU (1 TECU = 1×10^{16} electrons m^{-2}) was observed along the path of the eclipse shadow. A few sites inadvertently located on the sliding slopes are used in landslide monitoring, e.g., a site located near Uttarkashi in Garhwal Himalaya, shows that the site has been sliding along the slope at a rate of ~12-22 mm/year since 2006. CSIR-4PI has established several Continuous GNSS stations, in the Kashmir valley, Bhuj, the Indian subcontinent, and the north-eastern provinces, including an IGS (International GNSS Service) station at Bengaluru, which serves as a reference station for all the crustal deformation research in the country (Jade et al., 2020).

2.1 Stable India region:

The stable region in India has a considerably good network of GPS stations (Figure.3), which has facilitated the calculation of the Euler pole for the Indian plate, which is located at 51.992±0.22°N, 2.832±0.83°E with an angular velocity of 0.5205±0.002°/myr. Additionally, the velocity of the Indian plate at HYDE is estimated to be 54 mm/year towards N49°. Using this Euler pole, the researchers at CSIR-NGRI, has determined - India's fixed site velocity (Rajewar et al., 2021; Figure.3).

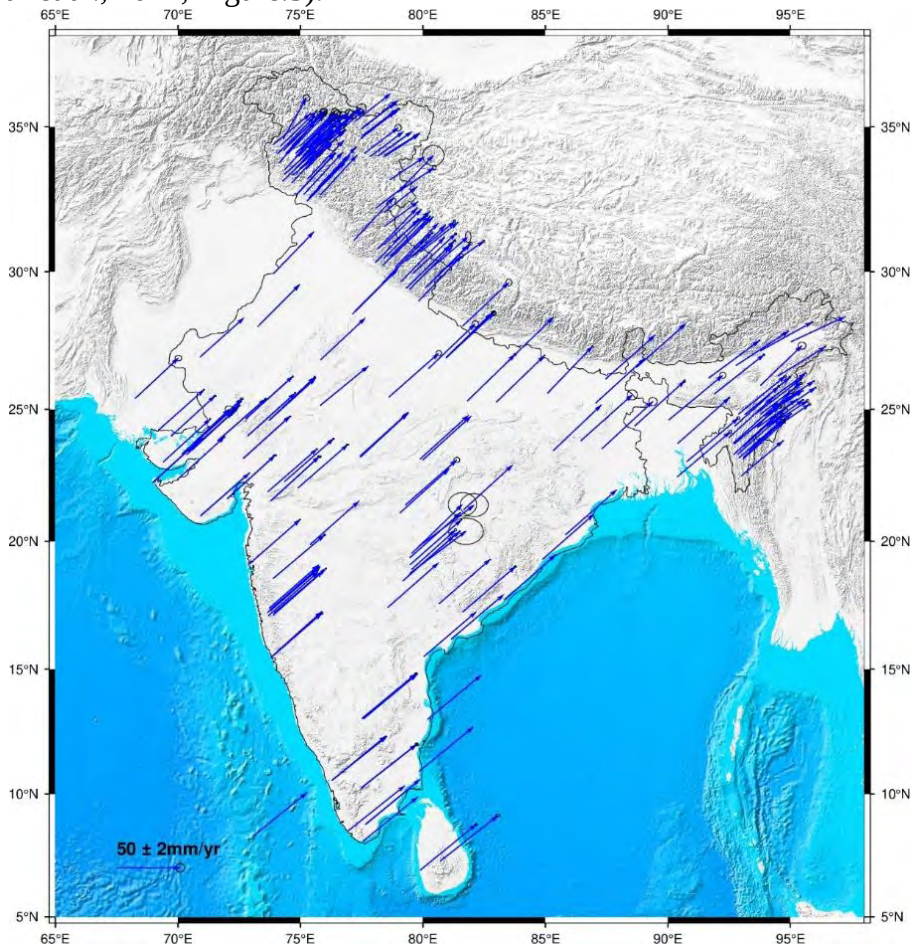

Figure.3: Site velocity at permanent GPS stations (Rajewar et al., 2021).

The residual velocity at various sites indicates that the deformation in the plate interior region is relatively low, with an estimated velocity of ~ 1 mm/year, whereas the plate boundary regions show significant strain accumulation. They have also calculated the two-dimensional strain rate using the site velocity estimates in the stable Indian region. The plate interior region generally, displays significantly lower shear strain rates ranging approximately ~1-3 μ strain/yr, while the Kachchh (~9 μ strain/yr) and the Godavari failed rift (~6 μ strain/yr) are exhibiting higher and moderate shear strain rates, respectively. Presently, both of these paleo-rift regions are experiencing compression (Rajewar et al.,2021; Yadav et al.,2019; Gahalaut et al., 2019). Some new findings related to the Indian continental plate and adjoining regions are also reported; like, segmentation of the Indian plate through the Narmada-Son diffuse plate boundary (Sen, 2022) and groundwater extraction-induced seismicity around the Delhi region (Tiwari et al., 2021).

2.2 Himalayan Region:

The Garhwal-Kumaun region of Himalayan arc has a dense network of permanent and campaign mode GPS stations established by various research institutes (Yadav et al., 2019 & 2021). This region of Himalayan arc is accumulating strain due to the convergence of about 18 mm/yr. A homogeneous strong coupling on the Main Himalayan Thrust (MHT) beneath the Outer and Lesser Himalaya is suggested except in the very shallow updip part of the MHT with a coupling width of ~ 85 km. Whereas the mid crustal ramp, the locales of earthquakes exhibits low coupling. It appears that the nature of the coupling is not significantly influenced by the subduction of sediments from the Indo-Gangetic plains or the Delhi Haridwar ridge. The continued accumulation of high rate of strain over the past ~ 500 years on a strongly coupled MHT, makes this segment of the Himalayan arc one of the most susceptible to earthquake.

The Central Himalayan seismic gap consisting of Himachal, Garhwal and Kumaon region is devoid of any great earthquakes. The geodetic coverage is comparatively sparse considering the complex deformation pattern of the region. Using 40 campaign mode GPS observations made by IIG for the period from 2003 – 2016, which essentially fills large data gaps in the region supported by other published velocities in the region, the study aims at the estimation of inter-seismic strain rate, fault coupling pattern of the sub surface decollement and seismic hazard probabilities (Figure 4).

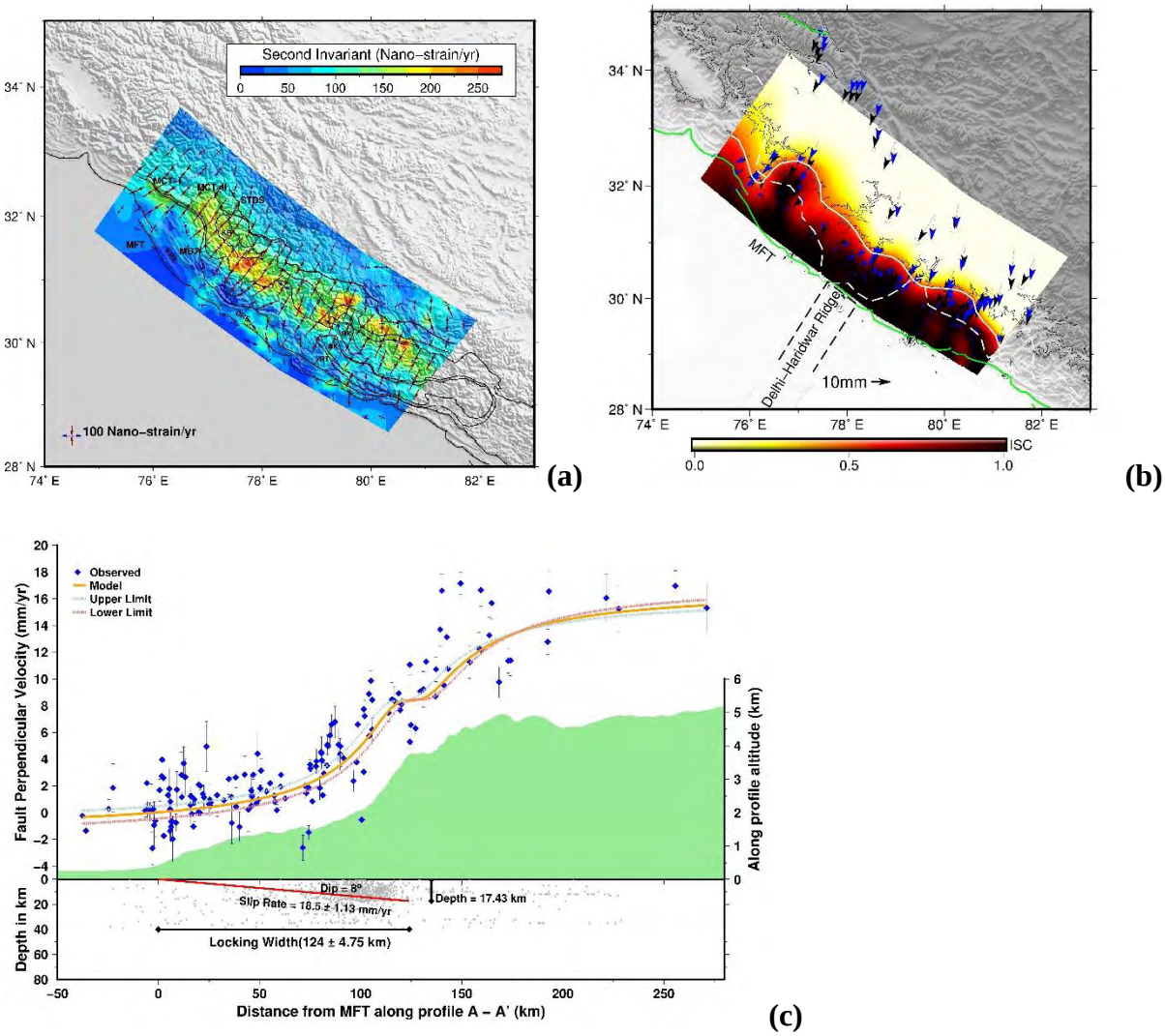

Figure 4 a,b and c represent the strain rate, interseismic coupling pattern and elastic dislocation modelling of the central seismic gap portion of Himalaya.

The study on strain rate patterns agrees that the dominant strain rate is of compressional nature and is situated along the Main Central Thrust (MCT) zone in the study region. The elastic dislocation modelling yielded consistent results with the previous studies. No low coupling zones were observed in the Inter-seismic Coupling model of the present study in contrast to the recent reports. This is possibly due to the additional new velocity vectors which substantially improved the geodetic coverage. A detailed study reveals that the total arc normal shortening rates in the NW Himalayan region are approximately 14 mm/year across the transect of the Himalaya, which falls in the range from 10 to 20 mm/year reported from the 2500 km Himalayan Arc. ((Jade et al.,2020; Figure 5). Furthermore, the study recorded an arc-parallel extension rate of approximately 7 mm/year in the Kashmir valley. Using inverse modelling, they inferred an oblique slip of around 16 mm/year along the decollement in the Kashmir valley. The locking depth is estimated to be around 15 km and a width of slip is approximately 145 km.

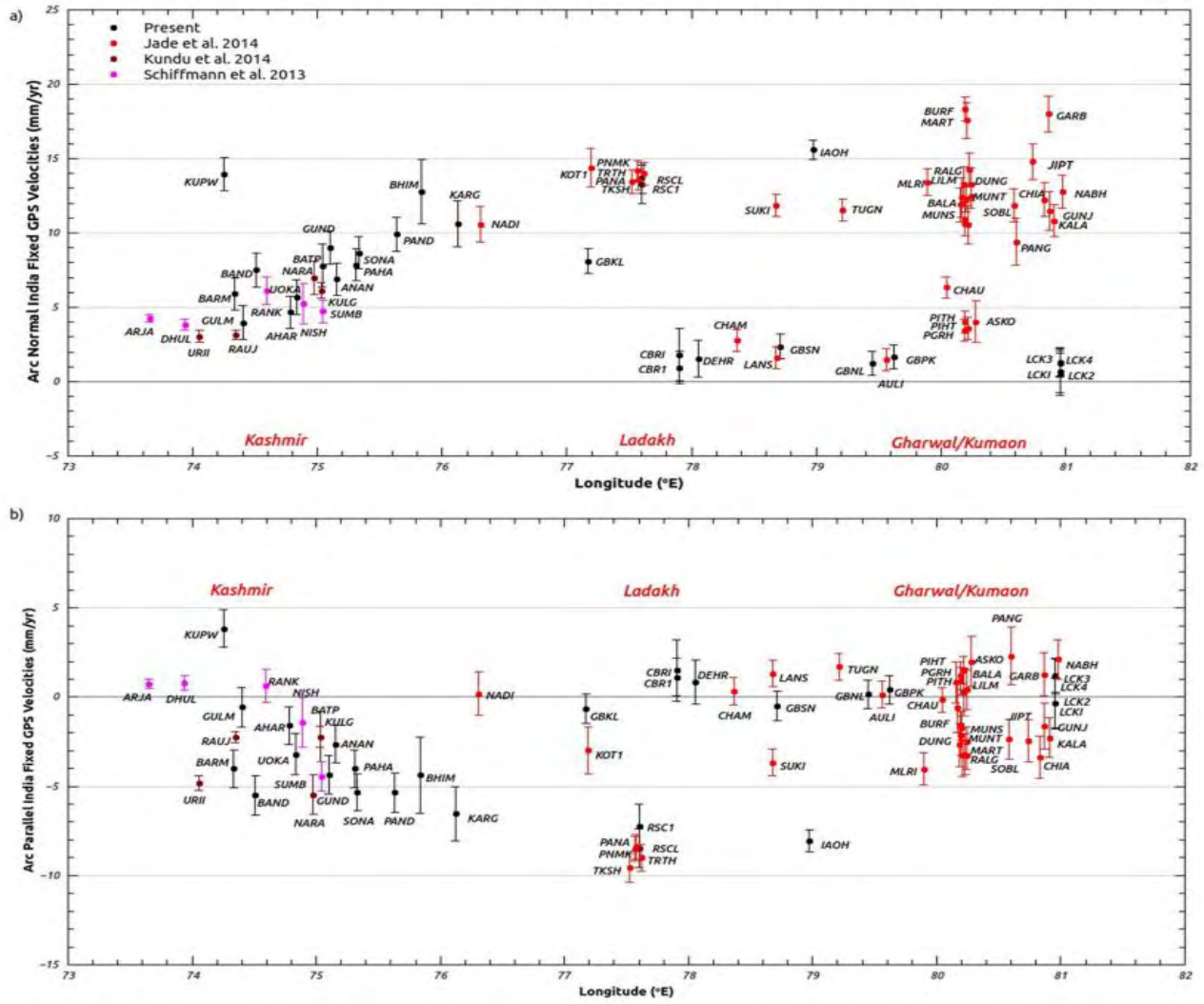

Figure 5. (a) Arc-normal and (b) Arc-parallel rates of GPS sites in northwest Himalaya with error bars (Jade et al.,2020).

The analyses of both geodetic and seismic strain rates in the Kumaun-Garhwal region indicate that a substantial amount of strain energy, estimated to be approximately 5E+21 Nm, has been accumulated over the past centuries and has the potential to cause a megathrust earthquake ($Mw \geq 8$) (Ghavri and Jade, 2022). Using the GPS network in the Indo-Burmese arc, strain accommodation in the wedge, status of active convergence and seismic vulnerability in the outer wedge, are being assessed. The estimated India-Sunda relative plate motion of ~37 mm/year oriented along N11°E is separated among three major active units, namely, the Sagaing Fault (~18 mm/year), Churachandpur-Mao Fault (~17 mm/year), and the blind megathrust (~7 mm/year), from west to east of the IBA, respectively. Kundu et al. (2022) made significant progress in understanding the Indo-Burmese Arc plate circuit, while Panda & Kundu (2022) examined the geodynamic complexity of the Indo-Burmese Arc region and its interaction with the Northeast Himalayas. Panda (2022) identified a low-effective fault strength of a blind detachment beneath the Indo-Burmese Arc (NE-India) induced by frictional-viscous flow. In a study Panda et al., 2020, they investigated the India-Sunda Plate Motion, Crustal Deformation, and Seismic Hazard in the Indo-Burmese Arc. Their research indicated that the convergence across the blind megathrust is significantly lower than that previously estimated.

However, due to a significant scatter in the data near the updip edge of the blind megathrust, it is uncertain whether the deformation is accommodated through shallow creep or in stick -slip manner, leading to uncertainty in the seismic hazard in this densely populated region.

2.3 Kachchh paleorift region:

GPS measurements of crustal deformation since 2009 in the Kachchh paleorift region are analysed and are consistent with the model in which strain accumulates on the opposite verging reverse faults located on the northern and southern flanks of the paleorift (Gahalaut et al.,2019). The 2001 Bhuj earthquake's postseismic deformation seems to have little significance, especially in distant locations, because of the weak mantle rheology. Despite their late Triassic rifting origins, these previously normal faults are now reactivated with reverse motion and show a high rate of compression. This results in a slip rate of around 4-5 mm/year from both sides, making it a seismically active paleorift. (Figure 6). Interestingly, the estimated geodetic strain accumulation rate is consistent with the seismic moment release rate from earthquakes of past 200 years, which suggests that the accumulation of slip in the region is mostly seismic (Gahalaut et al.,2019). The depth extent of the fault's updip edge is not well constrained and could also vary with time. Moreover, variations in slip along the faults' strike could occur, resulting in fault segmentation across their length and depth. The slip may even distribute among different faults located on the paleorift flanks, leading to all faults being active at some point with a minimal amount of strain accumulation on each individual fault resulting in all the faults being active at some point with minimal strain accumulation on each individual fault. Other paleorifts worldwide may exhibit similar behavior with varying compression rates. To detect such compression, a dense GPS network for measuring crustal deformation over an extended period could yield valuable evidence.

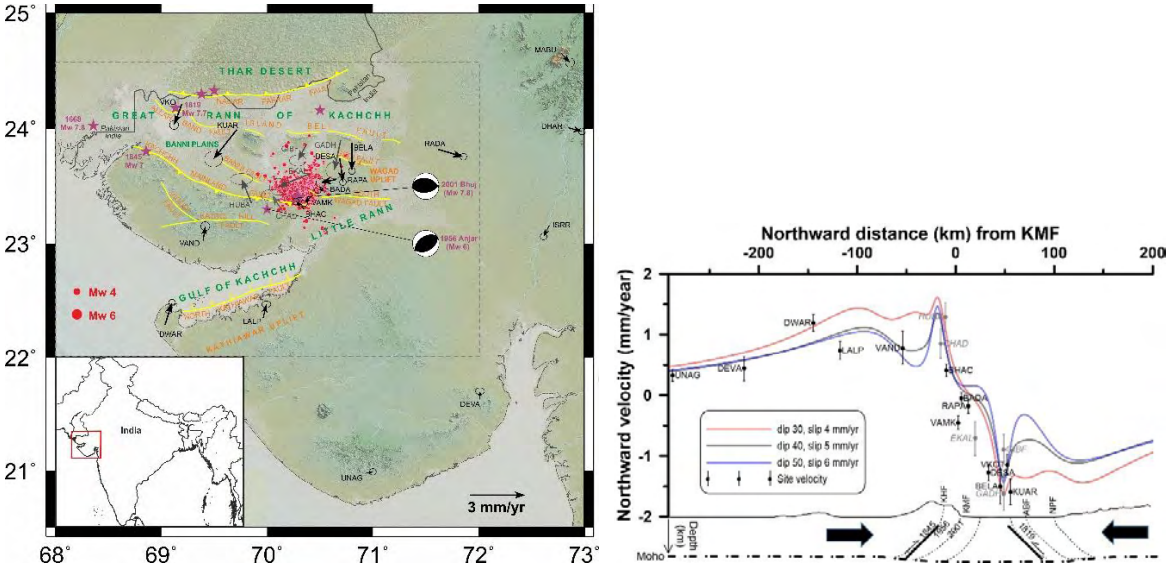

Figure. 6 GPS measurements of crustal deformation (2006/2009–2016) from the Kachchh and adjoining region (Gahalaut et al., 2019). Estimates of site velocity (black vectors, continuous sites; gray vectors, survey mode sites) are shown in Indian reference frame. Focal mechanism solutions of the 2001 Bhuj and 1956 Anjar earthquakes are also shown. Red filled circles are the aftershocks of the 2001 Bhuj earthquake (2001–2016). The Figure 6 displays historical earthquakes from the past two centuries, marked with stars. Major faults in the region are

depicted with yellow lines. The north-south profile on the right panel exhibits the northward site velocity variation. The three curves correspond to the modelled slip response on faults situated on both sides of the paleorift. In the lower panel, there is a schematic depth section of the Kachchh paleorift, indicating the faults' location on the paleorift flanks. Locations of 1845, 1956, 2001, and 1819 earthquakes are only representative. Topography is exaggerated. KHF = Katrol Hill fault; KMF = Kachchh Mainland fault; ABF = Allah Bund fault; NPF =Nagar Parkar fault.

2.4 Hydrological Induced Deformation

Hydrological loads deform earth's surface at varied time scales and space geodetic observations using GPS, INSAR have been used to quantify the deformation and earth's properties. CSIR-NGRI, as a part of a national network project has established a network of GNSS & Soil Moisture Sensors to monitor the surface deformation and constrain hydrological models in the Ganga Basin. Figure. 7 shows an example of deployment.

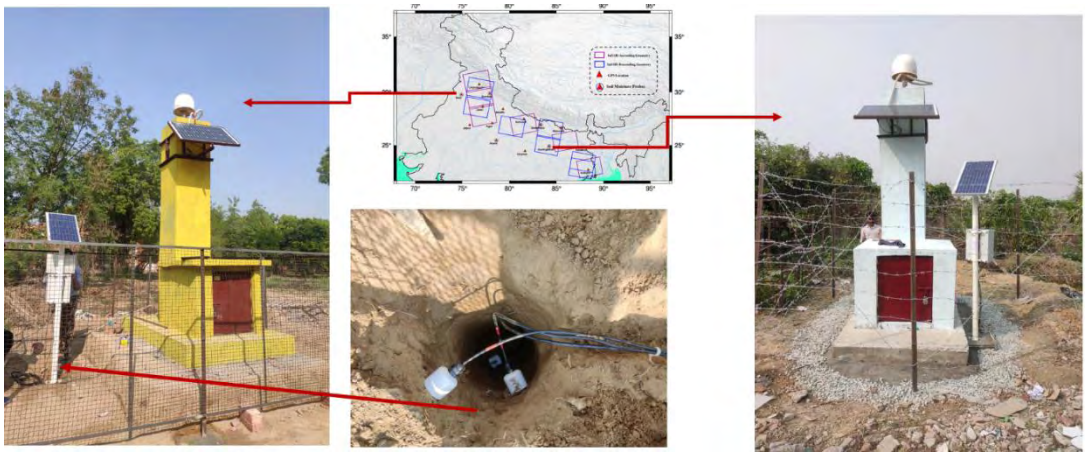

Figure 7: GNSS CORS & collocated Soil Moisture sensors.

The data from, from cGPS at 50 sites, located over North India and Himalaya and GRACE data for the period of 2004–2015 have been analysed to determine the vertical crustal deformation (Saji et al., 2020). Analyses indicate the dominance of hydrological mass variations, especially in the Indo-Gangetic plains and sub-Himalaya and also reveal that the sub-Himalaya and IGP are undergoing subsidence and the surrounding areas show uplift. In addition to the tectonic and nontectonic forcing, unsustainable consumption of groundwater associated with irrigation and other anthropogenic uses influence this subsidence rate. The geophysical modelling (Figure. 8) performed over the collision zone using GRACE-corrected and uncorrected GPS vertical velocity brings out a 12% contribution in slip rate from the hydrological mass variations (Saji et al., 2020).

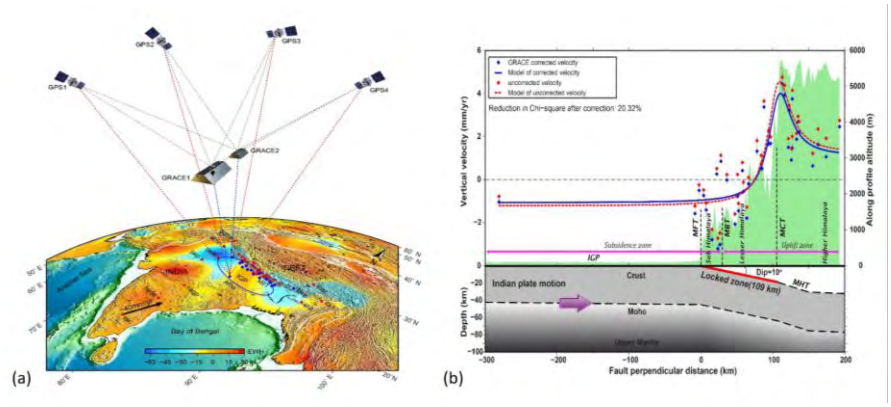

*Figure 8(a) :Schematic illustration of the study area in a GPS and GRACE satellite perspective view. (b) Cross-sectional view of the observed and modelled GPS vertical rates before (red) and after (blue) GRACE correction on a cross profile across the Himalaya. (*Saji et al., 2020).

3. Hydrological Studies

Satellite geodetic data, particularly from altimetry and gravimetry are widely used by the Indian geophysical community for studying hydrological changes, like water-level variations in rivers, and terrestrial stored water. The Spatio-Temporal variability of Terrestrial Water Storage (TWS) is explored from time variable gravity data of the GRACE & GRACE FO. A consistent water storage decline in northern India is interpreted to be caused by a combination of climatic and anthropogenic factors and a. substantial increase in TWS in the central India by the surge in surface water storage (Munagapati et al., 2021). The geodetic observations are also used for cryosphere studies, snow accumulation and storage changes of the glaciers, which are important sources of water for a large part of the country. A method to estimate snow density using bi-temporal fully polarimetric C-band RADARSAT-2 synthetic aperture radar (SAR) data is proposed, which can be used in determination of the hydrological potential of snow without a prior knowledge of the study region (Varade et al., 2020). This is further used for modleling of early winter snow density (Varade et al., 2020 a). Munagapati, and Tiwari, (2021), studied spatio-temporal patterns of mass changes in Himalayan glaciated region from GRACE Data. A mathematical approach of empirical orthogonal functions (EOFs), is utilized to identify mass variability and identified the three broad divisions of Himalayan glaciated region, i.e., western, central, and eastern, based on the seasonal mass gain or loss that corresponds to prevailing climatic changes (Figure. 9).

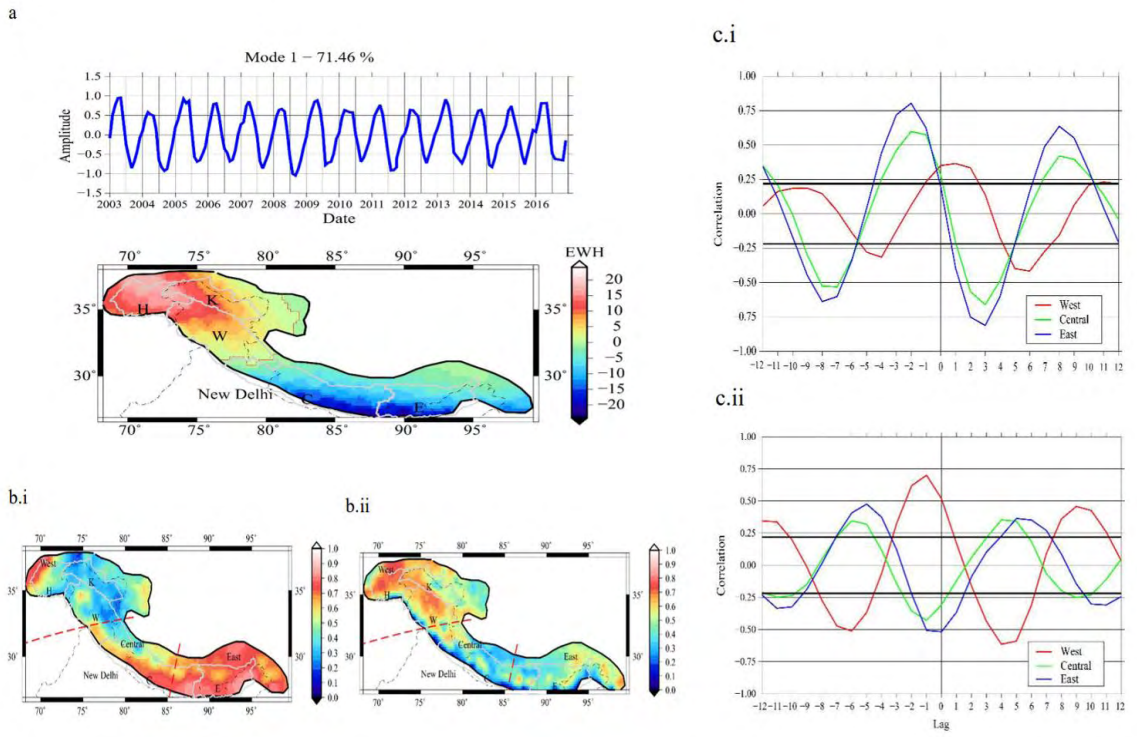

Figure 9: Analysis of EOF mode 1 of Himalaya. a. EOF Mode1 of Himalaya (red line defines the 'zero' contour). b. Grid-wise correlation of (i)Mode vs rainfall and (ii) Mode vs snowfall, three regions demarcated and marked in red. c. Cross correlations of each region against (i.) Rainfall (ii). Snowfall

A different pattern is observed in the western region compared to the rest of the Himalaya. A mass gain over the Hindukush and Karakoram glaciers is found from EOF analysis (Figure. 9). EOF of SWE deciphers that this mass gain was initiated due to a result of high precipitation and accumulation of ground snow cover up to 2007.The mass gain has been steadily increasing in spite of the dampening of snow cover rates after 2008, which is attributed to the lowering and stabilizing of temperature in this region (Munagapati, & Tiwari, 2021).

4. Lithospheric Density Models

Researchers across country have paid a wide attention in recording new gravity data and constructing lithospheric density models of different regions of the Indian plate utilizing ground and satellite gravity data and new computational methods. These studies have revealed important information about the crustal thickness, density inhomogeneities, and subsurface structures, which have allowed to comprehend the dynamics of active and ancient continental collision zones, magmatic underplating beneath large igneous provinces, evolutionary models of Dharwar and Singhbhum cratons, and passive continental margins of India. They are described in the following sections. Kumar et al. (2020) have prepared a merged (ocean and land) Bouguer Anomaly Map (Figure. 10) and discussed the long-wavelength gravity anomalies, effective elastic thickness, and lithospheric thickness in the Indian subcontinent.

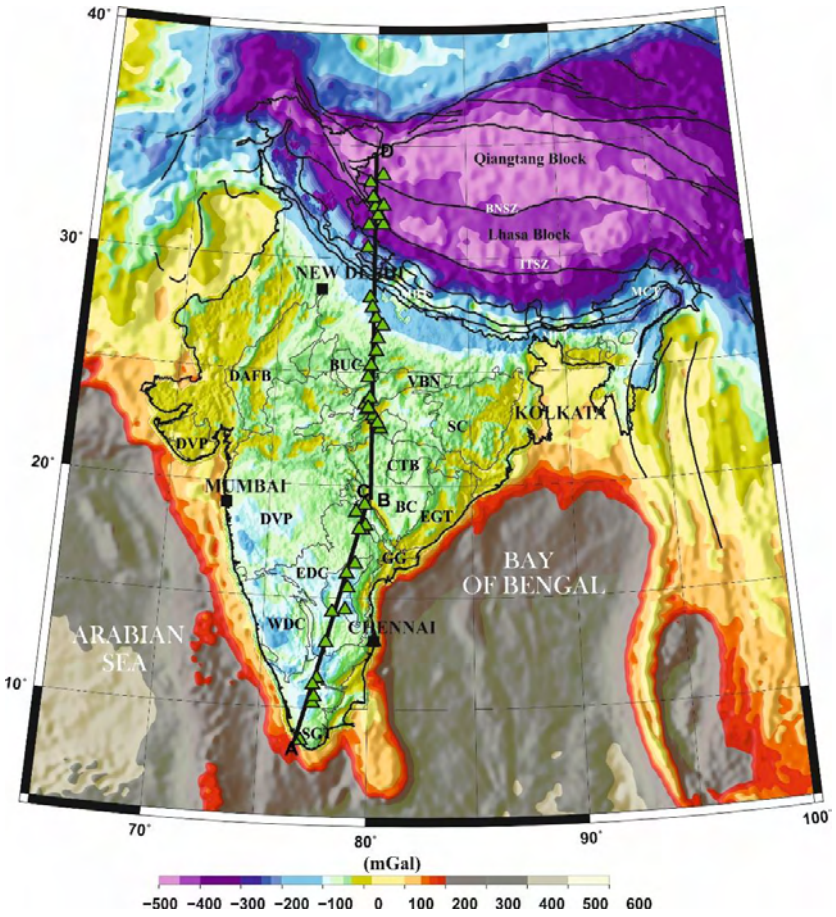

Figure 10: Composite Bouguer Anomaly Map of India and adjoining ocean. Location of transect is marked along which lithospheric model is constructed (Kumar et. al., 2020)

3.1 Indo-Eurasia Collision Zone:

Exploration of deep crustal and lithospheric structures in the Himalaya and Tibetan plateau is central for understanding the geodynamic processes in the Indo-Eurasian collision zone. In recent years, researchers, Arjun et al. (2022), Chamoli et al. (2020), Manglik et al. (2022), Hajra et al. (2022), Ghosh et al. (2022), Kumar et al. (2020), and Ravikumar et al. (2020) have utilized both the ground and satellite gravimetry to examine these structures. Arjun et al. (2022) investigated the lithospheric strength in the NW Himalaya and Ladakh-region using a joint modelling approach with teleseismic residuals, gravity, and topography data. Ravikumar et al. (2020) constructed three 2-D density models across the Indo-Eurasian collision zone based on global models of gravity, geoid, and topography data, as well as geodetic and seismic observations. Manglik et al. (2022) have analysed the gravity anomalies and topography to propose the segmentation of Himalayan collision zone arc, while using the integrated 2-D modelled lithospheric density cross sections, Ravikumar et al. (2020) demarcated the northern front of the underthrusting Indian lithosphere (Figure. 11).

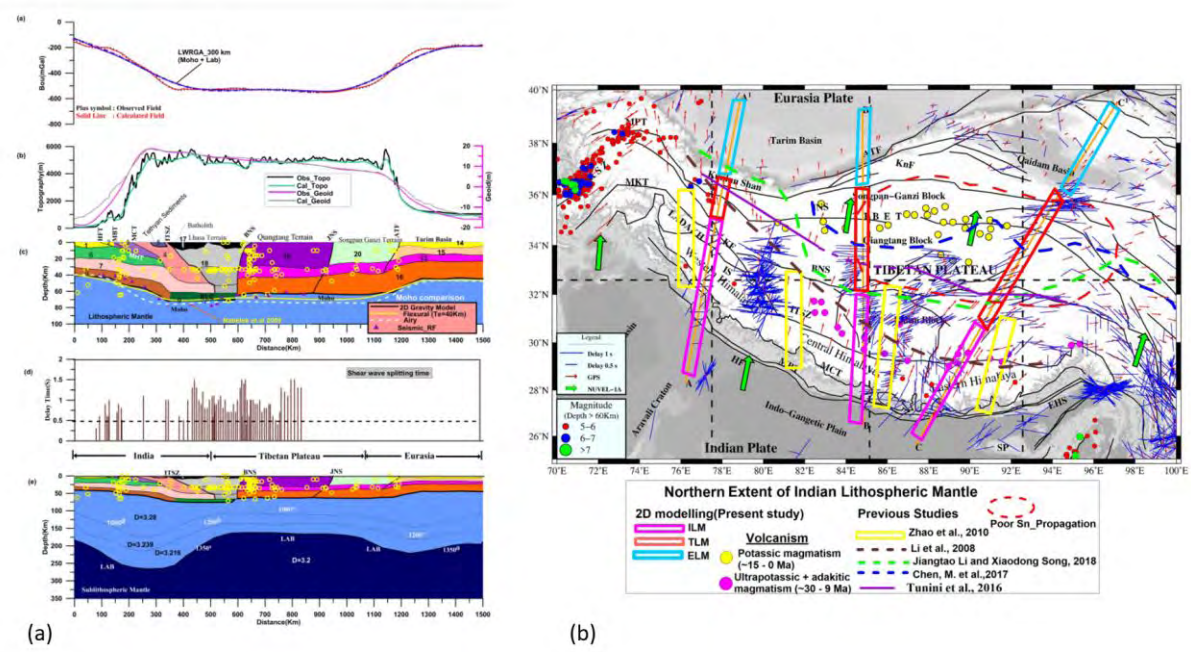

Figure 11: (a) 2-D density structures of the crust and upper mantle lithosphere beneath the central part of the Himalaya and Tibetan plateau along N-S Profile (b) Northern extent of the Indian lithospheric Mantle (Ravikumar et al., 2020)

3.2 Indian Peninsula.

A large part of India that remained tectonically stable over a significant geological time period is ~~over~~ referred as peninsular shield though it does not match to the idea of definition of shield. Several cratons and mobile belts are located in the Peninsular India and have been investigated through analyses of gravity and geoid anomalies. Singh et al. (2021) conducted a study on the western Indian shield to identify the crustal and lithospheric boundaries beneath the northwest India, revealing important insights into tectonomagmatic events at depths of 130-140 km and 170-200 km below the foreland Ganga basin. The thinning of lithosphere is reported beneath the Kachchh, Saurashtra, and Barmer-Pokhran regions, which are characterized by two rift systems and two major magmatic episodes, as well as a potential low-velocity zone in the subcrustal upper mantle region. Based on these observations, Kumar et al. (2022) have suggested a connection between the mantle lithosphere's thermal modification and evolution in this area (Figure. 12).

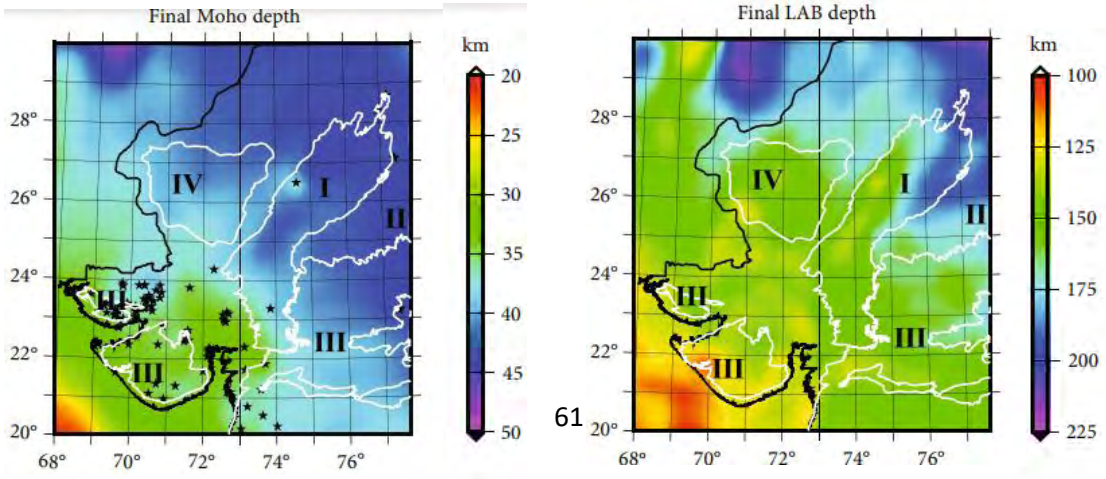

Figure 12: Moho depth and depth of the LAB in km (Modified from Kumar et al., 2022).

A new and complete Bouguer gravity map of Singhbhum craton had been prepared by compiling newly acquired data and all the existing data (Vasanthi et al., 2021). The conspicuous presence of high-order residual gravity low anomalies, together with estimated low densities, suggested voluminous presence of Singhbhum granitic batholiths that built the dominant crustal architecture. The studies by Vasanthi and Santosh (2021a, 2021b, 2022a, 2022b) and Vasanthi (2022b) utilized the ground and satellite gravity observations to investigate the geodynamics of Archean cratons and mobile belts. Based on the 2D and 3D integrated potential field modelling, the crustal and lithospheric structure of the west central India was described (Prakash et al., 2020; Prasad et.al 2021). Some new edge enhancement functions (BHG, ImpTAHG, ETG) are proposed which overcome the limitations of conventional edge detection techniques (Prasad et al.,2022a, b, c, d,). Satyakumar et al. (2022) utilized the gravity and SAR data to delineate the structural and tectonic features of Mahanadi basin. The tectonic and lithological boundaries identified on remote sensing imaginary correlate well with the structural trends from shallow source edge gravity techniques with some spatial variation. Hydrocarbon Exploration and Mineral exploration related studies have also been carried out during this period (Singh and Rao, 2021; Singh and Rao, 2021; Arasada et al., 2023; Rao et al., 2019; Babu et al., 2023).

3.3 Adjoining Oceanic Regions:

The early break-up history of conjugate East Indian-East Antarctic margin segments is often questionable due to the lack of information on the extent of stretched continental crust and unambiguous magnetic anomalies. Dubey et al., 2022, described the Lithospheric-mantle modification beneath the thick sedimentary fan of Bay of Bengal based on the 3D gravity model. Giri et al., 2022, also described the crustal architecture of the Eastern Ghats Mobile Belt and tectonic implications constraints from aeromagnetic, gravity and geological data. In a study (Vasanthi, 2022), the satellite gravity field over the Laxmi Ridge and its adjoining areas had been analysed to address the incongruity of the nature of the crust beneath this ridge structure. Rao and Radhkrishna, 2021 described that the central and northern conjugate segments are characterized by higher β (>3.0) and Te (15-30 km) values compared to southern conjugate segments (Te= 5km) from both the crustal stretching factors (β) and effective elastic strength (Te) values. They concluded that the Elan bank micro continent may have detached from the central part of the East Indian margin (16°-20°) (Rao and Radhkrishna, 2021). The Maldive Ridge (MR) forms the middle segment of the Chagos-Laccadive Ridge system, a vast submarine mountain range in the Indian Ocean. Kunnummal, et al 2019, used the satellite derived gravity data along with geoid and bathymetry data to understand the crustal structure (Figure 13*)*, isostasy and tectonic evolution of MR and Deep-Sea Channel region (region between MR and Chagos Bank, Maldive Ridge together with DSC region will herein be called Greater Maldive Ridge-GMR). Integrating with the available previous geophysical studies, the shallow interface at an average depth of 5.5km is inferred to represent the depth to the top of the acoustic basement underlying 1–1.5 km thick lava flow unit while the deeper one is associated with the interface between the crust and initial Moho before the underplating took

place (presently top of the underplated material). Further, they (Kunnummal, et al, 2020) also estimated the elastic thickness (Te) values along the GMR from 2D and 3D flexural modelling ranges from 6.5–16.5 km with comparatively lower Te values over MR (7–9 km) and slightly higher values over the DSC region (>10 km).

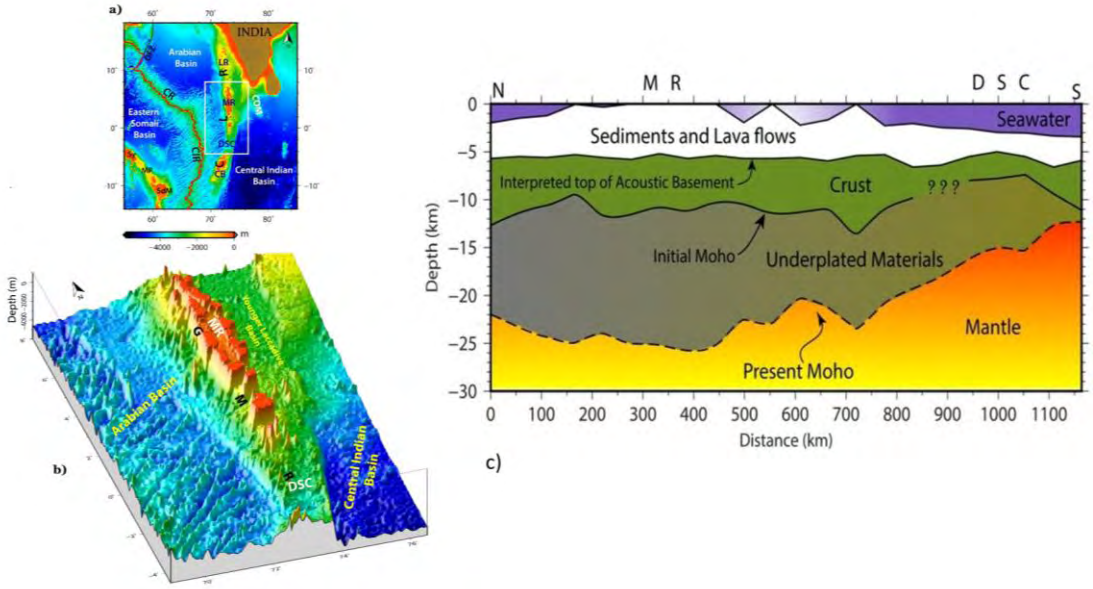

Figure 13: a) Bathymetry map of the Western Indian Ocean generated from satellite altimetry depicting the major structural features in the northwest Indian Ocean. The study region is shown in white rectangular box. b) 3D bathymetry of the Greater Maldive Ridge. MR: Maldive Ridge, DSC: Deep Sea Channel, GMR: Greater Maldive Ridge, CIR: Central Indian Ridge, CR:Carlsberg Ridge, CLR: Chagos Laccadive Ridge, LR: Laccadive Ridge, OFZ: Owen Fracture Zone, Sy: Seychelles, MP: Mascarene Plateau, SdM: Saya de Malha, COM: Comorin Ridge (c) Sketch showing a possible geological cross-section along two N-S profiles across the Maldive Ridge (MR) and the Deep Sea Channel (DSC).(Kunnummal, et al,. 2019, 2022)

Andaman-Sumatra–subduction is produced by the oblique subduction of the Indo-Australian plate beneath Burmese–Sumatra plate and has witnessed two great megathrust earthquakes (Mw 9.1, 2004 Sumatra and Mw 8.6, 2005 Nicobar) in the recent past. A Review" (Yadav and Tiwari, 2019) presents an overview of the lithospheric structure below the Andaman–Sumatra region and highlighted the significance of gravity–geoid modelling for better imaging of structure in this region. A three-dimensional density model of north Andaman subduction zone (10°–15°N, Figure.14) has also been constructed through the joint modelling of satellite free-air gravity and geoid anomalies with constraints from previous studies (Yadav and Tiwari 2020) which provides a better resolved structure of the inadequately known part of the subduction zone. Haripriya et al, 2019, further described the crustal Model for the Andaman Outer Arc constraints from Gravity and Receiver Function Data, including Earthquake, dealing with the seismologically constrained gravity interpretation for delineating the crustal structure below the Andaman outer arc region which suggested a thicker oceanic crust approaching the subduction zone. Overall, the recent Indian contributions on the Andaman Subduction Zone

have focused on better understanding of the lithosphere and crustal structure of the region and investigating the seismicity and tectonics of the area to improve the hazard assessments.

Figure:14 (a) Map of the study area in Andaman (b) Construction of an initial model along the cross-section showing the geometries prepared from the available geological and geophysical constraints and its gravity and geoid responses along with observed anomalies (Yadav and Tiwari 2020).

Acknowledgements

Director, CSIR-NGRI is thanked for permission to publish this manuscript. Report highlights the type of work being carried out through a few examples and is not a reflection of all the work carried out by Indian researchers. We also thank A.P. Dimri (IIG), O. Dixit (IITK), N. Gujjar (SoI), S. Rao (IIT-ISM), and V. K. Gahalaut, A. Vasanthi and N. Kumar, KND Prasad, A.V.Satya Kumar (CSIR-NGRI), for their inputs.

Bibliography:

Arasada, R. C., G. Srinivasa Rao, & P. R. Sahoo. Integrated geological and geophysical studies for delineation of laterite covered chromiferous ultramafic bodies around Bhuban, southwestern part of Sukinda ultramafic complex, Odisha. Ore Geology Reviews, 119, 103402, 1-9, 2020, https://doi.org/10.1016/j.oregeorev.2020.103402.

Arasada, R. C; Rao, G. S; Anand, R. Crustal architecture of North Singhbhum Mobile Belt, Eastern Indian Shield: Constraints from two-dimensional and three-dimensional modelling of Bouguer gravity and aeromagnetic data. Geological Journal, 0072-1050, 2022, http://dx.doi.org/10.1002/gj.4434.

Arjun, V. H; Gupta, S; Tiwari, V. M. Lithospheric structure of the Dharwar Craton (India) from joint analysis of gravity, topography, and teleseismic travel-time residuals. Journal of Asian Earth Sciences, 1367-9120, 2022, http://dx.doi.org/10.1016/j.jseaes.2022.105397

Arjun, V. H., Tiwari, V. M., Gupta S., 2021. Lithospheric strength across NW Himalaya and Ladakh - Inferences from joint modelling of teleseismic residuals, gravity and topography, Earth and Planetary Science Letters (Revision submitted)

Bahuguna, A., Shanker, D. Simulation of Intraplate Stress Distribution of the Indian Tectonic Plate Using the Finite Element Method. Pure & Applied Geophysics. 179, 125–148 (2022). https://doi.org/10.1007/s00024-021-02906-9

Basantaray, A. K; Mandal, A.Interpretation of gravity-magnetic anomalies to delineate subsurface configuration beneath east geothermal province along the Mahanadi rift basin: a case study of non-volcanic hot springs. Geothermal Energy, 2195-9706, 2022, http://dx.doi.org/10.1186/s40517-022-00216-4

Bisht, H; Kotlia, B.S; Kumar, K; Dumka, R.K; Taloor, A.K; Upadhyay, R. GPS derived crustal velocity, tectonic deformation and strain in the Indian Himalayan arc. Quaternary International, 1040-6182, 2021, http://dx.doi.org/10.1016/j.quaint.2020.04.028

Boazman, S.J., Shah, J., Harish, Gawronska, A.J., Halim, S.H., Satyakumar, A.V., Gilmour, C.M., Bickel, V.T., Barrett, N., Kring. D.A. The distribution and accessibility of geologic targets near the lunar south pole and candidate Artemis landing sites. The Planetary Science Journal, 3 (12), 275, 2022, https://doi.org/10.3847/PSJ/aca590.

Chouhan, A. K. Structural fabric over the seismically active Kachchh rift basin, India: insight from world gravity model 2012. Environmental Earth Sciences, 1866-6280, 2020, http://dx.doi.org/10.1007/s12665-020-09068-2

Chouhan, A. K; Choudhury, P; Pal, S. K. New evidence for a thin crust and magmatic underplating beneath the Cambay rift basin, Western India through modelling of EIGEN-6C4 gravity data. Journal Of Earth System Science, 2347-4327, 2020,http://dx.doi.org/10.1007/s12040-019-1335-y

Chouhan, A.K; Chopra, S; Chaube, H; Singh, D; Mishra, AK. Integrated analysis of the gravity and the magnetic data to infer structural features and their role in prospective mineralisation in and around the Ambaji-Deri-Danta-Chitrasani region, NW India. Journal of Earth System Science,2347-4327, 2022 http://dx.doi.org/10.1007/s12040-022-01979-x

Chouhan, A.K; Chopra, S; Singh, D. Structural Interpretation Over the Epicentre Zone of 1819 Allah-Bund Earthquake, North-Western India in An Intraplate Setup Using Global Gravity Data. Journal of The Indian Society Of Remote Sensing 0255-660X 2021 http://dx.doi.org/10.1007/s12524-021-01422-6.

Coudurier-Curveur. A, P. Tapponnier, E. Okal, J. Van der Woerd, E. Kali, S. Choudhury, S. Baruah, M. Etchebes, Ç. Karakaş, A composite rupture model for the great 1950 Assam earthquake across the cusp of the East Himalayan Syntaxis, Earth and Planetary Science Letters, 531, 0012-821, 2020, https://doi.org/10.1016/j.epsl.2019.115928.

DeMets. C, S Merkouriev, S Jade, High-resolution reconstructions and GPS estimates of India–Eurasia and India–Somalia plate motions: 20 Ma to the present, Geophysical Journal International, Volume 220, Issue 2, February 2020, Pages 1149–1171, https://doi.org/10.1093/gji/ggz508

Devara, M., Tiwari, A., Dwivedi, R. Landslide susceptibility mapping using MT-InSAR and AHP enabled GIS-based multi-criteria decision analysis. Geomatics, Natural Hazards and Risk, 12(1), 675-693, 2021. https://doi.org/10.1080/19475705.2021.1887939.

Dhar, S., Balasubramanian, N., Dikshit, O., Schuh, H, Stable and upgraded horizontal datum for India. Current Science, 123(1), 43-51, 2022. https://doi.org/10.18520/cs/v123/i1/43-51

Dhar, S., Glaser, S., Heinkelmann, R., Schuh, H., Balasubramanian, N., Dikshit, O., Favorable locations for new VGOS antennas in India depending on the assessment of geodetic parameters and environmental factors. Earth Planets Space, 75, 47, 2023. https://doi.org/10.1186/s40623-023-01794-8

Dhar, S., Tiwari, A., Balasubramanian, N., Devaraju, B., Dikshit, O., Prakash, J., Mishra, P., Agarwal, D., Sharma, V., Varade, D., Laha, A., Kumar, A., Singh, S., Bihari Narayan Singh, A., Goyal, R., and Kumar, V (2021). Establishment of State-of-the-Art Geodesy Village in India: Current status and Outlook, EGU General Assembly 2021, online, 19–30 Apr 2021, EGU21-16068, https://doi.org/10.5194/egusphere-egu21-16068.

Dikshit, O., Sharma, A., Nagarajan, R., Khuswaha, R., Goyal, R., Balasubramanian, N., Quality assessment of SOI established CORS stations in Uttar Pradesh. Unpublished,2022.

Dimri, A. P; S. Allen, C. Hugge, S. Mal, J. A. Ballesteros-Cánovas,M. Rohrer, A. Shukla, P. Tiwari, P. Maharana, T. Bolch, R. J. Thayyen ,M. Stoffel and Aayushi Pandey. Climate change, cryosphere and impacts in the Indian Himalayan Region. Current Science, 120, 5, 2021.

DST, Draft National Geospatial Policy, Department of Science and Technology, Government of India, New Delhi, 2021. (https://dst.gov.in/sites/default/files/National%20Geospatial%20Policy.pdf)

Dubey, C.P; Tiwari, V.M. Lithospheric-mantle modification beneath the thick sedimentary fan of Bay of Bengal: Inference from the 3D gravity model. Tectonophysics, 0040-1951, 2022, http://dx.doi.org/10.1016/j.tecto.2022.229253

Dumka, R. K., Prajapati, S., SuriBabu, D., Swamy, K. V., Kothyari, G. C., & Malik, K. GPS and InSAR derived evidences of intra-basin stress and strike-slip tectonics in the vicinity of 2001 (M7.7) earthquake, Kachchh, western India. Geological Journal, 58 (2), 683– 699. 2023 https://doi.org/10.1002/gj.4618

Dumka, R. K; Kotlia, B. S; SuriBabu, D; Narain, P; Prajapati, S. Present-day crustal deformation and geodetic strain in the vicinity of Dholavira - Harappan civilization site, Kachchh, western part of the Indian plate. Quaternary International 1040-6182, 2019,http://dx.doi.org/10.1016/j.quaint.2018.10.035

Dumka, R. K; Suribabu, D; Prajapati, S. PSI and GNSS derived ground subsidence detection in the UNESCO Heritage City of Ahmedabad, Western India. Geocarto International 37:25, 7639-7658, 2021 https://doi.org/10.1080/10106049.2021.1980618

Dwivedi, D; Chamoli, A; Pandey, AK, Crustal structure and lateral variations in Moho beneath the Delhi fold belt, NW India: Insight from gravity data modeling and inversion. Physics of The Earth and Planetary Interiors, 0031-9201,2019, http://dx.doi.org/10.1016/j.pepi.2019.106317

Ekka, M.S; Sahoo, S.D; Pal, S.K; Roy, P.N. S; Mishra, O.P. Comparative analysis of the structural pattern over the Indian Ocean basins using EIGEN6C4 Bouguer gravity data. Geocarto-International,1010-6049, http://dx.doi.org/10.1080/10106049.2022.2087748

Featherstone, W.E., Goyal, R., Digitisation and analysis of historical vertical deflections in India. online first. Survey Review,2022. https://doi.org/10.1080/00396265.2022.2088016

Gahalaut, V.K; Gahalaut, K; Dumka, R.K; Chaudhury, P; Yadav, R.K. Geodetic Evidence of High Compression Across Seismically Active Kachchh Paleorift, India. Tectonics, 0278-7407, 2019. http://dx.doi.org/10.1029/2019TC005496

Ganguli, S. S; Mondal, S; Pal, S. K; Lakshamana, M; Mahender, S. Combined analysis of remote sensing, gravity and magnetic data across Moyar Bhavani Shear Zone, Southern Granulite Terrane (SGT), India: appraisals for crustal architecture and tectonics. Geocarto International,1010-6049, 2022. http://dx.doi.org/10.1080/10106049.2022.2086627

Ganguli, S. S; Pal, S. K; Rao, J. V. R; Raj, B.S. Gravity-magnetic appraisal at the interface of Cuddapah Basin and Nellore Schist Belt (NSB) for shallow crustal architecture and tectonic settings, Journal of Earth System Science, 2347-4327, 2020. http://dx.doi.org/10.1007/s12040-020-1354-8

Ganguli, S. S; Pal, S. K; Singh, S. L; Rao, J.V. R; Balakrishna, B. Insights into crustal architecture and tectonics across Palghat Cauvery Shear Zone, India from combined analysis of gravity and magnetic data. Geological Journal, 0072-1050, 2021. http://dx.doi.org/10.1002/gj.4041

Ganguli, S.S; Pal, S. K; Sundaralingam, K; Kumar, P. Insights into the crustal architecture from the analysis of gravity and magnetic data across Salem-Attur Shear Zone (SASZ), South-ern Granulite Terrane (SGT), India: an evidence of accretional tectonics., Episodes,0705-3797, 2021.http://dx.doi.org/10.18814/epiiugs/2020/020095

Gawronska, A.J, Barrett, N, Boazman, S, Gilmour, C.M, Halim, S.H, Harish, McCanaan, K, Satyakumar, A.V., Shah, J, Kring, D.A., 2020. Geological Context and Potential EVA Targets at the Lunar South Pole. Advances in Space Research, 66 (6), 1247-1264 https://doi.org/10.1016/j.asr.2020.05.035

Ghavri, S; Jade, S., Seismic potential of megathrust in the Kumaun-Garhwal region of NW Himalaya: implications from geodetic and seismic strain rates. International Journal of Earth Sciences. 1437-3254, 2021. http://dx.doi.org/10.1007/s00531-021-02023-x

Ghosh, G.K., Delineation of major subsurface structural features and source depth locations using 3-D Euler deconvolution of gravity data at north-eastern part of India. Acta Geophysica,1895-6572, 2022, http://dx.doi.org/10.1007/s11600-022-00829-0

Giri, Y; Radhakrishna, M; Betts, PG; Biswal, TK; Armit, R; Sathapathy, SK., Crustal architecture of the Eastern Ghats Mobile Belt and tectonic implications: Constraints from aeromagnetic, gravity and geological data. Tectonophysics,0040-1951, 2022. http://dx.doi.org/10.1016/j.tecto.2022.229386

Gokul, V. S., Sreejith, K. M., Rao, G. S., Radhakrishna, M., & Betts, P. G. Crustal and upper mantle density structure below the Indian Ocean Geoid Low based on 3-D constrained potential field modelling: Inferences on causative sources. Tectonophysics, 822, 229161, 2022, https://doi.org/10.1016/j.tecto.2021.22916.

Goyal, R., Ågren, J., Featherstone, W.E., Sjöberg, L.E., Dikshit, O., Balasubramanian, N., 2022a. Empirical comparison between stochastic and deterministic modifiers over the French Auvergne geoid computation test-bed. Survey Review, 54(382), 57-69. https://doi.org/10.1080/00396265.2021.1871821

Goyal, R., Claessens, S.J., Featherstone, W.E., Dikshit, O. Investigating the congruence between gravimetric geoid models over India. Accepted. ASCE Journal of Surveying Engineering. 2023a, https://doi.org/10.1061/JSUED2/SUENG-1382

Goyal, R., Dikshit, O., Tiwari, A., 2023b. National Geospatial Policy: status of the Indian geodetic data. Accepted. Current Science

Goyal, R., Featherstone, W.E., Claessens, S.J., Dikshit, O., Balasubramanian, N. An experimental Indian gravimetric geoid model using Curtin University's approach. Terrestrial, Atmospheric and Oceanic Sciences, 32, 813-827. 2021a, https://doi.org/10.3319/TAO.2021.08.10.02

Goyal, R., Featherstone, W.E., Dikshit, O., Balasubramanian, N. Comparison and Validation of Satellite-Derived Digital Surface/Elevation Models over India. Journal of The Indian Society of Remote Sensing, 49, 971–986, 2021b. https://doi.org/10.1007/s12524-020-01273-7

Goyal, R., Featherstone, W.E., Tsoulis, D.V., Dikshit, O. Efficient spatial-spectral computation of local planar gravimetric terrain corrections from high-resolution digital elevation models. Geophysical Journal International, 221(3), 1820-1831, 2020. https://doi.org/10.1093/gji/ggaa107.

Goyal, R., Tiwari, A., Dikshit, O., Balasubramanian, N. Draft national geospatial policy: a few salient observations. Current Science, 123(3), 256-258, 2022b. https://currentscience.ac.in/Volumes/123/03/0256.pdf

Goyal, R., Towards a gravimetric geoid model for the mainland India. PhD Thesis. IIT Kanpur, India and Curtin University, Australia. 2022, http://hdl.handle.net/20.500.11937/89060

Gupta, S.K, Roy, P.N.S; Pal, S.K. Scale invariance behavior for pre and post-2015 Nepal Gorkha earthquake GPS time series based on fractal analysis. Chaos, Solitons & Fractals, 0960-0779, 2021. http://dx.doi.org/10.1016/j.chaos.2021.111341

Gupta, S; Singharoy, P. N; Yadav, R. K; Catherine, J. K; Burgmann, R; Gahalaut, V. K. Anomalous transients in GPS measurements due to induced changes in local site conditions. Journal of Earth System Sciences. 2347-4327, 2019. http://dx.doi.org/10.1007/s12040-019-1213-7

Hajra, S; Hazarika, D; Mondal, S; Pal, S.K; Roy, P.N.S. Deformation of the upper crust in the Kumaon Himalaya analysed from seismic anisotropy and gravity lineament studies. Physics of The Earth and Planetary Interiors 0031-9201, 2022. http://dx.doi.org/10.1016/j.pepi.2021.106827

Halim, S.H, Barrett, N, Boazman, S, Gawronska, A.J, Gilmour, C.M, Harish, McCanaan, K, Satyakumar, A.V., Shah, J, Kring, D.A., 2021. Numerical modeling of the formation of Shackleton Crater at the lunar south pole. Icarus, 351, 113992, https://doi.org/10.1016/j.icarus.2020.113992

Haripriya, K. , Radhakrishna, M, Manoj Mukhopadhyay, Crustal Model for the Andaman Outer Arc: Constraints from Earthquake, Gravity and Receiver Function Data The Andaman Islands and Adjoining Offshore: Geology, Tectonics and Palaeoclimate, 2020,978-3-030-39842-2 (Chapter)

Hebert, H; Occhipinti, G; Schindele, F; Gailler, A; Pinel-Puyssegur, B; Gupta, H.K; Rolland, L; Lognonne, P; Lavigne, F; Meilianda, E; Chapkanski, S; Crespon, F; Paris, A; Heinrich, P; Monnier, A; Jamelot, A; Reymond, D. Contributions of Space Missions to Better Tsunami Science: Observations, Models and Warnings. Surveys in Geophysics. 0169-3298, 2020. http://dx.doi.org/10.1007/s10712-020-09616-2

Jade, S; Mir, R. R; Vivek, C. G; Shrungeshwara, T. S; Parvez, I. A; Chandra, R; Babu, D. S; Gupta, S. V; Ankit; Rajana, S. S. K; Gaur, V. K. Crustal deformation rates in Kashmir valley and adjoining regions from continuous GPS measurements from 2008 to 2019, Scientific Reports, 2045-2322, 2020. http://dx.doi.org/10.1038/s41598-020-74776-5

Kandregula, R. S; Kothyari, G. C; Swamy, K. V; Taloor, A. K; Lakhote, A; Chauhan, G; Thakkar, M. G; Pathak, V; Malik, K. Estimation of regional surface deformation post the 2001 Bhuj earthquake in the Kachchh region, Western India using RADAR interferometry. Geocarto International, 1010-6049, 2022. http://dx.doi.org/10.1080/10106049.2021.1899299

Kannaujiya, S; Yadav, R. K; Ray, P. K. C; Sarkar, T; Sharma, G; Chauhan, P; Pal, S. K; Roy, P.N. S; Gautam, P. K; Taloor, A. K; Yadav, A. Unraveling seismic hazard by estimating prolonged crustal strain buildup in Kumaun-Garhwal, Northwest Himalaya using GPS measurements. Journal of Asian Earth Sciences, 1367-9120, 2022. http://dx.doi.org/10.1016/j.jseaes.2021.104993

Kothyari, G. C; Joshi, N; Taloor, A. K; Malik, K; Dumka, R; Sati, S. P; Sundriyal, Y. P. Reconstruction of active surface deformation in the Rishi Ganga basin, Central Himalaya using PSInSAR: A feedback towards understanding the 7th February 2021 Flash Flood. 0273-1177, 2022. http://dx.doi.org/10.1016/j.asr.2021.07.002

Kothyari, GC; Malik, K; Dumka, RK; Naik, SP; Biswas, R; Taloor, AK; Luirei, K; Joshi, N; Kandregula, RS. Identification of active deformation zone associated with the 28th April 2021 Assam earthquake (Mw 6.4) using the PSInSAR time series. Journal of Applied Geophysics. 0926-9851, 2022. http://dx.doi.org/10.1016/j.jappgeo.2022.104811

Kumar, C. R; Kesavan, R; Ramachandrappa. Crustal heterogeneities and geothermal gradients beneath thrust and fold belts of northeast India from scaled spectral analysis of aeromagnetic and gravity modelling. Journal of Earth System Science, 2347-4327, 2022. http://dx.doi.org/10.1007/s12040-022-01885-2

Kumar, C. R; Raj, A. S; Pathak, B; Maiti, S; Naganjaneyulu, K. High density crustal intrusive bodies beneath Shillong plateau and Indo Burmese Range of northeast India revealed by gravity modeling and earthquake data. Physics of The Earth and Planetary Interiors 0031-9201, 2020. http://dx.doi.org/10.1016/j.pepi.2020.106555

Kumar, K. S; SivaSankar, P; Begum, S. P; Laxman, B; Devidas, P. M; Naidu, V. M. L; Raju, P. S; Srinagesh, D. Appraisal of Veldurti-Kalva-Gani (VKG) fault, Cuddapah Basin, India: Gravity and magnetic approach. Journal of Earth System Science, 2347-4327, 2021. http://dx.doi.org/10.1007/s12040-020-01519-5

Kumar, N; Singh, A. P; Tiwari, V. M. Gravity Anomalies, Isostasy and Density Structure of the Indian Continental Lithosphere, Episodes, 0705-3797, 2020. http://dx.doi.org/10.18814/epiiugs/2020/020040

Kundu, B; Gahalaut, V. K; Panda, D. Two decades of progress in the understanding of the Indo-Burmese Arc plate circuit. Current Science 0011-3891,2022, https://www.currentscience.ac.in/Volumes/123/03/0259.pdf

Kundu, B; Vissa, N. K; Gahalaut, K; Gahalaut, V. K; Panda, D; Malik, K. Influence of anthropogenic groundwater pumping on the 2017 November 12 M7.3 Iran-Iraq border earthquake. Geophysical Journal International, 0956-540X, 2019. http://dx.doi.org/10.1093/gji/ggz195

Kundu, B; Yadav, R. K; Burgmann, R; Wang, K; Panda, D; Gahalaut, V. K. Triggering relationships between magmatic and faulting processes in the May 2018 eruptive sequence at Kilauea volcano, Hawaii. Geophysical Journal International, 0956-540,2020, http://dx.doi.org/10.1093/gji/ggaa178

Kunnummal, P., Anand, S.P. Crustal structure and tectonic evolution of Greater Maldive Ridge, Western Indian Ocean, in the context of plume-ridge interaction using high resolution satellite derived gravity, geoid and bathymetry data. Gondwana Research, 103, 142-163. 2022. https://doi.org/10.1016/j.gr.2022.01.006

Kunnummal, P; Anand, S. P. Qualitative appraisal of high-resolution satellite derived free air gravity anomalies over the Maldive Ridge and adjoining ocean basins, western Indian Ocean. Journal of Asian Earth Sciences, 1367-9120, 2019. http://dx.doi.org/10.1016/j.jseaes.2018.08.008.

Lakhote, A; Thakkar, M. G; Kandregula, R. S; Jani, C; Kothyari, G. C; Chauhan, G; Bhandari, S. Estimation of active surface deformation in the eastern Kachchh region, western India: Application of multi -sensor DInSAR technique. Quaternary International, 1040-6182, 2021. http://dx.doi.org/10.1016/j.quaint.2020.07.010.

Maiti, G; Roy, A; Sen, J; Mandal, N. Impact of Decelerating India-Asia Convergence on the Crustal Flow Kinematics in Tibet: An Insight from Scaled Laboratory Modeling, 2021. http://dx.doi.org/10.1029/2021GC009967

Mandal, A; Chandroth, A; Basantaray, A.K; Mishra, U. Delineation of shallow structures in Madawara igneous complex, Bundelkhand Craton, India using gravity-magnetic data: Implication to

tectonic evolution and mineralization. Journal of Earth System Science, 2347-4327, 2020. http://dx.doi.org/10.1007/s12040-020-1360-x

Manglik, A; Kandregula, R. S; Pavankumar, G. Foreland Basin Geometry and Disposition of Major Thrust Faults as Proxies for Identification of Segmentation along the Himalayan Arc. Journal of the Geological Society of India, 0016-7622, 2022. http://dx.doi.org/10.1007/s12594-022-1928-y

Maurya, V. P; Fontes, S. L; Oliveira, V. C; La Terra, E. F. Gradient based first- and second-order filters for the demarcation of continental-oceanic boundaries using satellite gravity data. Geophysical Journal International, 0956-540X, 2020. http://dx.doi.org/10.1093/gji/ggaa084

Mishra, M. N. Active tectonic deformation of the Shillong plateau, India: Inferences from river profiles and stream-gradients. Journal of Asian Earth Sciences, 1367-9120, 2019. http://dx.doi.org/10.1016/j.jseaes.2019.103904

Mondal, S. K; Yadav, R. K; Bansal, A. K; Catherine, J. K; Gahalaut, V. K. Geodetic strain rate, slip deficit and seismicity analysis in Central Seismic Gap of the Himalayan arc. Himalayan Geology, 43, 0971-8966, 2022.

Mukhopadhyay, B; Mukhopadhyay, M; Elawadi, E; Ghosh, UK; Pramanik, K. Cinder cone morphometry in relation to gravity anomaly zones in the Harrat al Birk and Asir foreland, SW Saudi Arabia. Journal of Earth System Science 2347-4327, 2019. http://dx.doi.org/10.1007/s12040-019-1188-4

Mukhopadhyay, M; Mogren, S; Mukhopadhyay, B; Venkatesh, KD; Elawadi, E. Crustal control on basement uplift beneath the Ghawar Anticline, Saudi Arabia-gravity modeling with receiver function constraints" Arabian Journal of Geosciences, 1866-7511, 2020. http://dx.doi.org/10.1007/s12517-020-05433-4

Mukhopadhyay, M; Mukhopadhyay, B; Elawadi, E; Venkatesh, KD; Al-Arifi, N. Crustal structure beneath the volcanic field in the Tihamat Plains, Saudi Arabia: An integrated model constrained by gravity modelling and receiver function results. Journal of Asian Earth Sciences,1367-9120,2021,http://dx.doi.org/10.1016/j.jseaes.2020.104614

Mukul, M; Mukul, M. Uncertainties in Digital Elevation Models from Global Advanced Land Observing Satellite (ALOS) digital topography data in the Indian subcontinent, Journal of Earth System Sciences, 2347-4327, 2021. http://dx.doi.org/10.1007/s12040-020-01523-9

Munagapati, H and V.M. Tiwari, D.K. Panda (2021) An analysis of spatio-temporal variability of terrestrial water storage in India. https://doi.org/10.1016/j.wasec.2021.100099.

Munagapati. H and V. M. Tiwari Spatio-Temporal Patterns of Mass Changes in Himalayan Glaciated Region from EOF Analyses of GRACE Data Remote Sens. 2021, 13(2), 265; https://doi.org/10.3390/rs13020265.

Narayan, S; Kumar, U; Pal, S. K; Sahoo, S. D. New insights into the structural and tectonic settings of the Bay of Bengal using high-resolution earth gravity model data. Acta Geophysica, 1895-6572, 2021. http://dx.doi.org/10.1007/s11600-021-00657-8

Naskar, D. C; Nagaraja, P. N; Ramesh, M; Suru, P, Gravity and magnetic studies in parts of Odisha and Chhattisgarh (India): implications in regional geology Bulletin of Geophysics and Oceanography, 2785-339X, 2022. http://dx.doi.org/10.4430/bgo00378

Niraj Kumar, Om Prakash, A. P. Singh, V. M. Tiwari; Thermal Modification of the Northwest Indian Shield: As Evidenced by Integrated Geopotential Modelling. Lithosphere 2022; 2022 (Special 8): 8022620. doi: https://doi.org/10.2113/2022/8022620

Padmavathi 2022, PhD Thesis, AcSIR- National Geophysical Research Institute, Hyderabad.

Pallabee Choudhury, Sumer Chopra, Charu Kamra, Archana Das; New Insight into the Recent Earthquake Activity in North Cambay Basin, Western India: Seismological and Geodetic Perspectives. Bulletin of The Seismological Society of America 2019; 109 (6): 2240–2251. Doi: https://doi.org/10.1785/0120190126

Panda, D. K., Tiwari, V. M., & Rodell, M. (2022). Groundwater variability across India, under contrasting human and natural conditions. Earth's Future, 10, e2021EF002513. American Geophysical Union (AGU). https://doi.org/10.1029/2021EF002513

Panda, D; Kundu, B; Gahalaut, V. K, Rangin, C. India-Sunda Plate Motion, Crustal Deformation, and Seismic Hazard in the Indo-Burmese Arc. Tectonics,0278-7407,2020 http://dx.doi.org/10.1029/2019TC006034

Panda, D and Bhaskar Kundu, Geodynamic complexity of the Indo-Burmese Arc region and its interaction with Northeast Himalaya, Earth-Science Reviews, 226,103959,0012-8252,2022, https://doi.org/10.1016/j.earscirev.2022.103959.

Panda, D., Samanta, S.K., Singh, M.D. et al. Low-effective fault strength of a blind detachment beneath the Indo-Burmese Arc (NE-India) induced by frictional–viscous flow. J Earth Syst Sci 131, 9 2022, https://doi.org/10.1007/s12040-021-01754-4

Panda, D., Kundu, B., Gahalaut, V. K.,& Rangin, C. India-Sunda platemotion, crustal deformation, andseismic hazard in the Indo-BurmeseArc.Tectonics,39, e2019TC006034..2020. https://doi.org/10.1029/2019TC006034

Pappachen, J. P; Sathiyaseelan, R; Gautam, P. K; Pal, S. K. Crustal velocity and interseismic strain-rate on possible zones for large earthquakes in the Garhwal Kumaun Himalaya Scientific Reports, 2045-2322, 2021. http://dx.doi.org/10.1038/s41598-021-00484-3

Pasari, S; Neha. Nowcasting-Based Earthquake Hazard Estimation at Major Cities in New Zealand. Pure And Applied Geophysics,0033-4553,2022, http://dx.doi.org/10.1007/s00024-022-03021-z

Ponraj, M; Amirtharaj, S; Sunil, P. S; Saji, A. P; Kumar, K. V; Arora, S. K; Reddy, CD; Begum, SK. An assessment of present-day crustal deformation in the Kumaun Himalaya from GPS observations.1367-9120,2019 http://dx.doi.org/10.1016/j.jseaes.2019.02.019

Prakash, O.M, A.P. Singh, K.N.D. Prasad, B. Nageswara Rao, A.K. Pandey. Remnant plume head under Neoproterozoic Malani Igneous Suite, western India, Tectonophysics, 792, 2020, 0040-1951, https://doi.org/10.1016/j.tecto.2020.228576.

Prasad, K.N.D., Bansal, A.R., Singh, A.P., Prakash, O. Magneto-thermometric modelling of Central Indian crust and its implications on the thermal lithosphere. Journal of Applied Geophysics, 196, 104508, 1-14, 2022, DOI: 10.1016/j.jappgeo.2021.104508.

Prasad, K.N.D., Patel, V.C., Bansal, A.R. and Singh, A.P., 2023. New insights into the crustal magnetization of the eastern Indian Shield inferred from the aeromagnetic data-based depth to the bottom of the magnetic sources (DBMS). Journal of Asian Earth Sciences, 245, pp.105544, 2022, DOI: 10.1016/j.jseaes.2023.105544.

Prasad, K.N.D., Pham, L.T., Singh, A.P. Structural mapping of potential field sources using BHG filter. Geocarto International. 1-22, 2022, DOI: 10.1080/10106049.20 22.2048903.

Prasad, K.N.D., Pham, L.T., Singh, A.P., 2022. A Novel Filter "ImpTAHG" for Edge Detection and a Case Study from Cambay Rift Basin, India. Pure and Applied Geophysics, 179, pp. 2351-2364, 2022, DOI: 10.1007/s00024-022-03059-z.

Prasad, K.N.D., Pham, L.T., Singh, A.P., Eldosouky, A.M., Abdelrahman, K., Fnais, M.S., Gómez-Ortiz, D., 2022. A Novel Enhanced Total Gradient (ETG) for Interpretation of Magnetic Data. Minerals, 12(11), pp. 1468 (1-16), 2022, DOI: 10.3390/min12111468.

Prasad, K.N.D., Singh, A.P., Rao, P.R., Prakash, O., Begum, S.K., Imprints of multistage magmatic intrusions in Narmada-Tapti region, India: Insights from Geophysical Modelling. Journal of Earth System Sciences, 130, 227, 1-28, 2021, DOI: 10.1007/s12040-021-01721-z.

Prasath, R. A; Bansal, B. K; Verma, M. Stress distribution in the western India-Eurasia collision zone, its kinematics and seismotectonic implications. Journal of Asian Earth Sciences.1367-9120, 2022. http://dx.doi.org/10.1016/j.jseaes.2022.105208

Prasath, R. A; Paul, A; Singh, S. Earthquakes in the Garhwal Himalaya of the Central Seismic Gap: A Study of Historical and Present Seismicity and Their Implications to the Seismotectonic. Pure and Applied Geophysics,0033-4553 2019,http://dx.doi.org/10.1007/s00024-019-02239-8

Rajendran, CP; Sanwal, J; John, B; Anandasabari, K; Rajendran, K; Kumar, P; Jaiswa, M; Chopra, S. Footprints of an elusive mid-14th century earthquake in the central Himalaya: Consilience of evidence from Nepal and India. Geological Journal,0072-1050, 2019, http://dx.doi.org/10.1002/gj.3385

Rajewar, S.K; Lakshmi, C.M; Mohanty, A; Pandey, D.N; Pandey, A; Chaurasia, A; Pandey, A; Rao, V.R; Naidu, M.S; Kumar, A; Mondal, S.K; Yadav, R.K; Catherine, J.K; Giri, R.K; Gahalaut, V.K. Constraining Plate Motion and Crustal Deformation from GNSS Measurements: CSIR-NGRI Contribution. Journal of the Geological Society of India. 0016-7622, 2021, http://dx.doi.org/10.1007/s12594-021-1850-8

Rakesh K. Dumka, S. Chopra, Sandip Prajapati. GPS derived crustal deformation analysis of Kachchh, zone of 2001(M7.7) earthquake, Western India, Quaternary International, 507, ,295-301, 2019. https://doi.org/10.1016/j.quaint.2019.01.032.

Rao, G. S; Radhakrishna, M. India-Elan Bank-East Antarctica Breakup, Crustal Architecture, and Margin Evolution: Results from Constrained Potential Field and Process-Oriented Gravity Modelling of Conjugate Margin Segments. Tectonics. 0278-7407, 2021, http://dx.doi.org/10.1029/2019TC005804

Rao, J. V. R; Kumar, B. R; Kumar, M; Singh, R. B; Veeraiah, B. Gravity of Dharwar Craton, Southern Indian Shield. Journal of The Geological Society of India 0016-7622,2020. http://dx.doi.org/10.1007/s12594-020-1543-8

Rao, J.V.R; Kumar, B.R; Balakrishna, B; Veeraiah, B. Tectonic divisions and accretionary model within Dharwar Craton: New insights from gravity surveys on status of Chitradurga Schist Belt. Journal of Earth System Science, 2347-4327, 2021. http://dx.doi.org/10.1007/s12040-021-01621-2

Rao, J.V.R; Ravikumar, B; Golani, P.R. What lies beneath the Deccan volcanic province? Perspective on tectonic elements and sub-trappean geology from gravity signatures. Journal of Earth System Science, 2347-4327,2022, http://dx.doi.org/10.1007/s12040-021-01787-9

Rao, S, G & Singh, A. Crustal architecture and isostatic compensation of the Comorin Ridge, Central Indian ocean: implications for the breakup of East Gondwana. Journal of Asian Earth Sciences, 199, 104463,1-13, 2020, https://doi.org/10.1016/j.jseaes.2020.104463

Rao, S, G., Arasada, R. C., Sahoo, P. R., & Khan, I. Integrated geophysical investigations in the Mudiyawas-Khera block of the Alwar basin of North Delhi Fold Belt (NDBF): Implications on copper and associated mineralisation. Journal of Earth System Science, 128 (6), 161, 2019, https://doi.org/10.1007/s12040-019-1193-7

Ravikumar, M; Singh, B; Kumar, V.P; Satyakumar, A.V; Ramesh, D.S; Tiwari, V.M. Lithospheric Density Structure and Effective Elastic Thickness Beneath Himalaya and Tibetan Plateau: Inference From the Integrated Analysis of Gravity, Geoid, and Topographic Data Incorporating Seismic Constraints,Tectonics,0278-7407,2020, http://dx.doi.org/10.1029/2020TC006219.

Sahoo, S. D; Pal, S. K. Mapping of Structural Lineaments and Fracture Zones around the Central Indian Ridge (10 degrees S-21 degrees S) using EIGEN 6C4 Bouguer Gravity Data.Journal of The Geological Society of India, 0016-7622, 2019, http://dx.doi.org/10.1007/s12594-019-1323-5

Sahoo, S.D; Pal, S.K. Crustal structure and Moho topography of the southern part (18 degrees S-25 degrees S) of Central Indian Ridge using high-resolution EIGEN6C4 global gravity model data. Geo-Marine Letters, 0276-0460,2021http://dx.doi.org/10.1007/s00367-020-00679-z

Sahoo, S.D; Pal, S.K. The mantle temperature corrected gravimetric Moho using SGG-UGM-2 gravity data: An evidence of asymmetric distribution of thin and thick crust along the Central Indian Ridge (3 degrees S-16 degrees S). Marine Geophysical Research,0025-3235,2022, http://dx.doi.org/10.1007/s11001-022-09481-1

Sahoo, SD; Narayan, S; Pal, S.K. Appraisal of gravity-based lineaments around Central Indian Ridge (CIR) in different geological periods: Evidence of frequent ridge jumps in the southern block of CIR. Journal of Asian Earth Sciences,1367-9120 2022. http://dx.doi.org/10.1016/j.jseaes.2022.105393

Saji, A. P., Sunil, P. S., Sreejith, K. M., Gautam, P. K., Kumar, K. V., Ponraj, M., et al. Surface deformation and influence of hydrological mass over Himalaya and North India revealed from a decade of continuous GPS and GRACE observations. Journal of Geophysical Research: Earth Surface, 125, 2020. https://doi.org/10.1029/2018JF004943

Sarkar, P; Mondal, S; Pal, S. K; Roy, P.N.S; Sahoo, S.D; Widyadwatmaja, A; Gupta, S; Gupta, A. New insights on the tectonic framework using EIGEN6C4 gravity data, seismicity, and finite element stress analysis: An attempt to map earthquake vulnerable zones in parts of North-East India and surroundings. Physics and Chemistry of The Earth,1474-7065, 2022. http://dx.doi.org/10.1016/j.pce.2022.103195

Sastry, R. G; Sonker, M.K. Co-seismic grace gravity-based 11-layered 3-D thrust fault model for the Sumatra earthquake 2004. Journal of Earth System Science, 2347-4327, 2019, http://dx.doi.org/10.1007/s12040-018-1050-0

Satyakumar, A.V; Pandey, A.K; Singh, A.P; Tiwari, V.M. Delineation of structural and tectonic features in the Mahanadi basin, eastern India: New insights from remote sensing and land gravity data. Journal of Asian Earth Sciences, 1367-9120, 2022. http://dx.doi.org/10.1016/j.jseaes.2022.105116

Shamim, S; Khan, P. K; Mohanty, S. P; Mohanty, M. Andaman-Nicobar-Sumatra Margin Revisited: Analysis of the Lithospheric Structure and Deformation Based on Gravity Modelling and Distribution of Seismicity. Surveys in Geophysics, 0169-3298, 2021. http://dx.doi.org/10.1007/s10712-021-09633-9

Sharma, G; Kannaujiya, S; Gautam, PKR; Taloor, AK; Champatiray, PK; Mohanty, S. Crustal deformation analysis across Garhwal Himalaya: Part of western Himalaya using GPS observations. Quaternary International,1040-6182, 2021. http://dx.doi.org/10.1016/j.quaint.2020.08.025

Sharma, Y; Pasari, S; Ching, K.E; Dikshit, O; Kato, T; Malik, J.N; Chang, CP; Yen, J. Y., Spatial distribution of earthquake potential along the Himalayan arc, Tectonophysics, 0040-1951,2020. http://dx.doi.org/10.1016/j.tecto.2020.228556

Sen, R, Dibyashakti Panda, Bhaskar Kundu, M. Santosh,Mountain height as a proxy for the cessation of active plate convergence,Geosystems and Geoenvironment,2,4,100189,ISSN 2772-8838, 2023, https://doi.org/10.1016/j.geogeo.2023.100189.

Singh, A., & Rao, G. S. Crustal structure and subsidence history of the Mannar basin through potential field modelling and backstripping analysis: Implications on basin evolution and hydrocarbon exploration. Journal of Petroleum Science & Engineering, 206, 109000, 1-13, 2021.

Singh, A.P., Kumar, N., Rao, B.N. et al. A Short Walk through Gravity Studies at CSIR-NGRI, India. Journal of Geological Society of India, 97, 1121–1134 (2021). https://doi.org/10.1007/s12594-021-1841-9

Singh, A.P; Niraj Kumar, B. Nageswara Rao, V.M. Tiwari. Geopotential evidence of a missing lithospheric root beneath the eastern Indian shield: An integrated approach, Precambrian Research,356,2021,106116,0301-268, https://doi.org/10.1016/j.precamres.2021.106116.

Singh, K.K; Ranjan, S.K; Biswas, S; Mandal, B.C; Bagchi, J, Crustal Mapping of Northern Extremity of Aravalli Delhi Fold Belt (ADFB) by High Resolution Gravity Survey in Haryana, India. Journal of The Geological Society of India, 0016-7622, 2022, http://dx.doi.org/10.1007/s12594-022-2067-1

Singh, S; Ghosh, A. Surface Motions and Continental Deformation in the Indian Plate and the India-Eurasia Collision Zone. Journal of Geophysical Research Solid Earth, 2169-9313, 2019 http://dx.doi.org/10.1029/2018JB017289

Sreejith, K. M; Agrawal, R; Rajawat, A.S. Constraints on the location, depth and yield of the 2017 September 3 North Korean nuclear test from InSAR measurements and modelling. Geophysical Journal International,0956-540X, 2020, http://dx.doi.org/10.1093/gji/ggz451

Sreejith, K. M; Jasir, M.C.M; Agrawal, R; Rajawat, A. S. The 2019 September 24, M-w=6, Mirpur earthquake, NW Himalaya: Geodetic evidence for shallow, near-horizontal decollement rupture of the Main Himalayan Thrust. Tectonophysics, 0040-1951,2021,http://dx.doi.org/10.1016/j.tecto.2021.229013

Srinivas, N., Tiwari, V. M. Gravity and geodetic studies in India: historical observations and advances during the past decade. Proceedings of The Indian National Science Academies, 85(2), 343-361, 2019. https://doi.org/10.16943/ptinsa/2018/49511

Swarnapriya C, Bijendra Singh, A.P. Singh,Anatomy of an intracratonic Son-Mahanadi Gondwana rift basin in Peninsular India: An integrated gravity, magnetic and remote sensing approach,Physics of the Earth and Planetary Interiors,328, 106888,0031-9201, 2022,, https://doi.org/10.1016/j.pepi.2022.106888.

Sutar, A. K; Roy, S; Tiwari, V.M. Revisiting the Koyna-Warna seismic zone: strain budget, present-day potential and associated hazard. Journal Of seismology,1383-4649,2021 http://dx.doi.org/10.1007/s10950-021-10024-1

Tiwari, A; Narayan, A. B; Dwivedi, R; Swadeshi, A; Pasari, S; Dikshit, O. Geodetic investigation of landslides and land subsidence: case study of the Bhurkunda coal mines and the Sirobagarh landslide. Survey Review, 0039-6265,2020, http://dx.doi.org/10.1080/00396265.2018.1531654

Tiwari, D.K., Jha, B., Kundu, B. et al. Groundwater extraction-induced seismicity around Delhi region, India. Sci Rep 11, 10097, 2021. https://doi.org/10.1038/s41598-021-89527-3Varade, D., Dikshit, O. Potential of multispectral reflectance for assessment of snow geophysical parameters in Solang valley in the lower Indian Himalayas. GIScience & Remote Sensing, 57(1), 107-126, 2020. https://doi.org/10.1080/15481603.2019.1672365

Varade, D., Manickam, S., Dikshit, O., Singh, G., Snehmani,. Modleling of early winter snow density using fully polarimetric C-band SAR data in the Indian Himalayas. Remote Sensing of Environment, 240, 111699, 2020. https://doi.org/10.1016/j.rse.2020.111699

Varade, D., Maurya, A.K., Dikshit, O., Singh, G., Manickam, S.,. Snow depth in Dhundi: an estimate based on weighted bias corrected differential phase observations of dual polarimetric bi-temporal Sentinel-1 data. International Journal of Remote Sensing, 41(8), 3031-3053, 2019. https://doi.org/10.1080/01431161.2019.1698076

Varade, D., Singh, G., Dikshit, O., Manickam, S.,. Identification of snow using fully polarimetric SAR data based on entropy and anisotropy. Water resources research. 56(2), 2020, e2019WR025449. https://doi.org/10.1029/2019WR025449

Vasanthi, A. and Santosh, M. A Gondwanan micro-fragment adjacent to southern granulite terrane of India: Evidence from satellite gravity studies. Physics of The Earth and Planetary Interiors, 322, 106832,2022b, https://doi.org/10.1016/j.pepi.2021.106832.

Vasanthi, A. and Santosh, M. Regional gravity field distribution over cratonic domains of the Indian Shield: Implications for lithospheric evolution and destruction. Geosystems and Geoenvironment, 1, 100010, 2022a, https://doi.org/10.1016/j.geogeo.2021.100010.

Vasanthi, A. Geotectonic evolution of prominent rift structures beneath Deccan Volcanic Province: Inferences from satellite gravity studies. Journal Earth System Science, JESS-Topical Collection: Deccan Traps and other Flood Basalt Provinces – Recent Research Trends, 131, 101, 2022c, https://doi.org/10.1007/s12040-022-01860-x

Vasanthi, A. Lithospheric structure and geodynamical evolution of the Laxmi Ridge: new inferences from satellite gravity studies. Geo-Marine Letters, 0276-0460, 2022, http://dx.doi.org/10.1007/s00367-022-00737-8

Vasanthi, A., Singh A.P., Niraj Kumar, Nageswara Rao B., Satyakumar A.V., Santosh, M. Crust-mantle structure and lithospheric destruction of the oldest craton in the Indian shield. Precambrian Research, 362, 106280, 2021a, https://doi.org/10.1016/j.precamres.2021.106280.

Vasanthi, A; Santosh, M. Lithospheric architecture and geodynamics of the Archean Dharwar craton and surrounding terranes: New insights from satellite gravity investigation. Gondwana Research, 1342-937X,2021b, http://dx.doi.org/10.1016/j.gr.2021.03.008

Vasanthi, A; Santosh, M. Overview of regional gravity field computation models and application of a novel method in imaging the lithospheric architecture and destruction of the North China Craton. Earth-Science Reviews,0012-8252, 2021, http://dx.doi.org/10.1016/j.earscirev.2021.103548

Xie, L; Xu, WB; Burgmann, R; Ding, XL; Gahalaut, VK; Mondal, S. Tehri Reservoir Operation Modulates Seasonal Elastic Crustal Deformation in the Himalaya. Journal of Geophysical Research Solid Earth,2169-9313,2021,http://dx.doi.org/10.1029/2020JB021122

Yadav, R. K; Gahalaut, V. K; Bansal, A. K; Sati, S. P; Catherine, J; Gautam, P; Kumar, K; Rana, N. Strong seismic coupling underneath Garhwal-Kumaun region, NW Himalaya, India, 0012-821X,2019, http://dx.doi.org/10.1016/j.epsl.2018.10.023.

Yadav R. K, Martin SS, Gahalaut VK Intraplate seismicity and earthquake hazard in the Aravalli–Delhi fold belt, India. J Earth Syst Sci 131:204, (2022), https://doi.org/10.1007/s12040-022-01957-3

Yadav, R.K; Gahalaut, V. K; Bansal, A. K. Tectonic and non-tectonic crustal deformation in Kumaun Garhwal Himalaya,1040-6182,2021,http://dx.doi.org/10.1016/j.quaint.2020.10.011

Yadav, R. Tiwari, V.M. A three-dimensional density model of north Andaman subduction zone, Journal of Geodynamics,129, 247-261,0264-3707, 2019, https://doi.org/10.1016/j.jog.2018.09.005.

Yadav, R. Tiwari, V. M. Lithospheric Framework of Sumatra–Andaman Subduction Zone—A Review The Andaman Islands and Adjoining Offshore: Geology, Tectonics and Palaeoclimate, 2020, 978-3-030-39842-2(Chapter)

Indian National Report for IAGA (2019 - 2023)

Kusumita Arora

CSIR-National Geophysical Research Institute, Hyderabad, India

Salient points of progress of the research on various aspects of geomagnetism and aeronomy from India during 2019–2023 are presented in this report. It may be noted that the report cannot be considered as a fully comprehensive review of all the achievements during 2019–2023 in these fields of science in India. A report on the 3rd IAGA IASPEI Joint Scientific Assembly hosted by CSIR National Geophysical Research Instituted in August 2021 is also included.

Salient Scientific Results

1 Internal Magnetic Fields

1.1 Numerical Dynamo Simulation

Earth's magnetic field is generated by a dynamo in its liquid core, which convects in response to non-uniform heat flow in the overlying mantle. Research performed at the Centre for Earth Sciences, Indian Institute of Science, has aimed at understanding the axial dipole structure of the magnetic fields of rotating planets and how the Earth's field evolved, subject to a large mantle heterogeneity.

Isolated density disturbances in planetary cores generate fast and slow dynamo waves, called Magnetic-Archimedean-Coriolis (MAC) waves, under the combined influence of background rotation, magnetic field and unstable stratification. Of these, the slow MAC waves are magnetostrophic waves, generated from localized balances between the magnetic (Lorentz), Coriolis and buoyancy forces. In a rotationally dominant regime, the slow waves were shown to be essential for dipole formation (*Sreenivasan & Maurya, 2021; Varma & Sreenivasan, 2022*). This study would in turn place a powerful constraint on the parameter space that admits magnetic polarity reversals in Earth and other planetary bodies. Reversals (Figure 1) occur in a regime where the slow MAC waves are suppressed in a strongly driven dynamo. The analysis of dynamo waves in a forced damped system also placed a lower bound of ~10 km for the flow length scale that supports slow waves in the Earth's core.

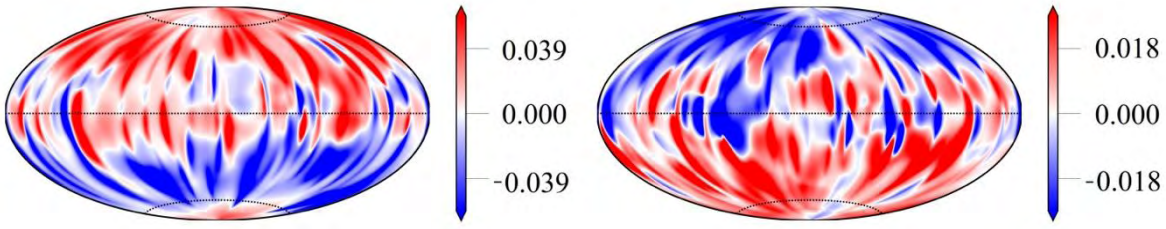

Figure 1: Normal and reversed field polarity in a numerical dynamo simulation.

A simplified two-fold pattern of convection in the Earth's core is often used to explain the non-axisymmetric magnetic flux concentrations (or lobes) in the present-day geomagnetic field. For large lateral variations in the lower mantle heat flux, however, a substantial east–west dichotomy in core convection is expected. Strongly forced convection in an annulus subject to lateral variations in heat flux at the outer boundary indicated a coherent long-lived downwelling beneath Siberia and time-varying convection beneath Canada in the Earth's core (see Figure 2 and *Sahoo & Sreenivasan, 2020*). This pattern of convection was reproduced in spherical shell convection models. Spherical shell dynamo models in turn showed that this eastward preference for coherent convection may cause the relative instability or even the occasional disappearance of the high-latitude magnetic flux in the Western hemisphere.

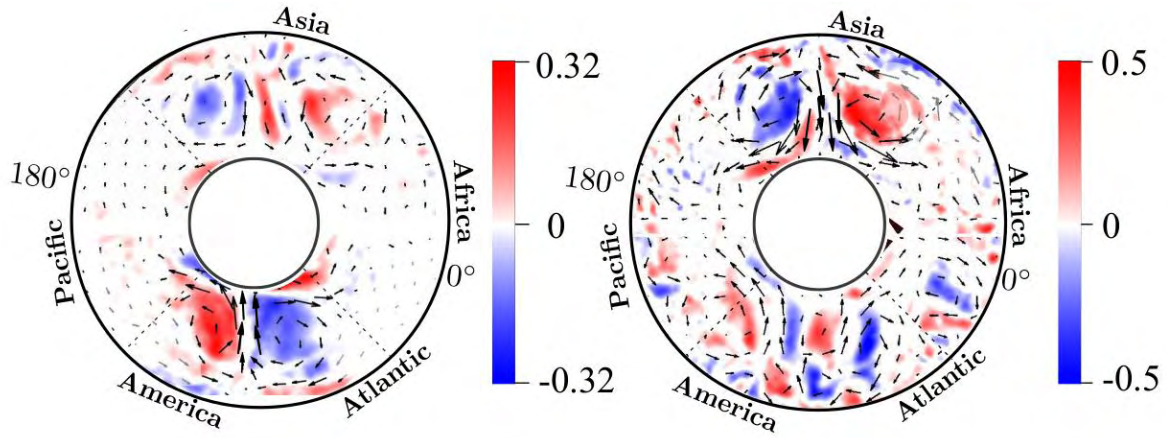

Figure 2: Axial vorticity (colours) and radial velocity (arrows) on a horizontal section in annulus experiments at moderate and strong forcing, shown in the left and right panels respectively.

1.2 Archeointensity Studies

Archaeointensity investigation were carried out at the Indian Institute of Geomagnetism, on bricks from a Buddhist monument at Adurru in the Godavari delta and a medieval fort at Kolleti Kota site situated on an island in the Kolleru Lake, Andhra Pradesh. The archaeointensity value of 44.6±1.4 μT for Adurru site (third century BCE) and mean site value of 36.6±2.9 μT for Kolleti Kota (4^{th} and 7^{th} centuries CE) were obtained. New archaeointensity results were derived from four historical sites situated at Ter, Junnar, Nalasopara and Kanheri in Maharashtra region (*Deenadayalan et al., 2020*). After anisotropy and cooling rate corrections, the calculated archaeointensity value for Nalasopara (third century BCE) is B_{anc}=37.07 ±3.8 μT and for Kanheri (first century BCE) it is B_{anc}=34.52±4.9 μT. Ter has given a mean archaeointensity value of B_{anc}=39.44±4.6 μT (fourteenth century CE) and a mean B_{anc} value of 37.46±3.0 μT (third century BCE) was obtained for Junnar. The secular variation curve in comparison to other global data sets in shown in Figure 3.

Figure 3: The new Indian archeointensity values along with earlier data, compared to global models (calculated to Maharashtra region coordinates)

A relative palaeointensity determination was obtained using the pseudo-Thellier technique on sediment from Ther, Tirna Basin, Latu-Osmanabad District, Maharashtra, India. The stability of the natural remanent magnetization was investigated by alternating field (AF) demagnetization. To varying degrees, the smoothed palaeo inclination and palaeo declination patterns of the Tirna Basin are similar to other Asian palaeosecular variation records CALS3k.4, CALS10k.1 and SED3k.1, with an age offset (*Lakshmi et al., 2020*).

2. **Aeronomic Phenomena**

2.1 MLT region dynamics

PRL has conducted research in the areas of Mesosphere Lower Thermospheric (MLT) dynamics; effects of Sudden Stratospheric Warming events; Characterizing gravity waves; Long term variability of equatorial electrodynamic processes; Dayglow and nightglow observations; Interplanetary medium-magnetosphere connection, Solar wind and suprathermal energetic particles etc. The relationship between the quasi-two-day wave (QTDW) and solar variability during summer in the MLT is studied using long-term meteor wind observations from an extratropical station, Cachoeira Paulista (22.7°S, 45°W) in the Southern hemisphere. Overall, the seasonal (summer) mean and monthly mean zonal amplitude of the QTDW show a negative correlation and the meridional amplitude exhibits a positive correlation with the solar F10.7 flux in the MLT. Both amplitude and period of the QTDW show slightly higher values in solar minimum and lower values in solar maximum within the limit of standard deviation indicating a weak, but measurable response to the solar cycle (*Guharay et al., 2019*).

The modulation of the dominant atmospheric tides in the mesosphere and lower thermosphere (MLT) is investigated using long-term meteor wind database from three Southern hemispheric

low-latitude locations. The spectral analysis reveals an evident and intermittent signature of a 27-day oscillation in the tidal amplitudes. The strong correlation between the solar variability and tidal modulation in the concerned period with positive lags at certain intervals indicates solar influence on the MLT tides (*Guharay et al., 2020*). A signature of quasi-90-day oscillation is found in the winds and tides in the MLT from an equatorial station, São João do Cariri. The maximum amplitude of the oscillation is found to be around 10 m/s in the zonal wind. Similar oscillation feature in the tropospheric zonal wind and ozone may imply its lower atmospheric origin as a component of the intra-seasonal oscillation (ISO) that moves upward by modulating the tides. Subsequently, the propagating tides (mainly semidiurnal) are enhanced by the ozone in the stratosphere through absorption of solar UV radiation and finally manifest the oscillation in the MLT (*Guharay et al., 2021*).

A conspicuous and intermittent signature of a 120-day oscillation is found in the winds and tides in the mesosphere and lower thermosphere (MLT) over a Southern hemispheric equatorial station, São João do Cariri for the first time using meteor radar observations during the interval 2004–2008. The 120-day modulation amplitude is higher (maximum ~ 5 m/s) in the diurnal and semidiurnal tides and relatively smaller in the terdiurnal tide (peak ~ 2 m/s). Existence of the same periodicity in the solar UV flux may indicate a plausible indirect solar connection with the MLT circulation although direct solar influence cannot be ascertained (Figure 4), (*Guharay et al., 2020*).

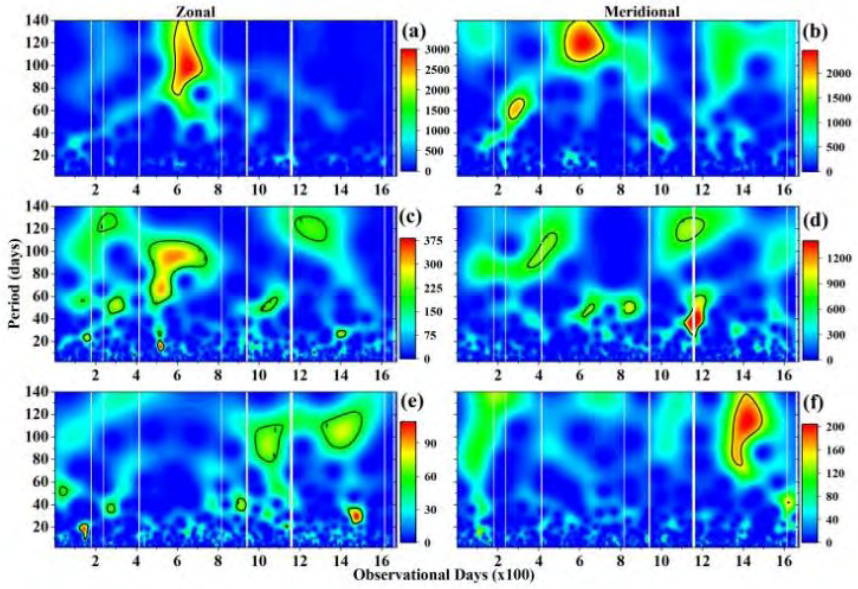

Figure 4: Wavelet power ($m^2sec^{-2}day^{-1}$) spectra estimated using daily tidal amplitudes at 90 km for diurnal tide (a-zonal, b-meridional), semidiurnal tide (c-zonal, d-meridional) and ter-diurnal tide (e-zonal, f-meridional).

Solar cycle dependence of the dominant tides, i.e. diurnal and semidiurnal components in the mesosphere and lower thermosphere (MLT) is investigated from a Southern hemispheric low-latitude station, Cachoeira Paulista (22.7oS, 45oW) using long-term meteor wind observations (1999–2018). The diurnal tide seasonal profiles show negative correlation with the solar activity and the semidiurnal tide exhibits both negative and positive correlations. The zonal diurnal tide shows positive correlation with the solar flux in the upper MLT in solar minima. However, the meridional semidiurnal tide reveals negative correlation in solar minima

condition. No evident relationship between the tides and solar flux is found in solar maxima condition (*Guharay et al., 2019*).

2.2 Thermosphere-Ionosphere System

Earth's upper atmosphere is enveloped by a coupled thermosphere-ionosphere (T-I) system, which acts as a first line of defence for earth to the upcoming solar energy during solar or geomagnetic storms. PRL investigated the response of the T-I system during such events. One of the objectives is to analyse the heating and cooling mechanisms of this coupled system. This aspect is investigated during multiple geomagnetic storms including a composed superstorm (the Halloween storms), which occurred in late October (27 Oct. to 1 Nov.) 2003 (*Ranjan et. al., 2023*). Nitric Oxide is a very important trace species which plays a significant role acting as a natural thermostat in Earth's thermosphere during strong geomagnetic activity. NO radiative cooling converts the enhanced kinetic energy of the lower thermosphere (caused by storm induced Joule heating) to the radiative energy of 5.3 μm, and thus cools the T-I system. The contribution of the 135.6 nm emission originating from the ionospheric O^+ radiative recombination can significantly alter the magnitude and location of the O/N_2 ratio increase as observed by GUVI (both TEC or O^+ density and O/N_2 enhancements are in low-mid northern hemispheric latitudes of northern American region; *Ranjan et. al, 2023*).

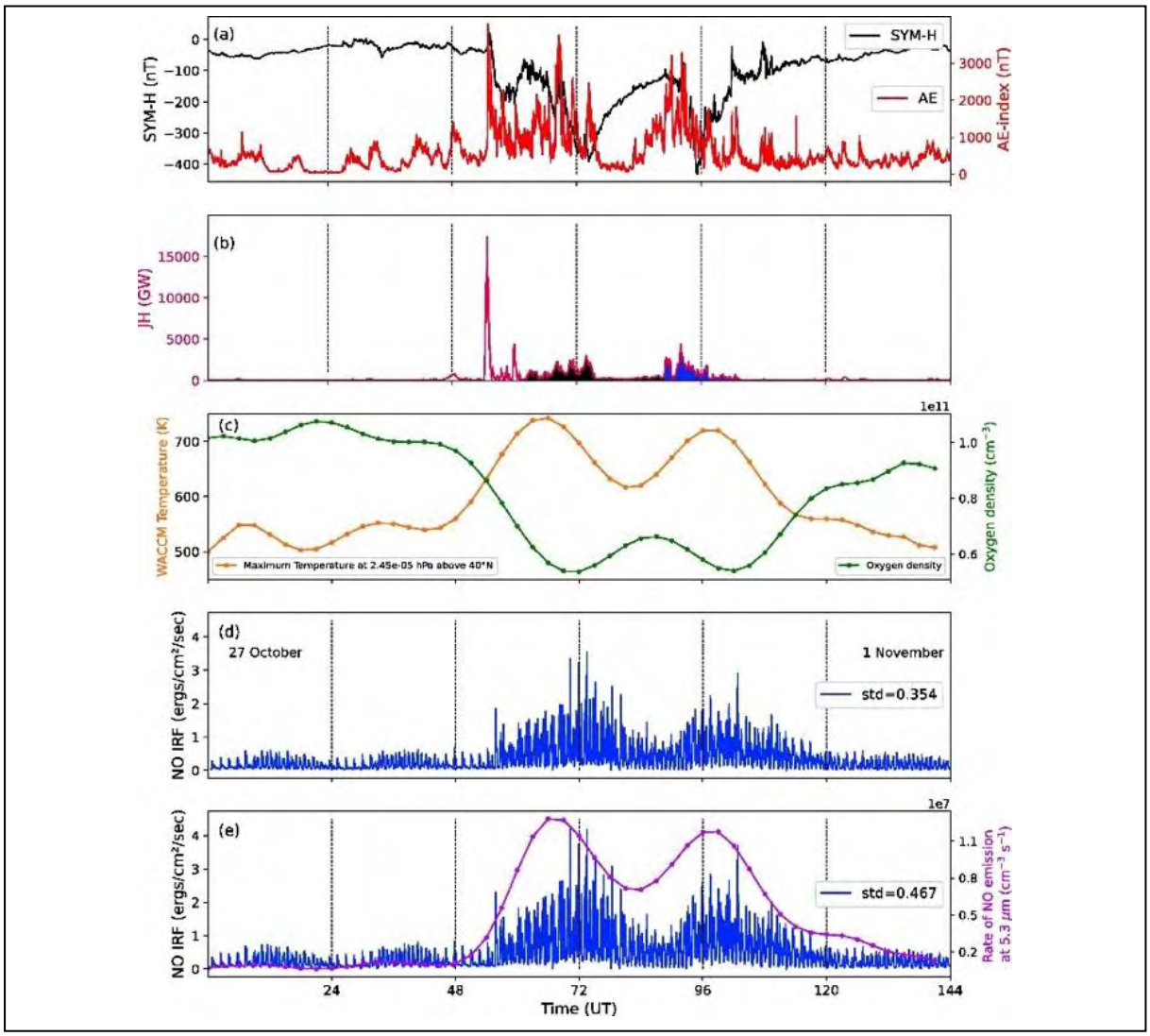

Figure 5: NO cooling response in Asian sector

In another study, the NO cooling response in the thermosphere over Asian sector during two other geomagnetic storms during 26–29 September 2011 and 18–21 February 2014 (*Bharti et al., 2019*) is analysed. It was found that the peak emission of NO cooling is strongly influenced by the storm conditions, being maximum at higher latitudes during the storms and gradually decreasing towards the Equator, shown in Figure 5. The modelled atomic oxygen number density showed depletion at the higher latitudes corresponding to peak altitude of NO cooling (Figure 6).

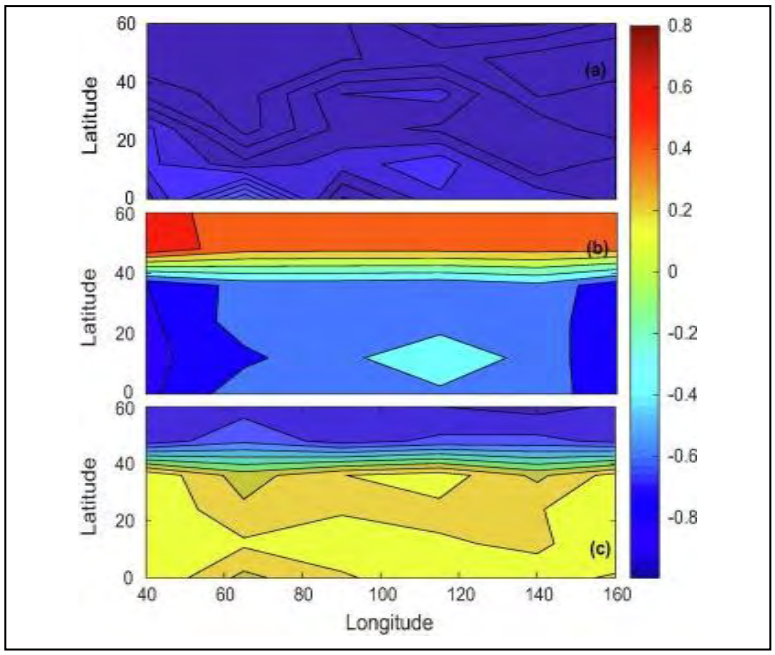

Figure 6: Radiative cooling due to NO at 5.3 μm emission

Investigation of the middle atmospheric tidal response to the September 2002 sudden stratospheric warming (SSW) is carried out from a southern hemispheric extra-tropical location Cachoeira Paulista (22.7°S, 45°W) using meteor radar observations and reanalysis database. Significant diurnal and semidiurnal tidal amplitudes are found in the mesosphere and lower thermosphere (MLT) a few days prior to the warming onset consistent with the high latitude observations. A preferential modulation of the tidal amplitudes by long/short period planetary waves are observed in the MLT/TS. The migrating diurnal tide (DW1) and nonmigrating semidiurnal tide (SW1) at 10 hPa pressure level show considerable variability during the warming episode (*Guharay et al., 2019*).

Tidal variability in the mesosphere and lower thermosphere (MLT) during September 2019 southern hemisphere minor sudden stratospheric warming (SSW) is investigated utilizing ground-based meteor radar wind observations from the equatorial, extratropical, middle, and high latitude stations and global reanalysis dataset. A few global tidal modes, DW1, DE3, and SW2 show significant variability during 2019 minor SSW. It is found that the seasonal broad changes in the DW1, DE3, and SW2 amplitudes can be explained by the variability in the tidal sources, i.e., water vapour, convective activity, ozone, etc. during the observational period. The de-seasoned tidal features do not seem to correlate well with that of the source species unlike the seasonal ones (*Mitra et al., 2022*).

2.3 Influence of the Sudden Stratospheric Warming (SSW) effect on the Equatorial Ionosphere

This study by SPL, brought out that the equatorial ionosphere responds in distinctly different ways to the Sudden Stratospheric Warmings (SSWs) that occurred during different phases of the stratospheric Quasi-Biennial Oscillation (QBO). The peaking time of the Equatorial Electrojet (EEJ) and occurrence time of Counter Electrojet (CEJ) displayed shift towards morning/evening sector during the westward/eastward phase of the QBO (Figure 7). The

analysis revealed that the enhancement and depletions seen in TEC over both the equatorial and low-latitude ionosphere displayed shifts towards morning/evening during the westward/eastward phase of the QBO. The upper mesospheric tides (diurnal and semidiurnal) estimated using a co-located meteor radar also exhibit similar shift in their phases. These observations clearly indicate that the phase of the QBO plays a crucial role in structuring the equatorial electrodynamics and electron density distribution over the low-latitudes during the SSW events.

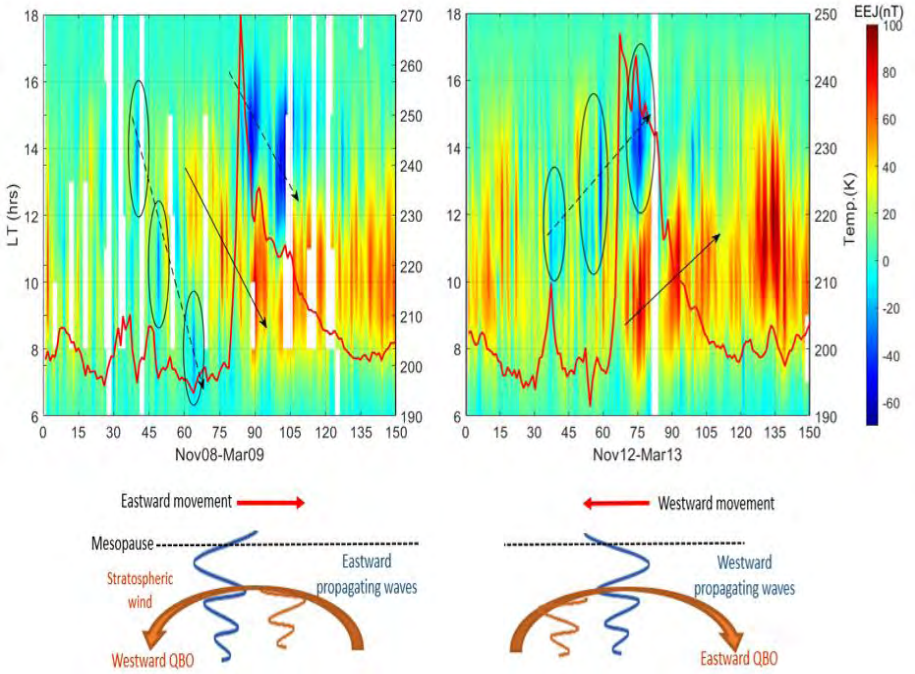

Figure 7: Schematic of the wave filtering during different phase of QBO and its manifestation of EEJ (*Yadav et al., 2019*).

Planetary wave (PW) associated dynamical variability in the equatorial and extratropical middle atmosphere during the September 2019 southern hemisphere minor sudden stratospheric warming (SSW) is investigated utilizing meteor radar wind observations from São João do Cariri and Cachoeira Paulista and reanalysis data. Signature of the mesospheric warming in conjunction with the stratospheric cooling is found at low latitudes. The wind spectra reveal a prevalent quasi-16-day wave (Q16DW) prior to the SSW and existence of a quasi-6-day wave (Q6DW) after the warming event. The Eliassen-Palm flux diagnosis shows the propagation of the Q6DW and Q16DW from mid to low latitudes during the warming event (*Mitra et al., 2021*). Based on the analysis of Ionosonde and Thermosphere Ionosphere Mesosphere Energetics and Dynamics (TIMED) satellite observations, SPL found that the dominant Planetary Wave (PW) in the equatorial ionosphere is of 16-day periodicity and its strength is maximum in winter solstice/ autumnal equinox and minimum in summer solstice in high solar activity conditions. In low solar activity years, the PW activity is more or less comparable in vernal equinox, autumnal equinox and winter solstice, while it is observed to be least in summer solstice. Further, the PW activity shows direct correlation with solar activity for different seasons (Figure 8). The off-equatorial E-region zonal winds measured by TIMED

satellite were found to be strong westward in high solar activity years compared to low solar activity years. The role of PWs in modulating the pre-reversal enhancement, equatorial spread-F duration and its spread range on a day-to-day basis is brought out quantitatively for both high and low solar activity conditions.

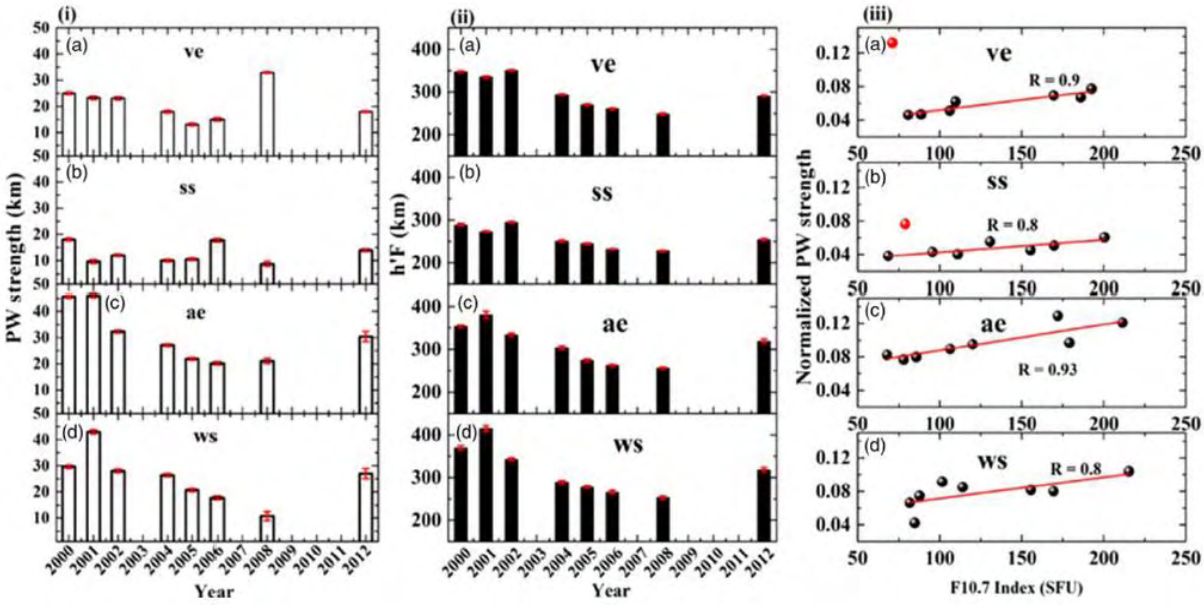

Figure 8: (i) Yearly variation of the seasonal average of the extracted power (strength) of PWs from h'F fluctuations. (ii) Yearly variation of the seasonal mean of h'F. (iii) The correlation of seasonal mean of F10.7 index and seasonal mean of normalized planetary wave strength (*Manju and Aswathy, 2021*).

SPL studied the response of the equatorial ionosphere to the noon time annular solar eclipse of January 15, 2010. The observations were made using collocated Digisonde, Meteor Wind Radar and Proton Precession Magnetometer over Trivandrum, (8.5^o E; 77^o N; diplat 0.5^o N). It was found that the E, F_1 and F_2 regions of the equatorial ionosphere responded to solar eclipse with different time delays, F1 responding fast and the E and F2 regions relatively slow (Figure 9). Though the delayed response of F2 region is known, the delayed response of E region is quite unexpected since it is dominated by the recombination chemistry and expected to respond immediately. The plausible reasons for the observed delay has been explored and it is suggested that the downward diffusion of atomic oxygen plays a major role as the diffusion rates are known to be slower than the chemical recombination rates.

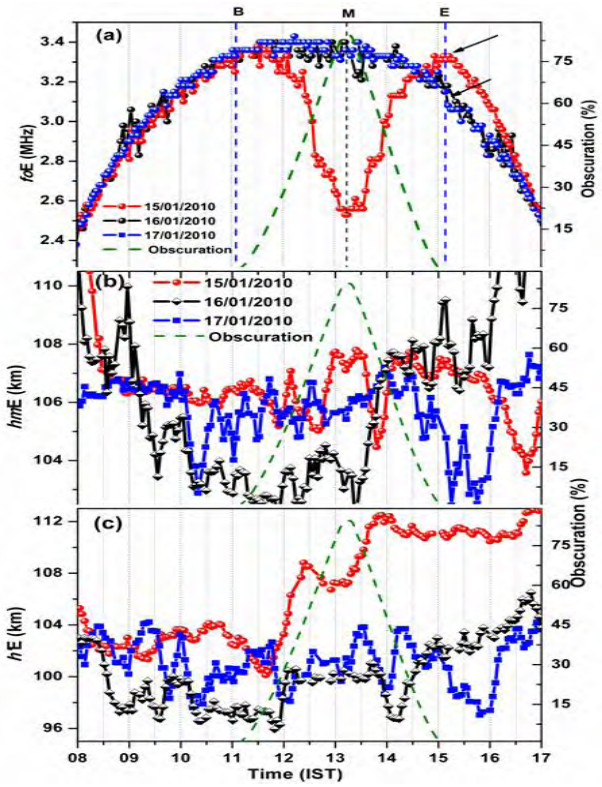

Figure 9: The time variation of (a) critical frequency of E-region (foE),(b) peak height (hmE) and (c) minimum virtual height of E region (h'E) on the day of the eclipse (15/01/2010) and the background days (16/01/2010 and 17/01/2010). The dashed green line shows the percentage of obscuration and the arrows represent the foE enhancement after the eclipse (*Jose et al., 2020*).

2.4 Characterizing gravity waves

PRL used radio wave measurement technique (digisonde) to obtain information on the neutral GW behavior. It involves monitoring of variations in the heights of isoelectron densities as a function of time, and their phase shifts, if any, to derive vertical propagation speeds and scale sizes of GWs. The daytime values of GW time periods, vertical phase speeds, and vertical scale sizes obtained for the duration of 16–21 May 2015 are in the range of 1.47 ± 0.05 to 2.64 ± 0.07 hr, 30.06 ± 4.35 to 45.69 ± 11.84 m/s, and 183.21 ± 39.23 to 393.07 ± 66.38 km, respectively. This method of deriving neutral GW characteristics is effective for the daytime conditions and opens up new possibilities of investigations of the wave dynamical behavior in the upper atmosphere during all weather conditions (Figure 10), (*Mandal et al., 2019*).

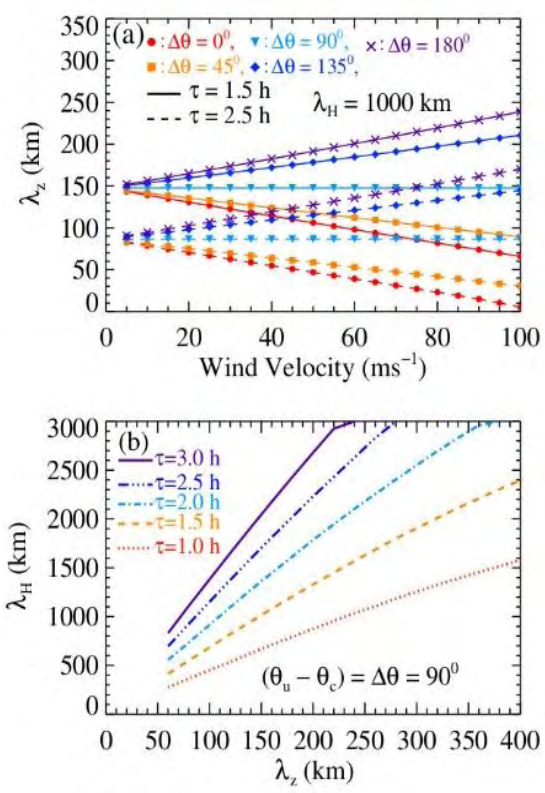

Figure 10: a) Simulation of gravity wave (GW) vertical scale sizes (λz) for horizontal scale size (λH) of 1,000 km (b) Simulation of λ H obtained for range of values of λz , at θ = 90◦ for GW time periods in the range of 1 - 3 hr

The seasonal variability in the vertical propagation characteristics of GWs in the daytime thermosphere over low-latitudes are examined during both geomagnetic quiet and disturbed times using digisonde observations over Ahmedabad. During geomagnetic quiet times, the magnitudes of vertical propagation speeds of GWs and their vertical wavelengths show seasonal variation and vary in the range of 10–70 ms−1 and 70–520 km, respectively. Changes in the vertical propagation characteristics of GWs during geomagnetic disturbed days show good correlation with the integrated values of the AE index. Such information can form definitive inputs to the modelling and simulation studies to understand the GW dynamics in the daytime (*Mandal et al., 2020*).

The systemic behaviour of gravity wave dynamics during daytime, in terms of their occurrence and propagation characteristics in the vertical direction and their relation to changes in Solar flux are examined using digisonde observations. Investigation of gravity waves by radio measurements, unlike the conventional optical techniques, which are limited to clear sky conditions alone, enable an unhindered study of gravity wave dynamics in all weather conditions. We find that the gravity wave activity shows a very good correlation with Solar F10.7cm flux. Also, we have found a very good correlation between the variations in derived vertical phase speeds of gravity waves in the thermosphere and Solar F10.7cm flux (Figure 11), (*Mandal et al., 2020*).

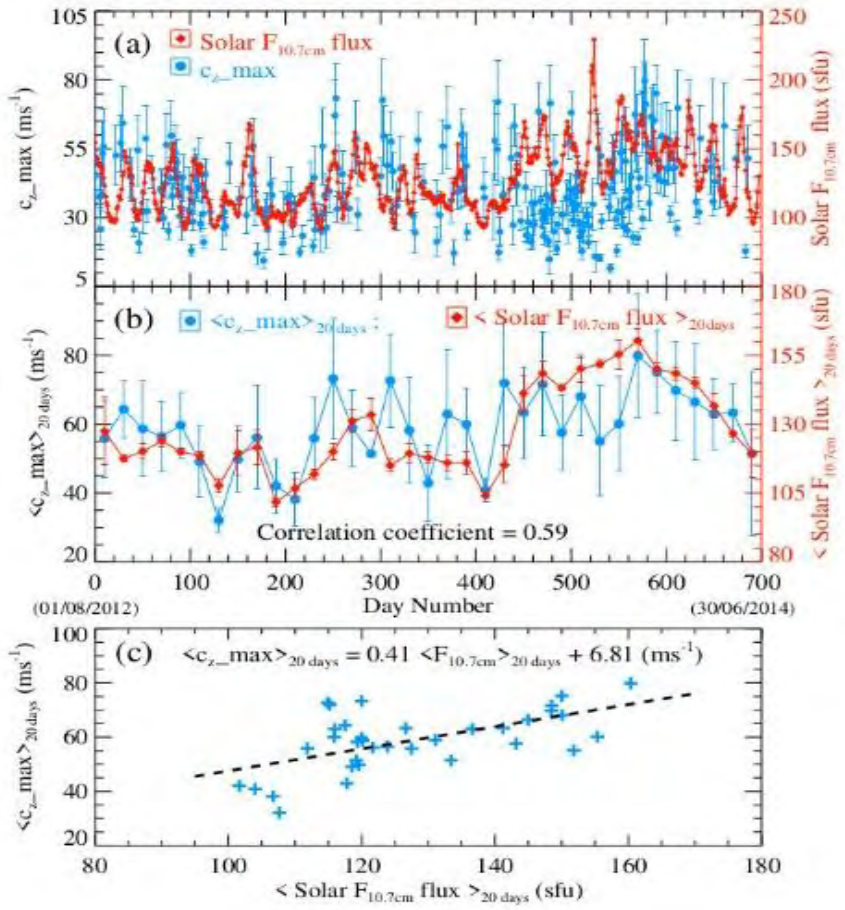

Figure 11: a) Distribution of daily maximum values of vertical phase propagation speeds (cz) (cyan colored circles) along with variation in Solar F10.7cm flux (red colored diamonds). (b) Maximum values of cz over 20 days window (cyan colored curve with circles) and 20-day averaged values of the Solar F10.7cm flux (red colored curve with diamonds). (c) Maximum cz in every 20 day window is plotted as a function of 20- day averaged values of Solar F10.7cm flux. The least- square fit between these two is shown as a dashed line.

2.5 TIDs and Equatorial Spread F during geomagnetically disturbed periods

The control of magnetic disturbance induced seed perturbations on the daily variation in ESF occurrence over Trivandrum is studied using ionospheric and thermospheric (neutral) density measurements through ionosonde and GUVI onboard TIMED satellite respectively. The study revealed that there is a requisite threshold seed amplitude for the ESF to occur at a particular altitude, which increases as the altitude decreases. This dependence of requisite seed perturbation on altitude for multiple years was used as the basis for developing an empirical model to hind-cast ESF. The model is also validated for high and low solar activity periods with 92% and 50% success rate respectively (Figure 12). The geomagnetically disturbed period requisite seed amplitudes are higher than those for quiet periods at a given altitude. This study underlines the importance of disturbance induced seed perturbations and neutral density in controlling the occurrence of ESF.

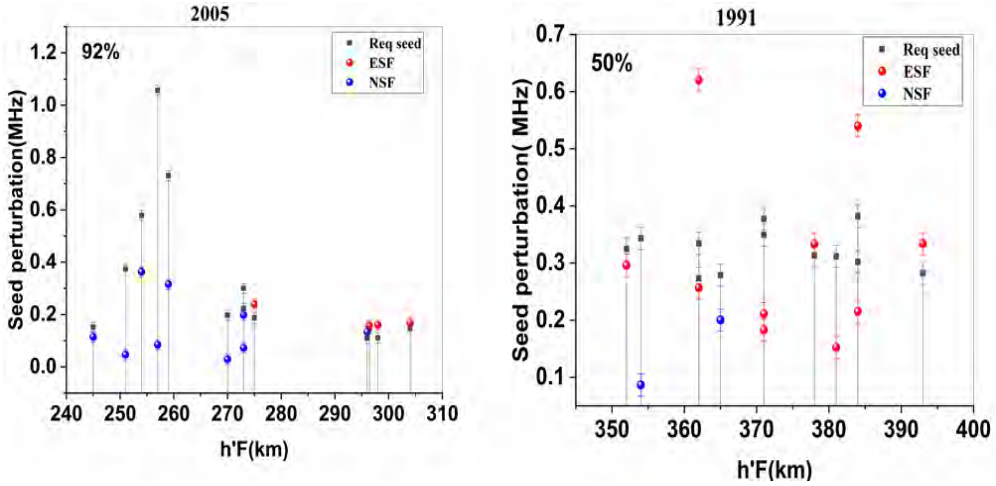

Figure 12: Variation of h'F-vs-Seed perturbation's amplitude for the ESF and NSF days of 2005 (left panel) and 1991 (right panel) along with the model derived requisite seed perturbations (*Shruthi and Manju, 2022*).

An observational evidence of medium-scale traveling ionospheric disturbances (MSTIDs) reaching to magnetic latitude as low as ~3.5° over the Indian sector is provided for the first time based on OI 630-nm airglow imaging observation from a low-latitude station, Gadanki (13.5°N, 79.2°E; 6.6° magnetic latitude), on 12 January 2016. Quasiperiodic southward moving waves (QPSMW) and a small-scale southward moving wave signature are also observed in addition with the MSTID. Global Positioning System-total electron content maps suggest that the weak and asymmetric equatorial ionization anomaly helped deep ingression of the MSTID on this night. It is found that the midlatitude MSTIDs can influence the F region plasma processes even over very low latitudes under favourable background conditions (*Mani et al., 2019*).

2.6 Mid-latitude spread-F structures during solar minimum

Equatorial spread F (ESF) is usually observed after sunset, but during solar minimum periods it can also be seen in the later hours of the night. Using coincident airglow imaging, VHF radar, and ionosonde observations, IIG demonstrated that midlatitude-type instabilities can cause ESF over low and equatorial latitudes in the later hours of the night. The all-sky airglow imaging observations from Silchar (24.68°N, 92.76°E), India, during December 2018 revealed two simultaneous mesospheric fronts propagating orthogonally to each other on the night of 9 December 2018. Though one of the frontal structures resembled a mesospheric bore, the other frontal events did not satisfy a few of the requirements to be met for a bore. A notable finding has been a significant reduction in the OH emission gleaned from TIMED-SABER observations at the time of the frontal propagation noticed in all-sky images (*Chauhan et al., 2022*).

2.7 Ionospheric critical frequency foF2 in the Indian Sector

TIE-GCM model (Thermosphere Ionosphere Electrodynamics Global Circulation Model), run has been performed to understand its performance over Indian region. An extensive

intercomparison of ionospheric foF2 observations over Trivandrum and corresponding TIE-GCM simulations has been carried out for geomagnetically quiet days of the years 2002, 2006 and 2008, representing solar maximum, solar minimum and deep solar minimum conditions. In general, TIE-GCM simulations reproduced the trends of temporal and seasonal changes of foF2 over Trivandrum reasonably well for all the three solar activity conditions. The model underestimates the magnitude of changes in general, but, for the periods when ionospheric density bite out is prominent, the model gives an over estimation (Figure 13). This study brings out the efficacy of the model in simulating the temporal, seasonal and solar cycle variability of ionospheric foF2 over the equatorial Indian region.

Figure 13: The four panels, depict the TIE-GCM simulated foF2 values (red lines) and ionosonde measured foF2 values (black lines) during the four seasons of vernal equinox, summer solstice, autumnal equinox and winter solstice for the year 2008 (*Mridula et al., 2022a*).

2.8 Evolution of F3 layers over equatorial location of Thiruvananthapuram

Using long term data, a study has been carried out on various aspects of occurrence as well as vertical drift of F3 layer over the magnetic equatorial location, Trivandrum in India for the period 1990-2009 using ionosonde observations. The F3 layer occurrence exhibits a seasonal pattern which is prominent only during low solar activity periods. The solar cycle variability of F3 is brought out in the present study using data from solar cycle 22 and 23. The seasonal as well as solar activity dependence of the vertical drift of F3 layers is also brought out (Figure 14). The role of Counter Electrojet and the ensuing thermosphere-ionosphere coupling processes are proposed to be the reason for the above stated features of F3 layers' occurrence. The influence of thermospheric winds in determining the drift velocity is promulgated.

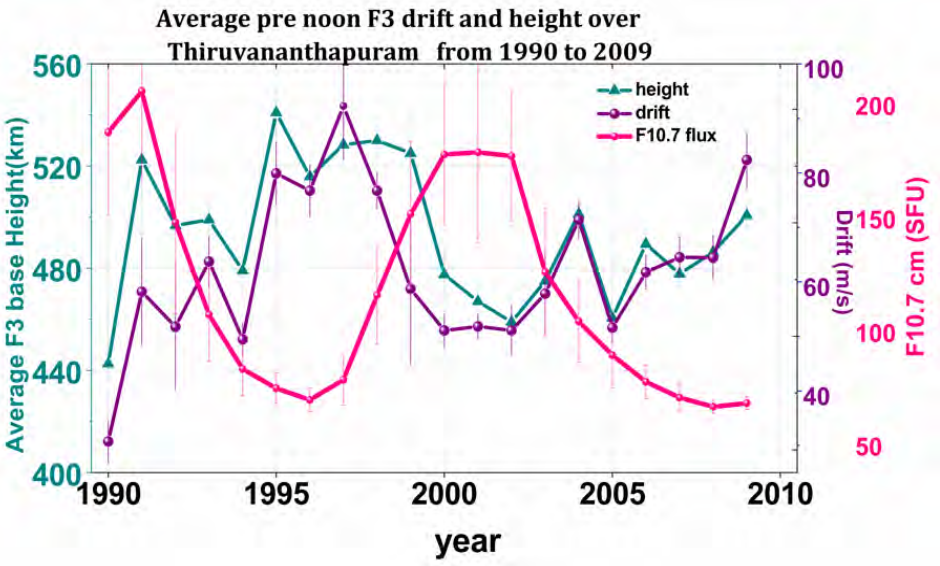

Figure 14: The annual mean drift and mean base height of pre-noon F3 layer over Thiruvananthapuram along with F10.7 cm solar flux. The error bars signify the standard error (*Mridula and Pant, 2022b*).

2.9 F-region zonal plasma drift variability

The study analysed the delayed occurrence of the F-region ionospheric features like peak vertical drift and Equatorial Spread-F (ESF) onset time in summer solstice of low solar activity years, using the ionosonde data over Trivandrum (8.5^o N, 76.9^o E) and Republic of China Satellite-1 data. The analysis revealed the unambiguous role of the time of ionospheric F-region zonal plasma drift/ wind reversal in modifying the above-mentioned phenomena. The direct control of ESF onset by the F-region drift/wind reversal was clearly established on a day-to-day basis in summer season. The role of the time of zonal wind/drift reversal in modulating the ESF onset was examined quantitatively by exploring its effect on the growth rate of Rayleigh-Taylor instability. Further, the study brings out the solar activity variation of the time of F-region zonal plasma drift/wind reversal for all seasons (Figure 15). The dependence of the F-region post sunset vertical drift on the zonal plasma drift was also brought out. The results highlight the need to have systematic neutral wind measurements to better address the enigmatic and multi-dimensional problem of ESF day-to-day variability.

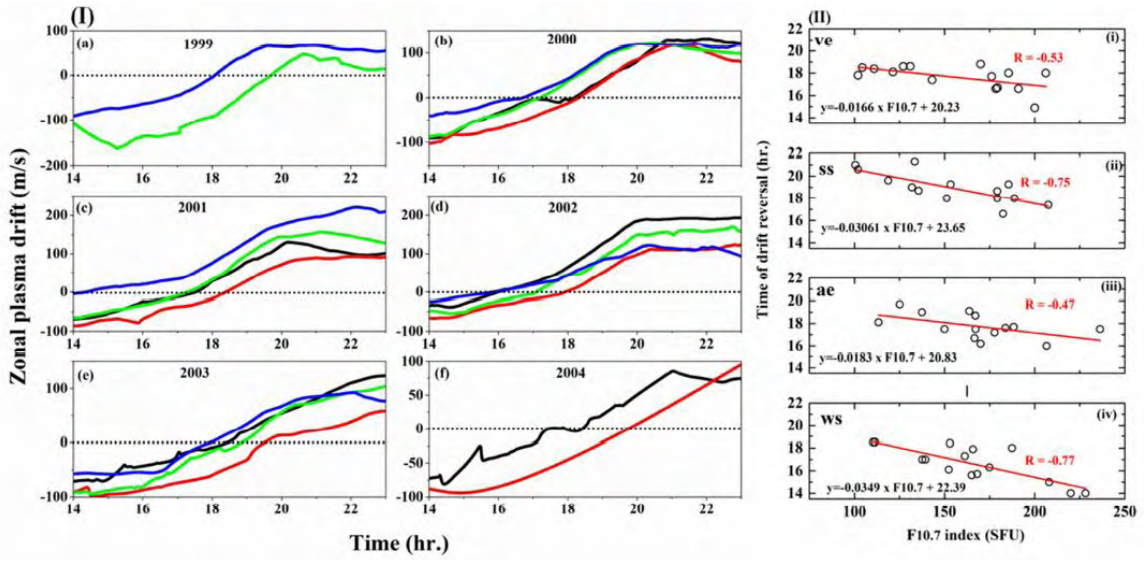

Figure 15: Seasonal pattern of the temporal variation of zonal plasma drift for the years 1999 to 2004 (ve - black curve, ss -red curve, ae -green curve and ws -blue curve) (II) The F10.7 variation of time of drift reversal for different months of all seasons (Aswathy and Manju, 2020).

2.10 The Post Sunset Equatorial F- region Zonal Drift Variability

The seasonal and solar activity variation of the post sunset F-region zonal plasma drift over Indian longitudes is examined using Republic of China Satellite-1 data for period January 2000 to April 2004. The dependence of the F-region peak vertical drift on the zonal plasma drift at 18.5 IST (Indian Standard Time) and the time difference of the conjugate points sunset times, were quantitatively analysed. Further, an integrated parameter, which is able to predict the peak vertical drift and growth rate of Rayleigh Taylor instability is proposed (Figure 16). The other major outcome is the successful prediction of the Equatorial Spread-F (ESF) onset time and duration using the new integrated parameter. The present methodology for the prediction of the characteristics of these nocturnal irregularities becomes significant in mitigating the hazardous implications of the same for communication and navigation.

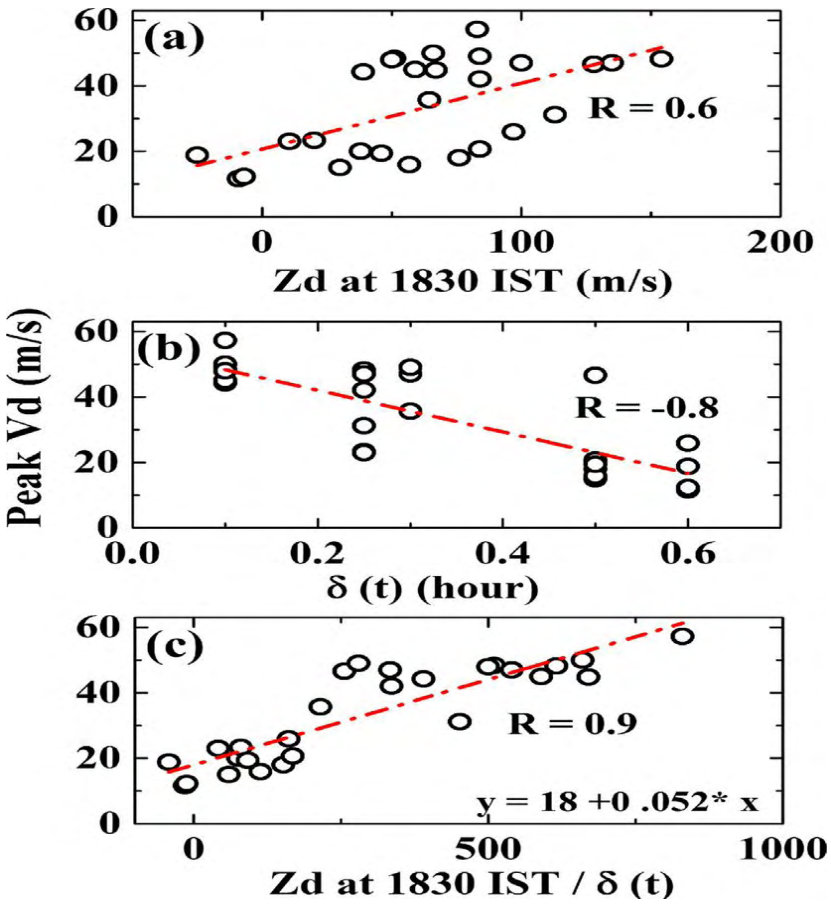

Figure 16: (a) Variation of monthly mean peak vertical drift V_d with peak zonal drift Z_d (b) Variation of the same with time difference 'dt' (c) Variation of the same with the integrated parameter (*Aswathy and Manju, 2021*).

2.11 Thermospheric Oxygen Airglow Emissions: Results from the First Ship-Borne Aeronomy Experiments from the Indian Region

This paper discusses the results from the aeronomy experiment carried out using a multiwavelength photometer operated onboard Sagar Kanya ship from the Indian region, which covered a latitude region from 14.5^o N to 2^o S (7^o to -10^o dip latitude) along the same longitude region (~72-75^o E). It has been found that the thermospheric airglows, especially the OI 630.0 nm emission near to the geographic equator exhibits 'Midnight Brightness' on different days of observations (Figure 17). Though the magnitudes were found to be less, the OI 777.4 nm and OI 557.7 nm emissions also exhibit intensity variations on those days, indicating a common causative mechanism for the same. The simulation studies using a quasi-two dimensional ionospheric model suggest that such an enhancement could be due to the F-region collapse associated with the Midnight Temperature Maximum (MTM) phenomenon.

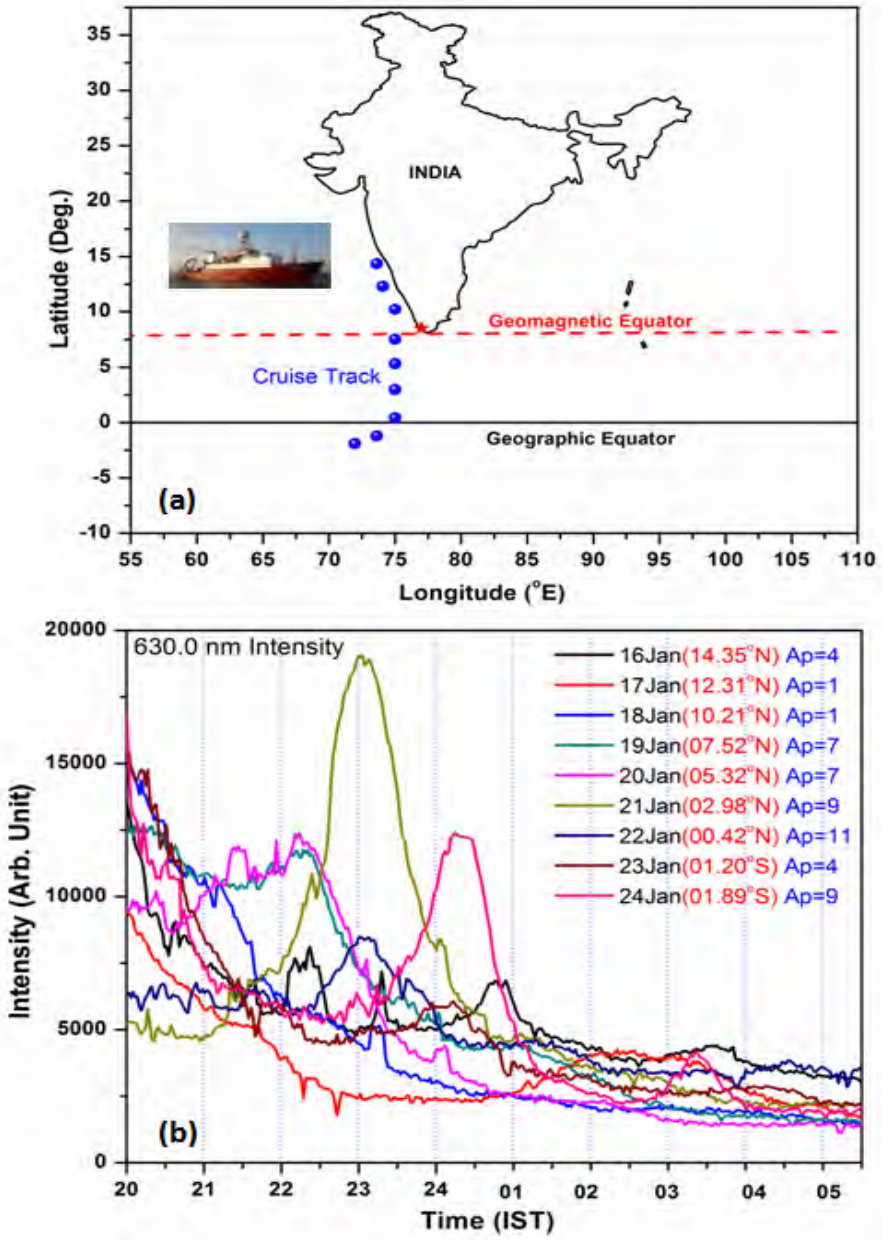

Figure 17: (a) Position of the ship during the period 16 January to 24 January 2018, where it traveled through the same longitude region. The location of the magnetic and geographic equators are shown in the figure as red dashed line and black solid lines respectively. (b) Time-latitude plot of the nocturnal OI 630.0 nm intensity during this period (*Vineeth et al., 2022*).

2.12 Behavior of Thermospheric O^1D 630.0 nm Dayglow Emission during Counter Electrojet Events

This study presents the response of thermospheric O^1D 630.0 nm dayglow emission to the variability associated with equatorial Counter Electrojet (CEJ) events. The analysis based on the data from a meridian scanning Dayglow Photometer, Digital Ionosonde and Proton Precession Magnetometer over Trivandrum (8.5°N, 77°E, 0.5°dip lat.), revealed that the O^1D 630.0 nm emission shows enhancement during the negative excursion of the ΔH, followed by an unusual depletion during the peak CEJ time (Figure 18). The observed variability was found to be more pronounced in a latitudinal region of ±3° centered at around the dip equator. In

addition, the emission intensities also exhibit the presence of enhanced short period oscillations of periodicity 20-30 minutes during the CEJ events. The simulation studies using a Quasi 2 dimensional ionospheric model showed that the modified plasma fountain during the CEJ can alter the plasma density at the emission centroid and hence explain the observed variability in dayglow emissions.

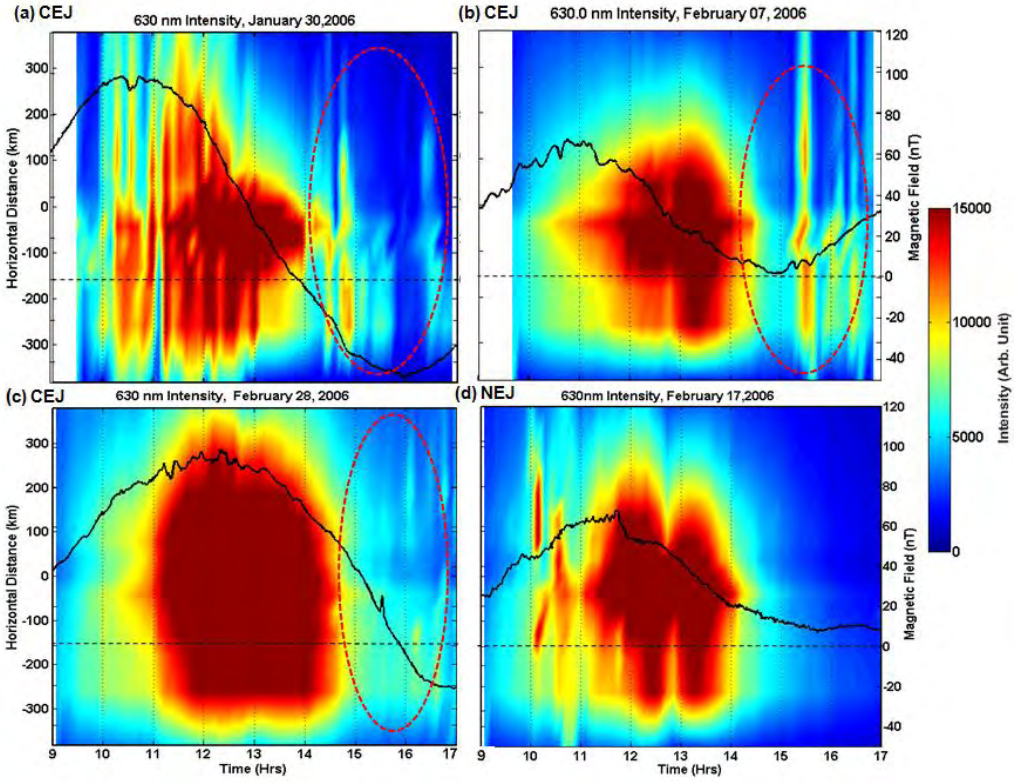

Figure 18: Time variation of EEJ Induced magnetic field and Spatio-temporal variation of thermospheric O^1D 630.0 nm emissions on January 30, 2006, February 07, 2006 and February 28, 2006 (CEJ days) along with the same on February 17, 2006 (NEJ day).

2.13 Airglow Imager in Himalayan region

IITR has installed a multi-wavelength airglow imager over the Indian Himalayan region at Hanle, Leh Ladakh, (32.77°N, 78.97°E; Magnetic latitude ~24.1°). This is the first of its kind that is installed in the Indian Himalayan region at an altitude of around 4200 m above the mean sea level, Figure 19. It is intended to observe intriguing phenomena in the mid-latitude of F region ionosphere: a least explored area over the Indian sector. The high-sensitive thermoelectrically cooled CCD based imager is equipped with two interference filters (557.7 nm and 630.0 nm with a bandwidth of 2 nm). The airglow imaging observation is being carried out during the moonless nights from June 2018 for the estimation of gravity wave parameters (Phase velocity, horizontal wavelength, propagation direction etc.) from the processed images. In addition, we report a few interesting events like Mesospheric Bores and Ripple-type structures in the mesosphere and the plasma disturbances in the ionospheric F region observed for the first time over Hanle, Leh Ladakh.

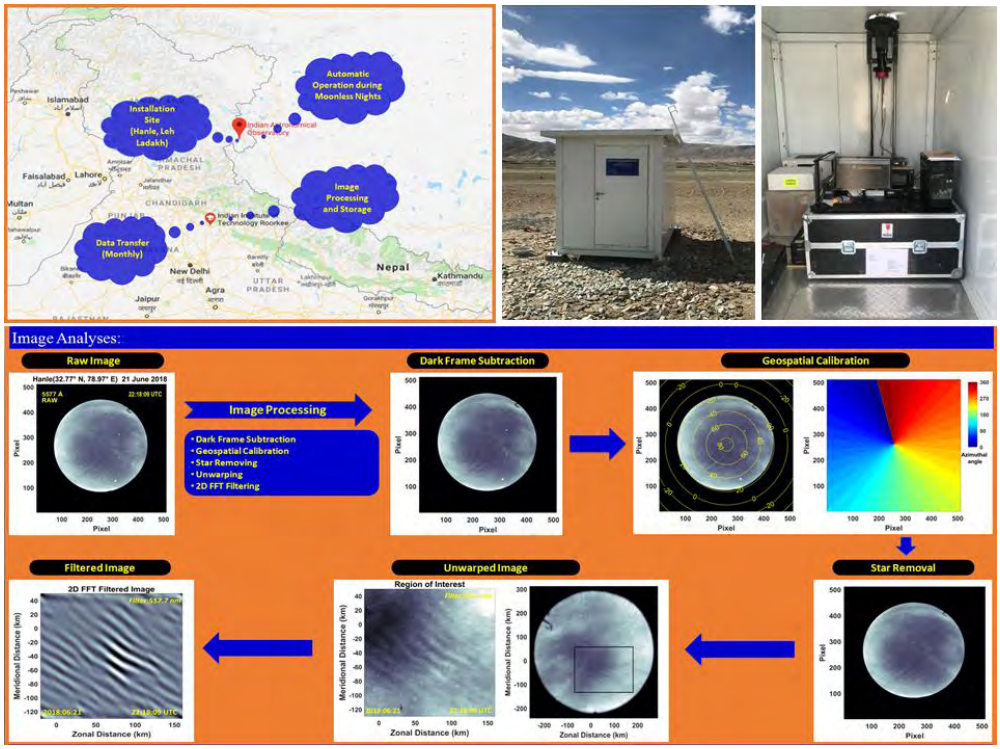

Figure 19: Map of Indian subcontinent indicating the position of the all-sky imager over Hanle, Leh Ladakh. (Upper Right) The weather-proof PUF container and the multi-wavelength all-sky airglow imager. (Bottom) The different stages of image processing.

An observational evidence of a unique plasma depletion event was captured by an O(1D) 630.0 nm airglow imager on 13 June 2018 over a transition region of geomagnetic low-mid latitude, Hanle, Leh Ladakh, India (32.77°N, 78.97°E; Mlat. ~24.1°N). Simultaneous ionosonde measurements from Delhi, India (28.70°N, 77.10°E; Mlat. ~20.2°N) shows spread-F signatures while radar observations over the low-latitude station Gadanki, India (13.5°N; 79.2°E; Mlat. ~6.5°N) reveal the absence of equatorial plasma bubbles. These observations strongly suggest that the observed structures in the airglow images over Hanle are associated with mid-latitude spread-F (MSF). These observations, for the first time, bring out the presence of MSF structures over geomagnetic low-mid latitude transition region (*Mani et al., 2020*).

A unique plasma depletion event was also captured by an O(^{1}D) 630.0 nm airglow imager on 13 June 2018 over Hanle, Ladakh, India. These observations, for the first time, bring out the presence of MSF structures over geomagnetic low-mid latitude transition region. It is suggested that the plasma distribution over low latitudes plays an important role in the occurrence of MSF structures over this transition region. A sequence of processes constituted this unique interaction that includes developing phase of the MSTID within the imager's field of view, gradual bending of the field-aligned plasma depletion structure and eventual merging with the MSTID, and propagation of the merged structure in the form of a single MSTID structure post-interaction. On a geomagnetic quiet night of October 29, 2018, observational evidence of the onset of dark band structures within the field-of-view was captured. Our analyses reveal that the growth time of the plasma depletion is ~2 h if one considers only the Perkins instability mechanism. This is not consistent with the present observations as the plasma depletion

developed within ~25 min. By invoking possible Es layer instabilities and associated E-F region coupling, we show that the growth rate increases roughly by an order of magnitude (Figure 20).

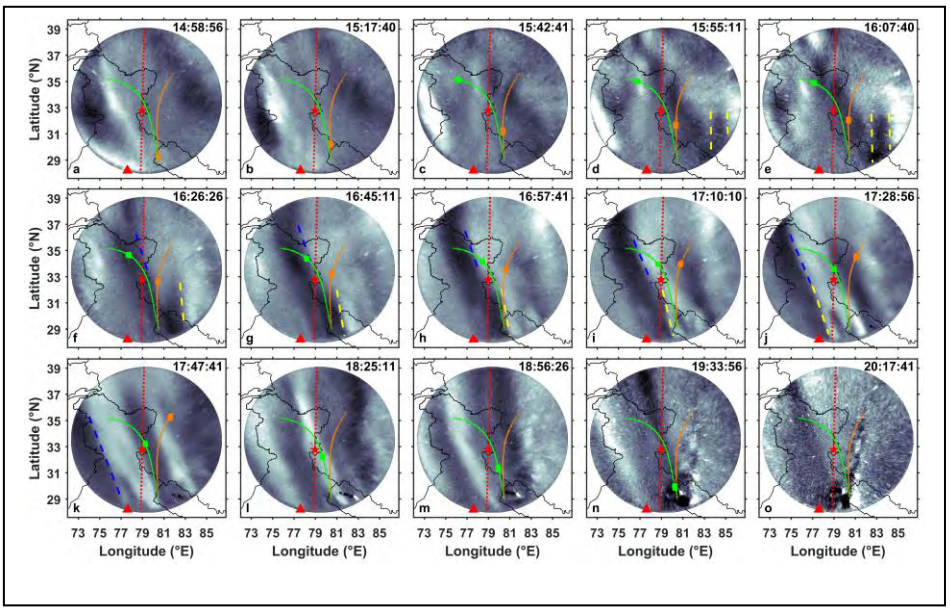

Figure 20: Interaction between nighttime MSTID and mid-latitude field-aligned plasma depletion structure over the transition region of geomagnetic low-mid latitude

2.14 Equatorial Electrojet and Sq

A detailed investigation on longitudinal and decadal variations of general characteristics (amplitude, width, peak altitude) of the equatorial electrojet (EEJ) is carried out using a physics-based model of electrojet. A few important aspects that emerge from this investigation include (i) changes in the half-width of EEJ with longitude, (ii) changes in EEJ strength as large as 10–20% over the Peruvian and Brazilian sectors from 1960 to 2020, (iii) wave-4 structure in the EEJ current density. It is shown that the peak EEJ current density over different longitudes inversely depends on the strength of geomagnetic field. This comprehensive account of the longitudinal and decadal variations of EEJ can be used in observational and modelling studies to understand the low-latitude ionospheric electrodynamics in greater detail (*Pandey et al., 2021*).

A study by CSIR-NGRI investigated the variations of the Sq foci in the northern and southern hemispheres over the 24th solar cycle. The Sq focus in the northern hemisphere exhibits annual variation with maximum Equatorward movement at the summer solstice and maximum poleward movement at the winter solstice. Whereas the Sq focus in the southern hemisphere exhibits semi-annual variation, with maximum Equatorward movement at the spring and autumn equinoxes and maximum poleward movement at the summer solstice (in the northern hemisphere). The seasonal variations in Equatorial Electrojet (EEJ) show a weak relationship with Sq focus movement. EEJ shows higher amplitudes for spring and autumn equinoxes when the Sq focus of both hemispheres moves towards Equator, and EEJ is weak for winter and summer solstice when either of the foci is far away from the Equator. The occurrence pattern of CEJs shows a clear seasonal trend, with large numbers of CEJs for the winter and summer solstices and fewer CEJs during the equinoxes (*Archana and Arora, 2022*; Figure 21).

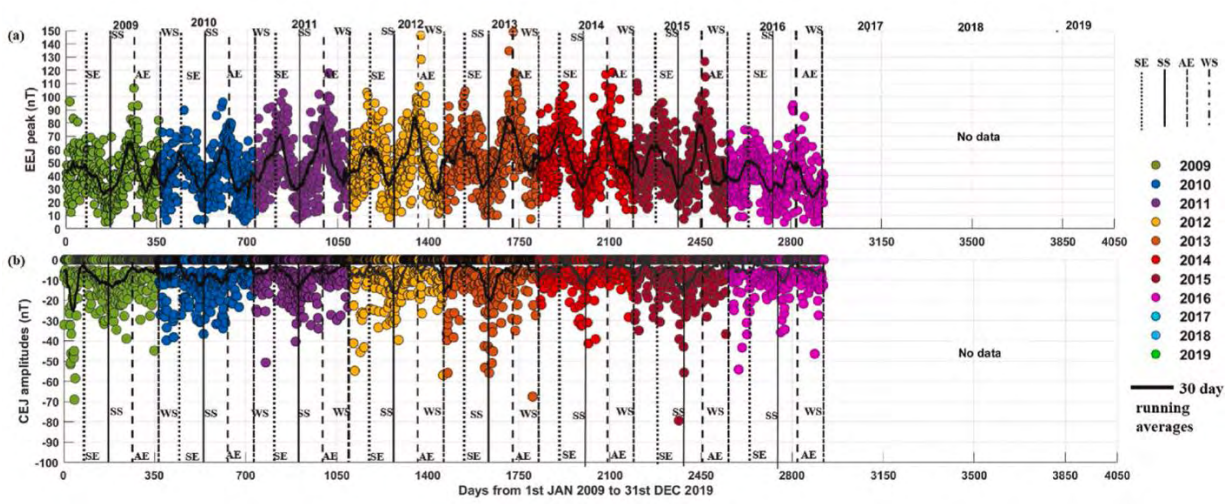

Figure 21: Day to-day latitudinal position of Sq focus in the northern hemisphere (a) and southern hemisphere (b); radial distance between the foci (c); the 30-day running means are plotted in thick black.

A study reveals, for the 'first time', a delayed response of O^1D 630.0 nm dayglow emissions measured using a daytime photometer over Thumba, a geomagnetic dip equatorial station in India, to the noontime X-class solar flare event of July 30, 2005. The Equatorial Electrojet (EEJ) induced magnetic field, measured using a proton precession magnetometer, showed a magnetic spike of ~90 nT during this flare with a time delay of ~7.2 minutes. The O^1D 630.0 nm dayglow over the dip equator exhibited a fourfold enhancement during the noontime flare after a time delay of ~45 minutes as shown in Figure 22. Analysis of satellite measured electron density and simulations using a quasi 2D ionospheric model indicate that the thermospheric O^1D 630.0 nm dayglow emission over the dip equatorial region during a solar flare is primarily driven by the electrodynamics, rather than the direct solar control. This finding is new, unique and very important for the studies related to plasma-neutral coupling and also for modelling studies on the equatorial thermosphere-ionosphere region.

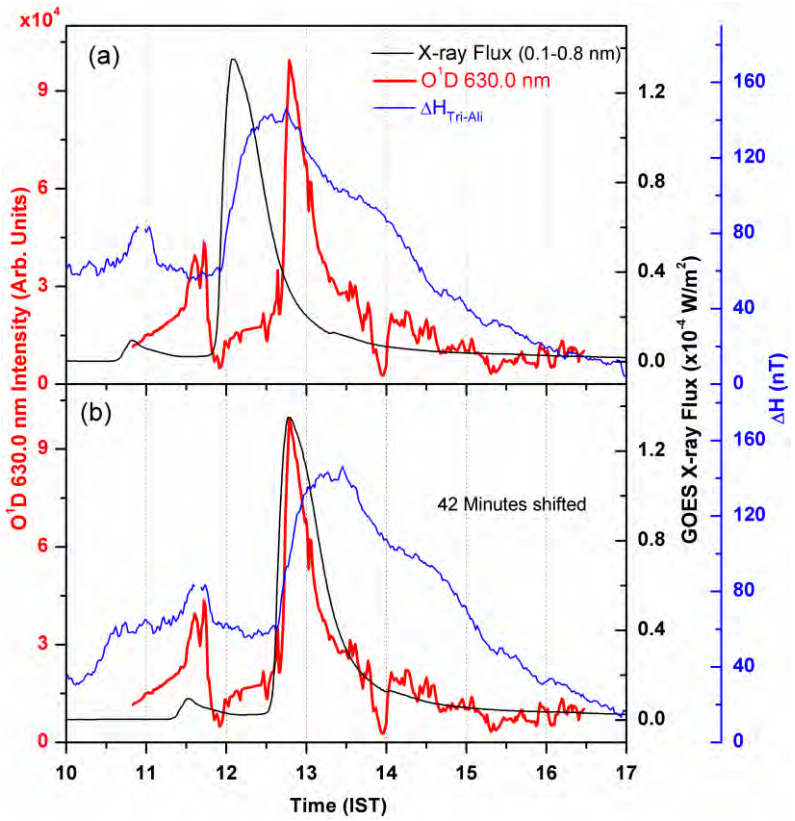

Figure 22: Time variation of (a) O^1D 630.0 nm dayglow emissions, X-ray flux and EEJ induced magnetic field on July 30, 2005, (b) same as Figure 2a but for the X-ray flux and EEJ induced magnetic field forward time shifted by 42 minutes (Vineeth et al., 2021).

2.15 Evidence for the significant differences in response times of equatorial ionization anomaly crest corresponding to plasma fountains during daytime and post-sunset hours

Based on 10 years of vertical total electron content (VTEC) data from Ahmedabad and OI 630.0 nm airglow intensity measurements from Mt. Abu, it is shown that plasma density over the equatorial ionization anomaly (EIA) crest region increases in varying degrees during post-sunset hours (2000–2100 LT) in magnetically quiet periods (Figure 23). It is shown that pre-reversal enhancement (PRE) of the zonal electric field causes these enhancements over the EIA crest region. Post-sunset enhancements in VTEC occurs ~1.7 h after the PRE, which is almost half compared to the average response time (3–4 h) associated with the daytime fountain. It is proposed that the PRE drives plasma from 5°N to 10°N magnetic latitudes to the EIA crest region leading to shorter response time (Figure 5), (Kumar et al., 2021). Based on these observations and Thermosphere Ionosphere Electrodynamics-General circulation model (TIE-GCM) outputs, it is argued that the pre-reversal enhancement (PRE) in the zonal electric field works in tandem with latitudinal gradient in the F region plasma density to determine the degree of VTEC enhancement over the EIA crest region during post-sunset hours (*Kumar et al., 2022*).

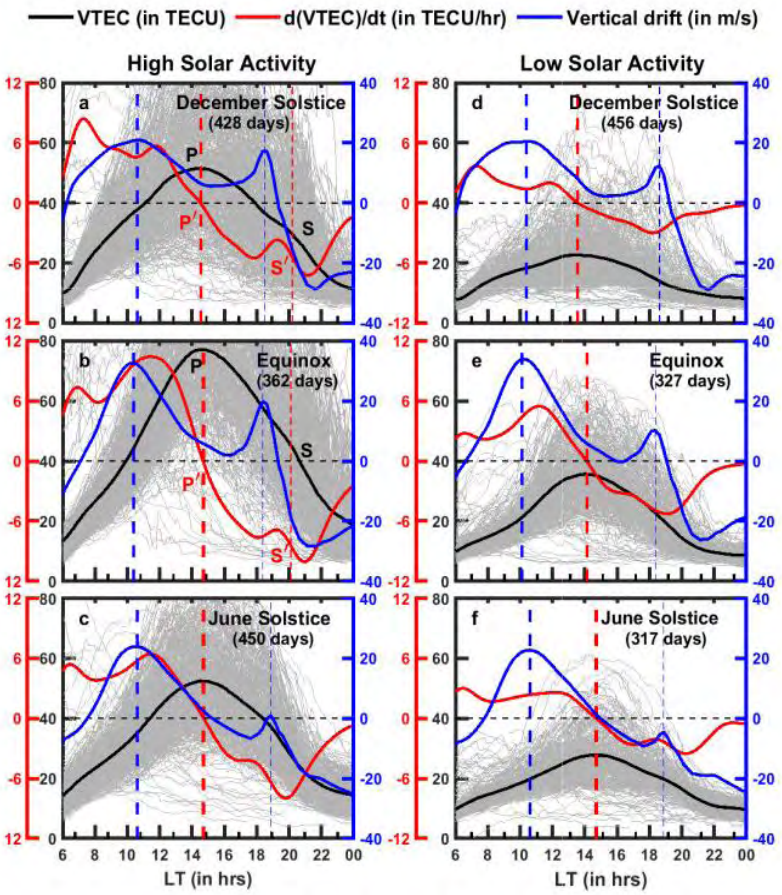

Figure 23. Variation of VTEC over Ahmedabad (gray), average of seasonal VTEC (black), temporal derivative of seasonal VTEC (red), and model-derived vertical drift (blue) in December solstice (top), Equinox (middle), and June solstice (bottom) under high (left panel) and low (right panel) solar activity years. The number of days used to calculate the seasonally averaged VTEC curve is also mentioned in each subplot. The points P and S represent primary (afternoon) and secondary (post-sunset) maxima of VTEC. P and S are determined based on P' and S' that are overall and local zero crossing points of d(VTEC)/dt. The intervals between the thick and thin vertical dashed lines (blue and red) are the response times of the EIA crest region during noon and post-sunset hours respectively.

2.16 Formation of the evening time F_3 layer

One of the hypotheses for the formation of the evening time F_3 layer relies on the height gradient in the vertical plasma drift. This hypothesis is tested for the first time, using Jicamarca Incoherent Scatter Radar observations of electron density and vertical plasma drift profiles. It is found that the evening F_3 layer could occur even when the height gradient in vertical drift is small and insignificant. It is proposed that, in addition to the known role of vertical plasma drift, the height variation in the recombination loss of electrons plays an important role in the formation of evening time F_3 layer over the geomagnetic equator (*Venkatesh and Patra, 2022*).

2.17 Low latitude ionospheric dynamics

A novel approach is developed to estimate the daytime equatorial vertical drifts using ground-based optical neutral oxygen dayglow emission intensity measurements over Hyderabad. The extent of asymmetric nature in the diurnal patterns of the day emissions is characterized by a parameter called Asymmetry in Time (AT), which shows similar variations with the integrated Equatorial Electrojet (EEJ) strength. AT values obtained from the dayglow measurements are used to infer the vertical drifts. Vertical drifts derived by this method match well with the global climatological model estimates and with radar measurements. This new approach provides an alternative method for obtaining vertical drifts to enable systematic investigations of equatorial electrodynamics (*Karan and Pallamraju, 2020*).

Analysis of systematic observations of daytime optical OI 630.0 nm emission rates from a low- and a mid-latitude location obtained during 2015 and 2003–2004 are compared. The variability in the low-latitude emission rate is primarily dependent on that of the solar flux. However, such primary dependence on the solar flux is not reflected on the emission rate variability seen over mid-latitudes. This discrepancy is understood to be due to the relative effects of solar flux and the globally changing compositional variability, characterized by the oxygen to molecular density ratios (O/N2), that show varying behavior from mid- to low-latitudes (*Pallarmaju et al., 2020*).

The relative effect of the equatorial electrodynamics and meridional winds on the upper atmospheric variability as a function of latitude are investigated using the OI 630.0 dayglow data from two large field-of-view (FOV) imaging spectrographs, which collectively cover a large latitudinal extent from 5-18 MLAT. It is found that the poleward meridional wind contributes to an enhancement in the OI 630.0 nm dayglow emission rates closer to the magnetic equator and a decrement as one moves away from the equator. The equatorial electric field effect, however, continues to be equally effective in the low-latitudes (Figure 24; *Kumar et al., 2022*)

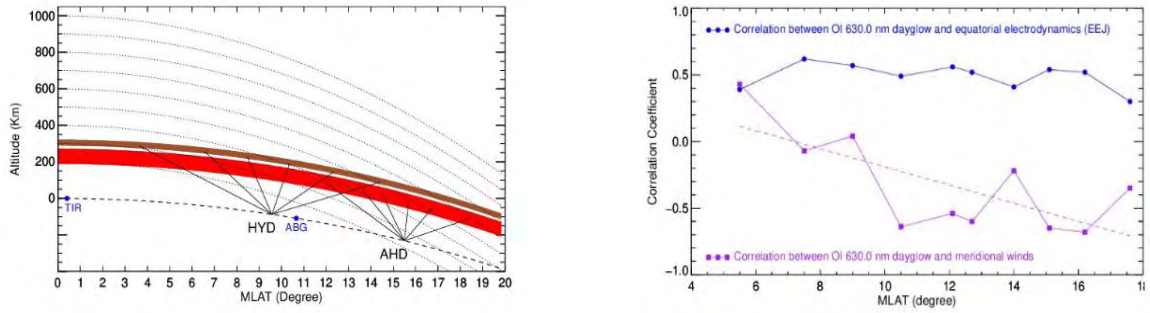

Figure 24. (a) Schematic showing the regions of IO630.0 nm dayglow emissions over different MLAT in red colour. The field-of-view of MISE is shown by black solid lines from HYD and AHD. The geomagnetic field lines are represented by dotted black line. TIR and ABG indicate the locations of geomagnetic measurements. (b) Values of correlation coefficients of OI 630.0 nm dayglow emission with EEJ and meridional winds are shown along with MLAT in blue and purple coulored lines, respectively. The linear fit between the correlation coefficients of the OI 630.0 nm averaged dayglow emission intensities with meridional wind and MLAT is shown in the dashed purple colour.

2.18 Variability of the Equatorial Ionization Anomaly Trough

In this study, a novel method using single station beacon Relative Slant Total Electron Content (RSTEC) measurements, obtained through the Coherent Radio Beacon Experiment was proposed to estimate the location of Equatorial Ionization Anomaly Trough (EAT) and study the variability therein. The feasibility of this method is established based on simulations of RSTEC using IRI model electron densities. It was seen that the EAT location moves 13^{o}N to 3^{o}N (~±5^{o} on either side of the dip equator) and exhibits a systematic seasonal variability. During solsticial months, the EAT location was found to be determined by the trans-hemispheric winds. During equinoctial months, when thermospheric winds were weak, the EAT location was determined by the combined effect of field aligned diffusion and the thermospheric winds (Figure 25). The transition of EIA from winter to summer side of the dip equator, depends on the balance between the field aligned diffusion and thermospheric winds.

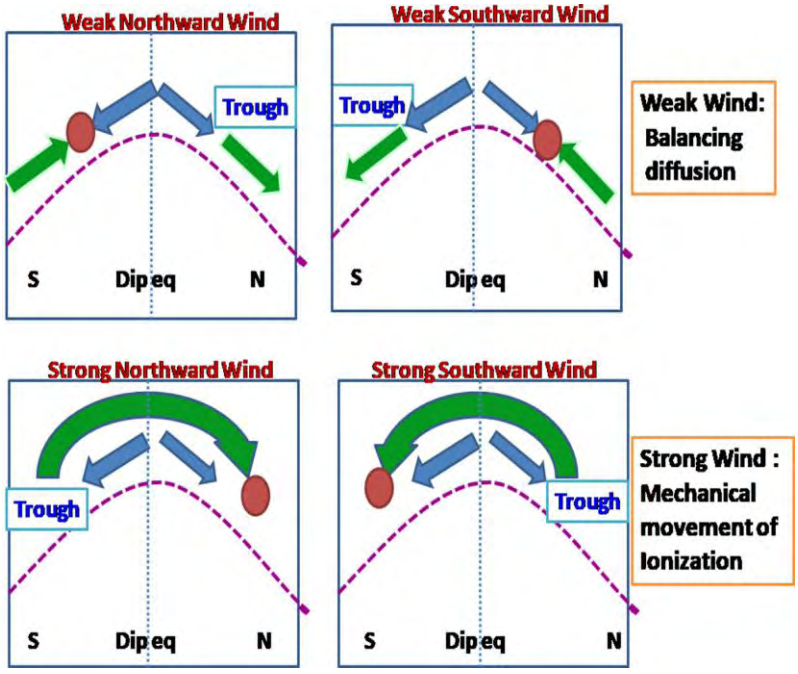

Figure 25: Gives the schematic explaining the mechanism of trough movement over the dip equatorial region (*Mridula et al., 2020*).

2.19 In-situ observations of rocket burn induced modulation of the top side ionosphere

The fourth stage (PS4) of the Polar Satellite Launch Vehicle (PSLV) of the C-38 mission, was used for the first time as an orbiting platform to carry out measurements of ionospheric parameters, on June 23, 2017. The Ionization Density and Electric-field Analyzer (IDEA) payload onboard the PS4 stage provided electron density (Ne) and electric field (EF) information in the F region altitudes. The presence of a top side enhancement, was revealed in the initial phase IDEA measurements and simulations using IRI and TIE-GCM models confirm the possibility (Figure 26). The first of their kind in-situ observations of top side electron density enhancement concurrent with the operation of the PS4 stage of PSLV demonstrates the

plausible role of rocket burn and exhaust gases in modulating the ionosphere in the vicinity. The results indicate that the unique trajectory of the PS4 orbiting station (in the initial phase) serves as an ideal one to investigate top side electron density enhancements.

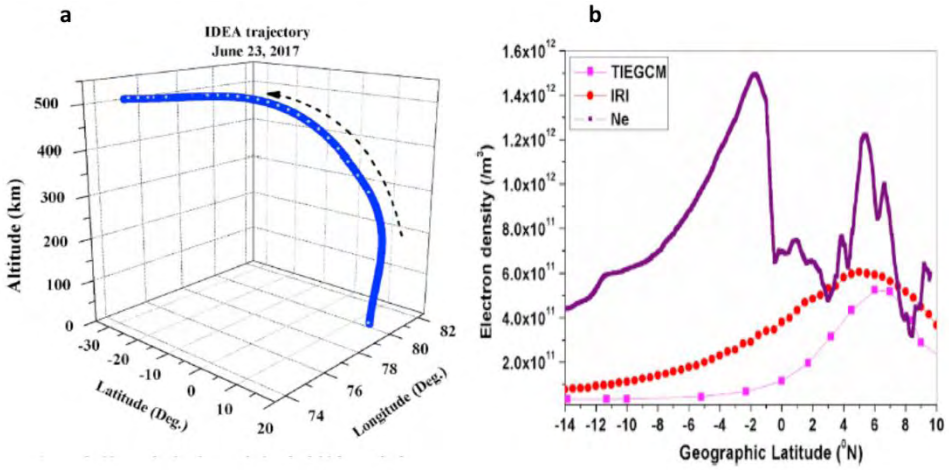

Figure 26: a)Trajectory of payload in the launch phase b) Comparison of IDEA LP electron density observations with IRI model output and TIEGCM model simulation for 23 June 2017(*Manju et al., 2020*).

2.20 Equatorial Ionization Anomaly crest magnitude

The association of Equatorial Ionization Anomaly (EIA) with various post sunset ionospheric irregularity manifestations is brought out empirically for vernal equinox season of different solar activity conditions. The GPS-TEC from five stations centred around 77°E longitude as well as ionosonde measurements over Trivandrum, have been used. The study reveals that the magnitude of the EIA crest in the evening hours has a direct control on the base height of post sunset ionospheric F-layer on a day-to-day level (Figure 27). During conditions of strong (weak) EIA crest, the Equatorial Spread-F (ESF) irregularities are observed to be manifested earlier (later) and are sustained for a longer (shorter) duration. Further, the GPS signal scintillation intensity (quantified by the parameter S4 index) exhibits a direct association with EIA crest strength. This work emphasizes the need for understanding effects of EIA and incorporating them into models for better prediction of ESF. The vertical propagation of gravity waves in daytime thermosphere has also been shown to be a crucial parameter for the generation of ESF during post-sunset hours (*Mandal et al., 2022*).

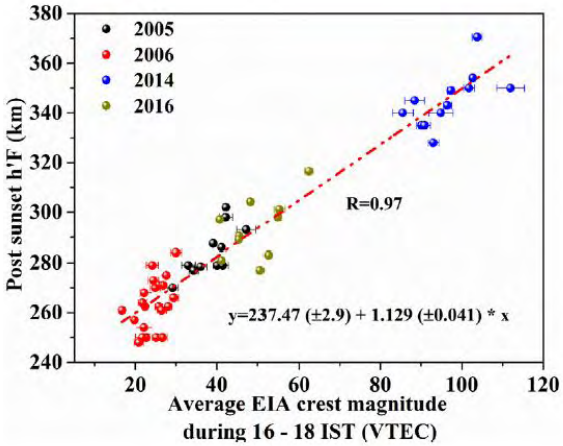

Figure 27: The day-to-day association of the mean of EIA crest strength during 16 – 18 IST and post sunset h'F for the days of vernal equinox for the years 2005, 2006, 2014 and 2016 (Aswathy and Manju, 2021).

2.21 Characteristics and precursors to the equatorial plasma bubbles

OI 630 nm night time airglow emissions have been investigated over Mt. Abu and Kolhapur using a High Throughput Imaging Echelle spectrograph (HiTIES) and All-Sky Imager (ASI), respectively. Plasma depletions are seen in simultaneity in OI 630 nm nightglow from two different low-latitudinal locations. Strength of PRE decides the latitudinal extent of plasma bubbles over the low-latitudes. Based on the analysis of around 1300 images of data, it is revealed that the gravity waves with scale sizes in the range of 250–300 km are omnipresent, whereas, shorter scale sizes (50–250 km) are present only during the presence of EPBs. It is inferred that these shorter scale size gravity waves played a significant role in the seeding the perturbation of the EPBs (Figure 28; *Saha et al., 2022*).

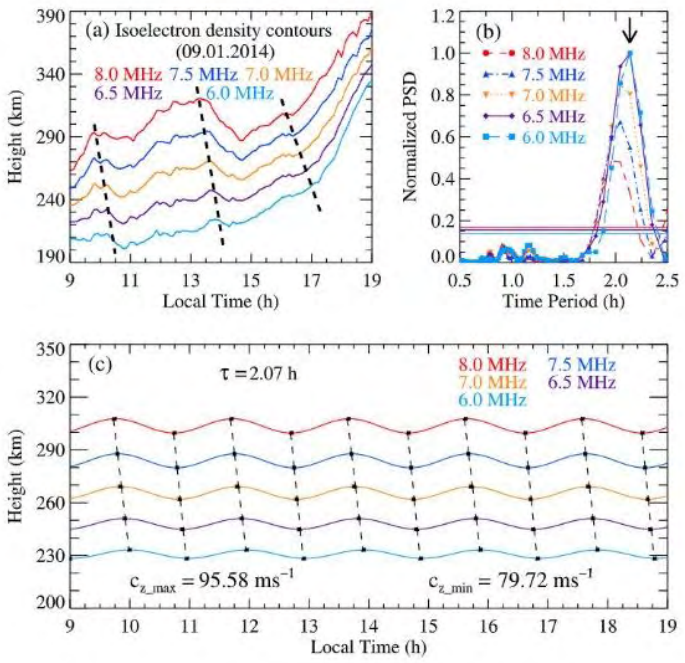

Figure 28: (a) Variations in the true heights of isoelectron densities corresponding to five transmission frequencies (6.0, 6.5, 7.0, 7.5, and 8.0 MHz) on a sample day of January 9, 2014 obtained from digisonde of Trivandrum, India are shown. (b) Lomb-Scargle spectral analyses show a period of 2.07 hr (as indicated by a black arrow) to be significant in height variations of all the isoelectron density contours. (c) Fluctuations in the heights of those isoelectron density contours due to the gravity wave of time period of 2.07 hr are shown.

Equatorial plasma bubbles (EPBs) are noticed as airglow depletions aligned along the geomagnetic field. During the geomagnetic storm on 17 March 2015, all-sky airglow images from the IIG equatorial station, Tirunelveli (8.7°N, 77.8°E, 1.7°N dip latitude) revealed an interhemispheric asymmetry in the tilt of the EPBs about the equator (*Hickey et al., 2020*). It was suggested that it could be the result of the difference in airglow layer altitude between the northern and southern regions, attributed to a difference in the height of the ionosphere. EPBs from Equatorial Atmosphere Radar (EAR) provides hitherto undisclosed evidence for the smaller (3-meter) scale irregularities initially developing at higher altitudes and subsequently developing to lower altitudes. This is likely to have significant impact on the latitudinal development of L-band scintillations. The case of intense and periodic EPBs observed during

April 8-9, 2013 by the 47 MHz EAR at Kototabang, Indonesia has been investigated in view of its possible connection with the tropical cyclone Victoria (*Ajith et al., 2020*). It is found that the secondary gravity waves generated by the dissipation of primary gravity waves associated with tropical cyclone Victoria could have served as a seeding source on the generation of periodic EPBs during these two consecutive days (Figure 29). As a coupled system of atmosphere-ionosphere system, the exclusive role of solar wind density changes on the prompt equatorial electric field disturbances using the long term observations of equatorial electrojet (EEJ) from the Indian sector has been studied. The underlying physical mechanisms for the prompt equatorial electric field disturbances has been discussed in light of enhanced high-latitude convection and additional field-aligned currents due to sudden enhancement of solar wind density. Planar magnetic structures (PMS) are often observed in sheath regions driven by interplanetary coronal mass ejections (ICMEs) and in corotating interaction regions (ClRs). Statistical studies of plasma properties within planar and non-planar ICME sheath regions using in situ data from the Advanced Composition Explorer (ACE) spacecraft revealed that the strength of the southward/northward magnetic field component is almost double in planar sheath regions compared with non-planar sheath regions and that planar sheaths are more geo effective than non-planar sheaths (*Shaikh et al., 2020*).

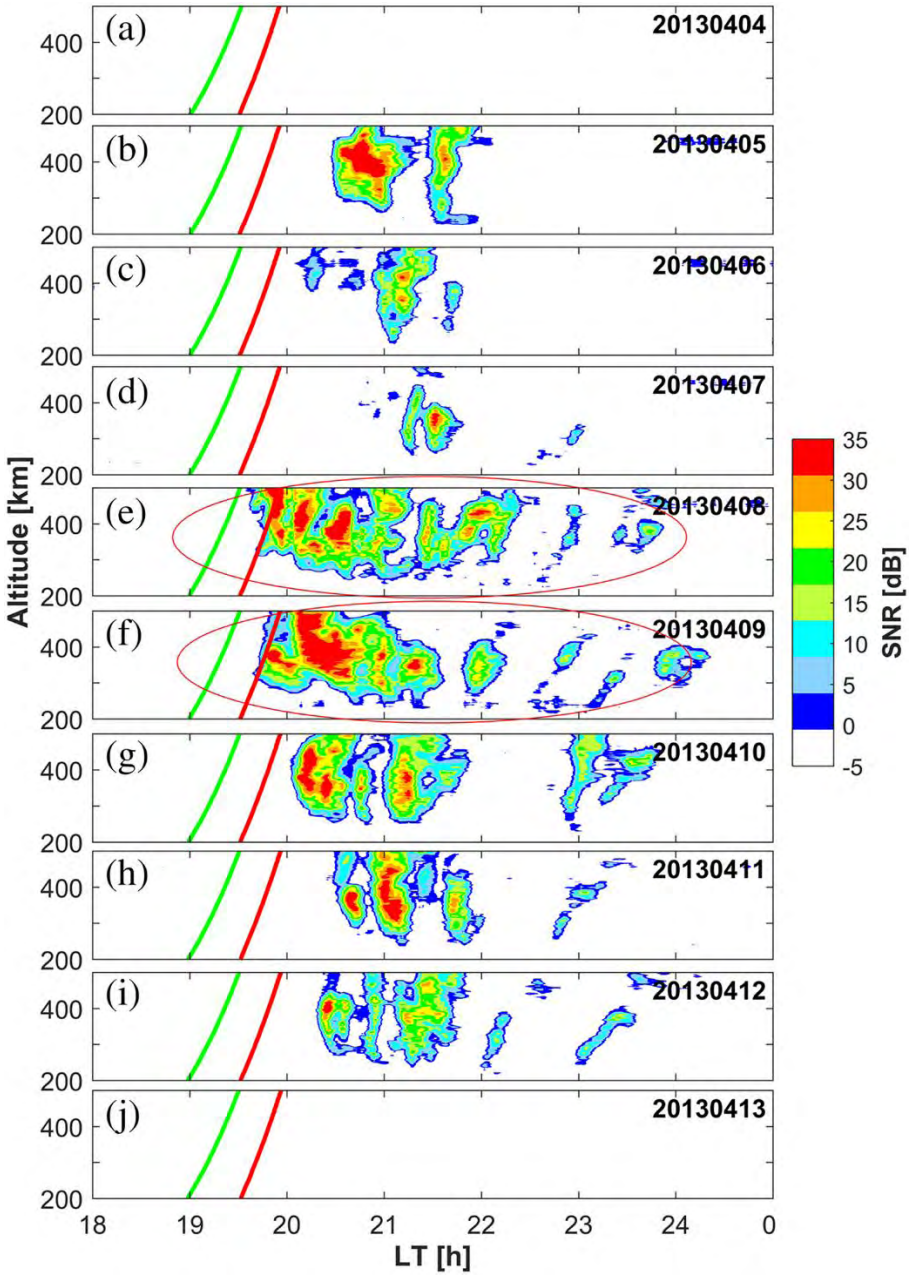

Figure 29: Altitude-time-intensity (ATI) maps of backscatter echo observed by the central beam (180°) of EAR during 4–13 April 2013. The green and red curves indicate the local and apex sunset.

2.22 Thermosphere-Ionosphere dynamics through nightglow observations

Nocturnal variations of OI 630 nm nightglow emissions are investigated using optical spectrograph observation over Mt. Abu (24.6°N, 72.7°E, 19°N Mag.). The post-sunset poleward movement of EIA crest correlates well with the strength of PRE. It is demonstrated that the reversal in EIA as inferred by the OI 630 nm nightglow emissions in our measurements is due to the westward equatorial electric field. It is hereby proposed that the reversal speed derived from optical nightglow measurements can serve as a proxy for the determination of westward electric field over equator for that longitude sector (*Saha and Pallamaraju, 2022*).

The effects of both equatorial electrodynamics and meridional winds have been investigated to understand the variations in the post-sunset emissions in the OI 630 nm airglow over the low-latitude location, Mt. Abu. Following the expected monotonic decrement in the emissions after sunset, an enhancement is observed on several nights that peaks at around 20–21 local time (LT). It is found that the neutral winds, as obtained using digisondes at two locations, show a very good correlation between a poleward directed wind or cessation of equatorward wind over AMD and the observed airglow emission enhancement in the post-sunset time (*Saha et al., 2021*).

2.23 The Response of the D and E Regions of the Equatorial Ionosphere to Solar Flare Event

The response of equatorial ionospheric current systems to solar flare events was studied using the data from a magnetometer and an in-house developed ionospheric model (Figure 30). During an X1.9 class flare event which occurred on 24 September 2011, magnetic field (ΔH) showed a crochet, whereas during an M1.5 class flare on 20 February 2002, in addition to an enhancement, a reduction in ΔH with a time delay was also observed. Using model simulations, it has been shown that integrated Hall to Pedersen conductivity ratio in the D and E-regions of the ionosphere plays a key role in controlling flare response. It was found that the ratio had a reduction at 105 km while it was enhanced at 90 km. The changes in conductivity modulate the east-west electric field, which, in turn, leads to modifications in the ionospheric current systems and thereby the ΔH. It is found that modifications observed in ionospheric currents during solar flare events depend not only on the changes in conductivity but also on the variations in the zonal electric field.

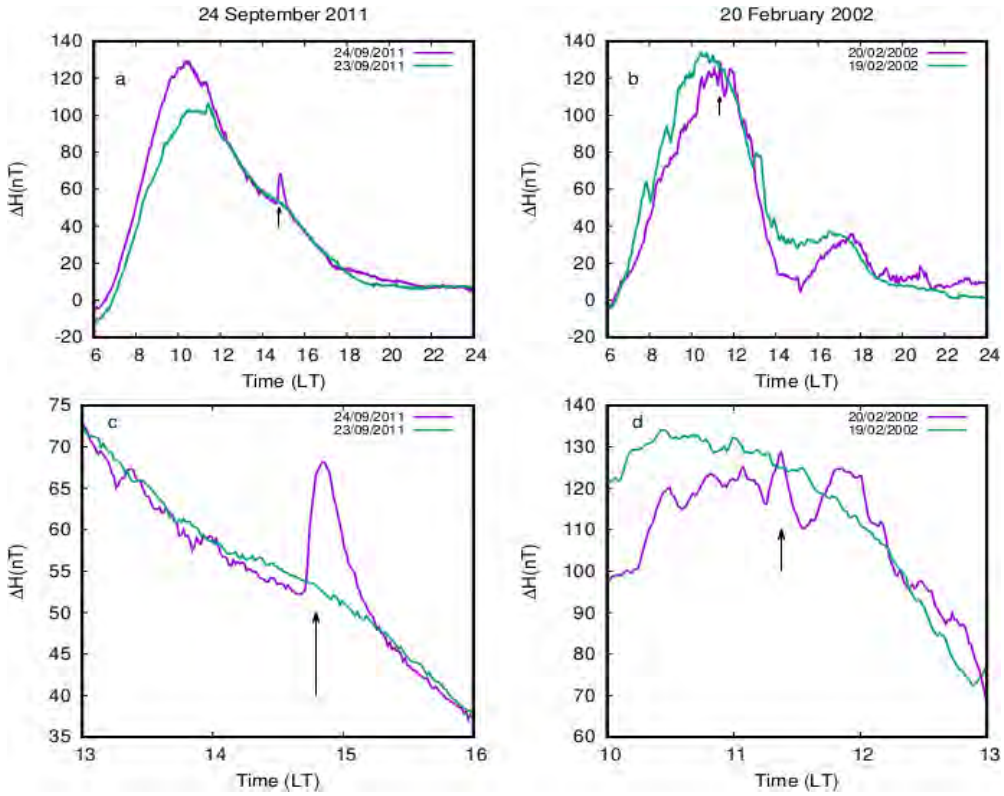

Figure 30: Temporal variation of (a) ΔH over Tirunelveli 24 September 2011 (b) ΔH over Tirunelveli on 20 February 2002. Panels (c) and (d) are enlarged portions of (a) and (b), respectively (*Gopika et al, 2021*).

Latitudinal and longitudinal variations of the disturbance ionospheric (Ddyn) current during 12 geomagnetic storms with Dst −50 to −130 nT was investigated from 5 geomagnetic stations along three longitudinal sectors with *Dst* ranging between −50 and −130 nT. For this purpose, data from 15 geomagnetic stations along three longitudinal sectors at 70°E, 77°E, and 93°E, ranging from middle to equatorial latitudes in both hemispheres are analyzed. Our study reveals the pattern of PP in the different phases of the storm and the competing effects of PP and Ddyn during the recovery phase of the storms. The PP signatures are mainly comparable across longitudes, irrespective of the strength and phase of the storm. The effect of Ddyn shows a seasonal pattern, which is influenced by the strength of the storm. The location of the antifoci during each storm shows latitudinal variability (*Bulusu et al, 2020a*)

2.24 Electron density distribution over the Indian equatorial and low latitude ionospheric region during a severe geomagnetic storm

Using a chain of ground-based GPS receivers and magnetometers, the importance of thermospheric meridional wind circulation in controlling the distribution of plasma over the Indian low latitude ionosphere during a severe noontime geomagnetic storm (Sym-H ~ -305 nT) of May 2005 has been studied. A steep increase in the Total Electron Content (TEC) of the ionosphere over the entire Indian ionospheric region was observed on May 15 (Figure 35). The enhancement in the TEC was well correlated with the increase in ΔH at the dip-equator due to the prompt penetration electric field (PPEF) associated with the storm. Enhancements in the TEC were observed on May 16, a day after the storm, as well, though the ΔH at the dip-equator was quite below the quite-time mean. The TEC remained well above its monthly mean over the entire Indian ionospheric region during the storm recovery period. We suggest that the TEC enhancement on May 16, even though it looked to be due to the PPEF effect, was directly related to the compositional disturbances as given by the O/N_2 ratio. In view of this, the study concludes that the meridional wind circulation plays an important role in the distribution of electron density over the equatorial and low latitudinal region during the period of a geomagnetic storm.

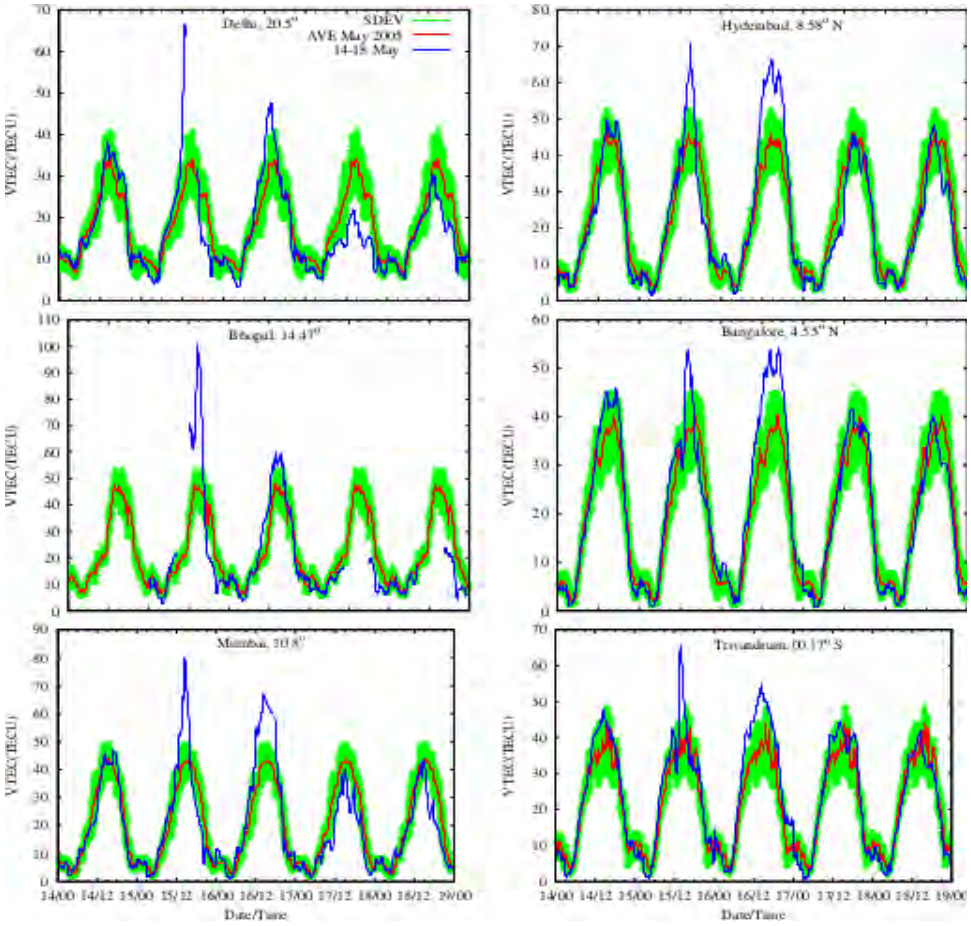

Figure 31: The electron density distribution over the Indian sector (6 stations) during May 14-18 2005. The magnetic latitude of each station is shown in Figure (*Ambili and Choudhary, 2022*).

3. Magnetospheric phenomena

3.1 Pulsations

Manjula et al. (*2020*) analyze the characteristics of non-substorm Pi2 (impulsive pulsations [3–25 mHz]) from low and middle latitudes (HYB, *L* ¼ 1.03) and Paratunka (PET, *L* ¼ 2.1) and investigates the trends of these oscillations during 2015–2016. Variation of non-substorm Pi2 periods with geomagnetic activity index Kp and solar wind speed (*V*sw) show inverse relations with Pi2 period at HYB. In addition, non-substorm Pi2s are distributed equally in all local time sectors with ratio of second harmonic to fundamental Pi2 ranging within 1.3–2.2. These trends of non-substorm Pi2s indicate plasmaspheric cavity resonance (PCR) as the dominant source at low latitude, confirmed using a theoretical model. In contrast, non-substorm Pi2 periods do not show a steady trend with Kp and *V*sw at midlatitude station PET. Local time variations show an increased period in the premidnight sector at PET. A close agreement between theoretical estimates and observed periods of non-substorm Pi2-s at PET, leads to the inference of Alfvenic nature of these modes, attributable to a resonant oscillation (Figures 31, 32).

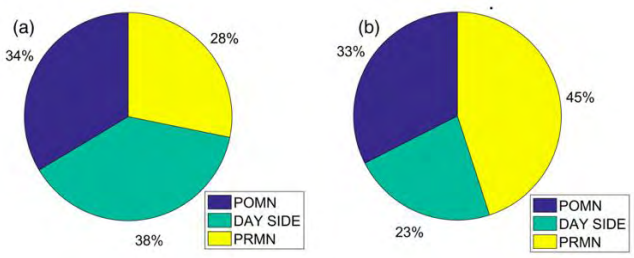

Figure 32: Distribution of non-substorm Pi2s over different local time sectors at HYB (a) and PET (b).

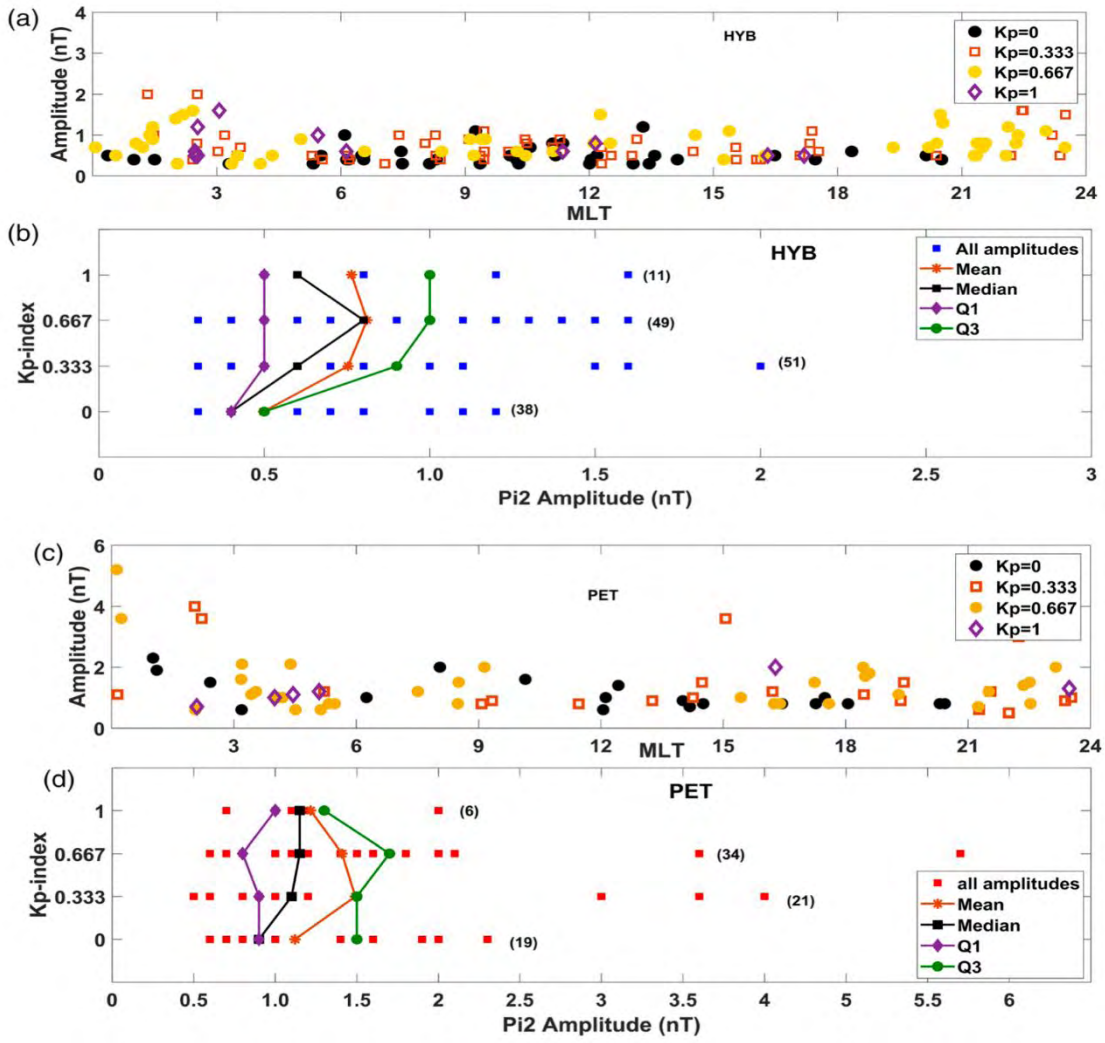

Figure 33: Local time variation of Pi2 amplitudes at HYB (a) and PET (c), respectively. Amplitude variations with Kp is plotted for HYB (b) and PET (d). The numbers in brackets report the number of events occurring at the particular Kp.

The spatial features of low-latitude Pi2 (6.6–25 mHz) pulsations, which are indicators of auroral susbtorms are investigated. A comprehensive study is carried out for the first time using magnetic field measurements from a global network of low-latitude ground stations (Mlat: ± 2° − 51°) and the Swarm multisatellites located simultaneously at day and night local times.

These Pi2 characteristics observed globally at ground and at the topside ionosphere suggest that the sources for nighttime and daytime low-latitude Pi2s are oscillating field-aligned currents and ionospheric currents, respectively (*Thomas et al., 2019*).

In another study Pc4 signatures for the year 2013, are investigated vis-à-vis the prevalent interplanetary parameters (IMF) as well as the geomagnetic activity indices. A clear dominance of Pc4-5 (467 events) over Pc3 (17 events) is observed. Local time variation of Pc4 shows a peak in the noon sector in both X and Y components. Our investigations show that the dominant peak frequency is 10 mHz at low latitude region. Correlations with solar wind and IMF parameters illustrate highest occurrence of Pc4 for a solar wind speed of 300–400 km/s and average IMF B field of 3–6 nT. The amplitude of Pc4s at DSP shows an increase with increasing solar wind speed, plasma density, solar wind dynamic pressure and average B field which is also reflected in the trend of frequency variation of these pulsations. We report that IMF clock angle at low latitude does not have influence on Pc4 occurrence. Based on the characteristics of these events, detected in latitudinally distributed stations from low and mid-latitudes from northern and southern hemisphere, we infer that modes were compressional, which could be driven by K-H instability or solar wind dynamic pressure, as compressional modes can propagate to low latitude with little attenuation (*Bulusu et al 2020*).

3.2 Electromagnetic ion cyclotron

The observations of rising tone emissions of EMIC waves by THEMIS A, D, and E spacecraft in the outer magnetosphere are examined which indicate a left-handed polarization with wave normal angles less than 30 degree (*Ojha et al., 2022*). There is a rapid nonlinear growth of the EMIC subpackets within one wavelength. Subpackets are dynamic in nature as their structure changes within one wave period, which is further supported by the nonlinear wave growth theory. Observed ion energies and pitch angle spectra of the ion fluxes are consistent with the energy associated with the Landau and cyclotron resonance conditions. Although substorms are much more frequent than geomagnetic storms, all substorms are not associated with EMIC waves. Our aim was to determine the conditions under which a substorm can trigger EMIC waves. A statistical survey of EMIC wave events during the Van Allen Probes (VAP) era showed that the injection events associated with EMIC waves enhancements also showed associated signatures of strong magnetospheric plasma convection (Figure 33, 34). The enhanced convection during injections can push more ions, more quickly and to deeper locations in the magnetosphere, leading to higher fluxes and greater anisotropies, which in turn lead to wave excitation (*Remya et al., 2020*). EMIC waves and their seasonal, local time distributions using long-term observations of EMIC waves from ground Indian, Antarctic station Maitri, in solar cycle 24 (*Upadhyay et al., 2020*)**.**

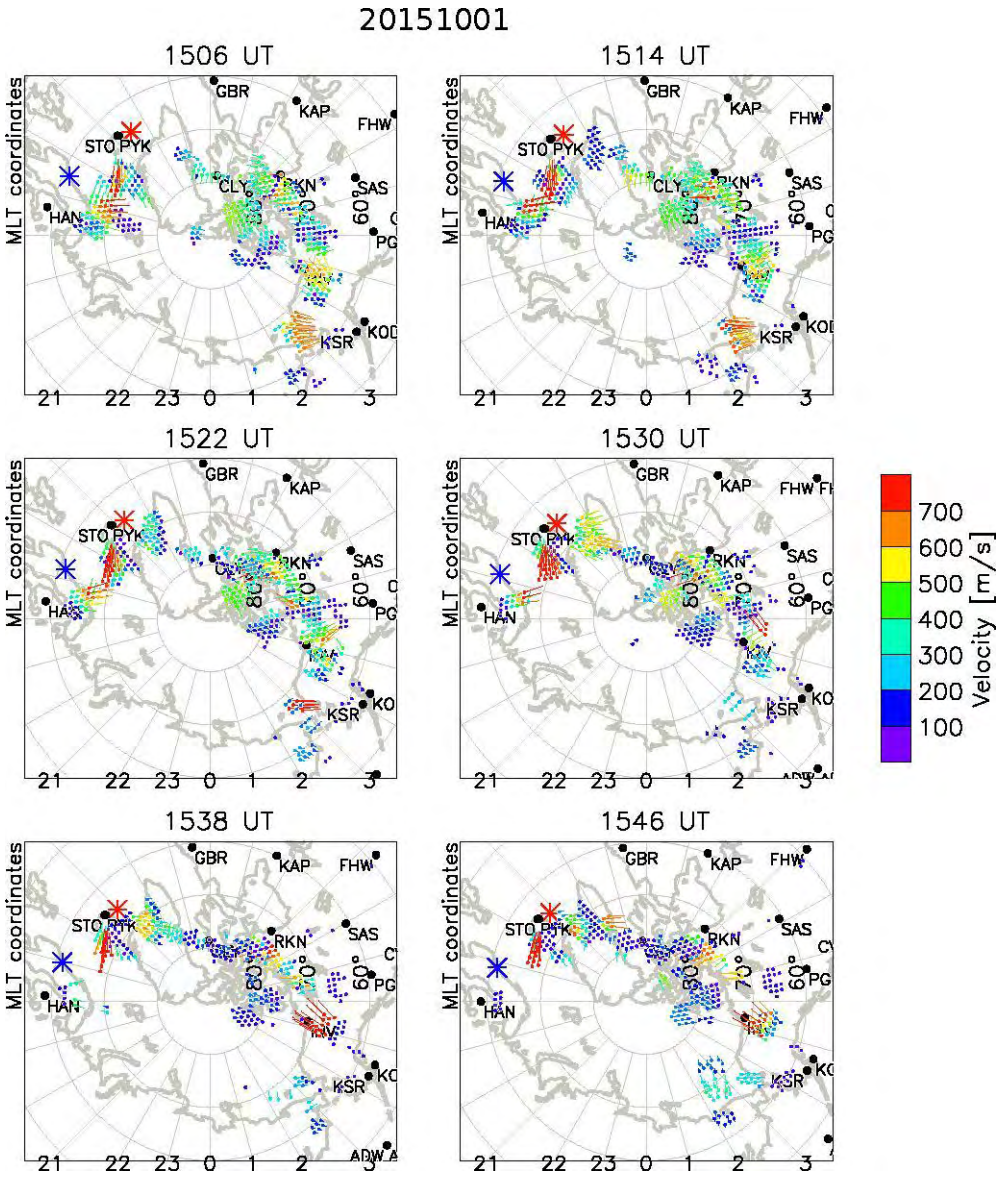

Figure 34: Maps showing gridded line-of-sight velocity vectors derived from the northern hemisphere SuperDARN radars, between 15:00 - 16:00 UT on 01 October 2015. The observed EMIC wave events are associated with these strong sunward convection at dusk local times (14-18 MLT). The red and blue stars indicate the footpoint locations of Van Allen Probes A and B, respectively (*Remya et al., 2020*).

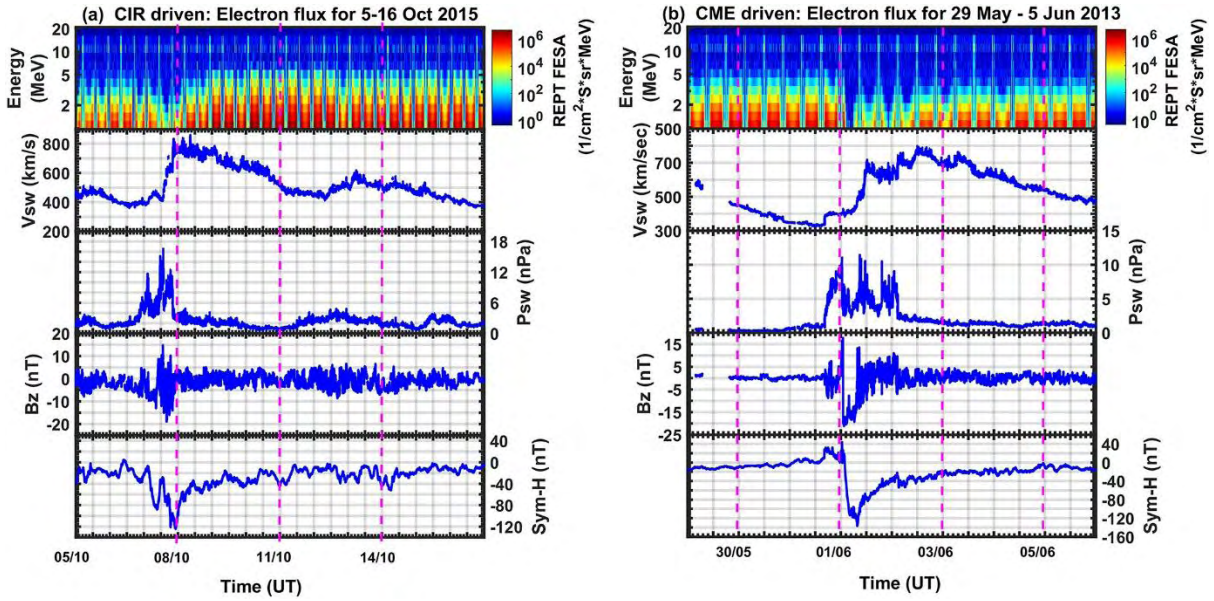

Figure 35: Energy versus time spectra for spin averaged differential electron flux for (a) CIR-driven geomagnetic storm of 5–16 October 2015 and (b) CME-driven geomagnetic storm of 29 May to 5 June 2013 is shown. The lower panels show corresponding solar wind parameters, *V*sw, *P*sw, and IMF *Bz*. The lower most panel gives the intensity of the geomagnetic storm *Sym-H*. CIR = corotating interaction region; CME = coronal mass ejection; REPT = Relativistic Electron-Proton Telescope (Pandya et al., 2019).

3.3 Geomagnetic storm induced plasma density enhancements in the southern polar region

The evolution of positive ionospheric storms at the southern polar stations Bharati (76.6°S MLAT) and Davis (76.2°S MLAT) and its causative connection to the solar wind driving mechanisms during the St. Patricks day (17 March 2013 and 2015) storms was studied using GNSS receiver system. During the main phase of these storms, significant enhancements in TEC and phase scintillation were observed in the magnetic noon/midnight period at Bharati and Davis. The TEC in the midnight sector on 17 March 2015 was significantly higher compared to that on 17 March 2013, in line with the storm intensity. The strong and sustained magnetopause erosion led to the prevalence of stronger storm time electric fields for long duration on 17 March 2015. This combined with the action of neutral winds at mid latitudes favored the formation of higher plasma densities in the regions of storm enhanced densities formation on this day. The same was weaker during the 17 March 2013 storm due to the fast fluctuating nature of IMF B_z (Figure 36). This study shows that the duration and extent of magnetopause erosion plays an important role in the spatio temporal evolution of the plasma density distribution in the high & mid latitude ionosphere.

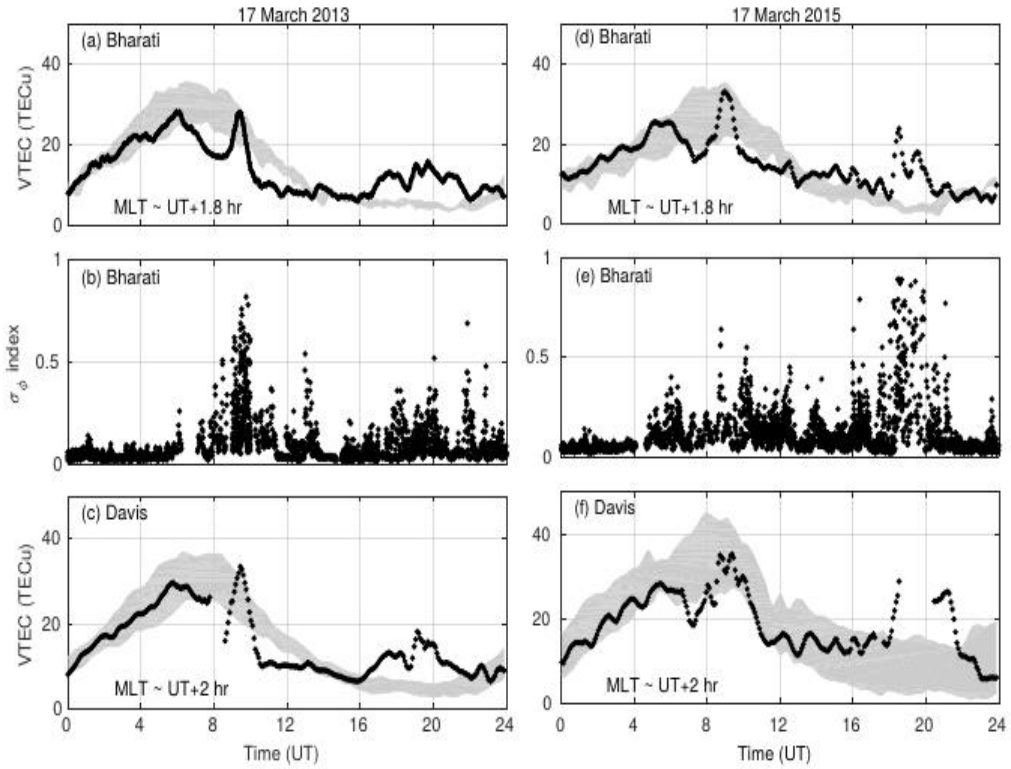

Figure 36: Panels (a) and (b) represent the diurnal variation of TEC and σ φ index, respectively, at Bharati 254 on 17 March 2013 while panel (c) represent the diurnal variation of TEC at Davis station on 17 March 2013. 255 Similarly, panels (d) and (e) represent the diurnal variation of TEC and σ φ index, respectively at Bharati on 17 256 March 2015 while panel (f) represents the diurnal variation of TEC at Davis station on 17 March 2015. The 257-black curve in panels (a), (c), (d), and (f) represent the variation in TEC respectively on the day of the storm 258 and the gray shade represents the quiet day standard deviation. *(Shreedevi et.al., Space Weather, 2020).*

3.4 Electrostatic waves

Electrostatic solitary waves (ESWs) have been observed in the reconnection jet region in the Earth's magnetotail by the Magnetospheric Multiscale spacecraft (MMS). The jet plasma is modeled by a three-component magnetized plasma consisting of hot electrons and two cold ion beams streaming parallel and anti-parallel to the magnetic field, respectively (*Lakhina et al., 2021*). The theoretical model predicts bipolar electric fields amplitudes, the soliton widths which are in good agreement with the observed characteristics of ESWs in the reconnection jet region. A new class of ion-acoustic solitons that can exist below the critical Mach number is reported for the first time in a three-component plasma consisting of hot Maxwellian electrons, and two counter streaming ion beams. The results show that when the streaming velocity is below or at a threshold value, only the regular solitons having Mach numbers greater than critical Mach number can exist. The new class of slow ion-acoustic solitons can exist in the parametric regime where the system is stable to counter streaming ion beams instability.

Statistical investigation (September 2012 - September 2017) of pitch angle distribution (PAD) of energetic electrons (∼30 keV - 1 MeV) in the outer radiation belt (L ≥ 3) during CME- and

CIR-driven geomagnetic storms is carried out using Van Allen Probe measurements. We found that several hundreds of keV electrons exhibit clear dependence on local time, storm phases and storm drivers, with increased anisotropy for CME-driven storms during main and early recovery phases. On the contrary, we found that tens of keV electrons do not exhibit significant dependence on these parameters. Magnetic field line stretching and drift-shell splitting during disturbed times resulted in the MLT dependent PAD of 346–909 keV electrons (*Chakraborty et al., 2022*).

During geomagnetic storm period, the magnetic field variations obtained after removing the internal geomagnetic field and quiet time contributions can be considered as a proxy for storm time currents and are found to follow the temporal profile of Dst index very closely. These variations at the equatorial crossings are recorded by multiple-spacecraft are used to estimate the Dst values and are found to have a good match with the ground-based Dst index. The average deviation between these two is around 4–13% (*Vichare et al., 2019*).

The observations of variation of Radiation Belt Electron Flux during CME- and CIR-Driven Geomagnetic Storms from Van Allen Probes Observations. Relativistic electron flux responses in the inner magnetosphere are investigated for 28 magnetic storms driven by corotating interaction region (CIR) and 27 magnetic storms driven by coronal mass ejection (CME), using data from the Relativistic Electron-Proton Telescope instrument on board VanAllen Probes from October 2012 to May 2017. It is seen that at $L \sim 5$, CIR storms are responsible for the electron flux enhancements, while this effect is seen at $L \sim 3$ for CME storms (*Pandya et al., 2019*) (Figure 37).

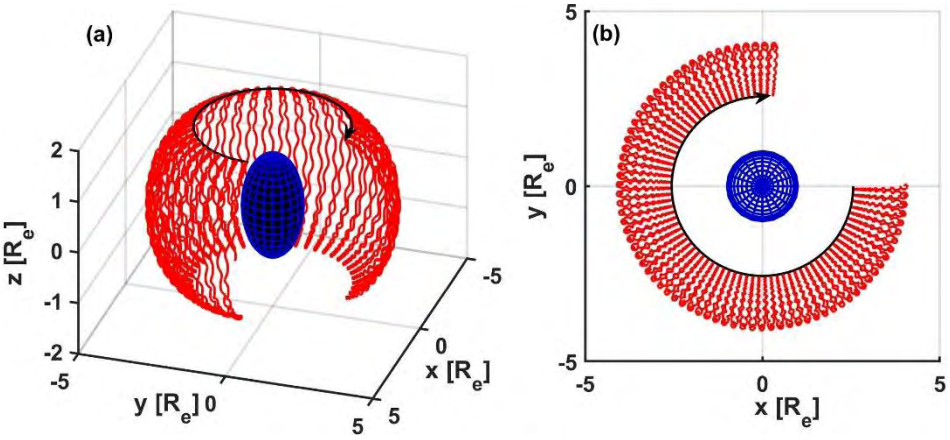

Figure 37: The trajectories of proton of energy 5 MeV at L=4 with pitch angle of αeq=30° in Earth's dipolar magnetic field for 120 s. The dipole moment is in -$\hat{z}$ direction. The black arrows show westward motion of proton due to ∇B×B drift. (a) shows three-dimensional trajectory of proton (b) the top view of the proton motion in *xy* plane as seen from the north magnetic pole.

In Polar Science program, a series of sub-storms called high-intensity long-duration continuous AE activity events (HILDCAAs) were studied. To understand the mechanism, global Cosmic Noise Absorption (CNA), auroral images by a space-based Imager, energetic electron flux data from geostationary satellites and magnetic field measurements covering almost all latitudinal

and local time sectors were studied. These shock-induced super-substorms (SSSs) have extremely high intensities and long durations.

4. Solar Wind and Interplanetary Field

4.1 Effects of IMF By on ring current asymmetry

PRL has evaluated the role of interplanetary magnetic field (IMF) B_y on the asymmetry of the ring current during the main phase of geomagnetic storms. The investigation brings out for the first time, the additional role of IMF B_y in influencing the MLT distribution of ring current observed at ground magnetic stations. Under southward IMF B_z conditions, it is shown based on SuperDARN and AMPERE data that IMF B_y can alter the MLT distribution of ring current under suitable conditions. Under steady convection state, IMF B_y can rotate the convection cells based on its polarity, which in turn can change the MLT distribution of ring current observed by low-latitude ground stations. This investigation, thus, brings out the important role of IMF B_y on the asymmetric MLT distribution of ring current under southward IMF B_z (*Kumar et al., 2020*).

4.2 Van Allen probe observations of disappearance, recovery and patchiness of plasmaspheric hiss

A plasmaspheric hiss event observed by the Van Allen probes in response to two successive interplanetary (IP) shocks occurring within an interval of ∼2 h on December 19, 2015 is reported for the first time. Both the shocks triggered substorms that played important roles in the variability of plasmaspheric hiss. It is shown that an enhanced growth rate and additional contribution from shock-induced poloidal Pc5 mode (periodicity ∼240 s) ultralow frequency (ULF) waves resulted in the excitation of hiss waves during this period. The hiss wave amplitudes were found to be additionally modulated by background plasma density and fluctuating plasmapause location. The investigation highlights the important roles of IP shocks, substorms, ULF waves, and background plasma density in the variability of plasmaspheric hiss (*Chakraborty et al., 2021*).

4.3 Solar wind and suprathermal energetic particle studies

By systematically analysing inter-calibrated alpha particle abundance (A_{He}) data obtained from the first Lagrangian point of the Sun–Earth system, we show that A_{He} variations are distinctively different in solar cycle 24 as compared to the last three cycles. The frequency of A_{He} = 2–3 per cent events is significantly higher in slow/intermediate solar winds in solar cycle 24 as opposed to the dominance of the typical A_{He} = 4–5 per cent events in the previous three cycles. The investigation suggests that the coronal magnetic field configuration started undergoing systematic changes starting from cycle 23 and this altered magnetic field configuration affected the way helium got processed and depleted in the solar atmosphere (Figure 38), (*Yogesh et al., 2021*).

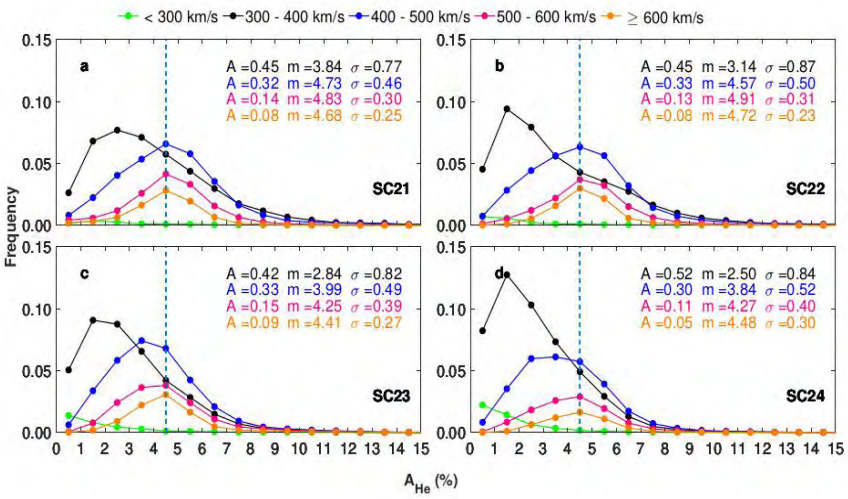

Figure 38: Frequency distribution of A H e events with 1% bin size for four velocity bins, viz. (1). 300 km/s (2) 300-400 km/s (3) 400-500 km/s (4) 500-600 km/s (6) > 600 km/s in solar cycles 21 (a), 22 (b), 23 (c) and 24 (d). The frequency distributions are approximated by log-normal distributions wherein A, σ and m are the fit parameters namely normalization coefficient, standard deviation and median in linear scale respectively. The vertical dashed lines mark A H e of 4.5%.

Based on an extensive analysis of 275 ICME events, we show that there is a solar activity variation of ICME averaged A_{He} values. We also found that the first ionization potential effect and localized coronal heating due to magnetic reconnection are not the major contributing factors for A_{He} enhancements in ICMEs. Investigation on concurrent solar flares and ICME events for 63 cases reveals that chromospheric evaporation in tandem with gravitational settling determines the A_{He} enhancements and variabilities beyond 8 per cent in ICMEs. We show that the intensity and timing of the preceding flares from the same active region from where the CME erupts are important factors to understand the A_{He} enhancements in ICMEs (*Yogesh et al., 2022*).

Recently the sunspot number series has been corrected and new Version II sunspot number data are released. Therefore, one has to check the applicability of different solar cycle prediction models using Version II sunspot data. In this context, we have developed a new model to forecast the peak sunspot activity of the upcoming solar cycle by utilizing Shannon entropy estimates in the declining phase of the preceding solar cycle. This model predicts the peak smoothed Version II sunspot number as 137±24 for the solar cycle 25 (*Kakad et al., 2020*).

Solar cycle variations of "quiet" time suprathermal elements (H and other heavy ions like 4He, 3He, C, O, and Fe) are investigated using < ~ 1 MeV n−1 particle flux data obtained from the Ultra-Low Energy Isotope Spectrometer on board the Advanced Composition Explorer satellite during solar cycles 23 and 24. These results suggest that generation mechanisms responsible for suprathermal 4He and Fe underwent changes in cycle 24 and these mechanisms are probably dependent on the first ionization potential and mass-to-charge ratio. This proposition gets credence from the fact that changes in the lags and spectral slopes for C and O are not significantly different in cycles 23 and 24 (Figure 39), (*Dalal et al., 2022*).

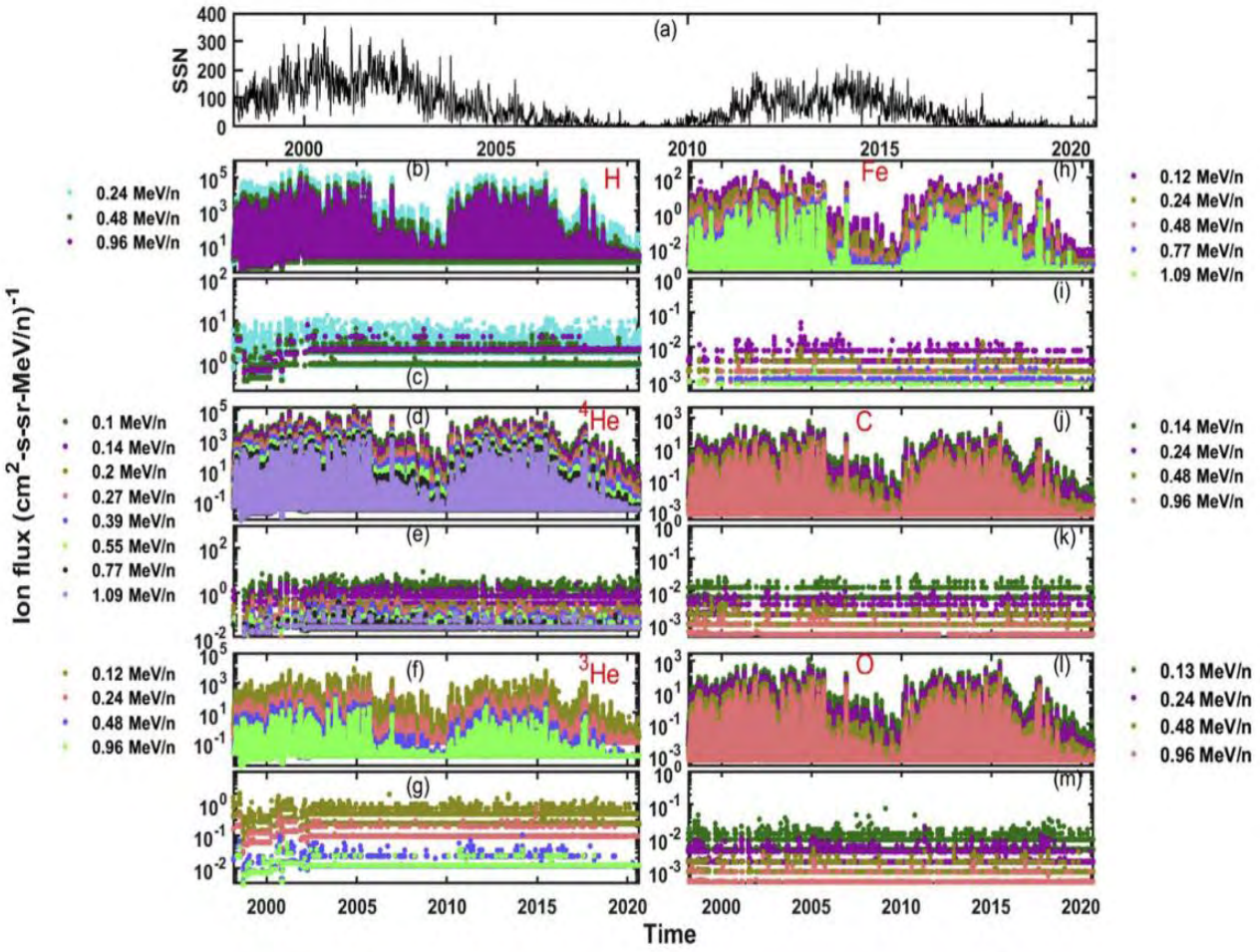

Figure 39. Original vis-à-vis modified (after removal of the transient events) variations of the fluxes of different elements for the entire period (1998–2020) along with the SSN data used in this paper (panel (a)). Subplots (b), (d), (f), (h), (j), and (l) show the original flux variations of H, 4 He, 3He, Fe, C, and O, respectively. The modified ("quiet") fluxes of the elements in the similar order are plotted in subplots (c), (e), (g), (i), (k), and (m). Legends for the different energy channels of an element are marked by colored dots and are appropriately placed at the left and right of the plots.

5. Geomagnetic Observatory, Surveys and Analysis

Magnetic observatories used indigenously developed PPMs for absolute observations. Spectral Resonance Structures (SRS) of Ionospheric Alfven Resonator (IAR) are investigated by analysing the magnetic field data of a high sampling frequency induction coil magnetometer, installed at a low latitude Indian station, Shillong(25.56∘N, 91.86∘E, dipoleL=1.08) (Adhitya et al., 2022). It is observed that the excitation of double SRS is related to the E-region to F-region variability of refractive index of the ionosphere (*Adhitya et al., 2022*).

CSIR-NGRI Geomagnetic Observatories (GO) has been measuring the strength and direction of the Earth's magnetic field for the past 58 years, and the measurements were recently upgraded to 1s. Manjula et al. (*2021*) found noticeable differences in the noise levels present in vector and scalar variation data, due to the vehicular noise observed before and during the lockdown periods by the noise spectrum estimates. Vijay Kumar and Chandrasekhar (*2022*) developed a robust real-time data transmission system by using Python language and transmitted real-time from a remote observatory to GIN with a time frame of less than 300s.

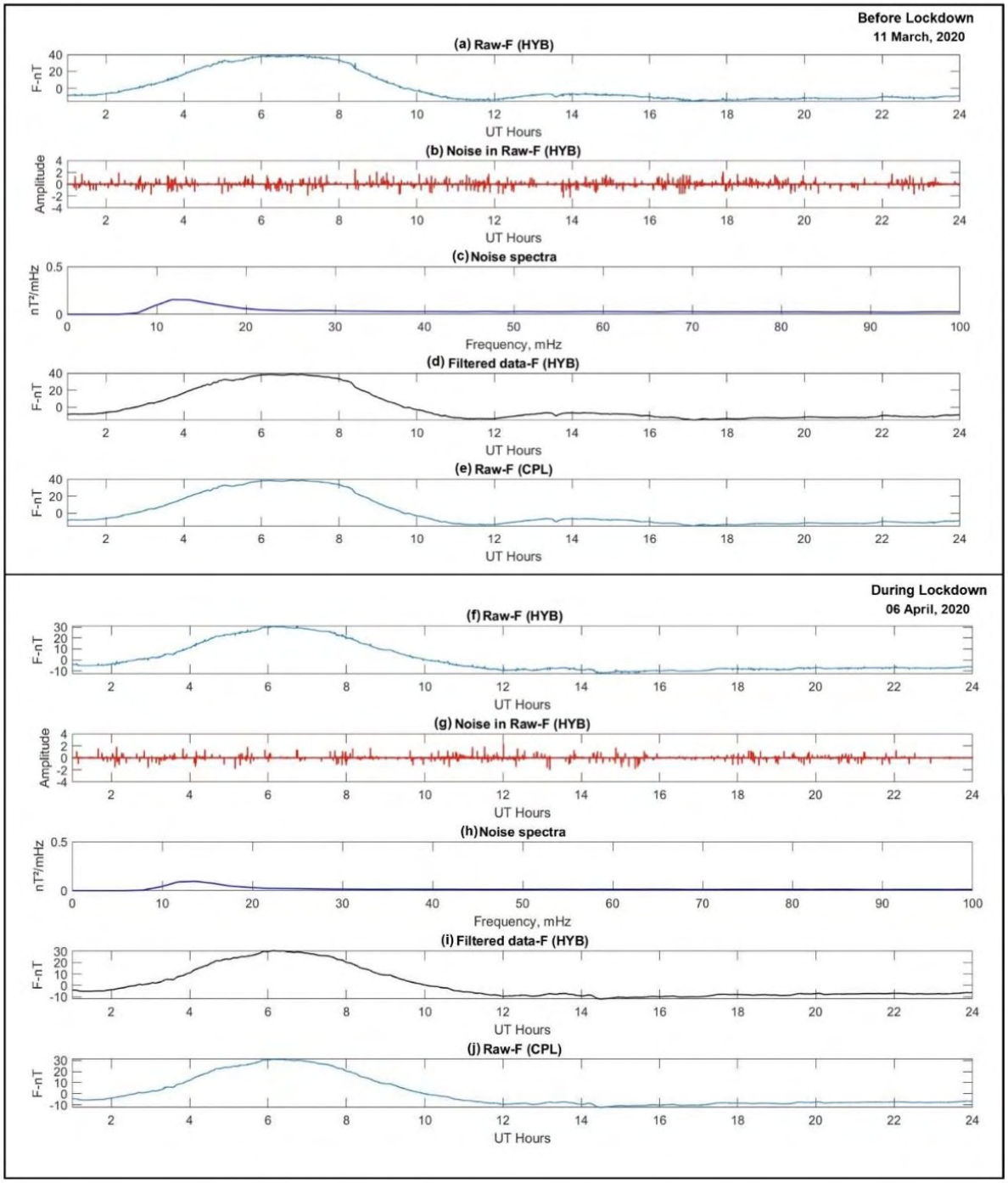

Figure 40: Plots of HYB 1 Hz F component data before and after the lockdown period in the raw data and filtered data

6. Electromagnetic Induction in Earth and Planetary Bodies

6.1 Magnetotelluric measurements in Precambrian terranes

The CSIR-NGRI has carried out magnetotelluric (MT) studies in the diverse geological terranes of the Indian sub-continent, spanning from the Indian Himalayas in the north to the Dharwar terrane in the south, and the Andaman Nicobar Islands in the Indian Ocean, to understand the present day crustal as well as upper mantle resistivity structure that helped to identify potential earth resource structures and unfold the tectonic evolution of key geological domains. As the manual analysis and processing of MT time-series data is a tedious and time consuming job, a new automated software tool (SigMT: an open source Python package) for noise removal from measured time-series and MT tensor estimation was developed and made available to the EM community (*Ajithabh et al., 2023*).

MT investigations across Precambrian terranes of Marwar and Aravalli-Delhi Mobile Belt (ADMB) in the NW Indian shield showed imprints of Proterozoic as well as Phanerozoic tectono-thermal events in the lithosphere structure and meta-cratonization of the Aravalli craton (Figure 41; *Azeez et al., 2023*).

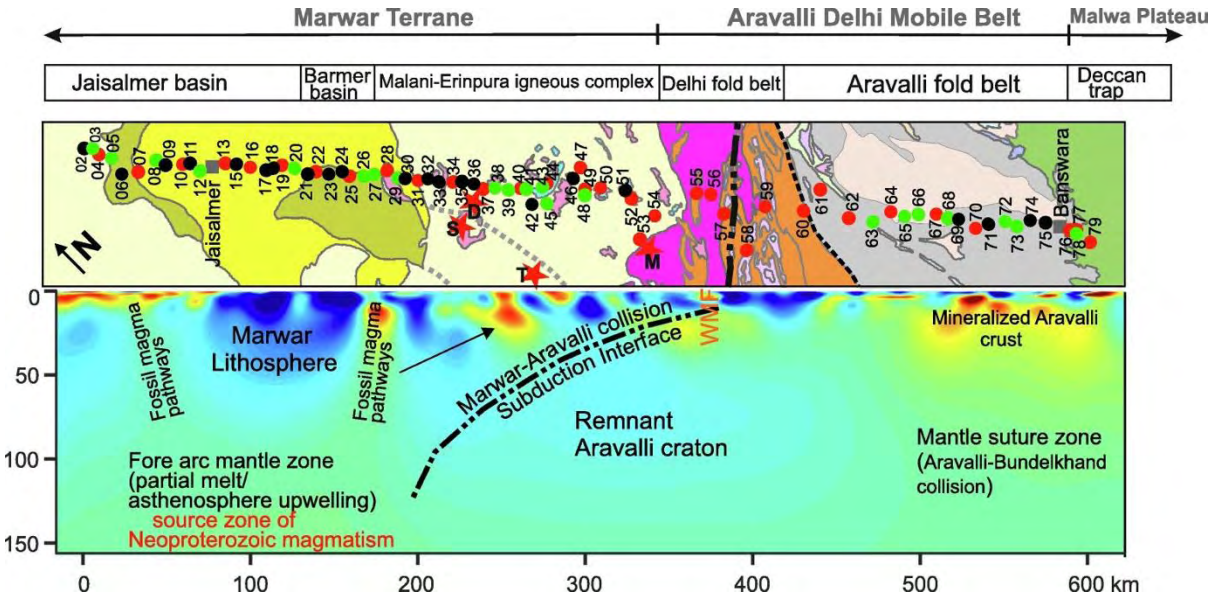

Figure 41: Interpreted lithospheric resistivity section from the 3D inversion modelling of MT data along Jaisalmer-Banswara transect across the Marwar Terrane and Aravalli-Delhi Mobile Belt in the NW Indian shield (*Azeez et al., 2023*).

The lithosphere architecture of the well-known Dharwar craton in south India was studied using MT data to understand the complex geological processes that evolved this largest cratonic terrane in the Indian subcontinent. The lithospheric resistivity models revealed that Chitradurga shear zone (CSZ) acts as a contact zone between east and west Dharwar carton and also indicated an eastward subduction polarity of the accretion process between the western and eastern Dharwar blocks (*Malleswari et al., 2019; Kusham et al., 2019, 2021a, b*).

6.2 Magnetotelluric measurements in Kachchh, CITZ and Sikkim

The crustal and upper mantle resistivity character of the Kachchh intraplate seismic zone was studied using 3D inversion modelling. The models indicated significant level of fluids in the crust and upper mantle, and provided clue to the prolonged aftershock activity in this unique intraplate seismic zone (*Azeez et al., 2020*). Another study in the Deccan flood basalt covered Saurashtra peninsula, using 2D and 3D inversion approaches, successfully imaged thick sub-basaltic Mesozoic sediment (*Ajithabh et al., 2020*; *Ajithabh and Patro, 2021*; *Borah et al., 2023*). Apart from this, the importance of Uniform grid Laplacian operator and Standard grid Laplacian operator in 2D inversion of MT data has been demonstrated (*Ajithabh and Patro, 2021*). Evolutionary history of the ENE-WSW trending Central Indian Tectonic Zone (CITZ), the mega lineament that divide the Indian peninsular shield into North and South Indian blocks, was investigated through magnetotelluric imaging of the complex geologic structures encompassing the CITZ. Multiple tectonic boundaries along the Central Indian shear and Tan shear are inferred from the MT results, which suggest that the developed under the transition of oceanic subduction to continental collision processes at multiple geological times (*Raju et al., 2020; 2023*).

Using broad-band and long-period magnetotelluric (MT) IIG acquired data along an east-west trending traverse of nearly 200 km across the Kachchh, Cambay rift basins, and Aravalli-Delhi fold belt (ADFB), western India. The regional strike analysis of MT data indicated an approximate N59°E geoelectric strike direction under the traverse and it is in fair agreement with the predominant geological strike in the study area. The decomposed transverse electric (TE)- and transverse magnetic (TM)-data modes were inverted using a nonlinear conjugate gradient algorithm to image the electrical lithospheric structure across the Cambay rift basin and its surrounding regions (Figure 42). These studies show a thick (~1–5 km) layer of conductive Tertiary–Mesozoic sediments beneath the Kachchh and Cambay rift basins. The resistive blocks indicate presence of basic/ultrabasic volcanic intrusives, depleted mantle lithosphere, and different Precambrian structural units (*Danda et al., 2020*).

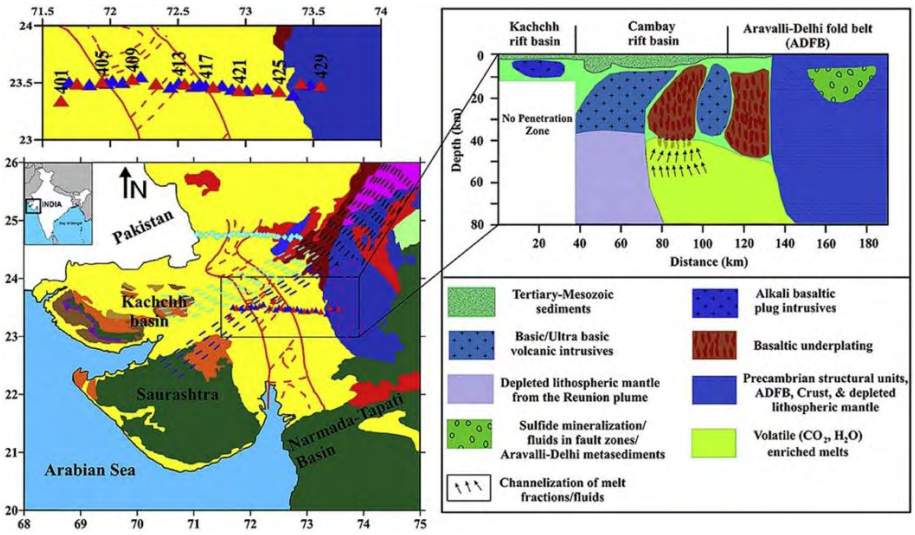

Figure 42: Regional geological map of the western India (modified from *Biswas, 1982, Biswas, 1987, Mishra et al., 1998*). Red triangles represent LMT + BBMT stations, blue triangles represent BBMT stations, and red star for Mehsana town. A cartoon sketch showing possible geological interpretation across the profile. The geological domains crossed by the profile are shown at the top.

A case study on the MT data from Sikkim Himalaya demonstrated the importance of 3D topography correction on 2D modelling of MT data (Figure 43; *Kumar et al., 2022*). New insights on the lateral as well as vertical variations in crustal electrical structure and rheology in the Sikkim Himalaya was obtained from 3D inversion of MT data (*Konda et al., 2023*).

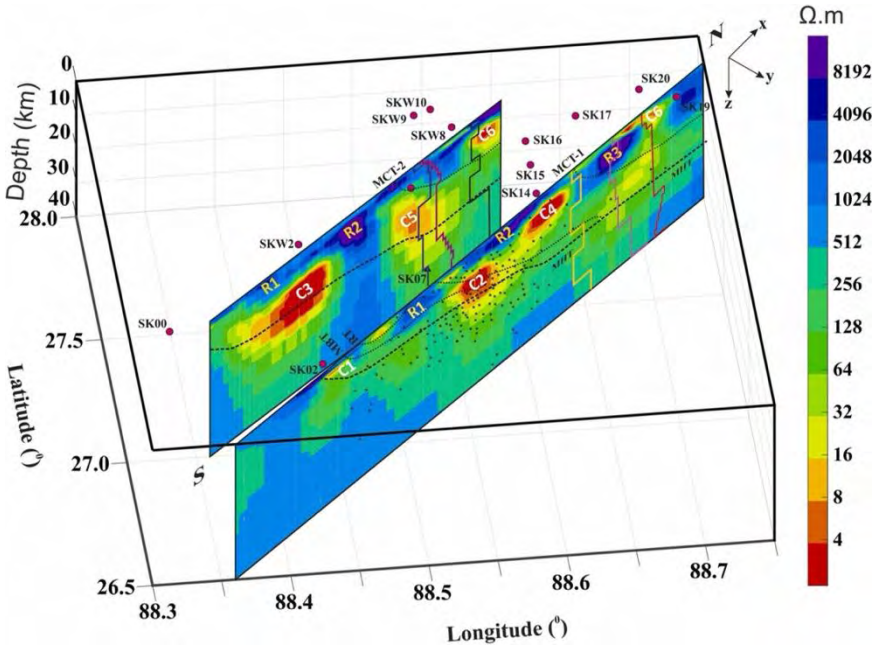

Figure 43: 3D geoelectric cross sections obtained from full impedance tensor inversion of MT data from Sikkim Himalaya (*Konda et al., 2023*).

Andaman-Nicobar is the unique region in India, which forms the outer-arc accretionary sedimentary complex and inner igneous arc is related to the Andaman-Sumatra active subduction zone. To understand this region LMT data acquired at three locations. The forward modelling of LMT data along with other geophysical constraints reveals the complexity of the subsurface structure from north to south of the Andaman Islands (*Anusha et al., 2020*). Apart from routine MT work, continuous monitoring magnetotelluric (MT) time series data in Koyna and Warna region is carried out. This study revealed the electrokinetic and seismic dynamo mechanisms are the feasible mechanisms playing a major role for generation of co and pre seismic electromagnetic signatures (*Vijaya Kumar et al., 2020*).

Magnetotellurics method for delineating crustal and lithospheric structure of Himalayan region is being extensively used by Wadia Institute of Himalayan Geology, Dehradun,India. Several MT profiles covering different litho-tectonic segments are undertaken for study. MT profiles along Satluz Valley, along Saharanpur-Yamunotri, across Tso-Morari crystallines and along Lohit valley are being investigated in different regions of Himalaya for subsurface geoelectrical characterization and for understanding Himalayan tectonics in order to develop a geodynamic model of the Himalaya. The important observation from these studies is presence of intra crustal low resistivity layer (IC-LRL) at mid crustal depth along all profiles (Figure 44). The resistivity of this ICLRL is not same across different segments of Himalaya signifying varying intensity of tectonics all along the Himalaya. IC-LRL is interpreted as the Main Himalayan Thrust (MHT) or detachment to which all major thrust of the Himalayas appears to sole down.

The other important observation in geoelectrical images along Himalayan transects is the change of depth of IC-LRL from the MCT zone to the higher Himalayas and Northward. This change of depth is the location of the ramp structure in MHT. The conductivity of this transition zone varies along strike. In order to understand whether this along strike variability may be affecting or controlling the seismicity pattern of Himalayan seismic belt beside the transverse structure, an integrated approach is required where more number of multidisciplinary profiles, 3D modelling and joint inversion of different parameters may provide significant insight.

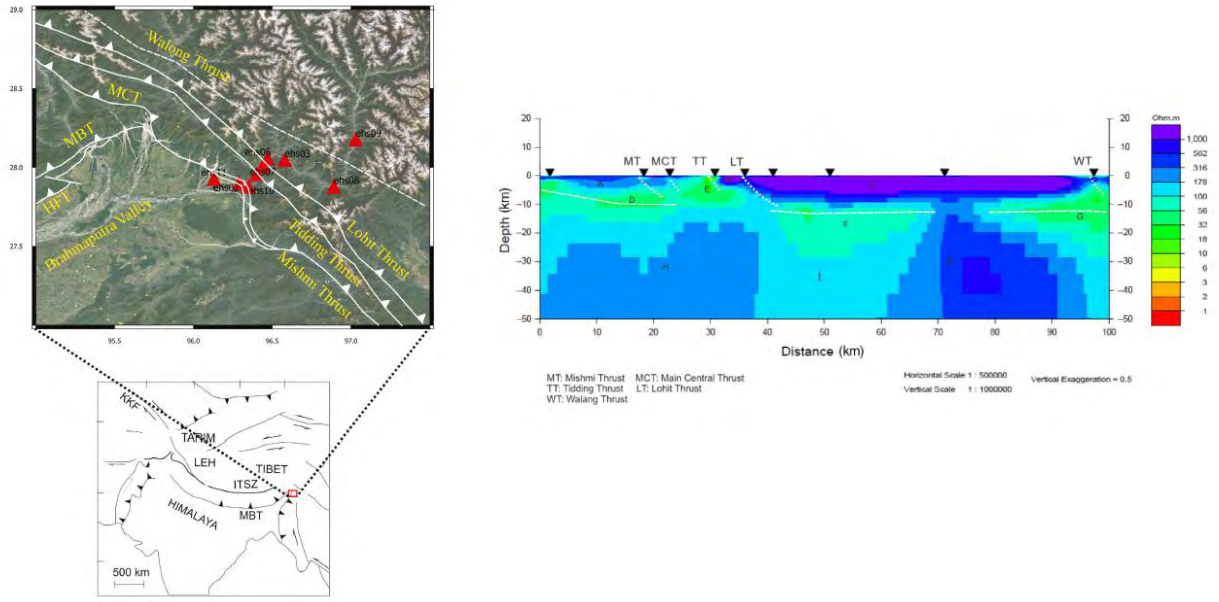

Figure 44: MT profile in Lohit Valley (Arunachal Pardesh,India) and geoelectrical section along the profile.

6.3 Electrical resistivity Tomography

Electrical resistivity tomography for shallow subsurface image in Kala-amb region is used for active tectonics studies at Kala Amb region, across the Himalayan Frontal Thrust based on a previous trench excavation survey, in the northwestern Frontal Himalaya. An electrical resistivity tomography 2D profile survey is conducted along two lines in Kala Amb region. The lines are selected with the primary objective of extending the features identified in the trench section into the subsurface. The inverted resistivity model has lateral and vertical resistivity variations according to different depositional units in the area. The presence of a north dipping fault at 54-m distance from zero electrode position towards south clearly distinguishes two separate lithological units. The liquefaction feature identified on the trench wall section which is also inferred from the resistivity section appears to be originated from greater depth. Similarity of resistivity features and spatial distance of two profiles allow us to interpret the lateral continuity of subsurface features and to identify the thickness of Quaternary deposit over river bed level. The study found to be helpful in understanding the efficacy of this method for the recognition and geometrical characterization of faults across morphotectonic scarps or fault traces in a region which experienced late Quaternary tectonic activity.

6.4 Earthquake precursory studies

ULF band induction coil magnetic field variations recorded at MPGO Tejpur has been studied with NEIST, Jorhat. Fractal analysis, polarization analysis methods were employed to find the seismo-electromagnetic signatures. The study suggest signature of SEM emissions, in the form of enhancements in SZ/SH. The fractal dimensions, calculated with the spectral density method, ambiguously depicted a gradual increase prior to the intense phase of seismicity.

3rd IAGA IASPEI Joint Scientific Assembly hosted by CSIR National Geophysical Research Institute

The IAGA IASPEI 2021 Joint Scientific Assembly (JSA) was held virtually from 21-27 August, 2021, due to the global Covid 19 pandemic conditions. It was hosted by CSIR-NGRI and INSA (the National Adhering body of IUGG) and supported by CSIR, MoES and DST. The week before, the 5th IAGA and 1st IASPEI Schools and the GIFT Workshop were conducted. 30 doctoral students attended each of the Schools, and more than 50 school teachers attended the GIFT Workshop. The Joint Scientific Assembly was inaugurated by Dr. Jitendra Singh, Hon'ble Minister of State for Science and Technology and Earth Sciences (Independent Charge). 827 scientists and researchers were registered for the conference. 778 abstracts were submitted for presentations during the 53 symposia: 8 Joint symposia, 1 Diamond Jubilee symposium commemorating 60 years of CSIR-NGRI, 27 IAGA symposia and 17 IASPEI symposia, including one from the Asian Seismological Commission (ASC). The 217 poster and 562 oral contributions including 121 invited talks were presented in virtual mode from all over the world. Three Plenary lectures on topics of interest both for IAGA and IASPEI were also presented during the JSA. This assembly also facilitated 24 business meetings of IAGA and 20 business meetings of IASPEI, including one for Asian Seismological commission. The sessions were organized during 1645 to 1845 Indian Standard Time, and also 2015 to 2215 Indian Standard Time to optimize global coverage. 57 countries participated in this joint scientific assembly.

The Chief Guest Dr. Jitendra Singh, Hon'ble Minister of State for Science and Technology and Earth Sciences (Independent Charge), along with the dignitaries in person and online, released the Abstract Volume of the JSA IAGA IASPEI 2021.

Address by Dr. Mioara Mandea, President, International Association of Geomagnetism and Aeronomy (IAGA) at the inaugural ceremony.

Address by Dr. Kenji Satake, President, International Association of Seismology and Physics of the Earth's Interior (IASPEI) at the inaugural ceremony.

Address by Dr. Kathryn Whaler, President, The International Union of Geodesy and Geophysics (UGG) at the inaugural ceremony.

Acknowledgements

The following scientists from national institutes participated in the preparation of this report:

Dr. B.P.K. Patro, CSIR-National Geophysical Research Institute, Hyderabad, India
Dr. Kusumita Arora, CSIR-National Geophysical Research Institute, Hyderabad, India
Dr. Jayashree Bulusu, Indian Institute of Geomagnetism, Mumbai, India
Dr. Binod Sreenivasan, Indian Institute of Science, Bengaluru, India
IIT Indore,
Dr. Sumanta Sarkhel, Indian Institute of Technology, Roorkee, India
(Name?), National Atmospheric Research Laboratory, Gadanki, India
Dr. D. Pallamraju, Physical Research Laboratory, Ahmedabad, India
Dr. C. Vineeth, Space Physics Laboratory, Thiruvananthapuram, India
Dr. Gautam Rawat, Wadia Institute of Himalayan Geology, Dehradun, India

REFERENCES

1. A. Guharay, P. P. Batista and V. F. Andrioli, (2019), Investigation of solar cycle dependence of the tides in the low latitude MLT using meteor radar observations, Journal of Atmospheric and Solar-Terrestrial Physics, 193, 105083, https://doi.org/10.1016/j.jastp.2019.105083.
2. A. Guharay, S. Mondal, S. Sarkhel, M. Sivakandan, M. V. Sunil Krishna, (2021), Signature of a mesospheric bore in 557.7 nm airglow emission using all-sky imager at Hanle (32.7N, 78.9E), Advances in Space Research, 69, 5, 2020-2030, https://doi.org/10.1016/j.asr.2021.12.006
3. A. Guharay, S. Mondal, S. Sarkhel, M. Sivakandan, M. V. Sunil Krishna, (2021), Signature of a mesospheric bore in 557.7 nm airglow emission using all-sky imager at Hanle (32.7N, 78.9E), Advances in Space Research, 69, 5, 2020-2030, https://doi.org/10.1016/j.asr.2021.12.006
4. A. Kumar, D. Chakrabarty, K. Pandey, A.K. Yadav, (2022), Solar flux dependence of post-sunset enhancement in vertical total electron content over the crest region of equatorial ionization anomaly, JGR Space Physics, 127, e2021JA030156. https://doi.org/10.1029/2021JA030156.
5. Kumar A., Chakrabarty D., Pandey K., Fejer B. G., Sunda S., G. K. Seemala, S. Sripathi, A. Yadav K., (2021), Evidence for the significant differences in response times of equatorial ionization anomaly crest corresponding to plasma fountains during daytime and post-sunset hours, JGR Space Physics, 126, e2020JA028628, https://doi.org/10.1029/2020JA028628.
6. Varma A. and Sreenivasan B., The role of slow magnetostrophic waves in the formation of the axial dipole in planetary dynamos, *Physics of the Earth and Planetary Interiors*, 106944, 2022.
7. Adhitya, P., Nosé, M., Bulusu, J., Vichare G., Sinha A.K.. Observation of ionospheric Alfven resonator with double spectral resonance structures at low latitude station, Shillong (dipole L=1.08 dipole L=1.08). *Earth Planets Space* **74**, 169 (2022). https://doi.org/10.1186/s40623-022-01730-2

8. Ajith, K. K., Li, G., Tulasi Ram, S., Yamamoto, M., Hozumi, K., Abadi, P.,& Xie, H. (2020). On the seeding of periodic equatorial plasma bubbles by gravity waves associated with tropicalcyclone: A case study. Journal of Geophysical Research: Space Physics,125, e2020JA028003. https://doi.org/10.1029/2020JA028003
9. Ajithabh, K.S. and Patro, P.K., 2021. Crustal deformation in Volcanic covered area as inferred from magnetotelluric studies: An example from India. *Journal of Geodynamics*, *145*, p.101840.
10. Ajithabh, K.S. and Patro, P.K., 2023. SigMT: An open-source Python package for magnetotelluric data processing. *Computers & Geosciences*, *171*, p.105270.
11. Ajithabh, K.S., Patro, P.K., Azeez, K.A. and Veeraswamy, K., 2020. Basalt–sediment configuration in the Tapti rift of central Indian region as derived from magnetotelluric (MT) studies and hydrocarbon prospects. *Arabian Journal of Geosciences*, *13*, pp.1-12.
12. Ambili, K. M and Choudhary R. K., "Three-dimensional distribution of ions and electrons in the lunar ionosphereoriginated from the photochemical reactions", Monthly Notices of the Royal Astronomical Society, 3734, https://doi.org/10.1093/mnras/stab3734, 2021.
13. Ambili, K. M. and Choudhary R. K., "On the impact of meridional wind circulation changes in the electron density distribution over the Indian equatorial and low latitude ionospheric region during a severe geomagnetic storm", Advances in Space Research, 70 (7), 2058-2069, https://doi.org/10.1016/j.asr.2022.06.027, 2022.
14. Anusha, E., Arora, K., Nagarajan, N. and Azeez, K.A., 2020. Constraints on the configuration of Andaman-Nicobar Subduction zone from EM modeling. *Tectonophysics*, *792*, p.228575
15. Aswathy R. P. and G. Manju, "Equatorial Ionization Anomaly crest magnitude and its implications on the nocturnal equatorial ionospheric plasma irregularity characteristics", Adv. Space Res., 68(10), 4129-4136, https://doi: 10.1016/j.asr.2021.07.019, 2021.
16. Aswathy, R. P. and G. Manju, "The post sunset equatorial F- region zonal drift variability and its linkage with equatorial spread F onset and duration over Indian longitudes", Advances in Space Research, 67 (4), 1254-1260, https://doi.org/10.1016/j.asr.2020.11.024, 2021.
17. Aswathy, R.P., Manju, G., Time of evening zonal drift reversal in F- region and its implications for post sunset ionosphere, Journal of Atmospheric and Solar-Terrestrial Physics, DOI:10.1016/j.jastp.2020.105210, (2020).
18. Azeez, K.A., Mohan, K., Veeraswamy, K., Rastogi, B.K., Gupta, A.K. and Harinarayana, T., 2021. Lithospheric resistivity structure of the 2001 Bhuj earthquake aftershock zone. *Geophysical Journal International*, *224*(3), pp.1980-2000
19. B. Dalal, D. Chakrabarty, and N. Srivastava, (2022), Differential behaviors of suprathermal 4He and Fe populations in the interplanetary medium during solar cycle 24, Astrophys. J., 938:26 (15pp), https://doi.org/10.3847/1538-4357/ac88d8
20. B. R. Kalita, P. K. Bhuyan, S. J. Nath, M. C. Choudhury, D. Chakrabarty, K. Wang, K. Hozumi, P. Supnithi, T. Komolmis, C. Y. Yatini, M. L. Huy, (2022), The investigation on daytime conjugate hemispheric asymmetry along 100°E longitude using observations and model simulations: new insights, Adv. Space Res., 69, 3726-3740, https://doi.org/10.1016/j.asr.2022.02.058.
21. B. Sreenivasan and G. Maurya, Evolution of foced magnetohydrodynamic waves in a stratified fluid, *Journal of Fluid Mechanics*, 922, A32, 2021.

22. B. Veenadhari,, T. Kikuchi, S. Kumar, S. Tulasiram, D. Chakrabarty, Y. Ebihara, G. D. Reeves, (2019), Signatures of substorm related overshielding electric field at equatorial latitudes under steady southward IMF Bz during main phase of magnetic storm, Adv. Space Res., 64, 1975-1988, https://doi.org/10.1016/j.asr.2019.04.001
23. B.V. Lakshmi, Deenadayalan K. and Gawali P.B. (2020). A test of the pseudo-Thellier technique for determining relative palaeointensity in the Tirna Basin, Osmanabad, Maharashtra, India. Geological Society, London, Special Publications, 497, https://doi.org/10.1144/SP497-2019-77
24. Bharti, G., Sunil Krishna, M. V, & Singh, V. (2019). Radiative cooling due to NO at 5.3 μm emission as observed by TIMED/SABER over Asian sector. *Advances in Space Research*, *64*(10), 1989-2001. https://doi.org/10.1016/j.asr.2019.07.016
25. Bhattacharyya, A., Fedrizzi, M., Fuller-Rowell, T. J., Gurram, P., Kakad, B., Sripathi, S., & Sunda, S. (2019). Effect of magnetic storm related thermospheric changes on the evolution of equatorial plasma bubbles. Journal of Geophysical Research: Space Physics, 124. https://doi.org/10.1029/2018JA025995.
26. Bhattacharyya, A., Gurram, P., Kakad, B., Sripathi, S., & Sunda, S. (2019). Signal frequency dependence of ionospheric scintillations: An indicator of irregularity spectrum characteristics, Journal of Geophysical Research: Space Physics, 124. https://doi.org/10.1029/2019JA026987
27. Borah, U.K. and Patro, P.K., 2019. Estimation of the depth of investigation in the magnetotelluric method from the phase Magnetotellurics depth of investigation. *Geophysics*, *84*(6), pp.E377-E385.
28. Borah, U.K., Patro, P.K., Reddy, K.C. and Babu, N., 2023. Deccan Trap configuration in and around Koyna-Warna Seismic Zone, India: A magnetotelluric approach. *Journal of Applied Geophysics*, *208*, p.104875.
29. C. Vineeth, A. Ajesh, Pant T. K. and Ruohoniemi J.M., Response of Thermospheric Nightglow Emissions over the magnetic Equator to Prompt Penetration Electric Field Events, Journal of Geophysical Research: Space Physics,2019, DOI: 10.1029/2018JA026317.
30. Chakraborty S., Chakrabarty D., Reeves G. D., Baker D. N., Claudepierre S. G., Breneman A. W., Hartley D. P., Larsen B. A., (2021), Van Allen probe observations of disappearance, recovery and patchiness of plasmaspheric hiss following two consecutive interplanetary shocks: First results, JGR Space Physics, 126, e2020JA028873. https://doi.org/10.1029/2020JA028873
31. Chakraborty S., Chakrabarty D., Reeves G. D., Baker D. N., Rae J., (2022), Statistical investigation on equatorial pitch angle distribution of energetic electrons in Earth's outer radiation belt during CME-and CIR-driven storms, Front. Astron. Space Sci. 9:986061, https://doi.org/10.3389/fspas.2022.986061
32. Chauhan N., Gurubaran S., Moulik S., Das P.K., Bagiya M., Advances in Space Research, 70, 699-709, 2022.All-Sky Imaging Observations of Mesospheric Fronts from Silchar (24.7° N, 92.8° E)
33. D. Rout, K. Pandey, D. Chakrabarty, R. Sekar, Xian Lu, (2019), Significant electric field perturbations in low latitude ionosphere due to the passage of two consecutive ICMEs during 6-8 September 2017, JGR Space Physics, 124, https://doi.org/10.1029/2019JA027133.

34. D. Rout, R. Singh, K. Pandey, T. K. Pant, C. Stolle, D. Chakrabarty, S. Thampi, T. Bag (2022), Evidence for Presence of a Global Quasi-Resonant Mode of Oscillations During High-Intensity Long-Duration Continuous AE Activity (HILDCAA) events, Earth, Planets and Space, 74:91, https://doi.org/10.1186/s40623-022-01642-1
35. Dalal B., Chakrabarty D., and Srivastava N., (2022), Differential behaviors of suprathermal 4He and Fe populations in the interplanetary medium during solar cycle 24, Astrophys. J., 938:26 (15pp), https://doi.org/10.3847/1538-4357/ac88d8
36. Danda N., Rao C.K., Kumar A., Rao P.R., Subba Rao P.B.V., Implications for the lithospheric structure of Cambay rift zone, western India: Inferences from a magnetotelluric study, Geoscience Frontiers, 11, 5, 2020, 1743-1754, https://doi.org/10.1016/j.gsf.2020.01.014.
37. de Abreu, A.J., Correia, E., Denardini, C.M., de Jesus, R., Venkatesh, K., Roberto, M., Abalde, J.R., Fagundes, P.R., Bolan, M.J.A. and Gende, M., (2022), Ionospheric GPS-TEC responses from equatorial region to the EIA crest in the South American sector under intense space weather conditions, J. Atmos. Sol. Terr. Phys., 227, 105801, 1-16, doi: https://doi.org/10.1016/j.jastp.2021.105801.
38. Deenadayalan K., Gawali P.B., B.V. Lakshmi and Manish Rai, Rock-magnetic and archaeomagnetic investigations on archaeological artifacts from Maharashtra, India. *Geological Society, London, Special Publication*, 2020, 497. https://doi.org/ 10.1144/SP497-2019-119
39. Fagundes, P.R., Tasil Brown, V.Y., Pillat, V.G., arcanjo, M.O., Venkatesh, K., Habarulema, J.B., Bolzan, M.J.A, de Jesus, R., de Abreu, A.J., Tardelli, A., Vieira, F. and Denardini, C.M., (2023), Ionospheric storm due to solar Coronal mass ejection in September 2017 over the Brazilian and African longitudes, Adv. Space Res., 71 (1), 46-66, doi: https://doi.org/10.1016/j.asr.2022.07.040.
40. G. Manju and Aswathy R. P., "Ionospheric Planetary Wave Activity and Its Role in equatorial Spread F Day-to-Day Variability", Journal of Geophysical Research, https://doi.org/10.1029/2020JA027960, 2020.
41. G. Manju, Tarun K. Pant, N. Mridula, Aswathy R. P., P. Sreelatha, Rosmy John, Satheesh Thampi R., Aneesh. N. and Abhishek J. K., In-situ observations of rocket burn induced modulations of the top side ionosphere using the IDEA payload on-board the unique orbiting experimental platform (PS4) of the Indian Polar orbiting Satellite Launch Vehicle mission, Journal of Atmospheric and Solar Terrestrial Physics, DOI:10.1016/j.jastp.2020.105203, (2019).
42. G. Mitra, A. Guharay, P. P. Batista, R. A. Buriti, (2021), Impact of the September 2019 minor sudden stratospheric warming on the low-latitude middle atmospheric planetary wave dynamics, Journal of Geophysical Research: Atmospheres, 127, 1, e2021JD035538, https://doi.org/10.1029/2021JD035538
43. G. Mitra, A. Guharay, P. P. Batista, R. A. Buriti, T. Moffat-Griffin, (2022), Investigation on the MLT tidal variability during September 2019 minor sudden stratospheric warming, Advances in Space Research, 71, 869-882, https://doi.org/10.1016/j.asr.2022.08.017
44. Gopala Rao, D., Krishna, K.S., Harinarayana, T., Veeraswamy, K., Abdul Azeez, K.K., Ismaiel, M., Chaubey, A.K., Srinivas, K. and Sreejith, K.M., 2021. Crustal structure of the Gulf of Kachchh, northwest India. *Journal of Earth System Science*, *130*, pp.1-16.

45. Guharay A., Batista P. P., (2019), On the variability of tides during a major stratospheric sudden warming in September 2002 at Southern hemispheric extra-tropical latitude, Advances in Space Research, 63, 8, 2337-2344, https://doi.org/10.1016/j.asr.2018.12.037
46. Guharay A., Batista P. P., and V. F. Andrioli, (2019), Investigation of solar cycle dependence of the tides in the low latitude MLT using meteor radar observations, Journal of Atmospheric and Solar-Terrestrial Physics, 193, 105083, https://doi.org/10.1016/j.jastp.2019.105083
47. Guharay A., Batista P. P., Buriti R. A. (2020), Signature of a 120-day oscillation in the MLT winds and tides over Sao Joao do Cariri (7.4S, 36.5W), Journal of Atmospheric and Solar-Terrestrial Physics, 207, 1, 105337, https://doi.org/10.1016/j.jastp.2020.105337
48. Guharay A., Batista P. P., Buriti R. A. (2021), Observations of a quasi-90-day oscillation in the MLT winds and tides over an equatorial station using meteor radar winds, Advances in Space Research, 67, 10, 3125-3133, https://doi.org/10.1016/j.asr.2021.02.004
49. Guharay A., Batista P. P., Buriti R. A. and Schuch, N. J. (2020), Signature of the 27-day oscillation in the MLT tides and its relation with solar radiation at low latitudes, Earth, Planets and Space, 72, 51, https://doi.org/10.1186/s40623-020-01149-7
50. Hickey D.A., Sau S., Narayanan V. L., Gurubaran S., A possible explanation of interhemispheric asymmetry of equatorial plasma bubbles in airglow images, , Journal of Geophysical Research: Space Physics 125 (3), e2019JA02759212020, 2020.
51. Jose, L., C. Vineeth, T. K. Pant and K. K. Kuma, 2020, Response of the Equatorial Ionosphere to the Annular Solar Eclipse of January 15, 2010, Journal of Geophysical Research, DOI: 10.1029/2019JA027348, (2020).
52. K. Choraghe, A. Raghav, D. Chakrabarty, S. Kasthurirangan, and N. Bijewar, (2021), Properties of the recovery phase of extreme storms, JGR Space Physics, 126, e2020JA028685. https://doi.org/10.1029/2020JA028685.
53. K. Pandey, R. Sekar, D. Chakrabarty, and B. G. Anandarao, (2021), Investigation on Longitudinal and Decadal Variations of the Equatorial Electrojet using a Physical Model, Adv. Space Res., 68, 182-200, https://doi.org/10.1016/j.asr.2021.02.040, 2021
54. Karan, D. K., and D. Pallamraju, (2020), On estimation of daytime equatorial vertical (ExB) plasma drifts using optical neutral dayglow emission measurements, Journal of Geophysical Research: Space Physics, https://doi.org/10.1029/2019JA026775
55. Karan, D. K., and D. Pallamraju, (2020), On estimation of daytime equatorial vertical (ExB) plasma drifts using optical neutral dayglow emission measurements, *Journal of Geophysical Research: Space Physics*, https://doi.org/10.1029/2019JA026775 .
56. Konda, S., Patro, P.K., Reddy, K.C. and Babu, N., 2023. Three-dimensional magnetotelluric signatures and rheology of subducting continental crust: Insights from Sikkim Himalaya, India. *Journal of Geodynamics*, p.101961.
57. Kumar A., Chakrabarty D., Pandey K., Fejer B. G., Sunda S., Seemala G. K., Sripathi S., Yadav A. K., (2021), Evidence for the significant differences in response times of equatorial ionization anomaly crest corresponding to plasma fountains during daytime and post-sunset hours, JGR Space Physics, 126, e2020JA028628, https://doi.org/10.1029/2020JA028628
58. Kumar A., Chakrabarty D., Pandey K., Yadav A.K., (2022), Solar flux dependence of post-sunset enhancement in vertical total electron content over the crest region of

equatorial ionization anomaly, JGR Space Physics, 127, e2021JA030156. https://doi.org/10.1029/2021JA030156
59. Kumar S., Veenadhari B., Chakrabarty D., Tulasi Ram S., Kikuchi T., and Miyoshi Y., (2020), Effects of IMF By on ring current asymmetry under southward IMF Bz conditions observed at ground magnetic stations: Case studies, JGR Space Physics, 125, e2019JA027493. https://doi.org/10.1029/2019JA027493
60. Kumar, P. and Choudhary R. K., "A Study on the Various Modes of Parallel Heat Conduction in the Coronal Loopsof Small and Large Solar Flares Using Scaling Laws", Solar Physics, 296, 147, https://doi.org/10.1007/s11207-021-01884-4, 2021.
61. Kumar, S., D. Pallamraju, P. Suryawanshi, T. Vijayalakshmi, and S. Gopi (2022). Latitudinal Variation in OI 630.0 nm and OI 777.4 nm Dayglow Emissions due to the Equatorial Electrodynamic Processes, Advances in Space Research, https://doi.org/10.1016/j.asr.2021.10.034
62. Kumar, S., D. Pallamraju, P. Suryawanshi, T. Vijayalakshmi, and S. Gopi (2022). Latitudinal Variation in OI 630.0 nm and OI 777.4 nm Dayglow Emissions due to the Equatorial Electrodynamic Processes, *Advances in Space Research*, https://doi.org/10.1016/j.asr.2021.10.034
63. Kumar, S., Patro, P.K. and Chaudhary, B.S., 2022. Subsurface Resistivity Image of Sikkim Himalaya as Derived from Topography Corrected Magnetotelluric Data. *Journal of the Geological Society of India*, *98*(3), pp.335-343.
64. Kunjavaran, A.A.K., Koppireddy, V., Patro, P.K., Gupta, A.K. and Babu, N., 2023. Precambrian tectonics and metacratonization in the NW Indian shield inferred from magnetotelluric imaging across the Marwar Terrane and Aravalli-Delhi Mobile Belt. *Journal of Asian Earth Sciences*, p.105541.
65. Kusham, Naick, B.P., Pratap, A. and Naganjaneyulu, K., 2021a. 2-D versus 3-D Magnetotelluric Data Interpretation: A case study from the Dharwar craton, India. *Tectonophysics*, *816*, p.229028.
66. Kusham, Naick, B.P., Pratap, A. and Naganjaneyulu, K., 2021b. Magnetotelluric 3-D full tensor inversion in the Dharwar craton, India: Mapping of subduction polarity and kimberlitic melt. *Physics of the Earth and Planetary Interiors*, *315*, p.106708.
67. Kusham, Pratap, A., Naick, B.P. and Naganjaneyulu, K., 2019. Crustal and lithospheric mantle conductivity structure in the Dharwar craton, India. *Journal of Asian Earth Sciences*, *176*, pp.253-263.
68. Lakhina G. S., Singh, S. V. and Rubia, R., A mechanism for electrostatic solitary waves observed in the reconnection jet region of the Earth's magnetotail, Adv. Space Res, 68 (4), 1864-1875, 2021, doi:10.1016/j.asr.2021.04.026
69. Lakhina, G.S., Singh S.V. and R. Rubia, A new class of Ion-acoustic solitons below critical Mach number. Phys. Ser., 95(7), 10560, 2020, https:// doi.org/ 10.1088/1402-4896/abb2e0.
70. Laskar, F. I., J. P. McCormack, J. L. Chau, D. Pallamraju, P. Hoffmann, and R. P. Singh (2019), Interhemispheric Meridional Circulation During Sudden Stratospheric Warming, *Journal of Geophysical Research: Space Physics*, 124, https://doi.org/10.1029/2018JA026424
71. Laskar, F. I., Stober, G., Fiedler, J., Oppenheim, M. M., Chau, J. L., Pallamraju, D., Pedatella, N. M., Tsutsumi, M., and Renkwitz, T. (2019) Mesospheric Anomalous

Diffusion During Noctilucent Clouds, *Atmos. Chem. Phys.* https://doi.org/10.5194/acp-2018-1028.

72. Lissa, D., Venkatesh, K., Prasad, D.S.V.V.D. and Niranjan K., (2022), Distinct ionospheric response to three different geomagnetic storms during 2016 using GPS-TEC observations over the Indian equatorial and low latitudes, Adv. Space Res., 70(4), 1089-1103, doi: https://doi.org/10.1016/j.asr.2022.05.027.
73. M. Sivakandan, S. Mondal, S. Sarkhel, D. Chakrabarty, M. V. Sunil Krishna, P. P. Chaitanya, A. K. Patra, R. K. Choudhary, T. K. Pant, A. K. Upadhayaya, and T. Sori, (2020), Mid-latitude spread-F structures over the geomagnetic low-mid latitude transition region: An observational evidence, JGR Space Physics, 124, e2019JA027531. https://doi.org/10.1029/2019JA027531.
74. M. Sivakandan, S. Mondal, S. Sarkhel, D. Chakrabarty, M. V. Sunil Krishna, A. K. Upadhayaya, A. Shinbori, T. Sori, S. Kannaujiya, P. K. Champati Ray, (2021), Evidence for the in-situ generation of plasma depletion structures over the transition region of geomagnetic low-mid latitude, JGR Space Physics, 126, e2020JA028837. https://doi.org/10.1029/2020JA028837.
75. M. Sivakandan, S. Mondal, **S. Sarkhel***, D. Chakrabarty, M. V. Sunil Krishna, A. K. Upadhayaya, A. Shinbori, T. Sori, S. Kannaujiya, and P. K. Champati Ray, Evidence for the in-situ generation of plasma depletion structures over the transition region of geomagnetic low-mid latitude, *Journal of Geophysical Research: Space Physics, 126,* e2020JA028837, 2021. https://doi.org/10.1029/2020JA028837
76. Malleswari, D., Veeraswamy, K., Azeez, K.A., Gupta, A.K., Babu, N., Patro, P.K. and Harinarayana, T., 2019. Magnetotelluric investigation of lithospheric electrical structure beneath the Dharwar Craton in south India: Evidence for mantle suture and plume-continental interaction. *Geoscience Frontiers*, *10*(5), pp.1915-1930.
77. Mandal, S., and D. Pallamraju, (2020), Thermospheric gravity wave characteristics in the daytime over low-latitudes during geomagnetic quiet and disturbed conditions, J. Atmos. Sol.-Terr. Phys. https://doi.org/10.1016/j.jastp.2020.105470
78. Mandal, S., and D. Pallamraju, (2020), Thermospheric gravity wave characteristics in the daytime over low-latitudes during geomagnetic quiet and disturbed conditions, *J. Atmos. Sol.-Terr. Phys.* https://doi.org/10.1016/j.jastp.2020.105470
79. Mandal, S., D. Pallamraju, and P. Suryawanshi, (2020), Changes in the daytime thermospheric gravity wave propagation characteristics over low-latitudes in response to the variation in Solar flux, *J. Atmos. Sol.-Terr. Phys.*, https://doi.org/10.1016/j.jastp.2020.105414 .
80. Mandal, S., D. Pallamraju, and Pant T. K. (2022). Vertical propagation speeds of gravity waves in the daytime as a precursor to the onset of the Equatorial Spread-F, Journal of Geophysical Research - Space Physics 127, e2022JA030401, https://doi.org/10.1029/2022JA030401
81. Mandal, S., D. Pallamraju, and Suryawanshi P., (2020), Changes in the daytime thermospheric gravity wave propagation characteristics over low-latitudes in response to the variation in Solar flux, J. Atmos. Sol.-Terr. Phys., https://doi.org/10.1016/j.jastp.2020.105414
82. Mandal, S., D. Pallamraju, and T. K. Pant (2022). Vertical propagation speeds of gravity waves in the daytime as a precursor to the onset of the Equatorial Spread-F, *Journal of*

Geophysical Research - Space Physics 127, e2022JA030401, https://doi.org/10.1029/2022JA030401
83. Mandal, S., D. Pallamraju, D. K. Karan, K. A. Phadke, R. P. Singh, P. Suryawanshi, (2019), On deriving gravity wave characteristics in the daytime upper atmosphere using radio technique, *J. Geophys. Res.- Space Phys.* https://doi.org/10.1029/2019JA026723
84. Mandal, S., D. Pallamraju, D. K. Karan, Phadke K. A., Singh R. P., Suryawanshi P., (2019), On deriving gravity wave characteristics in the daytime upper atmosphere using radio technique, J. Geophys. Res.- Space Phys. https://doi.org/10.1029/2019JA026723
85. Mani S., Chakrabarty D., T. Ramkumar, Guharay A., Taori A. and Parihar N., (2019), Evidence for deep ingression of the mid-latitude MSTID into as low as ~3.5° magnetic latitude, JGR Space Physics,124, 749-764. https://doi.org/10.1029/2018JA026103
86. Mitra G., Guharay A., Batista P. P., Buriti R. A., (2021), Impact of the September 2019 minor sudden stratospheric warming on the low-latitude middle atmospheric planetary wave dynamics, Journal of Geophysical Research: Atmospheres, 127, 1, e2021JD035538 https://doi.org/10.1029/2021JD035538.
87. Mitra G., Guharay A., Batista P. P., Buriti R. A., Moffat-Griffin T., (2022), Investigation on the MLT tidal variability during September 2019 minor sudden stratospheric warming, Advances in Space Research, 71, 869-882, https://doi.org/10.1016/j.asr.2022.08.017
88. Murthy, D.N., Veeraswamy, K. and Harinarayana, T. (2020) Deep Geoelectric Structure and Its Relation to Seismotectonics of the Saurashtra Region, Western India. Open Journal of Earthquake Research, 9, 181-200.
89. N. Mridula and G. Manju, On the seasonal evolution of the diurnal pattern of the longitudinal structures in MAVEN NGIMS derived CO2 densities over Martian upper atmosphere", Journal of Atmospheric and Solar–Terrestrial Physics, 212, 105508, https://doi.org/10.1016/j.jastp.2020.105508, 2021.
90. N. Mridula and Pant T.K., "On the F3 layer occurrence and drift over the equatorial location of Thiruvananthapuram", Advances in Space Research 69, 3717–3725, https://doi.org/10.1016/j.asr.2022.02.057, 2022.
91. N. Mridula and Tarun Kumar Pant, "Occurrence features of Intermediate Descending Layers [IL] over the equatorial location of Thiruvananthapuram", Advances in Space Research 69, 2102–2110, https://doi.org/10.1016/j. asr.2021.12.003, 2022.
92. N. Mridula, G. Manju, Sijikumar S., Pant T.K., "The geoeffectiveness of TIE-GCM simulations of ionospheric critical frequency foF2 at the equatorial station of Thiruvananthapuram in the Indian sector", Advances in Space Research, 69, 3386–3397, https://doi.org/10.1016/j.asr.2022.02.018, 2022.
93. N. Mridula, Pant T.K., G. Manju, On the variability of the Equatorial Ionization Anomaly Trough over Indian region: A novel analysis using Beacon TEC measurements, Advances in Space Research, DOI:10.1016/j. asr.2020.04.040, (2020).
94. N. Mridula, Pant T.K., G. Manju, Subrahmanyam K V, Kumar K.K., On the role of F3 layers as well as increase in solar flux in modulating the topside ionization over Indian region during increasing phase of solar cycle 24: An analysis, Journal of Atmospheric and Solar-Terrestrial Physics, 189, 52-64, 2019, DOI: 10.1016/j.jastp.2019.04.004.
95. N. P. S. Mithun, S. V. Vadawale, A. R. Patel, M. Shanmugam, D. Chakrabarty, P. Konar, T. N. Sarvaiya, G. D. Padia, A. Sarkar, P. Kumar, P. Jangida, A. Sarda, M. S. Shah, A.Bhardwaj, (2021), Data Processing Software for Chandrayaan-2 Solar X-ray Monitor, Astron. Comp., 34, 100449, https://doi.org/10.1016/j.ascom.2021.100449.

96. Narayanan V.L., Patra A.K., Gurubaran S., P. Pavan Chaitanya, Emperumal K., Coincident airglow, VHF radar, and ionosonde observations of electrified medium-scale traveling ionospheric disturbances in the equatorial latitudes, Geophysical Research Letters 46 (13), 7173-7181, 2019.
97. Nilam, B., and Tulasi Ram, S. (2022). Large geomagnetically induced currents at equator caused by an interplanetary magnetic cloud. Space Weather, 20, e2022SW003111. https://doi. org/10.1029/2022SW003111.
98. Ojha, B., Omura, Y., Singh, S., & Lakhina, G. S. (2021). Multipoint analysis of source regions of EMIC waves and rapid growth of subpackets. Journal of Geophysical Research: Space Physics, 126, e2021JA029514. https://doi.org/10.1029/2021JA029514
99. P. G. Gopika,, Ambili K. M., and Choudhary R. K., (2021). "The response of the D and E regions of the equatorial ionosphere to solar flare events". Journal of Geophysical Research: Space Physics, 126, e2021JA029350, https://doi.org/10.1029/2021JA029350, 2022.
100. P. R. Shreedevi, Choudhary R. K., Yadav S., Thampi S., and A. Ajesh, Variation of the TEC at a dip equatorial station, Trivandrum and a mid latitude station, Hanle during the descending phase of the solar cycle 24 (2014–2016).; Journal of Atmospheric and Solar-Terrestrial Physics, 179, pp.425-434, 2018, DOI: 10.1016.j.jastp.2018.09.010.
101. P. R. Shreedevi, Choudhary R. K., Yu. , Thomas E. G., Morphological study on the ionospheric variabilities at Bharati, a polar cusp station in the southern hemisphere. Journal of Atmospheric and Solar-Terrestrial Physics, 2019, DOI:10.1016/j.jastp.2019.105058.
102. P. R. Shreedevi, Choudhary R.K., Yu., Thomas E.G., Morphological study on the ionospheric variability at Bharati, a polar cusp station in the southern hemisphere, Journal of Atmospheric and Solar Terrestrial Physics, Volume 193, doi: DOI:10.1016/j.jastp.2019.105058, (2019).
103. P. R. Shreedevi, Choudhary, R. K., Thampi, S. V., Yadav, S., Pant, T. K., Yu, Y., et al., Geomagnetic storm induced plasma density enhancements in the southern polar ionospheric region: a comparative study using St.Patrick's day storms of 2013 and 2015, 2020, Space Weather, 18, DOI:10.1029/2019SW002383, (2020).
104. Pallamraju, D., D. K. Karan, F. I. Laskar, T. Vijaya Lakshmi, S. Chakrabarti, (2020), Effect of solar flux versus compositional variations on the variability of daytime oxygen optical emission rates over low- and mid-latitudes, *J. Atmos. Sol.-Terr. Phys.*, 205, 105293, 2020. https://doi.org/10.1016/j.jastp.2020.105293
105. Pallamraju, D., D. K. Karan, Laskar F. I., T. Vijaya Lakshmi, Chakrabarti S., (2020), Effect of solar flux versus compositional variations on the variability of daytime oxygen optical emission rates over low- and mid-latitudes, J. Atmos. Sol.-Terr. Phys., 205, 105293, https://doi.org/10.1016/j.jastp.2020.105293
106. Pandey K., Sekhar R., Chakrabarty D., and Anandarao B. G., (2021), Investigation on Longitudinal and Decadal Variations of the Equatorial Electrojet using a Physical Model, Adv. Space Res., 68, 182-200, https://doi.org/10.1016/j.asr.2021.02.040
107. Pandya M., B. Veenadhari, Ebihara Y., Kanekal S. G., Baker D. N., Variation of Radiation belt electron flux during CME and CIR driven geomagnetic storms: Van Allen Probes observations, *DOI:10.1029/2019JA026771 JGR Space Physics, 2019*

108. Patro, P.K., 2020. Electrical conductivity structure along a few transects over the Indian Lithospheric domains. *Episodes Journal of International Geoscience*, *43*(1), pp.638-649.
109. Patro, P.K., Kumar, P.V. and Sarma, S.V.S., 2021. MT/LMT Studies for Crust and Upper Mantle Structure of India and Its Adjoining Regions: Contribution of CSIR-NGRI. *Journal of the Geological Society of India*, *97*, pp.1251-1259.
110. Prateek Mayank, Bhargav Vaidya, and D. Chakrabarty (2022), SWASTi-SW: Space Weather Adaptive SimulaTion framework for Solar Wind and its relevance to ADITYA-L1 mission, Astrophys. J. Suppl. Ser, 262:23 (16pp), https://doi.org/10.3847/1538-4365/ac8551
111. R. Rathi, V. Yadav, S. Mondal, **S. Sarkhel***, M. V. Sunil Krishna, A. K. Upadhayaya (2021), Evidence for simultaneous occurrence of periodic and single dark band MSTIDs over geomagnetic low-mid latitude transition region, *Journal of Atmospheric and Solar-Terrestrial, 215, 105588.* https://doi.org/10.1016/j.jastp.2021.105588
112. R. Rathi, V. Yadav, S. Mondal, **S. Sarkhel***, M. V. Sunil Krishna, A. K. Upadhayaya, S. Kannaujiya, P. Chauhan, A case study on the interaction between MSTIDs' fronts, their dissipation and a curious case of MSTID's rotation over geomagnetic low-mid latitude transition region, *Journal of Geophysical Research: Space Physics, 127,* e2021JA029872, 2022. https://doi.org/10.1029/2021JA029872
113. Raju, K. and Patro, P.K., 2020. Dimensionality analysis of MT data using Mohr circle: A case study from Rewa–Shahdol region, India. *Journal of Earth System Science*, *129*, pp.1-15.
114. Raju, K., Patro, P.K., Borah, U.K., Srivastava, S. and Reddy, K.C., 2022. Evolution of eastern segment of the Central India Tectonic Zone: an insight from a magnetotelluric study. *Geophysical Journal International*, *230*(1), pp.272-287.
115. Ranjan, A. K., Sunil Krishna, M. V, Kumar, A., Sarkhel, S., Bharti, G., Bender, S., & Sinnhuber, M. (2023). Aspects related to variability of radiative cooling by NO in lower thermosphere, TEC and O/N_2 correlation, and diffusion of NO into mesosphere during the Halloween storms. *Advances in Space Research*, *71*(1), 29-45. https://doi.org/10.1016/j.asr.2022.07.035
116. Remya, B., Sibeck D.G., Ruohoniemi J.M., Kunduri B., Halford A.J., Reeves G. D., and Reddy R. V., Association between EMIC wave occurrence and enhanced convection periods during ion injections, Geophysical Research Letters, 47(3), e2019GL085676, Doi: 10.1029/ 2019GL085676, 2020.
117. S. Chakraborty, D. Chakrabarty, G. D. Reeves, D. N. Baker, J. Rae, (2022), Statistical investigation on equatorial pitch angle distribution of energetic electrons in Earth's outer radiation belt during CME-and CIR-driven storms, Front. Astron. Space Sci. 9:986061, https://doi.org/10.3389/fspas.2022.986061.
118. S. Chakraborty, D. Chakrabarty, G. D. Reeves, D. N. Baker, S. G. Claudepierre, A. W. Breneman, D. P. Hartley, B. A. Larsen, (2021), Van Allen probe observations of disappearance, recovery and patchiness of plasmaspheric hiss following two consecutive interplanetary shocks: First results, JGR Space Physics, 126, e2020JA028873. https://doi.org/10.1029/2020JA028873.
119. S. Kumar, B. Veenadhari, D. Chakrabarty, S. Tulasi Ram, T. Kikuchi, and Y. Miyoshi, (2020), Effects of IMF By on ring current asymmetry under southward IMF Bz

conditions observed at ground magnetic stations: Case studies, JGR Space Physics, 125, e2019JA027493. https://doi.org/10.1029/2019JA027493.

120. S. Mani, D. Chakrabarty, T. Ramkumar, A. Guharay, A. Taori and N. Parihar, (2019), Evidence for deep ingression of the mid-latitude MSTID into as low as ~3.5° magnetic latitude, JGR Space Physics,124, 749-764. https://doi.org/10.1029/2018JA026103.
121. S. Mondal, A. Srivastava, V. Yadav, **S. Sarkhel***, M.V. Sunil Krishna, Yamini K. Rao, Vir Singh (2019), Allsky airglow imaging observations from Hanle, Leh Ladakh, India: Image analyses and first results, *Advances in Space Research, 64, 1926-1939,* https://doi.org/10.1016/j.asr.2019.05.047
122. S. Mondal, M. Sivakandan, **S. Sarkhel***, M. V. Sunil Krishna, Martin G. Mlynczak, James M. Russell III, and G. Bharti (2021), A case study of a thermally ducted undular mesospheric bore accompanied by ripples over the western Himalayan region, *Advances in Space Research, 68,* 1425-1440, https://doi.org/10.1016/j.asr.2021.03.026
123. S. Mondal, S. Sarkhel, J. Agarwal, D. Chakrabarty, R. Sekar, Tao Yuan, X. Cai, A. Liu, S. Nozawa, N. Saito, T. Kawahara, M. Mlynczak, J. Russell, (2019), On the long-lasting "C-type" structures in the sodium lidargram: The life-time of Kelvin-Helmholtz billows in the mesosphere and lower thermosphere region, JGR Space Physics,124. https://doi.org/10.1029/2019JA026630.
124. S. Sahoo and B. Sreenivasan, Response of Earth's magnetic field to large lower mantle heterogeneity, *Earth and Planetary Science Letters*, 549, 116507, 2020.
125. S. Sarkhel, S. Mondal, R. Sekar,D. Chakrabarty,S. Sridharan, (2019), A review on the upper atmospheric sodium observations from India: Insights, Adv. Space Res., 63, 3568-3585, https://doi.org/10.1016/j.asr.2019.02.019
126. S. Tulasi Ram, B. Nilam, N. Balan, Q. Zhang, K. Shiokawa, D. Chakrabarty, Z. Xing, K. Venkatesh, B. Veenadhari and A. Yoshikawa, (2019), Three different episodes of prompt equatorial electric field perturbations under steady southward IMF Bz during St. Patrick's day storm, JGR Space Physics, 124, https://doi.org/10.1029/2019JA027069.
127. Saha, S., and D. Pallamraju, (2022). Latitudinal Variations in the Nocturnal behaviour of OI 630 nm Airglow Emissions and their relationship to the Equatorial Electrodynamics, Journal of Atmospheric and Solar-Terrestrial Physics . https://doi.org/10.1016/j.jastp.2022.105965
128. Saha, S., and D. Pallamraju, (2022). Latitudinal Variations in the Nocturnal behaviour of OI 630 nm Airglow Emissions and their relationship to the Equatorial Electrodynamics, *Journal of Atmospheric and Solar-Terrestrial Physics* . https://doi.org/10.1016/j.jastp.2022.105965
129. Saha, S., D. Pallamraju, Pant T. K., and Chakrabarti S. (2021). On the cause of nocturnal OI 630 nm airglow variability over low-latitude thermosphere, Journal of Geophysical Research - Space Physics , https://doi.org/10.1029/2021JA029146
130. Saha, S., D. Pallamraju, and Ghodpage R., (2022). Investigation of equatorial plasma bubbles as observed in the OI 630 nm nightglow emissions over off-equatorial and low-latitudinal locations over Indian longitudes, Advances in Space Research, https://doi.org/10.1016/j.asr.2022.08.023
131. Saha, S., D. Pallamraju, and R. Ghodpage, (2022). Investigation of equatorial plasma bubbles as observed in the OI 630 nm nightglow emissions over off-equatorial and low-latitudinal locations over Indian longitudes, *Advances in Space Research,* https://doi.org/10.1016/j.asr.2022.08.023

132. Saha, S., D. Pallamraju, T. K. Pant, and S. Chakrabarti (2021). On the cause of nocturnal OI 630 nm airglow variability over low-latitude thermosphere, *Journal of Geophysical Research - Space Physics* , https://doi.org/10.1029/2021JA029146 .
133. Santos, A.M., Brum, C.G.M., Batista, I.S., Sobral, J.H.A, Abdu, M.A., Souza, J.R., Chen, S.S., Denardini, C.M., de Jesus, R., Venkatesh, K., Nogueira, P.A.B., (2022), Anommalous responses of the F2 layer over the Brazilian equatorial sector during a counter electrojet event: A case study, J. Geophys. Res., Space Physics, e2022JA030584, 27(9), 1-12, doi: https://doi.org/10.1029/2022JA030584.
134. Shaikh Z.I., Raghav A.N., Vichare G., Bhaskar A., Mishra W., Comparative statistical study of characteristics of plasma in planar and non-planar ICME sheaths during solar cycles 23 and 24, *Monthly Notices of the Royal Astronomical Society*, Volume 494, Issue 2, May 2020, Pages 2498–2508, https://doi.org/10.1093/mnras/staa783
135. Shiokawa, K., S. Dasso, R. Miteva, D. Pallamraju, S. Zhang, (2021), Preface of the special issue: "Variability of the Sun and Its Terrestrial Impact (VarSITI) Completion Symposium 2019 and the SCOSTEP 14th Quadrennial Solar-Terrestrial Physics Symposium (STP14)" *J. Atmos. Sol.-Terr. Phys.*, https://doi.org/10.1016/j.jastp.2021.105593
136. Sivakandan M., Mondal S., Sarkhel S., Chakrabarty D., Sunil Krishna M. V., P. P. Chaitanya, Patra A. K., Choudhary R. K., Pant T. K., Upadhayaya A. K., and Sori T., (2020), Mid-latitude spread-F structures over the geomagnetic low-mid latitude transition region: An observational evidence, JGR Space Physics, 124, e2019JA027531. https://doi.org/10.1029/2019JA027531
137. Sivakandan, M., Mondal, S., **S. Sarkhel***, Chakrabarty, D., Sunil Krishna, M. V., Chaitanya, P. P., et al. (2020). Mid-latitude spread-F structures over the geomagnetic low-mid latitude transition region: An observational evidence. *Journal of Geophysical Research: Space Physics, 124, e2019JA027531*. https://doi.org/10.1029/2019JA027531
138. Soni P.K., Kakad B., Kakad A., Deepening of radiation belt particles in South Atlantic Anomaly Region: A scenario over past 120 years, Advances in Space Research 69 (5), 2090-2101, 2022
139. Sruthi, T.V. and G. Manju, "Quantification of the role of gravity wave induced TIDs in modulating ESF day to day variability during geomagnetically disturbed periods", Adv. Space Res., 69(5), 2081-2081, https://doi:10.1016/j.asr.2021.11.038, 2022.
140. Sumanjit Chakraborty and D. Chakrabarty, (2023), Global asymmetry in ΔX variations during the 06 April 2000 geomagnetic storm: Relative roles of IMF Bz and By, Accepted, JGR Space Physics.
141. Thomas, N., Shiokawa, K., and Vichare, G. (2019). Comprehensivestudy of low-latitude Pi2 pulsationsusing observations from multisatelliteSwarm mission and globalnetwork of ground observatories.Journal of Geophysical Research:Space Physics,124, 1966–1991.https://doi.org/10.1029/2018JA026094
142. Upadhyay A., Kakad B., Kakad A., Y. Omura, A. K. Sinha, Occurrence characteristics of electromagnetic ion cyclotron waves at sub-auroral Antarctic station Maitri during Solar Cycle 24, EPS, 2020
143. V. F. Andrioli, J. Xu, P. P. Batista, L. C. A. Resende, L. A. Da Silva, J. P. Marchezi, H. Li, C. Wang, Z. Liu , and A. Guharay, (2022), New Findings Relating Tidal Variability and Solar Activity in the Low Latitude MLT Region, Journal of Geophysical Research: Space Physics, 127, 3, e2021JA030239, https://doi.org/10.1029/2021JA030239

144. V. Yadav, R. Rathi, G. Gaur, S. Sarkhel, D. Chakrabarty, M. V. Sunil Krishna, P. Pavan Chaitanya, A. K. Patra, R. K. Choudhary, T. K. Pant, A. K. Upadhayaya, (2021), Interaction between nighttime MSTID and mid-latitude field-aligned plasma depletion structure over the transition region of geomagnetic low-mid latitude: First results from Hanle, India, J. Atm.Sol-Terr. Phys., 217, 105589, https://doi.org/10.1016/j.jastp.2021.105589, 2021

145. V. Yadav, R. Rathi, G. Gaur, **S. Sarkhel***, D. Chakrabarty, M.V. Sunil Krishna, P. Pavan Chaitanya, A.K. Patra, R.K. Choudhary, T.K. Pant, A.K. Upadhayaya (2021), Interaction between nighttime MSTID and mid-latitude field-aligned plasma depletion structure over the transition region of geomagnetic low-mid latitude: First results from Hanle, India, *Journal of Atmospheric and Solar-Terrestrial Physics, 217, 105589*. https://doi.org/10.1016/j.jastp.2021.105589

146. V. Yadav, R. Rathi, S. Sarkhel, D. Chakrabarty, M. V. Sunil Krishna, and A. K. Upadhayaya, (2020), A unique case of complex interaction between MSTIDs and mid-latitude field-aligned plasma depletions over geomagnetic low-mid latitude transition region, JGR Space Physics, 126, e2020JA028620. https://doi.org/10.1029/2020JA028620.

147. Veeraswamy, K., Azeez, K.A., Patro, P.K., Gupta, A.K. and Babu, N., 2020. Electrical resistivity structure across the Jaisalmer Basin (Rajasthan, NW India) derived from magnetotelluric data: Inferences on basin architecture and basement morphology. *Journal of Applied Geophysics*, *181*, p.104147.

148. Venkatesh, K., and A.K. Patra, (2022), Formation of the evening time F3 layer investigated using Jicamarca incoherent scatter radar observations, J. Geophys. Res. Space Physics, 127 (2), e2021JA029684, 1-8, doi: https://doi.org/10.1029/2021JA029684.

149. Venkatesh, K., and Patra A.K., (2022), Formation of the evening time F_3 layer investigated using Jicamarca incoherent scatter radar observations, J. Geophys. Res. Space Physics, 127 (2), e2021JA029684, 1-8, doi: https://doi.org/10.1029/2021JA029684

150. Vichare, G., Thomas, N., Shiokawa, K., Bhaskar, A., & Sinha, A. K. (2019). Spatial gradients in geomagnetic storm time currents observed by Swarm multi-spacecraft mission, Journal of Geophysical Research: Space Physics,124, 982–995. https://doi.org/10.1029/2018JA025692

151. Vieira, F., Fagundes, P.R., Pillat V.G., Agyei-Yeboah, E., Venkatesh, K., Arcanjo, M.O., (2022), Ionospheric disturbances over the American and African sectors due to the 2019 major Sudden Stratospheric Warming (SSW 2019) under low solar activity conditions, J. Atmos. Sol. Terr. Phys., 240, 105945, 1-16, doi: https://doi.org/10.1016/j.jastp.2022.105945.

152. Vijaya Kumar, P.V., Rawat, V.S., Patro, P.K., Gupta, A.K. and Babu, N., 2021. Assessment and recognition of pre-and co-seismic electromagnetic signatures from magnetotelluric data: A case study from Koyna–Warna seismoactive region, India. *Acta Geophysica*, *69*, pp.1-15.

153. Vineeth, C., Ambili K. M. and Pant T. K. (2023), On the Behavior of Thermospheric O^1D 630.0 nm Dayglow Emission during Counter Electrojet Events, Adv. Space Res., 71 115–128, DOI: 10.1016/j.asr.2022.08.048.

154. Vineeth, C., Ambili K. M. and Pant T. K., "Signature of the MTM Phenomenon in Thermospheric Oxygen Airglow Emissions: Results from the Ship-Borne Airglow

Measurements from the Indian Region", Advances in Space Research. 69, 4129-4139, https://doi.10.1016/j.asr.2022.03.015, 2022.
155. Vineeth, C., Ambili, K. M., Pant, T. K., and Subrahmanyam, K. V., "Role of equatorial fountain for the delayed response of thermosphere O1D 630.0 nm dayglow over the dip equator during an X-class flare", Journal of Geophysical Research: Space Physics, 126, 2020JA028624, https://doi.org/10.1029/2020JA028624, 2021.
156. Ward, W., A. Seppälä, E. Yigit, T. Nakamura, C. Stolle, J. Lastovicka, T. Woods, Y. Tomikawa, F-J Lübken, S. Solomon, D. Marsh, B. Funke, D. Pallamraju . (2021), Role Of the Sun and the Middle atmosphere/thermosphere/ionosphere In Climate (ROSMIC): A Retrospective and Prospective View, *Progress in Earth and Planetary Science* , 8, https://doi.org/10.1186/s40645-021-00433-8
157. Yadav S, C. Vineeth, Kumar K. K., Choudhary R. K., Pant T. K., S. Sunda, The role of the phase of QBO in modulating the influence of the SSW effect on the Equatorial Ionosphere, Journal of Geophysical Research: Space Physics, 2019, DOI: 10.1029/2019JA026518.
158. Yadav, S., Choudhary, R. K., Kumari, J., Sunda, S., P. R., Shreedevi, & Pant, T. K., Reverse fountain and the nighttime enhancement in the ionospheric electron density over the equatorial region: A case study. Journal of Geophysical Research: Space Physics, 124, DOI:/10.1029/2019JA027286, (2020).
159. Yadav, S., Shiokawa, K., Oyama, S., & Otsuka, Y, Multievent analysis of oscillatory motion of medium scale traveling ionospheric disturbances observed by a 630 nm airglow imager over Tromsø, Journal of Geophysical Research: Space Physics, 125, DOI: 10.1029/2019JA027598, (2020).
160. Yadav, V., Rathi, R., **S. Sarkhel***, Chakrabarty, D., Krishna, M. V. S., & Upadhayaya, A. K. (2021). A unique case of complex interaction between MSTIDs and mid-latitude field-aligned plasma depletions over geomagnetic low-mid latitude transition region. *Journal of Geophysical Research: Space Physics*, *126*, e2020JA028620. https://doi.org/10.1029/2020JA028620
161. Yogesh, Chakrabarty D., and Srivastava N., (2022), A holistic approach to understand Helium enrichment in Interplanetary coronal mass ejections: New insights, MNRAS-Letters, MNRAS 513, L106-L111, https://doi.org/10.1093/mnrasl/slac044
162. Yogesh, Chakrabarty D., Srivastava N., (2021), Evidence for distinctive changes in the solar wind helium abundance in solar cycle 24, MNRAS-Letters, MNRAS 503, L17-L22 https://doi.org/10.1093/mnrasl/slab016
163. Yogesh, D. Chakrabarty, and N. Srivastava, (2022), A holistic approach to understand Helium enrichment in Interplanetary coronal mass ejections: New insights, MNRAS-Letters, MNRAS 513, L106-L111, https://doi.org/10.1093/mnrasl/slac044.
164. Yogesh, D. Chakrabarty, N. Srivastava, (2021), Evidence for distinctive changes in the solar wind helium abundance in solar cycle 24, MNRAS-Letters, MNRAS 503, L17-L22 https://doi.org/10.1093/mnrasl/slab016, 2021

Glimpses of Surface and Ground Water Studies in India During 2019-2022

V.M. Tiwari and N. Srinivas

CSIR-National Geophysical Research Institute, Hyderabad, India

This report documents a concise overview of R&D activities in the areas of surface and ground water and a short note on the national programs initiated to provide the potable water for public in India. Data from Web of Science for the four calendar years (2019-2022) indicate that about ~ 1600 peer-reviewed papers authored by at least one researcher affiliated to Indian institution were published on the topic related to the surface water and ground water (both quantity and quality), which suggests the breadth of research being carried out in the country. The research activities conducted during the period 2019 -2022 in India have contributed significantly to deepening the understanding of surface hydrological processes, aquifer mapping, water quality monitoring, water resources management, and climate change impacts. The government programs are focused to implement projects to recharge/conserve the water resources and recycle/reuse of treated wastewater for meeting the water demand and providing enough clean water to every rural/urban family of India

1. Water Resources of India and their Monitoring

Annual rainfall over Indian territorial region is ~ 3,830 BCM and utilizable water resource is 1,122 BCM which includes 432 BCM of ground water and 690 BCM of surface water (MoSPI, 2009). These estimates change from time to time depending upon the amount of rainfall during the specific year. As per a recent report, the total water requirement of the country for the years 2025 and 2050 are 843 BCM and 1180 BCM respectively, which are in the order of the annual water avaialbility. However, the uneven distribution of water poses furure challenge of its adequate availability. India's water requirement is mostly met from the twenty river basins and hydro-meteorological related data for all the river basins are recorded in a systematic manner by the relevant government departments and institutes for monitoring, planning and development of water resource projects, and research purposes. The surface water levels, discharge, water quality and silt are recorded in the all twenty river basins by the Central Water Commission (CWC) through a well distributed network of 1543 hydrological observation (HO) stations and 187 meteorological observation stations. Snowfall observations are also recorded at some crucial stations. Glacial lakes, stored glacial ice melts lead to flash floods in the downstream reaches sometimes. Therefore, CWC also monitors about 475 glacial lakes and water bodies in higher reaches of the Himalaya having dimension of more than 50 Ha water spread area. The ground water levels of 22835 ground water observation wells (Dug Wells: 16271, Piezometers: 6394, Hand Pump: 129, spring: 41) spread across India in a network are being monitored by the Central Ground Water Board (CGWB). The same wells are utilized to collect ground water samples and these samples are analysed to determine chemical quality of ground water and its variation over time. A review of knowledge of hydrology and water resources engineering in ancient India was reported by Singh et al, 2020.

Total annual ground water recharge over the entire country is ~ 438 BCM, which is estimated based on a standard methodology (GEC–2015) of rainfall and recharge relation, including other related parameters (CGWB, 2022). Satellite based data from the GRACE &

GRACE FO missions which also allow to quantify the water storage changes and spatio-temporal variabilities. Satellite derived Terrestrial Water Storage (TWS) data are widely analysed and studied (e.g. Munagapati et al., 2021). In India, presently, ~ 83 per cent of the water resources are used for irrigation and the rest are utilized for drinking, domestic, industrial and recreational purposes. Since the 1960's, the water demand has increased in many ways due to the rapidly growing population, urbanization, industrialization and irrigation demands. Figure 1 shows the assessment of recharge versus exploitation. It is obvious from the Figure 1 that a considerable part of the country is classified as ground water overexploited, critical and semi-critical, which is also reflected in satellite-based estimates of decreasing ground water storage (Munagapati et al., 2021; Panda et al, 2022).

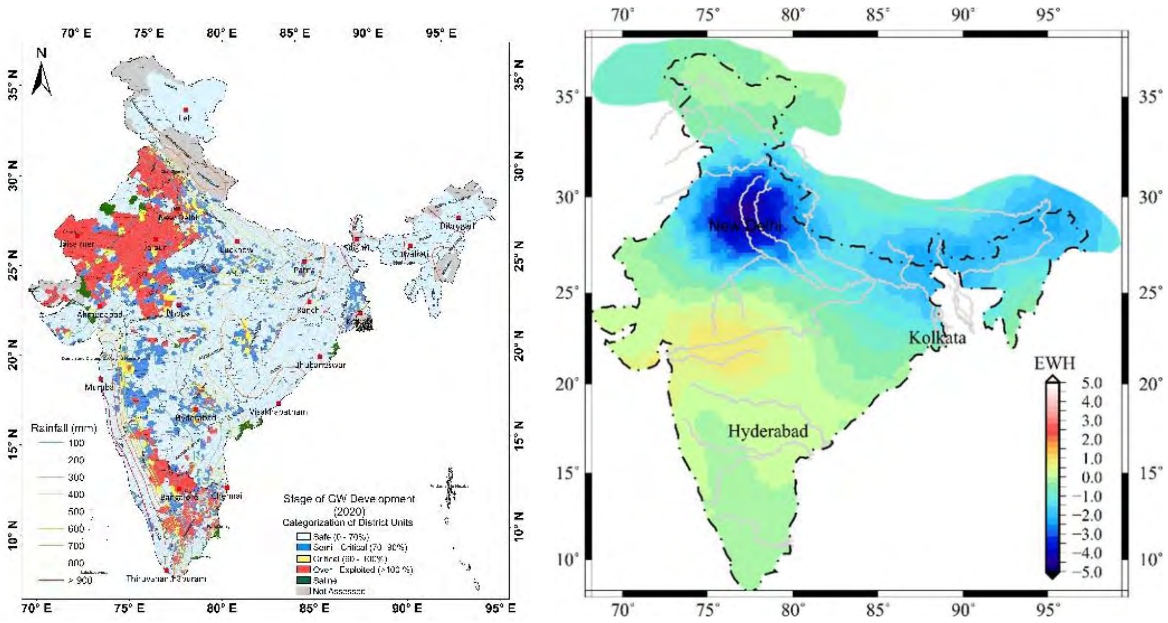

Figure 1a Categorization of assessment of ground water withdrawal (modified after CGWB Report, 2020 and NWIC ArcGIS Sever) with rainfall contours superimposed on it. Figure 1b: Seasonal removed trend of TWS over India derived from time varying gravity data of GRACE from 2002-2016 (Munagapati et al., 2021).

A continuous declining trend of TWS and ground water over exploited regions in northern India are probably caused by a combination of climatic and anthropogenic factors where as a substantial increase in TWS over the Narmada river basin region appears to be mainly caused by the water storage rise in the surface reservoir (Munagapati et al., 2021; Dangar et al, 2021). During the period of 2002-2016, the Ganga basin lost ~225 km^3 of ground water, which is equivalent to approximately 20 times the storage capacity of India's largest reservoir, Indira Sagar. An alarming 95% of India's ground water loss (498 km^3) occurred between 2002 and 2022 in the northern region of the country, a global hotspot for ground water depletion (Dangar, Mishra, 2021). The main cause is excessive pumping from non-renewable ground water sources, which is expected to continue despite projected increases in rainfall (~ 4-6%). Although there is a projected increase in ground water recovery in the near future (2021-2040), it is only estimated to be about half of the total ground water loss. Therefore, the increase in rainfall may not be enough to recover the lost ground water, highlighting the need for managing ground water resources sustainably.

To meet the sustained demand and achieve optimal use, it is necessary to have an all-inclusive approach for water resource development through comprehensive and integrated river basin planning and management.

2. Water Informatics

National Water Informatics Centre (NWIC) (https://nwic.gov.in/) was set up in 2018 by Government of India, for archival, display and dissemination of all water resources data. It houses water resource data for both surface and ground water resources through two integrated web-enabled water resources data platforms. At initiation stage, National Remote Sensing Agency (NRSC) has helped in developing the web portal of water data - India-WRIS. Subsequently, NRSC has also developed Telangana Water Resource Information System (TWRIS) and Andhra Pradesh Water Resources Information and Management System (APWRIMS) on the Bhuvan platform for systematic integration of water resources related geospatial information for these States.

The near real time information of water spread area in the country are being extracted from multiple remote sensing data using an automated feature extraction algorithm by NRSC. Even small size water bodies of 0.25 Ha are also identified. These data are continuously uploaded on a Web-GIS portal (https://bhuvan-wbis.nrsc.gov.in/) of the Water Body Information System (WBIS) for visualisation and downloads. WBIS comprises water spread area information for over 1.6 million water bodies monitored regularly. The latest version of WBIS is enriched with water spread area delineated using data from MSI sensor of Sentinel-2.

To address the present concern on the dynamics of ground water quality, NRSC, in collaboration with state remote sensing centres had taken up the ground water quality mapping for entire country using geo-spatial data analytics and data mining techniques for understanding the seasonal variability of geo-chemical parameters obtained from the habitation wise ground water quality observations, provided by state line departments, both in spatial and temporal domain. After several brainstorming sessions between the hydrologists from various state ground water departments in the country, academic institutions and NRSC scientists, a technical methodology and Standard Operating Procedure (SOP) for ground water quality mapping were formulated and successfully implemented and validated for few pilot studies by NRSC. Seasonal observations of 12 essential geo-genic elements (e.g. Arsenic Fluoride, Nitrate, Sulphate, Chloride, Hardness, Total Dissolve Solids, Alkalinity, Calcium, Magnesium & Iron) in the ground water are recorded for the entire county (except Sikkim) with 7.5 lakh habitation wise observations (Fig. 2). The Ground Water Quality (GWQ) database has been launched through Bhuvan–Bhujal portal (www. https://bhuvan-app1.nrsc.gov.in/gwis/) for public usage.

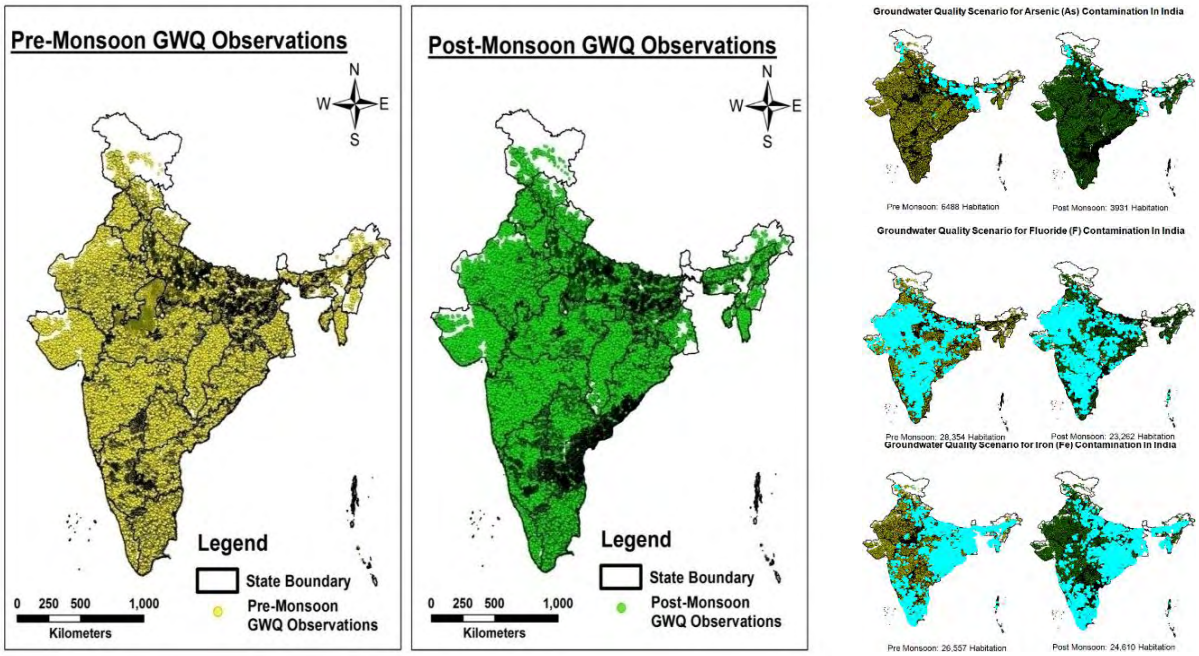

Fig:2. Habitation wise Seasonal Ground Water Quality database for the Country. (a.) Pre-Monsoon observation ;(b) Post monsoon observation;(c) Seasonal (Pre-& Post) distribution/ variation of Arsenic contamination;(d) Seasonal (Pre-& Post) distribution/variation of Fluoride contamination;(e) Seasonal (Pre-& Post) distribution/ variation of Iron contamination (Source NRSC)

3. Ground water Exploration

Ground water is a major hidden source of the fresh water. Exploration of ground water involves studying sub-surface hydrogeological set-up and evaluating hydrological parameters of aquifer systems. India has diverse hydrogeological settings and ground water resource variability. To deal with the growing issues of ground water, a national level program of management of ground water resources through aquifer mapping is launched by the government. This programme envisages to cover ~25 lakh km^2 mappable area of the country in a time-bound manner (Saha et al., 2019). The CGWB and researchers from different organizations are using remote sensing, geophysical investigations and drilling at appropriate locations to map and characterize the aquifers across different geological terrains of India. As per the CGWB reports, aquifer maps and management plans for an area of 18.7 lakh km^2 spread over various parts of the country have been prepared. Researchers from CSIR-NGRI have developed an approach to map cluster of bedrock fracture network that facilitates ground water occurrences due to drying of saprolite zone by employing airborne electromagnetic (AEM) surveys in combination with magnetic, borehole data and geological information (Chandra et al., 2019; Chandra and Tiwari, 2022). Encouraged by the success of AEM investigation in diverse hydrogeological settings of India covering major hydrogeological settings viz., flood basalt, Archean granite, gneiss and schist, alluvial, coastal formation (Tiwari et al., 2021; Chandra and Tiwari, 2022; Sonkamble et al., 2022), CSIR-NGRI in collaboration of CGWB have initiated a large-scale experiment of high-resolution aquifer mapping in water scarce arid region of north west India covering 400,000 sq.km area starting from part of Himachal Pradesh

at Himalayan foot hill to downstream side of states of Haryana, Punjab, Rajasthan and coastal Gujarat for developing comprehensive and effective management plan for transforming the dry land into green land (Figure:3) in two phases. Phase- I of the project covering an area of 1 lakh km^2 was completed.

Fig:3. Area of Arid project for aquifer mapping and management using integrated heliborne and ground hydro-geophysical studies.

A 45 km long buried river (Figure 4), having comparable dimensions and similar meandering pattern to those of Ganga and Yamuna rivers is discovered near Prayagraj, India from Airborne electromagnetic study supplemented with drilling and logging data, (Chandra et al., 2021). The AEM results have also revealed hydrogeological linkages amongst Ganga, Yamuna and Paleo rivers at places, making them a unified system. These hydrogeological linkages facilitate exchange of water and hence pollution depending on hydraulic gradient. The location of discovered paleoriver coincides with site of the lost mythological Ancient River "Sarashwati". This finding has a large hydrogeological significance.

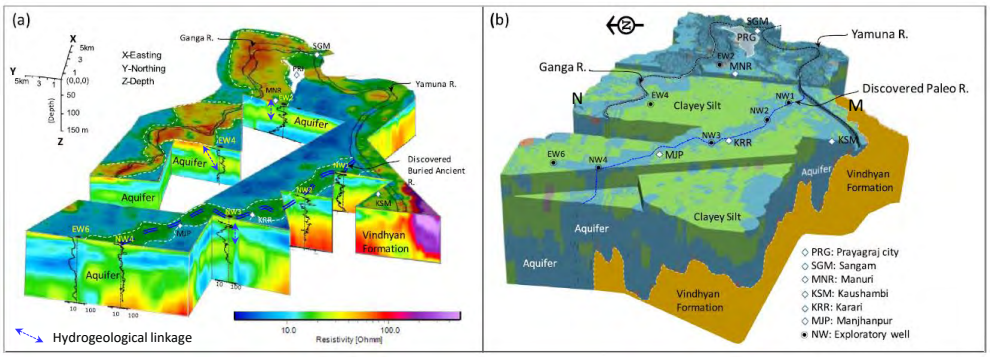

Fig:4. 3D models: (a) resistivity cutaway showing disposition of rivers, discovered paleoriver and exploratory wells with LN64 borehole resistivity logs, hydrogeological linkages and (b) hydrostratigraphical model (after Chandra et al., 2021).

NRSC has started a project to develop and operationalize the methodology for ground water prospects mapping on 1:10,000 scale and five pilot studies are investigated in granitic hard rock terrain, basalts, Gondwana rocks, Vindhayans rocks and hilly terrain of North East. These are over-exploited zones where ground water availability is low due to variability in rainfall and excessive ground water usage for irrigation. Pre and post managed aquifer recharge (MAR) tank Time-lapse ERT experiments carried out in an experimental hydrogeological park located in granitic hard rock terrain has clearly mapped and modelled the signature of fracture network forming ground water flow path (Maurya et al., 2021). The fractured aquifers mapped by geophysical methods are used to set up a simulation for operational decision support tool for ground water management under variable agro-climatic conditions (Paswan et al, 2022). The futuristic simulation suggests several possible options to enhance aquifer recharge and reduce the ground water extraction by changing the cropping pattern to arrest the depleting condition and achieving long-term sustainable management solution. Researchers from CSIR NGRI have tried to understand the ground water flow processes in a highly evaporative environment through identification of possible sites for ground water recharge, recharge sources, hydrogeochemical processes and mechanism behind ground water salinization in the semi-arid region.

Geo-electrical signatures of the earth's subsurface such as Dar-Zarrouk parameters (T&S) are explored and utilized for detecting water-bearing zones. Aquifer parameters estimated indicates that the high value of permeability is the presence of a possible shear zone as more productive for providing a good yield of groundwater (Mondal, 2021). Water-bearing zones are explored by merging of partial curve matching, factor analysis and inverse techniques from surficial geophysical data in a sedimentary area (Mondal et al., 2020). Microtremor (H/V spectral ratio) investigation is utilized for aquifer deposition (Mondal and Rajewar, 2020). Spatial distribution of groundwater potential zones deduced using the RS, GIS and AHP Techniques in a part of Deccan Volcanic Province (DVP), Maharashtra, and compared with the existing borehole yields. The yield value is an average of 8.63 lps in the deduced Good to Very Good Groundwater Potential Zones, whereas an average of 0.84 lps within the Poor to Very Poor Zones (Ajaykumar et al., 2020). Further, these groundwater potential zones are used to demarcate groundwater recharge zones using groundwater level and precipitation adopting cross-correlation technique for constructing recharge structures (Venkatarao et al., 2019). An

information-based model has been hypothesized and developed to estimate natural groundwater recharge with the measurement of groundwater level and rainfall data at the proximity of Deccan Trap Basalt in Central India (Mondal and Ajaykumar, 2021), and Gangetic plains, Northern India (Mondal and Ajaykumar, 2022). Static Groundwater Reserve (SGWR), Dynamic Groundwater Reserve (DGWR), and Monsoon Groundwater Reserve (MGWR) estimated using the GEC-2015 Methodology in both regional and local scales of a typical DVP part, Nagpur, Maharashtra. Their spatial and temporal variabilities also observed the help of Thiessen Polygons. The comparison in the reserves of regional scale found to be higher than the dense well network data, which could be useful for the implementation of groundwater development and sustainable management in future (Ajaykumar and Mondal, 2022).

Water Quality Studies

In recent years, considering direct or indirect human health consequences of water quality, both surface and ground water samples from all over India are analysed which indicated the source of these contaminants to be both geogenic and anthropogenic. The monthly water quality data of 85 measured parameters are being archived and can be accessed from NWIC (https://nwic.gov.in/). Fluoride, Arsenic, Iron, lead, nitrate and uranium are major ground water contaminants reported in India. Figure 5 shows locations of Fluoride, Arsenic, and Iron and their concertation in the ground water. To assess both the ground and surface quality, water quality indices are devolved based 25 selected parameters.

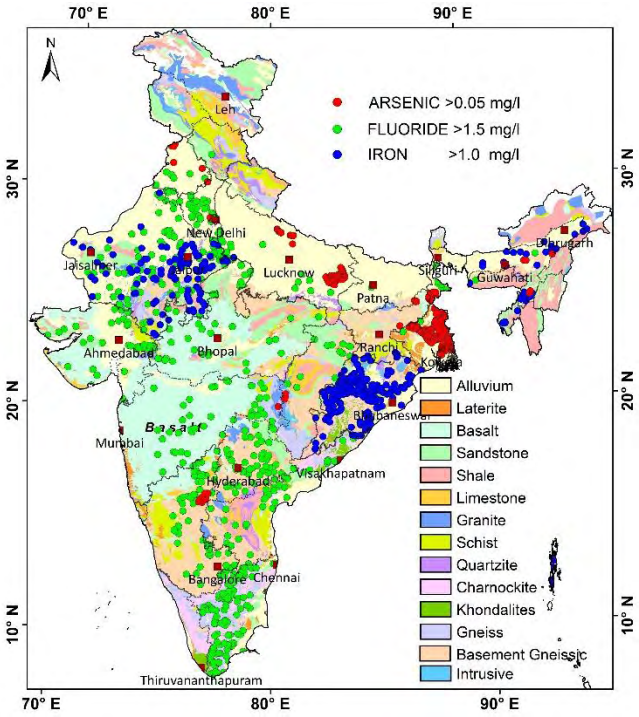

Fig 5: Locations of Arsenic, Fluoride and Iron, where concentration of these are reported high in ground water (after CGWB)

Arsenic in ground water is reported to be as high as 300 times the safe levels at some places (Kajal, 2020). Chakraborty et al., 2022 have used a dense network of 3112 borehole lithologs spread across the Ganga River delta of India and Bangladesh to develop

hydrostratigraphic model of the transboundary aquifer architecture of the delta and to interpret regional-scale arsenic distribution based on about one hundred thousand ground water arsenic data points utilizing multiple statistical tools to conclusively establish the control of the architectural variability between the aquifer sub-system on the arsenic distribution within the delta. They have suggested that the depth distribution of arsenic within the delta aquifers spatially varies as a function of the aquifer architecture and concurrently identified among the potential arsenic-safe aquifers on a regional-scale. Artificial Intelligence (AI) models are applied to predict ground water Arsenic using numerous tubewells data across India and it was found that several areas which were not well-studied earlier, have the possibility of Arsenic contamination, apart from the Indus-Ganges-Brahmaputra River basin areas (Mukherjee et al., 2020). This study also indicates that a large Indian population could be exposed to Arsenic contamination in ground water. Another study has used a multi-model approach to determine fluoride contamination with more prediction accuracy and suggests that the dry-climate granitic and metamorphic rock areas in the southern peninsular and north western Indus basin parts of India are highly susceptible to ground water fluoride contamination (Sarkar et al., 2023). The nitrate contamination is also predicted using AU models and it was found that fertilizer usage and population density as some of the major controlling factors of ground water nitrate contamination, along with the influence of rainfall and aridity-like climate factors (Sarkar et al., 2022).

Seawater intrusion (SWI) into coastal aquifer is a common phenomenon occurring in several coastal areas across the Indian coast. NRSC in association with PRIST University, Thanjavur has carried out several pilot studies in the coastal aquifers of Andhra Pradesh, Tamil Nadu to address /assess coastal aquifer vulnerability in terms of sea water intrusion (SWI) and sub-surface ground water discharge (SGD) using remote sensing and ground based observations. Detailed hydro-geological studies (micro geomorphology, topography, well inventory) have been carried out using Earth Observation (EO) data and ground based Ground Penetrating Radar (GPR) observations and detailed well inventory in both pre and post monsoon to understand the sea water intrusion scenario and its possible impact on SHAR Island due to opening of the Rayadoruvu/ SHAR inlet. In a study to understand the sea water intrusion and effects of anthropogenic factors like salt pans and fish ponds in coastal areas, a study using SEAWAT model was carried out to delineate the saltwater intrusion effect in the Nizampatnam coastal area, Andhra Pradesh. An integrated geophysical mapping, soil moisture measurements along with groundwater level monitoring in a pharmaceutical industrial area has allowed propose a management plan for perpetually polluted groundwater seepage in the highly industrial watershed (Suri Naidu et al, 2021). Chloro-Alkaline Indices (CAI) and Corrosivity Ratios (CR) have been explored to utilize for clearly distinguishing recharge and discharge zones, and demarcating areas in Dausa district, Rajasthan (Rahman et al., 2020a). It reveals that the metallic pipes could be used for groundwater supply particularly irrigation purpose. A novel technique using cumulative probability plots of analytical hydrochemical data is developed to segregate natural backgrounds (NBs) of major ions including As, F^- and NO_3^- which are essential for mass transport modelling and understanding the loadings/impacts of contamination/ pollution in groundwater system, It has been applied at an active floodplains of Ganga basin, Northern India (Rahman et al., 2021a), Dausa District, Rajasthan (Rahman et al., 2020b; 2021b), Krishna Delta, Southern India (Mondal, 2019) and an industrial belt of Peninsular India (Mondal, 2020). Spring water quality assessed at Anantnag district of Kashmir

Himalaya towards understanding the looming threats to spring ecosystem services (Bhat et al., 2022), and evaluated groundwater pollution with emphasizing heavy metal hotspots in an urbanized alluvium watershed of Yamuna River, Northern India (Ahmed et al., 2022).

Hydrological Modelling and forecasts

Optimal utilization of water requires detailed information of different components of hydrological cycle, their spatio-temporal variability and forecasting. Evapotranspiration (ET) is a critical variable required in hydrological and agricultural applications. Remote sensing (RS) is regarded as the best possible technology to map ET over large spatial domains in a repeated manner. The need for reliable ET datasets has led to the development of multiple ET products using different RS-based models at regional and global levels (e.g. Melton et al., 2021). Over India, several studies have been carried out to model ET from RS (e.g. Bhattarai et al., 2019 and reference therein). Bhattarai et al. (2019) have demonstrated the applicability of RS based models for ET mapping over entire India. However, development of an operational-capable ET product was still lacking. In addition to this, RS based ET products. Thermal Infrared (TIR) remote sensing are affected due to the cloud cover and over India, there could be data gaps even for months together affecting the continuous availability of the ET dataset. In this scenario, the India ET product was developed to map ET across India at 0.05° spatial resolution and with 8-day temporal frequency. The product was developed only using satellite observations (land surface temperature (LST), Normalized Difference Vegetation Index (NDVI), surface reflectance and digital elevation data) and meteorological data (solar radiation and air temperature) from reanalysis models. Data from MODIS and IMDAA reanalysis were used primarily towards product development. The solar radiation data from IMDAA model was found to have positive bias and hence, a statistical bias correction model (Jain et al., 2022) was applied to the data before being used in ET product generation. The LST-NDVI triangle model was used as the basis for modelling ET. The gaps in the ET dataset due to cloud cover were filled using k-nearest neighbor machine learning model. Validation of ET was carried out using in situ observations from three eddy covariance towers and five Bowen Ratio Energy Balance micrometeorological towers. The RMSE in the ET product varied across the sites in the range of 6 mm to 11 mm per an 8-day period. The product based on the methodology of Eswar et al., 2017 was found to perform consistent compared to the most widely used MODIS ET product at all sites. The variation of ET across India for different months of year 2019 is depicted in Figure 6. The dataset is now available for the years 2001-2019 and will be continuously updated. This product has exhibited negative bias over a few sites and steps are being undertaken to reduce the bias and further improve the product's accuracy.

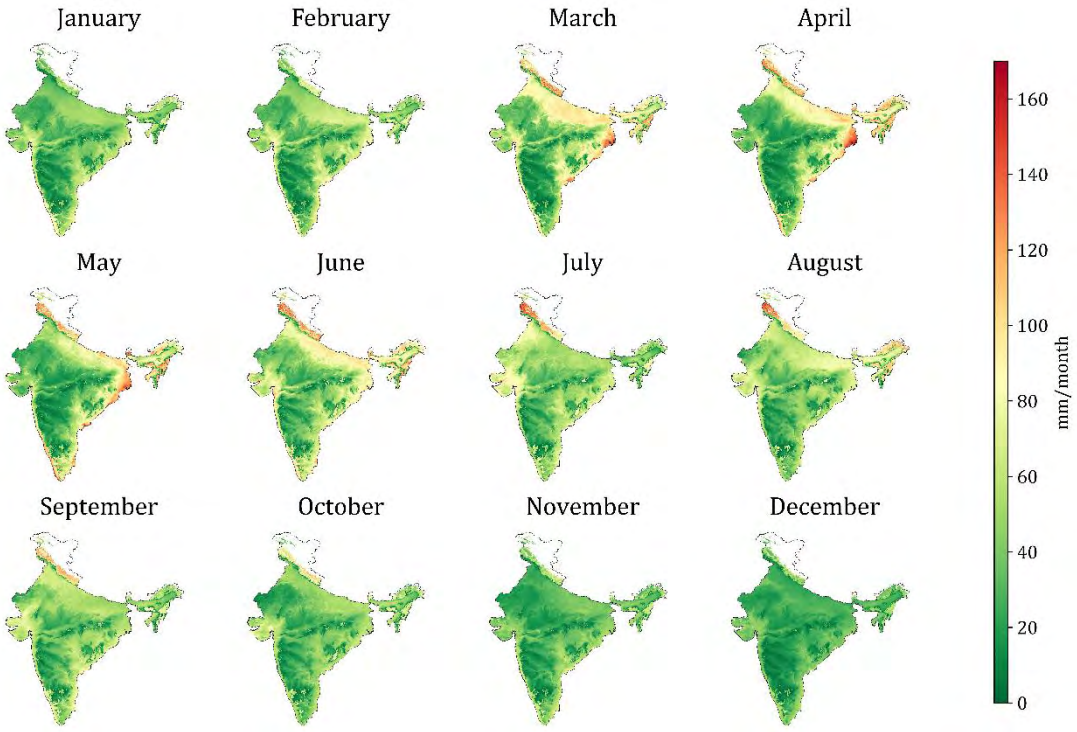

Figure 6 Monthly variation of ET across India for the year 2019(Source S Muddu).

Soil moisture data at different scales can also be reliably estimated from space-based microwave sensors (Moran et al., 2006). Passive microwave sensors provide soil moisture at a relatively coarser spatial resolution (~25 km), whereas active microwave sensors provide a relatively better spatial resolution (less than 100 m) but with a relatively lower temporal resolution (1-4 weeks). Passive microwave sensors provide readily available global soil moisture products. However, in the case of active microwave sensors, only raw satellite data is provided. Tomer et al. (2015) developed an algorithm to operationally estimate the soil moisture data using the active microwave space-based sensors. Zribi et al. (2019) developed another algorithm to estimate soil moisture under relatively denser vegetation using space-based L-band active microwave data. Using the Merging Active and Passive microwave Soil Moisture (MAPSM) approach, Tomer et al., 2016, estimated soil moisture products by operationally combining with passive band global products to provide soil moisture with a relatively better spatial (less than 100 m) and temporal resolution (1-3 days). Figure 7 provides snapshot of one weekly soil moisture over India.

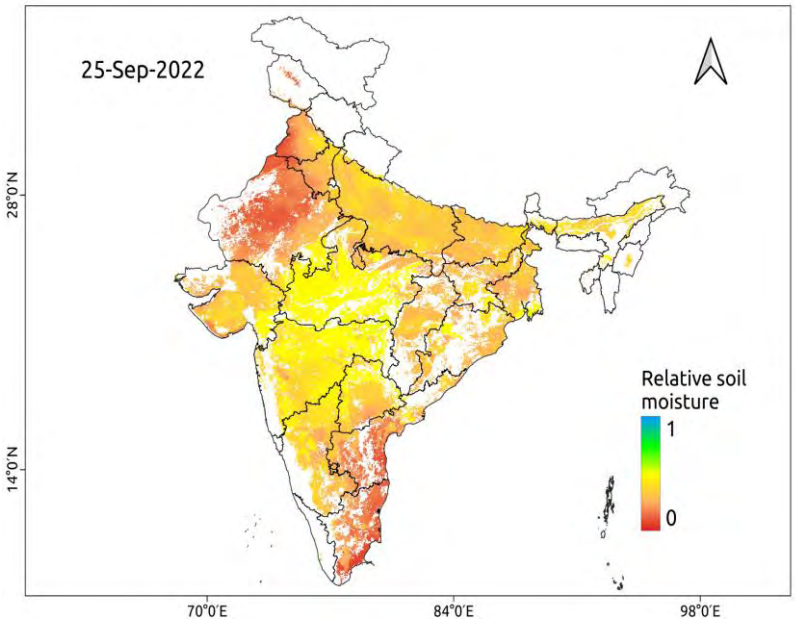

Figure 7: Relative Soil moisture for entire India. Here 0 means driest possible soil moisture and 1 means wettest possible soil moisture at that location. Relative soil moisture is obtained by considering the historical soil moisture and rescaling it to 0 to 1.

NRSC uses space-based inputs to re-assess the water availability in the country using geo-spatial and meteorological data of the last three decades. The study established a standard geospatial data based hydrological framework with a transformation from basin terminal runoff aggregation to precipitation-based water budgeting exercise. The various hydrological information products & services at NRSC are: Actual Evapotranspiration (AET) for India at daily time-step, inventory of glacial lakes (size greater than 0.25 ha) for entire Himalayan river basin catchments (Indus, Ganga & Brahmaputra) using Resourcesat-2 LISS-IV MX data. A total of 28,004 glacial lakes were mapped along with 21 attributes. daily snowmelt rate and snowmelt discharge for entire Himalayan river basin catchments (Indus, Ganga & Brahmaputra) during Apr-Jun months, spatial flood early warning systems for Godavari & Tapi river basins integrating high resolution

A study (Kushwaha et al 2021) has provided estimates of the water budget in river basins across the Indian subcontinent using a multimodel (VIC, CLM, Noah-MP, H08, and CWatM models) and showed that ensemble mean provided better results compared to individual models. The Brahmaputra, Ganga, and Indus, transboundary river basins, show the highest water yield. Brahmaputra, and Brahmani basins are the wettest river basins, while Sabarmati, Indus, and Pennar are the three driest basins. The atmospheric water demands of the river basins are identified using Budyko framework analysis which shows that two river basins, are in the energy-limited conditions, and the other sixteen river basins are in water-limited conditions suggesting low and high atmospheric water demands respectively (figure 8). These findings are crucial for sustainable water management to ensure the equitable distribution of water resources.

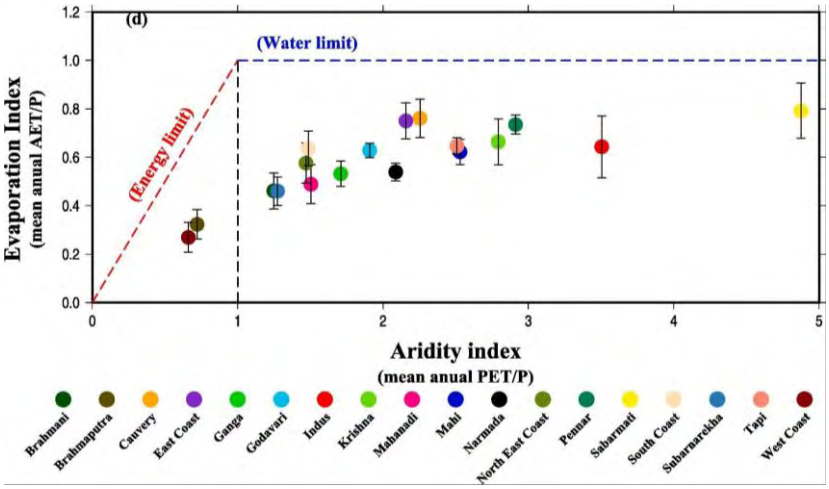

Fig 8: Indian sub-continental river basins on Budyko's diagram. Error bars show inter-model uncertainty in the evaporative index estimated using the multimodel hydrological models.
Reference:

A comprehensive study was conducted to quantify water availability and water demands of the Cauvery basin, which can help in framing improved water management policies to ensure improved water security. A significant trends in the baseflow, evapotranspiration, runoff and rainfall are noticed and modification of streamflow are observed after the construction of dams, which may affect the downstream water availability (Gowri et al., 2021). Catchments can be considered as complex systems, and hence the interactions between catchment and climate will impart distinct patterns in the temporal dynamics of streamflow. Complexity measures and information-theoretic measures such as emergence and self-organization are used to capture the streamflow characteristics. The role of memory in identifying the causal structure of bivariate systems is investigated, revealing that the state of the memory of the causal variables influences the inference of the causal methods (Dey & Mujumdar, 2022). Hydrological extremes such as droughts and floods may be caused either predominantly by a single meteorological or hydrological variable or by a combination of such variables. Concurrent occurrences of extreme events can have more severe consequences than individual occurrences. Therefore, it is crucial to accurately estimate joint probabilities to develop effective risk management strategies and plan preventive actions. A framework is developed to characterize the complex dependence structure of concurrent hydroclimatic extremes in higher dimensions, investigate extremal behaviour, and assess risk in drought-prone regions (Sharma & Mujumdar, 2022). Figure 9 shows the estimated angular densities of the best selected Hüsler-Reiss model for all the districts of a drought-prone region in India - Marathwada, Maharashtra. Significant relation is found between soil moisture deficits and high temperatures, while deficit in rainfall are mildly related dependent on these two variables.

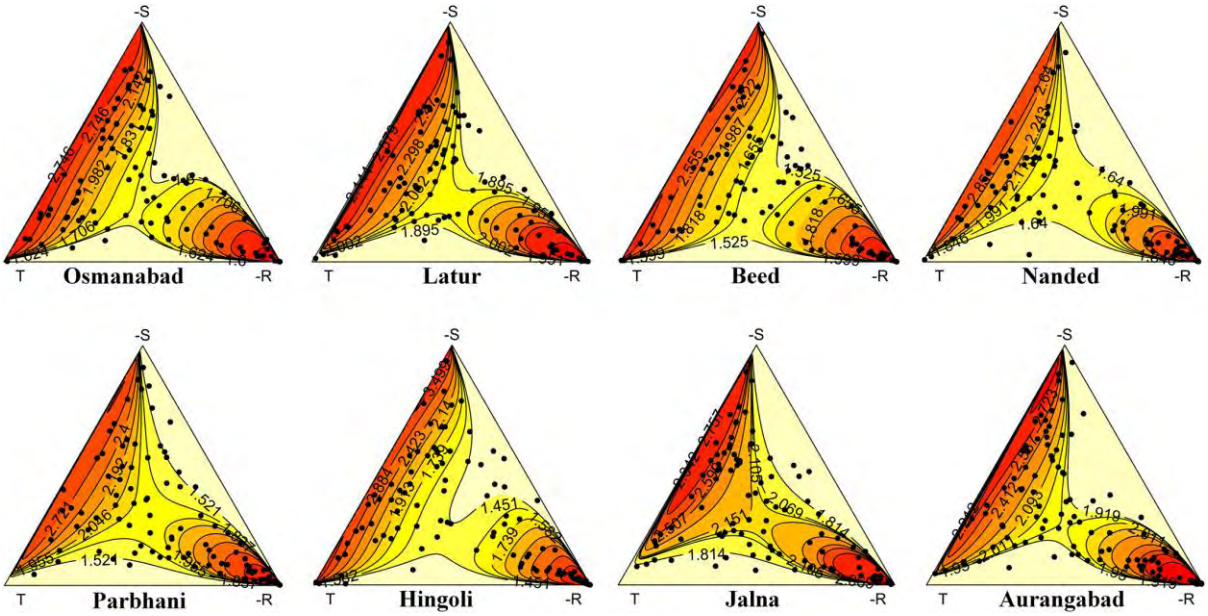

Fig:9. Estimated angular densities of the best selected Hüsler-Reiss model for all districts of Marathwada, Maharashtra. (Sharma & Mujumdar, 2022).

Several analyses are carried out to study the influence of various causal factors on extreme rainfall values. The impact of urbanization on hydro-meteorologic variables across seven cities in the United States is investigated (Rajulapati et al., 2020). The results indicate that changes in short-duration precipitation and temperature have been prominent in the recent past. The influence of threshold selection in modelling extreme rainfall under a non-stationary scenario is performed. It is found that threshold uncertainty is more for high return period events. Additionally, a methodology is proposed to investigate the association of extreme rainfall events with physical drivers and to model their dependence structure (Sharma & Mujumdar, 2019).

Entropy measures such as Relative Entropy (RE) are used to investigate the spatial variability and change in uniformity of rainfall distribution over India (Dey & Mujumdar, 2019). It is concluded that uniformity in rainfall distribution is altered as rise in temperature modifies both high and low-intensity rainfall events. Figure 11 shows the temporal statistics of RE (1951–2010), trends and their statistical significance. In addition, the temporal asymmetry of a streamflow hydrograph is explored by correlating streamflow indices and catchment attributes with the rising and falling limbs of the hydrograph (Mathai & Mujumdar, 2019). The streamflow indices and their regional variability in the Contiguous United States is also prepared (Mathai & Mujumdar, 2022).

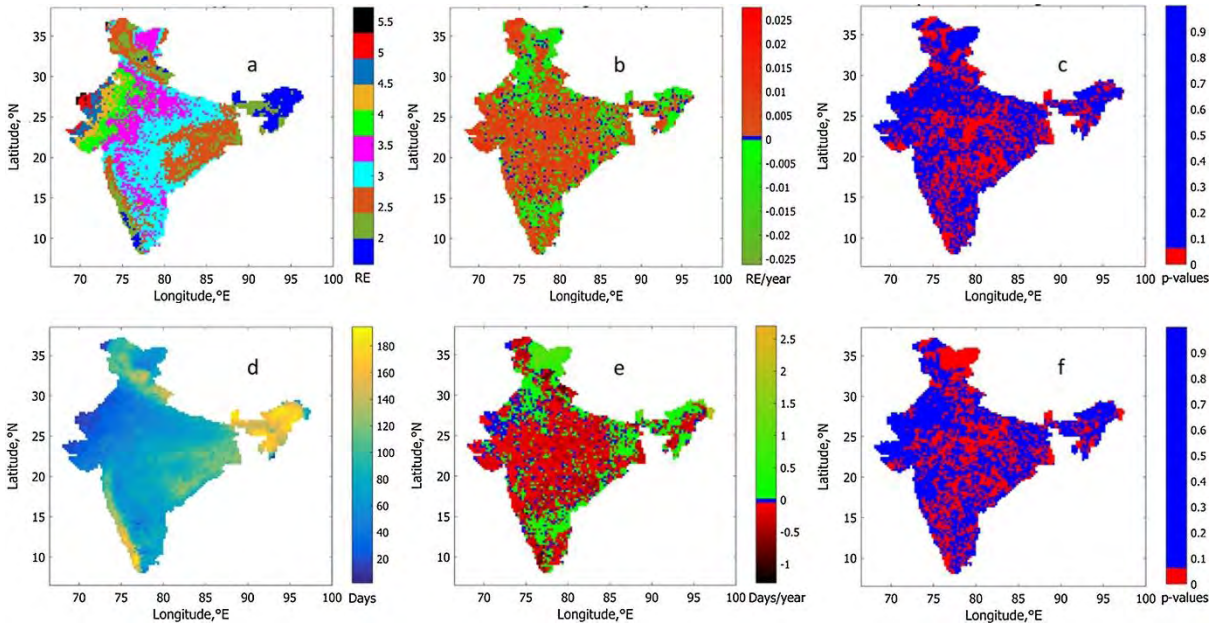

Fig: 10. Spatial plots of Relative Entropy (RE) and the annual number of wet days during 1951–2010. The spatiotemporal behaviour of the degree of uniformity of annual rainfall distribution as measured by RE. a) The mean RE from 1951 to 2010, b) trends in the evolution of RE from 1951 to 2010 and c) the significance of the trend denoted by p-values. A day with rainfall greater than 0.1 mm is considered a wet day. d) The mean annual number of wet days, e) its trend and f) significance of the trend (Dey & Mujumdar, 2019).

Flooding in urban areas is one of the most severe natural disasters humanity has been facing for several years. Rapid urbanization and climate change have exaggerated the severity of these events. The development of an indigenous flood forecasting system with enough lag time to alert citizens during extreme events is vital for ensuring adequate preparedness and effective planning of mitigation activities. To achieve this, an integrated urban flood model is developed for Bangalore, Karnataka, which includes a dense network of telemetric rain gauge stations and a Weather Research and Forecasting (WRF) model further integrated with a hydrological model for obtaining short-term rainfall and flood forecasts (Davis et al., 2022; Kaginalkar et al., 2022). This framework generates 15-minute forecasts for Bangalore city and provides a comprehensive overview of integrated urban environmental systems in Indian cities. Additionally, a comprehensive analysis of the 2018 Kerala floods is carried out to analyze the role of reservoir operations during the flood period. Major dam spills are assessed to determine their contribution, and reservoir operations are checked against the existing rule curves. A calibrated hydrological model is utilized to estimate flows and assess the amount of floodwater resulting from extreme rainfall. Modelling heavy rainfall events is challenging due to multi-scale interactions and model configuration factors. The WRF model is implemented to investigate the impact of different processes on extreme rainfall simulation considering a representative event in the Ganga Basin, India (Chawla & Mujumdar, 2020). The inclusion of detailed land surface model schemes improves model results by representing soil moisture. The model parameters are found to vary over time, suggesting the need for non-stationary parameters in future streamflow simulations. Evaluation of reanalysis data and satellite products shows that fine-resolution datasets do not always produce better rainfall simulations. Further, a study is conducted to explore the hydrological implications of increasing reservoir-

induced and climate-related stressors in the Upper Ganga River basin (Swarnkar et al., 2021). The study highlights the disruptions of upstream-downstream geomorphological linkages due to hydraulic structures. The results show that the hydrological regimes of low and moderate flows of the Upper Ganga basin have been significantly altered and the operation of hydraulic structures in the Bhagirathi basin attenuates the flood peaks. The downstream reaches of the basin experience reservoir-induced flow alteration and increased extreme flood magnitudes. Substantial siltation upstream of the reservoirs has disrupted the geomorphologic linkages in the basin.

An analysis using Extended Range Forecast System (ERFS) and Global Ensemble Forecast System (GEFS) forecast for streamflow prediction shows that the ensemble streamflow forecast from the GEFS has better performance than the ERFS during 2019-2020 for Narmada River Basin (Vegad and Mishra, 2022). The findings of the study can be useful in evolving a flood early warning system. Combined in situ and satellite-based datasets, along with meteorological model simulations, provide valuable insights into the impact of irrigation on extreme moist heat in South Asia. The findings indicate that intensive irrigation in the region leads to a cooling of the land surface and air by 1°C and 0.5°C, respectively (Mishra et al, 2021). However, the decrease in sensible heat flux due to irrigation results in a reduction of the planetary boundary layer height, leading to an increase in low-level moist enthalpy. Consequently, irrigation leads to an increase in specific and relative humidity, which contributes to the rise in moist heat stress metrics. The intense irrigation practices in the region lead to a significant increase in moist heat stress in India, despite the cooling of the land surface. These findings highlight the need for sustainable irrigation practices and underscore the importance of addressing the issue of extreme moist heat.

The climate change could also impact the occurrence and distribution of ground water contaminants. The impacts of climate change and land use change on the water quality across the industrialized Kanpur region along the Ganga river are assessed (Santy et al., 2020, 2022). It is found that dissolved oxygen is more sensitive towards climate, while nutrients and faecal coliform concentrations are sensitive to land use change, respectively. Eutrophic conditions are observed for different climate change and land cover scenarios, implying severe impacts on aquatic life. A study using AI models and two climate change scenarios under the RCP 4.5 and 8.0 conditions, predicted that the areas affected by high ground water nitrate in Punjab can rise to 50% by 2030 and 65% by 2040. (Sarkar et al., 2022). An information-based model has been hypothesized and developed to estimate natural groundwater recharge with the measurement of groundwater level and rainfall data at the proximity of Deccan Trap Basalt in Central India (Mondal and Ajaykumar, 2021), and Gangetic plains, Northern India (Mondal and Ajaykumar, 2022).

Government Initiatives

During 2019-2022, the government has started various measures and initiatives to ensure the sustainable management of water resources in the country and include water conservation and rainwater harvesting; renovation of traditional and other water bodies/ tanks; creation of ground water recharge structures, and intensive afforestation. A program named Atal Bhujal Yojana was launched to address the issues related to depletion of ground water in the country and selected some critical areas for ground water management for improving the

recharge of ground water and and promoting justifiable use of ground water. The scheme emphasizes on community-led ground water management, which involves the active participation of local communities. A linked initiative to water management is Jal Jeevan Mission (JJM) which envisages to create a network of piped drinking water to all rural houses. Since the source (surface and ground) water is critical for continued supply of water, these programmes utilize the present day scientific and technological knowledge base for source sustainability for good quality water. These government missions also proliferate awareness about water conservation and management among rural communities.

Acknowledgments

The information included in the report does not include all the work carried by Indian water scientists rather it is indicative of the kind of water related research work pursued in India during 2019-2023. The inputs received from PP Muzumdar (IISc), S Muddu (IISc), IC. Das (NRSC-ISRO), V Mishra (IITGn), S Chandra, NC Mondal and S More (NGRI) are appreciated. Permission by Director, CSIR-NGRI to publish this report is duly acknowledged.

References

Ahmed, S., Akhtar, N., Rahman, A., Mondal, N.C., Khurshid, S., Sarah, S., Ali Khan, M.M., and Kamboj, V., 2022. Evaluating groundwater pollution with emphasizing heavy metal hotspots in an urbanized alluvium watershed of Yamuna River, Northern India. Environmental Nanotechnology, Monitoring & Management, Vol. 18, 100744, pp.1-13.

Ajaykumar, V. and Mondal, N.C., 2022. Estimating static, dynamic and monsoon groundwater reserves in a dense well network of basaltic terrain, central India. Journal of the Geological Society of India, Vol. 98, No.6, pp.787-794.

Ajaykumar, V., Mondal, N.C. and Ahmed, S., 2020. Identification of groundwater potential zones using RS, GIS and AHP techniques: a case study in a part of Deccan Volcanic Province (DVP), Maharashtra, India. Journal of the Indian Society of Remote Sensing, Vol. 48, No. 3, pp.497-511.

Asoka, A., Wada, Y., Fishman, R., & Mishra, V. (2018). Strong linkage between precipitation intensity and monsoon season groundwater recharge in India. Geophysical Research Letters, 45(11), 5536-5544.

Bhat, S.U., Nisa, A.U., Sabha, I. and Mondal, N.C., 2022. Spring water quality assessment of Anantnag district of Kashmir Himalaya: Towards understanding the looming threats to spring ecosystem services. Applied Water Science, Article: 180, Vol. 12, No.8, pp.1-17.

Bhattarai, N., Mallick, K., Stuart, J., Vishwakarma, B.D., Niraula, R., Sen, S., & Jain, M. 2019. An automated multi-model evapotranspiration mapping framework using remotely sensed and reanalysis data. Remote Sensing of Environment, 229: 69-92.

Boisson, A., Villesseche, D., Selles, A.,Alazard, M., Chandra, S., Ferrant, S., & Maréchal, J.-C. (2022). Long term monitoring of rainwater harvesting tanks: Ismulti-years management possible in crystalline South Indianaquifers? Hydrological Processes,36(12), e14759. https://doi.org/10.1002/hyp.14759

Central Ground Water Board, Department of Water Resources, River Development & Ganga Rejuvenation, Ministry of Jal Shakti, Government of India (2022), National Compilation on Dynamic Ground Water Resources of India, 2020

Chakraborty, M., Mukherjee, A. & Ahmed, K.M., 2022. Regional-scale hydrogeochemical evolution across the arsenic-enriched transboundary aquifers of the Ganges River Delta system, India and Bangladesh. Science of the Total Environment, 823, p.153490.

Chandra S., & Tiwari V.M., 2022 Rapid 3d Geophysical Imaging of Aquifers in Diverse Hydrogeological Settings. Water Security (published online), 15 February 2022, 100111, https://doi.org/10.1016/j.wasec.2022.100111

Chandra S., Auken E., Maurya P.K., Ahmed S., & Verma S.K, 2019. Large scale mapping of fractures and groundwater pathways in crystalline hardrock by AEM, Scientific Reports 9: 398, DOI:10.1038/s41598-018-36153-1

Chandra S., Choudhury J., Maurya P.K., Ahmed S., Auken E., & Verma S.K. 2021. Geological significance of locating paleo-channels with AEM. Exploration Geophysics. Exploration Geophysics, 51 (1): 74-83 DOI: 10.1080/08123985.2019.1646098

Chandra S., Jacobsen B.H., Christensen N.B. Ahmed S. & Verma, S.K., 2020. Multiparametric Coupling and Constrained Interpolation to Improve Natural Recharge Estimation, J. Earth Syst. Sci. (2020) 129:8, https://doi.org/10.1007/s12040-019-1253-z

Chandra, S., Raju, K.B., Vidyasagar, M., Choudhury, J., Kumar, K.L., Chandrapuri, S. & Ahmed S (2020). High Resolution 3-D Aquifer Mapping along Tapi River and the Adjoining Region near Surat City employing Heliborne and Ground Geophysical Surveys-Heliborne survey and report, NGRI-2020-GW-978.

Chandra, S., Tiwari, V. M., Vidyasagar, M., Raju, K. B., Choudhury, J., & Lohithkumar, K., (2021). Airborne electromagnetic signatures of an ancient river in the water-stressed Ganga Plain, Prayagraj, India: A potential groundwater Repository. Geophysical Research Letters, 48, e2021GL096100. https://doi.org/10.1029/2021GL096100

Chawla, I., & Mujumdar, P. P. (2020). Evaluating rainfall datasets to reconstruct floods in data-sparse Himalayan region. Journal of Hydrology, 588(November 2019), 125090. https://doi.org/10.1016/j.jhydrol.2020.125090

Dabas, J., Sarah, S., Mondal, N.C. and Ahmed, S., 2022. Geostatistical spatial projection of geophysical parameters for practical aquifer mapping. Scientific Reports, 12, 4641, 1-14.

Dangar, S., & Mishra, V. (2021). Natural and anthropogenic drivers of the lost groundwater from the Ganga River basin. Environmental Research Letters, 16(11), 114009.

Dangar, S., & Mishra, V. (2023). Excessive pumping limits the benefits of a strengthening summer monsoon for groundwater recovery in India. One Earth.

Dangar, S., Asoka, A., & Mishra, V. (2021). Causes and implications of groundwater depletion in India: A review. Journal of Hydrology, 596, 126103.

Davis, S., Pentakota, L., Saptarishy, N., & Mujumdar, P. P. (2022). A Flood Forecasting Framework Coupling a High Resolution WRF Ensemble With an Urban Hydrologic Model. Frontiers in Earth Science, 10, 876.https://doi.org/10.3389/FEART.2022.883842/BIBTEX

Dey, P., & Mujumdar, P. (2022). On the statistical complexity of streamflow. Hydrological Sciences Journal, 67(1), 40–53. https://doi.org/10.1080/02626667.2021.2000991

Dey, P., & Mujumdar, P. P. (2019). On the uniformity of rainfall distribution over India. Journal of Hydrology, 578, 124017. https://doi.org/10.1016/J.JHYDROL.2019.124017

Eswar, R., Sekhar, M., & Bhattacharya, B.K., 2017. Comparison of three remote sensing based models for the estimation of latent heat flux over India. Hydrological Sciences Journal 62, 2705–2719. https://doi.org/10.1080/02626667.2017.1404067

Gowri, R., Dey, P., & Mujumdar, P. P. (2021). A hydro-climatological outlook on the long-term availability of water resources in Cauvery river basin. Water Security, 14, 100102. https://doi.org/10.1016/j.wasec.2021.100102

Jain, A., Eswar, R. & Bhattacharya, B. K. (2022), Validation and bias correction of incoming solar radiation from two reanalysis products over India, Journal of Earth System Science, 131, 1276, DOI: 10.1007/s12040-022-01873-6

Kaginalkar, A., Ghude, S. D., Mohanty, U. C., Mujumdar, P., Bhakare, & S., Darbari, H., (2022). Integrated Urban Environmental System of Systems for Weather Ready Cities in India. Bulletin of the American Meteorological Society, 103(1), E54–E76. https://doi.org/10.1175/BAMS-D-20-0279.1

Kumar Singh, P., Dey, P., Kumar Jain, S., & Mujumdar, P. P. (2020). Hydrology and water resources management in ancient India. Hydrology and Earth System Sciences, 24(10), 4691–4707. https://doi.org/10.5194/HESS-24-4691-2020

Kushwaha, A. P., Tiwari, A. D., Dangar, S., Shah, H., Mahto, S. S., & Mishra, V. (2021). Multimodel assessment of water budget in Indian sub-continental river basins. Journal of Hydrology, 603, 126977.

Mathai, J., & Mujumdar, P. P. (2019). Multisite Daily Streamflow Simulation With Time Irreversibility. Water Resources Research, 55(11), 9334–9350. https://doi.org/10.1029/2019WR025058

Mathai, J., & Mujumdar, P. P. (2022). Use of streamflow indices to identify the catchment drivers of hydrographs. Hydrology and Earth System Sciences, 26(8), 2019–2033. https://doi.org/10.5194/HESS-26-2019-2022

Maurya, V.P., Chandra, S., Sonkamble, S., Kumar, K.L., Nagaiah, E., & Selles A., 2021. Electrically inferred subsurface fractures in the crystalline hard rocks of an Experimental Hydrogeological Park, Southern India. Geophysics 86 (5), WB59-WB146, https://doi.org/10.1190/geo2020-0327.1

Melton, F.S., J. Huntington, R. Grimm, J. Herring, M. Hall, D. Rollison, & T. Erickson et al. 2021. OpenET: Filling a Critical Data Gap in Water Management for the Western United States. Journal of the American Water Resources Association 1–24. https://doi.org/10.1111/1752-1688.12956.

Ministry of Water Resources, River Development & Ganga Rejuvenation, 2015, Report of the Ground Water Resource Estimation Committee. Govt. of India

Mishra, V., Ambika, A. K., Asoka, A., Aadhar, S., Buzan, J., Kumar, R., & Huber, M. (2020). Moist heat stress extremes in India enhanced by irrigation. Nature Geoscience, 13(11), 722-728.

Mondal, N. C., & Ajaykumar, V. (2021). Appraisal of natural groundwater reserve using entropy-based model at the proximity of Deccan Trap Basalt and Gondwana Sandstone in a part of Central India. Arabian Journal of Geosciences, 14, 1-15.

Mondal, N. C., & Ajaykumar, V. (2022). Assessment of natural groundwater reserve of a morphodynamic system using an information-based model in a part of Ganga basin, Northern India. Scientific Reports, 12(1), 1-12.

Mondal, N.C. and Ajay Kumar, V., 2021. Appraisal of natural groundwater reserve using entropy-based model at the proximity of Deccan Trap Basalt and Gondwana Sandstone in a part of Central India. Arabian Journal of Geosciences, vol.14, no.21 article: 2163, pp.1-15.

Mondal, N.C. and Ajaykumar, V., 2022. Assessment of natural groundwater reserve of a morphodynamic system using an information-based model in a part of Ganga basin, Northern India. Scientific Reports, 12(1), 6191, 1-12.

Mondal, N.C. and Rajewar, S.K., 2020. Estimating soil thickness using the H/V Spectral ratio technique in CSIR-NGRI Campus, Hyderabad, India. Bulletin of Pure and Applied Sciences-Geology, Vol. 39F, No.2, pp.150-162.

Mondal, N.C., 2019. Hydrochemical approach for irrigation suitability of groundwater in Krishkindapalem of Krishna delta, Andhra Pradesh. Journal of Geosciences Research, Vol. 4, No. 1, January 2019, pp. 1-10.

Mondal, N.C., 2020. Exploring hydrochemical backgrounds using cumulative probability approach for finding groundwater suitability in an industrial area from Peninsular India. Journal of Applied Geochemistry, Vol. 22, No. 2, pp. 132-141.

Mondal, N.C., 2021. Geoelectrical signatures for detecting water-bearing zones in a micro-watershed of granitic terrain from Southern India. Journal of Applied Geophysics, vol.191C, article: 104361.

Mondal, N.C., Vimala Supriya, T., Mahato, P.P. and Ahmed, S., 2020. Exploring water-bearing zones by merging of partial curve matching, factor analysis and inverse technique from surficial geophysical data in a sedimentary area of West Bengal. Hydrology Journal, Vol. 40&41, No. 1-4, pp. 38-51.

Moran, M. S., McElroy, S., Watts, J. M., & Peters-Lidard, C. D. (2006). Radar remote sensing for estimation of surface soil moisture at the watershed scale. Modeling and Remote Sensing Applied in Agriculture (US and Mexico), 91-106.

MoSPI (2009), Performance of AIBP, Ministry of Statistics and Programme Implementation, Government of India.

Mukherjee, A., Sarkar, S., Chakraborty, M., Duttagupta, S., Bhattacharya, A., Saha, D., Bhattacharya, P., Mitra, A. & Gupta, S., 2021. Occurrence, predictors and hazards of elevated groundwater arsenic across India through field observations and regional-scale AI-based modeling. Science of the Total Environment, 759, p.143511.

Munagapati, H. & Tiwari, V.M., 2021. Spatio-temporal patterns of mass changes in himalayan glaciated region from EOF analyses of GRACE Data. Remote Sensing, 13(2), p.265.

Munagapati, H., Tiwari, V.M. & Panda, D.K., 2021. An analysis of spatio-temporal variability of terrestrial water storage in India. Water Security, 14, p.100099.

Nicolas, M.,∗, Bourb, O., Sellesa, A., Dewandelc, B., Bailly-Comtec, V., Chandra, S., Ahmed, S., & Maréchalc, J-C., 2019. Managed Aquifer Recharge in fractured crystalline rock aquifers: Impact of horizontal preferential flow on recharge dynamics. Journal of Hydrology 573 (2019) 717–732.

Panda, D.K., Tiwari, V.M. & Rodell, M., 2022. Groundwater variability across India, under contrasting human and natural conditions. Earth's Future, 10(4), p.e2021EF002513.

Paswan, A.K., Mizan, S. A., Chandra S., & Tiwari, V.M., 2022. Hydrogeological simulation for groundwater management strategies in crystalline aquifers, Southern India, J. Earth System Sciences, 131 (3), 168.

Rahman, A., Mondal, N.C. and Fauzia F., 2021a. Arsenic enrichment and its natural background in groundwater at the proximity of active floodplains of Ganga River, Northern India. Chemosphere, Vol.265, Article-129096.

Rahman, A., Mondal, N.C. and Tiwari, K.K., 2021b. Anthropogenic nitrate in groundwater and its health risks in the view of background concentration in a semi-arid area of Rajasthan, India. Scientific Reports, 11, 9279, 1-13.

Rahman, A., Tiwari, K.K. and Mondal, N.C., 2020a. Hydrochemical characterization for groundwater suitability in a semi-arid area in Sanganer Block, Jaipur District, Rajasthan. Journal Geological Society of India, Vol. 96, No.4, pp. 399-409.

Rahman, A., Tiwari, K.K. and Mondal, N.C., 2020b. Assessment of hydrochemical backgrounds and threshold values of groundwater in a part of desert area, Rajasthan, India. Environmental Pollution, Vol. 266, Part 3, Article 115150, pp.1-12.

Rajulapati, C. R., Gupta, H., & Mujumdar, P. P. (2020). Diurnal variability of hydrological variables in urban areas. Urban Climate, 33, 100669. https://doi.org/10.1016/J.UCLIM.2020.100669

Saha, D., Marwaha, S., & Dwivedi, S.N. (2019). National Aquifer Mapping and Management Programme: A Step Towards Water Security in India. In: Singh, A., Saha, D., Tyagi, A. (eds) Water Governance: Challenges and Prospects. Springer Water. Springer, Singapore. https://doi.org/10.1007/978-981-13-2700-1_3

Santy, S., Mujumdar, P., & Bala, G. (2020). Potential Impacts of Climate and Land Use Change on the Water Quality of Ganga River around the Industrialized Kanpur Region. Scientific Reports 2020 10:1, 10(1), 1–13. https://doi.org/10.1038/s41598-020-66171-x

Santy, S., Mujumdar, P., & Bala, G. (2022). Increased risk of water quality deterioration under climate change in Ganga River. Frontiers in Water, 4, 140. https://doi.org/10.3389/FRWA.2022.971623/BIBTEX

Sarkar, S., Mukherjee, A., Chakraborty, M., Quamar, M.T., Duttagupta, S. & Bhattacharya, A., 2023. Prediction of elevated groundwater fluoride across India using multi-model approach: insights on the influence of geologic and environmental factors. Environmental Science and Pollution Research, 30(11), pp.31998-32013.

Sarkar, S., Mukherjee, A., Senapati, B. & Duttagupta, S., 2022. Predicting Potential Climate Change Impacts on Groundwater Nitrate Pollution and Risk in an Intensely Cultivated Area of South Asia. ACS Environmental Au, 2(6), pp.556-576.

Shaji, E., Santosh, M., Sarath, K.V., Prakash, P., Deepchand, V. & Divya, B.V., 2021. Arsenic contamination of groundwater: A global synopsis with focus on the Indian Peninsula. Geoscience frontiers, 12(3), p.101079.

Sharma, S., & Mujumdar, P. P. (2019). On the relationship of daily rainfall extremes and local mean temperature. Journal of Hydrology, 572, 179–191. https://doi.org/10.1016/J.JHYDROL.2019.02.048

Sharma, S., & Mujumdar, P. P. (2022). Modeling Concurrent Hydroclimatic Extremes With Parametric Multivariate Extreme Value Models. Water Resources Research, 58(2). https://doi.org/10.1029/2021WR031519

Singh, P.K., Dey, P., Jain, S.K. & Mujumdar, P.P., 2020. Hydrology and water resources management in ancient India. Hydrology and Earth System Sciences, 24(10), pp.4691-4707.

Sonkamble, S., Chandra, S. & Pujari, P.R. (2022). Application of airborne and ground geophysics to unravel the hydrogeological complexity of the Deccan basalts in central India. Hydrogeol J 30, 2097–2116 (2022). https://doi.org/10.1007/s10040-022-02503-7

Surinaidu, L., Nandan, M.J., Sahadevan, D.K., Umamaheswari, A. &Tiwari, V.M., 2021. Source identification and management of perennial contaminated groundwater seepage in the highly industrial watershed, south India. Environmental Pollution, 269, p.116165.

Swarnkar, S., Mujumdar, P., & Sinha, R. (2021). Modified hydrologic regime of upper Ganga basin induced by natural and anthropogenic stressors. Scientific Reports 2021 11:1, 11(1), 1–11. https://doi.org/10.1038/s41598-021-98827-7

Tiwari, V. M., Mondal, N.C., & Chandra S., 2021. A Brief Overview of Groundwater Studies at CSIR-NGRI During Six Decades. Journal Geological Society of India, 97: 285-1293

Tomer, S. K., Al Bitar, A., Sekhar, M., Zribi, M., Bandyopadhyay, S., Sreelash, K., ... & Kerr, Y. (2015). Retrieval and multi-scale validation of soil moisture from multi-temporal SAR data in a semi-arid tropical region. Remote Sensing, 7(6), 8128-8153.

Tomer, S. K., Al Bitar, A., Sekhar, M., Zribi, M., Bandyopadhyay, S., & Kerr, Y. (2016). MAPSM: A spatio-temporal algorithm for merging soil moisture from active and passive microwave remote sensing. Remote Sensing, 8(12), 990.

Vegad, U., & Mishra, V. (2022). Ensemble streamflow prediction considering the influence of reservoirs in Narmada River Basin, India. Hydrology and Earth System Sciences, 26(24), 6361-6378.

Venkatarao, A.V., Mondal, N.C. and Ahmed, S., 2019. Investigating groundwater recharge potential zones using a cross-correlation technique in a part of *Deccan Volcanic Province* (DVP), Central India. Environmental Earth Sciences, 78 (24):704, pp.1-12.

Zribi, M., Muddu, S., Bousbih, S., Al Bitar, A., Tomer, S. K., Baghdadi, N., & Bandyopadhyay, S. (2019). Analysis of L-band SAR data for soil moisture estimations over agricultural areas in the tropics. Remote Sensing, 11(9), 1122.

Quadrennial Report on Indian scientific contributions to IAMAS

A. P. Dimri

Indian Institute of Geomagnetism, New Panvel, Navi Mumbai

Atmospheric Aerosols

Outflow of Asian biomass burning aerosol pollution into the upper troposphere and lower stratosphere and radiative impacts

Biomass burning (BB) over Asia is a strong source of carbonaceous aerosols during spring. From ECHAM6–HAMMOZ model simulations and satellite observations, we show that there is an outflow of Asian BB carbonaceous aerosols into the upper troposphere and lower stratosphere (UTLS) (black carbon: 0.1 to 6 ng m^{-3} and organic carbon: 0.2 to 10 ng m^{-3}) during the spring season. The model simulations show that the greatest transport of BB carbonaceous aerosols into the UTLS occurs from the Indochina and East Asia region by deep convection over the Malay Peninsula and Indonesia. The increase in BB carbonaceous aerosols enhances atmospheric heating by 0.001 to 0.02 K d^{-1} in the UTLS. The aerosol-induced heating and circulation changes increase the water vapor mixing ratios in the upper troposphere (by 20–80 ppmv) and in the lowermost stratosphere (by 0.02–0.3 ppmv) over the tropics. Once in the lower stratosphere, water vapor is further transported to the South Pole by the lowermost branch of the Brewer–Dobson circulation. These aerosols enhance the in-atmosphere radiative forcing (0.68±0.25 to 5.30±0.37 W m^{-2}), exacerbating atmospheric warming, but produce a cooling effect on climate (top of the atmosphere – TOA: −2.38±0.12 to −7.08±0.72 W m^{-2}). The model simulations also show that Asian carbonaceous aerosols are transported to the Arctic in the troposphere. The maximum enhancement in aerosol extinction is seen at 400 hPa (by 0.0093 km^{-1}) and associated heating rates at 300 hPa (by 0.032 K d^{-1}) in the Arctic.

The impact of recent changes in Asian anthropogenic emissions of SO_2 on sulphate loading in the upper troposphere and lower stratosphere and the associated radiative changes

Convective transport plays a key role in aerosol enhancement in the upper troposphere and lower stratosphere (UTLS) over the Asian monsoon region where low-level convective instability persists throughout the year. We use the state-of-the-art ECHAM6–HAMMOZ global chemistry–climate model to investigate the seasonal transport of anthropogenic Asian sulfate aerosols and their impact on the UTLS. Sensitivity simulations for SO2 emission perturbation over India (48 % increase) and China (70 % decrease) are performed based on the Ozone Monitoring Instrument (OMI) satellite-observed trend, rising over India by ∼4.8 % per year and decreasing over China by ∼7.0 % per year during 2006–2017. The enhanced Indian emissions result in an increase in aerosol optical depth (AOD) loading in the UTLS by 0.61 to 4.17 % over India. These aerosols are transported to the Arctic during all seasons by the lower branch of the Brewer–Dobson circulation enhancing AOD by 0.017 % to 4.8 %. Interestingly, a reduction in SO2 emission over China inhibits the transport of Indian sulfate aerosols to the

Arctic in summer-monsoon and post-monsoon seasons due to subsidence over northern India. The region of sulfate aerosol enhancement shows significant warming in the UTLS over northern India, south China (0.2±0.15 to 0.8±0.72 K) and the Arctic (∼1±0.62 to 1.6±1.07 K). The estimated seasonal mean direct radiative forcing at the top of the atmosphere (TOA) induced by the increase in Indian SO2 emission is −0.2 to −1.5 W m−2 over northern India. The Chinese SO2 emission reduction leads to a positive radiative forcing of ∼0.6 to 6 W m−2 over China. The decrease in vertical velocity and the associated enhanced stability of the upper troposphere in response to increased Indian SO2 emissions will likely decrease rainfall over India.

Impacts of tropical volcanic eruptions on Indian droughts.

The Indian summer monsoon rainfall (ISMR) is vital for the livelihood of millions of people in the Indian region; droughts caused by monsoon failures often resulted in famines. Large volcanic eruptions have been linked with reductions in ISMR, but the responsible mechanisms remain unclear. Here, using 145-year (1871–2016) records of volcanic eruptions and ISMR, we show that ISMR deficits prevail for two years after moderate and large (VEI > 3) tropical volcanic eruptions; this is not the case for extra-tropical eruptions. Moreover, tropical volcanic eruptions strengthen El Niño and weaken La Niña conditions, further enhancing Indian droughts. Using climate-model simulations of the 2011 Nabro volcanic eruption, we show that eruption induced an El Niño like warming in the central Pacific for two consecutive years due to Kelvin wave dissipation triggered by the eruption. This El Niño like warming in the central Pacific led to a precipitation reduction in the Indian region. In addition, solar dimming caused by the volcanic plume in 2011 reduced Indian rainfall.

The impact of reduced air pollution during COVID-19 lockdown measures on the Indian summer monsoon.

Aerosol concentrations over Asia play a key role in modulating the Indian summer monsoon (ISM) rainfall. Lockdown measures imposed to prevent the spread of the COVID-19 pandemic led to substantial reductions in observed Asian aerosol loadings. Here, we use bottom-up estimates of anthropogenic emissions based on national mobility data from Google and Apple, along with simulations from the ECHAM6-HAMMOZ state-of-the-art aerosol-chemistry-climate model to investigate the impact of the reduced aerosol and gases pollution loadings on the ISM. We show that the decrease in anthropogenic emissions led to a 4 W m^{-2} increase in surface solar radiation over parts of South Asia, which resulted in a strengthening of the ISM. Simultaneously, while natural emission parameterizations are kept the same in all our simulations, the anthropogenic emission reduction led to changes in the atmospheric circulation, causing accumulation of dust over the Tibetan plateau (TP) during the pre-monsoon and monsoon seasons. This accumulated dust has intensified the warm core over the TP that reinforced the intensification of the Hadley circulation. The associated cross-equatorial moisture influx over the Indian landmass led to an enhanced amount of rainfall by 4% (0.2 mm d^{-1}) over the Indian landmass and 5%–15% (0.8–3 mm d^{-1}) over central India. These estimates may vary under the influence of large-scale coupled atmosphere–ocean oscillations (e.g. El Nino Southern Oscillation, Indian Ocean Dipole). Our study indicates that the reduced

anthropogenic emissions caused by the unprecedented COVID-19 restrictions had a favourable effect on the hydrological cycle over South Asia, which has been facing water scarcity during the past decades. This emphasizes the need for stringent measures to limit future anthropogenic emissions in South Asia for protecting one of the world's most densely populated regions.

Impacts of COVID-19 lockdown on black carbon

A nationwide lockdown was imposed in India due to the Coronavirus Disease 2019 (COVID-19) pandemic which significantly reduced the anthropogenic emissions. We examined the characteristics of equivalent black carbon (eBC) mass concentration and its source apportionment using a multiwavelength aethalometer over an urban site (Ahmedabad) in India during the pandemic induced lockdown period of year 2020. For the first time, we estimate the changes in BC, its contribution from fossil (eBC_{ff}) and wood (eBC_{wf}) fuels during lockdown (LD) and unlock (UL) periods in 2020 with respect to 2017 to 2019 (normal period). The eBC mass concentration continuously decreased throughout lockdown periods (LD1 to LD4) due to enforced and stringent restrictions which substantially reduced the anthropogenic emissions. The eBC mass concentration increased gradually during unlock phases (UL1 to UL7) due to the phase wise relaxations after lockdown. During lockdown period eBC mass concentration decreased by 35%, whereas during the unlock period eBC decreased by 30% as compared to normal period. The eBC_{wf} concentrations were higher by 40% during lockdown period than normal period due to significant increase in the biomass burning emissions from the several community kitchens which were operational in the city during the lockdown period. The average contributions of eBC_{ff} and eBC_{wf} to total eBC mass concentrations were 70% and 30% respectively during lockdown (LD1 to LD4) period, whereas these values were 87% and 13% respectively during the normal period. The reductions in BC concentrations were commensurate with the reductions in emissions from transportation and industrial activities. The aerosol radiative forcing reduced significantly due to the reduction in anthropogenic emissions associated with COVID-19 pandemic induced lockdown leading to a cooling of the atmosphere. The findings in the present study on eBC obtained during the unprecedented COVID-19 induced lockdown can provide a comprehensive understanding of the BC sources and current emission control strategies, and thus can serve as baseline anthropogenic emissions scenario for future emission control strategies aimed to improve air quality and climate.

Impact of COVID-19 lockdown on ozone build up over Ahmedabad

COVID-19 lockdown created a rare opportunity to study the air quality responses to dramatic reduction in man-made emissions. In contrast with the precursor species, the build-up of ozone has been observed to be enhanced by ~39% over Ahmedabad. To explain this observation, we incorporated the measurements of chemical species and prescribed environmental conditions of this region into a photochemical box model (NCAR Master Mechanism). Model, in a good agreement with measurements, reproduced the observed ozone enhancement during the lockdown. Sensitivity simulations unravelled that the ozone enhancement was contributed by both the non-linear chemistry (by ~25%) as well as the changes in meteorological conditions (by ~16%). We estimated that the net ozone production rate was higher by up to 1.2 ppbv h^{-1} during the lockdown as compared to the pre-lockdown. Our analyses highlight that the

lockdown impacts can be modulated profoundly by the complex chemistry plus meteorological changes, offsetting the benefits of lower precursor levels in the context of ozone pollution. The findings could prove valuable in planning strategies to curb ozone pollution in future by considering the effects of chemistry and meteorological variations in this semi-arid urban environment.

Strengthened Indian Summer Monsoon Precipitation Susceptibility Linked to Dust-Induced Ice Cloud Modification

A growing body of research has underscored the radiative impact of mineral dust in influencing Indian summer monsoon rainfall variability. However, the various aerosol-cloud-precipitation interaction mechanisms remain poorly understood. Here we analyse multi-satellite observations to examine dust-induced modification in ice clouds and precipitation susceptibility. We show contrasting dust-induced changes in ice cloud regimes wherein despite a 25% reduction in ice particle radius in thin ice clouds, we find ~40% increase in ice particle radius and ice water path in thick ice clouds resulting in the cloud deepening and subsequently strengthened precipitation susceptibility, under strong updraft regimes. The observed dust-ice cloud-precipitation interactions are supported by a strong correlation between the interannual monsoon rainfall variability and dust frequency. This microphysical-dynamical coupling appears to provide negative feedback to aerosol-cloud interactions, which acts to buffer enhanced aerosol wet scavenging. Our results underscore the importance of incorporating meteorological regime-dependent dust-ice cloud-precipitation interactions in climate simulations.

Contribution of light-absorbing aerosols to absorption over the Indo-Gangetic Plain and Himalayas

Analyzing new and high quality in situ observations, for the first time, the individual contributions of light-absorbing aerosols (black carbon (BC), brown carbon (BrC) and dust) to aerosol absorption are quantified over the Himalayan region, a relatively poorly studied region with several sensitive ecosystems of global importance, as well as highly vulnerable populations. The annual and seasonal average single scattering albedo (SSA) over Kathmandu is the lowest of all the locations. The SSA over Kathmandu is <0.89 during all seasons, which confirms the dominance of light-absorbing carbonaceous aerosols from local and regional sources over Kathmandu. The SSA decreases with increasing elevation over the Himalayas, confirming the dominance of light absorbing carbonaceous aerosols at higher elevations. In contrast, the SSA over the Indo-Gangetic Plain (IGP) did not exhibit a pronounced spatial variation. BC dominates (≥75%) the aerosol absorption over the IGP and the Himalayas throughout the year (Figure 1). Higher BC concentration at elevated locations in the Himalayas leads to lower SSA at elevated locations in the Himalayas. The contribution of dust to aerosol absorption is higher throughout the year over the IGP than over the Himalayas. The aerosol absorption over South Asia is very high, exceeding available observations over East Asia, and previous model estimates. This quantification will be valuable as observational constraints to help improve regional simulations of climate change, impacts on the glaciers and the hydrological cycle, and will help to direct the focus towards BC as the main contributor to aerosol-induced warming in the region.

Photochemistry and dynamics over Doon Valley of the Himalayan Foothills

Elevated ozone concentrations are observed every spring over the northern Indian region, however, studies investigating the influences of photochemistry and dynamics in the valleys of the central Himalaya are limited. In this direction, we combined observations (in situ and satellite-based) with model results (CAMS: Copernicus Atmosphere Monitoring Service) to study the O_3 variations at Dehradun (77.99^{o}E, 30.27^{o}N, 600 m amsl) in the Doon valley during April–July 2018. Entrainment through boundary layer dynamics is found to significantly enhance noontime O_3 in Doon valley, besides the photochemical production. CAMS model successfully reproduced the observed day-to-day variability in ozone at Dehradun (r = 0.86), however absolute ozone levels were typically overestimated. Positive relationship between modelled O_3 and CO (r = 0.65) together with O_3/CO slope of 0.16 are attributed to influences of biomass-burning. Model based calculations, supported by observations, show that O_3 was enhanced by 10–65% due to biomass burning over this region.

Asian Aerosol Dipole - Changing Content, Composition and Atmospheric Heating

Aerosol emissions from human activities have been extensive and changing rapidly over Asia. Model simulations and satellite observations indicate a dipole pattern in aerosol emissions and loading between South Asia and East Asia, two of the most heavily polluted regions of the world. We examine the previously unexplored diverging trends in the existing dipole pattern of aerosols between East and South Asia using the high quality, two-decade long ground-based time series of observations of aerosol properties from the Aerosol Robotic Network (AERONET), from satellites (Moderate Resolution Imaging Spectroradiometer (MODIS) and Ozone Monitoring Instrument (OMI)) and from model simulations (Modern-Era Retrospective Analysis for Research and Applications, version 2 (MERRA-2). The data cover the period since 2001 for Kanpur (South Asia) and Beijing (East Asia), two locations taken as being broadly representative of the respective regions. Since 2010 a dipole in aerosol optical depth (AOD) is maintained but the trend is reversed-the decrease in AOD over Beijing (East Asia) is rapid since 2010, being 17% less in current decade compared to first decade of twenty- first century, while the AOD over South Asia increased by 12% during the same period. Furthermore, we find that the aerosol composition is also changing over time.

The single scattering albedo (SSA), a measure of aerosol's absorption capacity and related to aerosol composition, is slightly higher over Beijing than Kanpur, and has increased from 0.91 in 2002 to 0.93 in 2017 over Beijing and from 0.89 to 0.92 during the same period over Kanpur, confirming that aerosols in this region have on an average become more scattering in nature. The spatial patterns in level-2 (unaffected by the row anomaly in OMI) and level-3 (affected by the row anomaly) SSA and their differences are similar. These changes have led to a notable decrease in aerosol-induced atmospheric heating rate (HR) over both regions between the two decades, decreasing considerably more over East Asia (− 31%) than over South Asia (− 9%). The annual mean HR is lower now, it is still large (≥ 0.6 K per day), which has significant climate implications. The seasonal trends in AOD, SSA and HR are more pronounced than their respective annual trends over both regions. The seasonal trends are caused mainly by the increase/decrease in anthropogenic aerosol emissions (sulphate, black carbon and organic carbon) while the natural aerosols (dust and sea-salt) did not change significantly over South

and East Asia during the last two decades. The MERRA-2 model was able to simulate the observed trends in AODs well but not the magnitude, while it also did not simulate the SSA values or trends well. These robust findings based on observations of key aerosol parameters and previously unrecognized diverging trends over South and East Asia need to be accounted for in current state-of-the-art climate models to ensure accurate quantification of the complex and evolving impact of aerosols on the regional climate over Asia. The findings open up a new area for research such as how the diverging trends might contribute to climate change and large-scale changes in regional atmospheric stability, circulation and hydrological cycle over both regions.

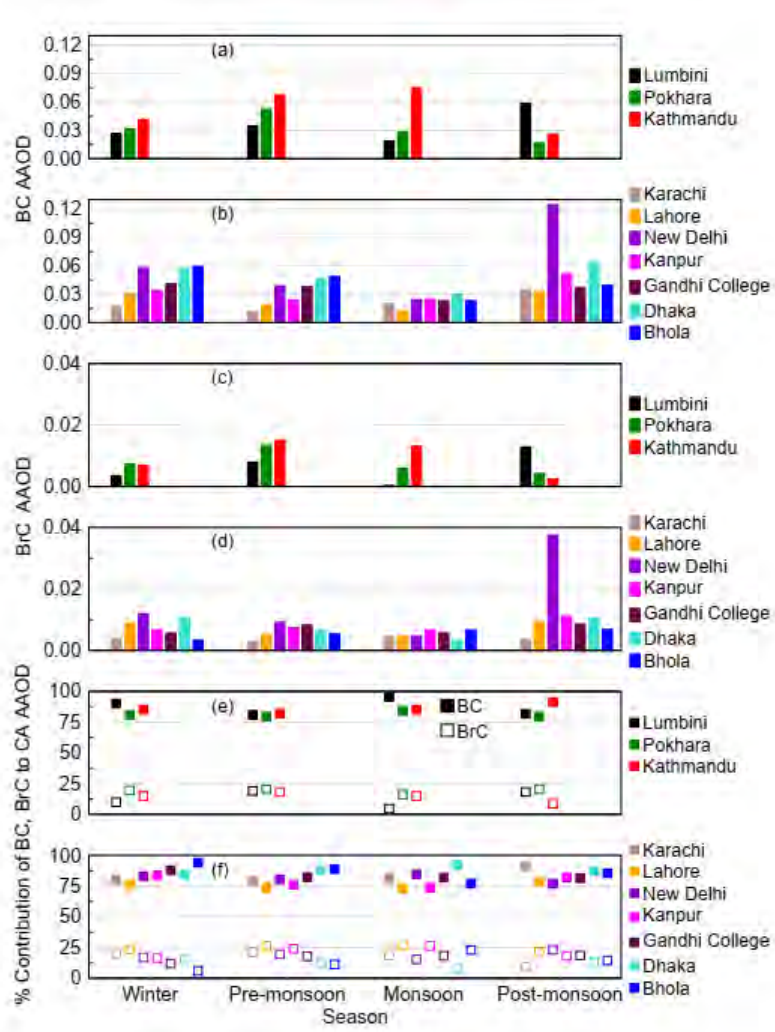

Figure 1: Black carbon (BC) and brown carbon (BrC) over the IGP and Himalayan foothills.

Widespread enhancement in fine particulate matter over the Indo-Gangetic Plain towards winter

Fine particulate matter ($PM_{2.5}$) influences the visibility, climate, and air quality. The Indo-Gangetic Plain (IGP) region, home to about one-seventh of the world's population, experiences strongly enhanced $PM_{2.5}$ pollution every post-monsoon and winter. We performed high-resolution modelling to unravel the role of dynamics and regional emissions over this region.

Model, in agreement with measurements, shows that the $PM_{2.5}$ distribution having patches of enhanced concentrations (≥100 μgm^{-3}) during post-monsoon, evolves dramatically into widespread enhancement across IGP during winter (Figure 2).

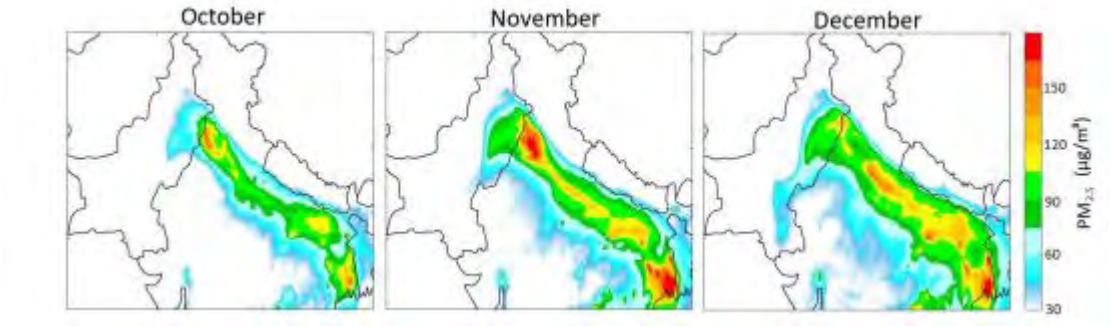

Figure 2: Mean distribution of $PM_{2.5}$ over the northern Indian region during October, November, and December 2016 as simulated by the WRF-Chem model.

Sensitivity simulation and satellite-based measurements revealed a dominant role of biomass-burning over northwest IGP during post-monsoon. Whereas, in contrast, towards winter, a large-scale decline in temperature, shallow atmospheric boundary layer, and weaker winds drastically reduced ventilation confining anthropogenic influences near the surface. The study highlights a west-east gradient in terms of sources, with western IGP dominated by biomass-burning and eastern IGP dominated by anthropogenic sources in post-monsoon. This gradient weakens in winter when entire IGP is dominated by anthropogenic sources. We argue that a generic emission reduction policy will not yield desired results, and advocate for a season-based source-focused policy taking unfavourable atmospheric dynamics into account, to minimize the air quality and climate impacts.

Aerosol size distribution in rural environment and implications for cloud droplet formation

Aerosol number size distributions in the diameter range of 5 nm-34 μm were measured in tropical southern India during the transition season from May (pre-monsoon) to June-July (monsoon). Averaged over the entire measurement period, the particle number size distributions were bimodal with a total particle number concentration of Ntot = (4.5±2.7) x 10^3 cm^{-3}. The ratio of Aitken to accumulation mode particle number concentrations (Nait/Nacc) ranged from 1.06 to 2.07, increasing from May to June-July due to a pronounced decrease in the accumulation mode particles with the onset of the monsoon. Cloud condensation nuclei concentrations at 0.4% supersaturation ($CCN_{0.4}$) were calculated under the assumption of an average continental hygroscopicity parameter of $\kappa = 0.3$. We found different regimes of CCN activation and cloud formation for the month of May (shifting from aerosol-limited regime to transitional regime) and for June-July (transitional regime), which was primarily due to the variability of particle number concentrations in the accumulation mode.

Environmental impacts of fireworks on aerosol characteristics and radiative properties

Present study investigates the variations in aerosol characteristics, concentrations, and radiative properties due to the burning of firecrackers during the Diwali festival event followed by New

year festival celebrations over a representative urban environment. A six day's long intensive in situ measurements of Black Carbon (BC), Particulate Matter (PM), and Aerosol Optical Depth (AOD) were collected to capture pre to post-Diwali and New Year festival celebrations marked with massive fireworks. We observed an increase of 286%, 89.5%, and 60.5% in BC, PM_{10}, and $PM_{2.5}$ concentrations, respectively, on the festival night as compared to pre-event days. An increase in in-situ measured AOD is comparable with concurrent satellite-derived AOD. Angstrom exponent, $\alpha > 1.0$ along with high turbidity coefficient; β estimated for the festival period clearly implies the abundance of fine-mode particles, probably the smoke aerosols loading from fireworks. The Mie-scattered return signals received by the ground-based Raman LiDAR at 532 nm showed an increased concentration of 'anthropogenic aerosols', attributed to the increased cracker's activity. Space-based CALIPSO LiDAR observations also validate the presence of 'polluted dust' and 'smoke' types of aerosols at the near-surface to 5 km altitude over the study area. A sharp increase in gaseous air pollutants like SO_2 and NOx concentrations exceeding the National Ambient Air Quality Standards is also observed. The investigations provide useful insights into the impact of burning firecrackers on urban air quality besides radiative impacts at a regional scale. Such celebration-induced air pollution events may lead to severe health impacts, particularly respiratory and cardiovascular ailments in the resident population.

Heterogeneity in single scattering albedo of aerosols: Radiative implications

The simultaneous near surface measurements of aerosol scattering and absorption coefficients over different environments (Ahmedabad, urban and Gurushikhar, a high altitude remote site) in western India were conducted to estimate SSA and investigate the importance of SSA in aerosol radiative forcing. The surface SSA is lower than the column SSA as emission sources for black carbon aerosols (absorbing in nature) are abundant near the surface (Ahmedabad, Gurushikhar). The atmospheric warming over the urban region estimated using column SSA is a factor of 3 lower (18 Wm^{-2}) than that of the warming (52 W m^{-2}) estimated utilising surface SSA. The significant difference in atmospheric warming arises due to the differences in the SSA as aerosol optical depth (a measure of column concentration of aerosols) is the same. Surface and column SSA are comparatively higher over the high altitude remote site as the abundance of absorbing aerosols is less over a non-source region. In addition, the differences between surface and column SSA are less (< 9%) resulting in comparable aerosol radiative forcing estimates. This study highlights the differences that can arise in aerosol radiative effects due to the differences in SSA as a function of altitude (surface vs. column) and environment (urban vs. remote), thereby providing regional bounds on aerosol radiative forcing which can further be used in climate assessment studies.

Climate Benefits of Cleaner Energy Transitions in East and South Asia Through Black Carbon Reduction

The state of air pollution has historically been tightly linked to how we produce and use energy. Air pollutant emissions over Asia are now changing rapidly due to cleaner energy transitions; however, magnitudes of benefits for climate and air quality remain poorly quantified. The associated risks involve adverse health impacts, reduced agricultural yields, reduced freshwater availability, contributions to climate change, and economic costs. We focus particularly on

climate benefits of energy transitions by making first-time use of two decades of high-quality observations of atmospheric loading of light-absorbing black carbon (BC) over Kanpur (South Asia) and Beijing (East Asia) and relating these observations to changing energy, emissions, and economic trends in India and China. Our analysis reveals that absorption aerosol optical depth (AAOD) due to BC has decreased substantially, by 40% over Kanpur and 60% over Beijing between 2001 and 2017, and thus became decoupled from regional economic growth. Furthermore, the resultant decrease in BC emissions and BC AAOD over Asia is regionally coherent and occurs primarily due to transitions into cleaner energies (both renewables and fossil fuels) and not due to the decrease in primary energy supply or decrease in use of fossil use and biofuels and waste. Model simulations show that BC aerosols alone contribute about half of the surface temperature change (warming) of the total forcing due to greenhouse gases, natural and internal variability, and aerosols, thus clearly revealing the climate benefits due to a reduction in BC emissions, which would significantly reduce global warming. However, this modeling study excludes responses from natural variability, circulation, and sea ice responses, which cause relatively strong temperature fluctuations that may mask signals from BC aerosols. Our findings show additional benefits for climate (beyond benefits of CO_2 reduction) and for several other issues of sustainability over South and East Asia, provide motivation for ongoing cleaner energy production, and consumption transitions, especially when they are associated with reduced emissions of air pollutants. Such an analysis connecting the trends in energy transitions and aerosol absorption loading, unavailable so far, is crucial for simulating the aerosol climate impacts over Asia which is quite uncertain.

Aerosol Oxidative Potential

One of the major societal concerns is degrading air quality which also affects human health and economy. Particulate matter smaller than 2.5 μm aerodynamic diameter (PM2.5) is often considered as sole measure of aerosol toxicity, and mitigation strategies focus to curb PM2.5 concentrations. Researchers are trying to establish link between aerosols and human health through cohort studies; however, such studies lack understanding underlying mechanisms. We initiated and established the study on 'Aerosol Oxidative Potential' in India, which is a newer and important aspect in aerosol research. Reactive oxygen species (ROS) generation or anti-oxidants depletion capacity of ambient aerosols is known as their oxidative potential (OP). Aerosol induced oxidative stress in human is the widely accepted mechanism explaining how aerosols with higher OP affect human health. Our research over urban, semi-urban, mountain, and marine regions in India revealed that: (1) OP of biomass burning (BB) derived species is much higher than those derived from fossil fuel burning (FFB), (2) OP of anthropogenic aerosols is higher than that of natural aerosols, (3) atmospheric ageing and fog processing increase aerosol OP, (4) aerosol OP is governed by chemical composition rather than total mass concentration, and (5) mitigation strategies for reducing aerosol concentrations alone may not be sufficient, and linking aerosol OP with health effects may be a better way to identify and regulate specific sources of toxic aerosol species (Patel and Rastogi, 2020; 2021; Patel et al., 2021, 2022). Such studies are inevitable in designing appropriate air pollution mitigation policies.

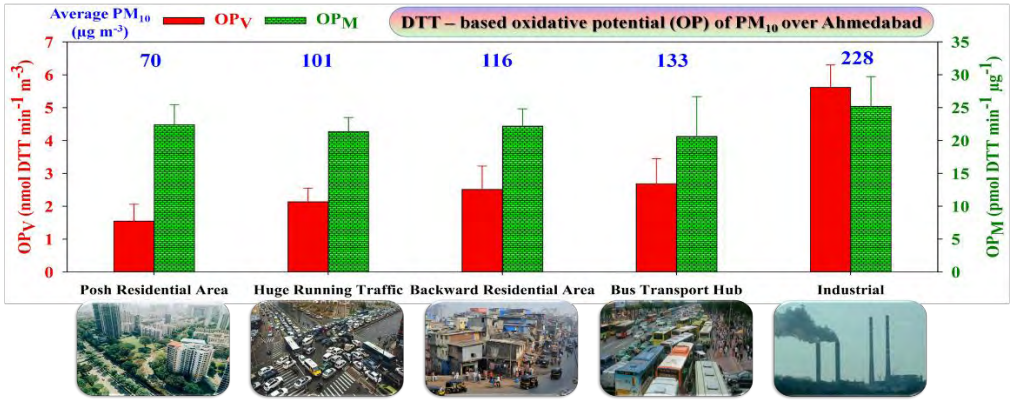

Fig. 1: PM10 mass concentration, volume-normalised oxidative potential (OPv), and mass-normalised oxidative potential (OPM) over different microenvironments of Ahmedabad (Patel et al., 2021b)

Organic Aerosols including Brown Carbon

Organic aerosols are the least understood component of ambient particles because of their numerous sources, complex composition, tedious formation mechanism, and complicated atmospheric evolution. Recent global models estimate that light absorption by brown carbon (BrC, also known as light-absorbing organic aerosols) in different regions of the world may be 27–70% of that due to black carbon (BC) absorption. In order to assess climatic effects of BrC, it is inevitable to understand their composition and characteristics, which is virtually lacking over India and limited over world. Our unique BrC measurements contributed significantly to this research gap over India. Our research work has provided an important contribution to the understanding of water-soluble brown carbon (BrC) aerosols through the first online measurements of water-soluble organic carbon (WSOC) and their absorption over urban sites in northern India using a unique assembled non-commercial analytical system. Our research has demonstrated that: (1) BrC is composed of variety of chromophores including at least humic-like substances and nitro-phenols, (2) Biomass burning (BB) derived primary BrC is most absorbing followed by that derived from fossil-fuel burning (FFB); whereas, secondary aged BrC is least absorbing (3) absorbing property of BrC diminishes with atmospheric ageing/oxidation and photo-bleaching, (4) organic aerosols (OA) are highly variable and composed of hydrocarbon-like OA, semi-volatile oxidized OA, and oxidized OA (OOA); and plausible major functional groups of OOA are the mixture of alcohols and carboxylic groups (Singh et al. 2019, 2021; Satish et al., 2020; Dave et al., 2021; Rastogi et al., 2021). We have also proposed a novel approach for understanding the composition and characteristics of BrC using only their absorption spectra, which otherwise needs a copious amount of work and expensive analytical facilities. Our work also showed a hitherto unknown feature that a majority of BrC species from BB are water-insoluble, and the ratio of absorption by water-soluble BrC to that by total BrC decreases with increasing wavelength from UV to visible range (Satish and Rastogi, 2019). We also showed that the atmospheric radiative forcing due to BrC over northwest India accounts for ~40 to 60% of that from EC, and water-insoluble BrC plays major role (Satish et al., 2020).

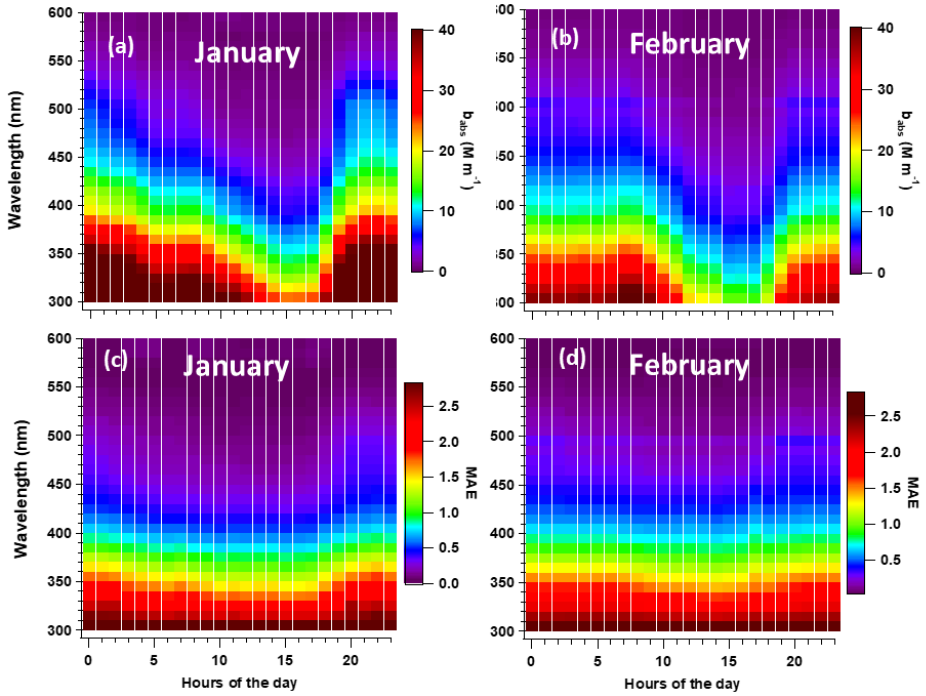

Fig. 2: Diurnal variability in (a) BrC spectra during January and (b) BrC spectra during February, and in (c) MAE during January and (d) MAE during February (Rastogi et al., 2021)

Aerosol Characterization using Isotopes:

Isotopes offer deeper insights in investigating the sources and processes affecting aerosols abundances and characteristics. Our multi-tracer/multi-isotope ($\delta^{13}C$, $\delta^{15}N$, and $\delta^{34}S$) investigation of ambient PM_{10} over the Port Blair island provides newer insights into complex aerosol chemistry occurring within marine atmospheric boundary layer over the Bay of Bengal, which can be utilized for atmospheric chemical transport models to assess dispersal of continental pollution in economically and ecologically sensitive marine zones. We have shown that a mixture of BB and FFB sources contribute to aerosol species over the BoB, and the variability in $\delta^{13}C$ confirmed the presence of aged organic aerosols (Rastogi et al., 2020). Using dual carbon isotopes (^{13}C and ^{14}C), we reported that the $\delta^{13}C$ of paddy-residue burning (PRB) in the Indo-Gangetic Plain is -28.9±1.1‰. Further, about 82% carbonaceous aerosols were PRB derived during October-November. We also showed that the aerosol mass spectrometer derived f60 (fraction of signal at m/z 60 to total signals for organics) can be used as a proxy of ^{14}C in PRB derived aerosols. We also reported the characteristics ratios of important species from PRB using radiocarbon, which can be used in modelling studies (Devaprasad et al., 2023).

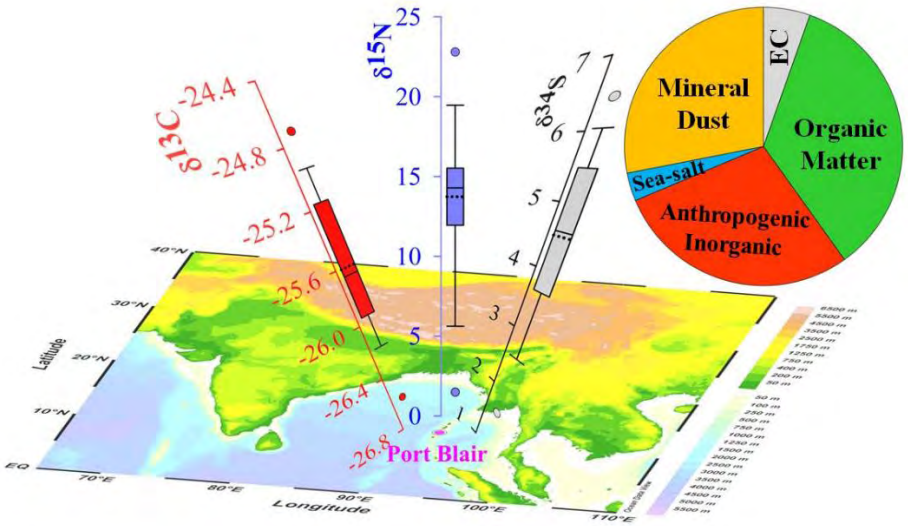

Fig. 3: Chemical composition and variability in the isotopic composition of carbon, nitrogen, and sulphur over the Bay of Bengal (Rastogi et al., 2020)

Emissions and atmospheric concentrations of α-pinene at an urban site of India: Role of changes in meteorology

The measurements of a monoterpenes (mainly α-pinene) were performed by the PTR-TOF-MS instrument at an urban site of India from mid-January to March 2014. The daytime concentration increased from 0.15 ppb in the second-half of January to 0.40 ppb in the second-half of March. Both the nighttime and daytime ratios of α-pinene/benzene in the second-half of March were 2-3 times higher their respective values from mid-January to first-half of February. The ratios of α-pinene/benzene increased from ~0.27 ppb ppb^{-1} at lower temperatures to ~0.51 ppb ppb^{-1} at higher temperatures indicating the increase of biogenic emissions in March. The concentration of α-pinene exhibited exponential decline with wind speed, but the rate of decrease in February was about twice that for March. The nighttime ratios of α-pinene/isoprene were greater than those measured in the daytime, suggesting temperature-dependent biogenic emissions of α-pinene. From mid-January to March, the increase of ~53% in the biogenic contributions of α-pinene were associated with the change in meteorological conditions. Our analysis suggests that the combined effect of the northwest wind flow and higher air temperatures in March favored the emissions of BVOCs from local vegetation. The exceptionally high concentrations of α-pinene up to 6 ppb were measured during the Holi bonfire festival. This is the first study reporting the change in α-pinene during winter-summer transition over India. In the urban regions of developing countries, high emissions of BVOCs from vegetation and of NOx from anthropogenic sources can act as a source of ozone.

Linkages of an aerosol layer over South Asia during El Niño and Indian droughts

Droughts have become more severe and recurrent over the Indian sub-continent during the second half of the twentieth century, leading to more severe hydro-climatic and socio-economic impacts over one of the most densely populated parts of the world. So far, droughts have mostly been connected to circulation changes concomitant with the abnormal warming over the Pacific Ocean, prevalently known as “El Niño”. In this study, exploiting observational data sets and a

series of dedicated sensitivity experiments, we show that the severity of droughts during El Niño is amplified (17%) by changes in aerosols. The model experiments simulate the transport of boundary layer aerosols from South Asian countries to higher altitudes (12–18 km) where they form the Asian Tropopause Aerosol Layer (ATAL) (~ 60–120°E, 20–40°N). During El Niño, the anomalous overturning circulation from the East Asian region further enriches the thickness of aerosol layers in the ATAL over the northern part of South Asia. The anomalous aerosol loading in the ATAL reduces insolation over the monsoon region, thereby exacerbating the severity of drought by further weakening the monsoon circulation. Future increases in industrial emissions from both East and South Asia will lead to a wider and thicker elevated aerosol layer in the upper troposphere, potentially amplifying the severity of droughts.

Lower and Middle Atmospheric Dynamics

Planetary wave dynamics

Planetary wave (PW) associated dynamical variability in the equatorial and extratropical middle atmosphere during the September 2019 Southern hemisphere minor sudden stratospheric warming (SSW) is investigated utilizing meteor radar wind observations from São João do Cariri (7.4°S, 36.5°W) and Cachoeira Paulista (22.7°S, 45°W) and reanalysis data. Signature of the mesospheric warming in conjunction with the stratospheric cooling is found at low latitudes. The strong westerly wind at low latitudes decelerates notably near 65 km at the onset of the warming episode, although no wind reversal is observed. The wind spectra reveal a prevalent quasi-16-day wave (Q16DW) prior to the SSW and existence of a quasi-6-day wave (Q6DW) after the warming event. Possible existence of barotropic/baroclinic instability in the low and mid latitude middle atmosphere may be responsible for exciting the Q6DW. Both traveling and stationary waves exhibit notable activities during the warming event. Although involvement of both zonal wavenumbers 1 and 2 PWs are found in the event, PW with zonal wavenumber 1 seems to play a vital role in preconditioning the same. Furthermore, significant latitudinal mixing of airmass between the tropics and high latitudes is evident in the potential vorticity map. The Eliassen-Palm flux diagnosis shows the propagation of the Q6DW and Q16DW from mid to low latitudes during the warming event (Figure 4).

Signature of a mesospheric bore

A prominent signature of dark bore front in the mesospheric O(1S) airglow emission is observed on a night in the late winter at Hanle (32.7ºN, 78.9ºE) located in the western Himalaya. The leading front was followed by a series of evident trailing waves and the event lasts for more than two hours. The characteristic features of the bore indicate it to be linear undular type. Instantaneous temperature profile shows presence of stable region through formation of thermal duct in the upper mesosphere possibly supported by chemistry and/or dynamics. With time, the bore fronts became faint in presence of ripples as they reached other side of imager field of view (FOV). During the initial period around 3–4 waves h^{-1} appear to enter the imager FOV. The observed average phase speed, period and horizontal wavelength are found to be 40 m/s, 12 min and 29 km, respectively. The bore fronts exhibit a clockwise rotation at a rate of around 5^{o} h^{-1}. The front edge perpendicular to the direction of propagation shows small-amplitude undulation indicating nonuniform duct structure. The tropospheric

meteorological conditions may indicate plausible contribution from jet stream, weather front (linked with the Himalayan orography), and nonmigrating tides to excite and sustain the mesospheric bore event although further investigations in this direction are being sought to understand the actual underlying physical processes.

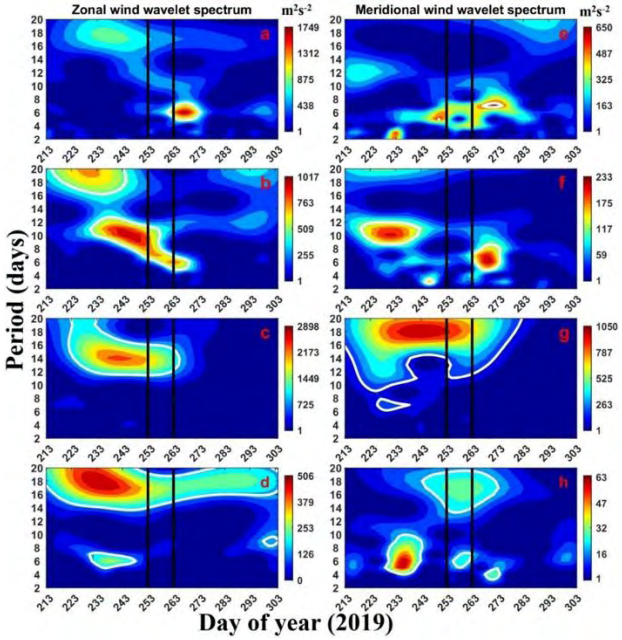

Figure 4: Wavelet power spectra at 90 km for (a) zonal wind, (e) meridional wind using meteor radar. Wavelet spectra in the zonal wind at (b) 0.02 hPa, (c) 1 hPa, (d) 10 hPa and meridional wind at (f) 0.02 hPa, (g) 1 hPa, (h) 10 hPa at Cachoeira Paulista using ERA5. Bold white curves in each plot represent 95% confidence level.

Quarterdiurnal tidal activity

The characteristic features of the quarterdiurnal tide (QDT) in the mesosphere and lower thermosphere (MLT) are investigated using meteor radar observations from three low-latitude southern hemispheric stations, Sao Joao do Cariri (7.4°S, 36.5°W), Cachoeira Paulista (22.7°S, 45°W) and Santa Maria (29.7°S, 53.7°W) in 2005. The QDT shows consistent appearance with a weak enhancement during late summer and fall interval. The QDT amplitudes are found to be much smaller (< 3 m/s) than the longer period tidal components most of the times of the year consistent with the previous investigations carried out from various locations over the globe. The vertical wavelength is found to reach up to 80 km in the MLT maximizing in winter although most of the times it remains within 20 km. Therefore, based on the observed characteristics of the QDT, it is surmised that both the migrating and nonmigrating components are involved in manifestation of the QDT at present locations.

A Rossby wave breaking-induced enhancement in the tropospheric ozone over the Central Himalayan region

The high-altitude regions in the Himalayas are prone to high ozone concentrations frequently resulting from diverse dynamical and transport mechanisms. Here, we report an unusual enhancement in the surface and tropospheric ozone concentrations over the central Himalayan

region from ground-based and space-borne measurements in the month of December 2010. The surface ozone levels (~80 ppbv) on 18–19 December 2010 is observed to be two-fold higher relative to the seasonal average (December-January-February) of about 40–50 ppbv in the central Himalayan region. The space-borne measurements from Tropospheric Emission Spectrometer and Ozone Monitoring Instrument onboard Aqua satellite also show higher values in the tropospheric column ozone over this region. The satellite observations indicate an increase in tropopause temperature of about 5 °C and decrease in tropopause altitude about 1 km during 18–19 December 2010 resulting in the occurrence of tropopause fold facilitating the stratospheric-tropospheric exchange processes over the study region. The plausible reason for the occurrence of tropopause fold and subsequent enhancement of tropospheric and surface ozone is found to be associated with the breaking Rossby waves in the upper troposphere. The wave breaking leads to the advection of high-PV (potential vorticity) air, with magnitudes of about 3–4 PVU, towards the central Himalayan region from high-latitudes. The vertical component of PV advection also shows a deep stratospheric intrusion of high-PV air into the troposphere. The isentropic transport of ozone across the folding tropopause due to the wave breaking is clearly depicted from the satellite and reanalysis datasets. Therefore, the present study has strong implications of upper tropospheric wave dynamics to the tropospheric and surface ozone over the Himalayan regions having complex topography.

Can Quasi-Periodic Gravity Waves Influence the Shape of Ice Crystals in Cirrus Clouds?

The study of gravity waves and their impact on the microphysical changes in cirrus clouds over the subtropical Indian region using Raman lidar, satellite, model simulations, and reanalysis data sets has been done. It is found that the cirrus clouds are formed from the convective outflow of large-scale convergence zone extending from south-west to north-east Indian region. These clouds are modulated by the upward propagating gravity waves with time periods ~40 min (at ~8.0-8.5 km) and ~20 min (at ~9.0-9.5 km) over the Raman lidar observational site as shown in Figure 5. The wave-induced enhancement of moisture leads to supersaturation, thereby controlling the ice crystals' size and shape through depositional freezing. The ice crystals size increases and they transform to irregular shapes in the presence of wave activity. Therefore, the present work is unique and will have implications toward the uncertainties associated with cirrus clouds in both regional and global climate models.

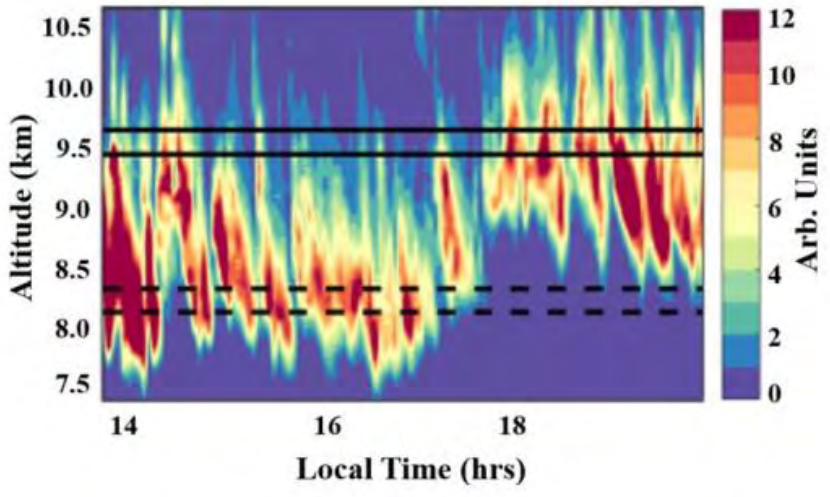

Figure 5: Modulation of Cirrus cloud patch by quasi-periodic gravity waves observed in range-corrected signals obtained at 532-nm using Raman Lidar. Horizontal lines represent regions of noticeable wave activity.

Analysis of the middle atmospheric ozone using SABER observations: a study over mid-latitudes in the northern and southern hemispheres

The present study focuses on the middle atmospheric ozone variability using 14 (2002–2015) years of Sounding of the Atmosphere using Broadband Emission Radiometry onboard Thermosphere Ionosphere Mesosphere Energetics and Dynamics satellite observations over the mid-latitude regions of northern and southern hemispheres. It is noted that ozone buildup starts late winter, and peaks during the springtime and gradually decreases in summer to autumn transitional period in both the hemispheres. The time series of ozone indicates the dominant annual and semi-annual oscillations in the middle atmosphere. The annual oscillation (AO) is found to be dominant over both the hemispheres, while the semi-annual oscillation (SAO) peaks at two different altitude regions: 30–60 km and 80–100 km. Further, the amplitude of AO is much significant than SSAO and MSAO. It is also noted another significant oscillation that peaks at ~4 months in the altitude range 60–80 km. The strength of these oscillations at different sites is studied by comparing it with the zonal mean spectrum to assess the longitudinal asymmetry. It is found that the longitudinal asymmetry is more significant in the northern hemisphere than the southern hemisphere. This can be attributed to the differences in the land (elevated topographies in the northern hemisphere) and primarily ocean (in southern hemisphere) contrast that further contributes to the differences in the strength of the vertically propagating planetary-scale waves modulating the middle atmospheric ozone.

Impact of dust storm on the atmospheric boundary layer: a case study from western India

The present study focuses on investigating the impacts of a sudden dust storm on the atmospheric boundary layer (ABL) over Ahmedabad (23.02°N, 72.57°E), an urban site located in the western region of India. The accumulation of dust particles in the atmosphere during the dust storm, originating from the Thar Desert in Rajasthan, led to the decrease in surface temperature as a consequence of dust–radiation interaction. Ambient particulate matter data obtained from Air Quality (AQ) station at Ahmedabad showed a spike of 118.5% and 44.5% in PM_{10} and $PM_{2.5}$ concentrations, respectively, during the event in comparison with the previous control day. Sudden exposure to an anomalous increase in the particulate matter may cause severe impacts on human health. These surface forcings have been reflected in the stable nocturnal ABL. Backscatter signals recorded by ground-based Ceilometer Lidar at Physical Research Laboratory (PRL) showed that ABL was shallow and collapsed during the dust storm episode (Figure 6). Turbulence has been detected in the ABL during the event which further assisted in the vertical mixing of dust particles in the ABL. These dust particles got trapped within the residual layer, preventing further percolation in the free atmosphere. Such sub-grid scale changes in the ABL during the dust storm were not reflected in the boundary layer height (BLH) obtained from the ERA-5 reanalysis dataset. A significant association between the ABL and the local radiative budget has been found. Coupled Ocean–Atmosphere Radiative Transfer Model (COART) simulations substantiated or showed a cooling event of the surface during the

dust storm. This study is important as it can be taken as feedback to improve local climate models with respect to dust storm meteorology.

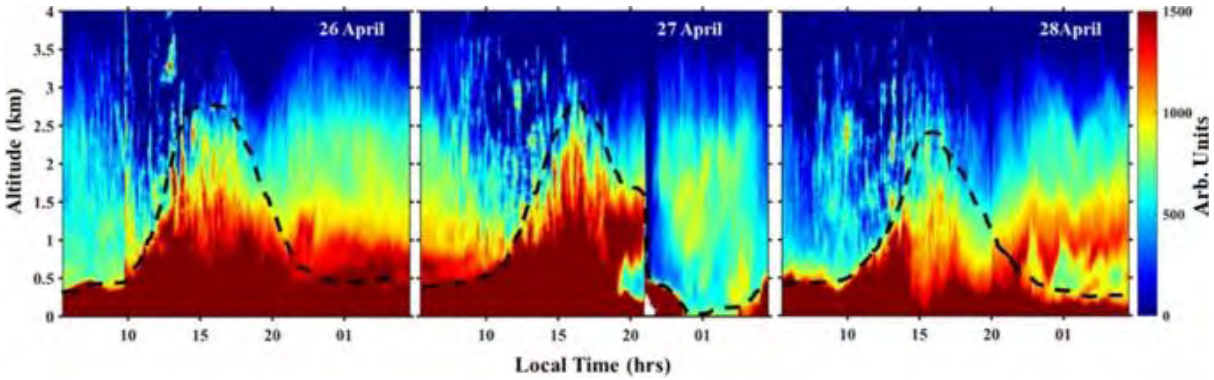

Figure 6: Range–time intensity plot of the backscatter received by Ceilometer over Ahmedabad

Paleo-climatic studies over India:

In a major implication to our understanding of paleo-salinity and paleo-monsoon based on foraminifera isotopic composition, our study suggested that the relationship of oxygen isotopic composition (δ18O) and salinity is variable in ocean (Kumar et al., 2018, 2023; Mehta et al., 2021; Rahman et al., 2021a). Concurrent with current observations, our records showed stronger El Niño events during 1715–1760 causing significant reduction and enhancement in rainfall amount over central India and northeast India, respectively (Kumar and Singh, 2021). The variations in organic carbon isotopic compositions, total organic carbon contents, along with major and trace element abundances suggested a strong effect of 8.2 dry event and a shift in chemical weathering at around 4.2 ka in the eastern coast of India (Ahmad Shah et al., 2022). We also found evidence of the effect of fossil fuel induced CO2 on the biota of Himalayan lake (Rahman et al., 2021b). A decrease in Arabian Sea surface salinity has been caused by transport of low salinity waters from the Bay of Bengal (Varna et al., 2021).

Biogenic non-methane hydrocarbons in the marine boundary layer of the Arabian Sea

Ocean surface acts as a source or sink for several trace gases including N_2O, CH_4, CO, and volatile organic compounds (VOCs). Among these gases, VOCs have profound effects in the marine atmosphere as their air-sea exchange can significantly influence the composition and chemistry of the marine atmosphere. The Arabian Sea is one of the most biologically productive ocean regimes, and hence possesses a perennially intense oxygen minimum zone. High productive oceans can potentially modify the production and sea-to-air exchange of trace gases including VOCs (Figure 3). We measured non-methane hydrocarbons (NMHCs) in the marine air and characterized the phytoplankton species in seawater of the Arabian Sea during the pre-monsoon season of the year 2017. The light alkenes namely ethene and propene were the dominant VOCs in the marine air with average mixing ratios of 8.92±3.5 and 3.38±1.3 ppbv, respectively. The high levels of alkenes were associated with the higher abundances of Trichodesmium and Thalassiosira species. We have calculated the emission fluxes of ethene using “top-down” and “bottom up” approaches and found the large discrepancies using these two methods. In the bottom-up approach, among the several sources of uncertainty, the major

cause of lower fluxes (one order of magnitude) than those estimated using the top-down approach could be the emissions of alkenes from the sea surface microlayer. The estimated emission flux of ethene using "bottom-up" approach was higher than those reported for several other oceanic regions. Such high emission rates of NMHCs in remote regions can significantly affect the regional tropospheric oxidation chemistry. Several studies reported that the emission of NOx from shipping over the northern Indian Ocean has increased significantly during last two decades. In the presence of NOx, VOCs act as an important source of atmospheric pollutant such as ozone, secondary organic aerosol and peroxy-acetyl nitrate. Our observations highlight the need to evaluate the biogeochemical processes controlling the oceanic emissions of NMHCs over the northern Indian Ocean.

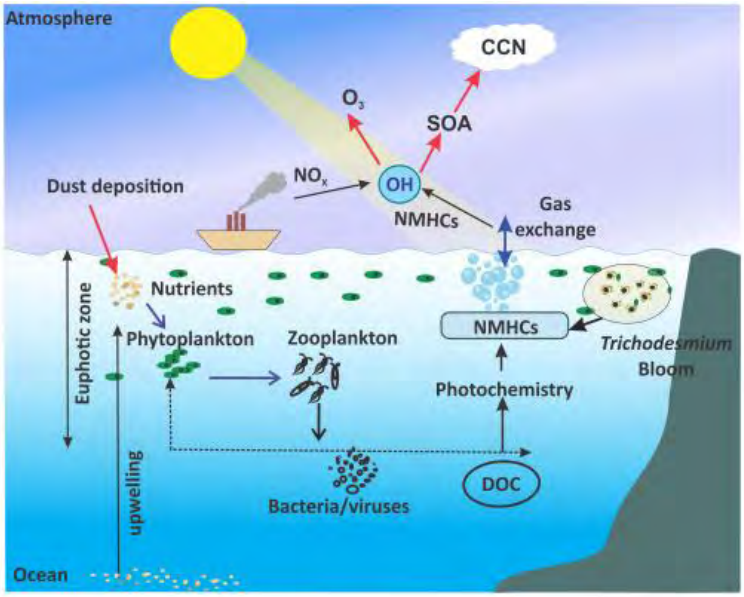

Figure 3: Emission from phytoplankton and dissolved organic carbon (DOC) present in seawater is an important natural source of many non-methane hydrocarbons (NMHCs) in the marine boundary layer (MBL).

SO_2 and NO_2 in tropical rural environment

Sulphur dioxide is a toxic pollutant in the atmosphere emitted from natural sources and human activities. We analysed the surface mixing-ratio of SO_2 and NO_2 measured over the time period from January 2010 to April 2012 at Gadanki, in Andhra Pradesh and found that SO_2 and NO_2 mixing-ratio are very low over this region. However, during January to May relatively higher concentrations of SO_2 are observed, mainly coming from power plants located in southern and eastern India as indicated by higher SO_2/NO_2 ratios of greater than 0.5. In one instance, on June 20th, 2011, it is found that the OMI SO_2 value was a factor of 13 higher than 2011 annual mean. Using the FLEXible PARTicle dispersion model (FLEXPART) and satellite data, it is found that the observed higher SO_2 value on 20th June was due to intercontinental transport of SO_2 from Nabro volcanic eruption. Using the FLEXPART model with ECLIPSE-v5 emission inventory, the observed seasonal variation of SO_2 could be well reproduced; however, the mixing ratios are found to be overestimated, possibly due to incorrect vertical profile used in the model.

Model simulation of VOC distribution over India

We investigate the distribution of volatile organic compounds (VOCs) over Indian subcontinent during a winter month of January 2011 combining the regional model WRF-Chem (Weather Research and Forecasting model coupled with Chemistry) with ground- and space-based observations and chemical reanalysis. WRF-Chem simulated VOCs are found to be comparable with ground-based observations over contrasting environments of the Indian subcontinent. WRF-Chem results reveal the elevated levels of VOCs (e. g. propane) over the Indo-Gangetic Plain (16 ppbv), followed by the Northeast region (9.1 ppbv) in comparison with other parts of the Indian subcontinent. Higher relative abundances of propane and ethane are simulated across the Indian subcontinent. WRF-Chem simulated formaldehyde and glyoxal show the western coast, Eastern India and the Indo-Gangetic Plain as the regional hotspots, in a qualitative agreement with the MACC (Monitoring Atmospheric Composition and Climate) reanalysis and satellite-based observations. Lower values of RGF (ratio of glyoxal to formaldehyde <0.04) suggest dominant influences of the anthropogenic emissions on the distribution of VOCs over Indian subcontinent, except the northeastern region where higher RGF (~0.06) indicates the role of biogenic emissions, in addition to anthropogenic emissions. Analysis of HCHO/NO2 ratio shows a NOx-limited ozone production over India, with a NOx-to-VOC transition regime over central India and IGP. The study highlights a need to initiate in situ observations of VOCs over regional hotspots (Northeast, Central India, and the western coast) based on WRF-Chem results, where different satellite-based observations differ significantly.

Characteristics of VOC Composition at Urban and Suburban Sites of New Delhi, India in Winter

Simultaneous measurements of volatile organic compounds (VOCs) using two PTR-TOF-MS instruments were conducted at urban and suburban sites of New Delhi during the winter of 2018. The time series of VOC mixing ratios show substantial variations mainly influenced by local emissions and meteorological conditions. Mixing ratios of methanol (∼28 ppbv), acetaldehyde (7.7 ppbv), acetone (10.6 ppbv), isoprene (2.8 ppbv) and monoterpenes (0.84 ppbv) at the suburban site were higher than those at the urban site, while levels of aromatic VOCs were almost similar. The strong nighttime correlations of isoprene and monoterpenes with CO and benzene at the urban site indicate their predominant anthropogenic origin. Higher emission ratios of ΔVOCs/ΔCO and ΔVOCs/Δbenzene than those reported for vehicular exhaust suggest the contributions of other sources. In addition to vehicular emissions, episodes of biomass burning, industrial plumes and aged air strongly influenced the levels of VOCs at the suburban site. Despite the predominant primary anthropogenic emissions, the higher daytime enhancements of OVOCs/CO ratios indicate additional contributions of OVOCs from secondary/biogenic sources. The secondary formation of OVOCs in moderately aged air masses was noticeable at the suburban site. Using the source-tracer-ratio method, the estimated biogenic contributions of isoprene (71%) and acetone (65%) during daytime at the suburban site were significantly higher than those for the urban site. The photochemical box model simulations suggest that daytime ozone formation was under the VOC-limited regime. The present study highlights the impact of different emission sources, photochemical processes and meteorological conditions on the composition and concentration of VOCs in the Delhi region.

Trends in sulfur dioxide over the Indian subcontinent during 2003–2019

Sulfur dioxide (SO_2) and its oxidation products profoundly impact the air quality and climate. In recent decades, contrasting SO_2 trends have been observed over different regions of the globe due to urbanization, energy generation and control measures. In this study, we have investigated the SO_2 trends over the rapidly developing Indian subcontinent using model reanalysis, satellite data, and emission inventories during 2003–2019 period. Copernicus Atmosphere Monitoring Service (CAMS) reanalysis shows rapid SO_2 growth up to 0.4 ppbv yr−1 during 2003–2009, particularly significant over the Indo-Gangetic Plain (IGP) and eastern India. However, the growth becomes slower after 2010 and is followed by a stabilization or slight reduction. The CAMS results agree with the satellite-based observations, however, the model underestimates enhancements over eastern India. The analysis of inventory datasets also suggests slower growths in SO_2 emissions and coal-fired electricity generation in recent years. Besides the changes in regional emissions, the enhancements in water vapor and OH radical coinciding with SO_2 stabilization indicate strengthening of the sink processes. Model simulation (Modern-Era Retrospective analysis for Research and Applications version 2—MERRA-2) with constant emissions shows reduction in SO_2 which confirms the stronger chemical losses. Overall, the SO_2 trends over the Indian subcontinent are found to be a manifestation of the combined effects of the regional emission change and chemistry. Our findings highlight the need for studies to assess the impacts of changing SO_2 trends in India on the regional and global climate.

Impact of COVID-19 Lockdown on Aromatic Volatile Organic Compounds

The real-time Benzene, Toluene, Ethylbenzene, and Xylenes (BTEX) concentrations were measured in a metropolitan city of India during January to May of 2020 and 2014-2015-2018 to assess the impact of emission reduction during the COVID-19 lockdown. The total BTEX (∑BTEX) concentrations were 11.5 ± 9.0, 15.7 ± 16, 5.3 ± 5.0, 2.9 ± 2.0, and 0.93 ± 1.2 ppbv in January–May 2020, respectively. The evening rush hour peaks of BTEX during lockdown decreased by 4–5 times from the same period of years 2014-2015-2018. A significant decline in background concentrations suggests a regional-scale reduction in anthropogenic emissions. The contributions of ∑TEX compounds to ∑BTEX increased from 42% to 59% in winter to 64%–75% during the lockdown under hot summer conditions. While emission reductions dominated during the lockdown period, the meteorological and photochemical factors may also have contributed. Meteorological influence on actual observed BTEX data was removed by normalizing with ventilation coefficient (VC). The actual ambient air reductions of 85%–90% and VC-normalized reductions of 54%–88% of the BTEX concentrations during lockdown were estimated compared to those during the same period of 2014-2015-2018. The estimated changes using nighttime data, which take into account BTEX photo oxidation removal, are ∼8% lower than the VC-normalized estimates using all data. These significant reductions in BTEX concentrations are consistent with the change in people's movement as inferred from mobility data during the lockdown. Although enforced, the significant decline in ambient BTEX levels during lockdown was a good change for the air quality. The study suggests a need for more effective science-based policies that consider local and regional factors.

Biogeochemical Processes over Northern Indian Ocean:

We provided the quantitative estimates of the elemental fluxes in biogeochemical processes that unravelled mysteries of these processes in the northern Indian Ocean. We conclude that eddies play an important role on C:N:P stoichiometry (Sahoo et al., 2021, 2020). We estimated that the diazotrophs supply surplus bioavailable nitrogen for photosynthetic organisms in the Arabian Sea (Singh et al., 2019). In addition, we found a significant contribution of dark C fixation to sinking C fluxes in the oxygen minimum zones of the Arabian Sea. Extrapolation of the measured dark C fixation rates to the global ocean ranged up to 7.4 Pg C y−1; amounting to ∼15% of the global ocean primary production (Saxena et al., 2022). Our N2O flux calculations revealed that out of eight, four stations acted as a minor source, whereas three were minor sink for it in the Bay of Bengal (Khan et al., 2022). Our studies have spurred biogeochemists under the ongoing IIOE-2 program to focus on such aspects in the Bay of Bengal (Saxena et al., 2020).

List of Publications

2019

1. S. Ramachandran, T. A. Rajesh and Sumita Kedia, 2019, "Influence of relative humidity, mixed-layer height, and mesoscale vertical-velocity variations on column and surface aerosol characteristics over an urban region", Boundary Layer Meteorology, 170, p. 161-181.

2. B. Sarangi, S. Ramachandran, T. A. Rajesh and V. K. Dhaker, 2019, "Black carbon linked aerosol hygroscopic growth: Size and mixing state are crucial", Atmospheric Environment, 200, p. 110-118.

3. Guharay, A., Batista, P. P., Andrioli, V. F., (2019), “Investigation of solar cycle dependence of the tides in the low latitude MLT using meteor radar observations”, J. Atmos. Sol.-Terr. Phys., 193(105083),https:// doi.org/10.1016/j.jastp.2019.105083.

4. Guharay, A., Batista, P. P., (2019), “On the variability of tides during a major stratospheric sudden warming in September 2002 at Southern hemispheric extra-tropical latitude”, Adv. Space Res., 63 (8), https://doi.org/10.1016/j.asr.2018.12.037.

5. T. A. Rajesh and S. Ramachandran, 2019, “Spatial, seasonal, and altitudinal heterogeneity in single scattering albedo of aerosols over an urban and a remote site: Radiative implications”,Atmospheric Environment., https://doi.org/10.1016/j.atmosenv.2019.116954.

6. T. A. Rajesh and S. Ramachandran, 2019, “Aerosol optical properties over Gurushikhar, Mt. Abu: A high altitude mountain site in India”, Aerosol and Air Quality Res., 19, 1259-1271., doi: 10.4209/aaqr.2018.05.0177.

7. Ojha, N., Girach, I., Sharma, K., Nair, P., Singh, J., Sharma, N., Singh, N., Flemming, J., Inness, A., Subrahmanyam, K. V., Surface ozone in Doon valley of the Himalayan foothills during Spring, Environ. Sci. Poll. Res., 26, 19155–19170 (2019), https://doi.org/10.1007/s11356-019-05085-2.

8. Chutia, L., Ojha, N., Girach, I. A., Sahu, L. K., Alvarado, L. M. A., Burrows, J. P., Pathak, B., Bhuyan, P. K., Distribution of volatile organic compounds over Indian subcontinent during winter: WRF-chem simulation versus observations, Environ. Poll., volume 252, pp. 256-269, 2019, doi: 10.1016/j.envpol.2019.05.097.

9. Sahu, L. K., Tripathi, N., Sheel, V., Ojha, N., The influence of local meteorology and convection on carbon monoxide distribution over Chennai., J. Earth Syst. Sci., doi: 10.1007/s12040-019-1156-z, 2019.

10. Kimothi, S., Pasbola, A. K., Thapliyal, A., Ojha,N., Soni, V. K., and Singh, N., Climate predictability in the Himalayan foothills using fractals, Mausam, 70, 2, 357-362, 2019.

11. Patel, N., Sharma, S., Joshi, V., Kumar, P., Ojha, N., Kumar, K. N., Chandra, H., Beig, G., Observations of middle atmospheric seasonal variations and study of atmospheric oscillations at equatorial regions, J. Atmos. Solar. Terr. Phy., v. 193, 2019., https://doi.org/10.1016/j.jastp.2019.105066.

12. Chandra, N., Venkataramani, S., Lal, S., Patra, P. K., Ramonet, M., Lin, X., & Sharma, S. K., 2019, "Observational evidence of high methane emissions over a city in western India", Atmospheric Environment, v. 202(January), p. 41–52. https://doi.org/10.1016/j.atmosenv.2019.01.007.

13. Ghosh, Priyanka; Sharma, Som and Ansari, Kamran, Investigation of Vertical Wavenumber Spectra during Sudden Stratospheric Warming (SSW) Events over the Indian Region, Remote Sensing Letters, 10 (7), 699-708, 2019. https://doi.org/10.1080/2150704X.2019.1601274.

14. Ghosh, Priyanka and Sharma, Som, Investigation of vertical wavenumber spectra of temperature from the troposphere to the mesosphere over tropical and subtropical regions, Journal of Atmospheric and Solar-Terrestrial Physics, 191, 105053, 2019, https://doi.org/10.1016/j.jastp.2019.05.017.

15. Patel, Nisha; Sharma, Som; Joshi, Vaidehi; Kumar, Prashant; Ojha, Narendra; Niranjan Kumar, Kondapalli; Chandra, Harish and Beig, Gufran, Observations of middle atmospheric seasonal variations and study of atmospheric oscillations at equatorial regions, Journal of Atmospheric and Solar-Terrestrial Physics, 193, 105066, 2019.https://doi.org/10.1016/j.jastp.2019.105066.

16. Niranjan Kumar, Kondapalli; Sharma, Som; Joshi, Vaidehi and Ramkumar, T. K., Middle atmospheric planetary waves in contrasting QBO phases over the Indian low latitude region, Journal of Atmospheric and Solar-Terrestrial Physics, 193, 105068, 2019.https://doi.org/10.1016/j.jastp.2019.105068.

17. Ravi Yadav, LK Sahu, Nidhi Tripathi, D Pal, G Beig, SNA Jaaffrey (2019), Investigation of emission characteristics of NMVOCs over urban site of western India, Environmental Pollution, 252, 245-255, https://doi.org/10.1016/j.envpol.2019.05.089.

18. Yadav Ravi, L.K. Sahu, G. Beig, Nidhi Tripathi, Sujit Maji, and S.N.A. Jaaffrey 2019, "The role of local meteorology on ambient particulate and gaseous species at an urban site of western India", Urban Climate, v.28, p.1-10, https://doi.org/10.1016/j.uclim.2019.01.003.

19. Sinha P.R., N. Nagendra, R. K. Manchanda, D. K. Ojha, B. Suneel Kumar, S. K. Koli, D. B. Trivedi, R. K. Lodha, L. K. Sahu and S. Sreenivasan, 2019, "Development of balloon-borne Impactor payload for profiling free tropospheric aerosol", Aerosol Science and Technology, v. 53, p. 231-243, https://doi.org/10.1080/02786826.2018.1546045.

20. Maurya, A. K; Cohen, M. B; Niranjan Kumar, Kondapalli; Phanikumar, D. V; Singh, R; Vineeth, P. K; & Kishore Kumar, K (2019) Observation of very short period atmospheric gravity waves in the lower ionosphere using very low frequency waves. J. Geophys. Res. Space Physics, 124. Doi: https://doi.org/10.1029/2019JA027360.

21. Ouarda, T. B. M. J; Christian Charron; Niranjan Kumar, Kondapalli; D. V. Phanikumar; Annalisa Molini; Ghouse Basha (2019), Nonstationary warm spell frequency analysis integrating climate variability and change with application to the Middle East, Clim. Dyn., DOI: https://doi.org/10.1007/s00382-019-04866-2

22. Valappil, V. K., M. Temimi, M. Weston, R. Fonseca, N. Narendra Reddy, Mohan Thota, Niranjan Kumar, Kondapalli (2019), Assessing Bias Correction Methods in Support of Operational Weather Forecast in Arid Environment, Asia-Pacific Journal of Atmospheric Sciences., DOI:https://doi.org/10.1007/s13143-019-00139-4

23. Niranjan Kumar, Kondapalli; Kentaroh Suzuki (2019), Assessment of seasonal cloud properties in the United Arab Emirates and adjoining regions from geostationary satellite data, Remote Sens. Envi., 228, 90-104, DOI: https://doi.org/10.1016/j.rse.2019.04.024

24. Eswaraiah, S; M. Venkat Ratnam; Y. H. Kim; Niranjan Kumar, Kondapalli; G. Venkata Chalapathi; L. Ramanjaneyulu; J. Lee; P. Vishnu Prasanth; K. Thyagarajan; S. V. B. Rao (2019), Advanced meteor radar observations of mesospheric dynamics during 2017 minor SSW over the tropical region, Advances in Space Research, DOI: https://doi.org/10.1016/j.asr.2019.05.039.

25. Niranjan Kumar, Kondapalli; D.V. Phanikumar; Sharma, Som; G. Basha; M. Naja; T. B. M. J. Ouarda; M. V. Ratnam; K. Kishore kumar (2019), Influence of tropical-extratropical interactions on the dynamics of extreme rainfall event: A case study from Indian region, Dynamics of Atmospheres and Oceans, 85, 28-40, DOI: https://doi.org/10.1016/j.dynatmoce.2018.12.002

26. Ghouse Basha; M. Venkat Ratnam; Niranjan Kumar, Kondapalli; T.B.M.J. Ouarda; P. Kishore; Isabella Velicogna (2019), Long-term variation of dust episodes over the United Arab Emirates, J. Atmos. Sol. Terr. Phys.,187, 33-39, DOI: https://doi.org/10.1016/j.jastp.2019.03.006.

27. Piyushkumar N. Patel, Ritesh Gautam, Takuro Michibata, Harish Gadhavi, 2019, Strengthened Indian Summer Monsoon Precipitation Susceptibility Linked to Dust-Induced Ice Cloud Modification, Geophysical Research Letters, v. 46 (14), p. 8431-8441.

28. Singh, A., Satish, R. V., and Rastogi, N, 2019. Characteristics and sources of fine organic aerosol over a big semi-arid urban city of western India using HR-ToF-AMS. Atmospheric Environment 208, 103-112. DOI: https://doi.org/10.1016/j.atmosenv.2019.04.009

29. Singh, A., and Rastogi, N, 2019. Quantification of organic carbon from biomass versus non-biomass burning emissions to fine aerosol. Proceedings of the Indian National Science Academy 85 (3), 629-636. DOI: https://doi.org/10.16943/ptinsa/2019/49585

30. Satish, R. V. and Rastogi, N, 2019. On the use of brown carbon spectra as a tool to understand their broader composition and characteristics: A case study from crop-residue burning samples. ACS Omega 4 (1). 1847-1853. DOI: https://doi.org/10.1021/acsomega.8b02637

31. Rastogi, N, Singh, A., and Satish, R. V., 2019. Characteristics of submicron particles coming from a big firecrackers burning event: Implications to atmospheric pollution. *Atmospheric Pollution Research 10, 629-634. DOI: https://doi.org/10.1016/j.apr.2018.11.002*

32. Singh, A., Gandhi, N., Ramesh, R., 2019. Surplus supply of bioavailable nitrogen through N2 fixation to primary producers in the eastern Arabian Sea during autumn. Cont. Shelf Res. 181, 103–110.

33. Fadnavis S., Müller R., Kalita G., Rowlinson M., Rap A., Frank Li J-L, Gasparini B., and Laakso A., The impact of recent changes in Asian anthropogenic emissions of SO2 on sulfate loading in the upper troposphere and lower stratosphere and the associated radiative changes, Atmos. Chem. Phys., 19, 9989–10008, 2019, https://doi.org/10.5194/acp-19-9989-2019.

34. Patel, P. N., Gautam, R., Michibata, T., & Gadhavi, H. (2019). Strengthened Indian summer monsoon precipitation susceptibility linked to dust-induced ice cloud modification. Geophysical Research Letters, 46, 8431– 8441. https://doi.org/10.1029/2018GL081634.

35**.** Fadnavis, S., Sabin, T.P., Roy, C. et al. Elevated aerosol layer over South Asia worsens the Indian droughts. Sci Rep **9**, 10268, 2019. https://doi.org/10.1038/s41598-019-46704-9

2020

36. Wang, L., Slowik, J. G., Tripathi, N., Bhattu, D., Rai, P., Kumar, V., Vats, P., Satish, R., Baltensperger, U., Ganguly, D., Rastogi, N., Sahu, L. K., Tripathi, S. N., and Prévôt, A. S. H., 2020, Source characterization of volatile organic compounds measured by proton-transfer-

reaction time-of-flight mass spectrometers in Delhi, India, Atmospheric Chemistry and Physics

37. S. Ramachandran and Maheswar Rupakheti, 2020, Year-round aerosol characteristics and radiative effects in the South Asian pollution outflow over a background site in the Maldives, Atmospheric Environment

38. Pragnesh N Dave, Lokesh Kumar Sahu, Nidhi Tripathi, Samiksha Bajaj, Ravi Yadav, Kashyap Patel, 2020, Emissions of non-methane volatile organic compounds from a landfill site in a major city of India: impact on local air quality, Heliyon

39. LK Sahu, Nidhi Tripathi, Ravi Yadav, 2020, Observations of trace gases in the earth's lower atmosphere: instrumentation and platform, CURRENT SCIENCE

40. LK Sahu, Ravi Yadav, Nidhi Tripathi, 2020, Aromatic compounds in a semi-urban site of western India: Seasonal variability and emission ratios, Atmospheric Research

41. S. Ramachandran and M. Rupakheti, 2020, Inter-annual and seasonal variations in columnar aerosol characteristics and radiative effects over the Pokhara Valley in the Himalayan foothills – Composition, radiative forcing, and atmospheric heating, Environmental Pollution

42. T. A. Rajesh and S. Ramachandran, 2020, Extensive and intensive properties of aerosol over distinct environments: Influence of anthropogenic emissions and meteorology, Journal of Atmospheric and Solar-Terrestrial Physics

43. Ravi Yadav, Pujal Trivedi, LK Sahu, G Beig, Nidhi Tripathi, 2020, Air Pollution Modeling, Air Pollution and Environmental Health. Environmental Chemistry for a Sustainable World

44. A. Guharay, P. P. Batista and R. A. Buriti , 2020, Signature of a 120-day oscillation in the MLT winds and tides over Sao ~ Joao ~ do Cariri (7.4S, 36.5W), Journal of Atmospheric and Solar-Terrestrial Physics

45. S. Ramachandran, Maheswar Rupakheti, Mark G. Lawrence, Black carbon dominates the aerosol absorption over the Indo-Gangetic Plain and the Himalayan foothills, Environment International, Volume 142, 2020, 105814, ISSN 0160-4120, https://doi.org/10.1016/j.envint.2020.105814.

46. N. Tripathi, L. K. Sahu, Emissions and atmospheric concentrations of α-pinene at an urban site of India: Role of changes in meteorology, Chemosphere, Volume 256, 2020, 127071, ISSN 0045-6535, https://doi.org/10.1016/j.chemosphere.2020.127071.

47. Nidhi Tripathi, L. K. Sahu, Arvind Singh, Ravi Yadav, and Kusum Komal Karati, 2020, High Levels of Isoprene in the Marine Boundary Layer of the Arabian Sea during Spring Inter-Monsoon: Role of Phytoplankton Blooms, ACS Earth and Space Chemistry

48.Tripathi, N., Sahu, L. K., Singh, A., Yadav, R., Patel, A., Patel, K., et al. (2020). Elevated levels of biogenic nonmethane hydrocarbons in the marine boundary layer of the Arabian Sea during the intermonsoon. Journal of Geophysical Research: Atmospheres, 125, e2020JD032869. https://doi.org/10.1029/2020JD032869.

49. I. A. Girach, N. Tripathi, P. R. Nair, L. K. Sahu, N. Ojha, 2020, O3 and CO in the South Asian outflow over the Bay of Bengal: Impact of monsoonal dynamics and chemistry, Atmospheric Environment

50. I. A. Girach, P. R. Nair, N. Ojha, L. K. Sahu, 2020, Tropospheric carbon monoxide over the northern Indian Ocean during winter: influence of inter-continental transport, Climate Dynamics

51. A. Guharay, P. P. Batista R. A. Buriti and N. J. Schuch, 2020, Signature of the 27-day oscillation in the MLT tides and its relation with solar radiation at low latitudes, Earth, Planets and Space

52. Sourita Saha, Kondapalli Niranjan Kumar, Som Sharma, Prashant Kumar, Vaidehi Joshi, 2020, Can Quasi-Periodic Gravity Waves Influence the Shape of Ice Crystals in Cirrus Clouds?, Geophysical Research Letters, https://doi.org/10.1029/2020GL087909.

53. Narendra Ojha, Amit Sharma, Manish Kumar, Imran Girach, Tabish U. Ansari, Som K. Sharma, Narendra Singh, Andrea Pozzer, Sachin S. Gunthe, 2020, On the widespread enhancement in fine particulate matter across the Indo-Gangetic Plain towards winter, Scientific Reports

54. K. Renuka, H. Gadhavi, A. Jayaraman, S. V. Bhaskara Rao, S. Lal, Study of mixing ratios of SO_2 in a tropical rural environment in south India, J. Earth Syst. Sci. (2020) 129 104, https://doi.org/10.1007/s12040-020-1366-4.

55. Kondapalli Niranjan Kumar, Som Kumar Sharma, Manish Naja, D.V. Phanikumar, A Rossby wave breaking-induced enhancement in the tropospheric ozone over the Central Himalayan region, Atmospheric Environment, Volume 224, 2020, 117356, https://doi.org/10.1016/j.atmosenv.2020.117356.

56. B. Sarangi, S. Ramachandran, T. A. Rajesh and V. K. Dhaker, 2020, Characteristics of black carbon aerosol mixing state over an urban region deduced using Single Particle Soot Photometer (SP2) and Differential Mobility Analyzer (DMA), Atmospheric Pollution Research

57. Joshi, V., Sharma, S., Kumar, K. et al. Analysis of the middle atmospheric ozone using SABER observations: a study over mid-latitudes in the northern and southern hemispheres. Clim Dyn 54, 2481–2492 (2020). https://doi.org/10.1007/s00382-020-05124-6.

58. Amit Sharma, Narendra Ojha, Tabish U. Ansari, Som K. Sharma, Andrea Pozzer, Sachin S. Gunthe, 2020, Effects of dry deposition on surface ozone over South Asia inferred from a regional chemical transport model, ACS Earth and Space Chemistry.

59. A. Chhabra, Turakhia, T., Som Sharma, Saha, S., Iyer, R., & Chauhan, P. (2020), "Environmental impacts of fireworks on aerosol characteristics and radiative properties over a megacity, India. City and Environment Interactions", 7, 100049. https://doi.org/10.1016/j.cacint.2020.100049.

60. P. Jindal, P. K. Thapliyal, M. V. Shukla, Som Sharma and D. Mitra (2020), "Trend analysis of atmospheric temperature, water vapour, ozone, methane and carbon-monoxide over few major cities of India using satellite data", J. Earth Syst. Sci. https://www.ias.ac.in/article/fulltext/jess/129/0060.

61. P. Saxena, S. Sonwani, Som Sharma, P. Kumar, N. Chandra (2020), "Carbonaceous Aerosol variations in Foggy Days: A critical analysis during the fireworks festival", Fresenius Environmental Bulletin Volume 29 – No. 08/2020 pages 6639-6656.

62. K. K. Shukla, D.V.Phanikumar, K N. Kumar, A Kumar, M. Naja, Som Sharma, Raju Attada, (2020), "Micro-Pulse Lidar observations of elevated aerosol layers over the Himalayan region", Journal of Atmospheric and Solar-Terrestrial Physics S 1364- 6826 (20) 30325-4. https://doi.org/10.1016/j.jastp.2020.105526.

63. S. Shika, H. Gadhavi, M. N. S. Suman, R. Ravikrishna, Sachin S. Gunthe, 2020, Atmospheric aerosol properties at a semi-rural location in southern India: particle size distributions and implications for cloud droplet formation, SN Applied Sciences, 2:1007.

64. Patel, A. and Rastogi, N, 2020. Chemical composition and oxidative potential of atmospheric PM10 over the Arabian Sea. ACS Earth and Space Chemistry 4, 112-121. DOI: https://doi.org/10.1021/acsearthspacechem.9b00285

65. Satish, R., Rastogi, N, Singh, A., and Singh D., 2020. Change in Characteristics of Water-soluble and Water-Insoluble Brown Carbon Aerosol during a Large-Scale Biomass Burning. Environmental Science and Pollution Research. 27, 33339-33350. DOI: https://doi.org/10.1007/s11356-020-09388-7 .

66. Rastogi, N, Agnihotri, R., Sawlani, R., Patel, A., Suresh Babu, S., and Satish, R, 2020. Chemical and isotopic and characteristics of PM10 over the Bay of Bengal: Effects of continental outflow on a marine environment. Science of the Total Environment 726, 138438. DOI: https://doi.org/10.1016/j.scitotenv.2020.138438

67. Sahoo, D., Saxena, H., Tripathi, N., Khan, A., Rahaman, A., Kumar, S., Sudheer, A., Singh, A., 2020. Non-Redfieldian C:N:P ratio in the inorganic and organic pools of the Bay of Bengal during the summer monsoon. Mar. Ecol. Prog. Ser. 653, 41–55. https://doi.org/10.3354/meps13498

68. Saxena, H., Sahoo, D., Khan, M.A., Kumar, S., Sudheer, A., Singh, A., 2020. Dinitrogen fixation rates in the Bay of Bengal during summer monsoon. Environ. Res. Commun. 2, 051007. https://doi.org/10.1088/2515-7620/ab89fa.

69. Saha, S., Niranjan Kumar, K., Sharma, S., Kumar, P., & Joshi, V. (2020). Can quasi-periodic gravity waves influence the shape of ice crystals in cirrus clouds? Geophysical Research Letters, 47, e2020GL087909. https://doi.org/10.1029/2020GL087909.

2021

70. Ambade, B., A. Kumar, and L. K. Sahu, 2021, Characterization and health risk assessment of particulate bound polycyclic aromatic hydrocarbons (PAHs) in indoor and outdoor atmosphere of Central East India, Environmental Science and Pollution Research, https://doi.org/10.1007/s11356-021-14606-x.

71. Chakraborty, P., Harish Gadhavi, Balasubramanian Prithiviraj, Moitraiyee Mukhopadhyay, Sanjenbam Nirmala Khuman, Masafumi Nakamura, Scott N. Spak, 2021, Passive Air Sampling of PCDD/Fs, PCBs, PAEs, DEHA, and PAHs from Informal Electronic Waste Recycling and Allied Sectors in Indian Megacities, Environmental Science and Technology.

72. Chavan P. Fadnavis S., Chakroborty T., Sioris C. E., Griessbach S., and Müller R., The outflow of Asian biomass burning carbonaceous aerosol into the upper troposphere and lower stratosphere in spring: radiative effects seen in a global model, Atmos. Chem. Phys., 21, 14371–14384, 2021, https://doi.org/10.5194/acp-21-14371-2021.

73. Chinmay Mallik, Harish Gadhavi, Shyam Lal, Rahul Kant Yadav, R. Boopathy and Trupti Das, 2021, Effect of Lockdown on Pollutant Levels in the Delhi Megacity: Role of Local Emission Sources and Chemical Lifetimes, Frontier in Environmental Science.

74. Dave, P. N., Shalini Chaturvedi, Lokesh Kumar Sahu, 2021, Impact of polychlorinated biphenyls on environment and public health, Handbook of Advanced Approaches Towards Pollution Prevention and Control.

75. Fadnavis, S., Müller, R., Chakraborty, T. *et al.* The role of tropical volcanic eruptions in exacerbating Indian droughts. *Sci Rep* **11**, 2714 (2021). https://doi.org/10.1038/s41598-021-81566-0

76. Fadnavis S. Sabin T P, Rap A., Müller R., Kubin A. and Heinold B. The impact of COVID-19 lockdown measures on the Indian summer monsoon, *2021* Environ. Res. Lett. ***16,*** *074054.*

77. Guharay, A., P. P. Batista and R. A. Buriti, 2021, Observations of a quasi-90-day oscillation in the MLT winds and tides over an equatorial station using meteor radar winds, Advances in Space Research, v. 67, 15 May 2021, Pages 3125-3133.

78. A. Guharay, S. Mondal, S. Sarkhel, M. Sivakandan, M.V. Sunil Krishna, Signature of a mesospheric bore in 557.7 nm airglow emission using all-sky imager at Hanle (32.7oN, 78.9oE), Advances in Space Research, Volume 69, Issue 5, 2022, Pages 2020-2030, ISSN 0273-1177, https://doi.org/10.1016/j.asr.2021.12.006.

79. Maji, S., R. Yadav, G. Beig, S. S.Gunthe, N. Ojha, 2021, On the processes governing the variability of PTR-MS based VOCs and OVOCs in different seasons of a year over hillocky mega city of India, Atmospheric Research, v. 261, 15 October 2021, 105736.

80. Mitra, G., Guharay, A., Batista, P. P., & Buriti, R. A., 2021, "Impact of the September 2019 minor sudden stratospheric warming on the low-latitude middle atmospheric planetary wave dynamics", Journal of Geophysical Research: Atmospheres, e2021JD035538, https://doi.org/10.1029/2021JD035538

81. Panda, U., R. Boopathy, H. S. Gadhavi, K. Renuka, Sachin S. Gunthe, Trupti Das, 2021, Metals in coarse ambient aerosol as markers for source apportionment and their health risk assessment over an eastern coastal urban atmosphere in India, Environmental Monitoring and Assessment

82. Rajesh, T. A., S.Ramachandran, Vishnu K.Dhaker, 2021, Black carbon aerosols: Relative source strengths of vehicular emissions and residential/open wood burning over an urban and a semi-urban environment, Atmospheric Pollution, v. 12, June 2021, 101060.

83. Ramachandran, S., T. A. Rajesh and R. Cherian, 2021, Black carbon aerosols over source vs. background region: Atmospheric boundary layer influence, potential source regions, and model comparison, Atmospheric Research, v. 256, 105573.

84. Ramachandran, S., and Rupakheti, M., 2021, "Inter-annual and seasonal variations in optical and physical characteristics of columnar aerosols over the Pokhara Valley in the Himalayan foothills", Atmospheric Research, 248, 105254.

85. Ramachandran, S., and Priyadarshini B., 2021, Biomass burning and impacts on aerosols: Optical properties and radiative effects, in "Biomass Burning in South and Southeast Asia".

86. Saha, S., Som Sharma, K. N. Kumar, P. Kumar, V. Joshi, S. Lal, 2021, A case study on the vertical distribution and characteristics of aerosols using ground-based raman lidar, satellite and model over Western India, International Journal of Remote Sensing

87. Sharma, S., and P Kumar, 2021, Impact of the COVID-19 Epidemic: Scenario in a Tropical Environment, Pure Appl. Geophys. 178 (2021), 3169–3177, https://doi.org/10.1007/s00024-021-02793-0.

88. Shukla, A. K., Lalchandani, V., Bhattu, D., Dave, J.S., Rai, P., Thamban, N.M., Mishra, S., Gaddamidi, S., Tripathi, N., Vats, P., Rastogi, N., Sahu L.K., Ganguly, D., Kumar, M., Singh, V., Gargava, P., and Tripathi S.N. , 2021, Real-time quantification and source apportionment of fine particulate matter including organics and elements in Delhi during summertime, Atmospheric Environment.

89. Singh, J., N. Singh, N. Ojha, A. Sharma, A. Pozzer, N. Kiran Kumar, K. Rajeev, S. S. Gunthe, and V. Rao Kotamarthi, 2021, Effects of spatial resolution on WRF v3.8.1 simulated meteorology over the central Himalaya, Geoscientific Model Development, v. 14, 1427–1443.

90. Soni, M., Ojha, N., Girach, I., Impact of COVID-19 lockdown on surface ozone build-up at an urban site in western India based on photochemical box modelling, Current Science, VOL. 120, NO. 2, 376-381, 2021, doi: 10.18520/cs/v120/i2/376-381.

91. Stewart, G. J., Beth S Nelson, W Joe F Acton, Adam R Vaughan, James R Hopkins, Siti SM Yunus, C Nicholas Hewitt, Oliver Wild, Eiko Nemitz, Ranu Gadi, Lokesh K Sahu, Tuhin K Mandal, Bhola R Gurjar, Andrew R Rickard, James D Lee, Jacqueline F Hamilton, 2021, Emission estimates and inventories of non-methane volatile organic compounds from anthropogenic burning sources in India, Atmospheric Environment: X, v. 11, October 2021, 100115.

92. Stewart, G. J., W Joe F Acton, Beth S Nelson, Adam R Vaughan, James R Hopkins, Rahul Arya, Arnab Mondal, Ritu Jangirh, Sakshi Ahlawat, Lokesh Yadav, Sudhir K Sharma, Rachel E Dunmore, Siti SM Yunus, C Nicholas Hewitt, Eiko Nemitz, Neil Mullinger, Ranu Gadi, Lokesh K Sahu, Nidhi Tripathi, Andrew R Rickard, James D Lee, Tuhin K Mandal, Jacqueline F Hamilton, 2021, Emissions of non-methane volatile organic compounds from combustion of domestic fuels in Delhi, India, Atmospheric Chemistry and Physics, v. 21, p. 2383-2406.

93. Stewart, G. J., Beth S Nelson, W Joe F Acton, Adam R Vaughan, James R Hopkins, Siti SM Yunus, C Nicholas Hewitt, Eiko Nemitz, Tuhin K Mandal, Ranu Gadi, Lokesh K Sahu, Andrew R Rickard, James D Lee, Jacqueline F Hamilton, 2021, Comprehensive organic emission profiles, secondary organic aerosol production potential, and OH reactivity of domestic fuel combustion in Delhi, India, Environmental Science: Atmospheres, Royal Society of Chemistry.

94. Tripathi, N., L. K. Sahu, Kashyap Patel, Ashwini Kumar & Ravi Yadav , 2021, Ambient air characteristics of biogenic volatile organic compounds at a tropical evergreen forest site in Central Western Ghats of India, Journal of Atmospheric Chemistry.

95. Mehta, S., Singh, A., Thirumalai, K., 2021. Uncertainty in palaeosalinity estimates from foraminiferal geochemical records in the northern Indian Ocean. Palaeogeogr. Palaeoclimatol. Palaeoecol. 569, 110326.

96. Rahman, A., Khan, M.A., Singh, A., Kumar, S., 2021a. Hydrological characteristics of the Bay of Bengal water column using δ18O during the Indian summer monsoon. Cont. Shelf Res. 226, 104491.

97. Rahman, A., Rathi, A., Nambiar, R., Mishra, P.K., Anoop, A., Bhushan, R., Kumar, S., 2021b. Signatures of natural to anthropogenic transition in lake sediments from the Central Himalaya using stable isotopes. Appl. Geochem. 134, 105095.

98. Varna, M., Singh, A., Sahoo, D., Sengupta, D., 2021. Strengthening of basin-scale ocean currents in winter drives decadal salinity decline in the eastern Arabian Sea. Geophys. Res. Lett. 48, e2021GL094516.

99. Kumar, P.K., Singh, A., 2021. Increase in summer monsoon rainfall over the northeast India during El Niño years since 1600. Clim. Dyn. 57, 851–863.

100. Sahoo, D., Saxena, H., Nazirahmed, S., Kumar, S., Sudheer, A., Bhushan, R., Sahay, A., Singh, A., 2021. Role of eddies and N2 fixation in regulating C: N: P proportions in the Bay of Bengal. Biogeochemistry 1–17.

101. Dave, J., Meena, R., Singh, A., and Rastogi, N, 2021. Effect of COVID-19 lockdown on the concentration and composition of NR-PM2.5 over Ahmedabad, a big city in western India. Urban Climate 37, 100818. DOI: https://doi.org/10.1016/j.uclim.2021.100818

102. Patel, A., Satish, R., and Rastogi, N, 2021a. Remarkably High Oxidative Potential of Atmospheric PM 2.5 Coming from a Large-Scale Paddy-Residue Burning over the Northwestern Indo-Gangetic Plain. ACS Earth and Space Chemistry 5, 2442-2452. https://doi.org/10.1021/acsearthspacechem.1c00125

103. Patel, A. and Rastogi, N, 2021. Oxidative Potential of Ambient PM and Related Health Endpoints over South Asia: A Review. Asian Journal of Atmospheric Environment 15 (1), 40-50. DOI: https://doi.org/10.5572/ajae.2020.123

104. Patel, A., Rastogi, N, Gandhi, U., and Khatri, N., 2021b. Oxidative Potential of Atmospheric PM10 at Five Different Sites of Ahmedabad, a Big City in Western India. Environmental Pollution. 268, 115909. DOI: https://doi.org/10.1016/j.envpol.2020.115909

105. Rastogi, N, Satish, R., Singh, A., Kumar, V., Thamban, N., Lalchandani, V., Shukla, A., Vats, P., Tripathi, S. N., Ganguly, D., Slowik, J., and Prevot, A. S. H. 2021. Diurnal Variability in the Spectral Characteristics and Sources of Water-Soluble Brown Carbon Aerosols over Delhi. Science of the Total Environment, 794, 148589. https://doi.org/10.1016/j.scitotenv.2021.148589 .

106. Singh, A. Rastogi, N, Kumar, V., Slowik, J., Satish, R., Lalchandani, V., Thamban, N., Rai., P., Bhattu, D., Vats, P., Ganguly, D., Tripathi, S.N., and Prevot, A.S.H., 2021. Sources and characteristics of light-absorbing fine particulates over Delhi through the synergy of real-time optical and chemical measurements. Atmospheric Environment 252, 118338. DOI: https://doi.org/10.1016/j.atmosenv.2021.118338

2022

107. V. Karthik, B. Vijay Bhaskar, S. Ramachandran and A.W. Gertler, 2022, Quantification of organic carbon and black carbon emissions, distribution, and carbon variation in diverse vegetative ecosystems across India, Environmental Pollution, Date of Publication: 15/09/2022

108. Narendra Ojha, Meghna Soni, Manish Kumar, Sachin S. Gunthe, Ying Chen, Tabish U. Ansari, 2022, Mechanisms and Pathways for Coordinated Control of Fine Particulate Matter and Ozone, Current Pollution Reports, Date of Publication: 15/08/2022

109. G. Mitra, A. Guharay, P. P. Batista, R. A. Buriti, T. Moffat-Griffin, 2022, Investigation on the MLT tidal variability during September 2019 minor sudden stratospheric warming, Advances in Space Research, Date of Publication: 10/08/2022

110. Mitra, G., Guharay, A., Batista, P. P., & Buriti, R. A. (2022). Impact of the September 2019 minor sudden stratospheric warming on the low-latitude middle atmospheric planetary wave dynamics. Journal of Geophysical Research: Atmospheres, 127, e2021JD035538. https://doi.org/10.1029/2021JD035538.

111. S. Ramachandran and Maheswar Rupakheti, 2022, Trends in the types and absorption characteristics of ambient aerosols over the Indo-Gangetic Plain and North China Plain in last two decades, Science of the Total Environment, Date of Publication: 20/07/2022

112. A. de Meij, N. Ojha, N. Singh, J. Singh, D. R. Poelman, A. Pozzer, 2022, The Impact of High-Resolution SRTM Topography and Corine Land Cover on Lightning Calculations in WRF, Atmosphere, Date of Publication: 30/06/2022

113. A. K. Gopinath, S. S. Raj, S. M. Kommula,C. Jose, U. Panda,Y. Bishambu, N. Ojha, R. Ravikrishna, P. Liu, S. S. Gunthe, 2022, Complex Interplay Between Organic and Secondary Inorganic Aerosols With Ambient Relative Humidity Implicates the Aerosol Liquid Water Content Over India During Wintertime, Journal of Geophysical Research: Atmospheres, Date of Publication: 20/06/2022

114. Pragnesh N Dave, Lakha V Chopda, and Lokesh Sahu, 2022, Applications of Nanomaterials in Corrosion Protection Inhibitors and Coatings, Functionalized Nanomaterials for Corrosion Mitigation: Synthesis, Characterization, and Applications, American Chemical Society (ACS), Date of Publication: 13/06/2022

115. Tripathi, N., Sahu, L. K., Wang, L., Vats, P., Soni, M., Kumar, P., Satish, R. V., Bhattu, D., Sahu, R., Patel, K., Rai, P., Kumar, V., Rastogi, N., Ojha, N., Tiwari, S., Ganguly, D., Slowik, J., Prévôt, A. S. H., Tripathi, S. N., Characteristics of VOC composition at urban and suburban sites of New Delhi, India in winter, Journal of Geophysical Research – Atmospheres, 127, e2021JD035342. https://doi.org/10.1029/2021JD035342, 2022.

116. Chutia, L., Ojha, N., Girach, I., Pathak, B., Sahu, L. K., Sarangi, C., Flemming, J., da Silva, A., Bhuyan, P. K., Trends in sulfur dioxide over the Indian subcontinent during 2003–2019, Atmospheric Environment, 2022, doi: 10.1016/j.atmosenv.2022.119189.

117. Vaishali Jain, Sachchida N. Tripathi, Nidhi Tripathi, Lokesh K. Sahu, Sreenivas Gaddamidi, Ashutosh K. Shukla, Deepika Bhattu, Dilip Ganguly, 2022, Seasonal variability and source apportionment of non-methane VOCs using PTR-TOF-MS measurements in Delhi, India, Atmospheric Environment, Date of Publication: 17/05/2022

118. S. Ramachandran and Maheswar Rupakheti, 2022, Trends in physical, optical and chemical columnar aerosol characteristics and radiative effects over South and East Asia: Satellite and ground-based observations, Gondwana Research, Date of Publication: 01/05/2022

119. T. A. Rajesh, S. Ramachandran, Assessment of the coronavirus disease 2019 (COVID-19) pandemic imposed lockdown and unlock effects on black carbon aerosol, its source apportionment, and aerosol radiative forcing over an urban city in India, Atmospheric Research, Volume 267, 2022, 105924, https://doi.org/10.1016/j.atmosres.2021.105924.

120. Yadav, R., Vyas, P., Kumar, P., Sahu, L.K., Kumar, U., Pandeya, V., Tripathi, N., Gupta, M., et al., 2022, Particulate Matter Pollution in Urban Cities of India During Unusually Restricted Anthropogenic Activities, Front. Sustain. Cities, Date of Publication: 22/03/2022

121. V. F. Andrioli, J. Xu, P. P. Batista, L. C. A. Resende, L. A. Da Silva, J. P. Marchezi, H. Li, C. Wang, Z. Liu , and A. Guharay, 2022, New Findings Relating Tidal Variability and Solar Activity in the Low Latitude MLT Region, Journal of Geophysical Research: Space Physics, Date of Publication: 15/03/2022

122. Sahu, L. K., Tripathi, N., Gupta, M., Singh, V., Yadav, R., & Patel, K. (2022). Impact of COVID-19 pandemic lockdown in ambient concentrations of aromatic volatile organic compounds in a metropolitan city of western India. Journal of Geophysical Research: Atmospheres, 127, e2022JD036628. https://doi.org/10.1029/2022JD036628.

123. S. Ramachandran, Maheswar Rupakheti, R. Cherian and Mark G. Lawrence, 2022, Climate Benefits of Cleaner Energy Transitions in East and South Asia Through Black Carbon Reduction, Frontiers in Environmental Science , Date of Publication: 09/03/2022

124. Sourita Saha, Som Sharma, Abha Chhabra, Kondapalli Niranjan Kumar, Prashant Kumar, Dharmendra Kamat & Shyam Lal, 2022, Impact of dust storm on the atmospheric boundary layer: a case study from western India, Nat Hazards 113, 143–155. https://doi.org/10.1007/s11069-022-05293-z.

125. Meghna Soni, Imran Girach, Lokesh K. Sahu, Narendra Ojha, 2022, Photochemical evolution of air in a tropical urban environment of India: A model-based study, Chemosphere, Date of Publication: 26/02/2022

126. S. Ramachandran, Maheswar Rupakheti and R. Cherian, 2022, Insights into recent aerosol trends over Asia from observations and CMIP6 simulations, Science of the Total Environment, Date of Publication: 10/02/2022

127. K. Gopalan, B. P. Shukla, Som Sharma, P. Kumar, A. Shyam, A. Gaur, and S. Sunda, 2022, An Observational Study of GPS-Derived Integrated Water Vapor over India, Atmosphere, Date of Publication: 31/01/2022

128. M. Jain, P. Saxena, Som Sharma, and S. Sonwani, 2022, Investigation of Forest Fire Activity Changes Over the Central India Domain Using Satellite Observations During 2001–2020, GeoHealth (AGU), Date of Publication: 31/01/2022

129. Ashish Soni, Stefano Decesari, Harish Gadhavi, Marco Paglione, Douglas Orsini, Vijay Shridhar, Ujjwal Kumar and Francesca Volpi , 2022, Chemical composition and radiative forcing of atmospheric aerosols over the high-altitude Western Himalayas of India, Environmental Science and Pollution Research, Date of Publication: 12/01/2022

130. Patel, A., Rastogi, N, Rangu, S., Dave, J., Borgohain, A., and Kundu, S. S. 2022. Oxidative potential and hydroxyl radical generation capacity of ambient PM2.5 over a high-altitude site in northeastern himalaya: Role of long-range transport, Atmospheric Environment, 119263, https://doi.org/10.1016/j.atmosenv.2022.119263

131. Khan, M.A., Rahman, A., Sahoo, D., Saxena, H., Singh, A., Kumar, S., 2022. Nitrous oxide in the central Bay of Bengal during the summer monsoon. Reg. Stud. Mar. Sci. 52, 102314.

132. Ahmad Shah, R., Khan, I., Rahman, A., Kumar, S., Achyuthan, H., Shukla, A.D., Kumar, P., Dash, C., 2022. Holocene climate events and associated land use changes in the eastern coast of India: Inferences from the Chilika Lagoon. The Holocene 32, 1081–1090.
132. Saxena, H., Sahoo, D., Nazirahmed, S., Rai, D.K., Khan, M.A., Sharma, N., Kumar, S., Singh, A., 2022. Contribution of carbon fixation toward carbon sink in the ocean twilight zone. Geophys. Res. Lett. 49, e2022GL099044.

134. Ramachandran, S., Rupakheti, M., Cherian, R., Lawrence, M. G., Climate Benefits of Cleaner Energy Transitions in East and South Asia Through Black Carbon Reduction, Frontiers in Environmental Science, VOLUME=10, 2022, doi:10.3389/fenvs.2022.842319.

2023

135. Devaprasad, M., N. Rastogi, R. Satish, A. Patel, A. Singh, A. Dabhi, A. Shivam, R. Bhushan, R. Meena. 2023. Characterization of paddy-residue burning derived carbonaceous aerosols using dual carbon isotopes, Science of The Total Environment, 864, 161044, https://doi.org/10.1016/j.scitotenv.2022.161044

136. Kumar, P.K., Singh, A., Ramesh, R., 2023. Convective mixing and transport of the Bay of Bengal water stir the δ18O-salinity relation in the Arabian Sea. J. Mar. Syst. 238, 103842.

National Report on Indian scientific contributions in the areas covered by the International Association for the Physical Sciences of the Oceans (IAPSO)

1. Physical Oceanography Section

High-resolution Operational Ocean Forecast and reanalysis System for the Indian Ocean

Considering the importance of providing accurate prediction of different oceanographic parameters for a wide spectrum of users ranging from traditional fisher folks to high-tech off-shore industries, INCOIS has developed the High-resolution Operational Ocean Forecast and reanalysis System (HOOFS), that comprises a suit of numerical ocean models to which near-real time ocean observations are assimilated. Major components of HOOFS are (i) a suite of numerical ocean models configured for the Indian Ocean and the coastal waters using Regional Ocean Modeling System (ROMS) for the analysis and forecasting physical and biogeochemical state of the ocean and (ii) the data assimilation based on Local Ensemble Transform Kalman Filter that assimilates in-situ and satellite observations in ROMS ((Regional Analysis for Indian Ocean, RAIN). The Indian Ocean configuration of the HOOFS takes initial and boundary conditions from the Global Ocean Data Assimilation System (GODAS) configuration at INCOIS, in which the insitu ocean observations are assimilated to Modular Ocean Model (MOM4p0d) using 3D-VAR data assimilation system. The ocean analysis system (both GODAS and RAIN) are forced with 6-hourly GFS atmospheric forcing provided by National Centre for Medium Range Weather Forecast (NCMRWF), while the forecast models are forced with 6-hourly NCUM atmospheric forcing provided by NCMRWF. Ten (10) tidal constituents are incorporated in the model for accurate simulation of tides. Since this system has a very high spatial resolution and is specifically configured to represent most of the physical processes in the coastal waters, it is capable of providing high quality forecasts of ocean circulation parameters such as currents, temperature and salinity structure, tides, depths of mixed layer and thermocline etc. The analysis and forecast products were statistically validated to make sure that they are useful for providing operational forecasts of different ocean parameters. The forecasts issued by INCOIS based on this system are extensively used by fishermen, maritime industries and shipping agencies. Apart from the routine forecasts of key oceanographic parameters, a few important applications such as (i) Potential Fishing Zone forecasting system and (ii) Search and Rescue Aid Tool were also developed as part of the HOOFS project. While developing the system, extensive research on the processes that are important to improve the quality of ocean forecasts and their representation in the numerical models were carried out.

Figure: A schematic representation of the components of HOOFS. GFS (Det.): GFS deterministic atmospheric analysis. GFS (Ens.): GFS ensemble analysis. Observ. : Observations. IC: initial condition. BC: boundary condition. Red arrows represent the observational data used for data assimilation in numerical models. Green Arrows represent the source of initial and boundary conditions used in various model configurations. Blue arrows indicate the data sets used for the atmospheric forcing in the HOOFS. Black arrows represent the model output used for the generation of analysis, forecast and value products.

***Ref**: Francis P. A., Jithin A. K, Effy B. John, Abhisek Chatterjee, Kunal Chakraborty, AryaPaul, Balaji B, S. S. C. Shenoi, Biswamoy P, Arnab Mukherjee, Prerna Singh, Deepsankar B, Siva Reddy S, Vinayachandran P. N, Girish Kumar M. S, Udaya Bhaskar T. V. S, Ravichandran M, Unnikrishnan A. S, Shankar D, Amol Prakash, Aparna S. G, Harikumar R, Kaviyazhaku K, Suprit K, Venkat Shesu R, Kiran Kumar N, Srinivasa Rao N, Annapurnaiah K,Venkatesan R, Suryachandra Rao A, Rajagopal E. N, Prasad V. S, Munmun Das Gupta, Balakirishnan Nair T. M, Pattabhi Rama Rao E, Satyanarayana B. V (2020): High-resolution Operational Ocean Forecast and reanalysis System for the Indian Ocean, Bulletin of the American Meteorological Society, 101(8), E1340–E1356.*

LETKF-based data assimilation system in ROMS

A high-resolution ocean circulation model for the Indian Ocean (IO) using Regional Ocean Modeling System (ROMS) is operational at Indian National Centre for Ocean Information Services (INCOIS) which provides ocean state forecasts for the Bay of Bengal (BoB) and the Arabian Sea (AS) to the Indian Ocean rim countries. To provide an improved estimate of ocean state, a variant of Ensemble Kalman Filter (EnKF), viz., the Local Ensemble Transform Kalman

Filter (LETKF) has been developed and interfaced with the present basin-wide operational ROMS. This system assimilates in-situ temperature and salinity profiles and satellite track data of sea-surface temperature (SST). The ensemble members of the assimilation system are initialized with different parameters like diffusion and viscosity coefficients and are subjected to an ensemble of atmospheric fluxes. In addition, one half of the ensemble members respond to K profile parameterization mixing scheme while the other half is subjected to Mellor–Yamada mixing scheme. This strategy aids in arresting the filter divergence which has always been a challenging task. The assimilated system simulates the ocean state better than the present operational ROMS. Improvements permeate to deeper ocean depths with better correlation and reduced root-mean-squared deviation (RMSD) with respect to observations particularly in the northern Indian Ocean which is data rich in density. Analysis shows domain averaged RMSD reduction of about 0.2–0.4^0 C in sea surface temperature and 2–4 cm in sea level anomaly. The assimilated system also manages to significantly improve the thickness of the temperature inversion layers and the duration of its occurrence in northern Bay of Bengal. The most profound improvements are seen in currents, with an error reduction of 15 cm/s in zonal currents of central Bay of Bengal.

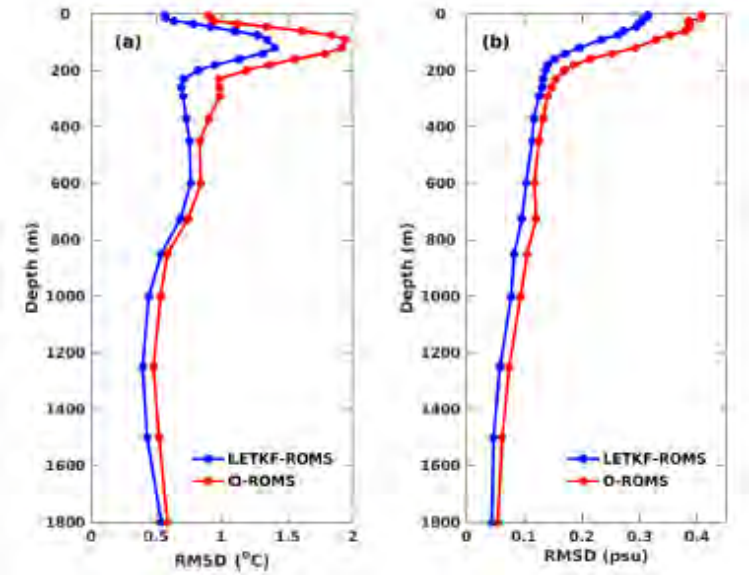

Figure: Vertical profile of RMS statistic of (a) temperature (in ^{o}C) and (b) salinity (in psu) derived from LETKF-ROMS (blue) and O-ROMS (red) in the observation space averaged over horizontal space and time.

Ref: *Baduru, B., Paul, B., Banerjee, D.S., Sanikommu, S., Paul, A. Ensemble based regional ocean data assimilation system for the Indian Ocean: Implementation and evaluation (2019) Ocean Modelling, 143, art. no. 101470*

Effect of Cyclones on the Biogeochemical Processes in the Bay of Bengal

It was shown that significant changes in upper ocean structure was observed in the physical and biogeochemical parameters observed by an autonomous profiling Argo float in the Bay of Bengal during the passage of tropical cyclone (TC) Hudhud (7–14 October 2014). TC Hudhud mixed

water from a depth of about 50 m into the surface layers through a combination of upwelling and turbulent mixing. Mixing was extended into the depth of nutricline, the oxycline, and the subsurface-chlorophyll-maximum and thus had a strong impact on the biogeochemistry of the upper ocean. Before the storm, the near-surface layer was nutrient depleted and was thus oligotrophic with the chlorophyll-a concentration of less than 0.15 mg m^{-3}. Storm mixing initially increased the chlorophyll by 1.4 mg m^{-3}, increased the surface nitrate concentration to about 6.6 μM kg^{-1}, and decreased the subsurface dissolved oxygen (30–35 m) to 31% of saturation (140 μM). These conditions were favorable for phytoplankton growth resulting in an estimated increase in primary productivity averaging 1.5 g $C \cdot m^{-2} \cdot day^{-1}$ over 15 days. During this bloom, chlorophyll-a increased by 3.6 mg m^{-3}, and dissolved oxygen increased from 111% to 123% of saturation. Similar observations during TC Vardah (6–12 December 2016) showed much less mixing. Analysis suggested that relatively small (high) translation speed and the presence of cold (warm) core eddy leads to strong (weak) oceanic response during TC Hudhud (TC Vardah). Thus, although cyclones can cause strong biogeochemical responses in the Bay of Bengal, the strength of response depends on the properties of the storm and the prevailing upper ocean structure such as the presence of mesoscale eddies.

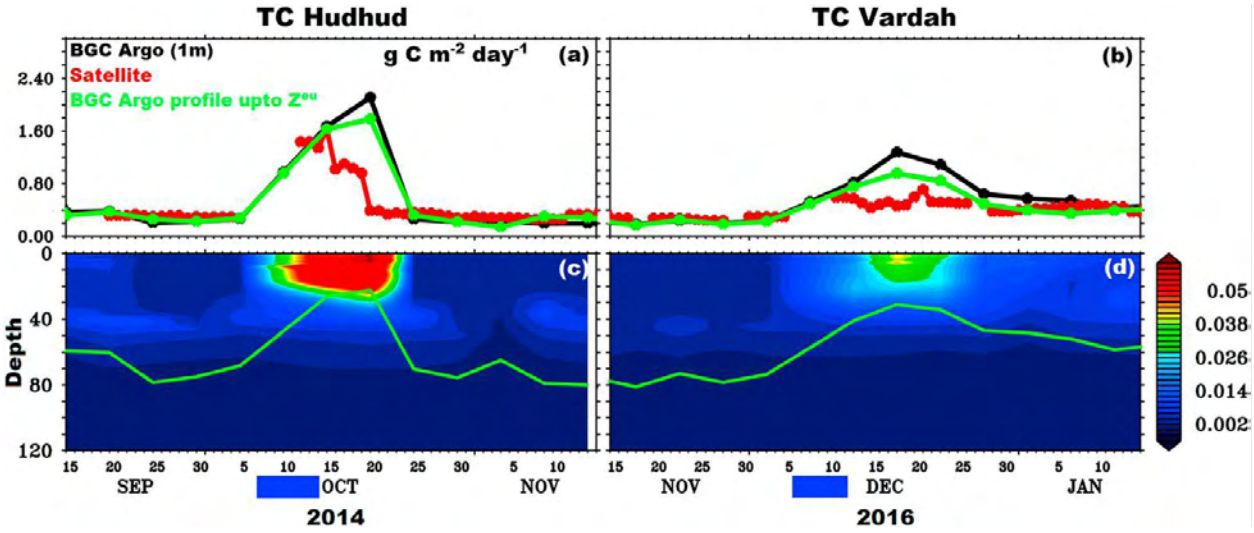

Figure: Temporal evolution of integrated primary productivity (PP) from the surface to euphotic depth (g $Cm^{-2}day^{-1}$):using satellite-merged chlorophyll-a (mg m^{-3}) and Microwave Optimum Interpolation Sea Surface Temperature (°C;PPSatzeu,redline); using surface chlorophyll-a (mg m^{-3}) and surface temperature (°C) from the C-Float and (PPSurfzeu black line);and using chlorophyll and temperature profiles from the C-Float (PPSTD-VGPM-Pzeu ; green line) during (a) TC Hudhud and(c) TC Vardah. Temporal evolution of PP profiles (PPSTD-VGPM-Pz ; g $Cm^{-3} \cdot day^{-1}$) estimated from the BGC-Argo chlorophylland temperature profiles during (b) TC Hudhud and (d) TC Vardah. The green solid line in the panels b and drepresents the euphotic depth. Blue thick line at the bottom of the figure indicates TC Hudhud period (7–14 October 2014;left panels) and TC Vardah (6–12 December, 2016) period. TC = tropical cyclone; C-Float = chlorophyll float.

Ref: *Girishkumar, M.S., Thangaprakash, V.P., Udaya Bhaskar, T.V.S., Suprit, K., Sureshkumar, N., Baliarsingh, S.K., Jofia, J., Pant, V., Vishnu, S., George, G., Abhilash, K.R., Shivaprasad, S. Quantifying Tropical Cyclone's Effect on the Biogeochemical Processes Using Profiling Float Observations in the Bay of Bengal (2019) Journal of Geophysical Research: Oceans, 124 (3), pp. 1945-1963*

La Nina Signature in the East India Coastal Current

Analysis of OSCAR (Ocean Surface Current Analysis Real-time) current and a linear, continuously stratified (LCS) model simulations showed significant interannual variation in the magnitude of the spring East India Coastal Current (EICC) with a decrease in its magnitude in the spring of 2000, 2008 and 2011- years with high negative value of Oceanic Nino Indices were observed due to the dominance of strong La Nina events. Numerical experiments using LCS model to identify the local and remote forcing response on EICC showed that the dynamics of the EICC during spring are dominated by four different forcing processes; local wind along east coast of India, remote forcing response from the eastern and northern boundary of the BoB including islands, interior BoB and the Equatorial Indian Ocean (EIO). During El Nino and normal spring years, strong poleward interannual EICC are due to very weak negligible (order of 0–5 cm s^{-1}) EICC from EIO remote response and in-phase poleward EICC formation using other three forcings. However, during La Nina spring years, weak (order of 0–10 cm s^{-1}) poleward interannual EICC are formed due to destructive interference between equatorward current (order of 10–25 cm s^{-1}) from EIO forcing and in-phase poleward current from the other three forcings. It was found that during with El Nino (La Nina) years, Kelvin wave from EIO via eastern and western boundary of the BoB during spring tend to be upwelling (downwelling). This interannual variation in the propagation of EIO Kelvin waves is associated with the changes in the direction of zonal winds in the EIO due to climate modes like ENSO.

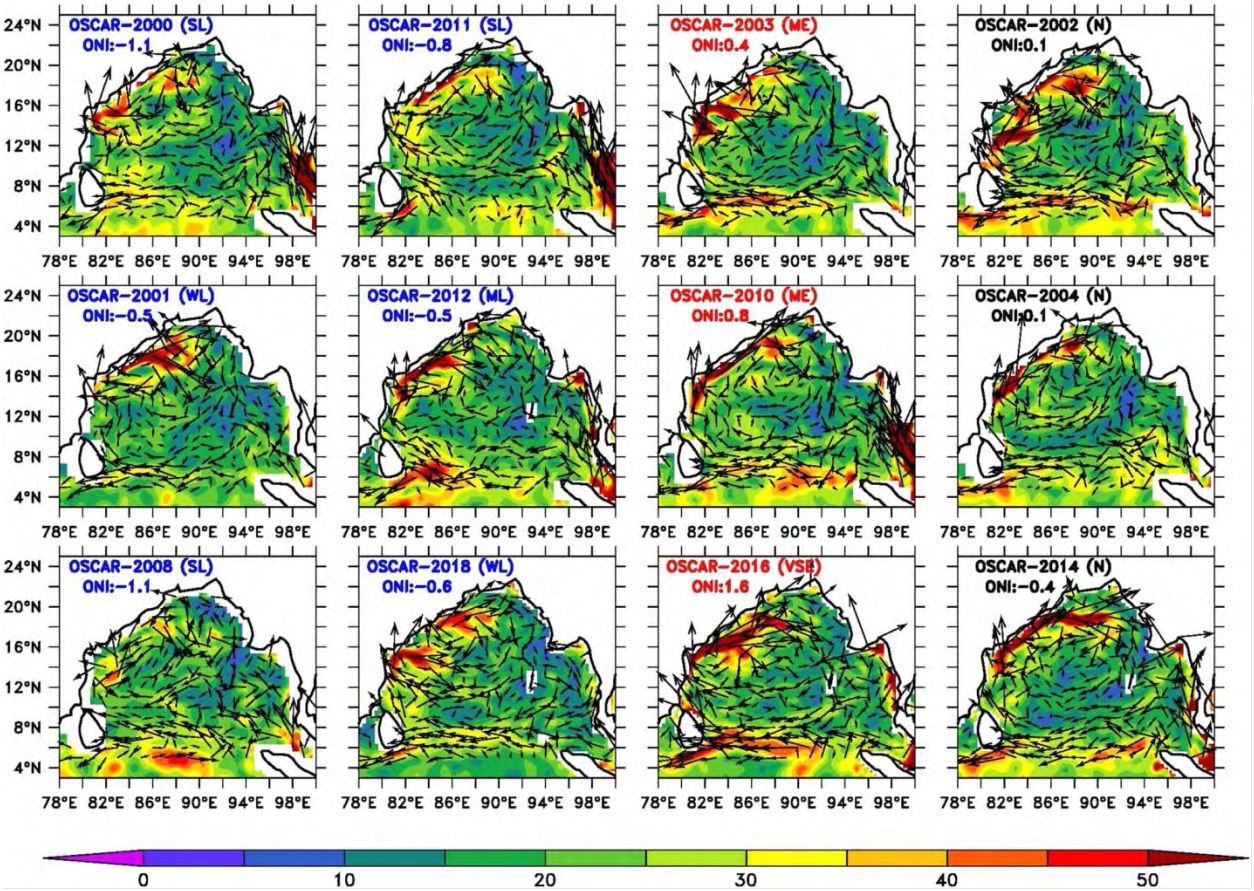

Figure: Magnitude of OSCAR current (cm s^{-1}) at BoB during spring (average of February–April) La Nina (left two column), El Nino (third column) and normal events (fourth column) with current vector overlay. ONI value during spring of the respective year are given in each box. Blue, red and black colour in each box represents La Nina, El Nino and normal event respectively.
Ref: *Mukherjee, A., Kalita, B.K. Signature of La Niña in interannual variations of the East India Coastal Current during spring (2019) Climate Dynamics, 53(1-2), pp. 551-568.*

Andaman and Nicobar Islands and eddies in the western Bay of Bengal

Eddies along western boundary of the Bay of Bengal (WBoB) play an important role in regulating regional climate and marine productivity of the north Indian Ocean. The role of Andaman and Nicobar islands (ANIs) in the formation of eddies along the WBoB was studied using an ocean general circulation model. This study showed that, in the absence of ANIs, there would be a significant reduction in the total number of mesoscale eddies in this region. The impact is particularly evident for the cyclonic eddies as a reduction of ~50% can be noticed in the absence of the islands. In contrast, influence of ANIs on anticyclonic eddies is not homogeneous in the WBoB; while absence of ANIs significantly increases anticyclonic eddies in the central part of the WBoB, a decrease can be noticed in the southern part. We further show that the reduction in number of cyclonic eddies along the WBoB is primarily driven by reduced baroclinic and barotropic instabilities. This process is more conspicuous during winter (October–January) season compared to summer (June–September) and spring (February–May) seasons.

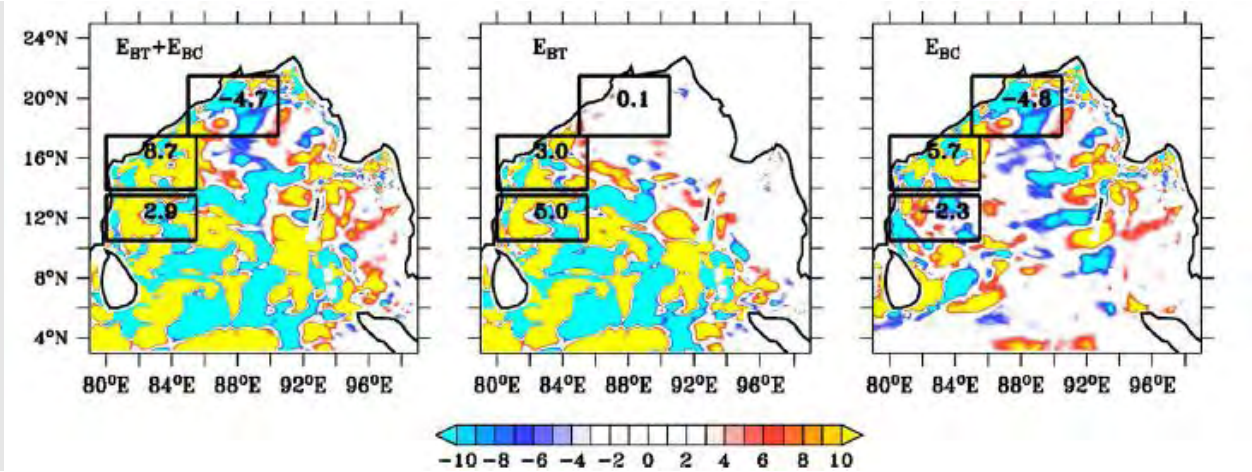

Figure: Winter (October–January) climatology of instabilities based on difference between the model simulations with and without Andaman Islands. Left, middle and right panel shows combination of both barotropic and baroclinic ((EBT + EBC, 10^{-3} m^2s^{-3}), barotropic (EBT, 10^{-3} m^2s^{-3}) and baroclinic (EBC,10^{-3} m^2s^{-3}) instability difference between the model configurations. Number in each square box denotes mean value of the respective domain.

Ref: *Mukherjee, A., Chatterjee, A., Francis, P.A., Role of Andaman and Nicobar Islands in eddy formation along western boundary of the Bay of Bengal, (2019) Nature Scientific Reports, 9, 10152.*

Surface and Sub-surface Ocean Response to Tropical Cyclone Phailin

The upper oceanic thermal response induced by Tropical Cyclone Phailin (9–14 October 2013) under the influence of East India Coastal Current (EICC) and a cyclonic eddy was investigated and contrasted with the response from open ocean region using a high-resolution HYbrid Coordinate Ocean Model simulation. It was found that there was significant cooling (7^o C) inside the cold core eddy and the cooling was negligible (0.5^o C) within the EICC region characterized by the shallow and deeper thermocline, respectively. Analysis of mixed layer heat budget terms showed that the horizontal advection played a significant role in determining the temperature tendency for the location within the EICC, in contrary to the general dominance of vertical processes as reported in previous studies during the cyclone period. The analysis for the locations inside eddy and open ocean concurs with the previous studies showing the dominance of vertical processes toward the temperature tendency. Further, near the coast, the surface cooling was minimal compared to the subsurface cooling, dominantly seen between 50 and 100 m depth. This disparity indicated that the factors responsible for the surface temperature anomalies were different from those of subsurface. Analysis of thermal signatures after the passage of cyclone showed that the EICC and cyclonic eddy contributed to the faster advection of cold wake and recovery of sea surface temperature to the prestorm state.

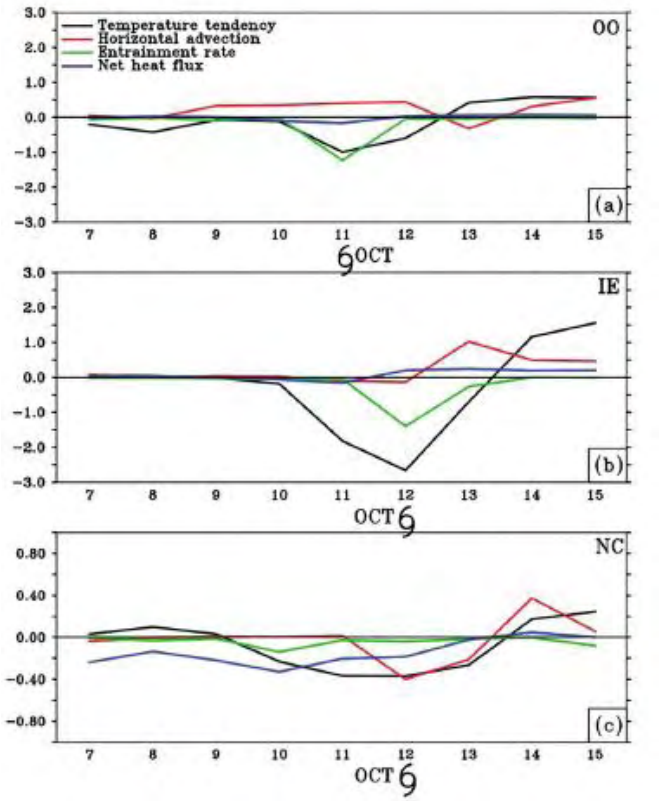

Figure: Time series of various mixed layer heat budget terms across box averaged regions of (a) open ocean, (b) inside eddy, and (c) near coast.

Ref: *Jyothi, L., Joseph, S., Suneetha, P., Surface and Sub-surface Ocean Response to Tropical Cyclone Phailin: Role of Pre-existing Oceanic Features (2019) Journal Geophysical Research Oceans, 124(9), pp. 6515-6530.*

Evaluation of the impact of high-resolution winds on the coastal waves

The efficiency of high-resolution winds in replicating fine-scale features throughout the coastal regions during the pre-monsoon season and explores the effects of high-resolution winds on coastal waves (March–May) has been analysed in this study. Utilizing wind fields from the European Centre for Medium-Range Weather Forecasts (ECMWF) and Weather Research and Forecast (WRF) (3 km), the impact of the diurnal variation of winds on waves is investigated for the coastal region of Tamil Nadu (27.5 km). Then, using readings from wave rider buoys, the improvement in the coastline forecast is calculated. The fine-scale features that the high-resolution wind fields replicated, like land-sea breeze occurrences, were in good agreement with the observational data. The overestimation of wave energy on high frequencies caused by overestimated WRF winds remains a concern in forecasting, however the inaccuracy in the wave height and period is decreased by 8% and 46%, respectively, with the use of high-resolution driving winds WRF over ECMWF. The analysis also demonstrates the value of precise wave forecasting during a pre-monsoon short-duration abrupt wind (12 m/s) event "Kondalkattu" in southern Tamil Nadu at

Rameswaram. Due to the heating of the land surface, a low-pressure area arises over Tamil Nadu, which causes an abrupt increase in winds locally termed as " Kondalkattu". In the high-resolution prediction system with WRF winds, severe winds and sharp waves that cause damage to the property of the coastal population close to Rameswaram were also well simulated.

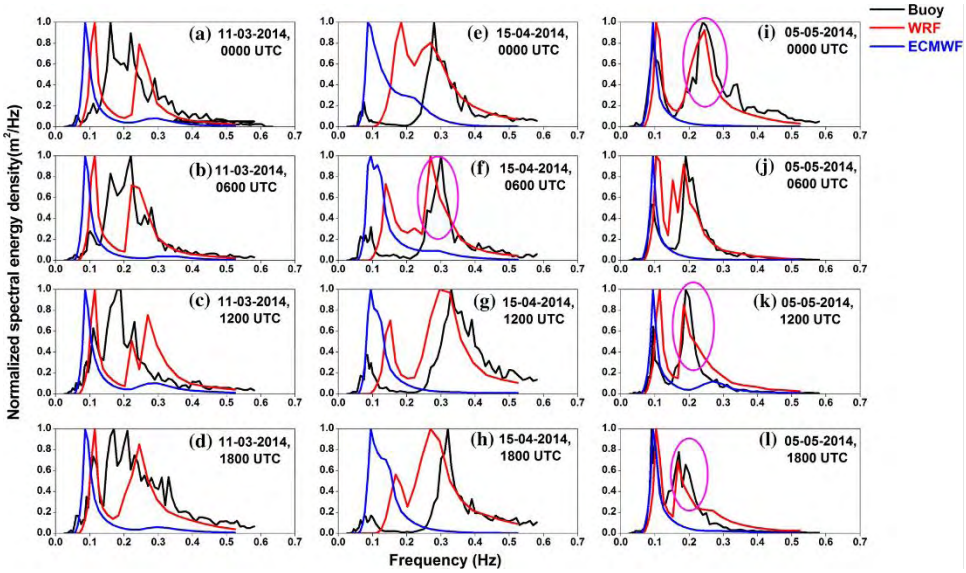

Comparison of frequency–energy wave spectra from (WRF & ECMWF) simulation with observation. The circles marked with pink colour shows good match of WRF spectrum with observation.

Ref: Sirisha, P., Remya, P.G., Modi, A. *et al.* Evaluation of the impact of high-resolution winds on the coastal waves. *J Earth Syst Sci***128**, 226 (2019). https://doi.org/10.1007/s12040-019-1247-x

Improved cyclonic wind fields over the Bay of Bengal

Tropical cyclone induced storm surge and extreme waves pose a significant threat and danger to coastal inhabitants as well cause significant damage to infrastructure. Nevertheless, significant progress has been achieved over the past several years in tropical cyclone modeling, there are however inherent limitations in the quality of real-time wind forecast for near-field and far-field regions surrounding the cyclone eye. The reliability and quality of computed storm surge and extreme wind-waves remains a challenge due to their primary association with the quality of input wind forcing. Parametric wind field models are widely used owing to their simplicity and also in realistically representing the inner core region of cyclones. On the other hand, global atmospheric models have inherent limitations in underestimating the inner core winds, although they produce outer core winds much better as compared to the parametric formulation. In this study a blending technique is proposed which takes advantage of both these wind fields thereby producing a blended wind field using a smoothing algorithm and superposition technique that provides realistic estimates of both inner and outer core winds. Numerical simulations with a coupled wave-hydrodynamic model using both blended and the parametric winds were also verified against in situ data. The study reveals that simulations using blended winds performed better and has practical relevance to real-time operational forecasts.

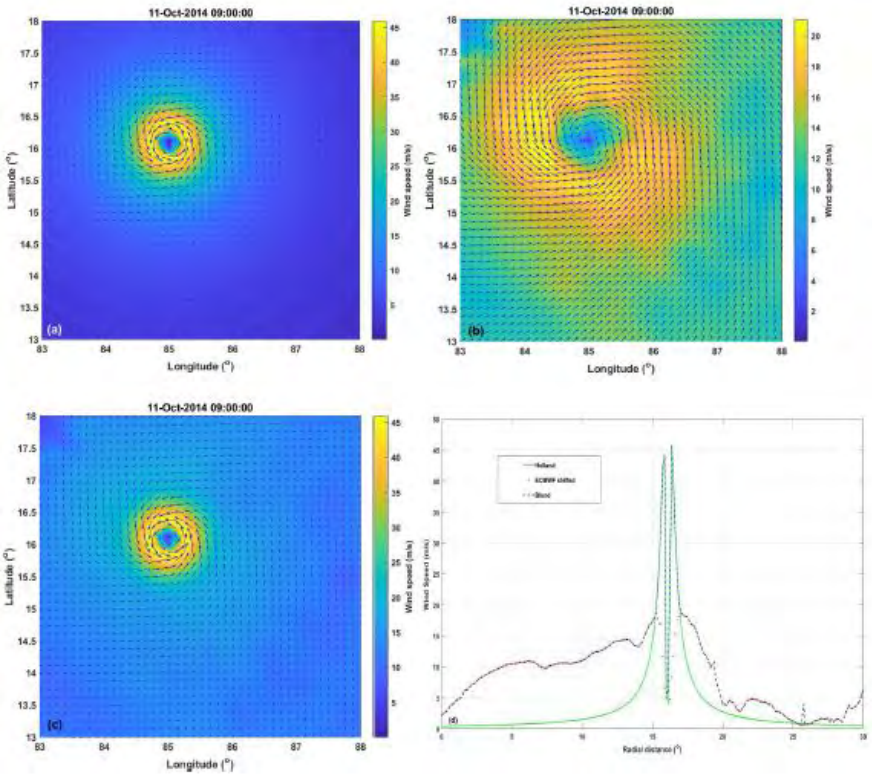

Figure: Depiction of (a) parametric wind field, (b) centered shifted ECMWF wind field, (c) blended wind field and (d) radial profile of parametric, ECMWF and blended wind fields. Hudhud cyclonic case is considered in this picture.

Ref: *Murty, P.L.N., Srinivas, K.S., Rama Rao, E.P., Bhaskaran, P.K., Shenoi, S.S.C., Padmanabham, J. (2020). Improved cyclonic wind fields over the Bay of Bengal and their application in storm surge and wave computations Applied Ocean Research, 95, art. no. 102048.*

Modeling slippery layers in the northern Bay of Bengal

A "slippery" layer observed during September 2011 at a National Institute of Ocean Technology (NIOT) mooring deployed at 18^0 N, 89^0 E in the northern Bay of Bengal (BoB) was modelled by a simple slab-type dynamical model and a turbulence closure-based model. The mooring was located close to the mouths of the huge rivers draining the Indian subcontinent. The lateral advection of riverine water masses past the mooring resulted in a shallow brackish layer 10–15m deep bounded by a strong halocline below, giving rise to the possibility of a slippery layer gliding past the layers below. The strong currents in this slippery layer were simulated by the simple. In addition, a second moment turbulence closure-based model, driven by surface data from the buoy was also used to simulate the water mass structure and upper layer currents during the event. Both the slab and turbulence-closure models reproduce currents in the slippery layer reasonably well overall, although the currents are somewhat overestimated. This "haline" slippery layer observed in the BoB complements well the "thermal" slippery layers that have been observed under certain conditions during strong diurnal heating of the upper layers of the ocean.

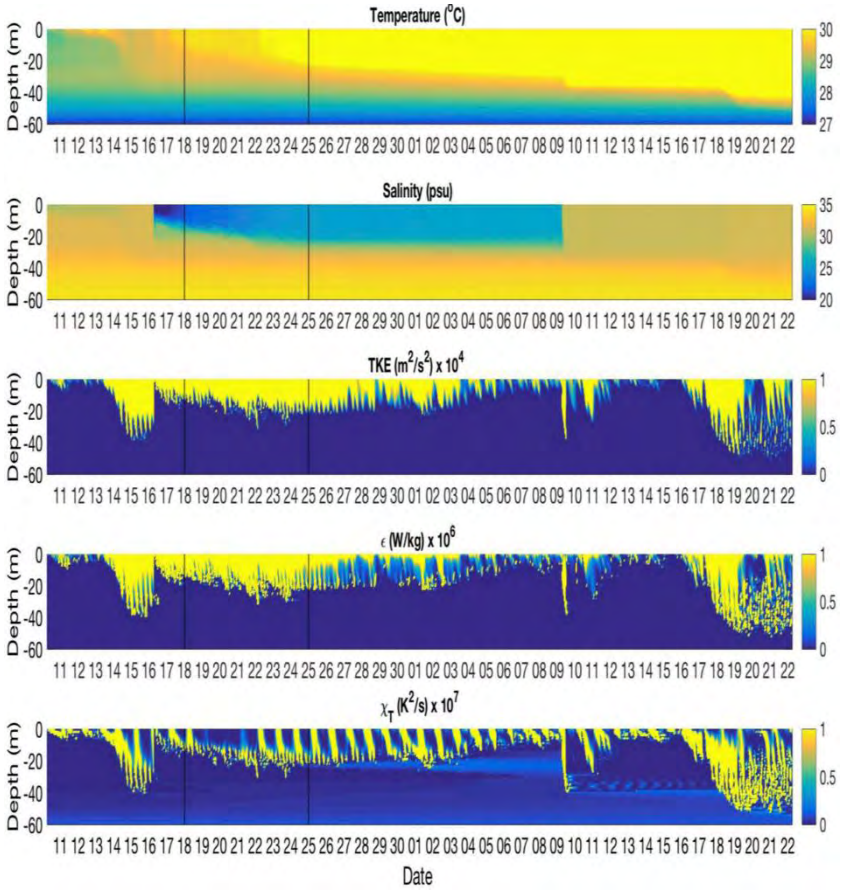

Figure: Time-depth plots of model results (temperature, salinity, turbulence kinetic energy, TKE dissipation rate, and the dissipation rate of temperature variance) from 10 September to 22 October 2011, the simulation period. Note the simulated intrusion of less saline water mass on 16 September and back to a more saline water mass on 9 October. The black vertical lines delineate the focus period containing slippery layers. Reinitializations of the model can be clearly seen in the salinity plot on 16 September and 9 October as a sharp change in the salinity profile.

Ref: *Jampana, V., Ravichandran, M., Kantha, L., Rahaman, H. Modeling slippery layers in the northern Bay of Bengal (2019) Deep-Sea Research Part II: Topical Studies in Oceanography, 168, art. no. 104616.*

Widespread cooling of the Bay of Bengal by tropical storm Roanu

Data from a Lagrangian float, measuring temperature, salinity and velocity profiles in the upper 80 m and 3 Argo floats were analyzed to investigate the widespread SST cooling (1.5–2^0 C) of the Bay of Bengal occurred in response to cyclone Roanu 2016, a weak, pre-monsoon storm. At the Lagrangian float, cooling was primarily due to mixing of the warm (32^0 C), fresh cap formed during the previous months of light winds and clear skies, accounting for about half of the cooling. Air-sea heat fluxes played a secondary role, accounting for about a quarter of the cooling. The depth of mixing was diagnosed by two measures: a traditional mixed layer depth and a "mixing depth" defined as the deepest depth unstable to shear instability. The mixing depth was roughly

twice (~65 m) the mixed layer depth (~35 m), illustrating the importance of the "transition layer" between them. The mixed layer restratified into 2 layers within a day after the end of the storm with near-inertial frequency waves gented by the storm increasing the diapycnal mixing rates at the depth of the transition layer to about 10^{-4} m^2s^{-1}. A popular upper ocean mixing model (PWP) driven by heat, moisture and momentum fluxes from reanalysis products (ERA-5 and CCMP) reproduced the maximum mixed layer depth to within a meter; maximum mixing depth was underpredicted by 10 m. These results were insensitive to uncertainties in the air-sea forcing. The change in SST was underestimated by 0.7^0 C and the model predicts few of the observed variations in mixed layer salinity. Some of these errors are due to uncertainties in air-sea fluxes, but lateral processes must also play a role, both during the storm and during the subsequent restratification. Data from the Argo floats, although much less detailed, show similar patterns with better simulations of mixed layer depth than of temperature and salinity evolution. Large-scale models generally underestimate the stratification of the upper 50 m of the Bay of Bengal leading to biases in modeling the important air-sea interactions that occur. These results suggest that although these errors may partially be due to errors in modelled vertical mixing rates, errors in modeling horizontal variability and its interaction with vertical mixing are also likely to be important.

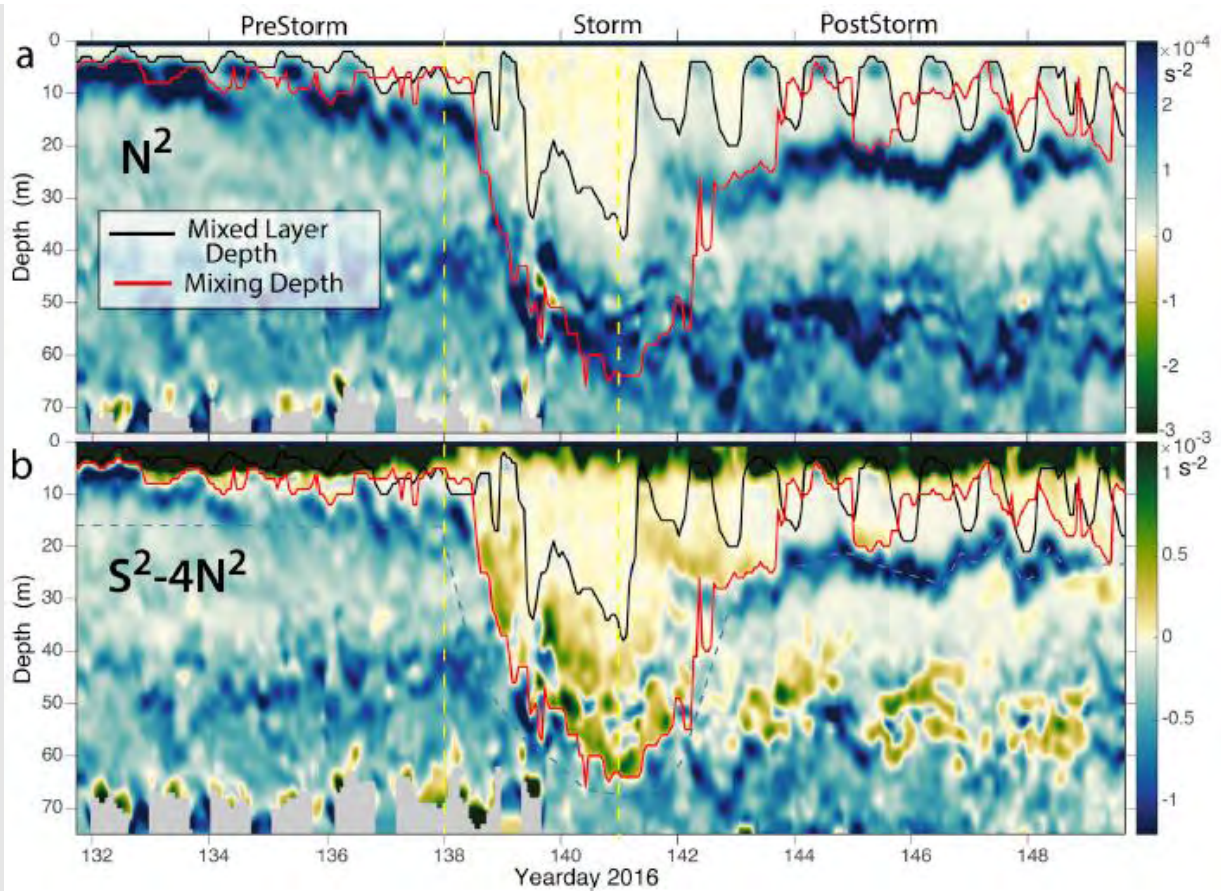

Figure: Comparison of mixed layer depth (black lines) and mixing depth from reduced shear (red lines) on plots of a) stratification and b) reduced shear. Thin dashed blue line shows depth limit imposed on computation of mixing depth. Yellow vertical dashed lines divide the pre-storm, storm

and post-storm periods. The color scales on the two panels are adjusted to scale N2 in the same way, so that for $S^2 = 0$, they would be identical.

Ref: *Kumar, B.P., D'Asaro, E., Suresh kumar, N., Ravichandran, M. Widespread cooling of the Bay of Bengal by tropical storm Roanu (2019) Deep-Sea Research Part II: Topical Studies in Oceanography, 168, art. no. 104652.*

Generation and Propagation of internal tides in the Bay of Bengal

Generation and propagation of internal tides in the western Bay of Bengal (BoB) were investigated using observations from Acoustic Doppler Current Profilers and simulations from a very high resolution numerical ocean model. Observations show that semidiurnal internal tides in the southern and northern parts of the western BoB are more energetic during neap phase of the local barotropic tide than those during spring phase. Numerical simulations indicate that internal tides generated over the Andaman-Nicobar Ridge propagate westward for about 1,000–1,450 km across the BoB and finally impinge on the continental slopes off the east coast of India after 5–7 days. Energetic internal tides observed during the neap phase of the barotropic tides in the western BoB are mainly due to the arrival of remotely generated internal tides. It is also shown that the variation in the onshore transmission of these remotely generated internal tides due to the topographic slope in the western BoB controls the strength of internal tide activity along the shelf. Superposition of reflected internal tides from continental slope, which are very steep in some regions and onshore propagating-waves generate partly standing waves. Numerical experiments suggest that internal tides coming from remote sources account for more than 80% of the total internal tide energy observed in the western BoB. Internal tide energy dissipation on the continental margins of the western BoB is about 3 to 4 times larger than the local generation, indicating that this region is a sink for remotely generated internal tide energy.

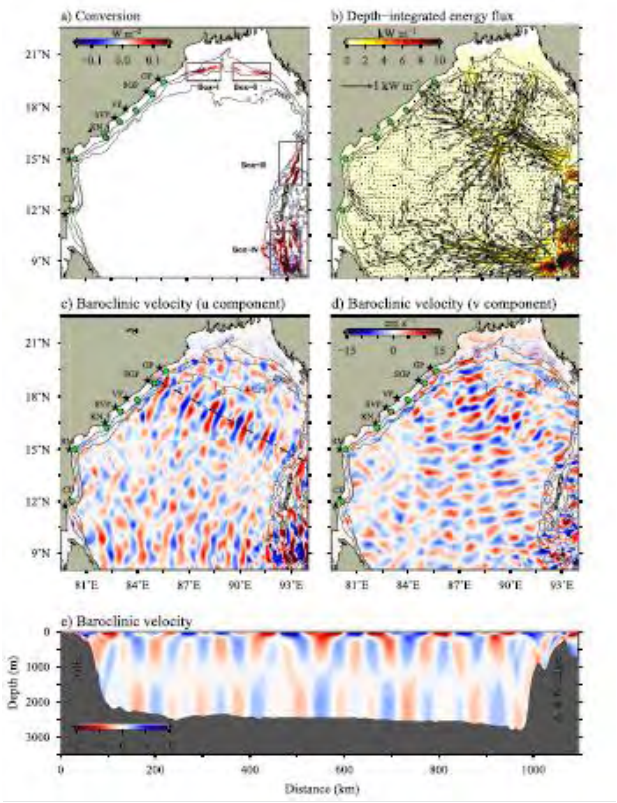

Figure: (a) Barotropic to baroclinic M2 energy conversion rate. Boxes indicate major internal tide generation regions in the BoB. (b) Depth-integrated baroclinic M2 energy flux in the BoB. Bathymetric contours of 100, 1,000, and 2,000 m are shown. Instantaneous zonal (c) and meridional (d) velocity component of semidiurnal internal tides at surface derived from model simulation (14 March 2012 18:00). Green circles represent the locations of ADCP moorings on the shelf. (e) Vertical section of instantaneous baroclinic velocity (14 March 2012 18:00) of semidiurnal internal tide along the east-west transects in the BoB (black dashed line) shown in (c).

Ref: *Jithin, A.K., Francis, P.A., Unnikrishnan, A.S., Ramakrishna, S.S.V.S. Modeling of Internal Tides in the Western Bay of Bengal: Characteristics and Energetics (2019) Journal of Geophysical Research: Oceans,124(12), pp.8720-8746.*

2. Chemical Oceanography Section

Impact of the model resolution on the simulation of upper-ocean biogeochemistry of the Arabian Sea

The resolution of the model emerges to be an important factor in simulating the real oceanic features. Validation of the physical and biogeochemical parameters simulated by two coupled bio-physical models having spatial resolutions 1/12° (~9 km) and 1/4° (~25 km) configured using Regional Ocean Modeling System (ROMS) with the observations from remote sensing, in-situ ship-borne, and Biogeochemical-Argo (BGC-Argo) floats showed that the high-resolution model reproduced the ocean physical and biogeochemical dynamics, and their seasonality more

efficiently. The upper ocean dynamics associated with the variability of mixed layer depth, persistent occurrence of deep chlorophyll maxima, and seasonal phytoplankton blooms. as well as deep ocean characteristics of oxygen minimum zone were much effectively captured by the high-resolution model than by its counterpart. Similarly, the former model performed very well in reproducing the upwelling dynamics over the eastern continental shelf indicating that the open ocean-coastal coupling has been better established. It was shown that the realistic representation of the eddy fields by the high-resolution model leads to the better representation of the ocean fields in comparison to the coarse resolution model.

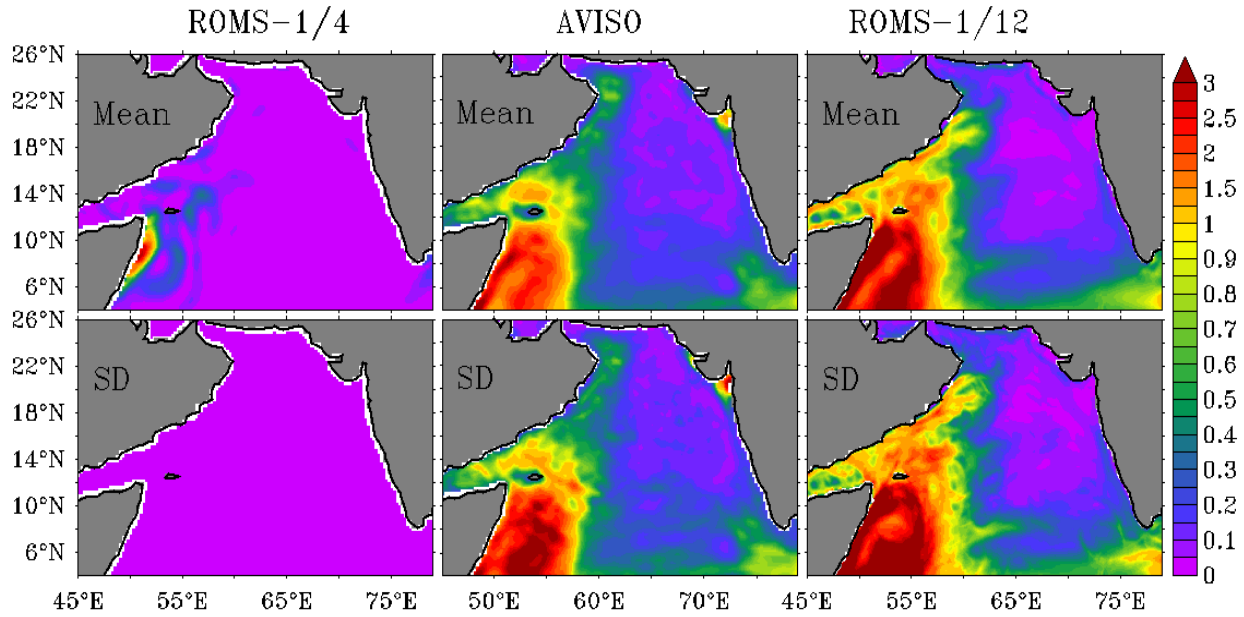

Figure: The capability of ROMS-1/12 model in capturing the eddy field is clearly evident in the comparison between model and observation to produce eddy kinetic energy. In particular, mean and variability of eddy kinetic energy field is reasonably captured by higher resolution model set-up in comparison with coarse resolution model. It is to be noted that mean eddy kinetic energy field in the ROMS-1/4 is one order less than satellite altimetry and ROMS-1/12.

Ref: *Chakraborty, K., Kumar, N., Girishkumar, M.S., Gupta, G.V.M., Ghosh, J., Udaya Bhaskar, T.V.S., Thangaprakash, V.P. Assessment of the impact of spatial resolution on ROMS simulated upper-ocean biogeochemistry of the Arabian Sea from an operational perspective (2019) Journal of Operational Oceanography, 12 (2), pp. 116-142*

Oil spill trajectory prediction with high-resolution ocean currents

Merchant Vessel (MV) Rak sunk at 72.4865°E, 18.7715°N, on 4 August 2011. As per the information from Indian Coast Guard, ~122.5 tons of fuel oil was spilled from the vessel during 5 to 12 August 2011. Oil spill trajectory model, GNOME, was forced with ocean currents from Indian Ocean Forecasting System (INDOFOS) and High-resolution Operational Ocean Forecasting and reanalysis System (HOOFS) individually, to simulate the oil drift pattern from

MV Rak during the spill period. Wind drift was obtained from European Centre for Medium Range Weather Forecast (ECMWF). The trajectory obtained while forcing oil spill model with wind drift and HOOFS currents is called HR track and the trajectory obtained from that of INDOFOS currents is called LR track.

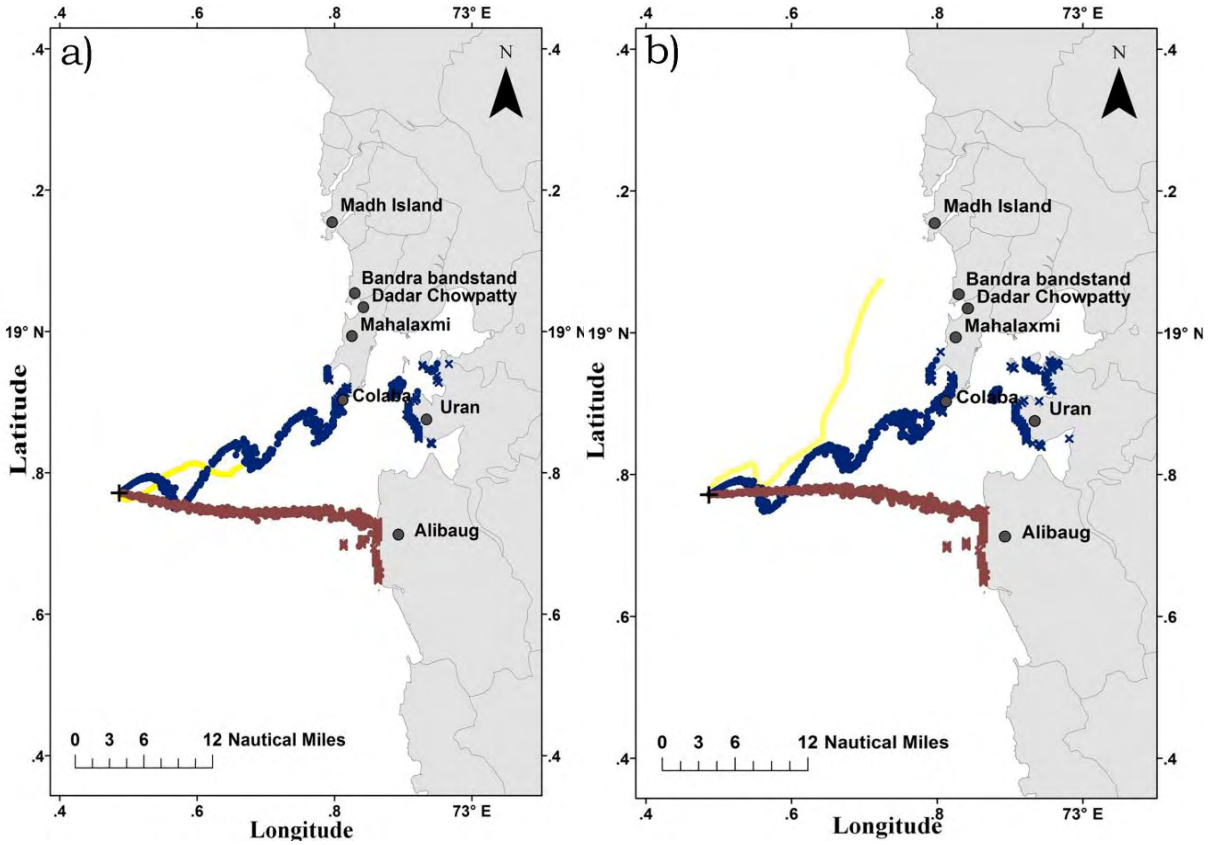

Comparison of LR and HR tracks with SAR observation: a) 08August 2011, 23.00 hours, b)09 August 2011, 23.00 hours. The black + symbol denote the spill location. The brown colored trajectory is generated from LR currents and the blue colored trajectory is generated from HR currents. The Yellow colored track is the observed track of the oil slick from SAR observation. The blue (brown) colored x symbol denotes the beached locations of oil slicks from HR (LR) track. The blue (brown) colored splots denote the floating locations of oil slicks from HR (LR) track.

It was found that, On 2300 hours of 8 August 2011, the Root Mean Square Error (RMSE) of the distance between the SAR track and LR track was ~3.24 NM and they were apart by a maximum distance of 3.9 Nautical Miles (NM). But the HR track was in agreement with the SAR track, which means RMSE is nil. The next day by 2300 hours, the RMSE of the distance between the SAR track and LR track was ~9.3 NM and a maximum distance of 18NM was found. But, with HR track a lesser RMSE (6.41 NM) was obtained with lesser separation distance of 12 NM. It was noticed from the above simulation that oil drift pattern obtained when forced with ocean currents from HOOFS was in better agreement with the actual track, compared to the one obtained while using INDOFOS currents.

***Ref**: Prasad, S.J., Francis, P.A., Balakrishnan Nair, T.M., Shenoi, S.S.C. Vijayalakshmi, T. (2020). Oil spill trajectory prediction with high-resolution ocean currents. Journal of Operational Oceanography, 13 (2), pp. 84-99*

Potential Mechanisms Responsible for Spatial Variability in Intensity and Thickness of Oxygen Minimum Zone in the Bay of Bengal

Spatial variability in boundaries and thickness of oxygen minimum zone (OMZ) is derived based on measured dissolved oxygen data obtained from sensors on board biogeochemical (BGC) Argo floats between 2013 and 2019 in the Bay of Bengal (BoB). Upper and lower boundaries of the OMZ varied from 60 to 200 m and 100 to 800 m respectively with the thickness of 80–650 m in the BoB. Relatively thicker OMZ is noticed in the northern than southern BoB associated with stratification. The oxygen concentrations in the OMZ in the NW was low (<1.5 µM) than NE BoB (2.5 µM) indicating that thick and intense OMZ occurs in the NW region associating with stratification and high primary production. Significant decrease in particle-back-scatter signal was observed toward offshore from shelf indicating organic matter from the shelf sediments may be supporting bacterial carbon demand in the OMZ. The particle backscatter signal peaked in the OMZ region with a higher signal in the north than southern BoB and it is consistent with the low oxygen concentration in the former indicating that organic matter from shelf sediments may be supporting carbon needs in the OMZ. In addition to this, the occurrence of eddies significantly controls the intensity of the OMZ in the BoB through mixing at the upper boundary of OMZ. Therefore, this study suggests that spatial variations in intensity of OMZ in the BoB are governed by stratification, primary and export productions, organic matter decomposition, and eddy-driven mixing

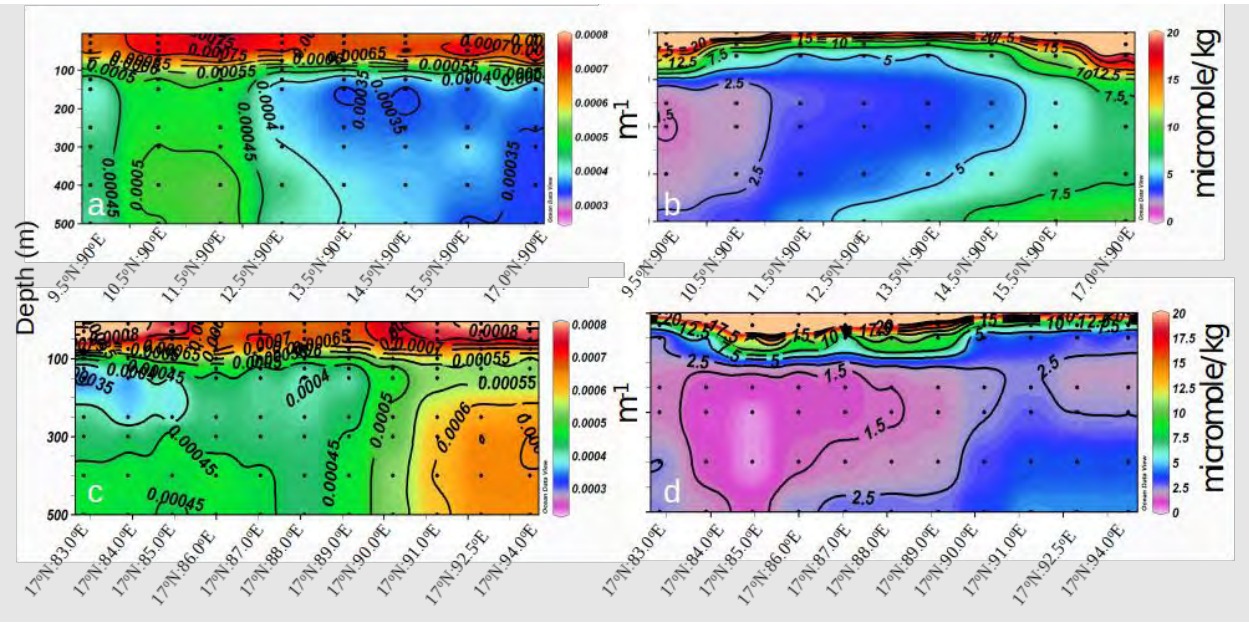

Figure: Depth profiles of a) particle back-scatter (m-1) and b) dissolved oxygen (M) along the 90° E and (c) and (d) representing 17° N respectively.

***Ref**: Udaya Bhaskar, T. V. S., Sarma, V. V. S. S., & Pavan Kumar, J. (2021). Potential mechanisms responsible for spatial variability in intensity and thickness of oxygen minimum zone in the Bay of Bengal. Journal of Geophysical Research: Biogeosciences, 126, e2021JG006341. https://doi.org/10.1029/2021JG006341*

Impact of coastal upwelling dynamics on the pCO_2 variability in the southeastern Arabian Sea

The Upwelling Systems are the most productive areas in the world ocean. Their high productivity is intimately linked with shallow, intense Oxygen Minimum Zones, which have high CO_2 concentrations, low pH values, and shallow aragonite saturation horizons. When these waters upwell and impinge on the euphotic zone, they impact the surface ecosystem and release CO_2 and N_2O, strong greenhouse gases, into the atmosphere. The physical and biogeochemical processes associated with upwelling strengthen the biological pump, which increases the biological contribution to the seasonal evolution of pCO_2 relative to the thermodynamic component. The upwelling zones are known to be biogeochemically active sites and are supersaturated with CO_2 with respect to the atmosphere due to the input of carbon-rich waters from deeper layers. However, the nutrient-rich water due to upwelling fuels the primary production and lowers the pCO_2. These two processes potentially have an effect on the variation of CO_2 across the sea-air interface.

The study examines the impact of the coastal upwelling dynamics on the surface ocean pCO_2 variability in the southeastern Arabian Sea during the southwest monsoon and discerns the factors controlling its spatio-temporal variability. The enhancement of upwelling-driven dissolved inorganic carbon is more in the near-surface waters than its removal by net biological processes in the southeastern Arabian Sea. The surface ocean pCO_2 variability driven biological processes is notable only in the southern part of the southeastern Arabian Sea but not significant in controlling pCO_2 variability. The upwelling-driven physical dynamics subjugates the biological processes in inducing the surface ocean pCO_2 variability in the southeastern Arabian Sea.

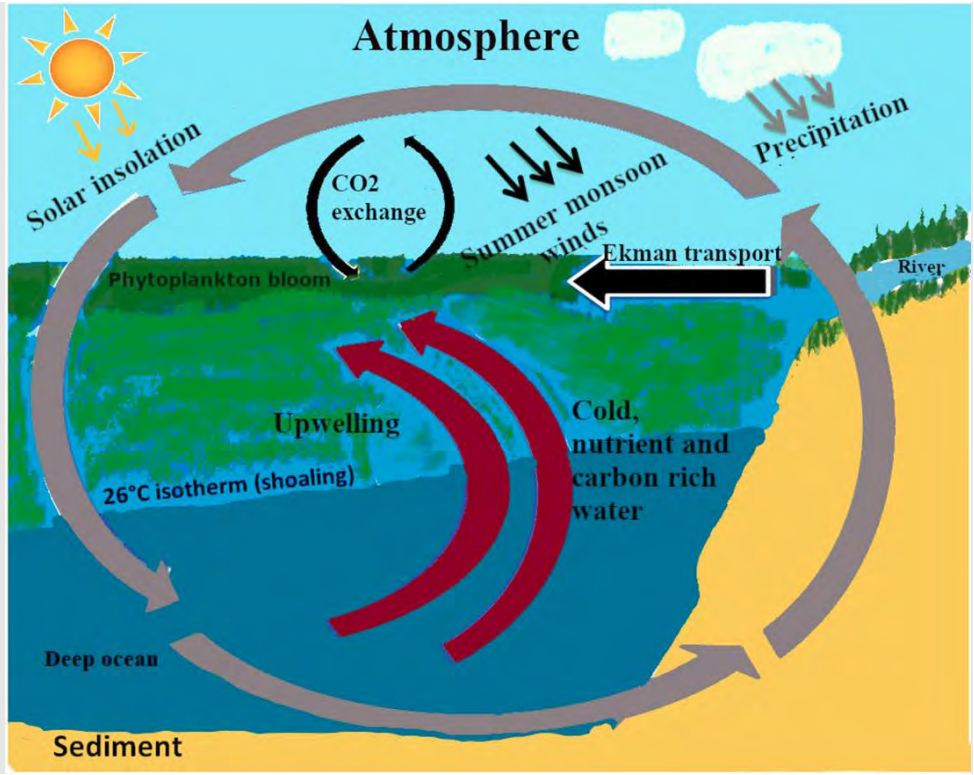

Figure. A schematic diagram illustrating the influence of coastal upwelling dynamics on the upper ocean carbon cycle.

Ref: *Ghosh, J., Chakraborty, K., Bhattacharya, T., Valsala, V., & Baduru, B. (2022). Impact of coastal upwelling dynamics on the pCO2 variability in the southeastern Arabian Sea. Progress in Oceanography, 203, 102785.*

Simulating the spatial and temporal distribution of oil spill over the coral reef environs along the southeast coast of Mauritius: A case study on MV Wakashio vessel wreckage

MV Wakashio spilled ~1000 tons of Fuel oil at 20°26'17.2"S 57°44'40.7"E off Mauritius on 06 August 2020. The spilled pollutant spread along the southeast coast of Mauritius. Simulated oil drift pattern agreed well with the oil slick signature obtained from Sentinel -1A data on 10 August 2020. Hence, the impact of oil spill over associated coral reef classes have been estimated by superimposing the oil drift pattern over coral reef region. It was found that on 08 August 2020, the reef flats were highly affected.

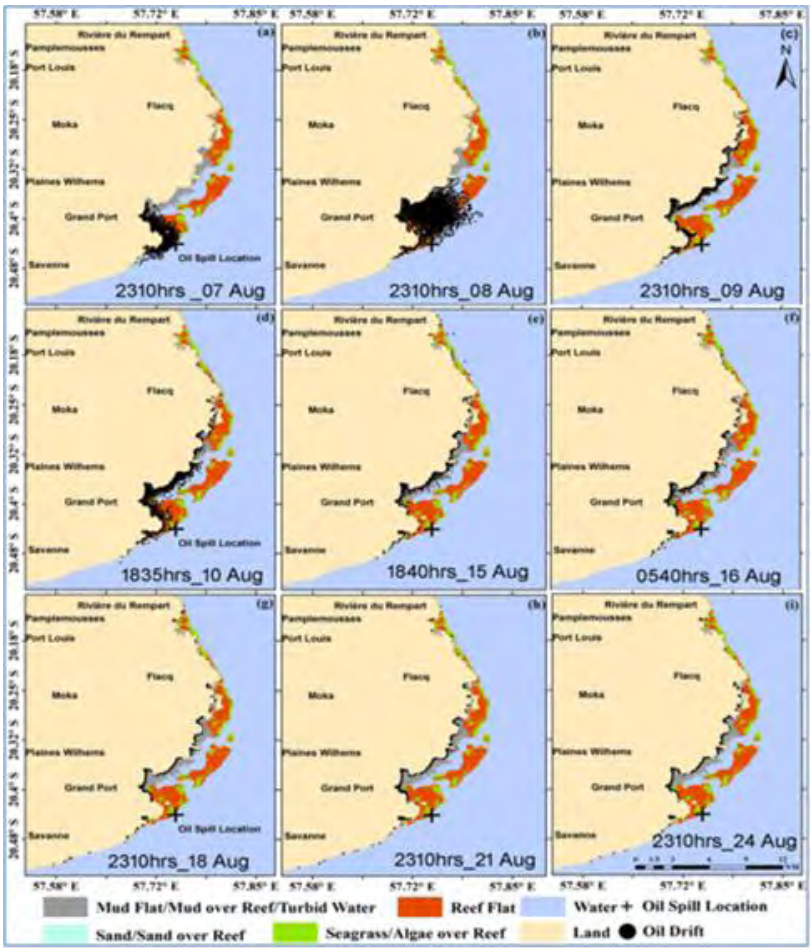

Figure: Simulation results depicting the trajectory of spilled oil and its spatial extent of impact on reef flats.

Ref: Prasad, S. J., Nair, T. M., Joseph, S., & Mohanty, P. C. (2022). Simulating the spatial and temporal distribution of oil spill over the coral reef environs along the southeast coast of Mauritius: A case study on MV Wakashio vessel wreckage, August 2020. *Journal of Earth System Science*, *131*(1), 1-10.

Improved prediction of oil drift pattern using ensemble of ocean currents

An attempt was made to generate an oil spill advisory using a weighted ensemble of ocean currents. In this study, the oil spill trajectory model, General National Oceanic and Atmospheric Administration (NOAA) Operational Modeling Environment (GNOME) was forced using a weighted ensemble of ocean currents for the Heavy Furnace Oil (HFO) spill reported off Ennore port during 0400 hours (IST) of 28 January 2017. The inverse-variance weighting method was used to estimate weights by comparing zonal and meridional components of individual model ocean currents, with that of High Frequency (HF) Radar currents. The zone of HFO spread obtained while using an ensemble of ocean currents was compared with oil slick signatures obtained from Synthetic Aperture Radar (SAR) data on 0600 hours (IST) of 29 January 2017. It

was noted that the trajectory patterns obtained from the weighted ensemble of ocean currents were well within the observed zone of oil slicks, compared to that of individual model ocean currents.

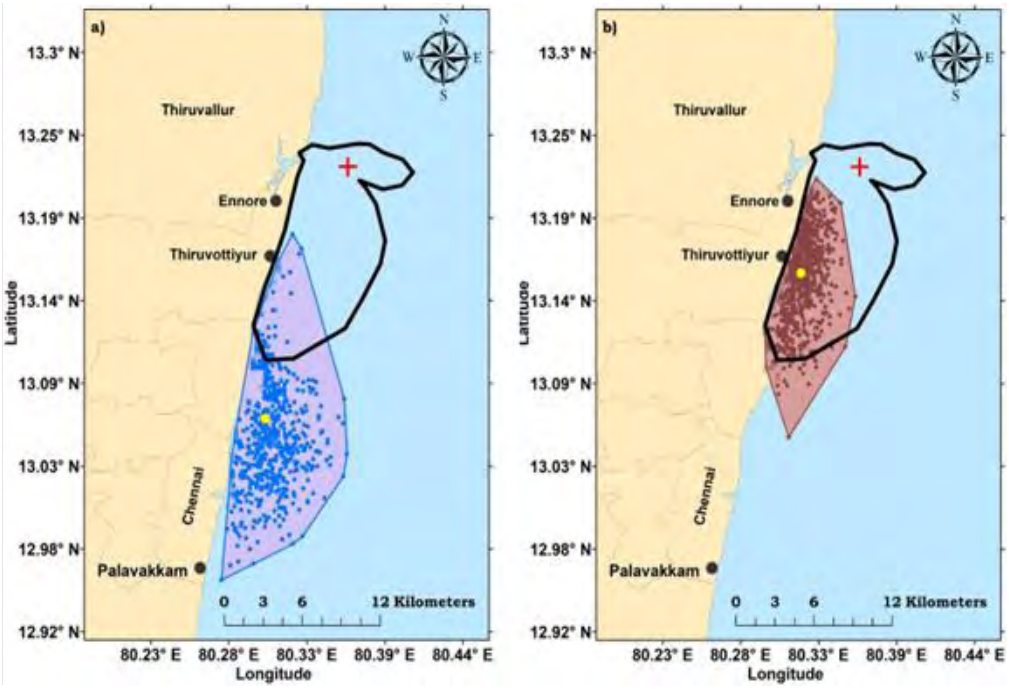

Figure: Comparison of oil drift patterns with SAR data. The red plus symbol denotes the HFO spill location. The black polygon is the zone of observed oil remnants on 0600 hours of 29 January 2017 from SAR data. The yellow circle denotes the mean position of oil particles. (a) The x (dot) denotes the beached (floating) status of drifted HFO while using Operational ROMS (R) currents. The blue polygon is the convex hull of HFO particles while using R currents. (b) The brown x (dot) denotes the beached (floating) status of drifted HFO particles while using Ensemble of currents. The brown polygon is the convex hull of HFO particles after using Ensemble of currents.

***Ref**: Prasad, S.J., Balakrishnan Nair TM and Balaji B. (2022) "Improved prediction of oil drift pattern using ensemble of ocean currents."Journal of Operational Oceanography 1-16.*

Assessment of an ocean-ecosystem model in simulating the Indian coastal marine ecosystem dynamics

This study describes an assessment of an ocean-ecosystem model in simulating marine ecosystem dynamics in the Indian coastal waters. Long-term sustained in-situ observations of temperature, salinity, chlorophyll-a and dissolved oxygen (DO) collected in the coastal waters of India, and ship-based observations are used for this assessment. The model captures observed trend of temperature, salinity and chlorophyll-a with high correlation in both eastern and western shelf waters except for salinity and DO along west and DO along east coast. The model performs very well in simulating the Indian coastal shelf ecosystem dynamics. The seasonal occurrence of prominent phytoplankton bloom in the central-east coast during pre-monsoon, south-west coast during monsoon and north-west coast during post-monsoon is realistically reproduced by the model. The model also reproduces the seasonal presence of significantly low DO content in the

upwelled water at a shallow depth leading to coastal hypoxia in the south-west and central east coast of India during summer monsoon. A fine-tuned model is useful in understanding better Indian coastal shelf ecosystem and predicting future changes in time and space, like the occurrence of coastal hypoxia or anticipating phytoplankton blooms. Such information is useful for predicting potential fishing grounds in coastal waters and fisheries management.

Figure: Schematic showing the study area. Long-term sustained time-series stations established under SATCORE project are shown as ( ). Blue dots are depicting the cruise stations along 100 m depth contour in the western continental shelf of India.

Ref: Chakraborty, K., Lotliker, A. A., Majumder, S., Samanta, A., Baliarsingh, S. K., Ghosh, J., ... & Shanmugam, P. (2019). Assessment of model-simulated upper ocean biogeochemical dynamics of the Bay of Bengal. Journal of Sea Research, 146, 63-76.

Evaluating controlling factors of the seasonal cycle of surface ocean pCO_2 and pH in the northern Indian Ocean

A study has been carried out examining the seasonal variability of surface ocean pCO_2 and pH in the northern Indian Ocean. It aims to identify their controlling factors using a high-resolution, regional ocean-ecosystem model simulation and available surface ocean carbon observations. The seasonal variability of pCO_2 and pH of the northern Indian Ocean is attributed to the changes in surface temperature (T), dissolved inorganic carbon (DIC), total alkalinity (ALK), and salinity (S). The western Arabian Sea has an enormous seasonal variance of pCO_2 due to coastal upwelling

dynamics. In contrast, the seasonal variance of pCO_2 in the Bay of Bengal is governed by the upper ocean mixed layer dynamics, albeit with smaller amplitudes. The contribution of T (DIC) in the seasonal variance of pCO_2 and pH at the western Arabian Sea is ±90 (∓100) µatm and ±0.18 (∓0.20) pH units, respectively. The contribution of ALK and S is complementary to each other in inducing seasonal variances of pCO_2 and pH in the southeastern Arabian Sea with a magnitude of ±5~10 µatm and ±0.02 pH units, respectively. In the northern Bay of Bengal, salinity plays a significant role in controlling seasonal variability of pCO_2 and pH with amplitudes of roughly ±20 µatm and ±0.18 pH units, respectively, along the pathways of freshwater spreading. The maxima of seasonal amplitudes of pCO_2 and pH occur during April-May and August-September for both basins. This study highlights the hotspots of pCO_2 and pH in the northern Indian Ocean, where observational efforts to monitor pCO_2 and pH become an essential requirement.

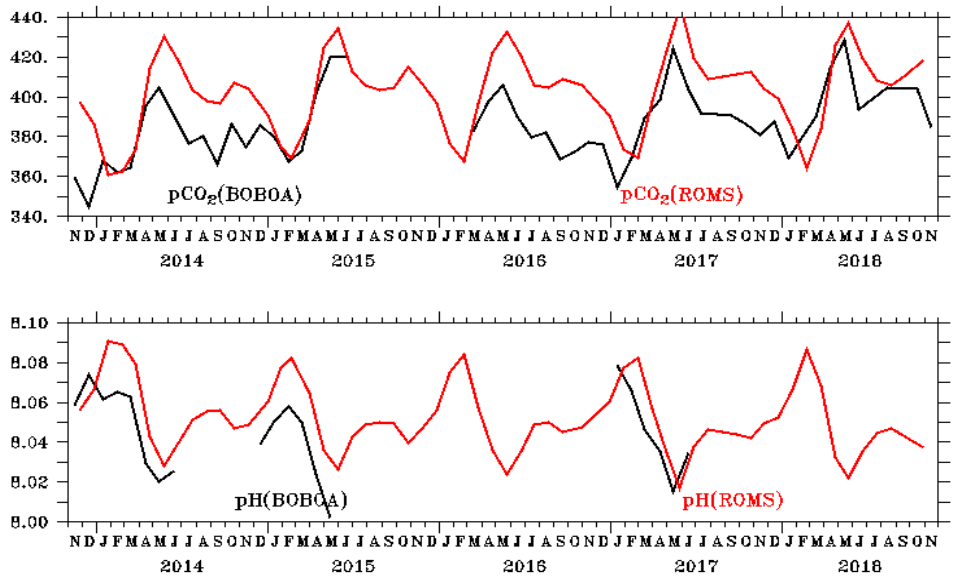

Figure: Comparison of surface ocean pCO_2 (µatm) and pH (unit in negative log of H+ ions) simulated by the model (in red colour) against BOBOA mooring measurements (in black colour).

Ref: Chakraborty, K., Valsala, V., Bhattacharya, T., & Ghosh, J. (2021). Seasonal cycle of surface ocean pCO2 and pH in the northern Indian Ocean and their controlling factors. Progress in Oceanography, 198, 102683.

Outwelling of total alkalinity and dissolved inorganic carbon from the Hooghly River to the adjacent coastal waters

The seasonal variability of the lateral flux of total alkalinity (TAlk) and dissolved inorganic carbon (DIC) of the tropical Hooghly estuary is analyzed in this work. In situ observations of water temperature, salinity, dissolved oxygen, TAlk, and pH were measured in four different stations of the Hooghly estuary. It was measured once every month during 2015–2016, and subsequently, DIC was estimated. A carbon budget was constructed to quantify carbon flows through the freshwater-marine continuum of the Hooghly estuary, and plausible impacts on the adjacent

coastal ocean, the northern Bay of Bengal, were examined. The biogeochemical mass balance box model was used to compute the seasonal flow of carbon flux, and subsequently, the annual budgeting of lateral fluxes of TAlk and DIC to the adjacent coastal ocean was carried out. The net annual TAlk and DIC flux from the Hooghly estuary to the adjacent coastal ocean were $4.45 \pm 1.90 \times 1011$ mol and $4.59 \pm 1.70 \times 1011$ mol, respectively. The net annual DIC flux of the Hooghly estuary is about 30 to 60 times higher than the surface area integrated air–water CO2 flux, which is an indication of promoting acidification in the adjacent coastal ocean. The present study indicates that the lateral DIC flux has increased substantially in the Hooghly estuary during the last two decades. The increase in inorganic carbon load in the Hooghly estuary due to the enhanced discharge of inorganic and organic matter load in the upper reaches of the estuary led to this increase in lateral DIC flux. The results strongly establish the need of having such regional studies for a better understanding of the estuarine carbon dynamics and its role in controlling the adjacent coastal ocean dynamics.

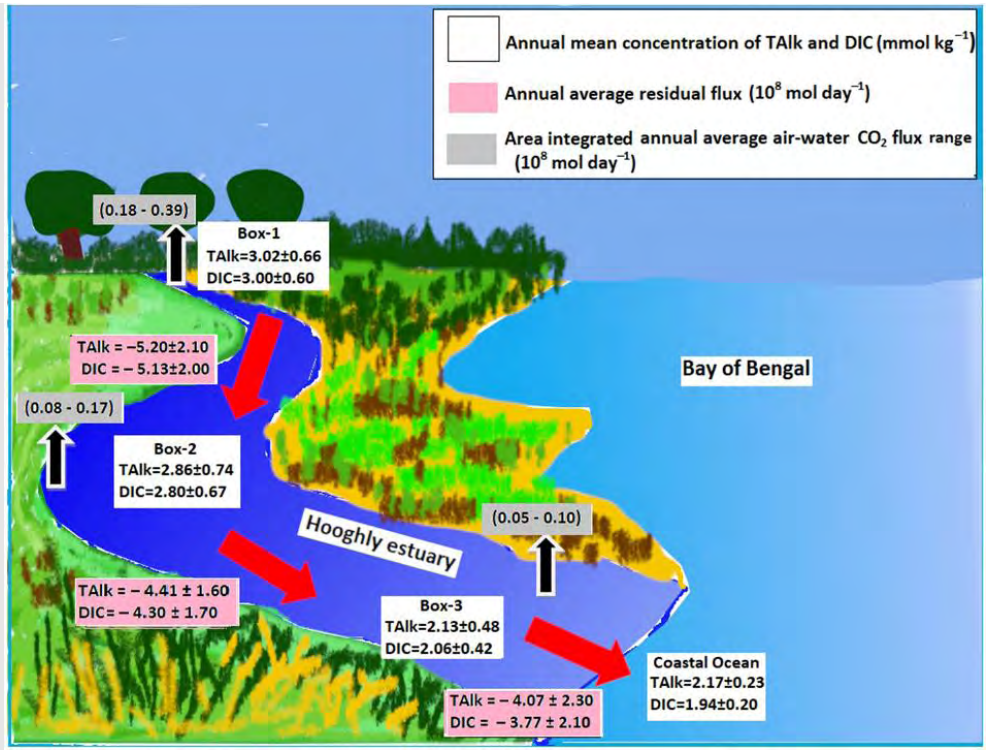

Figure: Schematic diagram depicting the transport of annual mean lateral fluxes of TAlk and DIC from the Hooghly Estuary to the coastal Bay of Bengal and area integrated annual average air–water CO_2 fluxes

Ref: Ghosh, J., Chakraborty, K., Chanda, A., Akhand, A., Bhattacharya, T., Das, S., ... & Wells, M. (2021). Outwelling of total alkalinity and dissolved inorganic carbon from the Hooghly River to the adjacent coastal Bay of Bengal. Environmental Monitoring and Assessment, 193(7), 1-14.

An observing system simulation experiment for Indian Ocean surface pCO2 measurements

Surface ocean partial pressure of CO2 (pCO2) information is vital for estimating sea-to-air CO2 exchanges. This parameter is least available from the Indian Ocean as compared to other global tropical and southern oceans. There has been no effort made so far to measure surface ocean pCO2 in the Indian Ocean with routine monitoring such as by mounting instruments to moorings or by underway sampling via any ship of opportunity program. Therefore there is a considerable demand to start pCO2 observations in the Indian Ocean. However, one key question that emerges is where to deploy pCO2 instruments in the Indian Ocean to learn the most with limited resources. This study addresses this question with inverse modeling techniques. The study finds that the existing moorings of the Indian Ocean are capable of hosting pCO2 sensors, and data from those are useful to reduce the uncertainty in the surface sea-to-air CO2 flux estimation by a quarter magnitude. In contrast, the Bio-Argo floats with pH sensors, and the ship of opportunity underway sampling of pCO2 may benefit from reducing the same up to 50% and 62%, respectively.

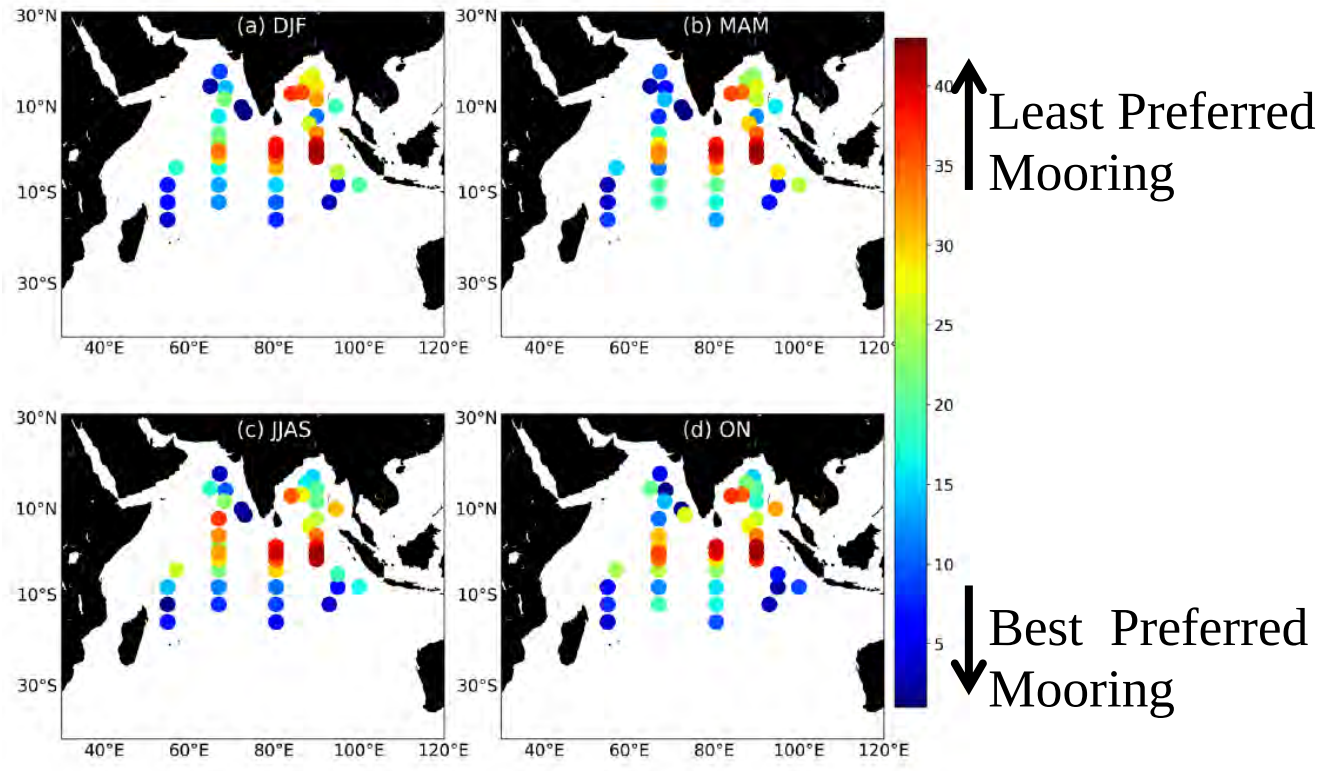

Figure: Rank of RAMA+OMNI moorings identified for each season for surface ocean pCO2 observation with deep blue (red) represents best (least) valued mooring for pCO2 observations from this OSSE experiment.

Ref: Valsala, V., Sreeush, M. G., Anju, M., Sreenivas, P., Tiwari, Y. K., Chakraborty, K., & Sijikumar, S. (2021). An observing system simulation experiment for Indian Ocean surface pCO2 measurements. Progress in Oceanography, 194, 102570

3. Biological Oceanography Section

Short term prediction of satellite-aided operational fishery advisories

The operational Potential Fishing Zone (PFZ) advisory generated and disseminated by the Indian National Centre for Ocean Information Services has a significant impact on the livelihood of coastal community of India. PFZs are identified as the relatively narrow zones in the ocean where horizontal gradients of physical and/or biological properties are enhanced. The advisories are provided to fishermen on a daily basis using remotely sensed sea surface temperature (SST) and chlorophyll-*a* (Chl-*a*) data from NOAA-AVHRR and MODIS-AQUA and/or Oceansat-2 satellites, respectively. Sometimes it becomes a major challenge to retrieve SST/Chl-a data from satellite images, particularly during the extensive cloud coverage. To overcome this operational difficulty, the satellite data is replaced by a coupled physical-biogeochemical model data capable of simulating ocean features leading to PFZs. The use of model data provides an additional advantage towards transforming the existing service from advisories to forecast. The average length of PFZs identified from satellite (model) data (2010–2016) for off Gujarat is 27.80 ± 7.2 km (33.07 ± 3.2 km) whereas for off Andhra Pradesh, it is 28.27 ± 10.9 km (52.48 ± 8.7 km). Considering the capability of the model in identifying PFZs, the existing advisory service can be transitioned into a short term PFZ forecast.

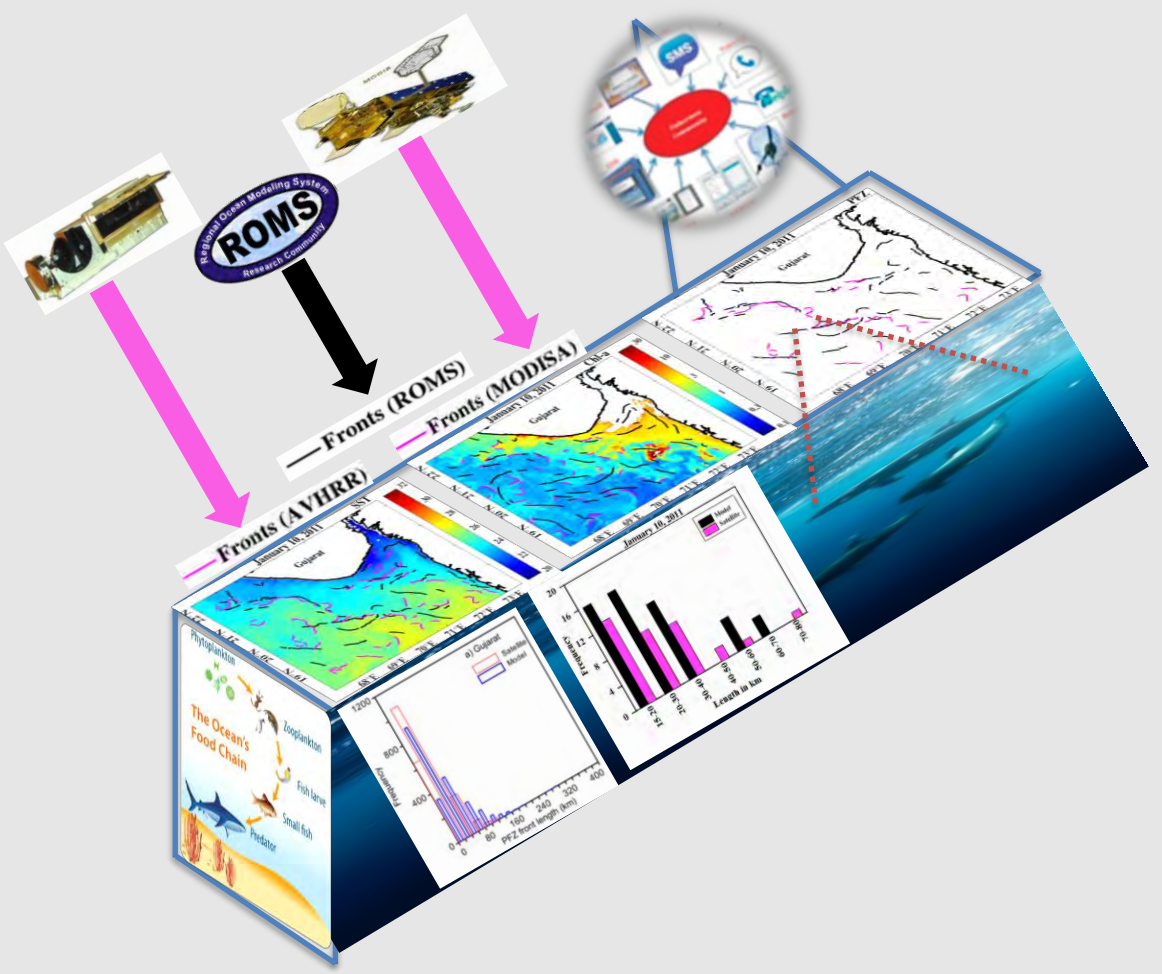

Figure: Graphical representation of the PFZ Forecasts Application developed using BIO Modelling System (high resolution, coupled numerical models) configured at INCOIS.

Ref: *Chakraborty, K., Maity, S., Lotliker, A.A., Samanta, A., Ghosh, J., Masuluri, N.K., Swetha, N., Bright, R.P. Modelling of marine ecosystem in regional scale for short term prediction of satellite-aided operational fishery advisories (2019) Journal of Operational Oceanography,12 (s2), s157-s175.*

Seasonal dynamics of phytoplankton in response to environmental variables in contrasting coastal ecosystems

Seasonal distribution of phytoplankton community and size structure was assessed in three different tropical ecosystems of the western Bay of Bengal viz. estuary (Mahanadi), lagoon (Chilika), and coastal waters (off Gopalpur) in response to ambient hydrobiology. Salinity regimes differentiated the study regions as contrasting ecosystems irrespective of seasons (pre-monsoon, monsoon, post-monsoon). Taxonomic account revealed a total no of 175, 65, and 101 phytoplankton species in the estuary, lagoon, and coastal waters respectively. Prevalence of marine, brackish, and freshwater types in the coastal waters, lagoon, and estuary, respectively, characterized the contrasting nature of the study regions in hosting the phytoplankton community. In general, phytoplankton abundance was observed in increasing order of coastal waters > estuary > lagoon during postmonsoon and pre-monsoon, while lagoon > coastal waters > estuary during monsoon. Bacillariophyta dominated the phytoplankton community in the estuary and coastal waters during all the seasons. In contrast, the lagoon exhibited a diverse array of phytoplankton group such as cyanophyta, dinophyta, and bacillariophyta during monsoon, post-monsoon, and pre-monsoon, respectively. Over the seasons, microphytoplankton emerged as the dominant phytoplankton size class in the coastal waters. Diversely, nanophytoplankton contributed to a major fraction of chlorophyll-a concentration in the estuary and lagoon. Interestingly, pre-monsoon dinophyta bloom (causative species: *Noctiluca scintillans*) and monsoon bacillariophyta bloom (causative species: *Asterionellopsis glacialis*) resulted in a decline in species diversity. Multivariate statistical analysis deciphered salinity as a major environmental player in determining the distribution, diversity, and composition of phytoplankton communities in the three contrasting environments. Trophic state indices signified the lagoon and estuary as hypereutrophic during all seasons. The coastal water was marked as highly eutrophic through trophic state index during monsoon and pre-monsoon.

Figure: Seasonal variation of percentage contribution of different phytoplankton groups to total phytoplankton abundance. b–d Seasonal variation of bacillariophyta abundance (BA), dinophyta abundance (DA), and cyanophyta abundance (CA), respectively. MON monsoon, POM post-monsoon, PRM pre-monsoon

Ref: *Srichandan, S., Baliarsingh, S.K., Prakash, S., Lotliker, A.A., Parida, C., Sahu, K.C. Seasonal dynamics of phytoplankton in response to environmental variables in contrasting coastal ecosystems (2019) Environmental Science and Pollution Research, 26 (12), pp. 12025-12041.*

Long-term chlorophyll-a dynamics in tropical coastal waters of the western Bay of Bengal

The long-term distribution of in situ optically active substances (OAS), accuracy assessment of satellite retrieved chlorophyll-a (chl-a) and its long-term trend has been carried out at a coastal site of the north-western Bay of Bengal. The temporal distribution of chl-a, total suspended matter (TSM) and absorption due to coloured dissolved organic matter at 440 nm (aCDOM440) discerned a common peak during southwest monsoon season (August–October). Chl-a also showed a prominent peak during pre-southwest monsoon period (March–April). The spatial variability of TSM and aCDOM440 was maximum during southwest monsoon, whereas in the case of chl-a, it was during pre-southwest monsoon. The accuracy assessment of chl-a retrieved from Moderate Resolution Imaging Spectroradiometer-Aqua (MODISA), Ocean Colour Monitor-2 (OCM-2) and Visible Infrared Imager Radiometer Suite (VIIRS) showed overestimation in nearshore waters. The error in satellite measurement of chl-a was within the range of 33 to 51%. The chl-a retrieved from MODISA was most accurate as indicated by statistical analysis. The long-term trend in satellite chl-a clearly indicated bi-modal distribution with a primary peak during pre-southwest

monsoon attributed to recurrent phytoplankton bloom that was mostly confined to nearshore waters. Whereas, the secondary peak in chl-a, during the end of southwest monsoon, spreads far offshore.

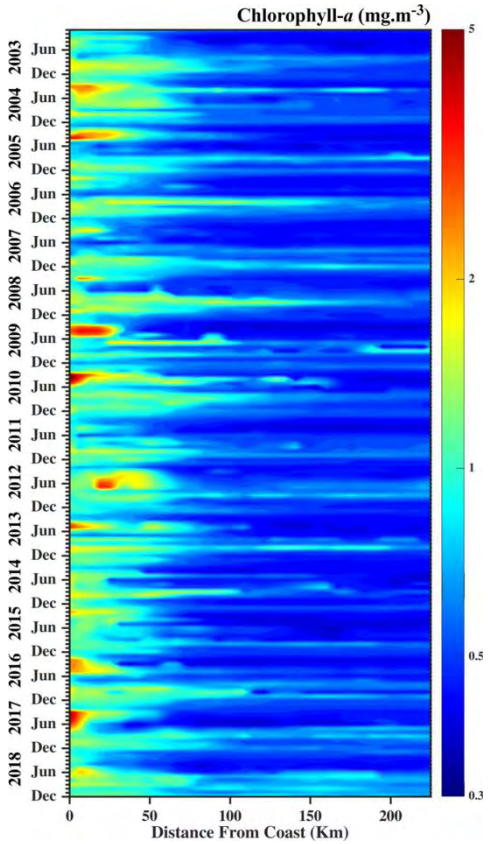

Figure: The latitudinal (18 to 20° N) averaged Hovmoller plot showing time series distribution of MODISA-retrieved chlorophyll-a from January 2003 to December 2018

Ref: *Lotliker, A.A., Baliarsingh, S.K., Sahu, K.C., Srinivasakumar, T. (2020). Long-term chlorophyll-a dynamics in tropical coastal waters of the western Bay of Bengal. Environmental Science and Pollution Research.27, pp. 6411-6419*

Biophysical Interactions in Driving the Summer Monsoon Chlorophyll Bloom Off the Somalia Coast

The biophysical interactions along the Somali coast are discussed during summer monsoon based on a numerical model study. The Somali coast is known to be the fifth largest upwelling region of the world ocean and one of the most productive regions of the globe. Based on scattered observations, mostly dated back to 1960s, it is widely accepted that the strong chlorophyll bloom along the Somali coast during summer is driven by upwelled nutrient flux.We show that the upwelling-driven productivity is primarily limited to the northern part of the coast when examined along the shelf break off the Somalia coast. In contrast, productivity in the south of 9◦N is driven by weaker upwelling in the early half of the summer monsoon but later dominated by the wind-

based mixing induced entrainment and therefore shows much weaker chlorophyll concentration than the north. Further, the strong poleward alongshore currents advect the upwelled nutrients away from the southern and central parts of the coast to the north, thereby controlling the biological community over the Somali region. This abundant locally upwelled and remotely advected nutrients support the enhanced growth of diatoms in the northern part of the transect as earlier observed from in situ measurements. However, limited nutrients allow smaller phytoplankton communities to grow in the southern and central sections.We show that nitrate is the primary limiting nutrient for the phytoplankton growth in the central and southern parts of the Somalia coast.

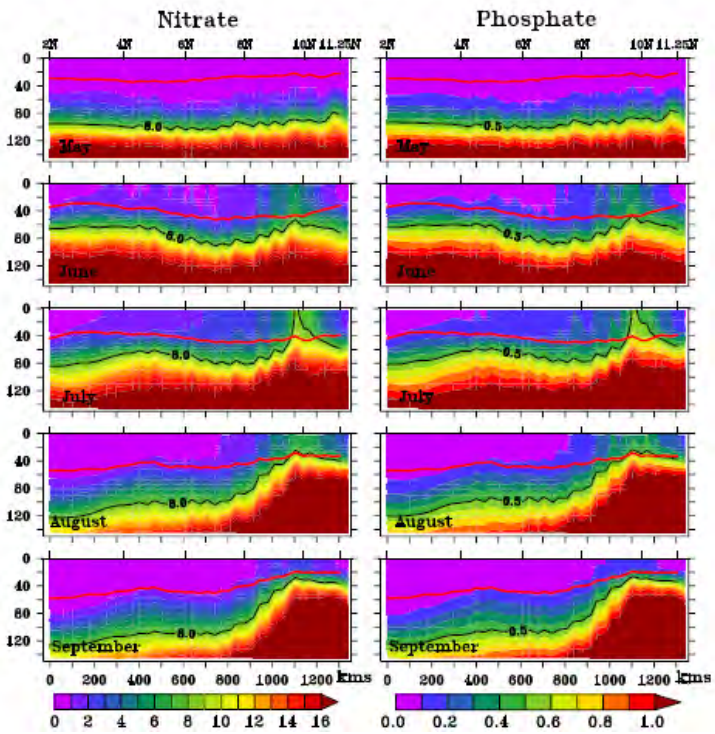

Figure: Evolution of model-simulated nitrate (µmol/kg) and phosphate (µmol/kg) along the 1,000 m isobath of Somalia coast (refer to Figure 1) from south to north during summer monsoon. The black lines represent the nutriclines, and the red line is the mixed layer depth computed using density criteria.

Ref: *Lakshmi, R.S., Chatterjee, A., Prakash, S., Mathew, T. (2020) Biophysical Interactions in Driving the Summer Monsoon Chlorophyll Bloom Off the Somalia Coast. Journal of Geophysical Research: Oceans, 125 (3), art. no. e2019JC015549*

Role of light limitation on the initiation of phytoplankton blooms in the northern Arabian Sea

The Arabian Sea is considered one of the highest productive regions of the world ocean. During boreal winter, the strong convective mixing deepens the mixed layer bringing nutrient-rich cold subsurface water into the euphotic zone making the basin one of the most productive regions of the globe. A winter monsoon cruise has been undertaken onboard FORV Sagar Sampada (Cr. No: SS383) in the northeastern Arabian Sea to understand the physicochemical coupling on the bloom dynamics. The studies conducted present new insights into the physicochemical forcings of phytoplankton blooms. Despite having a nutrient-enriched surface layer and a deeper mixed layer (>100 m), the observation shows a low chlorophyll concentration (0.1-0.3 µg/l) in the surface layer of the study region. Also, the study region showed a dominance of picophytoplankton with a negligible amount of diatom and *Noctiluca* bloom. Moreover, the euphotic depth was much shallower (~ 49 m) than the mixed layer suggesting the Sverdrup critical depth limitation in the northern Arabian Sea. We demonstrate that bloom begins in this region only when the mixed layer shoals toward the euphotic zone by the later winter monsoon. This strongly implies that the initiation of phytoplankton bloom depends on water column re-stratification.

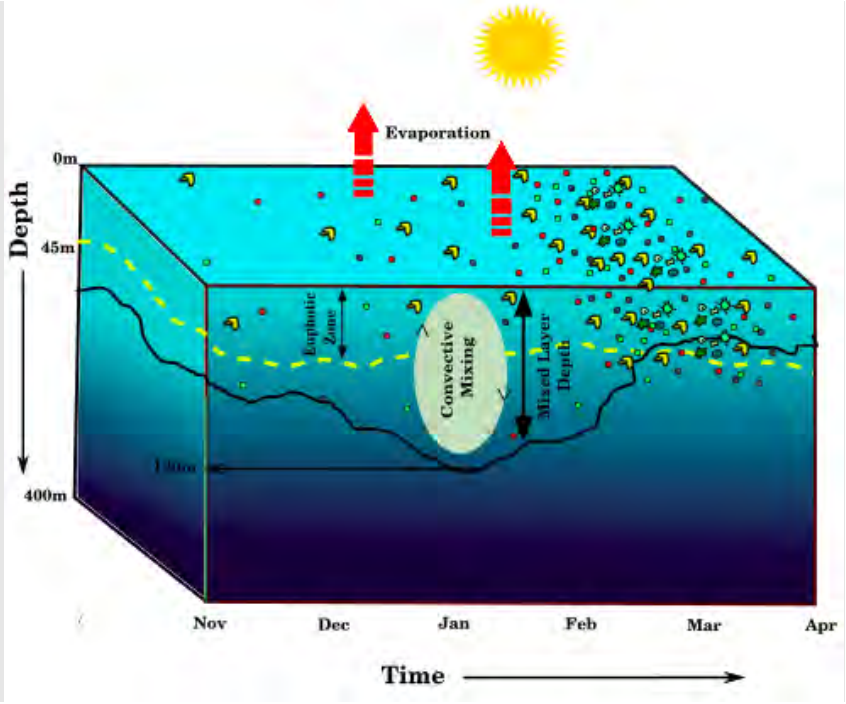

Figure: Schematic diagram which shows the relation between mixed layer depth and euphotic depth on the initiation of phytoplankton blooms.

Ref: *Lakshmi, R. S., Prakash, S., Lotliker, A. A., Baliarsingh, S. K., Samanta, A., Mathew, T., Chatterjee, A., Sahu, B. K. & Nair, T. M. (2021). Physicochemical controls on the initiation of phytoplankton bloom during the winter monsoon in the Arabian Sea. Scientific reports, 11(1), 1-10.*

Implication of monsoon blooms variability on the dissolved oxygen concentration in the OMZ: a Bio-Argo study

The inter-annual variability in surface productivity and its impact on the dissolved oxygen concentration in the deeper layer of the central Arabian Sea (CAS) is studied using four years (2013-2016) record of chlorophyll and dissolved oxygen (DO) concentration from a Bio-Argo float. The float has remained in a small region [65°E-68.5°E and 17°N-19°N], enabling to develop an understanding of the year to year variability of the physical and biogeochemical parameters in this region. It was observed that though the surface blooms occur during both the monsoons, winter blooms were more prominent compared to the summer bloom in the study region. The intensity and duration of the bloom have been decreasing over the study period. A detailed analysis shows that the observed inter-annual variability in the summer bloom can be attributed to the variability in wind speed, oceanic stratification, and advection of nutrient-rich water from the western Arabian Sea. It was found that during both the monsoons, stratification has played an important role in reducing productivity in recent years. During the winter monsoon, the upwelling Rossby wave propagating from the west coast of India influenced productivity as north as 15ºN. The chlorophyll data from Bio-Argo float shows that the total surface chlorophyll concentration and backscattering (a proxy for particulate flux) in the OMZ region have been decreasing during the study period. Consequently, the DO concentration in the deeper waters has also been increasing. The decrease in surface productivity, lateral advection from the west, and their manifestation on the export flux have reduced the oxygen demand in the deeper layer.

Figure 1:(a) Bar plot of mean surface chlorophyll in mg/m^3 during SM (blue),WM (red) and the annually averaged (black) during 2013-2016; (b) Volume transport (Sv) averaged for Jul-Sep in the upper 100 m across 65°E from 5°N to 20°N during 2013-2016;(c) Time series of integrated backscattering (m^{-1}) in the OMZ and (d)Mean oxygen concentration in the OMZ with trend line overlaid. The slope of trend line per 4years is listed on (c) and (d).

Ref: *Mathew, T., Prakash, S., Shenoy, L., Chatterjee, A., Udaya Bhaskar, T.V.S., Bozena, W. (2021). served variability of monsoon blooms in the north-central Arabian Sea and its implication on oxygen concentration A bio-argo study. Deep Sea Research Part II Topical Studies in Oceanography 184, 104935.*

Nutrient stoichiometry in the coastal waters of the western Bay of Bengal and its impact on the chlorophyll variability

The seasonal variability of chlorophyll concentration and its response to available nutrients along the BoB coastal waters are studied using two cruise data. These cruises were undertaken in 2017 in the coastal water of the western BoB during pre-southwest monsoon season (PRSWM) and post-southwest monsoon season (POSWM) along 50 m isobath. It is observed that the chlorophyll concentration is more during the PRSWM season compared to the POSWM season. The study reported the presence of a cold-core eddy during PRSWM enhancing the vertical movement of nutrients to the surface, well-mixed waters, leading to an increase in the chl–*a* concentration. However, during the POSWM period, despite having higher nitrate concentration and adequate light in the water column, the surface chl-*a* is substantially lower than PRSWM. This study shows that the main factor controlling the lower chl-*a* concentration during the POSWM period is the molar ratio of ambient inorganic macronutrients. Nitrate to phosphate (N:P) and nitrate to silicate (N: Si) ratios are less than the Redfield values, which resulted in lower chl-*a* concentration. This study also highlights phosphate limitation off the Godavari during the high river discharge period for the first time, which calls for a more intense study to understand the phosphate limitation in this region.

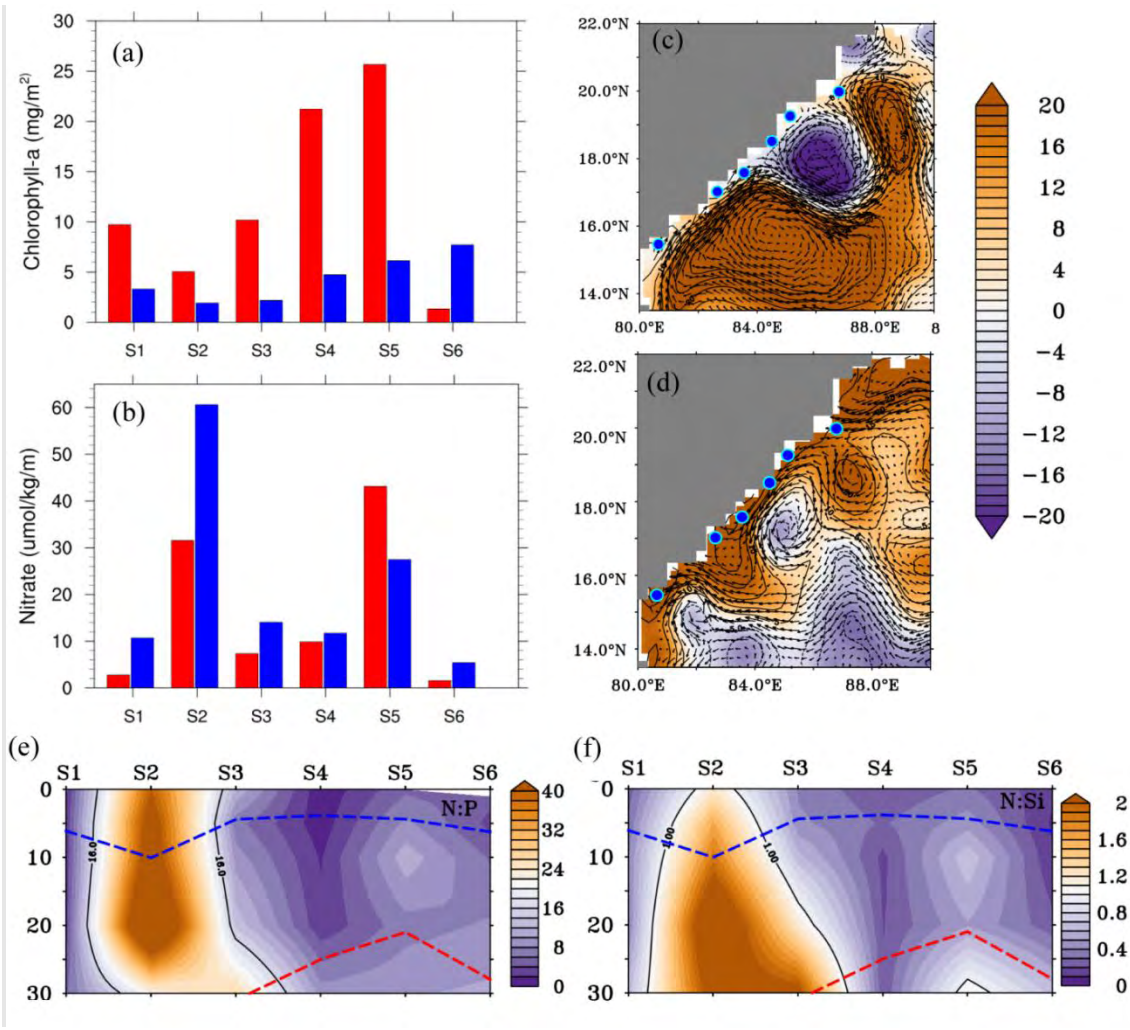

Figure: (a) Integrated chlorophyll and (b) nitrate concentration in the upper 10 meters for PRSWM (red) and POSWM (blue) cruises. Satellite derived sea level anomaly during the (c) PRSWM and (d) POSWM cruises with its contours overlaid. Overlaid vectors are surface currents. Blue dots indicate the location of cruise stations. Ratio of the nutrients at all the stations during (e) PRSWM and (f) POSWM cruises. blue and red dashed line over (e) and (f) indicates the MLD and the photic depth.

Ref: *Mathew, T., Prakash, S., Baliarsingh, S.K., Samanta, A., Lakshmi, R.S., Lotliker, A.A, Chatterjee, A., Balakrishnan Nair, T.M.* (2021). Response of phytoplankton biomass to nutrient stoichiometry in coastal waters of the western Bay of Bengal. Ecological Indicators 131, 108119.

Unravelling tidal effect on zooplankton community structure in a tropical estuary

The variability in zooplankton density and species composition in response to tidal oscillations were investigated in the lesser saline upper reaches (E1) and higher saline lower reaches (E2) of the Mahanadi Estuary, connected to the Bay of Bengal on the east coast of India at Paradip. The overall diversity of 92 taxa belonging to 13 groups was recorded during this study. The zooplankton community exhibited spatial, tidal, and diurnal patterns of distribution. The tidal

pattern shows the abundance of zooplankton was higher during the high tide than the low tide. On the diurnal scale, abundance is higher at night time than during the daytime indicating the upward migration of zooplankton. The migration is clearly represented by the high abundance of some groups such as Copepoda, Cladocera, and planktonic larvae during the night time. The spatial pattern exhibited migration of some zooplankton towards E1 during high tide. In contrast, the prevalence of limnetic taxa at E2 during low tide indicated a predominant riverine source. The tidal variability of Brachyura (zoea and megalopa) revealed different emergence times that indicated the dispersal of zoeas to the adjacent Bay of Bengal and the return of magalopa to the Mahanadi Estuary. Diversity indices such as species diversity, richness, and evenness were higher during high tide at E2, indicating an intrusion of several marine species from the adjacent Bay of Bengal. Several hydrological conditions drive the distribution of zooplankton, such as suspended matter influencing the detritivorous species at E1 and salinity influencing the dominant zooplankton taxa at E2. This study signifies the importance of tidal and diurnal cycles in zooplankton distribution and diversity in tropical estuaries. The study also highlighted the importance of sampling over the entire tidal cycle in the estuary as well as coastal water for a better understanding of the zooplankton migration pattern and population dynamics.

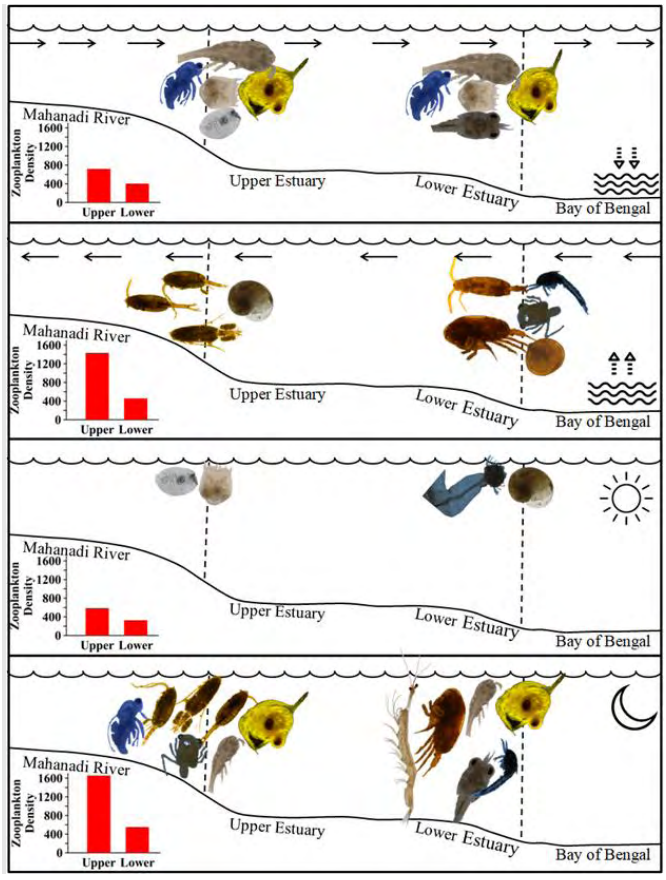

Fig: Graphical representation showing tidal variabilityof zooplankton in the Mahanadi estuary

Ref: *Srichandan, S., Baliarsingh, S. K., Lotliker, A. A., Sahu, B. K., Roy, R., & Nair, T. B. (2021). Unravelling tidal effect on zooplankton community structure in a tropical estuary. Environmental Monitoring and Assessment, 193(6), 362.*

Response of coastal phytoplankton pigment composition to tropical cyclone Fani

Phytoplankton pigment composition was evaluated during the pre-cyclone phase (PRCP) and post-cyclone phase (POCP) of tropical cyclone Fani in the coastal waters of the northwestern Bay of Bengal. The pigment analysis revealed higher pigment concentration and diversity during POCP. Chlorophyll–*a* (chl–*a*) was the dominant pigment during PRCP and POCP, followed by fucoxanthin. However, chl–*a* and fucoxanthin concentrations increased 18- and 14-folds, respectively, during the POCP, signifying Bacillariophyta bloom. Complementing microscopy confirmed the dominance of the toxic Bacillariophyta species *Pseudo-nitzschia pungens* during the POCP. The cyclone-induced nutrient recharge of the ambient medium could have promoted phytoplankton growth, causing the reappearance of diatom bloom during the later phase of the pre-southwest monsoon. Small-sized Prymnesiophyta and Cryptophyta were not detected microscopically; however, they were identified by chromatographic analysis through pigment markers during POCP. As the north Indian Ocean, especially the BoB, is experiencing frequent tropical cyclones, the resultant changes in the composition and biomass of the phytoplankton community need to be considered in ecological models and studies for a better understanding of the ecosystem for strategic management. In addition, this study recommended future studies on the triggers of HAB observed in the aftermath of cyclones which can be very useful in finding proxies for possible remote monitoring through ocean colour satellite sensors.

Fig: Phytoplankton pigment composition before and after the passage of cyclone Fani in the coastal waters off Gopalpur.

Ref: *Baliarsingh, S. K., Lotliker, A. A., Srichandan, S., Parida, C., Roy, R., Naik, R. C., ... & Barik, K. K. (2021). Response of coastal phytoplankton pigment composition to tropical cyclone Fani. Marine Pollution Bulletin, 173, 113038.*

A step towards genesis of Jellyfish Aggregation Advisory Service

Jellyfishes constitute an important group of marine animals that are broadly distributed in many coastal and open ocean regions. Some jellyfish species form dense aggregations during favorable environmental conditions. Jellyfish aggregations in coastal regions include swarming events and beach strandings that often result in water quality deterioration, trophic disturbance, and socio-economic losses. In addition, jellyfish outbreaks exert significant impacts on tourism, recreational activities, and coastal industries such as power plants. Episodes of jellyfish swarming have received substantial attention in recent times. However, the study of these organisms remains very subjective due to broad definitions and limited observational techniques. In peninsular Indian seas and coastal regions, jellyfish swarming and beach strandings have been reported sporadically. Therefore, an attempt has been made to enhance understanding of conducive conditions and subsequent ecological impacts of jellyfish aggregations in order to develop a Jellyfish Aggregation Advisory Service. A variety of natural (winds, tidal fronts, surface currents, water temperature, salinity, turbidity, dissolved oxygen) and anthropogenic (water quality deterioration, overfishing, translocation, habitat modification) factors play pivotal roles in triggering jellyfish aggregations. Based on the conducive factors, this study proposes a conceptual framework for the development of a jellyfish monitoring system for Indian waters using satellite and model data. The proposed conceptual scheme is aimed at being converted into an operational model by utilizing the institution's technical and data resources.

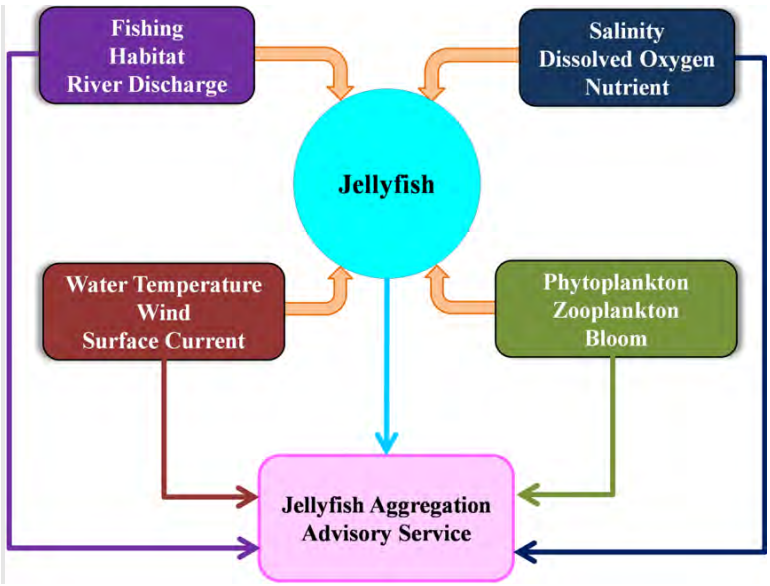

Figure: Conceptual framework for the development of jellyfish aggregation advisory service

Ref: *Baliarsingh, S.K., Lotliker, A.A., Srichandan, S., Samanta, A., Kumar, N. & Balakrishnan Nair, T.M. (2020). A review of jellyfish aggregations, focusing on India's coastal waters. Ecological Processes 9, 58.*

References

Physical Oceanography Section

1. Paul, A., Afroosa, M., Baduru, B., & Paul, B. (2023). Showcasing model performance across space and time using single diagrams. Ocean Modelling, 181, 102150.

2. Varna, M., Jithin, A. K., & Francis, P. A. (2023). Characteristics and dynamics of mesoscale eddies in the eastern Arabian sea. Deep Sea Research Part II: Topical Studies in Oceanography, 207, 105218.

3. Swapna, M., Raju, R., Nayak, R. K., Mohanty, P. C., SeshaSai, M. V. R., & Kumar, R. (2023). Spatiotemporal Characteristics of Thermal Fronts in Relation to Potential Fishing Zones in the Continental Shelf Sea Around India. Journal of the Indian Society of Remote Sensing, 1-14.

4. Mohanty, P. C., Mahendra, R. S., Nayak, R. K., Manche, S. S., Joseph, S., Nair, T. B., & Kumar, T. S. (2023). Characteristics of astronomical tides and their modulation on sea level extremes along the Indian coast. Ocean & Coastal Management, 231, 106398.

5. Rose, L., Rohith, B., & Bhaskaran, P. K. (2022). Amplification of regional tides in response to sea level. Ocean Engineering, 266, 112691.

6. Ramakrishnan, R., Remya, P. G., Mandal, A., Mohanty, P., Arayakandy, P., Mahendra, R. S., & Nair, T. M. (2022). Wave induced coastal flooding along the southwest coast of India during tropical cyclone Tauktae. Scientific Reports, 12(1), 1-11.

7. Ratheesh, R., Remya, P. G., Agrawal, R., Venkiteswarlu, C., Gireesh, B., Amarendra, P., ... & Rajawat, A. S. (2022). A numerical modelling approach for beach erosion forecast during the southwest monsoon season. Journal of Earth System Science, 131(4), 1-11.

8. Sreejith, M., PG, R., Kumar, B. P., Raj, A., & Nair, T. M. (2022). Exploring the impact of southern ocean sea ice on the Indian Ocean swells. Scientific Reports, 12(1), 1-9.

9. Prince, H. C., Nirmala, R., Mahendra, R. S., & Murty, P. L. N. (2020). Storm Surge Hazard Assessment Along the East Coast of India Using Geospatial Techniques.

10. Raju, R. M., Nayak, R. K., Mulukutla, S., Mohanty, P. C., Manche, S. S., Seshasai, M. V. R., & Dadhwal, V. K. (2022). Variability of the thermal front and its relationship with Chlorophyll-a in the north Bay of Bengal. Regional Studies in Marine Science, 56, 102700.

11. Murty, P. L. N., Kolukula, S. S., Ramarao, E. P., & Kumar, T. S. (2022). Finite Element Modeling of Tsunami-induced Water Levels and Associated Inundation Extent: A Case Study of the 26th December 2004 Indian Ocean Tsunami. Journal of the Geological Society of India, 98(10), 1356-1364.

12. Kumar, P., Sardana, D., Kaur, S., PG, R., & Weller, E. (2022). Influence of climate variability on wind-sea and swell wave height extreme over the Indo-Pacific Ocean. International Journal of Climatology.

13. Majumder, S., Remya, P. G., Nair, T. B., & Sirisha, P. (2022). Analysis of meteorological and oceanic conditions during freak wave events in the Indian Ocean. Ocean Engineering, 259, 111920.

14. Mukherjee, A., Shankar, D., Fernando, V., Amol, P., Aparna, S. G., Fernandes, R., ... & Vernekar, S. (2014). Observed seasonal and intraseasonal variability of the East India Coastal Current on the continental slope. Journal of Earth System Science, 123(6), 1197-1232.

15. Rose, L., & Bhaskaran, P. K. (2022). Tidal variations associated with sea level changes in the Northern Bay of Bengal. Estuarine, Coastal and Shelf Science, 272, 107881.

16. Borra, S., Nair, T. M., Jospeh, S., Kumar, S. V., Sridevi, T., Harikumar, R., ... & Prasad, K. V. S. R. (2022). Identifying rip channels along RK Beach, Visakhapatnam using video and satellite imagery analysis. Journal of the Indian Society of Remote Sensing, 1-18.

17. Afroosa, M., Rohith, B., Paul, A., Durand, F., Bourdallé-Badie, R., Joseph, S., ... & Shenoi, S. S. C. (2022). Investigating the robustness of the intraseasonal see-saw in the Indo-Pacific barotropic sea level across models. Ocean Dynamics, 72(7), 523-538.

18. Mohanty, S., Nadimpalli, R., Joseph, S., Srivastava, A., Das, A. K., Mohanty, U. C., & Sil, S. (2022). Influence of the ocean on tropical cyclone intensity using a high resolution coupled atmosphere–ocean model: A case study of very severe cyclonic storm Ockhi over the North Indian Ocean. Quarterly Journal of the Royal Meteorological Society, 148(746), 2282-2298.

19. Ashin, K., Girishkumar, M. S., Joseph, J., D'asaro, E., Sureshkumar, N., Sherin, V. R., ... & Shenoi, S. S. C. (2022). Double diffusion in the Arabian Sea during winter and spring. Journal of Physical Oceanography, 52(6), 1205-1231.

20. Jyothi, L., Joseph, S., Huber, M., & Joseph, L. A. (2022). Distinct oceanic responses at rapidly intensified and weakened regimes of tropical cyclone Ockhi (2017). Journal of Geophysical Research: Oceans, 127(6), e2021JC018212.

21. Castillo, J. M., Lewis, H. W., Mishra, A., Mitra, A., Polton, J., Brereton, A., ... & Valdivieso da Costa, M. (2022). The Regional Coupled Suite (RCS-IND1): application of

a flexible regional coupled modelling framework to the Indian region at kilometre scale. Geoscientific Model Development, 15(10), 4193-4223.

22. Harikumar, R., Sirisha, P., Modi, A., Girishkumar, M. S., Vishnu, S., Srinivas, K., ... & Mohapatra, M. (2022). Ocean state forecasting during VSCS Ockhi and a note on what we learned from its characteristics: A forecasting perspective. Journal of Earth System Science, 131(2), 1-20.

23. Aparna, A. R., & Girishkumar, M. S. (2022). Mixed layer heat budget in the eastern equatorial Indian Ocean during the two consecutive positive Indian Ocean dipole events in 2018 and 2019. Climate Dynamics, 58(11), 3297-3315.

24. Chatterjee, A., Anil, G., & Shenoy, L. R. (2022). Marine heatwaves in the Arabian Sea. Ocean Science, 18(3), 639-657.

25. Pottapinjara, V., & Joseph, S. (2022). Evaluation of mixing schemes in the HYbrid Coordinate Ocean Model (HYCOM) in the tropical Indian Ocean. Ocean Dynamics, 72(5), 341-359.

26. Pravallika, M. S., Vasavi, S., & Vighneshwar, S. P. (2022). Prediction of temperature anomaly in Indian Ocean based on autoregressive long short-term memory neural network. Neural Computing and Applications, 34(10), 7537-7545.

27. Prakash, K. R., Pant, V., Udaya Bhaskar, T. V. S., & Chandra, N. (2022). What Made the Sustained Intensification of Tropical Cyclone Fani in the Bay of Bengal? An Investigation Using Coupled Atmosphere–Ocean Model. Atmosphere, 13(4), 535.

28. Vishwakarma, V., Pattnaik, S., Chakraborty, T., Joseph, S., & Mitra, A. K. (2022). Impacts of sea-surface temperatures on rapid intensification and mature phases of super cyclone Amphan (2020). Journal of Earth System Science, 131(1), 1-21.

29. Kolukula, S. S., & Murty, P. L. N. (2022). Improving cyclone wind fields using deep convolutional neural networks and their application in extreme events. Progress in Oceanography, 202, 102763.

30. Kuttippurath, J., Akhila, R. S., Martin, M. V., Girishkumar, M. S., Mohapatra, M., Sarojini, B. B., ... & Chakraborty, A. (2022). Tropical cyclone-induced cold wakes in the northeast Indian Ocean. Environmental Science: Atmospheres.

31. Shesu, R. V., Ravichandran, M., Suprit, K., Rao, E. P., & Rao, B. V. (2022). Precipitation event detection based on air temperature over the Equatorial Indian Ocean.

32. Parida, C., Lotliker, A. A., Roy, R., & Vinayachandran, P. N. (2022). Radiant heating rate associated with chlorophyll dynamics in upper ocean of Southern Bay of Bengal: A case

study during Bay of Bengal Boundary Layer Experiment. Deep Sea Research Part II: Topical Studies in Oceanography, 196, 105026.

33. Pattiaratchi, C., van der Mheen, M., Schlundt, C., Narayanaswamy, B. E., Sura, A., Hajbane, S., ... & Wijeratne, S. (2022). Plastics in the Indian Ocean–sources, transport, distribution, and impacts. Ocean Science, 18(1), 1-28.

34. Samiksha, S. V., Tharani, A., Kumar, V. S., & Antony, C. (2022). Performance of ERA5 winds on computed storm surge and wave–current interaction using a coupled model during Ockhi cyclone. Natural Hazards, 1-16.

35. Sardana, D., Kumar, P., Bhaskaran, P. K., & Nair, T. M. (2022). The projected changes in extreme wave height indices over the Indian Ocean using COWCLIP2. 0 datasets. Climate Dynamics, 1-15.

36. Jha, R. K., & Bhaskar, T. U. (2022). Generation and Assessment of ARGO Sea Surface Temperature Climatology for the Indian Ocean Region. Oceanologia.

37. Maneesha, K., Ratheesh, S., & Bhaskar, T. V. S. (2022). Impact of the upper Ocean processes on intensification of cyclone Amphan. Journal of the Indian Society of Remote Sensing, 1-10.

38. Reddem, V. S., Jampana, V., Muthalagu, R., Bekkam, V. R., Eluri, P. R. R., & Tummala, S. K. (2022). On the non-parametric changepoint detection of flow regimes in cyclone Amphan. Oceanologia.

39. Vinayachandran, P. N., Neema, C. P., Chatterjee, A., & Prerna, S. (2022, February). Fate and impact of Bay of Bengal rivers in an intermediate resolution ocean model. In OCEANS 2022-Chennai (pp. 1-8). IEEE.

40. Papolu, J. S., Prasad, M. B., Vasavi, S., & Geetha, G. (2022). A Framework for Sea Breeze Front Detection from Coastal Regions of India Using Morphological Snake Algorithm. ECS Transactions, 107(1), 585.

41. Martin, M., Abhilash, S., Pattathil, V., Harikumar, R., Niyas, N. T., Nair, T. B., ... & Osella, F. (2022). Should I Stay or Should I Go? South Indian Artisanal Fishers' Precarious Livelihoods and Their Engagement with Categorical Ocean Forecasts. Weather, Climate, and Society, 14(1), 113-129.

42. Sirisha, P., Remya, P. G., Janardhanan, J., & Nair, T. B. (2022). Seasonal variation of wave power potential in the coastal areas of India. CURRENT SCIENCE, 122(5), 584.

43. Aditya, N. D., Sandhya, K. G., Harikumar, R., & Balakrishnan Nair, T. M. (2022). Development of small vessel advisory and forecast services system for safe navigation and operations at sea. Journal of operational oceanography, 15(1), 52-67.

44. Sen, R., Pandey, S., Dandapat, S., Francis, P. A., & Chakraborty, A. (2022). A numerical study on seasonal transport variability of the North Indian Ocean boundary currents using Regional Ocean Modeling System (ROMS). Journal of Operational Oceanography, 15(1), 32-51.

45. Chakraborty, K., Lotliker, A. A., Gupta, G. V. M., Narayanan Nampoothiri S, V., Paul, A., Ghosh, J., ... & Samanta, A. (2020). Assessment of an ocean-ecosystem model in simulating the Indian coastal marine ecosystem dynamics. Journal of Operational Oceanography, 1-19.

46. Elizabeth, A. I., Effy, J. B., & Francis, P. A. (2022). On the upper ocean response of Bay of Bengal to very severe cyclones Phailin and Hudhud. Journal of Operational Oceanography, 15(1), 17-31.

47. Remya, P. G., Rabi Ranjan, T., Sirisha, P., Harikumar, R., & Balakrishnan Nair, T. M. (2022). Indian Ocean wave forecasting system for wind waves: development and its validation. Journal of Operational Oceanography, 15(1), 1-16.

48. Afroosa, M., Rohith, B., Paul, A., Durand, F., Bourdallé-Badie, R., Sreedevi, P. V., ... & Shenoi, S. S. C. (2021). Madden-Julian oscillation winds excite an intraseasonal see-saw of ocean mass that affects Earth's polar motion. Communications Earth & Environment, 2(1), 1-8.

49. Chaudhuri, D., Sengupta, D., D'Asaro, E., & Shivaprasad, S. (2021). Trapping of Wind Momentum in a Salinity-Stratified Ocean. Journal of Geophysical Research: Oceans, 126(12), e2021JC017770.

50. Jithin, A. K., & Francis, P. A. (2021). Formation of an Intrathermocline Eddy Triggered by the Coastal-Trapped Wave in the Northern Bay of Bengal. Journal of Geophysical Research: Oceans, 126(12), e2021JC017725.

51. Srinivasa Kumar, T., & Manneela, S. (2021). A review of the progress, challenges and future trends in tsunami early warning systems. Journal of the Geological Society of India, 97(12), 1533-1544.

52. Anup, N., Vijith, V., Jithin, A. K., Rohith, B., Amol, P., & Francis, P. A. (2021). Quasi-biweekly oscillation in sea level along the western Bay of Bengal. Continental Shelf Research, 231, 104594.

53. Jain, V., Shankar, D., Vinayachandran, P. N., Mukherjee, A., & Amol, P. (2021). Role of ocean dynamics in the evolution of mixed-layer temperature in the Bay of Bengal during the summer monsoon. Ocean Modelling, 168, 101895.

54. Phillips, H. E., Tandon, A., Furue, R., Hood, R., Ummenhofer, C. C., Benthuysen, J. A., ... & Wiggert, J. (2021). Progress in understanding of Indian Ocean circulation, variability, air–sea exchange, and impacts on biogeochemistry. Ocean Science, 17(6), 1677-1751.

55. Vinayachandran, P. N. M., Masumoto, Y., Roberts, M. J., Huggett, J. A., Halo, I., Chatterjee, A., ... & Hood, R. (2021). Reviews and syntheses: Physical and biogeochemical processes associated with upwelling in the Indian Ocean. Biogeosciences, 18(22), 5967-6029.

56. Kumar, B. P., D'Asaro, E., Sureshkumar, N., Rama Rao, E. P., & Ravichandran, M. (2021). Thorpe Turbulence Scaling in Nighttime Convective Surface Layers in the North Indian Ocean. Journal of Physical Oceanography, 51(10), 3203-3216.

57. Shroyer, E., Tandon, A., Sengupta, D., Fernando, H. J., Lucas, A. J., Farrar, J. T., ... & Subrahmanyam, B. (2021). Bay of Bengal intraseasonal oscillations and the 2018 monsoon onset. Bulletin of the American Meteorological Society, 102(10), E1936-E1951.

58. Seemanth, M., Remya, P. G., Bhowmick, S. A., Sharma, R., Nair, T. B., Kumar, R., & Chakraborty, A. (2021). Implementation of altimeter data assimilation on a regional wave forecasting system and its impact on wave and swell surge forecast in the Indian Ocean. Ocean Engineering, 237, 109585.

59. Reddem, V. S., Muthalagu, R., Bekkam, V. R., Eluri, P. R. R., Jampana, V., & Nimit, K. (2021). Ocean Fronts detection over the Bay of Bengal using changepoint algorithms–A non-parametric approach. Oceanologia, 63(4), 438-447.

60. Girishkumar, M. S., Joseph, J., McPhaden, M. J., & Pattabhi Ram Rao, E. (2021). Atmospheric cold pools and their influence on sea surface temperature in the Bay of Bengal. Journal of Geophysical Research: Oceans, 126(9), e2021JC017297.

61. Jha, R. K., & Udaya Bhaskar, T. V. S. (2021). Optimal parameters for generation of gridded product of Argo temperature and salinity using DIVA. Journal of Earth System Science, 130(3), 1-14.

62. Tiwari, P., Dimri, A. P., Shenoi, S. C., Francis, P. A., & Jithin, A. K. (2021). Impact of Surface forcing on simulating Sea Surface Temperature in the Indian Ocean–A study using Regional Ocean Modeling System (ROMS). Dynamics of Atmospheres and Oceans, 95, 101243.

63. Modi, A., Munaka, S. K., Harikumar, R., Nair, T. M., & Srinivas, K. (2021). Evaluation of winds from SCATSAT-1 and ASCAT using buoys in the Indian ocean. Journal of the Indian Society of Remote Sensing, 49(8), 1915-1925.

64. Pradhan, M., Srivastava, A., Rao, S. A., Banerjee, D. S., Chatterjee, A., Francis, P. A., ... & Prasad, V. S. (2021). Are ocean-moored buoys redundant for prediction of Indian monsoon?. Meteorology and Atmospheric Physics, 133(4), 1075-1088.

65. Pottapinjara, V., Roxy, M. K., Girishkumar, M. S., Ashok, K., Joseph, S., Ravichandran, M., & Murtugudde, R. (2021). Simulation of interannual relationship between the Atlantic zonal mode and Indian summer monsoon in CFSv2. Climate Dynamics, 57(1), 353-373.

66. Modi, A., Nair, T. M., Remya, P. G., Harikumar, R., Srinivas, K., & Srinivas, G. (2021). The role of anomalous oceanic features on enhancing flooding duration in Kuttanad region, Kerala (India). Journal of Earth System Science, 130(2), 1-10.

67. Sen, R., Francis, P. A., Chakraborty, A., & Effy, J. B. (2021). A numerical study on the mixed layer depth variability and its influence on the sea surface temperature during 2013–2014 in the Bay of Bengal and Equatorial Indian Ocean. Ocean Dynamics, 71(5), 527-543.

68. Srinivas, G., Remya, P. G., Kumar, B. P., Modi, A., & Nair, T. B. (2021). The impact of Indian Ocean dipole on tropical Indian Ocean surface wave heights in ERA5 and CMIP5 models. International Journal of Climatology, 41(3), 1619-1632.

69. Satish, R. U. V. N., & Bhaskar, T. V. S. (2021). Metrics for the assessment of quantity and quality of the data by Argo floats.

70. Paul, B., Baduru, B., Paul, A., Francis, P. A., & Shetye, S. R. (2021). Absence of the annual cycle in shelf current inshore of the East Indian Coastal Current. Continental Shelf Research, 215, 104355.

71. Manche, S. S., Nayak, R. K., Mohanty, P. C., Shesasai, M. V. R., & Dadhwal, V. K. (2021). Assessment of mass-induced sea level variability in the Tropical Indian Ocean based on GRACE and altimeter observations. Journal of Geodesy, 95(2), 1-24.

72. Subeesh, M. P., Unnikrishnan, A. S., & Francis, P. A. (2021). Generation, propagation and dissipation of internal tides on the continental shelf and slope off the west coast of India. Continental Shelf Research, 214, 104321.

73. Joseph, J., Girishkumar, M. S., Varikoden, H., Thangaprakash, V. P., Shivaprasad, S., Rao, R., & Pattabhi, E. (2021). Observed sub-daily variability of latent and sensible heat fluxes in the Bay of Bengal during the summer. Climate Dynamics, 56(3), 917-934.

74. Joseph, J., Girishkumar, M. S., McPhaden, M. J., & Rao, E. (2021). Diurnal variability of atmospheric cold pool events and associated air-sea interactions in the Bay of Bengal during the summer monsoon. Climate Dynamics, 56(3), 837-853.

75. Gadgil, S., Francis, P. A., Rajendran, K., Nanjundiah, R. S., & Rao, S. A. (2020). Role of land-ocean contrast in the indian summer monsoon rainfall. In The Multiscale Global Monsoon System (pp. 3-12).

76. Gadgil, S., Francis, P. A., Vinayachandran, P. N., & Sajani, S. (2021). Interannual variation of the Indian summer monsoon, ENSO, IOD, and EQUINOO. In Indian Summer Monsoon Variability (pp. 29-48). Elsevier.

77. Murali, B., KUMAR, M. G., RAVICHANDRAN, M., & Bharathi, G. (2021). Role of equatorial Indian Ocean convection on the Indian summer monsoon. MAUSAM, 72(2), 457-462.

78. Das, A. K., Sharma, A., Joseph, S., Srivastava, A., & Pattanaik, D. R. (2021). Comparative performance of HWRF model coupled with POM and HYCOM for tropical cyclones over North Indian Ocean. MAUSAM, 72(1), 147-166.

79. Nair, P. J., Varikoden, H., Francis, P. A., Chakraborty, A., & Pandey, P. C. (2021). Atmospheric moisture as a proxy for the ISMR variability and associated extreme weather events. Environmental Research Letters, 16(1), 014045.

80. Francis, P. A., Jithin, A. K., Effy, J. B., Chatterjee, A., Chakraborty, K., Paul, A., ... & Satyanarayana, B. V. (2020). High-resolution operational ocean forecast and reanalysis system for the Indian ocean. Bulletin of the American Meteorological Society, 101(8), E1340-E1356.

81. Gayathri, R., Bhaskaran, P. K., & Murty, P. L. N. (2021). River-tide-storm surge interaction characteristics for the Hooghly estuary, East coast of India. ISH Journal of Hydraulic Engineering, 27(sup1), 483-495.

82. Sree Lekha, J., Lucas, A. J., Sukhatme, J., Joseph, J. K., Ravichandran, M., Suresh Kumar, N., ... & Sengupta, D. (2020). Quasi-Biweekly Mode of the Asian Summer Monsoon Revealed in Bay of Bengal Surface Observations. Journal of Geophysical Research: Oceans, 125(12), e2020JC016271.

83. Suneel, V., Alex, M. J., Antony, T. P., Gurumoorthi, K., Trinadha Rao, V., Harikrishnan, S., ... & Rama Rao, E. P. (2020). Impact of remote equatorial winds and local mesoscale eddies on the existence of “River in the Sea” along the East coast of India inferred from satellite SMAP. Journal of Geophysical Research: Oceans, 125(12), e2020JC016866.

84. Kolukula, S. S., Baduru, B., Murty, P. L. N., Kumar, J. P., Rao, E., & Shenoi, S. S. C. (2020). Gaps Filling in HF Radar Sea Surface Current Data Using Complex Empirical Orthogonal Functions. Pure and Applied Geophysics, 177(12), 5969-5992.

85. Srinivas, G., Remya, P. G., Malavika, S., & Nair, T. M. (2020). The influence of boreal summer intra-seasonal oscillations on Indo-western Pacific Ocean surface waves. Scientific Reports, 10(1), 1-12.

86. Jithin, A. K., & Francis, P. A. (2020). Role of internal tide mixing in keeping the deep Andaman Sea warmer than the Bay of Bengal. Scientific reports, 10(1), 1-10.

87. Thandlam, V., TVS, U. B., Hasibur, R., Luca, P. D., Sahlée, E., Rutgersson, A., & SSVS, R. (2020). A sea-level monopole in the equatorial Indian Ocean. npj Climate and Atmospheric Science, 3(1), 1-12.

88. Vijith, V., Vinayachandran, P. N., Webber, B. G., Matthews, A. J., George, J. V., Kannaujia, V. K., ... & Amol, P. (2020). Closing the sea surface mixed layer temperature budget from in situ observations alone: Operation Advection during BoBBLE. Scientific reports, 10(1), 1-12.

89. Jithin, A. K., Subeesh, M. P., Francis, P. A., & Ramakrishna, S. S. V. (2020). Intensification of tidally generated internal waves in the north-central Bay of Bengal. Scientific reports, 10(1), 1-11.

90. Mukhopadhyay, S., Shankar, D., Aparna, S. G., Mukherjee, A., Fernando, V., Kankonkar, A., ... & Ghatkar, S. (2020). Observed variability of the East India Coastal Current on the continental slope during 2009–2018. Journal of Earth System Science, 129(1), 1-22.

91. Saha, S. K., Hazra, A., Pokhrel, S., Chaudhari, H. S., Rai, A., Sujith, K., ... & Goswami, B. N. (2020). Reply to comment by ET Swenson, D. Das, and J. Shukla on "Unraveling the mystery of Indian summer monsoon prediction: Improved estimate of predictability limit". Journal of Geophysical Research: Atmospheres, 125(21), e2020JD033242.

92. Jithin, A. K., Francis, P. A., Unnikrishnan, A. S., & Ramakrishna, S. S. V. S. (2020). Energetics and spatio-temporal variability of semidiurnal internal tides in the Bay of Bengal and Andaman Sea. Progress in Oceanography, 189, 102444.

93. Wong, A. P., Wijffels, S. E., Riser, S. C., Pouliquen, S., Hosoda, S., Roemmich, D., ... & Park, H. M. (2020). Argo data 1999–2019: two million temperature-salinity profiles and subsurface velocity observations from a global array of profiling floats. Frontiers in Marine Science, 7, 700.

94. D'Asaro, E., Altabet, M., Kumar, N. S., & Ravichandran, M. (2020). Structure of the Bay of Bengal oxygen deficient zone. Deep Sea Research Part II: Topical Studies in Oceanography, 179, 104650.

95. Vinayachandran, P. N., Das, U., Shankar, D., Jahfer, S., Behara, A., Nair, T. B., & Bhat, G. S. (2020). Maintenance of the southern Bay of Bengal cold pool. Deep Sea Research Part II: Topical Studies in Oceanography, 179, 104624.

96. Levy, G., Kumar, N., Vigundelli, S., & Gower, J. (2020). Preface: Interdisciplinary multi-sensor studies of the Pacific and Indian Oceans. International Journal of Remote Sensing, 41(15), 5645-5652.

97. Sukhatme, J., Chaudhuri, D., MacKinnon, J., Shivaprasad, S., & Sengupta, D. (2020). Near-surface ocean kinetic energy spectra and small-scale intermittency from ship-based ADCP data in the Bay of Bengal. Journal of Physical Oceanography, 50(7), 2037-2052.

98. Shenoi, S. S. C., Murty, P. L. N., Kumar, C. P., Kumar, B. A., Sunanda, M. V., Srinivas, K. S., ... & Nayak, S. (2020). Are we ready for a major tsunami in the Indian Ocean?. CURRENT SCIENCE, 118(11), 1753.

99. Pokhrel, S., Dutta, U., Rahaman, H., Chaudhari, H., Hazra, A., Saha, S. K., & Veeranjaneyulu, C. (2020). Evaluation of different heat flux products over the tropical Indian Ocean. Earth and Space Science, 7(6), e2019EA000988.

100. Remya, P. G., Kumar, B. P., Srinivas, G., & Nair, T. M. (2020). Impact of tropical and extra tropical climate variability on Indian Ocean surface waves. Climate Dynamics, 54(11), 4919-4933.

101. Murty, P. L. N., Rao, A. D., Srinivas, K. S., Rao, E., & Bhaskaran, P. K. (2020). Effect of wave radiation stress in storm surge-induced inundation: a case study for the East Coast of India. Pure and Applied Geophysics, 177(6), 2993-3012.

102. Rajasekharan Nair, H. (2020). Discernment of near-oceanic precipitating clouds into convective or stratiform based on Z–R model over an Asian monsoon tropical site. Meteorology and Atmospheric Physics, 132(3), 377-390.

103. Jangir, B., Swain, D., Ghose, S. K., Goyal, R., & Bhaskar, T. V. S. (2020). Inter-comparison of model, satellite and in situ tropical cyclone heat potential in the North Indian Ocean. Natural Hazards, 102(2), 557-574.

104. Girishkumar, M. S., Ashin, K., McPhaden, M. J., Balaji, B., & Praveenkumar, B. (2020). Estimation of vertical heat diffusivity at the base of the mixed layer in the Bay of Bengal. Journal of Geophysical Research: Oceans, 125(5), e2019JC015402.

105. Anoop, T. R., Nair, L. S., Prasad, R., Reji, S., Ramachandran, K. K., Prakash, T. N., & Balakrishnan Nair, T. M. (2020). Locally and Remotely Generated Wind Waves in the Southwestern Shelf Sea of India. Journal of Coastal Research, 89(SI), 77-83.

106. Lakshmi, R. S., Chatterjee, A., Prakash, S., & Mathew, T. (2020). Biophysical interactions in driving the summer monsoon chlorophyll bloom off the Somalia coast. Journal of Geophysical Research: Oceans, 125(3), e2019JC015549.

107. Antony, C., Unnikrishnan, A. S., Krien, Y., Murty, P. L. N., Samiksha, S. V., & Islam, A. K. M. S. (2020). Tide–surge interaction at the head of the Bay of Bengal during Cyclone Aila. Regional Studies in Marine Science, 35, 101133.

108. Francis, P. A., Jithin, A. K., Chatterjee, A., Mukherjee, A., Shankar, D., Vinayachandran, P. N., & Ramakrishna, S. S. V. S. (2020). Structure and dynamics of undercurrents in the western boundary current of the Bay of Bengal. Ocean Dynamics, 70(3), 387-404.

109. Effy, J. B., Francis, P. A., Ramakrishna, S. S. V. S., & Mukherjee, A. (2020). Anomalous warming of the western equatorial Indian Ocean in 2007: Role of ocean dynamics. Ocean Modelling, 147, 101542.

110. Murty, P. L. N., Srinivas, K. S., Rao, E. P. R., Bhaskaran, P. K., Shenoi, S. S. C., & Padmanabham, J. (2020). Improved cyclonic wind fields over the Bay of Bengal and their application in storm surge and wave computations. Applied Ocean Research, 95, 102048.

111. Darshana, P., Chowdary, J. S., Gnanaseelan, C., Parekh, A., & Srinivas, G. (2020). Interdecadal modulation of the Indo-western Pacific Ocean Capacitor mode and its influence on Indian summer monsoon rainfall. Climate Dynamics, 54(3), 1761-1777.

112. Rahaman, H., Srinivasu, U., Panickal, S., Durgadoo, J. V., Griffies, S. M., Ravichandran, M., ... & Wang, Q. (2020). An assessment of the Indian Ocean mean state and seasonal cycle in a suite of interannual CORE-II simulations. Ocean Modelling, 145, 101503.

113. Jithin, A. K., Francis, P. A., Unnikrishnan, A. S., & Ramakrishna, S. S. V. S. (2019). Modeling of internal tides in the western Bay of Bengal: Characteristics and Energetics. Journal of Geophysical Research: Oceans, 124(12), 8720-8746.

114. Sirisha, P., Remya, P. G., Modi, A., Tripathy, R. R., Nair, B., & Venkateswara Rao, B. (2019). Evaluation of the impact of high-resolution winds on the coastal waves. Journal of Earth System Science, 128(8), 1-18.

115. Rahaman, H., Bharath Raj, G. N., & Ravichandran, M. (2019). Coupled Ocean–Atmosphere Summer Intraseasonal Oscillation over the Bay of Bengal. Pure and Applied Geophysics, 176(12), 5415-5429.

116. Srinivas, G., Chowdary, J. S., Gnanaseelan, C., Parekh, A., Dandi, R., Prasad, K. V. S. R., & Naidu, C. V. (2019). Impact of differences in the decaying phase of El Niño on South and East Asia summer monsoon in CMIP5 models. International Journal of Climatology, 39(14), 5503-5521.

117. Chatterjee, A., Kumar, B. P., Prakash, S., & Singh, P. (2019). Annihilation of the Somali upwelling system during summer monsoon. Scientific reports, 9(1), 1-14.

118. Sebastian, M., Behera, M. R., & Murty, P. L. N. (2019). Storm surge hydrodynamics at a concave coast due to varying approach angles of cyclone. Ocean Engineering, 191, 106437.

119. Baduru, B., Paul, B., Banerjee, D. S., Sanikommu, S., & Paul, A. (2019). Ensemble based regional ocean data assimilation system for the Indian Ocean: Implementation and evaluation. Ocean Modelling, 143, 101470.

120. Thandlam, V., & Rahaman, H. (2019). Evaluation of surface shortwave and longwave downwelling radiations over the global tropical oceans. SN Applied Sciences, 1(10), 1-25.

121. Ashin, K., Girishkumar, M. S., Suprit, K., & Thangaprakash, V. P. (2019). Observed upper ocean seasonal and intraseasonal variability in the Andaman Sea. Journal of Geophysical Research: Oceans, 124(10), 6760-6786.

122. Kumar, B. P., D'Asaro, E., & Ravichandran, M. (2019). Widespread cooling of the Bay of Bengal by tropical storm Roanu. Deep Sea Research Part II: Topical Studies in Oceanography, 168, 104652.

123. Sanikommu, S., Banerjee, D. S., Baduru, B., Paul, B., Paul, A., Chakraborty, K., & Hoteit, I. (2019). Impact of dynamical representational errors on an Indian Ocean ensemble data assimilation system. Quarterly Journal of the Royal Meteorological Society, 145(725), 3680-3691.

124. Kantha, L., Weller, R. A., Farrar, J. T., Rahaman, H., & Jampana, V. (2019). A note on modeling mixing in the upper layers of the Bay of Bengal: Importance of water type, water column structure and precipitation. Deep Sea Research Part II: Topical Studies in Oceanography, 168, 104643.

125. Busireddy, N. K. R., Ankur, K., Osuri, K. K., Sivareddy, S., & Niyogi, D. (2019). The response of ocean parameters to tropical cyclones in the Bay of Bengal. Quarterly Journal of the Royal Meteorological Society, 145(724), 3320-3332.

126. Jampana, V., Ravichandran, M., Kantha, L., & Rahaman, H. (2019). Modeling slippery layers in the northern Bay of Bengal. Deep Sea Research Part II: Topical Studies in Oceanography, 168, 104616.

127. Gadgil, S., Francis, P. A., & Vinayachandran, P. N. (2019). Summer monsoon of 2019. Current Science, 117(5), 783-793.

128. Jyothi, L., & Joseph, S. (2019). Surface and Sub-surface Ocean Response to Tropical Cyclone Phailin: Role of Pre-existing Oceanic Features. Journal of Geophysical Research: Oceans, 124(9), 6515-6530.

129. Chowdary, J. S., Patekar, D., Srinivas, G., Gnanaseelan, C., & Parekh, A. (2019). Impact of the Indo-Western Pacific Ocean capacitor mode on South Asian summer monsoon rainfall. Climate Dynamics, 53(3), 2327-2338.

130. Pottapinjara, V., Girishkumar, M. S., Murtugudde, R., Ashok, K., & Ravichandran, M. (2019). On the relation between the boreal spring position of the Atlantic intertropical convergence zone and Atlantic zonal mode. Journal of Climate, 32(15), 4767-4781.

131. Majumder, S., & Kanjilal, P. P. (2019). Application of singular spectrum analysis for investigating chaos in sea surface temperature. Pure and Applied Geophysics, 176(8), 3769-3786.

132. Kumar, B. P., D'Asaro, E., & Ravichandran, M. (2019). Widespread cooling of the Bay of Bengal by tropical storm Roanu. Deep Sea Research Part II: Topical Studies in Oceanography, 168, 104652.

133. Krishnamohan, K. S., Vialard, J., Lengaigne, M., Masson, S., Samson, G., Pous, S., ... & Madec, G. (2019). Is there an effect of Bay of Bengal salinity on the northern Indian Ocean climatological rainfall?. Deep Sea Research Part II: Topical Studies in Oceanography, 166, 19-33.

134. Mukherjee, A., Chatterjee, A., & Francis, P. A. (2019). Role of Andaman and Nicobar Islands in eddy formation along western boundary of the Bay of Bengal. Scientific reports, 9(1), 1-10.

135. Mukherjee, A., & Kalita, B. K. (2019). Signature of La Niña in interannual variations of the East India Coastal Current during spring. Climate dynamics, 53(1), 551-568.

136. Raj Deepak, S. N., Chowdary, J. S., Dandi, A. R., Srinivas, G., Parekh, A., Gnanaseelan, C., & Yadav, R. K. (2019). Impact of multiyear La Niña events on the South and East Asian summer monsoon rainfall in observations and CMIP5 models. Climate dynamics, 52(11), 6989-7011.

137. PRERNA, S., PAUL, B., FRANCIS, P., & SHENOI, S. (2019, June). Physical Sciences of the Ocean: A report to IAPSO/IUGG. In Proc Indian Natn Sci Acad (Vol. 85, No. 2, pp. 421-429).

138. Mishra, S. K., Nayak, R. K., Mahanty, P. C., Seshasai, M. V. R., & Dadhwal, V. K. (2019). Tidal Circulation in the Hooghly Estuary and Adjacent Coastal Oceans. Journal of the Indian Society of Remote Sensing, 47(4), 705-714.

139. Girishkumar, M. S., Thangaprakash, V. P., Udaya Bhaskar, T. V. S., Suprit, K., Sureshkumar, N., Baliarsingh, S. K., ... & Shivaprasad, S. (2019). Quantifying tropical cyclone's effect on the biogeochemical processes using profiling float observations in the Bay of Bengal. Journal of Geophysical Research: Oceans, 124(3), 1945-1963.

140. Saha, S. K., Hazra, A., Pokhrel, S., Chaudhari, H. S., Sujith, K., Rai, A., ... & Goswami, B. N. (2019). Unraveling the mystery of Indian summer monsoon prediction: Improved estimate of predictability limit. Journal of Geophysical Research: Atmospheres, 124(4), 1962-1974.

141. Umesh, P. A., Bhaskaran, P. K., Sandhya, K. G., & Nair, T. B. (2019). Numerical simulation and preliminary analysis of spectral slope and tail characteristics using nested WAM-SWAN in a shallow water application off Visakhapatnam. Ocean Engineering, 173, 268-283.

142. Rao, S. A., Goswami, B. N., Sahai, A. K., Rajagopal, E. N., Mukhopadhyay, P., Rajeevan, M., ... & Maini, P. (2019). Monsoon mission: a targeted activity to improve monsoon prediction across scales. Bulletin of the American Meteorological Society, 100(12), 2509-2532.

143. Gadgil, S., Francis, P. A., & Vinayachandran, P. N. (2019). Monsoon and EQUINOO. Current Science, 117(11), 1782-1784.

144. Goni, G. J., Sprintall, J., Bringas, F., Cheng, L., Cirano, M., Dong, S., ... & Volkov, D. (2019). More than 50 years of successful continuous temperature section measurements by the global expendable bathythermograph network, its integrability, societal benefits, and future. Frontiers in Marine Science, 6, 452.

Chemical Oceanography Section

1. Chen, J., Mueller, V., Durand, F., Lisco, E., Zhong, Q., Sherin, V. R., & Saiful Islam, A. K. M. (2022). Salinization of the Bangladesh Delta worsens economic precarity. Population and Environment, 44(3), 226-247.

2. Prakash, P., Prakash, S., Ravichandran, M., Kumar, N. A., & Bhaskar, T. V. S. (2022). On anomalously high sub-surface dissolved oxygen in the Indian sector of the Southern Ocean. Journal of Oceanography, 1-12.

3. Pandi, S. R., Chari, N. V. H. K., Sarma, N. S., Lotliker, A. A., Tripathy, S. C., & Bajish, C. C. (2022). Spatiotemporal variability in the optical characteristics of dissolved organic matter in the coastal Bay of Bengal. International Journal of Environmental Science and Technology, 19(10), 9393-9408.

4. John, P. M., Murali, V., Chakraborty, K., Lotlikar, A., Shameem, K., Rahman, K. H., & Gopinath, A. (2022). Spatial and seasonal trends of trace metals in the surficial sediments from off Kochi-Geochemistry and environmental implications. Marine Pollution Bulletin, 182, 114029.

5. Steiner, Z., Landing, W. M., Bohlin, M. S., Greaves, M., Prakash, S., Vinayachandran, P. N., & Achterberg, E. P. (2022). Variability in the Concentration of Lithium in the Indo-Pacific Ocean. Global Biogeochemical Cycles, 36(6), e2021GB007184.

6. Ghosh, J., Chakraborty, K., Bhattacharya, T., Valsala, V., & Baduru, B. (2022). Impact of coastal upwelling dynamics on the pCO2 variability in the southeastern Arabian Sea. Progress in Oceanography, 203, 102785.

7. Prasad, S. J., Nair, T. M., Joseph, S., & Mohanty, P. C. (2022). Simulating the spatial and temporal distribution of oil spill over the coral reef environs along the southeast coast of Mauritius: A case study on MV Wakashio vessel wreckage, August 2020. Journal of Earth System Science, 131(1), 1-10.

8. SJ, P., & TM, B. N. (2022). Improved prediction of oil drift pattern using ensemble of ocean currents. Journal of Operational Oceanography, 1-16.

9. Peter, R., Kuttippurath, J., Chakraborty, K., & Sunanda, N. (2022, February). Modelling the oceanic partial pressure of carbon dioxide in the North Indian Ocean. In OCEANS 2022-Chennai (pp. 1-3). IEEE.

10. Sahoo, S., & Pandey, S. (2022). Characteristics and Inter-citation Network of 100 Most Influential Studies on Ocean Acidification: A Bibliometric Analysis. Science & Technology Libraries, 41(1), 56-72.

11. Acharyya, T., Sudatta, B. P., Srichandan, S., Baliarsingh, S. K., Lotliker, A. A., Raulo, S., ... & Samanta, A. (2021). Deciphering long-term seasonal and tidal water quality trends in the Mahanadi estuary. Journal of Coastal Conservation, 25(6), 1-16.

12. Chakraborty, K., Valsala, V., Bhattacharya, T., & Ghosh, J. (2021). Seasonal cycle of surface ocean pCO2 and pH in the northern Indian Ocean and their controlling factors. Progress in Oceanography, 198, 102683.

13. Chatterjee, M., Shankar, D., Vijith, V., Sen, G. K., Sundar, D., Michael, G. S., ... & Das, M. (2021). Variation of salinity in the Sundarbans Estuarine System during the Equinoctial Spring tidal phase of March 2011. Journal of Earth System Science, 130(3), 1-25.

14. Roy, R., Vinayachandran, P. N., Sarkar, A., George, J., Parida, C., Lotliker, A., ... & Choudhury, S. B. (2021). Southern Bay of Bengal: A possible hotspot for CO2 emission during the summer monsoon. Progress in Oceanography, 197, 102638.

15. Peter, R., Kuttippurath, J., Chakraborty, K., & Sunanda, N. (2021). Temporal evolution of mid-tropospheric CO2 over the Indian Ocean. Atmospheric Environment, 257, 118475.

16. Ghosh, J., Chakraborty, K., Chanda, A., Akhand, A., Bhattacharya, T., Das, S., ... & Wells, M. (2021). Outwelling of total alkalinity and dissolved inorganic carbon from the Hooghly

River to the adjacent coastal Bay of Bengal. Environmental Monitoring and Assessment, 193(7), 1-14.

17. Nimit, K. (2021). Ideas and perspectives: Ushering the Indian Ocean into the UN Decade of Ocean Science for Sustainable Development (UNDOSSD) through marine ecosystem research and operational services–an early career's take. Biogeosciences, 18(12), 3631-3635.

18. Steiner, Z., Sarkar, A., Liu, X., Berelson, W. M., Adkins, J. F., Achterberg, E. P., ... & Turchyn, A. V. (2021). On calcium-to-alkalinity anomalies in the North Pacific, Red Sea, Indian Ocean and Southern Ocean. Geochimica et Cosmochimica Acta, 303, 1-14.

19. Udaya Bhaskar, T. V. S., Sarma, V. V. S. S., & Pavan Kumar, J. (2021). Potential mechanisms responsible for spatial variability in intensity and thickness of oxygen minimum zone in the Bay of Bengal. Journal of Geophysical Research: Biogeosciences, 126(6), e2021JG006341.

20. Valsala, V., Sreeush, M. G., Anju, M., Sreenivas, P., Tiwari, Y. K., Chakraborty, K., & Sijikumar, S. (2021). An observing system simulation experiment for Indian Ocean surface pCO2 measurements. Progress in Oceanography, 194, 102570.

21. Lotliker, A. A., Baliarsingh, S. K., Shesu, R. V., Samanta, A., Naik, R. C., & Balakrishnan Nair, T. M. (2021). Did the coronavirus disease 2019 lockdown phase influence coastal water quality parameters off major Indian cities and river basins?. Frontiers in Marine Science, 8, 648166.

22. Akhand, A., Chanda, A., Watanabe, K., Das, S., Tokoro, T., Chakraborty, K., ... & Kuwae, T. (2021). Low CO2 evasion rate from the mangrove-surrounding waters of the Sundarbans. Biogeochemistry, 153(1), 95-114.

23. Manickavasagam, S., Shukla, S. P., Kumar, S., Kumar, K., & Bhuvaneswari, R. (2021). Assessment of marine microplastics in floating plastic debris using a fixed sampling device: the example of South Juhu creek, Mumbai coast, India. Journal of Coastal Conservation, 25(1), 1-10.

24. Akhand, A., Watanabe, K., Chanda, A., Tokoro, T., Chakraborty, K., Moki, H., ... & Kuwae, T. (2021). Lateral carbon fluxes and CO2 evasion from a subtropical mangrove-seagrass-coral continuum. Science of the Total Environment, 752, 142190.

25. Mohanty, P. C., Shetty, S., Mahendra, R. S., Nayak, R. K., Sharma, L. K., & Rama Rao, E. P. (2021). Spatio-temporal changes of mangrove cover and its impact on bio-carbon flux along the West Bengal coast, Northeast coast of India. European Journal of Remote Sensing, 54(1), 525-537.

26. Jose, D. M., Mandla, V. R., Neerukattu, S. R., & Saladi, S. V. S. (2021). Development of Satellite Data-Based Multiple Regression Equations for the Estimation of Total Coliform and Petroleum Hydrocarbons Along South West Coast of India. In Advances in Civil Engineering (pp. 491-506). Springer, Singapore.

27. Valsala, V., Sreeush, M. G., & Chakraborty, K. (2020). The IOD impacts on the Indian Ocean Carbon cycle. Journal of Geophysical Research: Oceans, 125(11), e2020JC016485.

28. Sarma, V. V. S. S., Bhaskar, T. U., Kumar, J. P., & Chakraborty, K. (2020). Potential mechanisms responsible for occurrence of core oxygen minimum zone in the north-eastern Arabian Sea. Deep Sea Research Part I: Oceanographic Research Papers, 165, 103393.

29. Sherin, V. R., Durand, F., Papa, F., Islam, A. S., Gopalakrishna, V. V., Khaki, M., & Suneel, V. (2020). Recent salinity intrusion in the Bengal delta: Observations and possible causes. Continental Shelf Research, 202, 104142.

30. Pradhan, U. K., Wu, Y., Shirodkar, P. V., Kumar, H. S., & Zhang, J. (2020). Connecting land use− land cover and precipitation with organic matter biogeochemistry in a tropical river–estuary system of western peninsular India. Journal of Environmental Management, 271, 110993.

31. Prasad, S. J., Francis, P. A., Balakrishnan Nair, T. M., Shenoi, S. S. C., & Vijayalakshmi, T. (2020). Oil spill trajectory prediction with high-resolution ocean currents. Journal of Operational Oceanography, 13(2), 84-99.

32. Wojtasiewicz, B., Trull, T. W., Bhaskar, T. U., Gauns, M., Prakash, S., Ravichandran, M., ... & Hardman-Mountford, N. J. (2020). Autonomous profiling float observations reveal the dynamics of deep biomass distributions in the denitrifying oxygen minimum zone of the Arabian Sea. Journal of Marine Systems, 207, 103103.

33. Steiner, Z., Sarkar, A., Prakash, S., Vinaychandran, P. N., & Turchyn, A. V. (2020). Dissolved strontium, Sr/Ca ratios, and the abundance of Acantharia in the Indian and Southern Oceans. ACS Earth and Space Chemistry, 4(6), 802-811.

34. Minu, P., Souda, V. P., Baliarsingh, S. K., Dwivedi, R. M., Ali, Y., & Ashraf, P. M. (2020). Assessing temporal variation of coloured dissolved organic matter in the coastal waters of South Eastern Arabian Sea. Acta Oceanologica Sinica, 39(1), 102-109.

35. Danish, M., Tripathy, G. R., Panchang, R., Gandhi, N., & Prakash, S. (2019). Dissolved boron in a brackish-water lagoon system (Chilika lagoon, India): Spatial distribution and coastal behavior. Marine Chemistry, 214, 103663.

36. Chakraborty, K., Kumar, N., Girishkumar, M. S., Gupta, G. V. M., Ghosh, J., Udaya Bhaskar, T. V. S., & Thangaprakash, V. P. (2019). Assessment of the impact of spatial

resolution on ROMS simulated upper-ocean biogeochemistry of the Arabian Sea from an operational perspective. Journal of Operational Oceanography, 12(2), 116-142.

37. Chakraborty, K., Lotliker, A. A., Majumder, S., Samanta, A., Baliarsingh, S. K., Ghosh, J., ... & Shanmugam, P. (2019). Assessment of model-simulated upper ocean biogeochemical dynamics of the Bay of Bengal. Journal of Sea Research, 146, 63-76.

Biological Oceanography Section

1. Sarma, N. S., Baliarsingh, S. K., Lotliker, A. A., Pandi, S. R., Samanta, A., & Srichandan, S. (2023). Sea Surface Temperature and Phytoplankton Abundance as Crucial Proxies for Green Noctiluca Bloom Monitoring in the Northeastern Arabian Sea: A Case Study. Ocean Science Journal, 58(1), 1-13.

2. Pandi, S. R., Tripathy, S. C., Parida, C., Lotliker, A. A., Naik, R. C., Naik, R. K., ... & Anilkumar, N. (2022). Spatiotemporal variability in bio-optical characteristics of the southwestern tropical Indian Ocean during boreal summer: Biophysical influences. Progress in Oceanography, 208, 102883.

3. Srichandan, S., Baliarsingh, S. K., Samanta, A., Jena, A. K., Lotliker, A. A., Nair, T. M., ... & Acharyya, T. (2022). Satellite-Based Characterization of Phytoplankton Blooms in Coastal Waters of the Northwestern Bay of Bengal. Journal of the Indian Society of Remote Sensing, 50(11), 2221-2228.

4. Sarma, N. S., Baliarsingh, S. K., Pandi, S. R., Lotliker, A. A., & Samanta, A. (2022). Noctiluca blooms intensify when northwesterly winds complement northeasterlies in the northern Arabian Sea: Possible implications. Oceanologia, 64(4), 717-734.

5. Girishkumar, M. S. (2022). Surface chlorophyll blooms in the Southern Bay of Bengal during the extreme positive Indian Ocean dipole. Climate Dynamics, 59(5), 1505-1519.

6. Roy, R., Prakash, S., Lotliker, A., Sudhakaran, P. S., & Choudhury, S. B. (2022). Response of surface chlorophyll to aerosol dust input in the Central Arabian Sea.

7. Giri, S., Chanda, A., Maity, S., Chakraborty, K., & Hazra, S. (2022). Role of tide and lunar phases on the migration pattern of juvenile Hilsa shad (Tenualosa ilisha) within a meso-macrotidal estuary. Journal of Fish Biology, 100(4), 988-996.

8. Sahoo, C. K., Raulo, S., Singh, S., Srichandan, S., Baliarsingh, S. K., Acharyya, T., & Barik, K. K. (2022). Environmental–Economical Aspects of Protonibea diacanthus: A Heavily Priced Marine Fish of India. Proceedings of the National Academy of Sciences, India Section B: Biological Sciences, 1-10.

9. Kumari, P. V., Thomas, S., Mohanty, P. C., Jayappa, K. S., Mahendra, R. S., & Gupta, A. (2021). Effect of Sea Surface Temperature Variation on Productivity and Fisheries off

Karnataka, West Coast of India. Journal of the Indian Society of Remote Sensing, 49(12), 3027-3041.

10. Baliarsingh, S. K., Lotliker, A. A., Srichandan, S., Parida, C., Roy, R., Naik, R. C., ... & Barik, K. K. (2021). Response of coastal phytoplankton pigment composition to tropical cyclone Fani. Marine Pollution Bulletin, 173, 113038.

11. Retnamma, J., Kalathil, B. K., Loganathan, J., Chinnadurai, K., Gupta, G. V. M., Chakraborty, K., & Sahu, K. C. (2021). Why the Gulf of Mannar is a marine biological paradise?. Environmental Science and Pollution Research, 28(45), 64892-64907.

12. Lakshmi, R. S., Prakash, S., Lotliker, A. A., Baliarsingh, S. K., Samanta, A., Mathew, T., ... & Nair, T. M. (2021). Physicochemical controls on the initiation of phytoplankton bloom during the winter monsoon in the Arabian Sea. Scientific reports, 11(1), 1-10.

13. Kuttippurath, J., Sunanda, N., Martin, M. V., & Chakraborty, K. (2021). Tropical storms trigger phytoplankton blooms in the deserts of north Indian Ocean. npj Climate and Atmospheric Science, 4(1), 1-12.

14. Mathew, T., Prakash, S., Baliarsingh, S. K., Samanta, A., Lakshmi, R. S., Lotliker, A. A., ... & Nair, T. B. (2021). Response of phytoplankton biomass to nutrient stoichiometry in coastal waters of the western Bay of Bengal. Ecological Indicators, 131, 108119.

15. Mandal, S., Behera, N., Gangopadhyay, A., Susanto, R. D., & Pandey, P. C. (2021). Evidence of a chlorophyll “tongue” in the Malacca Strait from satellite observations. Journal of Marine Systems, 223, 103610.

16. Holmes, E. E., BR, S., Nimit, K., Maity, S., Checkley Jr, D. M., Wells, M. L., & Trainer, V. L. (2021). Improving landings forecasts using environmental covariates: A case study on the Indian oil sardine (Sardinella longiceps). Fisheries Oceanography, 30(6), 623-642.

17. Baliarsingh, S. K., Lotliker, A. A., Srichandan, S., Roy, R., Sahu, B. K., Samanta, A., ... & Jena, A. K. (2021). Evaluation of hydro-biological parameters in response to semi-diurnal tides in a tropical estuary. Ecohydrology & Hydrobiology, 21(4), 700-717.

18. Giri, S., Chanda, A., Mondal, P. P., Samanta, S., Chakraborty, K., Maity, S., & Hazra, S. (2021). Role of biogeochemical parameters in delineating suitable habitats of juvenile Hilsa (Tenualosa ilisha) within an estuary. Environmental Biology of Fishes, 104(9), 1057-1072.

19. Umamaheswari, T., Sugumar, G., Krishnan, P., Ananthan, P. S., Anand, A., Jeevamani, J. J. J., ... & Rao, C. S. (2021). Vulnerability assessment of coastal fishing communities for building resilience and adaptation: Evidences from Tamil Nadu, India. Environmental Science & Policy, 123, 114-130.

20. Sunanda, N., Kuttippurath, J., Peter, R., Chakraborty, K., & Chakraborty, A. (2021). Long-term trends and impact of SARS-CoV-2 COVID-19 lockdown on the primary productivity of the North Indian Ocean. Frontiers in Marine Science, 1176.

21. Mohanty, P. C., Kushabaha, A., Mahendra, R. S., Nayak, R. K., Sahu, B. K., Rao, E., & Kumar, T. S. (2021). Persistence of marine heat waves for coral bleaching and their spectral characteristics around Andaman coral reef. Environmental Monitoring and Assessment, 193(8), 1-9.

22. Padhi, S. K., Patro, S., Sahu, B. K., Baliarsingh, S. K., & Sahu, K. C. (2022). A preliminary study on the environmental factors triggering frequent bloom of diatom Asterionellopsis glacialis (Castracane) Round 1990 along west coast of Bay of Bengal. Indian Journal of Geo-Marine Sciences (IJMS), 50(07), 533-541.

23. Srichandan, S., Baliarsingh, S. K., Lotliker, A. A., Sahu, B. K., Roy, R., & Nair, T. M. (2021). Unravelling tidal effect on zooplankton community structure in a tropical estuary. Environmental Monitoring and Assessment, 193(6), 1-21.

24. Jayaram, C., Pavan Kumar, J., Udaya Bhaskar, T. V. S., Bhavani, I. V. G., Prasad Rao, T. D. V., & Nagamani, P. V. (2021). Reconstruction of gap-free OCM-2 chlorophyll-a concentration using DINEOF. Journal of the Indian Society of Remote Sensing, 49(6), 1419-1425.

25. Baliarsingh, S. K., Lotliker, A. A., Srichandan, S., Basu, A., Nair, T. M., & Tripathy, S. K. (2021). Effect of tidal cycle on Escherichia coli variability in a tropical estuary. Bulletin of Environmental Contamination and Toxicology, 106(4), 622-628.

26. Mathew, T., Prakash, S., Shenoy, L., Chatterjee, A., Bhaskar, T. U., & Wojtasiewicz, B. (2021). Observed variability of monsoon blooms in the north-central Arabian Sea and its implication on oxygen concentration: A bio-argo study. Deep Sea Research Part II: Topical Studies in Oceanography, 184, 104935.

27. Nair, T. B., Nimit, K., Lotliker, A. A., Modi, A., & Joseph, S. (2021, December). Oceansat3 Applications for Ocean State Forecast and Potential Fishing Zones Services. In 2021 IEEE International India Geoscience and Remote Sensing Symposium (InGARSS) (pp. 90-93). IEEE.

28. Jayaram, C., Bhaskar, T. U., Chacko, N., Prakash, S., & Rao, K. H. (2021). Spatio-temporal variability of chlorophyll in the northern Indian Ocean: A biogeochemical argo data perspective. Deep Sea Research Part II: Topical Studies in Oceanography, 183, 104928.

29. Miranda, J., Lotliker, A. A., Baliarsingh, S. K., Jena, A. K., Samanta, A., Sahu, K. C., & Kumar, T. S. (2021). Satellite estimates of the long-term trend in phytoplankton size classes in the coastal waters of north-western Bay of Bengal. Oceanologia, 63(1), 40-50.

30. Lakshmi, R. S., Chatterjee, A., Prakash, S., & Mathew, T. (2020). Biophysical interactions in driving the summer monsoon chlorophyll bloom off the Somalia coast. Journal of Geophysical Research: Oceans, 125(3), e2019JC015549.

31. Baliarsingh, S. K., Lotliker, A. A., Srichandan, S., Samanta, A., Kumar, N., & Nair, T. M. (2020). A review of jellyfish aggregations, focusing on India's coastal waters. Ecological Processes, 9(1), 1-9.

32. Pandi, S. R., Baliarsingh, S. K., Lotliker, A. A., Sarma, N. S., & Tripathy, S. C. (2020). Empirical relationships for remote sensing reflectance and Noctiluca scintillans cell density in the northeastern Arabian Sea. Marine Pollution Bulletin, 161, 111770.

33. Srichandan, S., Baliarsingh, S. K., Lotliker, A. A., Prakash, S., Samanta, A., & Sahu, K. C. (2020). A baseline investigation of phytoplankton pigment composition in contrasting coastal ecosystems of north-western Bay of Bengal. Marine Pollution Bulletin, 160, 111708.

34. Barik, K. K., Baliarsingh, S. K., Jena, A. K., Srichandan, S., Samanta, A., & Lotliker, A. A. (2020). Satellite Retrieved Spatio-temporal Variability of Phytoplankton Size Classes in the Arabian Sea. Journal of the Indian Society of Remote Sensing, 48(10), 1413-1419.

35. Amol, P., Vinayachandran, P. N., Shankar, D., Thushara, V., Vijith, V., Chatterjee, A., & Kankonkar, A. (2020). Effect of freshwater advection and winds on the vertical structure of chlorophyll in the northern Bay of Bengal. Deep Sea Research Part II: Topical Studies in Oceanography, 179, 104622.

36. Naik, S., Mishra, R. K., Sahu, K. C., Lotliker, A. A., Panda, U. S., & Mishra, P. (2020). Monsoonal influence and variability of water quality, phytoplankton biomass in the tropical coastal waters–a multivariate statistical approach. Frontiers in Marine Science, 7, 648.

37. Pramanik, S., Sil, S., Gangopadhyay, A., Singh, M. K., & Behera, N. (2020). Interannual variability of the Chlorophyll-a concentration over Sri Lankan Dome in the Bay of Bengal. International Journal of Remote Sensing, 41(15), 5974-5991.

38. Nimit, K., Masuluri, N. K., Berger, A. M., Bright, R. P., Prakash, S., TVS, U., ... & Varghese, S. P. (2020). Oceanographic preferences of yellowfin tuna (Thunnus albacares) in warm stratified oceans: A remote sensing approach. International Journal of Remote Sensing, 41(15), 5785-5805.

39. Prakash, P., Prakash, S., Ravichandran, M., Bhaskar, T. U., & Kumar, N. A. (2020). Seasonal evolution of chlorophyll in the Indian sector of the southern ocean: Analyses of Bio-Argo measurements. Deep Sea Research Part II: Topical Studies in Oceanography, 178, 104791.

40. Sahu, B. K., Baliarsingh, S. K., Samanta, A., Srichandan, S., & Singh, S. (2020). Mass beach stranding of blue button jellies (Porpita porpita, Linnaeus, 1758) along Odisha coast during summer season.

41. Lotliker, A. A., Baliarsingh, S. K., Samanta, A., & Varaprasad, V. (2020). Growth and decay of high-biomass algal bloom in the Northern Arabian Sea. Journal of the Indian Society of Remote Sensing, 48(3), 465-471.

42. Lotliker, A. A., Baliarsingh, S. K., Sahu, K. C., & Kumar, T. S. (2020). Long-term chlorophyll-a dynamics in tropical coastal waters of the western Bay of Bengal. Environmental Science and Pollution Research, 27(6), 6411-6419.

43. Souda, V. P., Minu, P., Lotliker, A. A., Shaju, S. S., & Ashraf, P. M. (2020). Inter-annual variability in the inherent optical properties along the southeastern Arabian Sea from 2009 to 2015. Arabian Journal of Geosciences, 13(2), 1-10.

44. Miranda, J., Baliarsingh, S. K., Lotliker, A. A., Sahoo, S., Sahu, K. C., & Kumar, T. S. (2020). Long-term trend and environmental determinants of phytoplankton biomass in coastal waters of northwestern Bay of Bengal. Environmental Monitoring and Assessment, 192(1), 1-13.

45. Chakraborty, K., Maity, S., Lotliker, A. A., Samanta, A., Ghosh, J., Masuluri, N. K., ... & Bright, R. P. (2019). Modelling of marine ecosystem in regional scale for short term prediction of satellite-aided operational fishery advisories. Journal of Operational Oceanography, 12(sup2), S157-S175.

46. Jayaram, C., Udaya Bhaskar, T. V. S., Kumar, J. P., & Swain, D. (2019). Cyclone enhanced chlorophyll in the Bay of Bengal as evidenced from satellite and BGC-Argo float observations. Journal of the Indian Society of Remote Sensing, 47(11), 1875-1882.

47. Parida, C., Baliarsingh, S. K., Lotliker, A. A., Dash, M., Srichandan, S., & Sahu, K. C. (2019). Seasonal variation in optically active substances at a coastal site along western Bay of Bengal. SN Applied Sciences, 1(10), 1-8.

48. Das, I., Hazra, S., Das, S., Giri, S., Maity, S., & Ghosh, S. (2019). Present status of the sustainable fishing limits for Hilsa Shad in the northern Bay of Bengal, India. Proceedings of the National Academy of Sciences, India Section B: Biological Sciences, 89(2), 525-532.

49. Srichandan, S., Baliarsingh, S. K., Prakash, S., Lotliker, A. A., Parida, C., & Sahu, K. C. (2019). Seasonal dynamics of phytoplankton in response to environmental variables in contrasting coastal ecosystems. Environmental Science and Pollution Research, 26(12), 12025-12041.

50. Bhendekar, S. N., Chellappan, A., Sonavane, A. E., Mohanty, P., Singh, R., & Shenoy, L. (2019). Geo-spatial distribution and faunal diversity in the trawling grounds off Mumbai coast, Maharashtra, India. Indian Journal of Geo-Marine Sciences, 48(9), 1435-1442.

51. Dutta, S., Chakraborty, K., & Hazra, S. (2019). Life History and Population Dynamics of Tenualosa ilisha of Sundarban Estuary in Bay of Bengal, India for Sustainable Fishery Management. Indian Journal of Geo-Marine Sciences, 48(12), 1870-1880.

Interdisciplinary Oceanography Section

1. Tiwari, A. K., Singh, A., Saikia, D., Singh, C., & Eken, T. (2022). Crustal anisotropy beneath southeastern Tibet inferred from directional dependence of receiver functions. Physics of the Earth and Planetary Interiors, 331, 106912.

2. Kameshwari, N., Bhaskar, T. V. S., Rao, E. Pattabhirama, & Jampana, V. (2022). Enhanced marine meteorological atlas for tropical Indian Ocean. Journal of Earth System Science, 131(2), 1-21.

3. Dubey, A. K., Singh, A., Kumar, M. R., Jana, N., Sarkar, S., Saikia, D., & Singh, C. (2022). Tomographic Imaging of the Plate Geometry Beneath the Arunachal Himalaya and Burmese Subduction Zones. Geophysical Research Letters, 49(8), e2022GL098331.

4. Manneela, S., & Kumar, S. (2022). Overview of the Hunga Tonga-Hunga Ha'apai Volcanic Eruption and Tsunami. Journal of the Geological Society of India, 98(3), 299-304.

5. Yusof, N., Idris, N. H., Darwin, N., Kanniah, K. D., Kumar, N., & Levy, G. (2022, July). Interactive Distance Learning for Virtual Capacity Building Development Intra-Pandemic Experiences: A Case of Mooc UTM-PORSEC. In IGARSS 2022-2022 IEEE International Geoscience and Remote Sensing Symposium (pp. 4619-4622). IEEE.

6. Yadav, A. B., Mohanty, P. C., & Singh, A. (2022, June). Coastal Vulnerability Assessment: A case study of the Ratnagiri coast, Maharashtra, India. In IOP Conference Series: Earth and Environmental Science (Vol. 1032, No. 1, p. 012038). IOP Publishing.

7. Aggarwal, R., Ugail, H., & Jha, R. K. (2022). A deep artificial neural network architecture for mesh free solutions of nonlinear boundary value problems. Applied Intelligence, 52(1), 916-926.

8. Mahendra, R. S., Mohanty, P. C., Francis, P. A., Joseph, S., Nair, T. M., & Kumar, T. S. (2021). Holistic approach to assess the coastal vulnerability to oceanogenic multi-hazards along the coast of Andhra Pradesh, India. Environmental Earth Sciences, 80(18), 1-14.

9. Singh, A., Saikia, D., & Kumar, M. R. (2021). Seismic imaging of the crust beneath Arunachal Himalaya. Journal of Geophysical Research: Solid Earth, 126(3), e2020JB020616.

10. Dash, M., Lotliker, A. A., Das, S. K., & Sahu, K. C. (2021). Characterization of Aerosol Types by Columnar Optical Properties Analysis at a Coastal Site on Eastern Seaboard of India. Aerosol Science and Engineering, 5(1), 56-69.

11. Kuttippurath, J., Murasingh, S., Stott, P. A., Sarojini, B. B., Jha, M. K., Kumar, P., ... & Pandey, P. C. (2021). Observed rainfall changes in the past century (1901–2019) over the wettest place on Earth. Environmental Research Letters, 16(2), 024018.

12. Barik, K. K., Mohanty, P. C., Nanda, S., Ramasamy, A., & Mahendra, R. S. (2021). Earth Observation Technique-Based Coastal Vulnerability Assessment of Northern Odisha, East Coast of India. Journal of the Indian Society of Remote Sensing, 49(2), 293-303.

13. Kushawaha, J., Borra, S., Kushawaha, A. K., Singh, G., & Singh, P. (2021). Climate change and its impact on natural resources. In Water conservation in the era of global climate change (pp. 333-346). Elsevier.

14. Mishra, S., Sahoo, S., & Pandey, S. (2021). Research trends in online distance learning during the COVID-19 pandemic. Distance Education, 42(4), 494-519.

15. Narayan, R., Pati, P. K., & Sahoo, S. (2021). Growth of Open Access Literature on Library and Information Science during 2011-2020: A Scientometrics Analysis.

16. Shesu, R. V., Bhaskar, T. U., Rao, E. P. R., Ravichandran, M., & Rao, B. V. (2021). An improved method for quality control of in situ data from Argo floats using α convex hulls. MethodsX, 8, 101337.

17. Meghana, B. P., Mamdapur, G. M. N., & Sahoo, S. (2021). Twenty-five Years Study (1995â 2019) of Food and Bioproducts Processing: An Overview of Research Trends. Library Philosophy and Practice, 2021.

18. Pradhan, B., Sahoo, S., & Padhan, A. (2021). A Scientometrics Study of Research Productivity of VSS University of Technology (VSSUT) as Reflected in Scopus Database during 2015-2020. Library Philosophy and Practice, 1-14.

19. Pandey, S., & Sahoo, S. (2020). Research collaboration and authorship pattern in the field of semantic digital libraries. DESIDOC J. Libr. Inf. Technol, 40, 375.

20. Sahoo, S., & Pandey, S. (2020). Evaluating research performance of Coronavirus and Covid-19 pandemic using scientometric indicators. Online Information Review.

21. Rao, B. P., Kumar, M. R., & Saikia, D. (2020). Seismic evidence for a hot mantle transition zone beneath the Indian Ocean Geoid Low. Geochemistry, Geophysics, Geosystems, 21(7), e2020GC009079.

22. Saikia, D., Kumar, M. R., & Singh, A. (2020). Palaeoslab and plume signatures in the mantle transition zone beneath Eastern Himalaya and adjoining regions. Geophysical Journal International, 221(1), 468-477.

23. Sahoo, S., & Pandey, S. (2020). Growth Analysis of Global Scientific Research on Covid-19 Pandemic: A Scientometrics Analysis. Growth, 4, 8-2020.

24. Abraham, M., Mahendra, R. S., Mandla, V. R., Merugu, C. S., & Peddinti, V. S. S. (2020). Geospatial-based Coastal risk assessment of Gujarat coastline. In Advances in Geotechnical and Transportation Engineering (pp. 41-57). Springer, Singapore.

25. Sahoo, S., & Pandey, S. (2020). Bibliometric analysis and visualization of global ocean acidification research. Science & Technology Libraries, 39(4), 414-431.

26. Mohanty, P. C., Panditrao, S., Mahendra, R. S., Kumar, H. S., Bharadwaj, S. P., Nayak, R. K., & Ramarao, E. P. (2019). Geospatial Assessment of Flood Hazard Along the Tamil Nadu Coast. Journal of the Indian Society of Remote Sensing, 47(10), 1657-1669.

27. Chowdary, J. S., Hu, K., Srinivas, G., Kosaka, Y., Wang, L., & Rao, K. K. (2019). The Eurasian jet streams as conduits for East Asian monsoon variability. Current Climate Change Reports, 5(3), 233-244.

28. Ghosh, S., Karmakar, S., Saha, A., Mohanty, M. P., Ali, S., Raju, S. K., ... & Nayak, S. (2019). Development of India's first integrated expert urban flood forecasting system for Chennai. Current Science, 117(5), 741-745.

29. Ved, M., & Rizwanahmed, B. (2019, July). Big data analytics in telecommunication using state-of-the-art big data framework in a distributed computing environment: a case study. In 2019 IEEE 43rd Annual Computer Software and Applications Conference (COMPSAC) (Vol. 1, pp. 411-416). IEEE.

30. Krishnan, P., Ananthan, P. S., Purvaja, R., Joyson Joe Jeevamani, J., Amali Infantina, J., Srinivasa Rao, C., ... & Ramesh, R. (2019). Framework for mapping the drivers of coastal vulnerability and spatial decision making for climate-change adaptation: A case study from Maharashtra, India. Ambio, 48(2), 192-212.

31. Barik, K. K., Annaduari, R., Mohanty, P. C., Mahendra, R. S., Tripathy, J. K., & Mitra, D. (2019). Statistical assessment of long-term shoreline changes along the Odisha Coast.

32. Bittig, H. C., Maurer, T. L., Plant, J. N., Schmechtig, C., Wong, A. P., Claustre, H., ... & Xing, X. (2019). A BGC-Argo guide: Planning, deployment, data handling and usage. Frontiers in Marine Science, 6, 502.

33. Roemmich, D., Alford, M. H., Claustre, H., Johnson, K., King, B., Moum, J., ... & Yasuda, I. (2019). On the future of Argo: A global, full-depth, multi-disciplinary array. Frontiers in Marine Science, 6, 439.

National Report on Seismological Research in India: 2019 – 2022

Ajay Manglik
CSIR-National Geophysical Research Institute, Uppal Road, Hyderabad - 500007, INDIA
(e-mail: ajay@ngri.res.in)

1. Introduction

The present chapter is a compilation for the International Association of Seismology and Physics of the Earth's Interior (IASPEI), encompassing the scientific activities carried out in the country during 2019-2022, in the field of seismology. The chapter is arranged to categorize the contributions under internal structure of the Indian lithosphere and sub-lithospheric mantle, crust and upper mantle deformation, seismic attenuation, seismic hazards, triggered seismicity, environmental seismology, paleoseismology and seismological networks. In addition, the chapter includes activities related to societal projects and outreach programs. It is not an exhaustive review of the entire Indian contribution to seismology and allied fields during this period but a window to the topics covered within the framework of IASPEI.

During the reporting period, researchers from several Indian R&D and Academic Institutions continued adding new results on the crustal and upper mantle structure of the Indian shield, both at regional and geological province scale. The Himalaya has been a major focus of seismological research for many Institutes who operated broadband seismological networks from Kashmir to Arunachal along the Himalayan arc. The data from these networks have facilitated in enhancing our understanding of the structure of the Main Himalayan Thrust, crustal and upper mantle structure as well as the dip of the underthrusting Indian plate, seismicity monitoring, and estimation of attenuation. Some of these networks also include accelerographs for strong ground motion studies. A few studies also focused on mapping of the mantle transition zone beneath the Indian Ocean Geoid Low. The studies on anthropogenic seismicity added near-field investigations in the Koyna - Warna region through borehole seismology. Organization of the Joint Scientific Assembly of IAGA and IASPEI during 21-27 August 2021 (JSA-2021) was a major event during this period related to the IUGG activities. Originally, the event was planned to be hosted at Hyderabad, India, but due to the COVID-19 pandemic it was organized in virtual mode. Initiatives have been taken to nucleate the field of environmental seismology in the country.

Many R&D Institutes and Academic Departments in the country pursue seismological research. The National Center for Seismology under the Ministry of Earth Sciences (MoES), Government of India, is the nodal agency for monitoring and reporting earthquake activity in the country. It has got a network of more than 150 broadband seismological stations spread across the country. In addition to this, several seismological networks are operated by R&D Institutes under CSIR, DST, MoES and State Government of Gujarat, and Academic departments under IITs and IISERs, mainly for region-specific seismological research. These are briefly covered in Section 10. The chapter has been prepared based on the inputs received from many researchers belonging to these Institutes/Departments. However, it is not an exhaustive review of all the Indian contribution to seismology and allied fields during this

period. Seismological Imaging of the Indian Lithosphere and Mantle

1.1. Indian Shield Region

Inversion of receiver functions (RF) revealed that the Deccan Volcanic Province (DVP) and the Eastern Dharwar Craton (EDC) have distinct crustal structure in terms of crustal thickness, average composition, shear wave velocity variation and nature of the crust-mantle boundary (Kumar S., et al., 2020). Using a similar methodology, Gupta and Kumar (2022) estimated the thickness of the lithosphere beneath EDC and DVP and found it to be ~50–60 km thinner in the DVP compared to that in the EDC. Arjun et al. (2022) carried out a joint modelling of teleseismic travel-time residuals, Bouguer gravity anomaly and surface topographic data to delineate the nature of the continental lithosphere beneath the Archaean Dharwar craton along an ENE-WSW traverse and reported an estimate of the Te and its role in supporting the topographic loads imposed by the Western Ghats, located near the western margin of the Southern Indian shield.

Rao and Ravi Kumar (2022a) studied the crustal and uppermost mantle structure of the Western Ghats (WG) by slant stacking, common conversion point imaging and harmonic decomposition of RFs. Their results reveal a large crustal thickness of ~45 km in the central part of the WG, which decreases to ~39 km in the southern and ~37 km in the northern parts. The RFs also reveal a strong sub-Moho low velocity layer. By jointly inverting receiver function and surface wave group velocity dispersion, Mandal et al. (2022a) found that the Moho depth ranges from 39.5 to 42 km, while the lithospheric thickness varies from 108 to 120 km across 6 stations beneath the Palghar region in Maharashtra. Inversion of receiver functions from a network of 10 stations in the vicinity of Hyderabad revealed a 4-layered crust with a 16-km-thick high-velocity lowermost crustal layer, a 9-km-thick upper crustal layer with a Vp of 6.27 km/s, a middle and upper lower crust between 9–22 km depth (Mandal et al., 2022c). The modelled Moho depths vary from 35.4 to 37.6 km across the region.

During 2013-2017, CSIR-NGRI maintained a seismic network of 15 three-component broadband stations in the Eastern Indian Craton (EIC). Results from joint inversion of receiver functions and surface wave group dispersion show a marked crustal thinning of 5–10 km and a ~90 km thick lithosphere below the Singhbhum-Odisha-Craton (SOC), with a flat crust having a thickness of 42 km below the Chotanagpur Granitic Gneissic Terrain (CGGT) (Mandal, 2019a). A marked crustal and lithospheric thinning beneath SOC is also seen (Mandal et al., 2021). In addition, this study showed a relatively smaller degree of crustal (2–4 km) and lithospheric thinning (4–10 km) beneath the Eastern Ghat Mobile Belt, south of the SOC. Despite a thick crust, they note a 15–20 km lithospheric thinning associated with the CGGT. Based on results from H-K stacking and CCP imaging, a secular variation of the Archean crust formation is inferred in the Eastern Indian Shield (Mandal, 2022a). They observed a correlation between crustal age and composition within the ellipsoidal Paleoarchaean cratonic domain in the SOC. In analogy with the Paleoarchaean and Mesoarchaean granite-greenstone terrains such as the eastern Pilbara, Barbeton, and Kappvaal cratons, Mandal et al. (2021) suggested that crust formation during the Paleoarchaean SOC may have involved a thick oceanic mafic plateau followed by polybaric melting resulting in pulses of felsic magmatism with concurrent gravitational reorganization via Rayleigh Taylor Instabilities.

A similar study indicated crustal and lithospheric thinning beneath Kachchh, along with a 2-

6% reduction of Vs across the Lithosphere-Asthenosphere-Boundary (Mandal, 2019b). Local earthquake tomography of the Kachchh rift zone (Mandal, 2020a, 2022b) showed two prominent high-velocity anomalies within the crust which were attributed to mafic plutons. Paul H., et al. (2021) estimated the crustal thickness and uppermost mantle velocity beneath the Gujarat region using Moho-reflected phases and found that the Kachchh region has a thicker crust (43 km) owing to a root and high uppermost mantle velocity.

Pn (Illa et al., 2021a) and Sn tomography (Illa et al., 2021b) of the Indian Shield and adjacent regions reveals that the upper mantle of the Indian shield is characterized by a Pn velocity of 8.12–8.42 km/s, while a large part of the central Indian shield has a higher mantle-lid velocity of ~8.42 km/s with a dominant anisotropic value of ~7.5% amounting to a variation of 0.2–0.3 km/s (Fig.1).

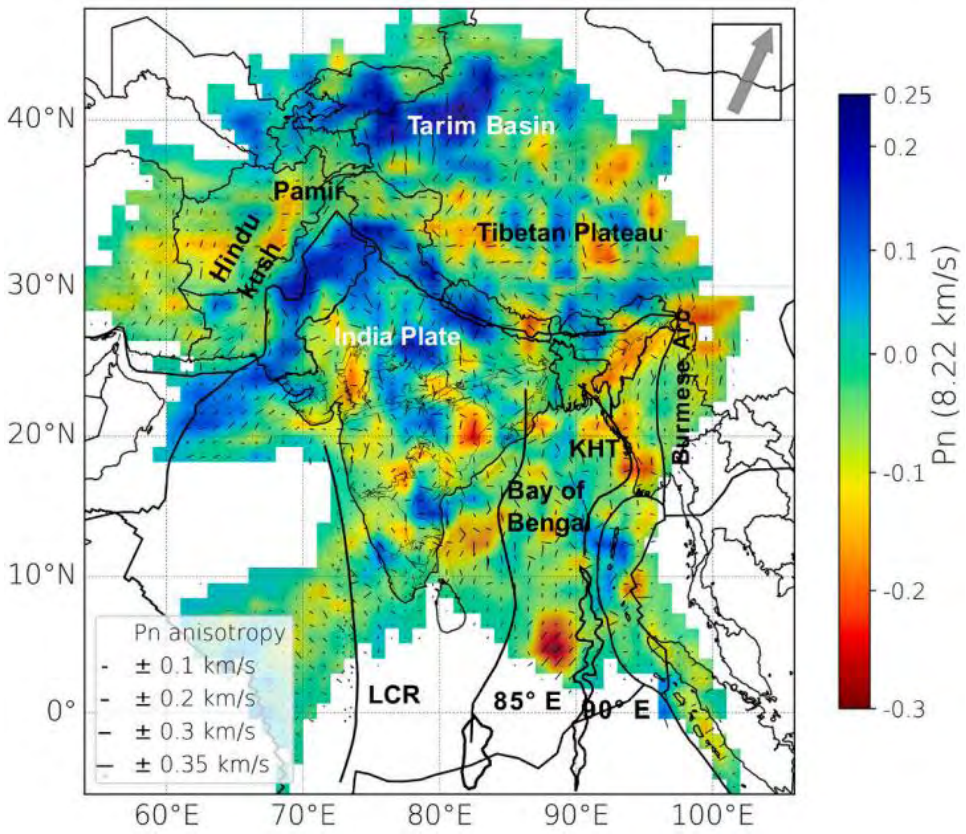

Figure 1. Pn velocity of the upper mantle of the Indian shield and adjoining regions obtained on a grid of 1°×1° size. Pn anisotropy results with magnitudes are also superimposed to illustrate the correspondence between anisotropy patterns and the major velocity anomalies. KHT- Kerguelen hotspot track. The gray arrow in the top right corner indicates the present-day Indian plate motion direction. (From Illa et al., 2021a) (*Reprinted from Tectonophysics, Vol 813, Bhaskar Illa, K.S. Reshma, Prakash Kumar, D. Srinagesh, C. Haldar, Sanjay Kumar, Prantik Mandal, Pn tomography and anisotropic study of the Indian shield and the adjacent regions, 228932, Copyright (2021), with permission from Elsevier*.)

Srinu et al. (2021) investigated the X-discontinuity beneath India, using P-RFs at seismological

stations deployed on the Indian shield and the Himalaya. They detect the X-discontinuity as a sporadic and thin feature in the depth range of 246–335 km, with a sharp shear velocity jump of 2.5-3.6%.

The DVP is considered to have its genesis in the interaction of the Indian plate with the Réunion mantle plume. Sharma J., et al. (2021) investigated the group velocity dispersion data in the period range of 6-100 s derived from waveforms of 77 regional earthquakes recorded at 38 broadband stations and performed surface wave tomography. The results revealed signatures of magmatic underplating and a thick crust beneath the Kachchh seismic zone and Western Ghats. A predominant low-velocity zone beneath the Cambay, Saurashtra, and adjoining regions was interpreted as a residual thermal anomaly and thin lithosphere as a result of weakening due to plume-lithosphere interaction.

Singh and Singh (2019) presented a high-resolution seismic image of the hitherto-elusive crustal architecture of the Eastern Ghat Mobile Belt (EGMB) and its contact with Archaean cratons using teleseismic receiver functions. The results reveal a thick crust (40 km) with oppositely dipping Moho below the contact between the EGMB and the Bastar craton. The crust of Bastar craton extends (~75 km) eastward beneath the EGMB-Bastar surficial contact. Jana et al. (2022) constrained the velocity model by jointly inverting the surface wave dispersion data with receiver function data (Fig.2). The lithospheric and asthenospheric velocity model excludes the possibility of southward accretionary growth of Singhbhum craton to form Rengali province. Also, a metasomatically altered zone has been reported in some areas. The signature of removal of lithospheric root beneath the investigating region indicates the thermo-mechanical destruction caused by plume hotspots during the northward drift of proto-India.

Mullick et al. (2022) obtained a 3-D shear velocity model of South Indian Precambrian terrains at a lateral resolution of 55 km down to 250 km depth by inversion of fundamental mode Rayleigh wave phase velocity dispersion data in the period range of 30-140s, which shows a 150-200 km thick lithosphere beneath most of the Archaean Dharwar craton. An extraordinary high shear velocity (up to 4.8 km/s) and thick lithosphere (150 km) are observed beneath the Proterozoic Carbonatite complex, located at the south-eastern edge of the Dharwar craton. They inferred a compositional modification of the lower lithosphere at the south-western margin of the Dharwar craton and lithospheric erosion in the Granulite terrain both possibly due to interaction with the Marion mantle plume at ~90 Ma.

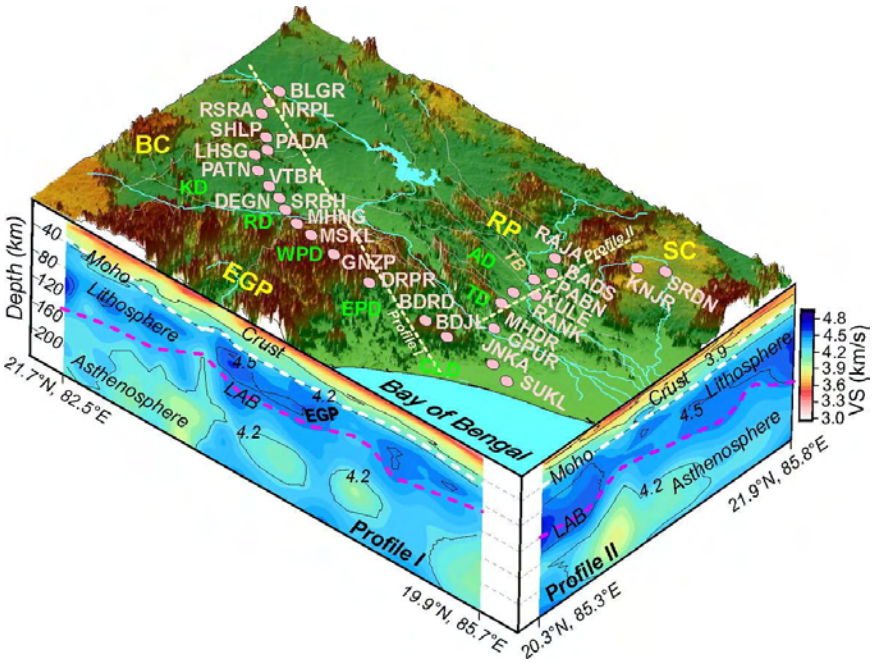

Figure 2. Shear velocity structure of the upper mantle along two profiles, obtained from joint inversion of the surface wave dispersion data and receiver functions. (From Jana et al., 2022) (*Reprinted from Gondwana Research, 111, Niptika Jana, Chandrani Singh, Arun Singh, Tuna Eken, Arun Kumar Dubey, Abhisek Dutta, Arun Kumar Gupta, Lithospheric architecture below the Eastern Ghats Mobile Belt and adjoining Archean cratons: Imprints of India-Antarctica collision tectonics, 209-222, Copyright (2022), with permission from Elsevier*.)

Das and Rai (2019) generated a 3-D shear velocity image of the crust through joint inversion of the P- RFs and Rayleigh wave group velocity dispersions, derived from cross correlation of ambient noise, to study the linkage and the boundary between the Dharwar craton and the Southern Granulite Terrain (SGT). The study delineated a 10–15 km thick high shear velocity layer in the lowermost crust of the southern part of the WDC continuing into the SGT up to 40 km beyond the E-W trending southern limb of the Palghat-Cauvery shear zone, suggesting that the Dharwar craton continues further south of the mapped orthopyroxene boundary to the Palghat shear zone.

Vashishtha et al. (2022) used surface wave data from the April 25, 2015, Nepal earthquake (Mw 7.8) and its aftershocks, recorded at eleven stations in India to estimate group velocities of both Love and Rayleigh waves. All stations are at regional distances from the earthquake sources. It is observed that the group velocities for both Love and Rayleigh waves obtained from the mainshock data are lower than those obtained from aftershock data for stations located towards W and SW of the earthquake source region. Such a variation of group velocity obtained from mainshock and aftershock data for different stations may be due to source directivity for the mainshock affecting the source group time, which in turn affects the travel time of surface waves at different periods.

1.2. Himalaya

Kanna and Gupta (2020) studied the crustal structure of the Garhwal Himalaya along a linear profile, using regional travel times and receiver function analysis. Their receiver function modeling showed a prominent intra-crustal low velocity layer with a flat–ramp–flat geometry

beneath the Main Central Thrust zone and a variation in the Moho depth from ~45 km beneath the Sub Himalaya to ~58 km to the south of the Tethys Himalaya. A similar study in the NW Himalaya and Ladakh-Karakoram indicates that the Moho depth increases from ~46 km below the Gangetic Plain to ~78 km at the southern flank of the Karakoram Fault. Several intra-crustal low-velocity layers were seen and the MHT is mapped as an LVL (Kanna and Gupta, 2021).

Gupta S., et al. (2022) examined the P-wave velocity (Vp) and Vp/Vs variations using local earthquake arrival time measurements recorded over 41 seismic stations operated during November 2006 to June 2008 in the Kumaun–Garhwal Himalaya. In the 0–25 km depth range, the Vp and Vp/Vs varies between 4.8–6.8 km/s and 1.55–1.85, respectively and show a heterogeneous structure in the upper-mid crust. The seismic images exhibit signatures of unconsolidated sediments, close to the Main Frontal Thrust, and Klippes (Lansdowne and Almora) in the uppermost crust. In the upper-mid crust, the observed low Vp and high Vp/Vs (1.82–1.85) along with available conductivity values indicate saline-rich aqueous fluid and partial melt. Using the inferred crustal composition and constraints from earlier information, they proposed the bottom of these fluid zones as the top of the underthrusting India Plate, which shows a flat-ramp-flat geometry at 16–21 km depth. The earthquakes of moderate and smaller magnitude mostly occur in the fluid-rich zone above the mid-crustal ramp in the underthrusting Indian Plate. Madhusudhan et al. (2022) calculated the uppermost mantle seismic (Pn and Sn) velocities using 12 regional earthquakes recorded by 33 digital broadband seismological stations from the Gangetic plain to the Tethys Himalaya along a ~160 km profile and showed that the Moho dips in the north direction with an overall dip angle of 3.43°- 4.2º in the Eastern Kumaun Himalaya.

Mandal et al. (2021c) imaged the lateral variations in the Moho depths and average crustal composition across the Kumaun–Garhwal Himalaya, through H-K stacking of 1400 radial P-RFs from 42 broadband stations. The modeled Moho depth and average crustal Vp/Vs values vary from 28.3 to 52.9 km and 1.59 to 2.13, respectively. They also mapped three NNE-SSW trending transverse crustal blocks in Uttarakhand Himalaya that extend down to the lithosphere-asthenosphere boundary. Local earthquake tomography of the Kumaun-Garhwal Himalaya (Mandal et al., 2022b; Gupta S., et al., 2022) shows a low velocity (Vp, Vs), high Vp/Vs mid-crustal layer, which was identified as the Main Himalayan Thrust associated with metamorphic fluid/partial melt.

The Himalaya-Karakoram-Tibet region characterizes a unique setup of crustal and upper mantle structure related to present-day geodynamics. Kumar N., et al. (2019) performed surface wave tomography studies that reveal highly variable shear wave velocity structure indicating signatures of underthrusting of the Indian plate beneath Eurasia. The study reveals a NE-dipping Moho with its depth increasing from ~40 km beneath the frontal Himalaya to 70-80 km below the collision zone. Low near-surface seismic velocities indicate thick sediments (5-6 km) in the Indo-Gangetic plains. Broader low-velocity zone at mid-crustal depth beneath the southern parts of Tibet and Karakoram fault is due to the presence of partial melting and/or aqueous fluids.

Kumar V., et al. (2022) used ambient noise cross-correlations from 530 seismological stations along with surface wave observations from 1,261 earthquakes to image the crust beneath the western Himalaya-Asia convergence zone encompassing western Himalaya-western Tibet-Ladakh-Karakoram-Pamir-Hindu Kush. The seismological data from the PASSCAL

experiments, the Global Seismograph Network, experiments in Kyrgyzstan, Kazakhstan, Tajikistan, China, Nepal and western Tibet, French deployments in western Kunlun and Kazakhstan and Indian deployments in the western Himalaya were used in this study that resulted in 22,726 inter-station Rayleigh wave dispersion measurements in the period band of 5 to 60 s at a horizontal resolution of less than 0.5°×0.5°. The 3-D shear wave velocity image revealed that the northern limit of the Indian crust extends beyond the Qiangtang block in western Tibet (77°-82°E) and till the central Pamir farther west. The study suggests a continuation of LVZs across the Karakoram Fault at a depth below 20 km, indicating the fault's upper crustal depth extent.

The seismicity in the Kumaun Himalaya is concentrated in the Chiplakot Crystalline Belt (CCB). WIHG conducted a passive seismological study using receiver functions (RFs) along a profile (see Fig.1 of Hazarika et al., 2021). The H-K stacking analysis of RFs of teleseismic earthquakes reveals a significantly high value of the Poisson's ratio (~0.28) in the Dharchula region of the CCB which is coincident with the earthquake cluster (Hajra et al., 2019). The RF inversion and Common Conversion Point (CCP) stacking imaging reveals a variation of crustal thickness from ~38 km in the Indo-Gangetic Plain to ~42 km near the Vaikrita Thrust (see Fig.6 of Hazarika et al., 2021). A ramp (~20º) structure on the MHT is revealed beneath the CCB. The spatial and depth distribution of seismicity pattern beneath the CCB and presence of steep dipping imbricate faults inferred from focal mechanism solutions suggest a Lesser Himalayan Duplex structure in the CCB above the MHT ramp (Hazarika et al., 2021; Hajra et al., 2021).

Medved et al. (2022) obtained 3D models of the crust and uppermost mantle beneath the NW Himalaya down to a depth of 120 km by local earthquake seismic tomography using data of India Meteorological Department (IMD) complemented by the Global International Seismological Centre (ISC) Catalogue. Their results suggest that the Indian Plate not only underthrusts northwards below the Himalaya but also bends westwards as it gets closer to the Hindukush Region. A peculiar feature of the model is a high-velocity anomaly in the Kaurik Chango Rift, interpreted as a remnant of the oceanic crust, left after the closure of the Indo-Tethys Ocean. In the seismically active Delhi-Haridwar Ridge, a low-velocity upper crustal layer is possibly associated with sediments of the Indo-Gangetic Plain and with a large number of fault structures.

Mir et al. (2021) estimated the shear wave velocity structure, together with Moho depths for the NW Himalaya, Hindu Kush and the Pamirs at a potential resolution of 0.5×0.5 degrees and at 1×1 degrees in the surrounding area (Fig.3), by inverting fundamental mode Rayleigh wave group velocities calculated from regional earthquake ($\Delta \leq 2500$ km) data, and also from their joint inversion with teleseismic receiver functions at 38 out of the 59 broadband stations in the region. The results illuminate a) the deeper root zone structures of the main geomorphic features, b) a pervasive low velocity layer (Vs ~3.1 km/s) at ~30 km depth beneath the NW Himalaya. Another notable result is the distinctly shallower Moho beneath the Kashmir Himalaya apparently segmented by arc-normal shear zones that cross the rupture zones of the 1905 Kangra and the 2005 Kashmir earthquakes, in turn, marked by the current epoch seismicity.

A high-resolution seismic image of the crust beneath the Arunachal Himalaya is documented by Singh A., et al. (2021), using RF analysis of data from 32 broadband seismic stations

deployed in the Arunachal Himalaya during 2010-2016, along with data from the HIMNT, SIKKIM, Hi-CLIMB, and GANSSER networks. Their results reveal lateral variations in the crustal structure with the Moho depth varying from 40-60 km. They also observe a comparatively less complex crust, absence of a prominent mid-crustal ramp, a highly deformed layer running parallel to the Main Himalayan Thrust, and an intermittent anisotropic low velocity layer in the middle crust.

In a recent study (Ravi Kumar et al., 2022), receiver function images of the detachment, mid-crustal ramp and the Moho of the underthrusting Indian plate along four profiles in the Arunachal Himalaya are documented (Fig.4). The results reveal a clear Moho signature in the depth range of 40 to 65 km, with the detachment mapped in the depth range of ~10 to 20 km. A mid-crustal ramp can be traced in the higher Himalaya especially along one profile. Singh A., et al. (2021) imaged the crust beneath the Arunachal Himalaya using teleseismic receiver functions. A mechanically weak middle crust beneath Arunachal Himalaya, highly deformed layer parallel to MHT, and comparatively less complex crust beneath Arunachal than Nepal and Sikkim are some important observations that have been reported in this study.

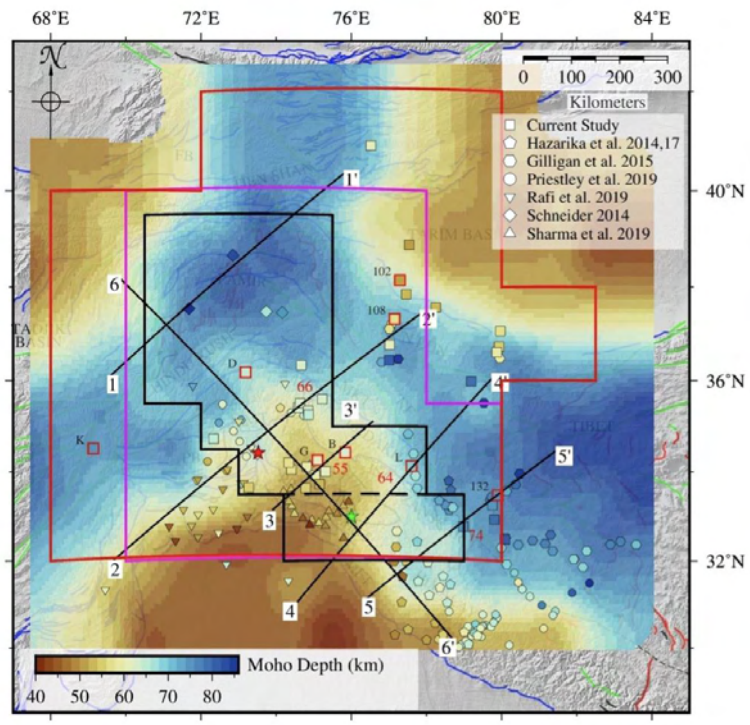

Figure 3. Posterior Moho depth estimates for the Kashmir Himalaya region. The average Moho depth in the region is found to be ~70 km, with higher depths beneath Tibet and the Pamir and shallower ones beneath the Tarim, Tadjik and Fergana basins, as well as the Himalayan foreland basin. (From Mir et al., 2021) (*Courtesy CSIR-4PI*)

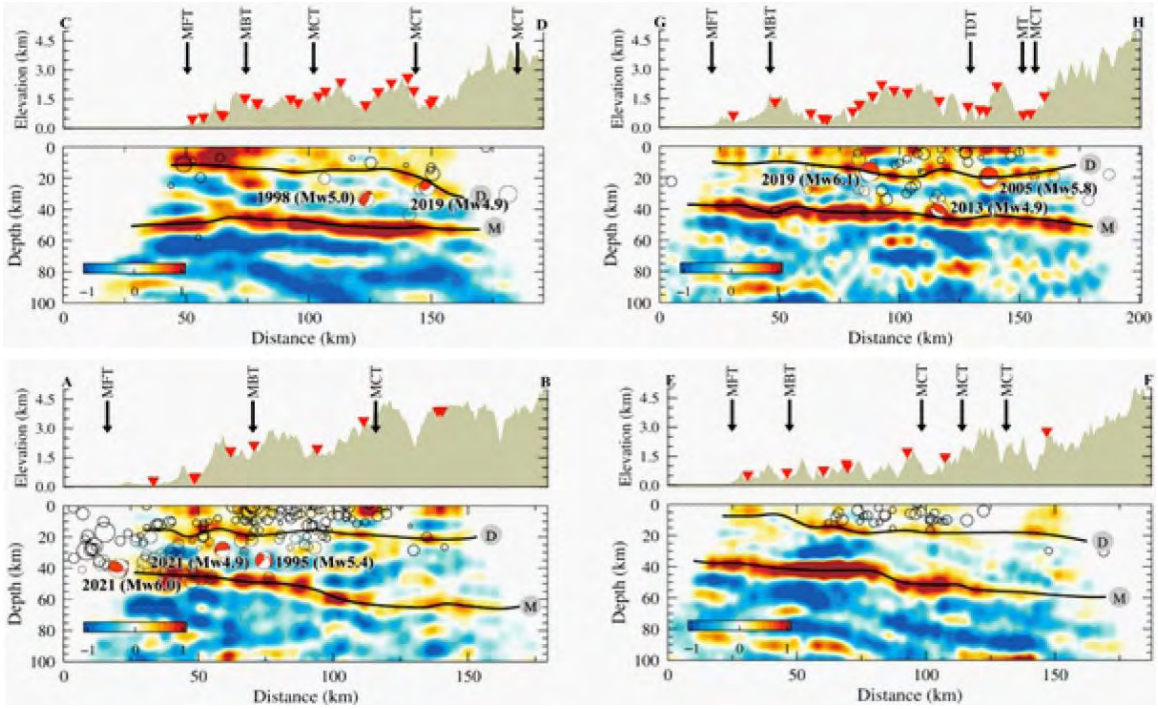

Figure 4. 3D migrated P-RF images along the Arunachal Himalaya profiles along with the elevation within ±50 km. Focal mechanisms of moderate magnitude earthquakes and local seismicity are superimposed on the 3D migrated images (circles). D: Detachment and M: Moho are marked based on P-RF images. (From Ravi Kumar et al., 2022) (*Reprinted from Journal of Asian Earth Sciences, 236, Ravi Kumar Mangalampalli, Padma Rao Bommoju, Mahesh Perugu, Vempati Venkatesh, Scattered wave imaging of the Main Himalayan Thrust and mid-crustal ramp beneath the Arunachal Himalaya and its relation to seismicity, 105335, Copyright (2022), with permission from Elsevier.*)

Crustal thickness in the NE India including the eastern Himalaya is investigated using surface wave tomography and the RF studies (Kundu et al., 2020; Kumar A., et al., 2021). The results reveal that the Bengal Basin comprises thick sediments (up to ~20 km) with thickness increasing from west to east. The Moho depth increases from ~40 km in the Shillong plateau and Brahmaputra valley to ~70 km beneath the Higher Himalaya and southern Tibet. The crustal thickness and Poisson's ratios reveal thickening of the crust from ~46 km beneath the Brahmaputra valley in the west to ~55 km in the western part of the Lohit Plutonic Complex (LPC). Similar analysis carried out in the Siang Window of the NE Himalaya reveals a variation of crustal thickness from ~38 km in the Brahmaputra valley (Pasighat) to ~53 km at the northern boundary of the window (Gelling area). The estimated Poisson's ratio in the Brahmaputra valley is low (0.23), suggesting a felsic composition of the crust. It is intermediate in the Mishmi Thrust zone (0.249–0.261) and in some parts of the LPC. A high Poisson's ratio (0.277–0.293) is obtained for the Tidding Tuting Suture Zone (TTSZ) and western part of the LPC, indicating the presence of aqueous fluid/partial melt in the crust (Kundu et al., 2020).

Shukla et al. (2022) investigated the crustal configuration beneath northeast India based on receiver function analysis of teleseismic earthquakes recorded by 19 broadband seismological stations using H-k stacking method. The study reveals a large variation in crustal thickness and Poisson's ratio which are correlated with the complex geology and tectonics of the region. The crust is observed to be thinner (36.5–41.6 km) beneath Bengal Basin, Shillong Plateau, and the

Brahmaputra valley compared to the Indo-Burma Ranges (IBR) (~40–54 km) and Arunachal Higher Himalaya (TAWA station, ~45 km) and Sikkim Himalaya (GTK station, ~46.5 km). A large variation of Poisson's ratio is observed in the region (~0.230–0.306).

On the occasion of the Diamond Jubilee Year of CSIR-NGRI in 2021, Manglik et al. (2021) reviewed the geophysical studies carried out by the Institute since 1961 for the crustal and upper mantle structure of the Himalaya.

1.3. Indo-Burmese Arc

Saikia et al. (2020) investigated the mantle transition zone (MTZ) structure beneath the eastern Himalaya, southern Tibet, Assam valley, Burmese arc and Bengal basin regions using receiver functions of 327 stations. A depression in the 410 and 660 km discontinuities is observed beneath the Bengal basin and to the east of the eastern Himalayan syntaxis. The 410 is elevated by ~10 km along the Himalayan collision front, while it deviates in the range of ±5 km beneath most parts of Tibet and the Himalayan Foredeep. The 410 and 660 km discontinuities are uplifted by nearly 10 km beneath the Arunachal Himalaya. They observe a thick (>20 km) transition zone beneath the Burmese Arc and close to the Tengchong volcano.

Dubey et al. (2022) presented 3-D P- and S-wave velocity perturbation maps of the upper-mantle beneath eastern Himalaya and Burmese subduction zones. Tomograms revealed that the subducting Indian lithospheric plate extends up to Bangong-Nujiang Suture Zone, overturns and descends steeply beyond 200 km below the Himalayan arc. A southward plunging detached slab can be traced beyond 600 km. Results reveal no evidence for the detachment of a S-E deflecting Indian lithospheric slab below the Burmese arc.

Surface wave tomography reveals thick sediments represented by low shear wave velocity down to ~21 km depth in the eastern Bengal Basin beneath the southern Indo-Burma Range (IBR) (Kumar A., et al., 2021; Chanu et al., 2022). Tomography images also report subduction of Indian plate beneath the Burmese arc with signatures of a medium of high shear wave velocity below ~50 km to ~75 km depth.

1.4. Indian Ocean and Bay of Bengal

Rao et al. (2020) investigated the mantle transition zone (MTZ) structure beneath the Indian Ocean Geoid Low (IOGL) region using P-RFs. 3-D time-to-depth migration of P-RFs reveals a thin MTZ primarily due to an elevation of the 660 km discontinuity. This is suggestive of anomalously hot temperatures in the mid-mantle beneath the IOGL region, possibly sourced from the African Large Low Shear Velocity Province (LLSVP). The seismic structure of the D″ layer beneath the Indian Ocean is investigated by modeling the ScS-S and PcP-P differential travel time residuals (Rao and Ravi Kumar, 2022b). Modeling of the residuals using a grid search approach revealed velocity perturbations in the range of -3.06% to 5.72% for the shear and -4.81% to 5.47% for compressional waves in the D″, which were positive below the Indian Ocean Geoid Low (IOGL) and negative below the adjoining region (Fig.5). The results reveal presence of high velocity material atop the Core Mantle Boundary (CMB) beneath the IOGL.

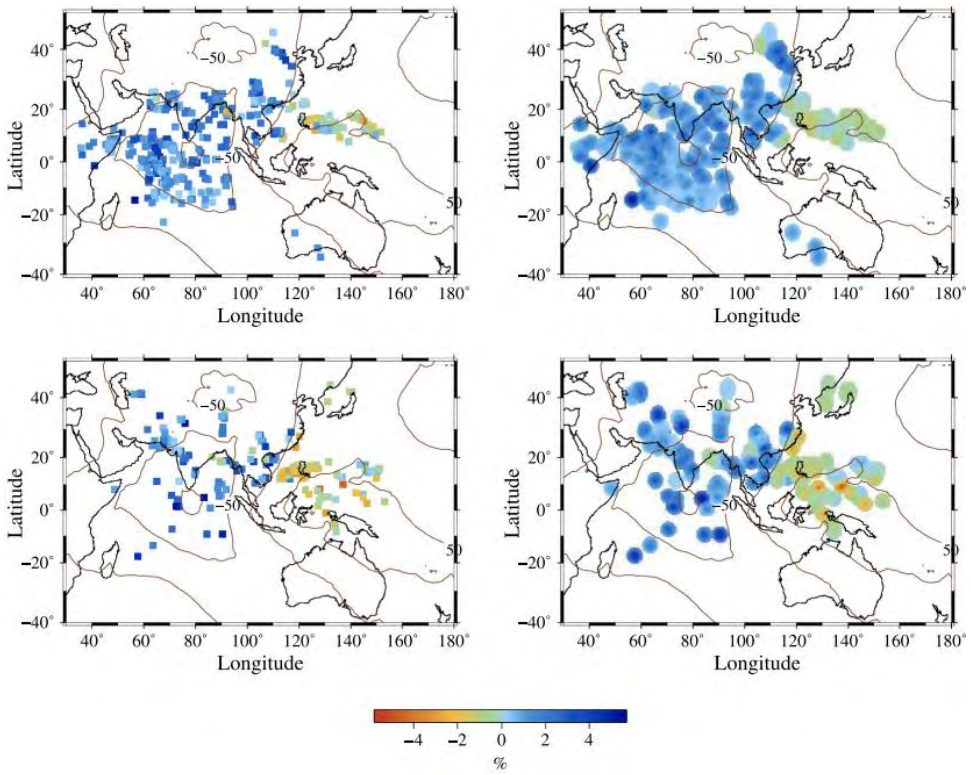

Figure 5. Percentage of shear (top left panel) and compressional wave velocity perturbations (bottom left panel) required to explain the observed differential travel time residuals in a 220 km thick layer above the CMB. Averaged shear (top right panel) and compressional wave velocity perturbations (bottom right panel) in the bottom 220 km of the mantle are inferred from the corrected travel time residuals. (From Rao and Ravi Kumar, 2022b) (*Reprinted from Journal of Asian Earth Sciences, 225, Padma Rao B., Ravi Kumar M., Lowermost structure beneath the Indian Ocean: Insights from modeling of ScS-S and PcP-P residuals, 105038, Copyright (2022), with permission from Elsevier*.)

Paul and Ravi Kumar (2022) identified salient features of the mantle beneath the Indian Ocean and Ross Sea, by analyzing 8 global tomographic models. Their study indicates low velocity anomalies of dVs ~1.1% in the ~400–680 km depth range and inconsistent high velocity anomalies of dVs ≥ 1% at depths below 1600 km beneath both Indian Ocean and Ross Sea. A consistent low velocity structure throughout the mantle beneath the southwestern Indian Ocean and east Africa is associated with a plume from the African LLSVP. Forward modeling of the Geoid indicated that the E-W extent of the IOGL, influenced by upper mantle anomalies, could be precisely predicted, however, the N-S extent is underestimated since the lower mantle anomalies are inconsistent.

Saha et al.(2021) mapped the 3-D shear wave velocity of the uppermost mantle beneath the Bay of Bengal using fundamental mode Rayleigh wave group velocities calculated along 21,600 crisscrossing paths from cross correlation of ambient noise as well earthquake seismograms. They obtained distinctly different lithospheres beneath the eastern and western Bay of Bengal, on either side of 86°E longitude. The western Bay of Bengal has > 120 km thick layered lithosphere and shear wave velocity of 4.7 km/s beyond 90 km depth whereas the eastern Bay of Bengal has thinner lithosphere (60–75 km) with minimum velocity of ~4.2 km/s, which is anomalously low for an old ocean.

2. Seismic Anisotropy, Crust and Mantle Flow

2.1. Crustal Deformation

2.1.1. Doda - Kishtwar Region, NW Himalaya

Splitting analysis of local earthquake waveforms in the Doda-Kishtwar region, NW Himalaya results in 47 individual shear wave splitting measurements (Roy et al., 2021b). The fast polarization azimuths (FPAs) primarily show two distinct patterns oriented along ENE-WSW and NW-SE directions. Both the patterns are in the Chamba sequence suggesting two deformation patterns. For the first pattern, both stations and events are located in the proximity of the Chenab River whereas for the second pattern the FPAs are parallel to the structural trend of the Chamba sequence. The FPAs are either perpendicular or sub-parallel to the maximum horizontal stress (SHmax), suggesting structure-induced anisotropy. A possible reason for the observation of the first pattern is that the shear wave samples the fluid-filled fractures in the fault zones resulting in FPAs parallel to the Chenab River, with large delay times. The extensional tectonic structures of the NW Himalaya could explain the second pattern of anisotropy.

2.1.2. Arunachal Himalaya

Shear wave splitting analysis beneath Arunachal Himalaya using waveforms of 396 local earthquakes recorded at 32 stations resulted in 76 well constrained splitting measurements (Nanajee et al., 2022). The delay times vary from 0.02 to 0.30 s, and are clustered around 0.07 s. There is a significant variation in the orientation of FPAs. The western part of Arunachal Himalaya is associated with smaller delay times (mostly < 0.10 s) and has large variation in the FPAs. The FPAs mostly vary from E-W to NNW-SSE along the westernmost profile. The observed anisotropy is associated with heterogeneities in the lithological properties, and the anisotropy is both stress-induced and structure-induced. There is a small crustal block in the central part of Arunachal, in which the FPAs are parallel to the strike of the Himalayan arc and are associated with structure-induced anisotropy. In the eastern part of the Arunachal Himalaya, a variation in the orientation of FPAs is observed from north to south. In the north, the FPAs are parallel to the strike of the Siang River in the eastern Himalaya syntaxis, suggesting structure-induced anisotropy. While in the south, the FPAs are mostly parallel to SHmax, suggesting stress-induced anisotropy.

2.1.3. Southeastern Tibet

Tiwari A.K., et al. (2022a) obtained a depth-dependent crustal anisotropic signature beneath SE Tibet using directional dependence of receiver functions. The obtained upper crustal (0-20 km) anisotropic orientations, which are orthogonal to major faults and suture zone, suggest structure induced anisotropy beneath the region. The anisotropic orientations of the middle (20-40 km) and lower (40-70 km) crust suggest ductile deformation due to crustal flow beneath the region. This study along with previous SK(K)S and direct-S splitting measurements suggests partial coupling between the crust and upper mantle beneath the region.

2.1.4. Shillong Plateau - Mikir Hill, NE India

Data from a 17-station broadband seismic network have been used to study correlation between

polarization direction of crustal anisotropy with seismogenic stress field at different locations of the Shillong-Mikir Plateau and its vicinity in northeast India (Baruah et al., 2021). The stress field has been determined around the stations using focal mechanism solutions (FMS) by waveform inversion. It is observed that polarization direction of crustal anisotropy is consistent with that of the maximum horizontal stress as well as the minimum horizontal stress. In addition, two orthogonal fast polarizations are also noted in some locations. The bivariate nature of suggests that the major mechanisms of seismic crustal anisotropy are not only due to the regional stress, but active faults and other geological conditions play a significant role in contemporary orientation of seismic crustal anisotropy and seismogenic stress field.

Earthquake source mechanisms obtained through waveform inversion reveal that the closely spaced Mishmi, Tidding, and Lohit faults are steeply dipping thrust sheets (dip ~ 50º) that accommodate large crustal shortening, owing to the indentation process and clockwise rotation tectonics. The Walong fault is characterized by strike-slip motion which helps to facilitate the clock-wise rotation of crustal material around the syntaxis (Hazarika et al., 2022). Radial anisotropy interpreted within the Eastern Himalaya Syntaxis (EHS) and the Indo-Burmese Ranges based on surface wave dispersion reveals stronger anisotropy in the deeper part below ~40 km depth (Chanu et al., 2022).

2.2. Upper Mantle Deformation

2.2.1. Ladakh – Karakoram zone (LKZ)

Seismic anisotropy of the upper mantle beneath the eastern LKZ and northwest Himalaya has been investigated based on splitting in SKS waveforms recorded at 28 broadband seismic stations (Fig.6). In the frontal part of the Himalaya, the Fast Polarization Directions (FPDs) are mostly parallel or sub-parallel to the strike of the Himalayan orogeny suggesting deformation in the shallow lithospheric mantle under compression owing to the India-Asia collision. On the other hand, FPDs observed in the Lesser, Higher, and Tethyan Himalaya largely follow the NE-oriented absolute plate motion (APM) of the Indian plate which can be attributed to basal shear as the Indian plate moves above the asthenospheric mantle, with a minor contribution from shallow lithospheric deformation. A complex anisotropy pattern is observed in the Indus Suture Zone. The FPDs near the Karakoram Fault Zone are parallel or sub-parallel to its strike. The study suggests that KF extends up to the lithospheric mantle accommodating the India-Asia collision and facilitating extrusion in the Tibetan Plateau (Paul A., et al., 2021).

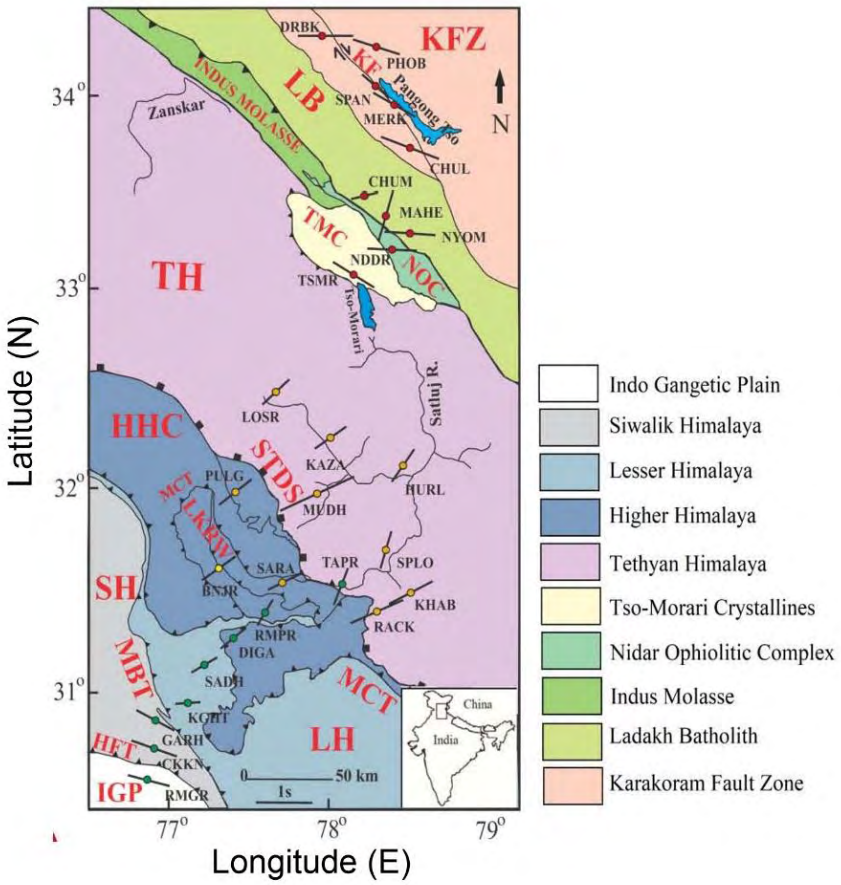

Figure 6. Simplified tectonic map of the Ladakh-Karakoram zone and northwest Himalaya. The orientation and length of the bar plotted with the red dots indicates predominant Fast Polarization Direction and splitting delay time (□t), respectively. (From Paul A., et al., 2021) (*Reprinted from Journal of Geodynamics, 144, Arpita Paul, Devajit Hazarika, Monika Wadhawan, Naresh Kumar, Upper mantle anisotropy in the northwest Himalaya and Ladakh-Karakoram zone based on SKS splitting analysis, 101817, Copyright (2021), with permission from Elsevier.*)

2.2.2. Western Himalaya

Upper mantle anisotropy beneath the western Himalaya is investigated using data from 62 broadband seismic stations (Biswal et al., 2020; Kumar V.P., et al., 2022). Of these 62 stations, around 18 stations are located along a linear profile in the Kumaun-Garhwal Himalaya traversing the Himalaya from south to north. The study region mostly comprises of Himachal (Biswal et al., 2020) and Kumaun-Garhwal (Kumar V.P., et al., 2022) Himalaya. The FPAs are mainly oriented along the ENE-WSW and ~E-W directions, respectively, and a few in the NE direction (see Fig.4 of Kumar, V.P., et al., 2022). Also, very few observations in the Kumaun-Garhwal Himalaya are oriented along the ~SE-NW direction. The delay times mostly vary from 0.2 and 1.7 s, mostly between ~0.4 to ~1.0 s. In the Kumaun-Garhwal Himalaya, the average delay time gradually decreases from 0.9 to 0.7 s in the sub- and lesser Himalaya to 0.6 s in the MCT zone and the higher Himalaya. There is not much variation in the orientation of FPAs from south to north in the Himachal and Kumaun-Garhwal Himalaya.

Another study on shear wave splitting (Kumar N., et al., 2021) reveals that both stress and structure-induced anisotropy prevail in the Kumaun Himalaya. The anisotropy directions are

mainly NE-SW, N-E and NW-SE, in agreement with the observed gravity lineaments (Hajra et al., 2022b).

2.2.3. Shillong Plateau

Mohanty and Singh (2022) investigated the shear wave splitting using SKS, SKKS, PKS phases for Shillong Plateau and have found that the deformation patterns beneath the northern and central Shillong Plateau are dominated by the asthenospheric forces controlling the absolute plate motion (APM) of the Indian plate in a no net rotation frame in a distinctive NE direction. Also, they have reported that at the southern proximity of the Shillong Plateau, the deformation pattern seems to be aligned parallel to the major regional geological structures. The coherent lithospheric deformation along with transpressional tectonics act as the major source of anisotropy at this southern end.

2.2.4. Rajasthan Craton

Shear wave splitting parameters are obtained at four broadband seismic stations in Rajasthan using core-refracted phases (Mandal, 2019c). The delay time was found to vary from 0.3 to 2.4 s and clustered around 1.6 and 1.7 s. The FPAs are found to vary from 8° to 175°. However, most of them are along the NE direction, parallel to the absolute plate motion (APM) direction of the Indian plate in the no-net-rotation frame. The basal drag could be the primary cause for the observed APM parallel anisotropy beneath the Rajasthan craton. It is inferred that the coherent lithospheric fabrics in the Rajasthan craton were formed during the Archaean and survived subsequent Paleoproterozoic tectonic events.

2.2.5. Kachchh rift zone

Shear wave splitting observations beneath twelve broadband seismic stations in the Kachchh rift zone (KRZ), Gujarat, are estimated using the core-refracted phases (Singh and Mandal, 2020; Mandal, 2021). In total, 443 new measurements are obtained. The mean value of FPAs varies from 49.41° to 103.78° at the stations, with an average value of 76.91°. Similarly, the delay times are found to cluster around 1.39 to 2.34 s at the stations. Most of the FPAs are clustered around 60° and 80°, suggesting an ENE-WSW direction, near parallel to the E-W trending Kachchh rift axis. It is suggested that the upper mantle anisotropy beneath the KRZ is parallel to the Kachchh rift axis. It is generally observed that rift zones are generally characterized by large delay times, which also suggests significant anisotropic contribution from the asthenospheric flow-induced anisotropy. Thus, the KRZ region is associated with a thick anisotropic layer, with mantle anisotropy parallel to the Kachchh rift axis direction caused by both frozen lithospheric anisotropy and asthenospheric flow-induced anisotropy.

2.2.6. Western Ghats

The mantle deformation pattern beneath the Western Ghats, India, is investigated using shear wave splitting of core-refracted phases at 17 broadband seismic stations (Sribin et al., 2021). In total, 193 measurements are obtained, comprising 52 splitting and 141 null measurements. The delay times are found to vary from 0.3 to 2.8 s, and the FPAs from N6° to N177°. The dominant direction is found to be NE, parallel to the APM direction of the Indian plate in a no-net-rotation frame. The dominant cause for the observed anisotropy is shear at the base of the lithosphere. The E-W orientation at stations close to the western coast, especially in the

northern part of the Western Ghats can be associated with the lithospheric stretching along the west coast, associated with rifting process. Also, the coast parallel FPAs oriented along N-S and NNW-SSE direction with delay times varying from 0.6 to 1.2 s at stations away from the coast could be associated with the edge flow due to the transition from a thick to a thin lithosphere.

2.2.7. Profile across the Dharwar Craton and the Cuddapah Basin

Upper mantle anisotropy is investigated along a west-to-east profile having 38 broadband seismic stations covering mid-Archaean Western Dharwar Craton (WDC), late-Archaean Eastern Dharwar Craton (EDC), and Proterozoic Cuddapah Basin (CB) (Saikia et al., 2019). The orientation of FPAs varies from -50° to 5° in the WDC, -40° to 30° in the EDC and -5° to 85° in CB and further east. The delay times vary from 0.4 to 2.0 s, with the average being 1 s. In the WDC, the orientation of FPAs is found to align along the strike of shear zones and faults. This suggests frozen-in anisotropy in the lithosphere, possibly established during the lithospheric evolution in mid-late Archaean. In the EDC, the orientation of the FPAs deviates from the APM direction, suggesting anisotropy frozen-in from the episodes of late Archaean to Proterozoic period. The splitting trend beneath the CB and Eastern Ghats (EG) follows the strike of the rift along with plate motion direction, indicating that the anisotropy is influenced by a combination of frozen anisotropy due to continental rifting along the eastern margin of the Indian plate and active asthenospheric flow.

2.2.8. NW-SE Profile across the DVP and the EDC

The upper mantle anisotropy is investigated beneath the DVP and the EDC at fifteen broadband seismic stations located along a NW-SE profile (Sivaram et al., 2022). In total, 71 measurements are obtained by performing shear wave splitting analysis of core-refracted phases. The orientation of FPAs suggests variation in splitting parameters along the profile. In the DVP, the orientation of FPAs is along NE-SW with the delay times varying from 0.5 to 1.2s. In the EDC and EGMB (Eastern Ghat Mobile belt), the FPAs are along NW-SE in EDC and NE-SW in EGMB, and the delay times vary from 1 to 1.4 s. The non-APM orientation in EDC suggests frozen-in anisotropy in a thick lithosphere, associated with the late Archaean to Proterozoic events or the last major episode of tectonic and magmatic activity during 2.6 Ga. In the DVP, the deformation seems to represent the predominant APM-trending asthenospheric anisotropy beneath a thinned lithosphere. Possibly, the upper mantle is influenced by shear interactions from the geologically recent ~65 Ma Deccan plume event. In the EGMB, the FPAs are sub-parallel to the APM direction, which suggests imprints of rifting.

2.2.9. Eastern Ghat Mobile Belt (EGMB)

Jana et al. (2019) carried out shear wave splitting analysis using core refracted PKS, SKS, SKKS phases to capture the collisional signature preserved beneath the EGMB. This is the first geophysical evidence deciphering the episodic collisional history of EGMB. The fast axis directions have shown absolute plate motion as the dominant cause. Though in Rengali province and Mahanadi rift zone, splitting shows signatures of previous collisions. Jana et al. (2021) evaluated the seismic anisotropic signatures and mantle deformation patterns using Reference Station Technique for the EGMB and its surroundings. This study found new evidence of frozen anisotropic signature demarcating eastern Phulbani domain from western

Phulbani domain. The dominant effect of absolute plate motion has been observed beneath the Bastar craton. The distinct nature of Chilka lake from its surroundings suggests Chilka lake to be a separate block.

2.2.10. Synthesis of upper mantle anisotropy beneath India

Around ~2500 published individual shear wave splitting measurements from more than 350 broadband seismic stations are synthesized to present the mantle deformation scenario beneath India (Roy et al., 2021a). On a continental scale, the delay times are found to cluster around 0.8 s, with the FPAs predominantly along the APM direction. This is attributed to basal shear due to the interaction between the lithosphere and asthenosphere. A significant deviation from the APM is observed from south to north. The deviation from APM is categorized into four sub-regions, namely northeastern (NE), north, central, and south India (Fig.7). For the NE and north India, it is attributed to the Indo-Eurasian collision tectonics. For NE India, it is found to be parallel to the strike of the orogens, suggesting coherent deformation in the upper mantle. For central India, the deviation is attributed to frozen anisotropy associated with widespread magmatism in the DVP, paleo-rifting and collisional events in the eastern Indian shield. The deviation is stronger in southern India than in central or northern India, primarily in the DVP, WDC and the northern part of Southern Granulite Terrain (SGT). This probably reflects the lithospheric evolution process in the mid-to-late-Archaean, continental rifting in the western and eastern margins, ocean closure and subduction in the northern part of SGT. Back azimuthal variation in the splitting measurements in southern India suggests layered anisotropy and/or variation among different blocks.

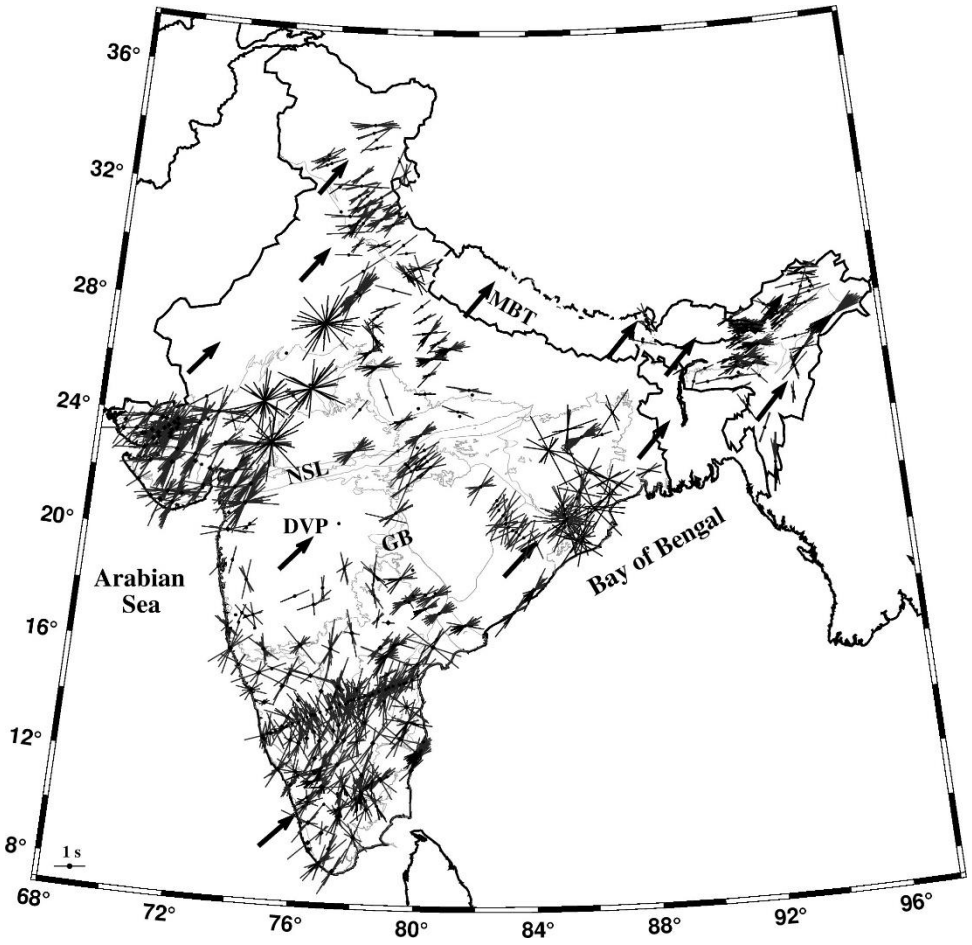

Figure 7. Map showing the individual splitting measurements at the station locations. The orientation and length of the lines correspond to the fast polarization azimuth (FPA) and delay time, respectively. Black arrow represents the absolute plate motion direction in a no-net rotation frame (DeMets et al., 2010, Geophy. J. Int., v.181, pp.1-80). MBT – Main Boundary Thrust, NSL – Narmada Son Lineament, DVP – Deccan Volcanic Province, GB – Godavari Graben. (*Courtesy Dr. M. Ravi Kumar and Dr. Sunil K. Roy, CSIR-NGRI*)

2.2.11. Pn anisotropy of the Indian shield

High-resolution P-wave velocity and anisotropy structure of the hitherto elusive uppermost mantle beneath the Indian shield and its surrounding regions are obtained using 19500 regional Pn phases from 172 broadband seismic stations (Illa et al., 2021a). The effect of continental rifting, collision and orogeny is reflected in the Pn velocity image. The cratons in the Indian shield have uppermost mantle velocities ranging from 8.02 to 8.42±0.05 km/s. Prominent highs and lows are observed in the shield region related to mantle deformation episodes, as the Indian plate has experienced major tectonic activity during and after the breakup from the Gondwanaland. The Pn and SKS anisotropic fast axis directions are consistent, except for the Indian shield, revealing that the Indian cratons are distinct with an altered uppermost mantle preserving the remnant anisotropy. The FPAs are consistent in the collision environments in the west, Himalaya, and Burmese arc region.

2.2.12. Anisotropy of NW DVP using Surface waves

The anisotropic and isotropic variations within the crust and upper mantle beneath the NW DVP are investigated using surface waves (Sharma J., et al., 2021). Results reveal different intra-crustal layers, lid, and a low-velocity zone (LVZ). The LVZ comprises a uniform asthenospheric low-velocity layer (LVL) of average V_{SV} 4.44 km/s and V_{SH} 4.47 km/s, and another LVL with an average V_{SV} 4.45 km/s and V_{SH} 4.41 km/s. A negative radial anisotropy is observed in the LVZ, indicating the dominance of vertical flow. This could be related to partial melts, volatile materials and/or a thermal anomaly.

3. Seismic Attenuation

Sivaram and Gupta (2022) investigated the frequency-dependent seismic attenuation characteristics of the crust beneath the Kumaun Himalaya using seismic coda waves (Qc-1) and high-frequency body waves (Qα-1 and Qβ-1). The results show that that the seismic attenuation is different for the Lesser Himalaya and the Higher Himalaya segments, which could possibly be due to the mechanism of underthrusting and deformation in the Lesser Himalaya segments, leading to a dominant scattering attenuation and the multitude of fractures and pores in the crust.

Seismic wave attenuation study has been performed for the Kinnaur and Garhwal-Kumaun regions of the NW Himalaya using data of low magnitude- and micro-earthquake events (Kumar and Yadav, 2019; Kumari et al., 2020, 2021; Monika et al., 2020; Kumar P., et al., 2021). Attenuation characteristic divide the Kinnaur Himalaya into three zones correlating with crustal/lithosphere structure and micro-earthquake activity. Decreasing attenuation with depth indicates more heterogeneities in the upper crust which can be explained by the effect of turbidity. The attenuation largely depends on the heterogeneities developed due to the collision of the Indian and the Eurasian plates. The attenuation is larger in the Tethys Himalaya than in

the High Himalayan crystallines. Small value of the resonance frequency and comparatively high attenuation to the north of the South Tibetan Detachment Zone indicate presence of low-grade meta-sedimentary rocks in the upper crust of the Tethys Himalaya (Kumar P., et al., 2021).

A series of studies on coda, body wave, and surface wave attenuation have been carried out for the Tibet and Nepal Himalaya regions. These studies suggest dominance of intrinsic attenuation for the Nepal Himalaya and southern Tibet. The second region shows dominance of scattering attenuation at higher frequencies (> 8 Hz) (Singh C., et al., 2019a; Biswas and Singh, 2019). Similar studies have been carried out for western Tibet and Karakoram fault region (Biswas and Singh, 2020a, 2020b, 2020c; Sarkar et al., 2021; Jaiswal et al., 2022), and southeastern Tibet (Tiwari A.K., et al., 2022b).

Singh C., et al. (2019a) investigated the spatial variations of coda wave attenuation structure using local events for Andaman-Nicobar Subduction Zone. The study shows high attenuation near Narcondum volcanic island, which also coincides with low-Vp zone, suggesting change in crustal properties. The results also reveal a good correlation between Q0 and seismicity, suggesting the presence of a highly scattered medium.

Singh C., et al. (2019b) investigated the spatial variations of Pg attenuation structure in Nepal Himalaya by the "Two-Station method" applied to 2325 waveforms obtained from 435 events recorded at 151 stations deployed across Nepal Himalaya. Their results suggest that the areas around the existing faults and lineaments exhibit very low Q values. They inferred that intrinsic attenuation plays a major role in causing the high apparent Pg attenuation in the crust of Nepal Himalaya. This may be mainly caused by highly pressurized fluids trapped within a thin low-velocity layer (LVL) at shallow depths.

Das and Mukhopadhyay (2020) studied the spatial variation in attenuation characteristics in Northeast India using coda Q. The average frequency dependencies of coda wave attenuation for a 30 s window length are estimated as Qc(f) = 135 ± 7f0.99± 0.03, Qc(f) = 109 ± 7f1.10±0.03 and Qc(f) = 90 ± 2f1.04±0.02 for Shillong Plateau, Mikir hills and surrounding River valley, and Indo-Burma Ranges respectively. It is observed that Q0 is greater for the Shillong Plateau than the other sub-regions. For window lengths ≥55 s, the central part of the Indo-Burma Ranges has higher Qc values at 10 and 12 Hz compared to the Shillong plateau.

Lg-Q for the Indian Shield derived from tomographic inversion varies from 50 to 650, while the frequency-dependent parameter varies between 0.4 and 1.1 with an average value of 0.7. Structural features such as rifts, suture zones, sedimentary, and active regions are characterized by high attenuation (Q_0<200) (Reshma et al., 2022).

4. Crustal Structure of Seismically Active Regions by Non-seismic Methods

4.1. Himalaya

4.1.1. Seismotectonics of the Sikkim Himalaya

The occurrence of deep crustal strike-slip earthquakes in the Sikkim Himalaya is indicative of the ongoing transverse tectonic deformation of the Indian plate, in addition to the N-S convergence related deformation within the Himalayan wedge. The two dominant tectonic

forces operating in this region could lead to a complex variable spatial deformation within the Indian lithosphere. Two-dimensional modeling of magnetotelluric data incorporating the NW-SE transverse tectonic trend within the Main Central Thrust zone (MCTZ) yields a lithospheric electrical resistivity structure of the region down to 100 km. By integration of these results with other geophysical information, seismological data and in conjunction with a kinematic wedge model, Pavankumar and Manglik (2021) proposed a comprehensive tectonic model for the Sikkim Himalaya that highlights the complex nature of the lithospheric structure (Fig.8). A major contact beneath the MCTZ separating two geologically and compositionally distinct blocks of the underthrusting Indian plate is suggested to be a NW-SE trending lithospheric-scale fault in this segment of the Himalaya. The tectonic model also demonstrates another crustal-scale tectonic feature beneath the Main Frontal Thrust that demarcates a transition zone of moderately conductive crust of the Ganga Foreland Basin and a resistive crustal block beneath the Sub-Himalaya.

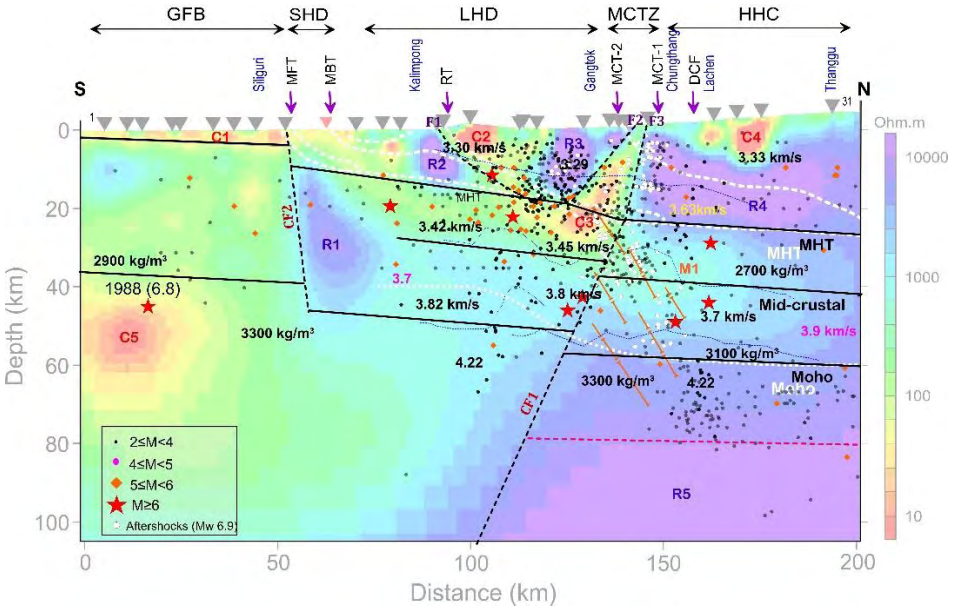

Figure 8. A tectonic model proposed for the Sikkim Himalaya based on the lithospheric geoelectric structure obtained by the present MT experiment and available seismic and density information as well as a kinematic model of the wedge structure. (From Pavankumar and Manglik, 2021) (*Reprinted from Physics and Chemistry of the Earth, Parts A/B/C, 124, G. Pavankumar, Ajay Manglik, Complex tectonic setting and deep crustal seismicity of the Sikkim Himalaya: An electrical resistivity perspective, 103077, Copyright (2021), with permission from Elsevier.*)

4.1.2. Gravity Modeling of the Kopili and Bomdila fault regions

An integrated approach based on seismotectonics, gravity and magnetic data is utilized to understand the tectonic activity of the Kopili and Bomdila Faults bounding the Mikir Hills (Sharma S., et al., 2018). The Kopili Fault dips NE at 75° whereas the Bomdila Fault dips NNE at 50-55° angle. The bottom of seismogenic zones is inferred to be 45±2 km and 50±2 km for the Kopili Fault and the Bomdila Fault regions, respectively. The low gravity values over the Bomdila Fault area indicate presence of thick alluvial deposits while lesser sediment thickness is observed along the Kopili Fault.

4.2. Indian Shield Region

4.2.1. Magnetotelluric investigations in the vicinity of the Delhi Seismic Zone

The Delhi Seismic Zone (DSZ) in the northwest Indian shield is one of the seismically active intraplate regions with frequent occurrence of small-to-moderate magnitude earthquakes. These earthquakes occur mainly along the NE-SW oriented Proterozoic Aravalli-Delhi Fold Belt (ADFB) and NNW-to-NW trending Delhi-Sargodha Ridge (DSR). However, the detailed subsurface architecture of DSZ and its surrounding areas concealed by alluvial sediments is still unclear. Pavankumar et al. (2021) and Manglik et al. (2022) conducted magnetotelluric (MT) experiments across the DSR and the ADFB, respectively, to image this region in terms of electrical resistivity structure. The results yield a northward dipping electrical conductor (< 10 Ωm) down to 20-25 km for the DSR whereas the ADFB buried beneath the alluvial sediments of the western Ganga Basin consists of a collage of nearly vertical conductive and resistive blocks and a sharp resistive contrast. These blocks appear to continue beneath the Kumaun-Garhwal Himalaya. These results have significant implications for earthquake hazard potential of both the region, the DSZ and the Uttarakhand Himalaya.

4.2.2. Pre-eruptive crustal electrical structure and tectonics of the recent Palghar earthquake swarm activity region, Maharashtra

The DVP is a major geological domain of the Indian peninsular shield. Though the region is considered to be seismically stable, it has experienced some significant intraplate earthquakes, as well as swarm type earthquake activity at Bhatsa, Silvasa, Navsari, Nasik, Valsad and more recently at Palghar. Pavankumar et al. (2020) carried out MT studies along two profiles covering the Bhatsa and the Palghar earthquake swarm regions. Geoelectric models of these two regions depict strong resistivity contrast suggesting that the crust below the basalt cover is fragmented. The zones of fragmentation coincide with the major pre- and post-eruptive tectonic structures, e.g. the West Coast fault, the Panvel Flexure and the Kurudwadi rift.

4.2.3. Seismogenesis of intraplate Kachchh rift in western India by Magnetotellurics

The Kachchh basin comprises a set of E-W trending faults and fault bounded uplifts. Since historic past, the region is experiencing moderate to large magnitude earthquakes and is considered as one of the most active intraplate regions of the world. Magnetotelluric studies carried out in various segments of the region yield well resolved electrical images of the deep crust, enabling delineation of the broad geometry of various active faults (Nagar et al., 2021). The MT models in conjunction with 3-D relocated hypocenters provide better constraints on the geometry of the seismogenic segments of the faults at depth. Among the various intra- basin faults, the South Wagad Fault (SWF) has a downward lower crustal extension that possibly connects to a fluid reservoir in the upper mantle. However, the Kachchh Mainland, Katrol Hill, Gedi and Allahbund faults are limited to the upper crustal depths. The North Wagad Fault is inferred as an antithetic splay of the SWF.

5. Seismic Hazard, Risk and Strong Ground Motion Studies

5.1. Strong Ground Motion and Earthquake Hazard Assessment

5.1.1. Plate boundary regions

Mir and Parvez (2020) simulated bedrock level peak ground motion at 2346 sites on a regular grid of 0.2°×0.2° in NW Himalaya from 543 simulated sources, using the stochastic finite-fault, dynamic corner frequency method, with particular emphasis on Kashmir Himalaya. Acceleration time series generated are then integrated to obtain velocity and displacement time series, which are all used to construct a suite of hazard maps of the region. The expected PGA values for the Kashmir Himalaya and Muzaffarabad are found to be ~0.3–0.5 g and for the epicentral region of the 1905 Kangra event, to be 0.35 g. The PGA values estimated in this study are in general found to be higher than those implied by the official seismic zoning map of India produced by the Bureau of Indian Standards. Major events in Kashmir Himalayas, such as those of 1555, 1885 and 2005, are simulated individually to allow comparison with available results. This study provides a first-order ground motion database for safe design of buildings and other infrastructure in the NW Himalayan region.

Kumar and Sharma (2019) performed a detailed study on the temporal evolution of seismicity in and around the seismic gaps in the Himalayan region. They segmented the region into four meridional regions (A) 80°E to 83.5°E, (B) 83.5°E to 87.5°E, (C) 87.5°E to 90°E, and (D) 90°E to 98°E along with a fixed latitude belt. A homogeneous catalogue with $3 \leq M_b \leq 6.5$ was used for the spatial and temporal analysis of seismicity in terms of b-value. It is found that pockets of lower b-values coincide over and around stress accumulated regions. The observed low b-value before the occurrence of the Nepal earthquake of 2015-04-25 supports the argument of impending occurrence of moderate to large magnitude earthquake in Sikkim and north-east Himalayan region in future.

Singh S.K., et al., (2020) documented the site amplification at 28 sites in the Indo-Gangetic Plains (IGP) using the RSS (ratio of the source spectrum) technique. The fundamental frequency (f_0) of the sites increases from 0.12 Hz near the foothills of Himalaya to 2.0 Hz at the southern edge of the basin and the amplification reaches about 10. At several sites, f_0 is difficult to select and an amplification of ~5 in broadband is in the range 0.12–0.7 Hz. Application of standard spectral ration (SSR) technique to teleseismic *S*-wave data recorded in the IGP reveals that this approach may be useful in the estimation of amplification at low frequencies (< 0.5 Hz).

Sharma N., et al. (2021) targeted two largest magnitude earthquakes (2017-02-06 M 5.1 and 2017-12-06 M 5.6) recorded by the CSIR-NGRI network in Uttarakhand. They estimated the peak ground acceleration (PGA), peak ground velocity (PGV) and peak ground displacement (PGD) from recorded waveforms and acceleration, velocity and displacement response spectra at different structural periods for districts like Haridwar, Rudraprayag, Almora, Tarikhet and Thakurdwar. Their simulation reveals that the displacement spectra for many Himalayan earthquakes obey a circular crack model with ω^{-2} fall. The high stress drop (70 and 100 bars) estimations suggest high release of energy in the seismic zone V region which hosted the 1991 Uttarkashi (M 6.8) and 1999 Chamoli (M 6.3) earthquakes. The PGA values estimated at Rudraprayag district (168 cm/s^2) bring the district under moderate to severe intensity zone even for moderate size earthquakes.

Strong motion data from the network operated by WIHG in the Himalaya have been used to quantify seismic hazard assessment in the form of attenuation, site effects, and simulation of strong ground motion for different sectors of the Himalaya, e.g. Garhwal and Kumaun (Uttarakhand), Kinnaur (Himachal Pradesh), Nubra-Shyok (Ladakh), and NE India (Sandeep

et al., 2019a, 2019b, 2019c, 2020, 2022; Kumar P., et al., 2019). This work provides great insight into exploring recent trends in seismology and earthquake engineering for seismic hazard evaluation.

In the Jammu & Kashmir sector of the Himalaya, the thrust faults are blind and large-scale folding is the only expression of active deformation at the surface, making it difficult to assess seismic hazard in this region. O'Kane et al. (2022) used field, satellite and seismological observations to determine the fault geometry for this region and modeled the potential hazard scenarios. Their results suggest that earthquakes that rupture the buried, shallow part of the locked Main Himalayan Thrust could generate PGVs that are >3 times larger than earthquakes of the same magnitude on its deeper portions.

Gogoi et al. (2023) estimated ground motion parameters (GMPs) by processing 125 accelerogram records of 26 earthquake events, with 375 components, that originated in NE India and its vicinity with special emphasis on the 2016-01-M6.7 Tamenglong earthquake. Moreover, Ground Motion Prediction Equations were developed through multiple regression analysis on observed data of 8 GMPs namely, PGA, PGV, Arias Intensity, Characteristics Intensity, Housner Intensity, Cumulative Absolute Velocity, Effective Design Acceleration and Acceleration Spectrum Intensity. The developed equations are representative of statistics on changes in amplitudes of parameters with varying distances and magnitude in connection to NE India. Besides, newly developed GMPEs can be applied to 4–6.8 magnitude earthquakes and valid up to 525 km of distance.

Boruah et al. (2022) attempted estimation of site amplification factors of different geomorphological units in Shillong city using the distribution of PGA due to maximum credible earthquakes that originated in nearby major faults and average shear wave velocity (Vs30) values for various geomorphological units. The amplification for the highly dissected land in the city is found to be maximum within a range of 2.77–2.92, while the high plateau segment is characterized by least values (2.01–2.16). Simultaneously, the effective ground motion mapped on the surface indicates a maximum value of 0.6–0.94 g for a probable earthquake of Mw 8.1 on the Dauki fault. Similarly, Dhubri and Kopili faults might produce a ground motion of 0.05–0.08 and 0.22–0.33 g for a maximum credible earthquake of Mw ~7.0, respectively.

The distribution and dissipation of post-seismic stress have been investigated for the Garhwal-Kumaun region based on spectral analysis of P-waveforms of local earthquakes (Hajra et al., 2022a). The study detects significantly lower stress drop compared to the overall values for the Central Seismic Gap region suggesting incomplete dissipation of the accumulated stress. The high-stress drop events are predominant along the MHT at mid-crustal depths, with the upper ~10 km of the brittle crust rarely hosting any strong earthquake. The b-value is estimated as 0.64±0.08 for the Kumaun Himalaya, which is low compared to the Garhwal and the rest of the NW Himalaya.

The Ladakh-Karakoram zone (LKZ) is a unique testing ground for understanding the geodynamic evolution of the Himalaya-Karakoram orogeny. Despite the accumulation of a large amount of strain energy that originated due to the India-Asia collision along the Karakoram fault, earthquakes of $M \geq 7.0$ are considerably less in the Karakoram Fault Zone compared to the Himalayan seismic belt in the northwest Himalaya. Earthquake source

parameter study in the LKZ through spectral analysis of P-waves of local earthquakes reveals low-stress drop earthquakes (~0.06-64.36 bar) caused by the possible presence of aseismic creeping patches in the Karakoram Fault. A partial stress drop mechanism is proposed for low-stress drop in the forearc region (Paul and Hazarika, 2022).

Although the 1950 Assam earthquake (Mw 8.7) endures as the largest continental earthquake ever recorded, its exact source and mechanism remain contentious. Coudurier-Curveur et al. (2020) analyzed the spatial distributions of reappraised aftershocks and landslides to estimate the hitherto unknown surface rupture extent along the Mishmi and Abor Hills. Their results from two key sites (Wakro and Pasighat) suggest over twice as large co-seismic surface throw (7.6±0.2 m vs. > 2.6±0.1 m) and average thrust dips (25–28° vs. 13–15°) on the Mishmi Thrust (MT) and Main Himalayan Frontal Thrust (MFT).

The Shillong Plateau is a peculiar geodynamic terrane hosting significant seismic activity outboard the Himalayan belt. This activity is often used as an argument to explain an apparent reduced seismicity in the Bhutan Himalayas. Although current geophysical and geodetic data indicate that the Bhutan Himalaya accommodates more deformation than the Shillong Plateau, it is aimed to quantify the extent to which the two geodynamic regimes are connected and potentially interact through stress transfer. Grujic et al. (2018) compiled a map of major faults and earthquakes in the two regions and computed co-seismic stress transfer amplitudes. Results indicate that the Bhutan Himalaya and the Shillong Plateau are less connected than previously suggested. The 1897 Assam earthquake (Mw 8.25) that affected the Shillong Plateau did not cause a stress shadow on the Main Himalayan Thrust in Bhutan as previously suggested. Similarly, the 1714 Bhutan earthquake (Mw 8±0.5) had negligible impact on stress accumulation on thrust faults bounding the Shillong Plateau.

An earthquake of magnitude Mw 5.7 shook the northeastern region of India on 2017-01-03 at 14:39:0.5 local time. The duration of the tremor lasted for about 5–6 s and had its epicenter in Dhalai District, Tripura, India. Even though the earthquake was of moderate magnitude, it caused damage to several masonry dwellings in Tripura and triggered soil liquefaction, lateral spreading, and landslides near the epicentral area. Anbazhagan et al. (2019) reported field reconnaissance observations of geotechnical effects and damage to buildings following this earthquake. In addition, the distribution of surface PGAs caused by the earthquake was estimated from the empirical equations based on the available data.

5.1.2. Intraplate regions

Surve et al. (2021) performed seismic hazard studies for the Mumbai city (financial capital of India), having a population of over 18 million. Two seismicity models, linear and areal, were used to compute the seismic hazard of Mumbai with an updated earthquake catalogue and latest knowledge on seismotectonics of the region. The hazard values for Mumbai corresponding to 475-year and 2475-year return periods are computed. Hazard maps at bedrock level for 2% and 10% probability of exceedance in 50 years were prepared. The hazard levels obtained in the present study are lower than those reported for the same area by previous researchers. The lower seismic hazard can be attributed to the fact that in this study, the Koyna–Warna region is used as one of the five independent source regions and reservoir triggered seismicity at times might reduce the overall seismic hazard in nearby regions.

Mandal and Asano (2019) modeled the low-frequency (0.1–1 Hz) ground motions excited by the 2006-04-06 event, using the finite difference method assuming a point source, to assess the robustness of the constructed velocity structure model. At most of the stations, the observed and simulated velocity waveforms are found to be in good agreement in terms of both amplitude and ground motion duration. They also computed synthetic ground velocities at numerous locations within the basin, for both the 2001 Bhuj mainshock (finite-fault source) and the 2006 aftershock (point source) cases, using a 3-D velocity model. Their work revealed that the presence of low velocity sediments within the Kachchh rift basin plays a key role in modifying/amplifying the ground motions in 0.1–1.0 Hz range.

The study of two earthquakes (2006-03-07 and 2006-04-06, Mw 5.5) in the Kachchh seismic zone by Mandal (2020) revealed that the estimated normalized response spectra at strong motion accelerograph sites in the Tertiary formations or near a zone of geological contact between the Jurassic/Tertiary formations, exceeded the design response spectra in the period range of 0.07–0.2 s, correlating with the complete collapse of low-rise buildings, water tanks and dams during the 2001 Bhuj earthquake. On the other hand, the normalized acceleration spectrum of corresponding to hard sediments (rock site) is found to not exceed the design spectrum, correlating with the lack of damage in the Mesozoic hill zone. It is also noticed that the spectral acceleration values at a few sites lying on the Quaternary formations have exceeded the design spectra at 3–4 s, suggesting these sites to be hazardous for engineered reinforced structures like bridges.

A rare lower crustal earthquake occurred on 2021-07-25 near Hyderabad, India. Mandal et al. (2022) used waveforms from 9 broadband stations and computed the average corner frequency, seismic moment, moment magnitude, stress drop, and source radius as 3.87 Hz, 7.14E+14 N-m, 3.75, 3.92 MPa, and 229 m, respectively. The mean crustal Q for the region was modeled to be 2182±1178, suggesting lower crustal attenuation below the Hyderabad region. However, the spatial distribution of the modeled crustal Q values revealed a high Q zone to the east of Hyderabad city, while a moderate Q zone was found west of the city. It is inferred that this lower crustal intraplate earthquake with a large stress drop of 3.9 MPa might have been generated due to the sudden movement on an almost vertical fault due to high pore-fluid pressure caused by the presence of CO_2-rich mantle fluids.

Srinagesh et al. (2021) analyzed a sequence of about 965 earthquakes in the magnitude range of 0.1–4.6. The main shock of moderate-sized earthquake (2020-01-26, M_L ~4.6) is located in the Palnadu sub-basin of the Cuddapah basin. It was felt both in the states of Telangana and Andhra Pradesh. The earthquakes prior and after the M_L 4.6 quake are located close to the thrust and along the periphery of the backwaters of the Pulichintala reservoir. The epicentral parameters obtained from double difference technique, using a minimum 1-D velocity model, illuminated a steep seismogenic structure extending down to 8 km depth,. The b-value estimate is 0.82 for a completeness magnitude of Mc 1.8 and could be associated with an intraplate event having a longer recurrence time. The focal mechanism solution obtained from waveform inversion reveals a pure double-couple mechanism of a strike-slip motion with a reverse component on a N–S trending focal plane.

Sharma A., et al. (2021) derived a new M_L scale, using the Grey Wolf Optimization, a swarm intelligence-based global optimization technique, for the first time, that is ML=logA+1.2588logR+0.0002789R-2.2265, where A is the amplitude measured in

millimeters, and R is the hypocentral distance in km. The new ML scale derived here is valid up to 400 km. The newly derived scale has a drop of 21.37% in the overall standard deviation of all magnitude residuals when station corrections are considered in comparison to the previously used scale.

Sivaram (2021) simulated high-frequency ground motions at five stations in the National Capital Region (NCR) of India for a large hypothetical Mw 8.5 earthquake and an intermediate Mw 6.8 earthquake in the Himalayan central seismic gap, at fault-distances of about 200–300 km, and indicated that the far-reaching and adverse ground-motion intensities might affect intermediate-high rise structures (period 0.4–0.8 s) in the NCR due to the predominance of fluvial deposits. Nagamani et al. (2020) identified different zones of seismic amplification in the Surat district of Gujarat, India, which are the hub of many mining and industrial projects like oil and natural gas.

Strong motion data from the network operated by ISR have been used in several engineering seismology applications, such as, estimation of source parameters, site characterization, development of ground motion prediction equation and ground motion modeling. The data recorded from the past decade have been used to characterize various sources in the Kachchh rift and other parts of Gujarat (Kamra et al., 2020). It is found from the study that stress drop of earthquakes (M 4.0-5.1) in the Kachchh rift are in the range 2.3-10.4 MPa with an average of 5.3 MPa. The estimated seismic moment and the source radius are in the range $1.02 \times 10^{22} - 5.3 \times 10^{23}$ dyne-cm and 0.43-1.32 km, respectively. The same exercise was carried out for the Saurashtra region (Kamra et al., 2021). For this region, the stress drop varies in the range 0.9-6.9 MPa with an average of 3.3 MPa. A regression relationship between observed accelerations and accelerations estimated from broadband data has been developed exclusively for the Gujarat region (Chaudhary et al., 2022).

5.1.3. Study of Earthquake Swarms

Srinagesh et al. (2020) studied earthquake activity in the Palghar region, Maharashtra, India. Until 31 August 2019, a total of 4854 earthquakes have been located here, whose local magnitude (M_L) varies from 0.1 to 4.1. Majority of the earthquakes (~94%) were located in the depth range of 4–16 km. The precise earthquake relocations reveal two clusters. The N–S trending cluster north of 20.04°N extends to a depth of 10 km, whereas the NE–SW trending cluster to the south of 20.04°N extends to 16 km depth. The shallow northern cluster is noticed to be sandwiched between two mapped mafic intrusions, whereas the deeper southern segment shows earthquakes clustering around the mafic intrusion. The modeled composite focal mechanism solutions for both the north and south clusters suggest normal faulting with a minor strike–slip component as the dominant deformation mode for the Palghar region. From relocated seismicity, they detected a deeper seismically active zone (with M > 3) at 4–16 km depth, occupying a crustal volume of 1440 km^3.

Mandal et. al. (2021b), conducted a comprehensive analysis of swarm activities in two regions of the Indian shield -- (i) Palghar (Maharashtra) and (ii) Pulichintala (Andhra Pradesh). The 3-D mapping of b-value and fractal correlation dimension (D2) reveals that the Palghar sequence follows typical characteristics of swarm activity (the b and D2 values vary from 0.1 to 2.5, and 0.39 to 2.62, respectively). On the contrary, the Pulichintala sequence (with b and D2 values varying from 0.2 to 1.68, and 0.68 to 3.0, respectively) shows negative characteristics. The

Palghar region is interpreted as a region of higher tectonic stresses.

Swarm activity similar to that at Palghar in Maharashtra (Mahesh et al., 2020), has been observed in Navsari and Jamnagar districts in South Gujarat and Saurashtra. At Navsari, a swarm activity was observed around the Keliya dam from Sep.2016 just after the Indian monsoon period that continued for about 4 months. Again, the swarm activity recurred in Aug.2017 and continued for about 5 months. A local network of four stations was installed by ISR to monitor the swarm activity, in addition to the Gujarat state seismic network (Sateesh, et al., 2019; Srijayanthi et al., 2022). A total of 1048 earthquakes were located around the Keliya dam and 229 events in the Dadra and Nagar Haveli (DNH) region from Sep.2016 to June 2018. The seismicity in both the regions followed a ~ NW–SE trend. It was confined to an area of 13 km × 2 km with a depth extent of 3 km at Navsari and 15 km × 2 km with depth of 6 km in DNH. In the Jamnagar district, ISR observed post-monsoon swarm activity in Sep.2019 with 76 clustered earthquakes having NW-SE trend that are in line with the strike of local lineaments and dykes.

Parija (2021) critically examined the 2011-09-18 Sikkim earthquake of M 6.9 and found it to be associated with episodes of precursory swarms, quiescence, mainshock and aftershocks. The precursory swarm and quiescence period consist of four earthquake swarms and one foreshock event of magnitude (mb ≥4.5) in the epicenter preparatory zone of the 2011 Sikkim earthquake. The 2011 Sikkim earthquake had about five aftershocks of magnitude (mb) ≥4.5 between 2011 and 2014 for the same region.

Parvin et al. (2021) analyzed two swarm activities in the Hyderabad region and found small absolute stress drop values (< 1 MPa) and a positive correlation between the static stress drop and the magnitude of the earthquake with seismic moment varying between $-0.09<M_L<1.52$. They observed a clear correlation of earthquakes associated with the fractures and faults in the vicinity of water bodies which are more sensitive to variations in hydrostatic pressures caused by vertical flow recharge from rainfall and deeper pore-fluid pressure diffusion.

Rekapalli and Gupta (2021) tried to understand the foreshock-aftershock patterns, main shock to the largest aftershock magnitude ratio, and difference in magnitude of two moderate injection-induced seismicity (IIS) earthquake sequences from Oklahoma, USA, namely, Prague (M 5.7, 2011) and Pawnee (M 5.8, 2016), and comprehend the shallow crustal heterogeneity. The analysis of temporal variation of "b" value from 2002 to 2018 suggests an increase in b-value after 2009. A reduction in b-value after 2016, in response to the reduced injection volumes is noted. A sharp fall in b-value usually precedes the main shocks of magnitude M ≥ 3.5. The foreshock b-values are lower than the regional b-value and aftershock b-values are higher than the regional b-value within the error limits. The investigated earthquake sequences fall under Type 2 of Mogi's model. The characteristics of IIS observed at Oklahoma are similar to the observations for the reservoir-triggered seismicity (RTS). However, with multiple injection wells operating from time to time in the region with varying amount of fluids injected, the entire IIS at Oklahoma has an appearance of a swarm.

Wadhawan et. al. (2021) studied a highly clustered shallow (<0.4 km) earthquake activity of low magnitude with accompanying rumbling sound in Sadrabadi and Zilphi villages in Dharni Taluka of the Amravati district, Maharashtra during the monsoon period of 2018 and found it to have the characteristics of a swarm. They found a strong correlation between rainfall and

swarm activity and categorized it as hydro-seismicity, resulting from hydro-fracturing of the soil/weathered basalt and collapsing and caving of the rocks. In the past, no such activity has been reported from the region during or after the monsoon, despite the fact that there was more rainfall in 2019. Therefore, they suggest that the low magnitude earthquake swarm at a very shallow depth might have been induced by the percolation of monsoonal rainwater through the weathered and fractured rock-mass associated with the fault system of the Narmada Son failed rift region.

5.1.4. Earth Observation for Crustal Tectonics and Earthquake Hazards

Elliott et al. (2020) illustrated the current methods for the exploitation of data from Earth Observing satellites to measure and understand earthquakes and shallow crustal tectonics. The aim of applying such methods to Earth Observation data is to improve our knowledge of the active fault sources that generate earthquake shaking hazards. Examples of the use of Earth Observation, including the measurement and modelling of earthquake deformation processes and the earthquake cycle using both radar and optical imagery are provided. They also highlighted the importance of combining these orbiting satellite datasets with airborne, in situ and ground-based geophysical measurements to fully characterize the spatial and timescale of temporal scales of the triggering of earthquakes from an example of surface water loading. Finally, they concluded with an outlook on the anticipated shift from the more established method of observing earthquakes to the systematic measurement of the longer-term accumulation of crustal strain.

5.1.5. Contributions of Space Missions to Better Tsunami Science: Observations, Models and Warnings

Global Navigation Satellite System (GNSS) data have a key role in better describing the ground deformation following a tsunamigenic earthquake close to the coast. The GNSS observations complement seismological data to constrain the rupture model rapidly and robustly. Interferometric Synthetic Aperture Radar (SAR) also contributes to this field, as well as optical imagery, relevant to monitoring elevation changes following subaerial landslides. The observation of the sea-level variations, in the near field and during the propagation across the ocean, can also increasingly benefit from GNSS data (from GNSS buoys) and from robust satellite communication: pressure gauges anchored on the seafloor in the deep ocean contribute to warning systems only by data continuously transmitted through satellites. The sounding of ionospheric Total Electron Content (TEC) variations through GNSS, altimetry, or a ground-based airglow camera, is a promising way to record tsunami initiation and propagation indirectly. Finally, GNSS, optical and SAR imagery are essential to map and quantify the damage following tsunami flooding. Satellite data are expected to contribute more to operational systems in the future provided they are reliably available and analyzed in real time (Hebert et al., 2020).

5.1.6. Aftershock Duration of Strong to Major Himalayan Earthquakes

Earthquakes of $M \geq 5$ tend to be locally damaging, specifically when these are the aftershocks of larger earthquakes, as the main shock would have weakened the structures. For the rescue operations and general well-being of the residents, it is helpful if an estimate is available as to how long $M \geq 5$ aftershocks would continue to occur. Earthquakes $M \geq 6.5$ tend to be followed

by aftershocks of M ≥ 5. In this study by Gupta and Rekhapalli (2022), aftershock sequences of seven earthquakes of magnitude M ≥ 6.5 were analyzed. Six among these are in the Himalayan region and the remaining one is in the near vicinity in China. The analysis suggests that the number of M ≥ 5 aftershocks and the duration of their occurrence decrease with the decrease of the mainshock magnitude. For the 2008 Sichuan earthquake of M 7.9 there were 136 M ≥ 5 aftershocks, while for 1975 Kinnaur earthquake of M 6.8 there were only 9. The aftershock duration of the Himalayan region earthquakes obeys the exponential law $T = Ae^{cM}$, where the A and c are constants associated with regional fault settings. This relation is helpful in providing an estimate of the time for which M ≥ 5 aftershock activity would continue after the occurrence of M ≥ 6.5 earthquakes.

5.2. Microzonation Studies

CSIR-NGRI prepared a first-cut Earthquake Disaster Risk Index (EDRI) map to capture the relative risk across Lucknow and Dehradun cities. These maps were handed over to the State Disaster Management Authority of respective States.

CSIR-4PI carried out microzonation of Srinagar region of the Kashmir Valley (Gupta S.V., et al., 2020, 2022). They conducted an extensive high-resolution microtremor ambient noise survey at 429 locations. The acquired dataset was processed using the Horizontal to Vertical Spectral Ratio (HVSR) technique to map the resonance frequency, the thickness of sedimentary cover and to identify areas prone to seismic amplification. The HVSR curves show the peaks in the range of 0.22 Hz to 9.96 Hz indicating heterogeneous and complex sedimentary cover in the region. Inversion of the HVSR curves gives the shear waves velocity distribution which highlights two distinct reflective surfaces in most of the areas. They also used the estimated fundamental frequency of various types of houses/buildings located in Srinagar city to assess the possibility of resonance in case of occurrence of any earthquake.

ISR has undertaken site-specific seismic hazard assessment and microzonation studies for areas of rapid growth, e.g. Special Investment Regions, Special Economic Zones, large and tall structures, and industrial hubs. These include Liquified Natural Gas / Liquid Petroleum Gas storage tanks at Mundra, Dhamra (Odisha), Dadra and Nagar Haveli, cable stayed bridge at Zuari River, Goa, and Indian Oil Corporation Ltd. Bongaigaon Refinery. The Institute has completed seismic microzonation of Bhuj city under a Ministry of Earth Sciences (MoES) sponsored project. In addition, it has undertaken seismic microzonation study of Amritsar, Meerut, Agra, Lucknow, Kanpur, Varanasi, Patna and Dhanbad towns under a project sponsored by MoES.

The concept of seismic vulnerability is a yard-stick of damage estimation from a probable earthquake, considering physical cum social dimension and enables a basis for decision-makers to develop preparedness and mitigation strategies. Baruah et al. (2020) used several parameters, e.g. shear wave velocity characteristics, geomorphology, slope angle, building typology, and the number of occupants, to estimate the dimension of vulnerability for the Shillong city. Based on this study, they inferred that more than 60% of Shillong city falls under moderate to high vulnerability and the rest is less vulnerable.

6. Triggered Seismicity and Borehole Seismology

Under certain suitable geological conditions, anthropogenic seismicity due to mining, geothermal and natural gas/oil production, filling of artificial water reservoirs, and high-pressure fluid injection has been reported globally. The reservoir-triggered seismicity (RTS) is most prominent, having been reported from hundreds of locations, with at least five sites where earthquakes exceeding M 6 occurred, claiming human lives and destruction of properties. The most important correlate for RTS to occur is the height of water column in the reservoir. Certain common characteristics of the RTS sequences have been identified, which discriminate them from normal earthquake sequences. During the reporting period, it was documented for the first time that the Injection Induced Seismicity (IIS) in Oklahoma, USA has characteristics like RTS (Rekhapalli and Gupta, 2021). An Editorial on Anthropogenic Seismicity (Gupta H.K., 2021a) and why Koyna is the most suitable site for near field investigations of earthquakes (Gupta H.K., 2021b, 2021c, 2021d, 2022b) were discussed in detail. It has been discovered that the DVP is hosting all the three types of earthquake sequences (Gupta H.K., 2022a).

Evidence for migration phenomenon:

An earthquake of Mw 4.0 occurred on 3 June 2017, south of Warna Dam, in the vicinity of the Western Ghat Escarpment (WGE), India. This earthquake is associated with a foreshock–aftershock sequence of 123 events of M_L 0.5–3.5, forming an intense cluster. This sequence occurred over a course of one month, beginning in the last week of May 2017, and seismicity continues. This earthquake sequence occurred at a new location compared with the past ~50 years of seismicity of the region. Prior to the new earthquake sequence of 2017, the earthquakes were bounded between latitude 17.1°–17.4°N, which supports the southward migration of seismicity in the region and suggests that the cluster is a part of the continuing RTS seismicity over the last five decades (Shashidhar et al., 2019a, 2019b).

Automatic detection of microearthquakes in borehole records:

For the first time, an automatic detection workflow was successfully implemented to seismological data recorded in deep boreholes situated in the Koyna-Warna region. This workflow allowed identification of about twice as many events as compared to the time-consuming manual data processing. Also, a two-stage grid-search algorithm provided additionally better constraints on the absolute event locations. Further, a relative location process of these events using a waveform similarity approach was performed. These new events provided a tighter clustering than was obtained earlier. The seismicity trend correlates well with the anomalies obtained from airborne lidar studies. It is believed that the improvements achieved in detection and locations of microearthquakes using the borehole seismograms will provide better understanding of the RTS of the Koyna-Warna region (Shashidhar et al., 2020).

Stress drop variations of triggered earthquakes at Koyna-Warna

The spectral ratio technique (SRT) is implemented for the estimation of source parameters of local earthquakes (M_L 0.5-4.0) of the Koyna–Warna region, western India. The SRT uses the concept of empirical Green's function and accounts for the path and site effects; thus, it contributes to the optimal estimates of the source parameters. Here, the corner frequencies and stress drops of a new earthquake sequence that occurred during 1 May - 25 June 2017 were calculated and compared with the stress drop behavior of the existing seismicity cluster in the region. The dependency of stress drop with increasing seismic moment of these earthquakes was also tested. A total of 689 P-wave spectra of earthquakes recorded by a short-period

borehole and a broadband surface seismic network are utilized for this purpose. It is found that the corner frequency varies from 1 to 25 Hz and stress drops vary from 0.01 to 14 MPa for earthquakes of both the clusters (Mahato and Shashidhar, 2022).

Site response and source parameters of RTS earthquakes using borehole seismic data: A linear scaling between seismic moment (M_o, in N-m) and stress drop ($\Delta\sigma$ in MPa) estimates is obtained for the Koyna earthquakes as: $\log_{10}\Delta\sigma = 0.62\ \log_{10} M_o - 8.03$. The maximum $\Delta\sigma$ of 34.2 MPa is modeled at 0.1 km depth for an event of Mw 4.09, while the largest apparent stress (σ_a) of 43.3 MPa is modeled at 4 km for an event of Mw 3.16. The hypocentral depth plot of $\Delta\sigma$ and σ_a reveals a seismogenic zone between 2.2 and 5.6 km depth, where most of the earthquakes (with large $\Delta\sigma$ and σ_a) have occurred. This could be attributed to the large stress/stain (associated with brittle, competent rocks) and high pore-fluid pressure (water saturated zone at hypocentral depths) beneath the Koyna seismic zone. The results suggest that most of the small Koyna events (Mw 2.9–4.2) satisfy the frictional overshoot stress-drop rupture model while only a few events follow the partial stress-drop rupture model. The reservoir-triggered Koyna earthquakes are associated with smaller stress drops in comparison with the rift-associated earthquakes in Kachchh, Gujarat and NSL (Mandal et al., 2021a).

7. Environmental Seismology and Earthquake Precursory Studies

7.1. Environmental Seismology

Cook et al. (2021) used seismic data from 76 broadband stations in Uttarakhand Himalaya to detect and evaluate the scope of early warning systems for mass wasting and floods in the Himalayan region. On 2021-02-07, Uttarakhand region of India experienced severe landslides and trolled over 200 lives. The signals of the events were observed up to 100 km from the disaster site and demonstrate the potential for these far-away monitoring stations to be useful for early warning. The records of the event at two of stations are shown in Fig.9. This discovery suggests a different way to monitor such remote Himalayan regions for mass wasting hazards.

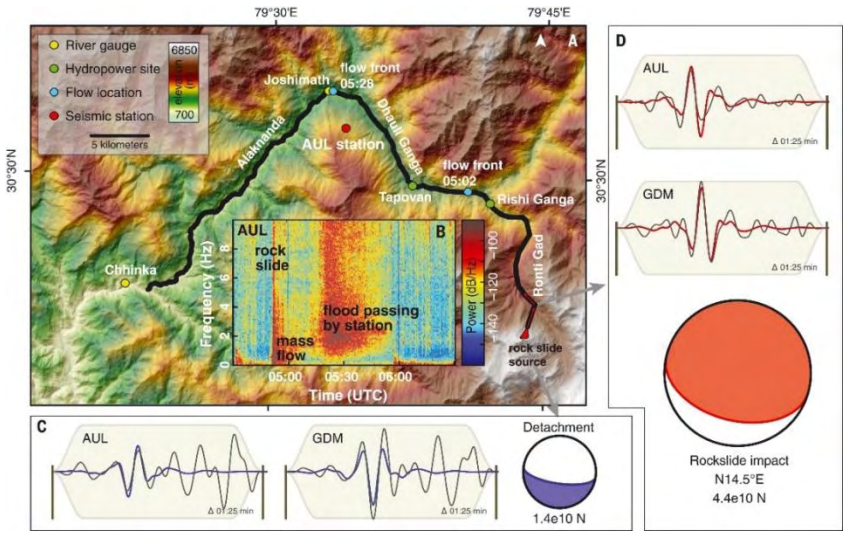

Figure 9. (A) Shaded relief map of 2021-02-07 slide event showing key geographic and instrument visual constraints of flow location; (B) Spectrogram at AUL station; (C&D) Lower hemisphere projections of single force focal sphere for the stations AUL and GDM. (From Cook et al., 2021) (*From Science, 374(6563), Kristen L. Cook, Rajesh Rekapalli, Michael Dietze, Marco Pilz,et al., Detection and potential early warning of catastrophic flowevents with regional seismic networks, 87-92. Reprinted with permission from AAAS.*)

WIHG studied this disaster using seismological data, satellite imagery and numerical modelling and estimated that $27 \times 10^3\ m^3$ of rock and glacier-ice collapsed from the steep north face of the Ronti Peak (Shugar et al., 2021; Tiwari A., et al., 2022). The main rock-fall followed by a noteworthy sequence of small events recorded by nearby seismic stations. The main event appears to have been initiated by precursory signals for nearly 2:30 h. The seismic data of three nearby stations within 50 km distance also distinguished debris flow and hitting obstacles from other seismic sources. The proximal high-quality seismic data allowed estimation of debris-flow speed and reconstruction of the complete chronological sequence, from the initiation of the nucleation phase to the occurrence of the rock-fall.

7.2. Earthquake Precursory Studies

Vijaya Kumar et al. (2020) recognized pre- and co-seismic signatures in MT data for the Mw 4.6 earthquake that occurred on 2007-11-24 in the Koyna-Warna region. Wavelet analysis of the MT time series data shows significant enhancement at 3–6 Hz frequency band in the scalogram during the earthquake in comparison with pre- and post-time. The spectral polarization ratio technique was implemented on these events to identify the precursory signatures. A few days before the earthquake, a significant anomaly was identified for most of the earthquakes using this technique. Akilan et al. (2021) studied changes in the zenith total delay (ZTD) and total electron content (TEC) associated with the 2015 Nepal earthquake (Mw 7.8). They analyzed the ZTD derived from GPS data received at HYDE, LCK3 International GNSS Service (IGS) stations and MSUN operated by CSIR-NGRI. The decrease in ZTD and TEC suggests hydration in the atmosphere by the joining of ions in the atmosphere during earthquakes. Almost the same results regarding the changes in ZTD and TEC were obtained for another large event (the 1999 Chamoli earthquake of Mw 6.8) in the Himalayan region, although they differ slightly in intensity depending on the observation distance.

Probabilistic analysis was performed on the seismic data of 100 years (1918–2018) for forecast of probable future earthquakes above Mw ≥ 5.0 in NE India (20°–30°N and 86°–98°E) and its vicinity to ascertain mean occurrence period E(t) for earthquakes of Mw ≥ 5 (Chetia et al., 2019a). Here, Kolmogorov–Smirnov statistics constrained by Weibull distribution has been utilized to achieve the best fit on the dataset. E(t) is found to be ~74 days with 50% probability. Similarly, cumulative probability function indicates a time of 140 days with 80% probability, while 400–500 days of recurrence time period is embedded with 90–100% probability for an earthquake of Mw ≥ 5.0 to recur following the occurrence of the last earthquake.

Mechanical deformations from within the earthquake preparation zones are believed to cause seismo-electromagnetic (SEM) emission in ultra-low frequency (ULF) band, i.e. between 0.001 and 10 Hz. The 3-component ULF induction coil magnetometer data from Multi-parametric Geophysical Observatory (MPGO), Tezpur were used to study SEM emissions employing both polarization ratio analysis and fractal analysis during the campaign period of

Apr.20 – Sep.3, 2019 (Dey et al., 2021). The findings show candidate SEM emissions, in the form of enhancements in SZ/SH, associated with all the seven credible events, even as nine enhancements could not be attributed to immediately adjacent credible events.

WIHG operates an MPGO at Ghuttu (Tehri, Uttarakhand) for earthquake precursory studies. Inert gas (soil Radon) and magnetic field changes before the occurrence of small-to-moderate magnitude earthquakes provide evidence for short-term (months-to-days, hours) earthquake precursors. However, this remote site in the Higher-Himalaya, away from human generated noise, indicates that there are different background natural noises to make the data very complex. There is a very high hydrological effect in the gravity and radon emanation (Shukla et al., 2020; Chauhan et al., 2021). After removing the background noises, anomalous changes are reported in case of 19-20 moderate magnitude local earthquakes. Earlier, this observatory has also reported precursory changes during the Mw 7.8 Nepal earthquake of 2015.

ISR has established three MPGOs in Gujarat for precursory studies. Soil radon (Rn-222) data of the Badargadh station were used to identify precursory signal of two earthquakes of M3.7 and M4.2 which occurred on March 26, 2011, and May 17, 2011, respectively through advanced processing of the time series (Sahoo et al., 2020, 2021). The ultra-low frequency geomagnetic variations were observed before the Dholavira earthquake (M 5.1) of 2012-06-20 in the Kachchh region (Joshi and Rao., 2021).

The apparent resistivity imaging at MPGO, Tezpur, operated by CSIR-NEIST, was carried out since 2016-08-31 for fixed interval time of 3 days to investigate precursory signatures prior to earthquake events. Anomalies in apparent resistivity prior to earthquake events are observed. These are not influenced by the rainfall activity in the region during the investigation period. Weibull distribution technique with observed apparent resistivity data is adopted to look for and revalidate the observations. The Weibull parameters, i.e. K and m, are estimated to be 0.26 and 1.04, respectively. No precise relation between magnitude and earthquake precursory time is found. Weibull probability distribution indicates that the probability of an earthquake occurrence exceeds the measure up to 80% (9 days) after the precursory signal is observed (Chetia et al., 2020). Similarly, temporal variability of the soil radon emanations measured at the MPGO was scrutinized using singular spectrum analysis (SSA) (Chetia et al., 2019b). The study concludes that SSA eliminates diurnal and semidiurnal components from time series of soil radon emanation for better correlation of soil radon emanation with earthquakes.

Mukherjee et al. (2021) have proposed a novel approach for Earthquake Early Warning (EEW) System Design using deep learning Techniques. The method converts a seismic signal into audio signals and then uses popular speech recognition techniques. Both Convolutional Neural Network (CNN) and a Long Short-Term Memory (LSTM) network have been trained.

7.3. Ionospheric Seismology

Ionospheric seismology refers to the study of events of earthquakes and tsunamis through co-seismic ionospheric waves produced by the dynamic coupling between the Earth's surface and the atmosphere. The ionosphere is a highly dynamic ionized region of the Earth's upper atmosphere extending from ~ 60 km to ~ 1000 km. The origin of any perturbations in the ionospheric electron density can be traced to various sources either from above (e.g. solar, geomagnetic, etc.) or below (e.g. lower atmospheric, earthquakes, tsunamis, volcano eruptions,

etc.) the ionosphere. In particular, short-period acoustic waves and long-period gravity waves emitted by earthquakes and tsunamis propagate upward in the region of exponentially decreasing atmospheric neutral density, and thus, their amplitude increases with atmospheric heights. On arrival at ionospheric heights, the waves redistribute ionospheric electron density and produce electron density perturbations known as co-seismic/co-tsunami ionospheric perturbations, respectively. Recently, it has been suggested that ionospheric signals produced by earthquakes and tsunamis can be inverted to infer the seismic source characteristics of large earthquakes and to envisage the propagation time and amplitudes of tsunami waves. It seems possible, but there are difficulties in terms of non-tectonic forcing mechanisms that act upon the ionospheric perturbation evolution at ionospheric altitudes (Bagiya et al., 2019).

A simple and direct 3D model is developed to estimate the combined effects of nontectonic forcing mechanisms of i) orientation between the geomagnetic field and tectonically induced atmospheric wave perturbations, ii) orientation between the GNSS satellite line of sight (LOS) geometry and coseismic atmospheric wave perturbations, and iii) ambient electron density gradients on the manifestations of Global Positioning System (GPS) – Total Electron Content (TEC) measured near field co-seismic ionospheric perturbations. This model can compute the nontectonic effects at various ionospheric altitudes depending on the propagation characteristics of seismo-acoustic rays (Fig.10). Further, this model is tested on earthquakes occurring at different latitudes. It is presumed that this model would induce and enhance a proper perception among the researchers about the seismic source characteristics derived based on the corresponding ionospheric manifestations (Bagiya et al., 2019).

Further, GPS-TEC observations provide adequate information on the spatial and temporal characteristics of earthquake induced ionospheric perturbations. However, one of the major limitations of this technique is the lack of altitude information of the recorded ionospheric perturbations. GPS derived TEC is an integrated quantity; hence it is difficult to relate the detection of ionospheric perturbations in TEC to a precise altitude. Using the modelled propagation of acoustic rays in space and time and their interaction with satellite-station line of sight (LOS) geometry, a novel method has been developed to infer the detection altitude of ionospheric perturbations observed through GPS-TEC. This modest method has been further upgraded to identify the distinct seismic sources that evolved along an extended rupture varying simultaneously in space and time akin to the seismic rupture of the Mw 9.0 2011-03-11 Tohoku-Oki earthquake (Bagiya et al., 2020).

In addition to the transient perturbations, prolonged ionospheric oscillations following large earthquakes (Mw > 8.0) have also been found to provide seismic source information from the ionosphere. Such ionospheric oscillations related to the earth-atmospheric resonance frequencies of ~3.7 and ~4.4 mHz following the 2012-04-11 Sumatra doublet (Fig.11) and 2011-03-11 Tohoku-Oki earthquakes were scrutinized (Nayak et al., 2021, 2022). The Earth's background free oscillations at ~3.7 and ~4.4 mHz resonantly couple with the atmospheric acoustic modes and thus energy cross-talk between the earth-atmosphere system is maximum at these frequencies. Our studies emphasized that resonant ionospheric signatures during the Sumatra doublet event were related to the seismic source. Therefore, resonant co-seismic ionospheric signatures could provide additional information on the low frequency features of seismic ruptures.

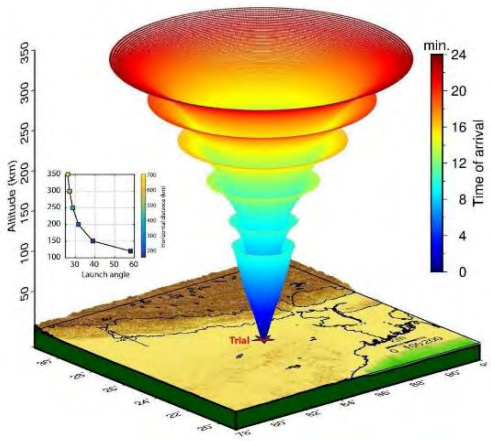

Figure 10. Propagation of seismo-acoustic waves in 3D space with time from the Trial seismic source assumed at 25°N 85°E. The propagation of six rays modeled at six different launch angles is shown. The first ray is launched at an angle of ~58° that is the threshold angle at 120 km altitude. The rays with launch angles higher than this refract downward while those lower than this propagate further upward. Similarly, the second ray is launched at an angle of ~38.8° that is the threshold propagation angle at 150 km altitude and so on. The inset shows the variation of the threshold angle and maximum horizontal distance along with the atmospheric altitudes. (From Bagiya et al., 2019) (*Courtesy IIG*)

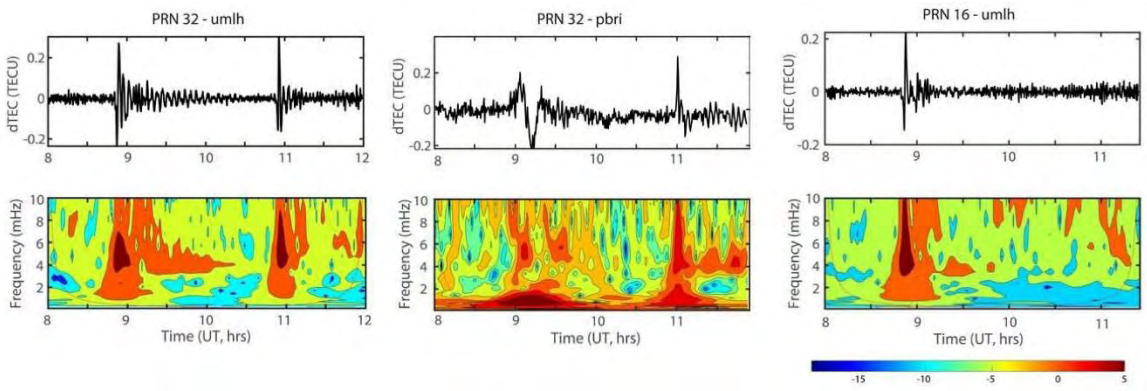

Figure 11. Power spectral analysis of Pseudo Random Number (PRN) 32 detrended TEC (dTEC) time series from umlh and pbri and of PRN 16 dTEC time series from umlh during 2012-04-11 Sumatra doublet earthquake. Resonant ionospheric signatures centered at ~4 mHz could be noticed. (From Nayak et al., 2021) (*Courtesy IIG*)

Rapidly moving objects excite short-period waves, and slow objects excite long-period waves. This has been confirmed for atmospheric waves excited by vertical crustal movements associated with large earthquakes. We compared atmospheric wave amplitudes excited by ordinary earthquakes and by "tsunami" earthquakes, characterized by slow fault movements. It has been found that the 2010 Mentawai earthquake, a typical tsunami earthquake, excited abnormally large internal gravity waves from ionospheric observations. This is the first slow earthquake signature found in space (Heki et al., 2022).

In another initiative, the Sumatra 2004 tsunami induced ionospheric signatures, which were detected simultaneously in GPS-TEC ~90 minutes before the arrival of actual tsunami over the Indian east coast, were successfully explained. This work offers an alternative tool to monitor

the offshore signatures that travel ahead of tsunami in the ionosphere could potentially be an important early warning tool for the tsunami over coastal regions. These findings, with a bearing on mitigation of hazards in coastal regions, are likely to impact tsunami forecast related research in a significant manner.

8. Paleoseismology

The E-W trending reverse Dauki Fault (DF) in NE India has played a major role in the regional deformation of the adjoining areas and was believed to be active during the Late Quaternary time. Previous paleo-seismological studies conducted on the eastern and western part of the DF, Bangladesh, revealed that the fault ruptured in AD 849-920 and AD 1548 respectively. However, there were no studies on the DF from the southern side of the Shillong Plateau (SP), India. IIG has reported soft sediment deformation structures (SSDS) from five trenches in and around the DF zone, SP. Close to the Dauki village, five trenches in the eastern part of the DF show micro-faulting, sand dykes, disturbed strata, and water escape structures. The detailed investigation of SSDS indicates that the origin of deformation is seismically triggered. The ^{14}C AMS (Accelerator Mass Spectrometry) dating of deformation structures generated by earthquakes suggests that three seismic events occurred between 130 and 920 yr BP, 5415 to 9140 yr BP, and at about 4285 yr BP. This study confirms that DF is indeed active, at least, since the mid-Holocene (Lakshmi and Gawali, 2022).

The major seismic source in the Kachchh basin, i.e. the Kachchh Mainland Fault (KMF), was studied using various geological investigations during 2019 and 2022. After thorough scrutiny of high-resolution satellite imageries and field investigations, several trenches were dug across prospective sites along the KMF for detailed paleo-seismic study. Based on these investigations, it was concluded that the KMF illustrates an oblique strike-slip fault in the western and central segments. A total of six paleo-seismic events have been identified during the period from 890 – 1980 years BP (Kothyari et al., 2021), out of which five were in the Holocene whereas one was in Late Pleistocene. The slip rate shows variability from lesser values in the western flank (0.08 – 0.04 mm/yr) to progressively increasing values (0.22 – 0.36 mm/yr) towards the eastern flank.

9. Seismological Networks

9.1. National Network

The National Center for Seismology (NCS) under the Ministry of Earth Sciences (MoES), Government of India, is the nodal agency for monitoring and reporting earthquake activity in the country. It has got a network of more than 150 broadband seismological stations spread across the country. The details of this national network are available on https://seismo.gov.in/. The web portal of NCS also reports earthquake activity in the region (https://riseq.seismo.gov.in/riseq/earthquake).

9.2. Regional Networks

CSIR-NGRI has been operating 174 broadband seismometers and 41 strong motion accelerometers in different parts of the country in network and profile modes (Fig.12). In recent years, Uttarakhand Himalaya has been a focus of seismological studies. A setup of 76 three-

component broadband stations (in network and profile modes) and 19 strong motion stations have been operating in this region since 2017 (Srinagesh et al., 2019). This network provides high-quality digital waveforms of thousands of local, regional, and teleseismic earthquakes. The data from this network have been used to pursue seismological studies, including research in environmental seismology, especially after the 2021-02-07 glacial burst and flood event in Uttarakhand.

WIHG is operating seismological networks in the NW and NE sectors of the Himalaya and adjoining parts for seismogenesis and subsurface structure investigations (Fig.13). The NW Himalaya network includes 72 broadband seismographs and 25 accelerographs and covers Jammu & Kashmir, Ladakh, Himachal Pradesh, Uttarakhand, Punjab, and Haryana. A network of 8 broadband seismographs is being operated in the Siang valley of Arunachal Pradesh in NE Himalaya. The institute also has state-of-the-art Multi-Parametric Geophysical Observatory at Ghuttu, Garhwal Himalaya.

Figure 12. The BBS and SMA stations operated by CSIR-NGRI in different regions of India. Inset shows the coverage in the Uttarakhand Himalaya. (Source: Seismological Observatory, CSIR-NGRI) (*Courtesy Dr. M. Ravi Kumar, Seismological Observatory, CSIR-NGRI*)

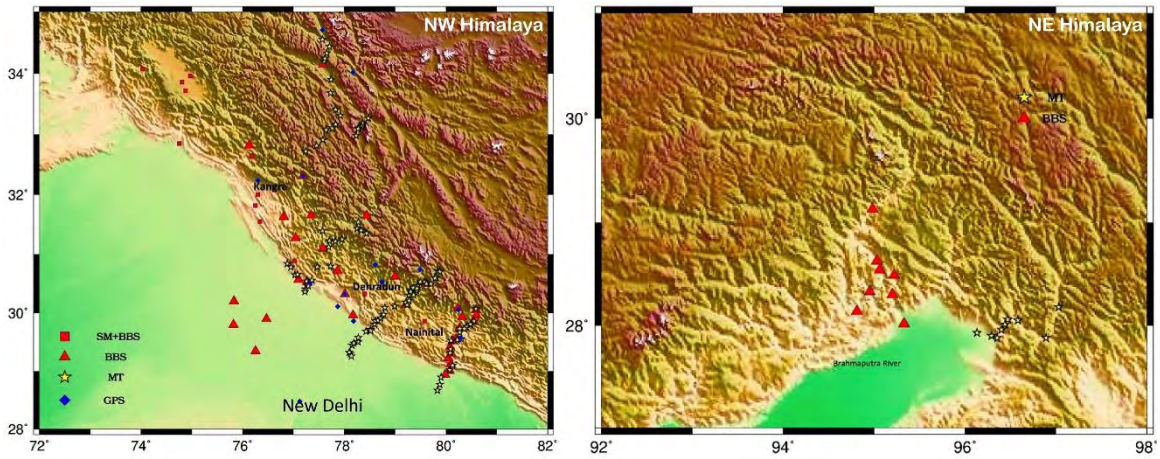

Figure 15. Geophysical Instrumentation network (permanent and temporary) operated by WIHG in the Himalaya and adjoining regions. Abbreviations: BBS - Broad Band Seismograph; SMS – Strong motion System; MT – Magnetotelluric; GPS – Global Positioning System; MCT – Main Central Thrust; MBT – Main Boundary Thrust; HFT – Himalayan Frontal Thrust. (*Courtesy WIHG*)

CSIR-4PI has established a regional broadband seismic and GNSS network in Kashmir Himalaya to assess earthquake hazard and risk in NW Himalaya with emphasis on Jammu & Kashmir, and Ladakh regions. This network started in 2013 with 8 stations in phase 1 and 7 stations were added in phase 2. Recently, 7 more stations are added in phase 3 (Fig.14). This network of collocated broadband seismic and GNSS stations enabled CSIR-4PI to initiate integrated broad seismic and GNSS studies for the first time in Kashmir valley. The network is running with 120 s broadband sensors and, in addition, CSIR-4PI is also equipped with 12 units of 5 s period seismometers useful for micro-tremor array measurements to image the subsurface geological mapping in terms of shear wave velocity. Mir et al. (2022) performed noise analysis of this seismic network for the period of 2014 – 2020.

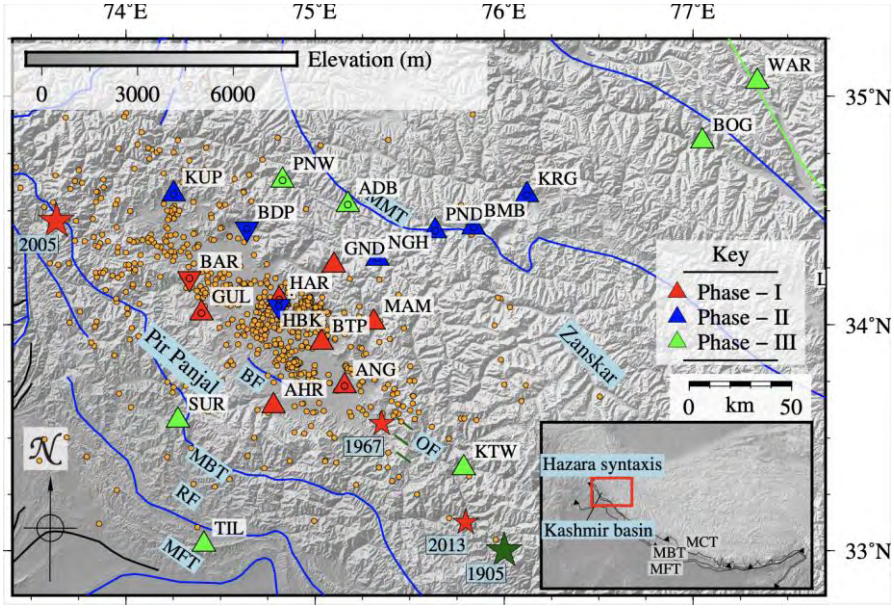

Figure 14. The location of broadband seismological and GNSS stations in Kashmir Himalaya operated by CSIR-4PI. (*Courtesy CSIR-4PI*)

A seismological network (Jammu and Kashmir Seismological Network [JAKSNET]) of 24 broadband three-component seismograph systems was installed in 2013 across Jammu and Kashmir, under joint collaborative efforts between Indian Institute of Science Education and Research (IISER)-Kolkata, Shri Mata Vaishno Devi University, Katra (J&K), and University of Cambridge, United Kingdom (Sharma S., et al., 2020).

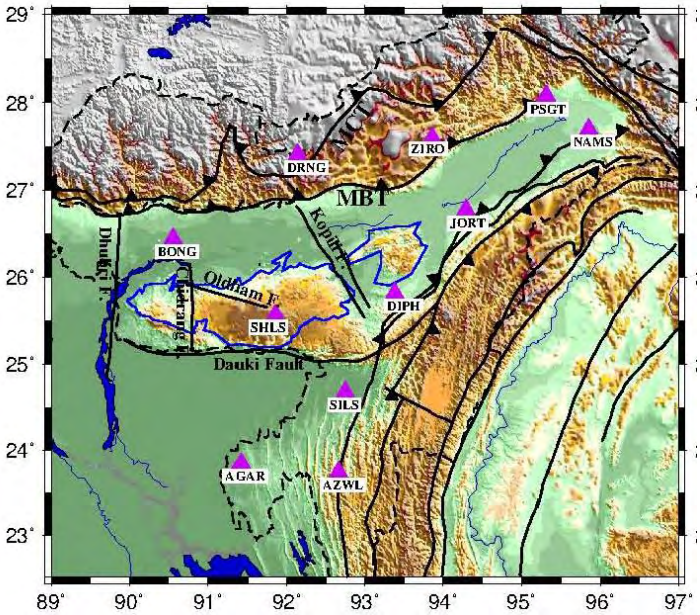

Figure 15. Regional network of 11 broadband seismological stations in NE India operated by Indian Institute of Geomagnetism. (*Courtesy IIG*)

A regional network of 11 broadband seismological stations has been established and operated by IIG in NE India (Fig.15) to study the geometry and continuity of crust and upper mantle discontinuities beneath the region, seismic ambient noise tomography focusing primarily on crustal and uppermost mantle structures, and crustal attenuation characteristics of high frequency body waves.

Strong motion accelerographs (SMA) have been installed and operated by CSIR-NEIST at different places in and around the Shillong Plateau and Mikir Hills. The acceleration time histories obtained from these accelerographs are filtered and processed for baseline corrections on a regular basis. These are then used as inputs for the estimation of several ground motion parameters including PGA, PGV and PGD, and Response spectra. A total of 234 earthquake events ($M \geq 3.5$) have been recorded by these SMA stations during Sep.2016 to Sep.2021.

The Gujarat State Seismic Network (GSNet) under the aegis of the ISR, Gandhinagar, is operational since July 2006 (Fig.16). Presently, the network consists of 54 broadband seismograph stations (BBS) spread out in the state and neighboring areas. The data from almost 45 BBS are transmitted to the Institute through VSAT, where the earthquake activity is monitored in near real time (24x7).The network has a detectability of M 1.5 in the Kachchh region and M 2.0 in the other areas of Gujarat. Based on earthquake data of the Gujarat region, ISR developed a calibrated local magnitude scale (M_L) for Kachchh and Saurashtra regions. ISR has also procured 10 compact broadband sensors with 4G connectivity. In addition, 54 strong motion accelerographs are also deployed by ISR. It has also established three MPGOs

in Kachchh for earthquake precursory studies.

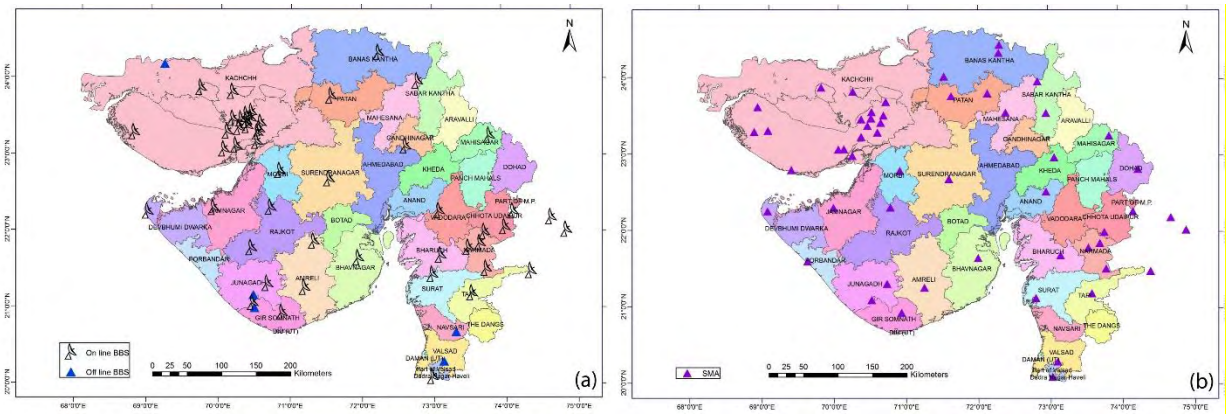

Figure 16. GSNet [(a) Broadband seismometers, (b) SMA] network operated by Institute of Seismological Research in Gujarat. (Source: https://isr.gujarat.gov.in/maps; accessed on 2023-01-31)

IIT-Kharagpur is operating a seismic network in the Sikkim Himalaya since 2019 (Fig.17). The network was deployed as an attempt to understand the seismic structure, lithospheric deformation, and seismicity of the Indian plate in Sikkim Himalaya (Uthaman et al., 2021, 2022).

10. Societal Projects

Monitoring of dams is an ongoing activity to keep a watch on the health of these dams. CSIR-NGRI has been involved in monitoring of many dams in different regions of the country, e.g. Srisailam dam (Andhra Pradesh), Bhatsa and Dhamni dams (Maharashtra), Kalpsar dam (Gujarat), Gandhisagar dam (Madhya Pradesh) to name a few. Estimation of seismic hazard for the cultural heritage sites like Shree Ram Mandir in Uttar Paradesh, and Somnath and Dwarka in Gujarat are among the most highlighted hazard based studies conducted by CSIR-NGRI.

10.1. Developing an Earthquake Resilient Society in the Vicinity of Himalaya

Among the seismically active continental regions, the Himalayan region is very significant with large human population in the immediate vicinity. The Himalayan region experienced four great earthquakes of M ~8 within a short span of 55 years from 1897 to 1952. The region has not experienced an earthquake of similar magnitude since 1952. Developing an earthquake resilient society through the process of developing earthquake scenarios, as to what would be the impact if one of the past earthquakes repeats today, is an extremely useful approach and sharing this information with all concerned, doing the needful to educate and enrich the concerned government departments, and making the public a shareholder, helps. The 1905 Kangra earthquake of M ~8 had claimed ~20,000 human lives in addition to causing widespread damage. A scenario was built by the National Disaster Management Authority (NDMA), Government of India, as to what would be the consequences if such an earthquake occurred today? It was discovered that ~0.9 million human lives would be lost in the states of Punjab, Haryana, Himachal Pradesh, and the Union Territory of Chandigarh if this earthquake occurred in the middle of the night. A year-long phase of training and educating at various

levels to develop an earthquake resilient society in the states of Punjab, Haryana, Himachal Pradesh, and the Union Territory of Chandigarh during 2012-2013 culminated in a mega mock drill on the 13 February 2013. It demonstrated what all had been achieved and what was missing. Encouraged by the success a similar exercise was carried out for the repeat of the 1897 Shillong earthquake for 8 northeast Indian states during 2013-2014 culminating in mega mock drills on 10 and 13 March 2014 (Gupta, 2020; Goff et al., 2020; Gupta and Sabnis, 2021).

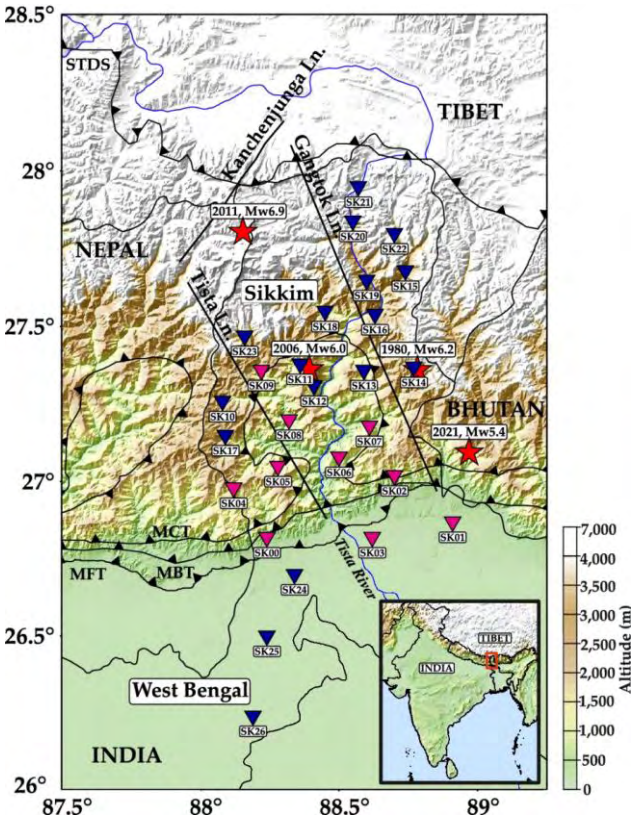

Figure 17. Seismological network operated by IIT-Kharagpur in the Sikkim Himalaya and adjoining Bengal basin. Stations with the sensor installed on pier are represented with pink inverted triangles and stations with the sensor buried are represented in blue inverted triangles. (From Uthaman et al., 2022) (*Courtesy Dr. Chandrani Singh, IIT-Kharagpur*)

11. Education and Outreach Programs

CSIR-NGRI along with various national agencies is involved in outreach activities to sensitize the general public to build a seismic resilient society. Gupta H.K., et al. (2020) opined that scenario-based research is important for disaster preparedness of the country, involving historical data of earthquakes superimposed on the current data pertaining to infrastructure, population, etc., for a Seismic Zone V. Such exercises carried out in NE India successfully raised awareness among the general public, and more importantly, among the various responders, streamlined the techniques and procedures of a diverse set of agencies – from administrative, to technical, including disaster response forces, fire-fighters, hospitals, etc. (Fig.18). All the concerned agencies successfully performed the mega mock exercises. This underscores that if the mitigation and preparedness measures are adequate, the impact of any great earthquake can be contained.

CSIR-NGRI is conducting various outreach activities in seismology by inviting students to the

Institute, conducting webinars for students and general public, distributing booklets in different languages, and visiting different schools in different parts of the country to spread awareness about earthquakes, earthquake risks and precautions. In the last three years, CSIR-NGRI has reached around 20,000 students and general public through these outreach activities. CSIR-NGRI has also conducted 6 training courses (online and offline) in seismology during 2019-2022. These courses were attended by nearly 250 participants. Fig.19 shows participation of school children in one such event.

Figure 18. Mock-drill exercise at military hospital, Shillong, Meghalaya. (*Courtesy Dr. M. Ravi Kumar, CSIRNGRI*)

Figure 19. Visit of students to CSIR-NGRI for an awareness program on seismology. (*Courtesy Dr. Sandeep K. Gupta, CSIR-NGRI*)

Figure 20. Demonstration during earthquake education awareness program on 30 Nov.2022 by WIHG in the Kendriya Vidyalaya, Raipur, Dehradun. (*Courtesy WIHG*)

Since 2017, WIHG is regularly conducting an outreach program titled "*Education and awareness program for earthquake preparedness and hazard mitigation: Uttarakhan*d". In this program, the Institute's scientists visit various schools, organizations and villages to deliver lectures on safety and prevention measures to be taken before, during and after an earthquake (Fig.20). To make the lecture more effective an earthquake recording system is also demonstrated exhibiting real-time recording by the seismograph.

12. Other Significant Contributions

Joint Scientific Assembly of IAGA and IASPEI:

A major international scientific event related to the IUGG during this period has been organization of the Joint Scientific Assembly of IAGA and IASPEI in India during 21-27 August 2021 (JSA-2021). The Assembly was hosted virtually by CSIR-NGRI and INSA (the National Adhering body of IUGG) with support from other Earth science institutes. The virtual conference was attended by 828 participants from 53 countries, over 500 from IAGA and about 300 from IASPEI. A total of 778 abstracts were submitted under 53 symposia, which included 8 joint symposia, 1 Diamond Jubilee symposium commemorating 60th anniversary of CSIR-NGRI, 27 IAGA symposia and 17 IASPEI symposia, including one from the Asian Seismological Commission. There were 3 joint plenary talks. The JSA-2021 was preceded by IAGA and IASPEI Schools for early carrier scientists and a GIFT Workshop for teachers.

Encyclopedia of Solid Earth Geophysics (ESEG) 2nd Edition:

The second edition of ESEG was compiled and published in 2021 with 257 articles spread over 1950 pages in two volumes (https://link.springer.com/referencework/10.1007/978-3-030-58631-7). Almost 100 of the 257 articles are seismology related (edited by Gupta H.K., 2021e).

Diamond Jubilee of CSIR-National Geophysical Research Institute:

To commemorate the Diamond Jubilee of the creation of the CSIR-National Geophysical Research Institute, Hyderabad, India, the Geological Society of India published a special issue with 9 seismology related papers (edited by Tiwari and Gupta, 2021).

Silver Jubilee of the Asian Seismological Commission:

The Asian Seismological Commission (ASC), established in 1996, completed 25 years in 2021. A special volume of the Journal of the Geological Society of India was published to commemorate the Silver Jubilee of the Asian Seismological Commission, with 18 articles dealing with various aspects of Seismology in Asia (edited by Gupta H.K., et al., 2021).

Acknowledgement

I am thankful to Prof. Archana Bhattacharyya, Chairperson, INSA IUGG-IGU National Committee, India, for entrusting the responsibility of preparing this chapter on IASPEI Activities in India to me for the INSA National Report. I approached several Institutes and individuals engaged in seismological research in India seeking inputs for this chapter. The response has been overwhelming. I gratefully acknowledge the inputs received from the following researchers: Prof. Harsh Gupta, NASI Senior Scientist, CSIR-NGRI, Hyderabad, Dr. Prakash Kumar, Director, CSIR-NGRI, Hyderabad, Dr. M. Ravi Kumar (CSIR-NGRI), Dr. Prantik Mandal (CSIR-NGRI), Dr. Sandeep Gupta (CSIR-NGRI), Dr. G. Pavankumar (CSIR-NGRI), Dr. K Sain, Director, WIHG, Dehradun, Dr. Naresh Kumar (WIHG), Dr. D. Hazarika (WIHG), Prof. A.P. Dimri, Director, IIG, Mumbai, Dr. Sridevi Jade, Head, CSIR-4PI, Bengaluru, Dr. Sumer Chopra, Officiating Director General, ISR, Gandhinagar, Dr. Saurabh Baruah (CSIR-NEIST, Jorhat), Prof. Sagarika Mukhopadhyay (IIT-Roorkee), Prof. Dinesh Kumar (Kurukshetra University), Dr. Chandrani Singh (IIT-Kharagpur), and Dr. Arun Singh (IIT-Kharagpur). I gratefully acknowledge Prof. Harsh Gupta, Dr. M. Ravi Kumar, and Dr. Sandeep Gupta for reviewing this chapter and providing their valuable suggestions. The chapter has been compiled under the project MLP6404-28(AM) of CSIR-NGRI.

Acronyms used in the Chapter

ASC : Asian Seismological Commission
CSIR : Council of Scientific and Industrial Research
CSIR-4PI : CSIR-Fourth Paradigm Institute
CSIR-NEIST : CSIR-North East Institute of Science and Technology
CSIR-NGRI : CSIR-National Geophysical Research Institute
DST : Department of Science and Technology, Ministry of Science & Technology, Government of India
IAGA : International Association of Geomagnetism and Aeronomy
IASPEI : International Association of Seismology and Physics of the Earth's Interior
IGU : International Geographical Union
IIG : Indian Institute of Geomagnetism
IISER : Indian Institutes of Science Education and Research
IIT : Indian Institute of Technology
INSA : Indian National Science Academy
IUGG : International Union of Geodesy and Geophysics

MoES : Ministry of Earth Sciences, Government of India
NCS : National Center for Seismology
NDMA : National Disaster Management Authority
WIHG : Wadia Institute of Himalayan Geology

ADFB : Aravalli-Delhi Fold Belt
AMS : Accelerator Mass Spectrometry
APM : Absolute Plate Motion
BBS : Broad Band Seismograph
CB : Cuddapah Basin
CCB : Chiplakot Crystalline Belt
CCP : Common Conversion Point
CGGT : Chotanagpur Granitic Gneissic Terrain
CMB : Core Mantle Boundary
CNN : Convolutional Neural Network
DF : Dauki Fault
DSZ : Delhi Seismic Zone
DVP : Deccan Volcanic Province
EDC : Eastern Dharwar Craton
EDRI : Earthquake Disaster Risk Index
EEW : Earthquake Early Warning
EIC : Eastern Indian Craton
ESEG : Encyclopedia of Solid Earth Geophysics
FPA : Fast Polarization Azimuth
FPD : Fast Polarization Direction
GNSS : Global Navigation Satellite System
GMP : Ground Motion Parameter
GPS : Global Positioning System
HVSR : Horizontal to Vertical Spectral Ratio
IOGL : Indian Ocean Geoid Low
KMF : Kachchh Mainland Fault
LKZ : Ladakh – Karakoram Zone
LLSVP : Large Low Shear Velocity Province
LOS : Line of Sight
LPC : Lohit Plutonic Complex
LVZ : Low Velocity Zone
MBT : Main Boundary Thrust
MCT : Main Central Thrust
MCTZ : Main Central Thrust zone
MFT : Main Frontal Thrust
MHT : Main Himalayan Thrust
MPGO : Multi-parametric Geophysical Observatory
MTZ : Mantle Transition Zone
PASSCAL : Portable Array Seismic Studies of the Continental Lithosphere
PGA : Peak Ground Acceleration
PGD : Peak Ground Displacement
PGV : Peak Ground Velocity
RF : Receiver Function
RTS : Reservoir-Triggered Seismicity
SAR : Synthetic Aperture Radar
SEM : Seismo-electromagnetic
SGT : Southern Granulite Terrain
SMA : Strong Motion Accelerograph
SOC : Singhbhum-Odisha-Craton
SP : Shillong Plateau
SSA : Singular Spectrum Analysis
STD ; South Tibetan Detachment
SWF : South Wagad Fault
TEC : Total Electron Content
ULF : Ultra-low Frequency
WDC : Western Dharwar Craton
WGE ; Western Ghat Escarpment
ZTD : Zenith Total Delay

Bibliography

References cited in the Chapter

Akilan, A., Padhy, S., Dimri, V.P., Schuh, H., Abdul Azeez, K.K. (2021) Co-seismic and Post-seismic Changes in ZTD and TEC of the 2015 Nepal Earthquake. Pure Appl. Geophys., 178: 3339–3354. https://doi.org/10.1007/s00024-021-02830-y

Anbazhagan, P., Mog, K., Rao, K.S.N., Prabhu, N.S., Agarwal, A., et al. (2019) Reconnaissance report on geotechnical effects and structural damage caused by the 3 January 2017 Tripura earthquake, India. Nat. Hazards, 98: 425-450.

Arjun, V.H., Gupta, S., Tiwari, V.M. (2022) Lithospheric Structure of Dharwar Craton from joint analysis of Gravity, Topography and Teleseismic Travel-Time Residuals, J. Asian Earth Sci., 239, 105397, https://doi.org/10.1016/j.jseaes.2022.105397

Bagiya, M.S., Sunil, A.S., Rolland, L., Nayak, S., Ponraj, M., et al. (2019) Mapping the Impact of Non-Tectonic Forcing mechanisms on GNSS measured Coseismic Ionospheric Perturbations. Sci. Rep., 9, 18640, https://doi.org/10.1038/s41598-019-54354-0

Bagiya, M.S., Thomas, D., Astafyeva, E., Bletery, Q., Lognonné, P., et al. (2020) The Ionospheric view of the 2011 Tohoku-Oki earthquake seismic source: the first 60 seconds of the rupture. Sci. Rep., 10, 5232, https://doi.org/10.1038/s41598-020-61749-x.

Baruah, S., Boruah, G.K., Sharma, S., Hoque, W.A., Chetia, T., et al. (2020) Seismic vulnerability assessment of earthquake-prone mega-city Shillong, India using geophysical mapping and remote sensing. Georisk: Assessment and Management of Risk for Engineered Systems and Geohazards, 14:2, 112-127, DOI: 10.1080/17499518.2019.1598560

Baruah, S., Sharma, A., Dey, C., Saikia, S., Boruah, G.K., et al. (2021) Correlation between crustal anisotropy and seismogenic stress field beneath Shillong–Mikir Plateau and its vicinity in North East India. Geomatics, Nat. Hazards Risk, 12(1): 2070-2086. https://doi.org/10.1080/19475705.2021.1947902

Biswal, S., Kumar, S., Roy, S.K., Kumar, M.R., Mohanty, W.K., et al. (2020) Upper Mantle Anisotropy beneath the Western Segment, NW Indian Himalaya, Using Shear Wave Splitting. Lithosphere, 1: 1-9. https://doi.org/10.2113/2020/8856812

Biswas, R., Singh, C. (2019) Lateral variation of crustal attenuation properties from southern Tibet to eastern Nepal Himalaya. Geophys. J. Int., 217: 257-270.

Biswas, R., Singh, C. (2020a) Attenuation of high frequency body waves in the crust of western Tibet. Phys. Earth Planet. Inter., 298, 106323.

Biswas, R., Singh, C. (2020b) An investigation of regional variations of coda wave attenuation in western Tibet. J. Seismol., 24(6): 1235-1254.

Biswas, R., Singh, C. (2020c) Seismic attenuation structure across the Karakoram fault in western Tibet. Geophys. J. Int., 223(2): 1418-1431.

Boruah, G.K., Baruah, S., Sharma, S., Barua, A.G., Baruah, S. (2022) Estimation of site-specific amplification factors and expected peak ground motion at Shillong city, Meghalaya: A deterministic approach. J. Earth Syst. Sci., 131(2), 69.

Chanu, N.M., Kumar, N., Kumar, A., Mukhopadhyay, S., Babu, V.G. (2022) Along-strike variation in the shear wave crustal structure of the NE Himalaya and Indo-Burmese arc: Evidence based on surface wave dispersion analysis. Geol. J., 57: 5161-5175. https://doi.org/10.1002/gj.4465

Chaudhary, P., Roy, K.S., Kamra, C., Chopra, S. (2022) Development of empirical relationship between the observed and the estimated ground acceleration values of small to moderate earthquakes in the northwest (Gujarat) and northeast (NE) regions of India. Geomatics, Nat. Hazards, Risk, 13(1): 364-389. https://doi.org/10.1080/19475705.2022.2028906

Chauhan, V., Kumar, N., Shukla, V., Verma, S.K. (2021) Multiple Linear regression analysis to estimate hydrological effects in Soil Rn-222 at Ghuttu, Garhwal Himalaya: A prerequisite to identify earthquake precursors. Curr. Sci., 120(12): 1905-1911.

Chetia, T., Baruah, S., Dey, C., Sharma, S., Baruah, S. (2019a) Probabilistic analysis of seismic data for earthquake forecast in North East India and its vicinity. Curr.Sci., 117(7): 1167-1173.

Chetia, T., Baruah, S., Dey, C., Sharma, S., Baruah, S. (2019b) Singular spectrum and principal component analysis of soil radon (Rn-222) emanation for better detection and correlation of seismic induced anomalies, Nonlinear Process. Geophys.: Discussions. https://doi.org/10.5194/npg-2019-37

Chetia, T., Baruah, S., Baruah, S., Dey, C., Sharma, S. (2020) Weibull distribution analysis of precursory time due apparent resistivity anomaly prior to earthquakes in the vicinity of multi-parametric geophysical observatory, Tezpur, India. Geomatics, Nat. Hazards Risk 11(1): 1093-1114. https://doi.org/10.1080/19475705.2020.1775714

Cook, K.L., Rekapalli, R., Dietze, M., Pilz, M., Cesca, S., et al. (2021) Detection and potential early warning of catastrophic flow events with regional seismic networks. Science, 374: 87-92.

Coudurier-Curveur, A., Tapponnier, P., Okal, E., Van der Woerd, J., Kali, E., et al. (2020) A composite rupture model for the great 1950 Assam earthquake across the cusp of the East Himalayan Syntaxis. Earth Planet. Sci. Lett., 531, 115928.

Das, R., Rai, S.S. (2019) Redefining Dharwar Craton-Southern Granulite Terrain boundary in south India from new seismological constraints. Precambrian Res., 332, 105394. https://doi.org/10.1016/j.precamres.2019.105394

Das, R., Mukhopadhyay, S. (2020) Regional variation of coda wave attenuation in Northeast India: An understanding of the physical state of the medium. Phys. Earth. Planet Inter., 299: 1-13. https://doi.org/10.1016/j.pepi.2019.106404.

Dey, C., Baruah, S., Rawat, G., Chetia, T., Baruah, S., et al. (2021) Appraisal of contemporaneous application of polarization ratio and fractal analysis for studying possible seismo-electromagnetic emissions during an intense phase of seismicity in and around Assam Valley and the Eastern Himalayas, India. Phys. Earth Planet. Inter., 318, 106759.

Dubey, A.K., Singh, A., Kumar, M.R., Jana, N., Sarkar, S., et al. (2022) Tomographic imaging of the plate geometry beneath the Arunachal Himalaya and Burmese subduction zones. Geophys. Res. Lett., 49, e2022GL098331.

Elliott, J.R., de Michele, M., Gupta, H.K. (2020) Earth observation for crustal tectonics and earthquake hazards. Surv. Geophys., 41: 1355-1389. https://doi.org/10.1007/s10712-020-09608-2

Goff, J., Gupta, H.K., Glade, T. (2020) Editorial at the occasion of the 100th volume of natural hazards. Nat. Hazards, 100(1): 1-2.

Gogoi, A., Baruah, S., Sharma, S. (2023) Regression analysis on ground motion parameters for the earthquakes (Mw≥ 4.0) in NE India with special emphasis on 3 Jan 2016 M6. 7, Tamenglong earthquake. Phys. Chem. Earth, Parts A/B/C 129, 103316

Grujic, D., Hetényi, G., Cattin, R., Baruah, S., Benoit, A., et al. (2018) Stress transfer and connectivity between the Bhutan Himalaya and the Shillong Plateau. Tectonophysics, 744: 322-332.

Gupta, H.K. (2020) Recent earthquakes in Delhi and developing an earthquake resilient society. J. Geol. Soc. India, 96: 1-4.

Gupta, H.K. (2021a) Understanding anthropogenic earthquakes. Curr. Sci., 120(9): 1415-1416.

Gupta, H.K. (2021b) Koyna, India, an ideal site for near field earthquake observations. J. Geol. Soc. India, 97(10): 1144-1151.

Gupta, H.K. (2021c) Studies of artificial water reservoir triggered earthquakes at Koyna, India: A Summary. J. Geol. Soc. India, 97(12): 1556-1564.

Gupta, H.K. (2021d) Artificial water reservoir-triggered seismicity (RTS): Most prominent anthropogenic seismicity. Surv. Geophys., https://doi.org./10.1007/s10712-021-09675-z

Gupta, H.K. (2021e) Encyclopedia of Solid Earth Geophysics, 2nd Edition, Vol.I & II, Springer ISBN: ISBN 978-3-030-58631-7 (Editor-in-Chief). https://link.springer.com/referencework/10.1007/978-3-030-58631-7

Gupta, H.K. (2022a) Three different types of earthquake sequences in the Deccan Volcanic Province of India. Geosystems and Geoenvironment. https://doi.org/10.1016/j.geogeo.2022.100035

Gupta, H.K. (2022b) Koyna, India: A very prominent site of artificial water reservoir-triggered seismicity. J. Earth Syst. Sci., https://doi.org/10.1007/s12040-021-01780-2

Gupta, H.K., Sabnis, K.A. (2021) Developing an earthquake resilient society in the vicinity of Himalaya. J. Geol. Soc. India, 97(12): 1593-1602.

Gupta, H.K., Rekapalli, R. (2022) A short note on the Aftershock Duration of Strong to Major Himalayan Earthquakes. J. Geol. Soc. India. https://doi.org/10.1007/s12594-022-xxxx-x

Gupta, H.K., Kanchan, A., Duarah, R., Saxena, R.S., Baruah, S. (2020). Himalayan Earthquakes and Developing an Earthquake Resilient Society, J. Geol. Soc. India, 96:433-446, https://doi.org/10.1007/s12594-022-1955-8

Gupta, H.K., Zhongliang, W., Banerjee, P., Li, L. (2021) 25 Years of Asian Seismological Commission. J. Geol. Soc. India, 97(12): 1475-1602.

Gupta, S., Kumar, S. (2022) Lithosphere thickness variation across the Deccan Volcanic Province-Eastern Dharwar Craton, South India: Insight into evolution of the Deccan Volcanic Province. J. Earth Syst. Sci., 131, 10. https://doi.org/10.1007/s12040-021-01748-2.

Gupta, S., Mahesh, P., Kanna, N., Sivaram, K., Paul, A. (2022) 3-D seismic velocity structure of the Kumaun–Garhwal (Central) Himalaya: insight into the Main Himalayan Thrust and earthquake occurrence, Geophys. J. Int., 229(1):138–149. https://doi.org/10.1093/gji/ggab449

Gupta, S.V., Parvez, I.A., Ankit, Khan, P.K., Chandra, R. (2020) Site Effects Investigation in Srinagar City of Kashmir Basin Using Microtremor and Its Inversion, J. Earthq. Eng., DOI: 10.1080/13632469.2020.1816232.

Gupta, S.V., Parvez I A and Khan P K (2022) Imaging sub-surface geological complexity (2D/3D) beneath Greater Srinagar region of Kashmir Basin, Northwest Himalaya. Near Surf. Geophys., 20(1): 94-114. DOI:10.1002/nsg.12186.

Hajra, S., Hazarika, D., Bankhwal, M., Kundu, A., Kumar, N. (2019) Average crustal thickness and Poisson's ratio beneath the Kali River Valley, Kumaon Himalaya. J. Asian Earth Sci., 173: 176-188.

Hajra, S., Hazarika, D., Kumar, N., Pal, S.K., Roy, P.N.S. (2021) Seismotectonics and stress perspective of the Kumaon Himalaya: A geophysical evidence of a Lesser Himalayan duplex. Tectonophysics, 806: 1-17, 228801.

Hajra, S., Hazarika, D., Shukla, V., Kundu, A., Pant, C.C. (2022a) Stress dissipation and seismic potential in the central seismic gap of the north-west Himalaya. J. Asian Earth Sci., 239, 105432. https://doi.org/10.1016/j.jseaes.2022.105432

Hajra, S., Hazarika, D., Mondal, S., Pal, S.K., Roy, P.N.S. (2022b) Deformation of the upper crust in the Kumaon Himalaya analyzed from seismic anisotropy and gravity lineament studies. Phys. Earth Planet. Inter. 322, 106827.

Hazarika, D., Hajra, S., Kundu, A., Bankhwal, M., Kumar, N., et al. (2021) Imaging the Moho and Main Himalayan Thrust beneath the Kumaon Himalaya: Constraints from receiver function analysis. Geophys. J. Int., 224: 858–870.

Hazarika, D., Kundu, A., Ghosh, P. (2022) Seismotectonic scenario of the indenting northeast corner of the Indian plate in the Tidding-Tuting Suture Zone of the Eastern Himalayan Syntaxis. Tectonophysics, 824, 229197, https://doi.org/10.1016/j.tecto.2021.229197

Hebert, H., Occhipinti, G., Schindele, F., Gailler, A., Pinel-Puyssegur, B., et al. (2020) Contributions of Space Missions to Better Tsunami Science: Observations, Models and Warning. Surv. Geophys., 41: 1535-1581. https://doi.org/10.1007/s10712-020-09616-2

Heki, K., Bagiya, M.S., Takasaka, Y. (2022) Slow fault slip signatures in coseismic ionospheric disturbances. Geophys. Res. Lett., 49, e2022GL101064. https://doi.org/10.1029/2022GL101064

Illa, B., Reshma, K.S., Kumar, P., Srinagesh, D., Haldar, C., et al. (2021a) Pn tomography and anisotropic study of the Indian shield and the adjacent regions. Tectonophysics, 813, 228932.

Illa, B., Kumar, P., Reshma, K.S., Srinu, U., Srinagesh, D. (2021b) Sn wave tomography of the uppermost mantle beneath the Indian shield and its adjacent regions. Phys. Earth Planet. Inter., 319, 106785.

Jaiswal, N., Singh, C., Sarkar, S., Tiwari, A.K., Jana, N. (2022) Pg attenuation tomography beneath western Tibet. J. Seismol., pp.1-13.

Jana, N., Singh, A., Tiwari, A.K., Singh, C., Biswas, R. (2019) Mantle deformation patterns and signatures of rift, beneath Eastern Ghats Mobile Belt. Phys. Earth Planet. Inter., 289: 20-33.

Jana, N., Singh, A., Tiwari, A.K., Eken, T., Singh, A., et al. (2021) Seismic anisotropy and mantle deformation beneath Eastern Ghats Mobile Belt using direct-S waves. Precambrian Res., 360, 106215.

Jana, N., Singh, C., Singh, A., Eken, T., Dubey, A.K., et al. (2022) Lithospheric architecture below the Eastern Ghats Mobile Belt and adjoining Archean cratons: Imprints of India-Antarctica collision tectonics. Gondwana Res., 111: 209-222.

Joshi, S., Rao, K.M. (2021) Ultra-low frequency geomagnetic variations before Dholavira earthquake (M 5.1) on 20th June 2012 in Kachchh region, Gujarat, India. Geotectonics, 55: 633–645. doi: 10.1134/S0016852121040142

Kamra, C., Chopra, S., Yadav, R.B.S., Joshi, V. (2020) Characterization of major fault systems in the Kachchh Intraplate Region, Gujarat, India, by focal mechanism and source parameters. Seismol. Res. Lett., 91(6): 3496-3517.

Kamra, C., Chopra, S., Yadav, R.B.S. (2021) Joint inversion for stress and fault orientations using focal mechanisms of earthquakes in the Saurashtra horst, a part of the stable continental region of India, and source parameter estimation. J. Seismol., 25(4): 1141-1159. https://doi.org/10.1007/s10950-021-10016-1

Kanna, N., Gupta, S. (2020) Crustal seismic structure beneath the Garhwal Himalaya using regional and teleseismic waveform modelling. Geophys. J. Int., 222: 2040-2052.

Kanna, N., Gupta, S. (2021) Seismic crustal shear velocity structure across NW Himalaya and Ladakh-Karakoram using receiver function modelling: Evidence of the Main Himalayan Thrust. Phys. Earth Planet Inter., 311, 106642. https://doi.org/10.1016/j.pepi.2020.106642

Kothyari, G.C., Kandregula, R.S., Kotlia, B.S., Lakhote, A., Swamy, K.V., et al. (2021) Palaeoseismic investigations along the Kachchh Mainland Fault: a comprehensive review and new insights of the past earthquakes in the Kachchh basin, Western India. Quat. Int., 599: 184-209.

Kumar, A., Kumar, N., Mukhopadhyay, S., Klemperer, S.L. (2021) Tomographic image of shear wave structure of NE India based on analysis of Rayleigh wave data. Front. Earth Sci., 9: 179-196, 680361. https://doi.org/10.3389/feart. 2021.680361

Kumar, N., Yadav, D.N. (2019) Coda Q estimation for Kinnaur region and surrounding part of NW Himalaya. J. Seismol., 23(2): 271-285.

Kumar, N., Aoudia, A., Guidarelli, M., Babu, V.G., Hazarika, D., et al. (2019) Delineation of lithosphere structure and characterization of the Moho geometry under the Himalaya-Karakoram-Tibet collision zone using surface wave tomography. Geol. Soc. Spec. Pub., SP481, 19-40. http://doi.org/10.1144/SP481-2017-172

Kumar, N., Kumar, K., Gautam, Mishra, M., Kumar, S., Kumar, P. (2021b) Upper mantle anisotropy from shear wave splitting of teleseismic earthquakes in the Kumaun-Garhwal and adjoining area of NW Himalaya. J. Asian Earth Sci., 5: 1-9, 100054.

Kumar, P., Devi, S., Monika, Srivastava, A., Sandeep, et al. (2019) Site response study based on H/V method using S-wave: A case study in the Kumaon Himalaya, India. Himal. Geol., 40(2): 213-219.

Kumar, P., Monika, Sandeep, Kumar, S., Kumari, R., Kumar, D., et al. (2021) Characterization of shear wave attenuation and site effects in the Garhwal Himalaya, India from inversion of strong motion records. J Earth Syst. Sci., 130:1-19.

Kumar, S., Sharma, N. (2019) The seismicity of central and north-east Himalayan region. Contrib. Geophys. Geod., 49(3): 265-281. https://doi.org/10.2478/congeo-2019-0014

Kumar, S., Gupta, S., Kanna, N., Sivaram, K. (2020) Crustal structure across the Deccan Volcanic Province and Eastern Dharwar Craton in south Indian shield using receiver function modelling. Phys. Earth Plant. Inter., 306, 106543.

Kumari, R., Kumar, P., Kumar, N., Sandeep (2020) Role of site effect for the evaluation of attenuation characteristics of P, S and coda waves in Kinnaur region, NW Himalaya. J. Earth Syst. Sci., 129: 1-18.

Kumari, R., Kumar, P., Kumar, N., Sandeep (2021) Implications of site effects and attenuation properties for estimation of earthquake source characteristic in Kinnuar Himalaya, India. Pure Appl. Geophys., 178: 4345-4366.

Kumar, V., Rai, S.S., Hawkins, R., Bodin, T. (2022) Seismic imaging of crust beneath the western Tibet-Pamir and western Himalaya using ambient noise and earthquake data. J. Geophys. Res. Solid Earth, 127, e2021JB022574. https://doi.org/10.1029/2021JB022574

Kumar, V.P., Gupta, S., Borah, K., Prakasam, K.S., Rai, S.S. (2022) Seismic anisotropy beneath the Kumaun–Garhwal Himalaya using core-refracted shear wave phases. Geophys. J. Int., 229(3): 1978-1989.

Kundu, A., Hazarika, D., Hajra, S., Singh, A.K., Ghosh, P. (2020) Crustal Thickness and Poisson's Ratio variations in the northeast India–Asia collision zone: Insight into the Tuting-Tidding Suture zone, Eastern Himalaya. J. Asian Earth Sci, 188, 104099. https://doi.org/10.1016/j.jseaes.2019.10409

Lakshmi, B.V., Gawali, P.B. (2022). Soft sediment deformation features in Dauki Fault region: Evidence of paleoeqrthquakes, Shillong Plateau, NE India. Environ. Earth Sci., 81.

Madhusudhan, S., Gupta,S., Kann, N., Sivaram, K., Sudesh Kumar (2022) Seismic characteristic of underthrusting Indian lithosphere beneath the eastern Kumaun Himalaya using regional earthquake waveform analysis, J. Asian Earth Sci., 237, 105356. https://doi.org/10.1016/j.jseaes.2022.105356

Mahato, C.R., Shashidhar, D. (2022) Stress drop variations of triggered earthquakes at Koyna-Warna, western India: A case study. J. Earth Syst. Sci. 131(2): 1-10. https://doi.org/10.1007/s11069-021-05096-8

Mahesh P., A. Sateesh, C. Kamra, S. Kumar, S. Chopra, et al. (2020) Earthquake swarms in Palghar district, Maharashtra, Deccan Volcanic province. Curr. Sci., 118(5): 701.

Mandal, P. (2019a) Passive source seismic imaging of the crust and upper mantle underlying the Archean Singhbhum Craton, Eastern India. J. Asian Earth. Sci., 176: 300-314.

Mandal, P. (2019b) A possible origin of intraplate earthquakes in the Kachchh rift zone, India, since the 2001 Mw7.7 Bhuj earthquake. J. Asian Earth Sci., 170: 56-72.

Mandal, P. (2019c) Shear-wave splitting in the Rajasthan craton, India. J. Asian Earth Sci., 173: 1-10.

Mandal, P. (2020) Strong ground motions from two moderate size (Mw5.5) Kachchh intraplate earthquakes, Gujarat, India. Nat. Hazards, 103: 2441–2458. https://doi.org/10.1007/s11069-020-04092-8

Mandal, P. (2020a) Three-dimensional seismic velocity imaging of the Kachchh rift zone, Gujarat, India: Implications toward the crustal mafic pluton induced intraplate seismicity. J. Asian Earth Sci., 192, 104226.

Mandal, P. (2021) Shear-wave splitting observations: Implications toward the variable anisotropic structure of the upper mantle below the Kachchh rift zone, Gujarat, India. Phys. Earth Planet. Inter., 310, 106618.

Mandal, P. (2021a) Seismic velocity images of a crystallized crustal magma-conduit (related to the Deccan plume) below the seismically active Kachchh rift zone, Gujarat, India. Nat. Hazards. https://doi.org/10.1007/s11069-021-05051-7

Mandal, P. (2022a) Evidence of secular variation in Archean crust formation in the Eastern Indian Shield. Sci. Rep., 12, 14040. https://doi.org/10.1038/s41598-022-18372-9

Mandal, P. (2022b) Seismic velocity images of a crystallized crustal magma-conduit (related to the Deccan plume) below the seismically active Kachchh rift zone, Gujarat, India .Nat. Hazards, 111: 239-260.

Mandal, P., Asano, K. (2019) Three-dimensional ground motion modelling in the Kachchh rift zone, Gujarat, India. Phys. Earth Planet. Inter., 297. https://doi.org/10.1016/j.pepi.2019.106322.

Mandal, P., Kumar, P., Sreenivas, B., Babu, EVSSK, Bhaskar Rao, Y.J. (2021) Variations in crustal and lithospheric structure across the Eastern Indian Shield from Passive Seismic source imaging: Implications to changes in the tectonic regimes and crustal accretion through the Precambrian, Precambrian Res., 360, 106207, 1-19.

Mandal, P., Satayanarayana, H.V.S., Shashidhar, D., Arti Devi, Srinagesh D. (2021a) Simultaneous estimation of site response and source parameters of reservoir-triggered earthquakes using data from the borehole seismic network in the Koyna–Warna seismic zone, Maharashtra, India. Nat. Hazards, 111: 1335 -1354. https://doi.org/10.1007/s11069-021-05096-8

Mandal, P., Srinagesh, D., Suresh, G, et al. (2021b) Characterization of earthquake hazard at the Palghar and Pulichintala swarm activity regions (India) through three-dimensional

modelling of b-value and fractal (correlation) dimensions. Nat. Hazards,108: 1183–1196. https://doi.org/10.1007/s11069-021-04726-5

Mandal, P., Srinivas, D., Suresh, G., Srinagesh, D. (2021c) Modelling of crustal composition and Moho depths and their Implications toward seismogenesis in the Kumaon–Garhwal Himalaya. Sci. Rep., 11, 14067. https://doi.org/10.1038/s41598-021-93469-1.

Mandal, P., Kumar, S., Gupta, S., Prasad, B.N.V., Saidixit, M. (2022) Delineation of detailed crustal seismic velocity structure and Moho depths in the Hyderabad region, eastern Dharwar craton, India. Nat. Hazards, 114: 2219-2241. https://doi.org/10.1007/s11069-022-05469-7

Mandal, P., Saha, S., Kumar, S., et al. (2022a) Modelling of Moment Tensors and Source Parameters of the 25 July 2021 Rare Lower Crustal Hyderabad (India) Earthquake of Mw 3.9. Pure Appl. Geophys, 179: 993–1010. https://doi.org/10.1007/s00024-022-02973-6

Mandal, P., Srinagesh, D., Vijayaraghavan, R., Suresh, G., Naresh, B., et al. (2022b) Seismic velocity imaging of the Kumaon–Garhwal Himalaya, India. Nat. Hazards, 111: 2241-2260. https://doi.org/10.1007/s11069-021-05135-4

Mandal, P., Srinivas, D., Vengala, P., Srinagesh, D., Suresh, G., Naresh, B. (2022c) Delineation of crustal and lithospheric structure below the 2019 Palghar swarm activity region, Maharashtra, India. Nat. Hazards, 114: 205-235. https://doi.org/10.1007/s11069-022-05387-8.

Manglik, A., Gupta, S., Tiwari, V.M. (2021) Geophysical studies for the crust and upper mantle structure of the Himalaya: Contributions of CSIR-NGRI. J. Geol. Soc. India, 97: 1190-1199.

Manglik, A., Suresh, M., Nagarjuna, D., Pavankumar, G. Demudu Babu, M., et al. (2022) Subsurface Expressions of the Aravalli-Delhi Fold Belt in the Western Ganga Basin by Magnetotellurics. J. Geol. Soc. India, 98(12): 1721-1727.

Medved, I., Koulakov, I., Mukhopadhyay, S., Jakovlev, A. (2022) Lithosphere Structure in the Collision Zone of the NW Himalayas Revealed by a Local Earthquake Tomography. J. Geodyn., 152: 1-11, https://doi.org/10.1016/j.jog.2022.101922.

Mir, R.R., and Parvez I A (2020) Ground motion modelling in NW Himalaya using stochastic finite-fault method, Nat. Hazards (10.1007/s11069-020-04068-8)

Mir, R.R., Parvez, I.A., Gaur, V.K. (2021) Shear wave velocity structure beneath North-Western Himalaya and adjoining areas. Preprint at EarthArxiv, https://doi.org/10.31223/X5DK68.

Mir, R.R., Parvez I A, Laske, G., Gaur, V.K. (2022) Sensor orientation and noise analysis of the Kashmir-Zanskar seismic network: an appraisal from 2014-2020, J. Seismol., 1-18, DOI:10.1007/s10950-022-10090-z

Mohanty, D.D., Singh, A. (2022) Shear wave birefringence and current configuration of active tectonics of Shillong plateau: an appraisal of Indian plate motion and regional structures. Int. J. Earth Sci., 111(1): 269-286.

Monika, Kumar, P., Sandeep, Kumar, S., Joshi, A., Devi, S. (2020) Spatial variability studies of attenuation characteristics of Qα and Qβ in Kumaon and Garhwal region of NW Himalaya. Nat. Hazards, 103: 1219-1237

Mukherjee, T., Singh, C., Biswas, P.K. (2021) A Novel Approach for Earthquake Early Warning System Design using Deep Learning Techniques. arXiv preprint arXiv:2101.06517.

Mullick, N., Rai, S.S., Saha, G. (2022) Lithospheric structure of the South India Precambrian terrains from surface wave tomography. J. Geophys. Res. Solid Earth, 127, e2022JB024244. https://doi.org/10.1029/2022JB024244

Nagamani, D., Sivaram K., Purnachandra Rao, N., Satyanarayana, H.V.S. (2020) Ambient noise and earthquake HVSR modelling for site characterization in southern mainland, Gujarat, J. Earth Syst. Sci., 129(1): 1-14.

Nagar, M., Pavankumar, G., Mahesh, P., Nikam, R., Nagarjuna, D., et al. (2021) Magnetotelluric evidence for trapped fluids beneath the seismogenic zone of the Mw6.0 Anjar earthquake, Kachchh intraplate region, northwest India. Tectonophysics, 228969. https:// doi.org/10.1016/j.tecto.2021.228969.

Nanajee, U., Roy, S.K., Kumar, M.R. (2022) Spatial variation of crustal anisotropy in the Arunachal Himalaya inferred from splitting of local S waveforms. J. Asian Earth Sci., 234, 105278. https://doi.org/10.1016/j.jseaes.2022.105278

Nayak, S., Bagiya, M.S., Maurya, S., Hazarika, N.K., Kumar, A.S.S., et al. (2021) Terrestrial resonant oscillations during the 11 April 2012 Sumatra doublet earthquake. J. Geophys. Res. Space Phys., 126, e2021JA029169. https://doi.org/10.1029/2021JA029169

Nayak, S., Bagiya, M.S., Sunil, A.S. (2022) Spatial manifestation of resonant ionospheric signatures during the 11 March 2011 Tohoku-Oki earthquake. Adv. Space Res., 69: 3000–3007. https://doi.org/10.1016/j.asr.2022.01.027

O'Kane, A., Copley, A., Mitra, S., Wimpenny, S. (2022) The geometry of active shortening in the northwest Himalayas and the implications for seismic hazard. Geophys. J. Int., 231: 2009-2033. https://doi.org/10.1093/gji/ggac303

Parija, M.P. (2021) Earthquake Swarm and Quiescence Precursory to the NE Himalaya 2011 Sikkim Earthquake (M 6.9) , J. Geol. Soc. India, 98: 178-180.

Paul, A., Hazarika, D. (2022) Occurrences of low-stress drop earthquakes in the eastern Ladakh-Karakoram zone and their tectonic implications. J. Asian Earth Sci.:X, 7 (2022) 100080, https://doi.org/10.1016/j.jaesx.2022.100080.

Paul, A., Hazarika, D., Wadhawan M, Kumar, N. (2021) Upper mantle anisotropy in the northwest Himalaya and Ladakh-Karakoram zone based on SKS splitting analysis. J. Geodyn., 144, 101817.

Paul, H., Ravi Kumar, M. (2022) Strong influence of tomographic models on geoid prediction: Case studies from Indian Ocean and Ross Sea geoids. Tectonophysics, 836, 229429.

Paul, H., Pandey, A., Ravi Kumar, M., Kumar, S. (2021) Investigation of crustal thickness and uppermost mantle velocity beneath Gujarat, western India, utilizing Moho reflected P phases. Phys. Earth Planet. Inter., 310, 106619.

Pavankumar, G., Manglik, A. (2021) Complex tectonic setting and deep crustal seismicity of the Sikkim Himalaya: An electrical resistivity perspective. Phys. Chem. Earth, Parts A/B/C, 124(2), 103077. 10.1016/j.pce.2021.103077

Pavankumar, G., Chakravarthi, N.N., Demudu Babu, M., Manglik, A. (2020) Magnetotelluric study of an intraplate seismic zone in the Palghar region of the Deccan Volcanic Province, India. J. Earth Syst. Sci.,129(1):1-16.

Pavankumar, G., Manglik, A., Demudu Babu, M., Chakravarthi, N.N. (2021) Magnetotelluric evidence for the presence of a deep electrical conductor in the vicinity of the Delhi Seismic Zone, India. J. Earth Syst. Sci., 130(2): 1-16.

Parvin, S.S., Naresh, B., Raghavan, R.V., et al. (2021) Source Parameters of Shallow Microtremors Induced by Seasonal Groundwater Recharge in Hyderabad, Southern

Peninsular India. J. Geol. Soc. India, 97: 1073–1079. https://doi.org/10.1007/s12594-021-1822-z

Rao, B.P., Ravi Kumar, M. (2022a) Evolution of the Western Ghats: Constraints from receiver function imaging and harmonic decomposition. Tectonophysics, 838, 229472.

Rao, B.P., Ravi Kumar, M. (2022b) Lowermost mantle (D″ layer) structure beneath the Indian Ocean: Insights from modeling of ScS-S and PcP-P residuals. J. Asian Earth Sci., 225, 105038.

Rao, B.P., Ravi Kumar, M., Saikia, D. (2020) Seismic Evidence for a Hot Mantle Transition Zone Beneath the Indian Ocean Geoid Low. Geochemistry, Geophysics, Geosystems, 21, e2020GC009079.

Ravi Kumar, M., Padma Rao, B., Mahesh, P., Venkatesh, V. (2022) Scattered wave imaging of the Main Himalayan Thrust and mid-crustal ramp beneath the Arunachal Himalaya and its relation to seismicity. J. Asian Earth Sci., 236, 105335.

Rekapalli, R., Gupta, H.K. (2021) Characterization of injection-induced seismicity at north central Oklahoma, USA (Short Communication). J. Seismol., 25: 327-337. https://doi.org/10.1007/s10950-020-09978-5

Reshma, K.S., Illa, B., Kumar, P., Srinagesh, D. (2022) Lg Q in the Indian Shield. Pure Appl. Geophys., 179: 149-168.

Roy, S.K., Kumar, M.R., Srinagesh, D. (2021a) Mantle deformation beneath India inferred from shear wave splitting. J. Geol. Soc. India, 97: 1200-1206. doi: 10.1007/s12594-021-1849-1

Roy, S.K., Srinagesh, D., Suresh, G., Srinivas, D. (2021b) Seismicity and Disparate deformation of the crust and upper mantle beneath the Doda-Kisthwar region, NW Himalaya. Phys. Earth Planet. Inter., 310, 106635. https://doi.org/10.1016/j.pepi.2020.10663.

Saha, G., Rai, S.S., Prakasam, K.S., Gaur, V.K. (2021) Distinct lithospheres in the Bay of Bengal inferred from ambient noise and earthquake tomography. Tectonophysics, 809, 228855. https://doi.org/10.1016/j.tecto.2021.228

Sahoo S.K., K.M. Rao, C. Barman, U. Lakshmi, G. (2020) Identification of earthquake precursors in soil radon-222 data of Kutch, Gujarat, India using empirical mode decomposition based Hilbert Huang Transform. J. Environ.Radioact., 222, 106353. Doi.org/10.1016/j.jenvrad.2020.106353.

Sahoo S.K., M. Katlamudi, U. Lakshmi G. (2021) Observation of ULF electromagnetic emissions before the M 7.8 New Zealand earthquake of November 13, 2016. Geodyn. Tectonophys., 12 (4), 891–901. Doi: 10.5800/GT-2021-12-4-0561.

Saikia, U., Kumar, V.P., Rai, S.S. (2019) Complex upper mantle deformation beneath the Dharwar craton inferred from high density splitting measurements: Distinct lateral variation from west to east. Tectonophysics, 755: 10-20.

Saikia, D., Ravi Kumar, M., Singh, A. (2020) Palaeoslab and plume signatures in the mantle transition zone beneath Eastern Himalaya and adjoining regions. Geophys. J. Int., 221: 468-477.

Sandeep, Joshi, A., Sah, S.K., Kumar, P., Lal, S., et al. (2019a) Modeling of 2011 Indo Nepal Earthquake and Scenario Earthquakes in the Kumaon Region and Comparative Attenuation Study Using PGA Distribution with the Garhwal Region. Pure Appl. Geophys., 176(11): 4687- 4700.

Sandeep, Joshi, A., Sah, S.K., Kumar, P., Lal, S., et al. (2019b) Modelling of strong motion generation areas for a great earthquake in central seismic gap region of Himalayas using the modified semi-empirical approach. J. Earth Syst. Sci., 128:100, 1-12.

Sandeep, Joshi, A., Devi, S., Kumar, P., Sah, S.K., et al. (2019c) Strong motion generation area modeling of the 2008 Iwate earthquake, Japan using modified semi-empirical technique. J. Earth Syst. Sci., 128:202, 1-16

Sandeep, A. Joshi, P. Kumari, Kumar, P., Sah, S.K., et al. (2020) Strong ground motion simulation techniques—a review in world context. Arab. J. Geosci., 13(673), 1-12.

Sandeep, S. Devi, Kumar, P., Monika, Kumar, R. (2022) Strong Motion Modelling of the 1999 Izmit Earthquake Using Site Effect in a Semi-Empirical Technique: A More Realistic Approach. Pure Appl. Geophys., 179: 483-497.

Sarkar, S., Jaiswal, N., Singh, C., Dubey, A.K., Singh, A. (2021) Source spectral studies using Lg wave in western Tibet. J. Seismol., 25(2): 625-638.

Sateesh A., Mahesh, P., Singh, A.P., Kumar, S., Chopra, S., et al. (2019) Are earthquake swarms in South Gujarat, northwestern Deccan Volcanic Province of India monsoon induced? Environ. Earth Sci., 78, 381. https://doi.org/10.1007/s12665-019-8382-1.

Sharma, A., Vashisth, D., Naresh, B., et al. (2021) An ML scale for Eastern Dharwar Craton and adjoining regions. J. Seismol., 25: 1251–1263. https://doi.org/10.1007/s10950-021-10028-x

Sharma, J., Kumar, M.R., Roy, S.K., Pal, S.K., Roy, P.N.S. (2021) Low-Velocity Zones and Negative Radial Anisotropy Beneath the Plume Perturbed Northwestern Deccan Volcanic Province. J. Geophys. Res. Solid Earth, 126(2), e2020JB020295.

Sharma, N., Srinagesh, D., Suresh, G., Srinivas, D. (2021) Stochastic simulation of strong ground motions From Two M > 5 Uttarakhand Earthquakes. Front. Earth Sci., 9, 599535. doi: 10.3389/feart.2021.599535

Sharma, S., Sarma, J.N., Baruah, S. (2018) Dynamics of Mikir hills plateau and its vicinity: inferences on Kopili and Bomdila Faults in Northeastern India through seismotectonics, gravity and magnetic anomalies. Ann. Geophys., 61(3), SE338-SE338.

Sharma, S., Mitra, S., Sharma, S., Priestley, K., Wanchoo, S.L., et al. (2020) A Report on Broadband Seismological Experiment in the Jammu and Kashmir Himalaya (JAKSNET). Seismol. Res. Lett., 91: 1915–1926, doi: 10.1785/0220190389

Shashidhar, D., Mallika, K., Mahato, C., et al. (2019a) A Catalogue of Earthquakes in the Koyna-Warna Region, Western India (2005–2017). J. Geol. Soc. India, 93: 7–24 . https://doi.org/10.1007/s12594-019-1115-y

Shashidhar, D., Mallika, K., Gahalaut, K., Mahato, C.R., Satyanarayana, H.V.S. (2019b) A New Earthquake Sequence at Koyna–Warna, India, and Its Implication for Migration of the Reservoir Triggered Seismicity. Bull. Seismol. Soc. Am., 109(2): 827-831.

Shashidhar, D., Rodriguez, I.V., Mallika, K., Kühn, D., Wilks, M., et al. (2020) Relative locations of an earthquake sequence recorded 1 during June 2017 on the Koyna-Warna borehole seismic network of western India. Bull. Seismol. Soc. Am., 110(6): 3130-3138. https://doi.org/10.1785/012020068

Shukla, N., Hazarika, D., Kundu, A., Mukhopadhyay, S. (2022) Spatial variations of crustal thickness and Poisson's ratio in the northeastern region of India based on receiver function analysis. Geol. J., https://doi.org/10.1002/gj.4469.

Shukla, V., Chauhan, V., Kumar, N., Hazarika, D. (2020) Assessment of Rn-222 continuous time series for the identification of anomalous changes during moderate earthquakes of the Garhwal Himalaya. Appl.Radiat. Isot., 166, 109327, 1-10.

Shugar, D.H., Jacquemart, M., Shean, D., Bhushan, S., Upadhyay, K., et al. (2021) A massive rock and ice avalanche caused the 2021 disaster at Chamoli, Indian Himalaya. Science, 373(6552): 300-306. https://doi.org/10.1126/science.abh4455

Singh, A., Singh, C. (2019) Seismic imaging of the deep crustal structure beneath Eastern Ghats Mobile Belt (India): Crustal growth in the context of assembly of Rodinia and Gondwana supercontinents. Precambrian Res., 331, 105343.

Singh, A., Saikia, D., Ravi Kumar, M. (2021) Seismic Imaging of the Crust beneath Arunachal Himalaya. J. Geophys. Res. Solid Earth, 126, e2020JB020616.

Singh, B., Mandal, P. (2020) Upper mantle seismic anisotropy beneath the Kachchh rift zone, Gujarat, India, from shear wave splitting analysis. J. Earth Syst. Sci., 129(1): 1-11.

Singh, C., Biswas, R., Jaiswal, N., Ravi Kumar, M. (2019a) Spatial variations of coda wave attenuation in Andaman–Nicobar subduction zone. Geophys. J. Int., 217(3): 1515-1523.

Singh, C., Jaiswal, N., Mukhopadhyay, S. (2019b) PgQ model for Nepal Himalaya. Phys. Earth Planet. Inter., 286: 13-20. doi.org/10.1016/j.pepi.2018.10.009

Singh, S.K., Srinagesh, D., Pérez-Campos, X., Srinivas, D., Suresh, G., et al. (2020). Seismic wave amplification in the central Indo-Gangetic Plains, India, estimated from the ratio of soft to hard site source spectrum. J. Seismol., 24: 679–692. https://doi.org/10.1007/s10950-020-09931-6

Sivaram, K. (2021) Simulation of Strong Ground Motion in the National Capital Region, India, from a Future 8.5 Magnitude Earthquake Using Two-Step Empirical Green's Function Method. Bull. Seismol. Soc. Am., 111(6): 3374–3386. doi: https://doi.org/10.1785/0120200239

Sivaram, K., Gupta, S. (2022) Frequency-dependent attenuation characteristics of coda and body waves in the Kumaun Himalaya: Implications for regional geology and seismic hazards. Pure Appl. Geophys., https://doi.org/10.1007/s00024-022-02963-8.

Sivaram, K., Kumar, V.P., Gupta, S., Prasad, B.N.V., Kumar, S. (2022) Upper mantle seismic anisotropy beneath the Deccan Volcanic Province and the adjacent Eastern Dharwar Craton in south Indian shield from shear wave splitting analysis. Phys. Earth Planet. Inter., 322, 106829.

Sribin, C., Rao, B.P., Kumar, M.R., Tomson, J.K. (2021) Mantle deformation beneath the Western Ghats, India: Insights from core-refracted shear wave splitting analysis. J. Asian Earth Sci., 218, 104848.

Srijayanthi G., Chatterjee, R.S., Kamra, C., Chauhan, M., Chopra, S., et al. (2022) Seismological and InSAR based investigations to characterise earthquake swarms in Jamnagar, Gujarat, India–An active intraplate region. J. Asian Earth Sci.: X, 8, pp.100118.

Srinu, U., Kumar, P., Haldar, C., Kumar, S. Ravi Kumar, M., et al. (2021) X-discontinuity beneath the Indian shield—evidence for remnant Tethyan Oceanic lithosphere in the mantle. J. Geophys. Res. Solid Earth, 126, e2021JB021890.

Srinagesh, D., Mandal, P., Vijaya Raghavan, R., Gupta, S., Suresh, G., et al. (2019) Digital seismic network: to map Himalayan orogen and seismic hazard, Curr. Sci., 116(4): 518-519.

Srinagesh, D., Singh, D.K., Vikas, G., Naresh, B., Roy, S., et al. (2020) An appraisal of recent earthquake activity in Palghar region, Maharashtra, India, Curr. Sci., 118(10): 1592-1596. doi: 10.18520/cs/v118/i10/1592-1598

Srinagesh, D., Sunil kumar, T.C., Naresh, B., Vitthal, S., Singh, D.K., et al. (2021) A study of Palnadu earthquake sequence in the Cuddapah basin and its tectonic implications. J. Earth Syst. Sci., 130, 52. https://doi.org/10.1007/s12040-021-01552-y

Surve, G., Kanaujia, J., Sharma, N. (2021) Probabilistic seismic hazard assessment studies for Mumbai region. Nat. Hazards 107: 575–600. https://doi.org/10.1007/s11069-021-04596-x

Tiwari, A., Sain, K., Kumar, A., Tiwari, J., Paul, A., et al. (2022) Potential seismic precursors and surficial dynamics of a deadly Himalayan disaster: an early warning approach. Sci. Rep., 12(1): 1-13.

Tiwari, A.K., Singh, A., Saikia, D., Singh, C., Eken, T. (2022a) Crustal anisotropy beneath southeastern Tibet inferred from directional dependence of receiver functions. Phys. Earth Planet. Inter., 331, 106912.

Tiwari, A.K., Singh, C., Sandvol, E., Mukhopadhyay, S., Singh, A., et al. (2022b) Sn attenuation tomography of southeastern Tibet: new constraints on lithospheric mantle deformation. Geophys. J Int., 228(2): 1038-1053.

Tiwari, V.M., Gupta, H.K. (2021) 60 Years of CSIR-National Geophysical Research Institute. J. Geol. Soc. India, 97(10): 1113-1324.

Uthaman, M., Singh, A., Singh, C., Dubey, A., Kumar, G. (2021) Discerning structure and seismic hazards in the Sikkim Himalayas. Eos, 102.

Uthaman, M., Singh, C., Singh, A., Jana, N., Dubey, A.K., et al. (2022) Spatial and temporal variation of the ambient noise environment of the Sikkim Himalaya. Sci. Rep., 12(1): 1-13.

Vashishtha, M., Karukola, B., Mukhopadhyay, S. (2022) Effect of Source Rupture Process on Surface Wave Group Velocity: An Example Using 2015 Nepal Earthquake Data. Pure Appl. Geophys. https://doi.org/10.1007/s00024-022-03008-w

Vijaya Kumar, P.V., Rawat, V.S., Patro, P.K., Gupta, A.K., Narendra Babu (2020) Assessment and recognition of pre- and co-seismic electromagnetic signatures from magnetotelluric data: a case study from Koyna–Warna seismoactive region, India. Acta Geophys., 69: 1–15. https://doi.org/10.1007/s11600-020-00510-4

Wadhawan, M., Rana, N., Gahalaut, V., et al. (2021) Monsoonal rainfall induced shallow earthquake Swarm in the Amravati district of the central India. J. Earth Syst. Sci., 130, 29. https://doi.org/10.1007/s12040-020-01511-z

Other publications during 2019-2022

Bhatia, M., Rekapalli, R., Kumar, M., Agrawal, M. (2022) Microseism source distribution inferred from noise recordings at the Gujarat Seismic Network, India. J. Earth Syst. Sci., 131, 23. doi: 10.1007/s12040-021-01779-9

Bhukta, K., Khan, P.K., Mandal, P. (2020) Estimation of source parameters of local earthquakes based on inversion of waveform data. Curr. Sci., 119: 1159-1168.

Bhukta, K., Paul, A., Khan, P.K. (2022) SKS and SKKS splitting measurements beneath the Northwest Himalaya. Pure Appl. Geophys. https://doi.org/10.1007/s00024-021-02935-4

Biswas, K., Mandal, P., Khan, P.K. (2019) Estimation of coda Q for the eastern Indian craton. J. Earth Syst. Sci., 128: 1-16.

Chaudhury, J., Mitra, S., Sarkar, T. (2021) Hales Discontinuity in the Southern Indian Continental Lithosphere: Seismological and Petrological Models. J. Geophys. Res. Solid Earth, 126, e2020JB020564. https://doi.org/10.1029/2020JB020564

Chaudhary, P., Chopra, S., Kamra, C., Das, A. (2019) New Insight into the Recent Earthquake Activity in North Cambay Basin, Western India: Seismological and Geodetic Perspectives. Bull. Seismol. Soc. Am., 109(6): 2240-2251.

Chetia, T., Baruah, S. (2022) Multi-Parametric Geophysical Observatory for Earthquake Precursory Research in Assam Valley, Eastern Himalaya (India): Seismotectonic Features of Kopili and Bomdila Faults. Geotectonics, 56(2): 212-227.

Chetia, T., Baruah, S., Dey, C., Baruah, S., Sharma, S. (2022) Seismic induced soil gas radon anomalies observed at multiparametric geophysical observatory, Tezpur (Eastern Himalaya), India: an appraisal of probable model for earthquake forecasting based on peak of radon anomalies. Nat. Hazards, 111(3): 3071-3098.

Das, A., Prizomwala, S.P., Solanki, T., Chauhan, G., Thakkar, M.G., et al. (2019) Relative assessment of tectonic activity along the seismically active Katrol Hill Fault, Kachchh, western India. J. Geol. Soc. India, 94(2): 179-187.

Devi, S., Kumar, S., Monika, P. (2021) Strong-Motion Simulation of the 1988 Indo-Burma and Scenario Earthquakes in NE India by Integrating Site Effects in a Semi-Empirical Technique. Pure Appl. Geophys., 178: 2839–2854.

Devi, S., Kumar, S., Monika, P., Joshi, A. (2022) Modelling of 2016 Kumamoto earthquake by integrating site effect in semi-empirical technique. Nat. Hazards, 111: 1931-1950.

Dey, C., Baruah, S., Abdelwahed, M.F., Saikia, S., Molia, N., et al. (2022) The 28 April 2021 Kopili Fault Earthquake (Mw 6.1) in Assam Valley of North East India: Seismotectonic Appraisal. Pure Appl. Geophys. https://doi.org/10.1007/s00024-022-03072-2

Dey, S., Powali, D., Chaudhury, J., Ghosh, M., Mandal, R., et al. (2019) 28 August 2018 (Mw 4.5) Bengal Basin earthquake highlights active basement fault beneath the sediments. Curr. Sci., 116(10): 1633-1636.

Dutta, A., Biswas, R., Singh, C., Kumar, M.R., Jana, N., et al. (2021) Depth-wise attenuation mechanism of seismic waves in the Andaman region. Soil Dyn. Earthq. Eng., 151, 107000

Dwivedi, V.K., Dubey, R.K., Pancholi, V., Rout, M.M., Singh, P., et al. (2020) Multi criteria study for seismic hazard assessment of UNESCO world heritage Ahmedabad City, Gujarat, Western India. Bull. Eng. Geol. Environ., 79(4): 1721-1733.

Gorshkov, A.I., Hasan, H., Mandal, P., Novikova, O. (2022) Identifying potential earthquake sources in the continental environments. Surv. Geophys., 43: 529-559. https://doi.org/10.1007/s10712-021-09683-z

Gupta, A.K., Mandal, P. (2020) Delineation of average 1-D shear velocity structure below north India, by surface wave dispersion study. J. Geol. Soc. India, 96: 58-64.

Gupta, V., Paul, A., Kumar, S., Dash, B. (2021b) Spatial distribution of landslides vis-à-vis epicentral distribution of earthquakes in the vicinity of the Main Central Thrust zone, Uttarakhand Himalaya, India. Curr. Sci., 120(12): 1927-1932.

Haldar, C., Sain, K., Kumar, S. (2022b) Seismic imaging of intra-crustal low-velocity layer beneath the Kishtwar region, North-West Himalaya, India using receiver function technique. Himal. Geol., 43(1A): 1-11.

Haldar, C., Kumar, P., Pandey, O.P., Sain, K., Kumar, S. (2022a) Lower crustal intraplate seismicity in Kachchh region (Gujarat, India) triggered by crustal magmatic infusion: Evidence from shear wave velocity contrast across the Moho. Geosystems and Geoenvironment, 1, 100073.

Hazarika, D., Kayal, J.R. (2022) Recent felt earthquakes (Mw 5.0–5.9) in Mizoram of north-east India region: Seismotectonics and precursor appraisal. Geol. J., 57(2): 877-885. doi.org /10.1002/ gj.4290.

Jaiswal, N., Singh, C., Singh, A. (2020) Crustal structure of western Tibet revealed by Lg attenuation tomography. Tectonophysics, 775, 228245.

Joshi, V., Chopra, S., Kumar, S. (2020) A local magnitude scale ML for the Saurashtra horst: An active intraplate region, Gujarat, India. J. Earth Syst. Sci., 129(1): 1-9.

Kanaujia, J., Mitra, S., Gupta, S.C., Sharma, M.L. (2019) Crustal anisotropy from shear-wave splitting of local earthquakes in the Garhwal Lesser Himalaya. Geophys. J. Int., 219(3): 2013-2033. doi: 10.1093/gji/ggz404

Kayal, J.R., Baruah, S., Hazarika, D., Das, A. (2022) Recent large and strong earthquakes in the eastern Himalayas: An appraisal on seismotectonic model. Geol. J., doi:10.1002/gj.4576.

Kumar, S., Gupta, V., Kumar, P., Sundriyal, Y.P. (2021a) Coseismic landslide hazard assessment for the future scenario earthquakes in the Kumaun Himalaya, India. Bull. Eng. Geol. Environ., 80: 5219–5235.

Kumar, S., Kumar, R.C., Roy, K.S., Chopra, S. (2021b) Seismic Monitoring in Gujarat, India, during 2020 Coronavirus Lockdown and Lessons Learned. Seismol. Res. Lett., 92(2A): 849–858.

Kumar, V., Rai, S.S. (2019) Complex seismic image of the Main Himalayan Thrust in Garhwal and implication for earthquake hazard. J. Earth Syst. Sci., 131, 79. https://doi.org/10.1007/s12040-022-0

Kumar, V., Chopra, S., Choudhury, P., Kumar, D. (2020) Estimation of near surface attenuation parameter kappa (κ) in Northwest and Northeast Himalaya region, Soil Dyn. Earthq. Eng, 136, 106237.

Kundu, A., Hazarika, D. (2022) Estimation of source parameters and scaling relations for local earthquakes of Lohit Valley in Arunachal Himalaya, Northeast India. Geol. J., DOI: 10.1002/gj.4423.

Kundu, A., Hazarika, D., Yadav, D.K., Ghosh, P. (2022). Crustal thickness and Poisson's ratio variations in the Siang Window and adjoining areas of the Eastern Himalayan Syntaxis. J. Asian Earth Sci., 231, 105225. https://doi.org/10.1016/j.jseaes.2022.105225.

Lakshmi, B.V. (2021) Seismically induced soft sediment deformation structures in and around Chamoli, Garhwal Himalaya, India. J. Earth Environ. Sci. Res., 3(2): 1-4.

Mandal, P. (2020) Relocations and local earthquake tomography: Implications toward the mafic pluton induced crustal seismicity in Kachchh, Gujarat, India, for last 18 years. J. Asian Earth Sci., 190: 1-9, 104196.

Mandal, P. (2021a) Structure of the seismically active Kachchh region. J. Geol. Soc. India, 10: 1163-1168.

Mandal, P. (2021b) Lessons Learned from the Occurrences of Major Devastating Mw≥7.5 Earthquakes in the Asian Countries during the last 25 years. J. Geol. Soc. India, 97: 1494-1497.

Mandal, P. (2022) Peak Ground Acceleration prediction using Artificial Neural Networks for Kachchh, Gujarat, India. Nat. Hazards, 114; 3043–3059. https://doi.org/10.1007/s11069-022-05504-7

Mandal, P., Srinagesh, D., Suresh, G., Naresh, B., Singh, D.K., et al. (2022) Three-dimensional b-value and fractal dimension mapping of the Uttrakhand Himalayan region, J. Geol. Soc. India, 98: 1365-1379.

Minocha, S., and Parvez, I A. (2020) Self-Organized Fractal Seismicity and b-Value of Aftershocks of the 2015 Gorkha Earthquake, Nepal. Int. J. Geosci., 11: 562-579. doi: 10.4236/ijg.2020.118030

Mitra, S., Wanchoo, S.K., Priestley, K. (2022) Seismic coda-wave attenuation tomography of the Jammu and Kashmir Himalaya. J. Geophys. Res. Solid Earth, 127, e2022JB024917. https://doi.org/10.1029/2022JB024917

Mittal, H., Sharma, B., Sandhu, M., Kumar, D. (2021) Spatial distribution of high-frequency spectral decay factor kappa (κ) for Delhi, India. Acta Geophysica, https://doi.org/10.1007/s11600-021-00674-7

Mohan K., Dugar, S., Pancholi, V., Dwivedi, V., Chopra S., et al. (2021) Micro-seismic hazard assessment of Ahmedabad city, Gujarat (Western India) through near-surface characterization/soil modeling. Bull. Earthq. Eng., 19: 623–656.

Naresh B., Mandal, P., Solomon Raju, P., Vijaya Raghavan, R., Suresh, G., et al. (2020). Magnitude estimation of regional earthquakes in India and its adjoining region. J. Earth. Syst. Sci., 129: 112. https://doi.org/10.1007/s12040-020-1374-4.

Nekrasova, A.K., Kossobokov, V.G., Parvez, I., Tao, X. (2020) Unified Scaling Law for Earthquakes as Applied to Assessment of Seismic Hazard and Associate Risks. Izvestiya, Phys. Solid Earth, 56: 83-94, DOI:10.1134/S1069351320010097

Pancholi, V., Bhatt, N.Y., Dwivedi, V.K., Choudhury, P., Chopra, S. (2020) Geotechnical Investigation for Estimation of Liquefaction Hazard for the Capital City of Gujarat State, Western India. Geotech. Geol. Eng., 38: 6551-6570. https://doi.org/10.1007/s10706-020-01454-8.

Pandey, P., Chauhan, P., Bhatt, C.M., Thakur, P.K, Kannaujia, S., et al. (2021) Cause and process mechanism of rockslide triggered flood event in Rishiganga and Dhauliganga River Valleys, Chamoli, Uttarakhand, India using satellite remote sensing and in situ observations. J. Indian Soc. Remote Sens., 49(5): 1011-1024. https:// doi.org/10.1007/s12524-021-01360-3.

Pandey, S., Yuan, X., Debayle, E., Geissler, W.H., Heit, B. (2022) Plume-lithosphere interaction beneath southwestern Africa -Insights from multi-mode Rayleigh wave tomography. Tectonophysics, 842, 229587.

Parshad, R., Kumar, P., Snehmani, Srivastva, P.K. (2019) Seismically induced snow avalanches at Nubra–Shyok region of Western Himalaya, India. Nat. Hazards, 99: 843-855.

Parvez, I.A. (2021) Application of neo-deterministic seismic hazard assessment to India. In: Panza, G., Kossobokov, V., De Vivo, B., Laor, E. (Eds) Earthquakes and Sustainable Infrastructure: neo-deterministic (NDSHA) approach guarantees prevention rather than cure. Imprint: Elsevier. Paperback ISBN: 9780128235034), pp. 525-541.

Paul, A., Hazarika, D. (2022) Seismic anisotropy for understanding the dynamics of crust and upper mantle: A case study in the northwest Himalaya and eastern Ladakh-Karakoram zone. In: Recent Developments in Using Seismic Waves as a Probe for Subsurface Investigations: Theory and Practices, Taylor & Francis Group, https://doi.org/10.1201/9781003177692, pp. 42

Paul, A., Tiwari, A., Upadhyay, R. (2019) Central Seismic Gap and Probable zone of large earthquake in North West Himalaya. Himal. Geol., 40 (2): 199-212.

Paul H., Kumar, M.R., Kumar, S. (2021) Evidence for reactivation of new faults and seismicity migration away from the causative fault of the 2001 MW 7.7 Bhuj earthquake, western India. Geophys. J. Int., 226 (3): 1800-1813.

Pavan Kumar, V., Gupta, S., Borah, K., Prakasam, K.S., Rai, S.S. (2022) Seismic anisotropy beneath the Kumaun-Garhwal Himalaya using core-refracted shear wave phases, Geophys. J. Int., 229(3): 1978–1989, https://doi.org/10.1093/gji/ggac043

Powali, D., Sharma, S., Mandal, R., Mitra, S. (2020) A reappraisal of the 2005 Kashmir (Mw 7.6) earthquake and its aftershocks: Seismotectonics of NW Himalaya. Tectonophysics, 789, 228501. https://doi.org/10.1016/j.tecto.2020.228501

Priestley, K., Ho, T., Mitra, S. (2019) The crust structure of the Himalaya: a synthesis. In: Treloar, P.J., Searle, M.P. (eds) Himalayan Tectonics: A Modern Synthesis. Geol. Soc. Spec. Pub., 483, 483–516. https://doi.org/10.1144/SP483-2018-127

Rawat, G., Luirei, K. (2022) Deep crustal resistivity structure of the Lohit Valley in the Eastern Himalayan Syntaxial region, Geol. J., 57: 4920-4928. doi:10.1002/gj.4422.

Roy, K.S., Sharma, J., Kumar, S., Kumar, M.R. (2021) Effect of coronavirus lockdowns on the ambient seismic noise levels in Gujarat, northwest India. Sci. Rep., 11, 7148. https://doi.org/10.1038/s41598-021-86557-9

Saha, G., Rai, S.S., Shalivahan (2019) Occurrence of diamond in peninsular India and its relationship with deep Earth seismic properties. J. Earth Syst. Sci. 128, 43. https://doi.org/10.1007/s12040-019-1088-7

Saha, G.K., Prakasam, K.S., Rai, S.S. (2020) Diversity in the peninsular Indian lithosphere revealed from ambient noise and earthquake tomography; Phys. Earth Planet. Inter. 306, 106523.

Sairam, B., Singh, A.P., Patel, V., Chopra, S., Kumar, M.R. (2019) VS30 mapping and site characterization in the seismically active intraplate region of Western India: implications for risk mitigation. Near Surf. Geophys., 17(5): 533-546.

Sandhu, K., Kumar, D. (2019) The 2011 Sikkim earthquake (MW 6.9) of the Himalaya: Estimates of earthquake source parameters and representability of attenuation characteristics, J. Asian Earth Sci., 169: 237-243.

Sandhu, M., Sharma, B., Mittal, H., Yadav R.B.S., Kumar, D., et al. (2020) Simulation of strong ground motion due to active Sohna fault in Delhi, National Capital Region (NCR) of India: an implication for imminent plausible seismic hazard. Nat. Hazards, 104: 2389-2408.

Sangwan, P., Kumar, D. (2020) Estimation of Coda Q for Northeast India using nonlinear regression. J. Earth Syst. Sci., 129, 229. https://doi.org/10.1007/s12040-020-01483-0

Sharma, A., Kumar, D., Paul, A. (2020) Estimation of site response functions for the Kumaun Garhwal region of Himalaya, India. J. Seismol., 24: 655-678. https://doi.org/10.1007/s10950-020-09920-9

Sharma, A., Yadav, R., Kumar, D., Paul, A., Teotia, S.S. (2021) Estimation of site response functions for the central seismic gap of Himalaya, India. Nat. Hazards, 109: 1899-1933. https://doi.org/10.1007/s11069-021-04903-6.

Shastri, A., Kumar, S. (2021) Estimation of Coda-Q for Mainland Gujarat region of Western Deccan Volcanic Province, India. J. Earth Syst. Sci., 130 (4), doi.org/10.1007/s12040-021-01731-x.

Shastri, A., Kumar, S. (2022) Source parameters and scaling relations for small earthquakes in mainland Gujarat region of Western Deccan Volcanic Province, India. Geomatics, Nat. Hazards Risk, 13 (1): 2925-2948.

Shreyasvi, C., Venkataramana, K., Chopra, S., Rout, M.M. (2019) Probabilistic seismic hazard assessment of Mangalore and its adjoining regions, a part of Indian Peninsular: an intraplate region. Pure Appl. Geophys., 176(6): 2263-2297.

Singh A.P., Koulakov, I., Kumar, M.R., Kumar, S., Kayal, J.R. (2019) Seismic velocity structure and intraplate seismicity beneath the Deccan Volcanic Province of western India. Phys. Earth Planet. Inter., 287: 21-36.

Singh, A.P., Sairam, B., Pancholi, V., Chopra, S., Kumar, M.R. (2020) Delineation of thickness of intrabasaltic rocks beneath the Deccan Volcanic province of western India through micro tremor analysis. Soil dyn. Earthq. Eng., 138, 106348. http://dx.doi.org/10.1016/j.soildyn.2020.106348.

Singh, K.D., Mohan, K., Chopra, S. (2021) Magnetotelluric investigation in the swarm prone intraplate Talala region of Saurashtra, Gujarat, western India. J. Appl. Geophys., 192: 104381. https:// doi.org/10.1016/j.jappgeo.2021.104381

Singh, R., Sharma, S., Mitra, S., Khan, P.K. (2019) Mapping of coda-wave attenuation and its frequency dependency over eastern Indian Shield. Pure Appl. Geophys., 176(12): 5291-5313. https://doi.org/10.1007/s00024-019-02284-3

Singh, R., Paul, A., Shalini, Joshi, P., Kumar, S., et al. (2020) Reverse migratory behaviour of the earthquakes aftershock sequences along Himalayan Seismic Belt, Northwest Himalaya. Quat. Int., 585: 163-170

Singh, S., Devbrat, B.P., Sinha, A., Rao, K.M., Guha, A., et al. (2020) Ultra-Low Frequency (ULF) Magnetic Field Emissions Associated With Some Major Earthquakes Occurred In Indian Subcontinent. Atmos. Sol. Terr. Phys, 211, 105469. doi:10.1016/j.jastp.2020.105469

Sunil, A.S., Bagiya, M.S., Bletery, Q., Ramesh, D.S. (2021) Association of ionospheric signatures to various tectonic parameters during moderate to large magnitude earthquakes: Case study. J. Geophys. Res. Space Phys., 126, e2020JA028709. https://doi.org/10.1029/2020JA028709

Thomas, D., Bagiya, M.S., Hazarika, N.K., Ramesh, D.S. (2022) On the Rayleigh wave induced ionospheric perturbations during the Mw 9.0 11 March 2011 Tohoku-Oki earthquake. J. Geophys. Res. Space Phys., 127, e2021JA029250. https://doi.org/10.1029/2021JA029250

Tiwari, A., Paul, A., Singh, R., Upadhyay, R. (2021) Potential seismogenic asperities in the Garhwal-Kumaun region, NW Himalaya: Seismotectonic implications. Nat. Hazards, 107: 73–95.

Vorobieva, I., Gorshkov, A.I., Mandal, P. (2021) Modelling the seismic potential of the Indo-Burman megathrust. Sci. Rep., 11:21200. https://doi.org/10.1038/s41598021-00586-y

Wadhwan, M., Hazarika, D., Paul, A., Kumar, N., Gupta, V., et al. (2022a) Seismic anisotropy and crustal deformation in the Satluj valley and adjoining region of northwest Himalaya revealed by the splitting analysis of Moho converted Ps phases. J. Asian Earth Sci., 238, 105377. https://doi.org/10.1016/j.jseaes.2022.105377

Wadhawan, M., Hazarika, D., Saikia, S. (2022b) Application of teleseismic receiver function in investigation of crustal thickness and Poisson's ratio. In: Recent Developments in Using Seismic Waves as a Probe for Subsurface Investigations: Theory and Practices, Taylor & Francis Group, https://doi.org/10.1201/9781003177692, pp. 32

Yadav, D.K., Hazariak, D., Kumar, N., Singh, A.K. (2021) Microseismicity study in the Siang valley of Arunachal Himalaya: Tectonic Implication of the 2019 Mw 5.9 Mechuka Earthquake. Himal. Geol., 42(2): 290-298.

Yadav, D.N., Kumar, N., Babu, G.B., Kumari, R., Pal, S.K. (2022) Crustal velocity structure and seismotectonics of the Kinnaur region of northwest Himalaya: New constraints based on recent micro-earthquake data. J. Asian Earth Sci., 224: 1-16, 105005.

Recent studies on volcanic materials and Chemistry of the Earth's Interior - An Indian Perspective: Progress made during the period 2019 - 2023

N. V. Chalapathi Rao[1] and G. Parthasarathy[2]

[1]Department of Geology, Institute of Science, Banaras Hindu University, Varanasi-221005, India (e-mail: nvcrao@bhu.ac.in)

[2]School of Natural Sciences and Engineering, National Institute of Advanced Studies, Indian Institute of Science Campus, Bengaluru- 560012, Karnataka, India (e-mail: partha@nias.res.in)

This report summarises *salient* recent research (2019-2023) on the physicochemical aspects of volcanic and mantle-derived material, from the Indian context. The paper essentially confines itself to the rock types of basalts and mafic dykes, kimberlites, lamproites, lamprophyres, and carbonatites with a focus on their regional representation from the various domains of the Indian shield in a chronological sequence.

I. Basalts and mafic dykes

Manu Prasanth et al. (2023) have presented trace elemental and Sr-Nd isotopic data for three major dyke swarms (ca. 2.7 Ga Ghatgaon dyke swarm, the Early Proterozoic Keonjhar dyke swarm, and the 1.76 Ga Pipilia dyke swarm. The authors invoke a sub-lithospheric mantle source in their origin with recycled components that satisfactorily explain the trace elements variations in these dyke swarms. Mafic (meta-volcanic) rocks from the Dhasan Formation, Bundelkhand craton, are categorized as tholeiitic basalt–basaltic andesite (Hiloidari et al. 2022) and originated from a parent rock similar to the primordial mantle in an intra-oceanic arc-backarc regime in a sub-arc mantle.Pandey and Paul (2022) reviewed the geochemistry of 2.8–0.8 Ga mafic dyke swarms of the Indian cratons and showed (i) their origin from a heterogeneous SCLM containing enriched and depleted components and (ii) subduction-driven metasomatism of global SCLM occurred during the Archean.The NW–NNW trending Paleoproterozoic (2.5–1.6 Ga) mafic dykes from Pakhanjore, Muramgaon, and Gariaband–Chhura areas of central Bastar craton reveal affinity towards subduction-modified lithospheric mantle field and support the generation of the magma from different degrees of interactions between plume and SCLM (Panda et al. 2022).Pandey (2022) reviewed the Paleoproterozoic mafic magmatism in Lesser Himalaya and showed that (i) the mantle source developed by mixing of a depleted mantle and a recycled component, (ii) the mafic rocks originated from olivine-poor lithologies, and (iii) continental arc-back-arc setting existed in this domain during the assembly of Columbia supercontinent. Based on a new *in situ* SIMS U-Pb baddeleyite date (1733 ± 23 Ma), Srivastava et al. (2022a) have shown that the Gwalior mafic sills were derived from a melt that originated from an SCLM source and bracketed the depositional age of the Gwalior sediments between 1980 and 1710 Ma.Zircon U-Pb data from the metabasalts of the Holenarsipur schist belt, Dharwar craton, gave an age of 3235 ± 54 Ma (Manikyamba et al. 2022). Holenarsipur and Chitradurga basalts show a partial melting trend whereas the Shimoga basalts show a fractional crystallization trend. Geophysical and

mineralogical studies of Paleoproterozoic Bonai volcanic rocks from Singhbhum craton revealed a new model supporting Pervasive Plume-Lithosphere Interaction and derivation from a relatively low melting ofuniform mantle source within the spinel lherzolite stability (Dwivedi et al. 2022). Pillow lavas from the Archaean Chitradurga schist belt, Western Dharwar craton, were generated during the initiation of an intra-oceanic subduction zone where a depleted upper mantle (MORB-source) was metasomatized with slab-derived aqueous fluids (Rose et al. 2022). The pillows show a whole-rock Sm–Nd errorchron age of 2433 ± 400 Ma. The Jhansi LIP mainly consists of the NW-trending ca. 1.98 Ga Jhansi swarm and the ca. 1.97 Ga Darguwan–Surajpura mafic sills within the Bijawar basin. Geochemically, they are all sub-alkaline tholeiitic in nature, and in general, they show very similar geochemical characteristics. Singh et al. (2021) show that some of these samples show geochemical similarities with the ca. 2.10 Ga mafic sills of the Gwalior basin and could represent another magmatic event. Srivastava et al (2021) reported a new precise U–Pb baddeleyite ID-TIMS age (2251 ± 4 Ma) for an ENE-trending mafic dyke from the Bastar craton. The age of this new swarm closely matches with the ca. 2.26–2.25 Ga dykes in the Dharwar craton and the ca. 2.26 Ga dykes in the Singhbhum Craton and together they define a ca. 2.26–2.25 Ga giant dyke swarm. Silpa et al. (2021) studied mafic dykes from the Tiptur area in the Western Dharwar craton and from the geochemical grounds, bringing out an interaction of DMM with an enriched mantle source.Manikyamba et al. (2021) report gold, uranium, thorium, and rare earth mineralization in the Kadiri schist belt of Eastern Dharwar Craton. The source of gold has been inferred to be from deep fractures (>200 km) at mantle depths that paved the magma to move upper crustal levels due to the partial melting of peridotites which tapped the siderophile elements (Au–Ag) from a deeper source. Deb et al (2021) reported coexisting arc and MORB signatures in the Sonakhan greenstone belt, and explain it to be due to late Neoarchean – early Proterozoic subduction rollback and back-arc formation. Samal et al. (2021a) reported Sr-Nd isotopic data for ca. 2.26–2.25 and 2.08 Ga mafic dyke swarms of the Dharwar cratonand show that both were derived from a MORB-like depleted mantle source and interacted with metasomatized SCLM mantle. The plume center of the ca. 2.08 Ga swarm is defined to be away from the cratonic margin.Hazarika et al. (2020) linked the widespread mafic dyke swarm activity of 1.42 Ga in the western Bastar craton to the extension events related to the breakup of the Columbia supercontinent. Radhakrishna and Vijaya Kumar (2020) reviewed the integrated U-Pb ages with palaeomagnetic results and identified at least four discrete Palaeoproterozoicmaficigneous events at 2.36-2.37 Ga, 2.1-2.2 Ga, 2.0-2.1 Ga 1.89-1.99 Ga and probably two other events at about 2.4 Ga and 1.8 Ga.Khanna and Sesha Sai (2020) reported coeval mafic-felsic Neoarchaean magmatism from the Peddavuru greenstone terrane, Eastern Dharwar craton. Dwivedi et al. (2023) showed derivation of 2.8-2.5 GaDhanjori volcanics, Singhbhum craton, from the garnet to spinel stability field due to decompressive melting ofa mantle plume head near the crust-mantle boundary, which is independently supported by the gravity studies.

Chen et al. (2023) have shown that the basalts from the southern Pir Panjal Range (see Shellnutt, 2019) yielded an age of 288.2 ± 0.3 Ma and have been derived from a modified sub-continental lithospheric mantle (SCLM) to a sub-lithospheric mantle source. Shellnutt et al. (2022) reported the PGE geochemistry of the Panjal Traps and question the notion that the coexistence of PGE-undepleted and -depleted magmas is prospective in the exploration of magmatic Ni–Cu–(PGE) sulfide mineralization. Baksi (2022) showed that samples from a ~300 m borehole near the northwestern corner of the Rajmahal lavas reveal the presence of

carbonatitic (aillikitic) material. This province, including the Bengal Traps, thus exhibits quartz and olivine tholeiites, andesitic basalts, alkali basalts as well as carbonatitic material. Baksi (2022) supported the postulated genetic link of the Rajmahal Traps with the Kerguelen hotspot and southern Indian ocean basalts. $^{40}Ar/^{39}Ar$ ages of Raniganj-Koderma swarm of dolerite dykes from Chhota Nagpur Gneissic Terrane, indicated three pulses of emplacement ca. 118–116 Ma, ca. 112–111 Ma, and ca. 109 Ma (Srivastava et al. 2023).The Lichi volcanic rocks crop out along the Main Boundary Thrust (MBT) of the Arunachal Himalaya, primarily of sub-alkaline basalt. Petrogenetic modelingimplies that the sub-alkaline basalts and intermediate rocks were derived from low-degree partial melting (1%–5%) of a garnet-bearing peridotite source and emplacement in a continental extensional regime and possibly resulted from the Cretaceous Kerguelen plume activities (Sharma et al. 2022a). Akhtar et al. (2022) suggested that arc-like basalts of the South Andaman ophiolite suite (India) of the Cretaceous agewere generated before the back-arc rifting initiated in an earlier stage of back-arc extension as a result of eastward subduction of the Neotethyan oceanic slab. On the other hand, the MORB-like pillow basalts erupted due to further back-arc spreading in response to the roll-back of the Neotethyan oceanic lithospheric slab.

Haase et al. (2019), Sheth et al. (2019), Cucciniello et al. (2019, 2023), Manu Prasanth et al. (2019), Krishnamurty (2020a and b),Eddy et al. (2020),Mittal et al (2022), Self et al. (2022), Kale and Pande (2022), Chalapathi Rao and Ray (2022 and references therein) and Pandey et al. (2022) contributed to the duration, transport, and eruption rates of the Deccan volcanism and associated alkaline rocks. KLR-1 scientific deep borehole, drilled in the 1993 Killari earthquake region of Maharashtra (India), penetrated 8 m thick infratrappean sediments below a 338 m-thick column of Deccan volcanics that rested over Neoarchean amphibolite to granulite facies. Detailed palynological studies of the sediments revealed the presence of characteristic Gondwanapalynomorphs which suggest an Asselian age (298-295 Ma) for their formation (Pandey et al. 2023). These findings provide the first evidence of the reactivation and rifting of Dharwarintracratonic regions during the earliest Permian Gondwana Period, which led to severe lithospheric mantle destruction, and massive regional uplift and erosion of the granitic-gneissic upper crust. Laxman et al. (2022) examined the spatial geochemical variations within the Deccan Volcanic Province and demonstrated that by 10% mixing and/or 20% AFC of lamprophyre source melts, original sub-lithosphere melts can exhibit visible SCLM signatures, and the entire Deccan data considered can be explained by 20% mixing and/or 50% AFC of plume-derived melts with calc-alkaline lamprophyre as an assimilate.Sr–Nd isotopic ratios of the Cenozoic tholeiitic dykes of the Multai area of the Deccan volcanic province indicate (Kumar et al. 2022) depleted mantle source and affinity to the Mahabaleshwar and Poladpur formations. Sheth et al. (2022) show that the outcrop structures and textures of ancient lava flows, such as those forming continental flood basalt sequences thousands of metersthick, provide clues to their cooling histories and the palaeoclimates. The jointing patterns in the entablatures (irregular, chevron, rosette, and skeleton jointing), and the textures of the sheet lobes and even some dykes (abundant glass, and quench crystals of plagioclase and Fe–Ti oxides) provide evidence for a wet climate in western India 65.5 million years ago. Ray et al. (2021)show that the basalt traps and the basement beneath Koyna-Warna show variations in thermal/physical properties that have been correlated to lithology/composition. Based on gamma and sonic logs as well as radioelements, the basalt trap can be divided into five sub-layers which can be correlated with basalt flows. Banerjee and Mondal (2021) show that Deccan basalts Koyna-KBH-7-borehole

show petrographic and geochemical variations, including contamination by Gondwana sediments alongside TTG.No signatures of sulfide supersaturation have been inferred due to the absence of crustal sulfur.

Cucciniello et al. (2020) inferred significant contamination of SE Saurashtra dyke swarm magmas by ancient granitic basement crust and that the AFC process played a significant role in their genesis. P-T estimates indicate crystallizationin upper crustal magma chambers.Basu et al (2020a) identified, based on the Sr-Hf-Pb isotopic variation in the volcano-stratigraphy and trace and major elements variation across the Deccan volcano-stratigraphy, mantle plume signatures in upper lavas, recycled crustal signatures in lower lavas in the Deccan Traps. Basu et al (2020b) also reported widespreadend-Cretaceoussilicic and alkaline magmatism synchronous with the Deccan Traps flood basalts, India.

II. Carbonatites

Reviews on alkaline carbonatite complexes from various domains of the Indian shield are provided by Paul et al (2020), Randive and Meshram (2020), Srivastava (2020) and Pandey et al. (2022). Much of the research has been confined to the Amba Dongar carbonatite complex, NW India, and the carbonatites from the Sung valley, Meghalaya. Brahma et al (2022)reported, for the first time, the occurrence of a carbonatite-syenite complex from Gundlupet area, western Dharwar craton, southern India. These carbonatites have high CaO content and are enriched in LRRE (5666 ppm to 7530 ppm). This ischaracterized dominantly as sövite with minor beforsite and iron-rich carbonatite which are associated with phenocrystic magnetite, apatite, amphibole, pyroxene, and monazite. Srivastava et al. (2022b) have performed stable isotope ($\delta^{13}C$ and $\delta^{18}O$)investigations on the carbonatites of the Pakkanadu Alkaline Complex, southern India.According to the study, O isotope exchange took place between carbonatite and its derived fluids, although the amount of CO_2 produced during the partial melting of the mantle source was negligible. Phdah and Konglah (2022) have documented the first occurrence of the orbicular carbonatites from the Sung valley ultramafic-alkaline-carbonatite complex, Shillong plateau, Meghalaya, northeast India. The authors have also provided petrogenetic implications concerning antiskarn due to metasomatic processes brought on by carbonatite magmatism. Chaudhary et al. (2023) have provided Raman spectroscopy and microthermometry analysis of aqueous-carbonic bi-phase, aqueous saline bi-phase, and poly-phase fluid inclusions study in calcite, as well as mineral inclusions study in accessory magnetite in the Sung Valley carbonatites from NE India. The presence of such rare hydrous minerals in magnetite demonstrates that ultra-hydrous conditions existed during the crystallization of carbonatitic magma. Srivastava et al. (2019) have reported new *in-situ* U–Pb ages and Sr–Nd–Hf isotopic data on mineral phases of the Sung Valley and Jasra ultramafic-alkaline-(carbonatite) intrusions (Shillong Plateau, India). Perovskite of a Jasra clinopyroxenite gave an age of 101.6 ± 1.2 Ma, different than the U–Pb age of 106.8 ± 0.8 Ma on zircon of Jasra syenites. The study suggests that the Sylhet tholeiitic magmatism is substantially older than the alkaline intrusions of northeastern India. Srivastava et al. (2022c)have reviewed six ultramafic-alkaline-carbonatite magmatic intrusions (115-120 Ma) of the Shillong Plateau (Sung Valley, Jasra, Swangkre-Rongjeng, and Mawpyut) and Mikir Hills (Samchampi-Samteran and Barpung).They inferred magmatic crystallization

from independently evolved variable liquid lineages and the role of shallow-level crustal contamination during their formation.

Aranha et al. (2022) utilized a fuzzy inference system, which is a knowledge-driven artificial intelligence technique, to identify and delineate prospective targets for REEs from carbonatite–alkaline complexes in the western part of Rajasthan, NW India. Dhote et al (2021) presented in-depth field, petrographic and geochemical characteristics of the potential area for economic REE deposit established from systematic geochemical sampling in the Ambadongar Carbonatite Complex. According to the authors, fertile carbonatite formation is caused by metasomatism from asthenospheric melts of the SCLM zone followed by low degree partial melting of the SCLM region. Banerjee and Chakrabarti (2019) have reported detailed geochemical and Nd, Sr, and stable Ca isotopic study of carbonatites and associated silicate rocks from the Ambadongar carbonatite complex and the Phenai Mata igneous complex. Hydrothermal alteration is invoked for the formation of massive fluorspar deposits, the role of the Reunion mantle plume has been inferred, and carbonatites are shown to have originated from a source that was deeper than the associated silicate rocks. Chandra et al. (2019) have proposedpetrogenetic model for the Amba Dongar Complex wherein the Reunion plume played a pivotal role in providing CO_2-rich fluids, heat, and low-degree plume-derived melts, which metasomatized parts of overlying SCLM. Their model proposed that a significant portion of the isotopic variability seen in global alkaline-carbonatite magmas may be inherited from their parent carbonated silicate magmas and may not solely reflect the isotopic heterogeneity of their ultimate asthenospheric or mantle plume sources.

Banerjee et al. (2021a)reported the major, trace element including stable Ca and radiogenic strontium isotopic compositions for 46 carbonatites from 22 occurrences worldwide (India included) that range in age from 2.61 Ga to Recent. The study suggests that the older (>300 Ma) carbonatites typically display mantle-like isotope composition, whereas, the younger (<300 Ma) carbonatites display low $\delta^{44/40}$Ca and radiogenic $^{87}Sr/^{86}Sr$ which highlight crustal input in the mantle source. This increasedcrustal recycling is linked with the amalgamation and breakup of Pangea and increased plume activity as well as Siberian Traps induced aragonite shelf weathering. Banerjee et al. (2021b) presented a variety ofsulfur isotope data from carbonatites from the Newania complex, NW India. It is suggested that the sulfurin the Newania carbonatites was predominantly derived from the mantle, based on the mantle-like sulfurisotope compositions as well as the $\delta^{13}C$ and $\delta^{18}O$ ratios. They inferred that carbonatite magmas that were deposited >400 Ma hada generally lower oxidation state. Samal et al. (2021b)have provided detailed major, trace, and REE Geochemistry of Nb-V rich Andradite-Schorlomite-Morimotoite garnet from Ambadungar-Saidivasan carbonatite Complex. The role of metasomatic reactions between earlier-formed minerals and hydrothermal fluid is suggested for the genesis of garnets. Viladkar et al (2021) presented a detailed account of the evolution of the pyrochlore group of minerals that are present as the common accessory rare metal-bearing minerals in the calcite and ankerite of the Amba Dongar complex. Patel et al. (2022) have presented a detailed account ofREE mineralization and C-O isotopic studies in carbonatites of the Amba Dongar carbonatite complex. REE enrichment in the groundmass/altered calcites rather than magmatic calcite is attributed to the presence of micron-sized REE phases.It is suggested that the interaction of the carbonatite with a sulfur-bearing, F-rich hydrothermal fluid that exsolved from late-stage carbonatitic magmas led to the REE mineralization. Singh et al. (2022) acquired in-situ analysis of the

major and trace element chemistry of fluid inclusion in fluorite as well as the host fluorite from the Amba Dongar complex. This study demonstrates that the fluid inclusions hosted by fluorite are unexpectedly Na, K, MREE- and HREE-enriched, considerably more than in many other hydrothermal settings.

Bhunia et al. (2022) have provided petrological and geochemical data of the Kamthai carbonatite plug in the Late Cretaceous polychronous (66–89 Ma) Sarnu Dandali alkaline complex, NW India. Petrological studies suggest them to be calcio-carbonatites dominated by calcite along with zircon and REE-bearing minerals. REE studies show extreme enrichment of LREE. U-Pb SHRIMP dating of zircon yielded an age of 68.4 ± 1.8 Ma linking their emplacement to the Deccan Large Igneous Province via the Reunion hotspot. Rapid CO_2 and SO_2 degassing from these carbonatites and the associated alkaline rocks, along with the concurrent eruption of Deccan lavas, has the potential to have a catastrophic effect that could contribute to the mass extinction at the K-Pg boundary.

III. Lamprophyres

Naushad et al. (2019), Khan et al. (2019), and Meshram et al. (2019) reported new occurrences of lamprophyres from various domains of the Indian shield. Pandey et al (2019) studied several post-Deccan lamprophyre dykes in the Narmada rift zone and Chhotaudepur alkaline province of the Deccan Large Igneous Province and proposed them to be small-volumeCO_2-rich melts derived from metasomatized the mantle source regions and have a HIMU-type geochemical character. Raghuvanshi et al (2019) explored the genetic relationship between kimberlites and lamprophyres from the Wajrakarur Kimberlite Field of the Eastern Dharwar Craton and demonstrated their ‘shoshonitic’ character. It is proposed that elevated Zr/Hf ratios in these rocks are a result of carbonatite metasomatism of the mantle source region.

Chalapathi Rao et al. (2020) presented a comprehensive review of the occurrence, petrology, geochemistry, and tectonic significance of the lamprophyres from the various parts of the Indian shield. Besides, the relationship between the lamprophyres and kimberlites where they occur in a close spatial and temporal association is also explored. Pandey et al. (2022) have presented a comprehensive review of diverse alkaline rocks associated with the Deccan Large Igneous Province. The lamprophyres show large mineralogical diversity and constitute an important component of the wide spectrum of alkaline rocks that are temporally and spatially associated with the Deccan basalts and derived from an enriched mantle. Dhote et al. (2022) have studied phlogopite-spinel-wehrlite xenoliths from lamprophyre dykes of the Sarnu-Dandali alkaline igneous complex of northwest India which portray three distinct stages of mantle modification. Sharma et al. (2022b) have identified texturally and compositionally distinct zoning in the mineral constituents of the lamprophyre dykes of the Mundwara alkaline complex, which is associated with the Deccan Large Igneous Province, and document the magma chamber processes such as crystal fractionation and corrosion in the magmatic plumbing system that played a crucial role in the generation of the alkaline complex. Meshram et al (2022) report two new meta-lamprophyre dykes near the margin of the Eastern Dharwar Craton and the Nellore Schist Belt. Based on the bulk-rock geochemistry of these rocks, their evolved nature is postulated and their Sr and Nd isotopic ratios are interpreted to be similar to the global back-arc basin basalts. Krmíček et al. (2022) carried out a bulk-rock lithium isotopic study on the Mesoproterozoic kimberlites,

lamproites, and lamprophyres from the Eastern Dharwar Craton. The δ7Li value ranges from 3.3‰ to 6.7‰ in the lamprophyres suggesting their derivation from a heterogeneous continental lithospheric mantle. Dongre et al (2022) carried out a petrological, geochronological, and paleomagnetic study of an alkaline lamprophyre dyke from the Sarnu-Dandali and Mundwara alkaline complexes of the Deccan Large Igneous Province. $^{40}Ar/^{39}Ar$ phlogopite geochronology revealed two distinct ages of 65.44±1.5 Ma and 68.17±1 Ma. The older age is suggested to represent the timing of the mantle metasomatism of the cratonic lithospheric mantle during the separation of India and the Seychelles. Vijaya Kumar and Randive (2022)have explored the platinum group element budget in the lamprophyre dykes, picrobasalt, gabbro, and basalts from the Phenai Mata alkaline complex of the Deccan Large Igneous Province. The presence of metal sulfides of Fe-Cu-Zn-Pb-Co-Ni in these rocks is identified to be a result of the 'accidental fertilization' of metals because of the mixing of the crustal sulfur. Dora et al. (2022) present geological, petrographic, mineralogical, bulk-rock geochemical as well as trace element geochemical data on a Proterozoic calc-alkaline lamprophyre (minette) dyke from the Thaneswana area of Bastar Craton. Enrichment in alkalis and large ion lithophile elements points to a mantle source that was metasomatized by hydrous fluids during a previous episode of subduction. Raghuvanshi et al (2022) explained the origin of chrome-diopside xenocrysts hosted in a Neoproterozoic lamprophyre dyke from the Mysore area of the Western Dharwar Craton and discussed its implications in understanding the lithospheric thickness in this area. It is suggested that the lithospheric thickness beneath the Western Dharwar Craton was at least ~115 km during the Neoproterozoic. Sharma et al (2021) have studied the mineralogy and petrology of fractionated alkaline lamprophyre dykes (camptonites) from the Phenaimata alkaline complex of the Deccan Large Igneous Province and highlighted the role of inter-connected magmatic plumbing systems beneath this alkaline complex. Giri et al (2021) studied Paleoproterozoic calc-alkaline lamprophyre dykes from the Sidhi Gneissic Complex of central India. The authors proposed a geodynamic model encompassing the northward subduction of the Southern Indian Cratonic Block beneath the Northern Indian Cratonic Block along the Central Indian Tectonic Zone. Sahoo et al (2020) studied fractionated lamprophyre dykes and associated syenites, diorites, and gabbros from the Mount Girnar igneous complex of northwestern India and suggested their genetic relation. $^{40}Ar/^{39}Ar$ dating of amphibole and biotite separated from the lamprophyre dykes revealed an emplacement age range of 65.9±0.3 Myr to 66.1±0.4 Myr. Dongre et al. (2020) have reclassified Pipe-8 kimberlite of the Eastern Dharwar Craton as an ultramafic lamprophyre in general and aillikite in particular. The phlogopite-rich groundmass of the rock yields a $^{40}Ar/^{39}Ar$ plateau age of 1115.8±7.9 Ma (2σ). Pandey et al. (2020) reported a $^{40}Ar/^{39}Ar$ Mesoproterozoic age of 1169±8 Ma for a calc-alkaline lamprophyre dyke from the Mudigubba area, Eastern Dharwar Craton. Bulk-rock Sr-Nd isotopic ratios reveal that the parental melts originated from an old enriched continental lithospheric mantle source. Giri etal. (2019) reported on an alkaline lamprophyre (camptonite) dyke from the Ankiraopalle area near the margin of the Cuddapah Basin and the Eastern Dharwar Craton whose bulk-rock geochemical data is similar to the ocean island basalts and other global alkaline lamprophyres suggesting its derivation from an enriched mantle source.

IV. Kimberlites

Babu et al (2023a) have presented major and trace element geochemical data of clinopyroxene megacrysts from one of the kimberlite pipes of the Chigicherla cluster of the Wajrakarur kimberlite field, Eastern Dharwar Craton. These megacrysts are classified into different types depending on their composition and a deeper silicate and a shallower carbonate melt-related metasomatism has been inferred. Babu et al (2023b) presented in situ U-Pb and Hf-O isotopic compositions of zircons that occur as xenocrysts in the kimberlites of the Eastern Dharwar Craton. Zircon U-Pb geochronology yields ages as old as ~3.6 Ga. Such old zircons are atypical of the granitoid of the Eastern Dharwar Craton but are common in the magmatic rocks of the Western Dharwar Craton and provide evidence for the transportation of older upper crustal rocks of the Western Dharwar Craton beneath the Eastern Dharwar Craton.Chatterjee et al (2023) have reported the occurrence of ultra-high pressure phases such as coesite, majoritic garnet, and supersilicic K-omphacite in an eclogite xenolith hosted in one of the kimberlites from the Kalyandurg cluster of kimberlites of the Eastern Dharwar Craton. Geothermobarometric estimates that the eclogitic assemblage equilibrated at ∼5–8 GPa pressure, while the majoritic garnet formed at a pressure of 8-19 GPa during an episode of ultra-deep subduction. Krmíček et al. (2022)have carried out a bulk-rock lithium isotopic study on the Mesoproterozoic kimberlites, lamproites, and lamprophyres from the Eastern Dharwar Craton as well as on the orangeite of the Bastar Craton. The kimberlites of the Dharwar Craton and the orangeites of the Bastar Craton show a heavy δ7Li isotopic signature (as high as 9.7‰) which is similar to the altered ancient oceanic crust. Sarkar et al (2021)have compared the compositions of different types of olivines (phenocrysts as well as xenocrysts) from the lamproites and kimberlites of the Dharwar Craton. Interestingly, the average Mg# of olivine macrocryst cores and the average Mg# of magmatic olivines show a good correlation in the lamproites and kimberlites of the Wajrakarur kimberlite field. The authors propose that the petrogenesis of cratonic lamproites is similar to that of the kimberlites. Dongre et al (2021) presented petrology, bulk-rock geochemistry, and perovskite U-Pb geochronology of pipe 12 of the Wajrakarur kimberlite field of the Eastern Dharwar Craton. The U-Pb geochronology of perovskite resulted in an emplacement age of 1122±7.7 Ma. The bulk-rock geochemistry is shown to be similar to the global hypabyssal kimberlites. Based on the new emplacement age, the authors relate the kimberlite magmatism of the Eastern Dharwar Craton to the mantle-plume generated 1110 Ma Large Igneous Provinces. Pattnaik et al (2021a) have analyzed the hydrogen content of anhydrous minerals found in the garnet-peridotite xenoliths hosted in the kimberlites of the Wajrakarur kimberlite field of Eastern Dharwar Craton. The reconstructed bulk-rock hydrogen concentration in the garnet-peridotite xenoliths is lower than that estimated for the lithospheric mantle and implies low-water activity in the proto-kimberlite melt. Mukherjee et al (2021) have reported the occurrence of gold and gold-platinum alloy grains in the bimineralic and kyanite-bearing eclogite xenoliths of the KL-2 kimberlite pipe of the Kalyandurg cluster in the Dharwar Craton Pattnaik et al (2021b) have reported mineralogy, petrology, and geochemistry of spinel- and garnet-bearing peridotite xenoliths from the Mesoproterozoic kimberlites of the Wajrakarur kimberlite field, Eastern Dharwar Craton. Based on the results, the authors infer the evidence of mantle plume activity and carbonate silicate melt-related metasomatism of the mantle related to proto-kimberlite melts. Sheikh et al. (2020) have presented major and trace element compositions of clinopyroxene and garnet xenocrysts recovered from different

kimberlite pipes of the Wajrakarur kimberlite field. Based on the compositions of these minerals and thermobarometric estimations, a vertically heterogeneous and layered cratonic lithospheric mantle has been inferred beneath the Dharwar Craton. The deeper layer is characterized by fertilized and Ti-metasomatized peridotite whereas the shallower layer is suggested to be depleted in nature. Choudhary et al (2020) have identified different associations and compositions of spinel in diamondiferous kimberlites of the Dharwar Craton. Besides, the schorlomite in the groundmass is observed to be enriched in Fe and Ti, which is interpreted to be because of metasomatism in the mantle source. Dongre et al (2020) studiedthe pipe-8 diamondiferous ultramafic intrusion in the Wajrakarur kimberlite field of the Eastern Dharwar Craton. Based on the mineralogy of the intrusion, it is classified as an ultramafic lamprophyre in general and aillikite in particular. Sr-Nd isotopic abundance in the intrusion suggests the derivation of the lamprophyre from a moderately depleted upper mantle source. The $^{40}Ar/^{39}Ar$ age of 1115.8±7.9 Ma for the pipe is consistent with the age of the Mesoproterozoic kimberlites of the craton. Such widespread magmatism is suggested to be the result of a plume-generated large igneous province. Kumar et al. (2020) used very low frequency electromagnetic (VLF-EM) to understand the depth, geometry, and aerial extension of the Wajrakarur kimberlite pipe 6 of the Eastern Dharwar Craton. The authors have validated their results with the borehole data of the Geological Survey of India. Pandey and Chalapathi Rao (2020) reviewed the available geochronological and radiogenic isotopic data (Sr-Nd-Hf isotopes) for the Mesoproterozoic (~1.1 Ga) kimberlites, lamproites, and ultramafic lamprophyres of the southern Indian shield. The authors proposed a plate reorganization model to explain the origin of these rocks. Sharma et al (2019) documented mineralogy, bulk-rock geochemistry, and Sr-Nd isotopic systematics of the kimberlite pipe-16 from the Wajrakarur kimberlite field of the Eastern Dharwar Craton. It is suggested that the kimberlite has originated by small-scale partial melting of a carbonated peridotite source.

V. Lamproites

Saini et al (2022a) have provided a detailed mineral chemical analysis on the Marepalli lamproite dyke from the Nalgonda district, Telangana, Southern India. Phlogopite, amphibole, pyroxene, and spinel compositional ranges in the Marepalli lamproite differ significantly from those from the Ramadugu Lamproite Field. Based on multiple evidence, such as low tetraferric iron content in phlogopite;low Fe^{3+}# and Ti# in spinels, and high F content in phlogopite and apatites, it is suggested that this lamproite evolved from common parent magma under reducing conditions. Saini et al (2022b)presented comprehensive mineral mineralogical characteristics of the Rajpura and Ramnagore sills in RaniganjGondawanasedimentary Basin of eastern India. Based on mineralogical characteristics, the Rajpura and Ramnagore sills are classified as phlogopite-diopside-K-feldspar-apatite olivine lamproite. Chemical variation in various minerals has been used to comprehend the magmatic evolution of lamproitic magma. Kumar et al (2021) studied the mineralogy and petrology of Mesoproterozoic olivine-lamproite dykes from Banganapalle, Dharwar craton, India. This work emphasizeshow various textural and compositional populations of spinel can shed light on the intricate history of lamproite magmas and antecedent metasomatic processes that have an impact on the cratonic mantle lithosphere. Sarkar et al (2021) have provided a comprehensive petrogenesis of two Wajrakarur olivine lamproites (P2 and P12) from the Eastern Dharwar Craton, by integrating in-depth

petrographic observations with fresh compositional information for olivine macrocrysts and phenocrysts. These findings suggest that Wajrakarur kimberlites and lamproites share a common genetic origin from primary melts, that later interacted with compositionally distinct lithospheric mantle wall rocks.Kaur et al (2019) studieda lamproite (pseudoleucite-phlogopite-amphibole-lamproite) dyke from Gundrapalli village (Nalgonda district), Telangana, India. This study highlights the rare mineral baotite's finding in an Indian lamproite for the first time. The mineralogy of the lamproite from Gundrapalli whichcontains baotite is analogous to the lamproite from Troms, Norway, whichcontains baotite, Kvalya. Sheikh et al (2019) presented comprehensive trace element studies of olivine from diamond-bearing intrusions, namely the (~1100 Ma), CC2, and P13 dykes in the Wajrakarur Kimberlite Field (WKF), Eastern Dharwar Craton, and ~65 Ma Kodomali and Behradih lamproite diatremes in the Mainpur Kimberlite Field (MKF), Bastar Craton. The authors have reclassified these dykes as olivine lamproites, which were previously classified as kimberlites or orangeites.

Concluding Remark: We summarised the most important findings in the area of Volcanology and Chemistry of the Earth's Interior (IUGG- IAVCEI): work carried out in India during the last four years 2019-2023. This effort is a continuation of our earlier review (Parthasarathy and Ray 2019) where we reviewed the progress made during 2015-2019; We would like to state here that if any omission of some work done in India in this area, it is purely inadvertent.

Acknowledgements

We thank Professor Archana Bhattacharya for inviting us to write this review under IUGG-IGU Joint National committee progress report for the period 2019-2023. NVCR thanks BHU for the sanction of the IOE faculty incentive grant which has facilitated this work. GP is grateful to INSA and NIAS for the support through INSA senior scientist program.

References

Akhtar, S., Saikia, A., Negi, P., Kalita, B.J., 2022. Back-arc basin origin for the basalts of the South Andaman Island Ophiolite (India). Episodes Journal of International Geoscience, 45(1), 5-27.

Aranha, M., Porwal, A., Sundarallngam, M., Gonzalez-Alvarez, I., Markan, A., Rao, K., 2022. Rare earth elements associated with carbonatite-alkaline complexes in western Rajasthan, India: exploration targeting at regional scale. Solid Earth, 13(3), 497-518, 10.5194/se-13-497-2022.

Babu, E.V.S.S.K., Dash, S., Santosh, G.H.N.V., Mukherjee, A., 2023. Origin of clinopyroxene megacrysts from the 1.1 Ga Chigicherla-4 kimberlite (CC4), Dharwar craton, southern India: Implications for multi-stage metasomatism of the sub-continental lithospheric mantle. Journal of Asian Earth Sciences 244, 105334.

Babu, E.V.S.S.K., Griffin, W.L., Norris, R., Belousova, E., O'Reilly, S.Y., Bhaskar Rao, Y.J., 2023. Zircon U–Pb ages and Hf and O isotope systematics of crustal zircons from Mesoproterozoic kimberlites of the Dharwar craton, India: Implications for Neoarchean craton assembly. Journal of Asian Earth Sciences 246, 105583.

Baksi, A.K., 2022. Geochemistry and geochronology of the Rajmahal Flood Basalt Province, northeastern India: Genetic links to Kerguelen hotspot activity. J Earth Sys Sci 131, 157 https://doi.org/10.1007/s12040-022-01855-8.

Banerjee, R., Mondal, S.K., 2021. Petrology and geochemistry of the Deccan basalts from the KBH-7 borehole, Koyna Seismic Zone (Western Ghats, India): Implications for nature of crustal contamination and sulfide saturation of magma. Lithos, 380, 105864.

Banerjee, A., Chakrabarti, R., 2019. A geochemical and Nd, Sr and stable Ca isotopic study of carbonatites and associated silicate rocks from the ~65 Ma old Ambadongar carbonatite complex and the Phenai Mata igneous complex, Gujarat, India: implications for crustal contamination, carbonate recycling, hydrothermal alteration, and source-mantle mineralogy. Lithos, 326-327, 572-585, https://doi.org/10.1016/j.lithos.2019.01.007.

Banerjee, A., Chakrabarti, R., Simonetti, A., 2021a. Temporal evolution of $\delta^{44/40}$ and $^{87}Sr/^{86}Sr$ of carbonatites: implications for crustal recycling through time. Geochimica et Cosmochimica Acta, 307, 168-191, https://doi.org/10.1016/j.gca.2021.05.046.

Banerjee, A., Kumar, M.S., Chakrabarti, R., 2021b. Sulfur, carbon, and oxygen isotopic compositions of Newania carbonatites, India: implications for source mantle characteristics. Journal of Mineralogical and Petrological Sciences, 116, 121-128, https://doi.org/10.2465/jmps.201130e.

Basu, A.R., Saha-Yannopoulos, A., Chakrabarty, P., 2020a. A precise geochemical volcano-stratigraphy of the Deccan traps. Lithos, 376, 105754.

Basu, A.R., Chakrabarty, P., Szymanowski, D., Ibañez-Mejia, M., Schoene, B., Ghosh, N., and Georg, R.B., 2020b. Widespread silicic and alkaline magmatism synchronous with the Deccan Traps flood basalts, India. Earth and Planetary Science Letters, 552, 116616.

Bhunia, S., Chalapathi Rao, N.V., Belyatsky, B.V., Talukdar, D., Pandey, R., Lehmann, B.,2022 U-Pb Zircon SHRIMP dating of the Carbonatite hosted REE deposit (Kamthai), Late Cretaceous polychronous Sarnu Dandali alkaline Complex, NW India: links to the Plume-related metallogeny and CO2 outgassing at the K-Pg boundary. Gondwana Research. DOI: 10.1016/j.gr.2022.09.012

Brahma, S., Sahoo, S., Durai, P., 2022. First report of Carbonatite from Gundlupeta area, Western Dharwar Craton, Karnataka, Southern India. Journal of the Geological Society of India, 98, 35–40, 10.1007/s12594-022-1924-2.

Chalapathi Rao, N.V., Ray, J.S., 2022. Deccan Traps and other flood basaltprovinces- Recent Research trends. Journal of Earth System Science v.130 and 131.

Chalapathi Rao, N.V., Giri, R.K., Sharma, A., Pandey, A., 2020. Lamprophyres from the Indian shield: A review of their occurrence, petrology, tectonomagmatic significance and relationship with the Kimberlites and related rocks. Episodes 43(1), 231-248, https://doi.org/10.18814/epiiugs/2020/020014

Chandra, J., Paul, D., Stracke, A., Chabaux, F., Granet, M., 2019. The origin of carbonatites within the Deccan Large Igneous province. Journal of Petrology 60(6), 1119-1134.

Chatterjee, A., Chalapathi Rao, N.V., Pandey, R., Pandey, A., 2023. Mantle transition zone-derived eclogite xenolith entrained in a diamondiferous Mesoproterozoic (~1.1 Ga) kimberlite from the Eastern Dharwar Craton, India: evidence from coesite, K-omphacite, and majoritic garnet assemblage. Geological Magazine, https://doi.org/10.1017/S0016756822001315.

Chen, W.Y., Shellnutt, J.G., Bhat, G.M., Tejada, M.L.G., Suzuki, K., Denyszyn, S.W., 2023. Geochronology and geochemistry of the Panjal Traps from the southern Pir Panjal Range, Kashmir, India. Lithos 436, 106967 https://doi.org/10.1016/j.lithos.2022.106967.

Choudhary, B.R., Santosh, M., Ravi, S., Babu, E.V.S.S.K., 2020. Spinel and Ti-rich schorlomite from the Wajrakarur kimberlites, southern India: Implications for metasomatism, diamond potential, and orangeite lineage. Ore Geology Reviews 126, 103727.

Choudhary, S., Rana, S., Sen, K., 2023. Ultra-hydrous conditions and local readjustment ofmagnetite in evolving carbonatitic magma at Sung Valley, Shillong Plateau: Evidence fromfluid inclusions in calcite and presence of manasseite, ferrohogbomite and amesite within magnetite. Himalayan Geology, 44(1), 35-46.

Cucciniello, C., Choudhary, A.K., Pande, K., Sheth, H., 2019. Mineralogy, geochemistry and ^{40}Ar–^{39}Ar geochronology of the Barda and Alech complexes, Saurashtra, northwestern Deccan Traps: early silicic magmas derived by flood basalt fractionation Geological Magazine 156(10), 1668-1690.

Cucciniello, C., Sheth, H., Duraiswami, R.A., Wegner, W., Koeberl, C., Das, T., Ghule, V., 2020. The Southeastern Saurashtra dyke swarm, Deccan Traps: magmatic evolution of a tholeiitic basalt–basaltic andesite–andesite–rhyolite suite. Lithos 376, 105759.

Cucciniello, C., Avanzinelli, R., Sheth, H., Casalini, M., 2022. Mantle and crustalcontributions to the Mount Girnar alkaline plutonic complex and the circum-Girnar mafic-silicic intrusions of Saurashtra, northwestern Deccan Traps. Journal of Petrology 63(3), egac007, https://doi.org/10.1093/petrology/egac007

Deb, G.K., Saha, D., Patranabis-Deb, S., Banerjee, A., 2021. Coexisting arc and MORB signatures in the Sonakhan greenstone belt, India: late Neoarchean–early Proterozoic subduction rollback and back-arc formation. American Journal of Science321(9), 1308-1349.

Dhote, P., Bhan, U., Verma, D., 2021. Genetic model of Carbonatites hosted Rare Earth Elements mineralization from Ambadongar Carbonatite Complex, Deccan Volcanic Province, India. Ore Geology Reviews 135(80), 10.1016/j.oregeorev.2021.104215.

Dhote, P., Zamarkar, P., Meshram, D.C., Dongre, A., 2022. Evidence and timing of metasomatism of the lithospheric mantle before large-scale Deccan magmatism: Insights from the phlogopite–spinel–wehrlite xenoliths from Sarnu–Dandali alkaline igneous complex, Rajasthan, northwestern India. Journal of Earth System Science 131, 150, https://doi.org/10.1007/s12040-022-01895-0

Dongre, A., Dhote, P.S., Zamarkar, P., Sangode, S.J., Belyanin, G., Meshram, D.C., Patil, S.K., Karmakar, A., Jain, L., 2022. Short-lived alkaline magmatism related to the Réunion plume in the Deccan Large Igneous Province: inferences from petrology, $^{40}Ar/^{39}Ar$ geochronology and palaeomagnetism of lamprophyre from the Sarnu-Dandali Alkaline Igneous Complex, Geological Society London Special Publications 513, 381-411, https://doi.org/10.1144/SP513-2021-34

Dongre, A., Viljoen, K.S., Belyanin, G., Le Roux, P., Malandkar, M., 2020. Petrogenesis of the diamondiferous Pipe-8 ultramafic intrusion from the Wajrakarur kimberlite field of southern India and its relation to the worldwide Mesoproterozoic (~1.1 Ga) magmatism of kimberlite and related rocks. Geoscience Frontiers 11(3), 793-805, https://doi.org/10.1016/j.gsf.2019.07.010

Dongre, A., Lavhale, P., Li, Q.-L., 2021. Perovskite U-Pb age and petrogenesis of the P-12 kimberlite from the Eastern Dharwar craton, southern India: Implications for a possible linkage to the 1110 Ma large igneous province. Journal of Asian Earth Sciences 213, 104750.

Dwivedi, S.K., Jafri, S.H., SrinivasaSarma, D., Tripathi, P., Parthasarathy, G., Pandey, O.P., 2022. Mineral chemistry, geochemistry and geophysical investigations of Simlipal volcanics from Eoarchean Singhbhum Craton (Eastern India): geodynamic implications of pervasive plume–lithosphere interaction. Int. J. Earth Sci. 111, 1149–1184. https://doi.org/10.1007/s00531-022-02170-9.

Dwivedi, S.K., Pandey, O.P., Tripathi, P., Jafri, S.H., SrinivasaSarma, D., Narsing Rao, A., Kanakdande, P., Parthasarathy, G., 2023. Petrogenesis of Bonai volcanic rocks from Singhbhum Craton (Eastern India): Geophysical and geodynamic implications for pervasive plume-lithospheric interaction. Geosystems and Geoenvironment 1, 100040. https://doi.org/10.1016/j.geogeo.2022.100040.

Eddy, M.P., Schoene, B., Samperton, K.M., Keller, G., Adatte, T., Khadri, S.F., 2020. U-Pb zircon age constraints on the earliest eruptions of the Deccan Large Igneous Province, Malwa Plateau, India. Earth and Planetary Science Letters, 540, 116249.

Giri, R.K., Chalapathi Rao, N.V., Rahaman, W., Kumar, A., Satyanarayanan, M., Keshav Krishna, A., 2021. Paleoproterozoic calc-alkaline lamprophyres from the Sidhi Gneissic Complex, India: Implications for plate tectonic evolution of the Central Indian Tectonic Zone. Precambrian Research 362, 106316.

Giri, R.K., Pankaj, P., Chalapathi Rao, N.V., Chakrabarti, R., Pandit, D., 2019. Petrogenesis of an alkaline lamprophyre (camptonite) with ocean island basalt (OIB)- affinity at the NW margin of the Cuddapah basin, eastern Dharwar craton, southern India. Neues Jahrbuch für Mineralogie 196(2), 149-177, https://doi.org/10.1127/njma/2019/0179.

Haase, K.M., Regelous, M., Schöbel, S., Günther, T., De Wall, H., 2019. Variation of melting processes and magma sources of the early Deccan flood basalts, Malwa Plateau, India. Earth and Planetary Science Letters 524, 115711.

Hazarika, B., Malpe, D.B., Dongre, A., 2020. Petrogenesis of mafic dykes from the western Bastar craton of Central India and their relation to outgrowth of Columbia supercontinent. Miner Petrol 114, 243–262. https://doi.org/10.1007/s00710-020-00695-y

Hiloidari, S., Sarma, D.S., Singh, S.P., 2022. Geochemical signatures and petrogenesis of Dhasan metabasalts from Kurrat–Girar–Badwar greenstone belt, southern Bundelkhand Craton, India. J Earth Sys Sci 131, 243. https://doi.org/10.1007/s12040-022-01986-y

Kale, V.S., Pande, K., 2022. Reappraisal of Duration and Eruptive Rates in Deccan Volcanic Province, India. J Geol Soc India 98, 7–17.

Kaur, G., Mitchell. R.H., 2019. Mineralogy of the baotite-bearing Gundrapalli lamproite, Nalgonda district, Telangana, India. Mineralogical Magazine 83(3), 401–411.

Kaur, G., Mitchell, R.H., Ahmed, S., 2018. Mineralogy of the Vattikod lamproite dykes, Ramadugu lamproite field, Nalgonda District, Telangana: A possible expression of ancient subduction-related alkaline magmatism along Eastern Ghats Mobile Belt, India. Mineralogical Magazine 82 (1), 35–58.

Khan, S., Dongre, A., Viljoen, F., Li, Q.-L., Le Roux, P., 2019. Petrogenesis of lamprophyres synchronous to kimberlites from the Wajrakarur kimberlite field: Implications for contrasting lithospheric mantle sources and geodynamic evolution of the eastern Dharwar Craton of southern India. Geological Journal 54(5), 2994-3016, https://doi.org/10.1002/gj.3394.

Khanna, T.C., Sesha Sai, V.V., 2020. Petrogenesis of low-Ti and high-Ti basalt, adakite and rhyolite association in the Peddavuru greenstone belt, eastern Dharwar craton, India: A Neoarchean analogue of Phanerozoic-type back-arc magmatism. Geochemistry 80(2), 125606.

Krmíček, L., Magna, T., Pandey, A., Chalapathi Rao, N.V., Kynický, J., 2022. Lithium isotopes in kimberlites, lamproites and lamprophyres as tracers of source components and processes related to supercontinent cycles. Geological Society London Special Publications 513, 209-236, https://doi.org/10.1144/SP513-2021-60.

Krishnamurthy, P., 2020a. The Deccan Volcanic Province (DVP), India: A Review. J Geol Soc India 96, 9–35. https://doi.org/10.1007/s12594-020-1501-5.

Krishnamurthy, P., 2020b. The Deccan Volcanic Province (DVP), India: A Review. J Geol Soc India 96, 111–147. https://doi.org/10.1007/s12594-020-1521-1

Kumar, S., Pal, S.K., Guha, A., 2020. Very low frequency electromagnetic (VLF-EM) study over Wajrakarur kimberlite pipe 6 in Eastern Dharwar Craton, India. Journal of Earth System Science 129, 102.

Kumar, R., Ahmad, T., Saikia, A. 2022. P–T estimates for the fractionated and primary melt of tholeiitic dykes from Multai area of Deccan flood basalt, Madhya Pradesh (India). J Earth Sys Sci 131, 104. https://doi.org/10.1007/s12040-022-01839-8

Kumar, S.P., Shaikh, A.M., Patel, S.C., Seikh, J.M., Behera, D., Pruseth, K. L., Ravi, S, R., Tappe, S., 2021. Multi-stage magmatic history of olivine–leucite lamproite dykes from Banganapalle, Dharwar craton, India: evidence from compositional zoning of spinel. Mineralogy and Petrology 115, 87–112, 10.1007/s00710-020-00722-y

Laxman, M.B., Nagaraju, B., Nagaraju, K., Vijaya Kumar, K., 2022. Spatial variations in the geochemical characteristics of basalts from the Deccan Volcanic Province, India: Role of mixing and assimilation fractional crystallisation. J Earth Sys Sci 131, 186.

Manikyamba, C., Ghose, N.C., Ganguly, S., Pahari, A., and Sindhuja, C.S., 2020. Gold, uranium, thorium, and rare earth mineralization in the Kadiri Volcanic Province of Eastern Dharwar Craton, India: An evaluation of mineralogical, textural, and geochemical attributes.Geological Journal56(1), 359-381. https://doi.org/10.1002/gj.3959

Manikyamba, C., Ganguly, S., Pahari, A., 2021. Geochemical Features of Bellara Trap Volcanic Rocks of Chitradurga Greenstone Belt, Western Dharwar Craton, India: Insights into MORB-BABB Association from a Neoarchean Back-Arc Basin. J. Earth Sci. 32, 1528–1544,https://doi.org/10.1007/s12583-021-1472-5.

Manikyamba, C., Pahari, A., Santosh, M., Subramanyam, K. S. V., Reddy, G. H., 2022. Geochemistry of basalts in unravelling the mantle processes and crustal evolution: Insights from the greenstone belts of western Dharwar Craton. Geosystems and Geoenvironment 1(4), 100070.

Manu Prasanth, M.P., Hari, K.R., Santosh, M., 2019. Tholeiitic basalts of Deccan large igneous province, India: An overview. Geological Journal 54(5), 2980-2993.

Manu Prasanth, M.P., Pang, K.N., Hari, K.R., Sahoo, B.B., Ravindran, A., Iizuka, Y., 2023. Geochemistry of Precambrian dyke swarms in the Singhbhum craton, India: Implications for recycled crustal components in the mantle source. Frontiers in Earth Science 10,https://doi.org/10.3389/feart.2022.1092823.

Meshram, R.R., Dora, M.L., Naik, R., Shareef, M., Gopalkrishna, G., Meshram, T., Baswani, S.R., Randive, K.R., 2019. A new find of calc-alkaline lamprophyres in Thaneswana area, Western

Dharwar Craton, India. Journal of Earth System Sciences 128, https://doi.org/10.1007/s12040-018-1037-x.

Meshram, T., Mahapatro, S.N., Aravind, J.K., Dora, M.L., Baswani, S.R., Gopalkrishna G., Meshram, R.R., Sesha Sai, V.V., Randive, K., Dash, J.K., 2022. Geochemistry and Sr-Nd isotopic studies of Paleoproterozoic (c. 2.3 Ga) meta-lamprophyre from the Rapuru area, Nellore Schist Belt, southern India: Implications for back-arc basin magmatism and its relevance to the Columbia supercontinent assembly. Geological Society London Special Publications 513, 103-132, https://doi.org/10.1144/SP513-2021-4.

Mittal, T., Sprain, C.J., Renne, P.R., Richards, M.A., 2023. Deccan volcanism at K-Pg time. Geological Society of America Special Paper,https://doi.org/10.1130/2022.2557(22).

Mukherjee, A., Tiwari, P., Verma, C.B., Babu, E.V.S.S.K., Sarathi, J.P., 2021. Native Gold and Au-Pt Alloy in Eclogite Xenoliths of Kalyandurg KL-2 Kimberlite, Anantapur District, South India. Journal of the Geological Society of India 97, 567-570.

Panda, A., Sarma, D.S., Patel, R., 2022. Geochemistry, magma flow characteristics and petrogenesis of Paleoproterozoic NW–NNW trending mafic dykes from central Bastar craton, India. Journal of Earth System Science 132(1), 1.

Pandey, A., Chalapathi Rao, N.V., 2020. Supercontinent transition as a trigger for ~1.1 Gyr diamondiferous kimberlites and related magmatism in India. Lithos 370-371, 105620.

Pandey, A., Chalapathi Rao, N.V., Chakrabarti, R., 2020. Mesoproterozoic 40Ar/39Ar age and Sr-Nd isotopic geochemistry of calc-alkaline lamprophyre from the Mudigubba area, eastern Dharwar Craton, India. Current Science 119(7), 1142-1148.

Pandey, R., Chalapathi Rao, N.V., Singh, M.K., Talukdar, D., 2022. Alkaline rocks from the Deccan Large Igneous Province: Time-space distribution, petrology, geochemistry and economic aspects. Journal of Earth System Sciences 131, 108.

Pandey, R., Pandey, A., Chalapathi Rao, N.V., Belyatsky, B., Choudhary, A.K., Lehmann, B., Pandit, D., Dhote, P., 2019. Petrogenesis of end-Cretaceous/Early Eocene lamprophyres from the Deccan Large Igneous Province: Constraints on plume-lithosphere interaction and the post-Deccan lithosphere-asthenosphere boundary (LAB) beneath NW India. Lithos 346-347, 105139, https://doi.org/10.1016/j.lithos.2019.07.006

Pandey, A., 2022. Geochemical evidence for a widespread Paleoproterozoic continental arc-back-arc magmatism in the Lesser Himalaya during the Columbia supercontinent assembly. Precambrian Research, 375, 106658.

Pandey, O.P., Paul, D., 2022. Secular evolution of the subcontinental lithospheric mantle beneath Indian cratons: Insights from geochemistry and geochronology of the Precambrian mafic dykes. Lithos, 106729.

Pandey, R., Chalapathi Rao, N.V., Singh, M.K., 2022. Alkaline rocks from the Deccan Large Igneous Province: Time–space distribution, petrology, geochemistry and economic aspects. J Earth Sys Sci 131, 108,https://doi.org/10.1007/s12040-022-01852-x,

Pankaj, P., Giri, R.K., Chalapathi Rao, N.V., Chakrabarti, R., Raghuvanshi, S., 2020. Mineralogy and petrology of shoshonitic lamprophyre dykes from the Sivarampeta area, diamondiferous Wajrakarur kimberlite field, Eastern Dharwar Craton, southern India. Journal of Mineralogical and Petrological Sciences 115(2), 202-215.

Parthasarathy, G., Ray J.S., 2019. Recent Advancement in Studies of Deccan Trap and Its Basement;Carbonatites and Kimberlites – An Indian Perspective in Last Five Years, Proc Indian National Sci Acad 85(2) 481-492.

Patel, A.K., Mishra, B., Upadhyay, D., Lochan, K., 2022 Mineralogical and geochemical evidence of dissolution-reprecipitation controlled hydrothermal Rare earth element mineralization in the Amba Dongar Carbonatite Complex, Gujrat, Western India. Economic Geology, 117(3), 683-702, 10.5382/econgeo.4890.

Pattnaik, J., Demouchy, S., Ghosh, S., 2021. Low hydrogen concentrations in Dharwar cratonic lithosphere inferred from peridotites, Wajrakarur kimberlites field: Implications for mantle viscosity and carbonated silicate melt metasomatism. Precambrian Research 352, 105982.

Pattnaik, J., Ghosh, S., Dongre, A., 2020. Plume activity and carbonated silicate melt metasomatism in Dharwar cratonic lithosphere: Evidence from peridotite xenoliths in Wajrakarur kimberlites. Lithos 376-377, 105726.

Paul, D., J. Chandra, M. Halder, 2020. Proterozoic Alkaline rocks and carbonatites of Peninsular India: A review. Episodes 43(1), 249-277, 10.18814/epiiugs/2020/020015.

Pdah, D.S.M., Khonglah, M.A., 2022. Orbicular and Nodular structures in Carbonatite of the Sung valley ultramafic-alkaline-carbonatite complex, Shillong plateau, Meghalaya, NE India: their petrogenetic implications. Journal of Geological Society of India 98, 635-640, 10.1007/s12594-022-2038-6.

Radhakrishna, T., Vijaya Kumar. K., 2020. Palaeoproterozoic Mafic magmatism in the Indian Shield: Petrologic, Geochemical and Thermal constraints on Proterozoic Mantle. Episodes Journal of International Geoscience 43(1), 187-202.

Raghuvanshi, S., Chalapathi Rao, N.V., Talukdar, D., Sharma, A., Pandey, R., 2022. Chrome-diopside xenocrysts entrained in a Neoproterozoic lamprophyre dyke from the Mysuru area: their origin and implications for lithospheric thickness beneath the Western Dharwar Craton, southern India. Journal of the Geological Society of India 98, 23-34.

Raghuvanshi, S., Pandey, A., Pankaj, P., Chalapathi Rao, N.V., Chakrabarti, R., Pandit, D., Pandey, R., 2019. Lithosphere–asthenosphere interaction and carbonatite metasomatism in the genesis of Mesoproterozoic shoshonitic lamprophyres at Korakkodu, Wajrakarur kimberlite field, Eastern Dharwar Craton, southern India. Geological Journal 54(5), 3060-3077, https://doi.org/10.1002/gj.3468.

Randive, K., Meshram, T., 2020. An Overview of the Carbonatites from the Indian Subcontinent. Open Geosciences, 12(1), 85-116, 10.1515/geo-2020-0007.

Ray, L., Gupta, R.K., Chopra, N., Gopinadh, D., Dwivedi, S.K., 2021. Thermal and physical properties of Deccan basalt and Neoarchean basement cores from a deep scientific borehole in the Koyna− Warna seismogenic region, Deccan Volcanic Province, western India: Implications on thermal modeling and seismogenesis. Earth and Space Science, 8(10), e2021EA001645.

Rose, R., Mukherjee, R., Frei, R., Mondal, S.K., Lingadevaru, M., 2022. Petrogenesis of the late Archean Pillow Basalts from the Chitradurga greenstone belt, Western Dharwar Craton (southern India). J Earth Sys Sci 131, 95, https://doi.org/10.1007/s12040-022-01818-z.

Sahoo, S., Chalapathi Rao, N.V., Monié, P., Belyatsky, B., Dhote, P., Lehmann, B., 2020. Petro-geochemistry,Sr-Nd isotopes and $^{40}Ar/^{39}Ar$ ages of fractionated alkaline lamprophyres from the Mount Girnar igneous complex (NW India): Insights into the timing of magmatism and the

lithospheric mantle beneath the Deccan Large Igneous Province. Lithos 374-375, 105712, https://doi.org/10.1016/j.lithos.2020.105712.

Saini, J., Kaur, P., Mitchell, R., Kaur, G., 2022. Mineralogy of the Marepalli lamproite dyke from the Nalgonda district, Telangana, Southern India. Mineralogical Magazine, 86(5), 799-813.

Saini, J., Patel, S.C., Tappe, S., Mitchell, R.H., Pruseth, K.L., Kaur, P., Singh, A., Kaur, G., 2022. Cretaceous potassic igneous activity in the Raniganj Basin, eastern India: Compositional variations in mica and apatite as recorders of lamproite magma evolution. Lithos434-435, 106916.

Samal, A.K., Srivastava, R.K., Rahaman, W. 2021a. Sr-Nd isotope geochemistry and petrogenesis of ca. 2.26–2.25 Ga and ca. 2.08 Ga mafic dyke swarms from the Dharwar craton, India: Insights into their mantle sources and geodynamic implications. Lithos 406, 106503.

Samal, A.K., Srivastava, R.K., Upadhyay, D., 2021b. Major, trace, and rare-earth element geochemistry of Nb-V rich Andradite-Schorlomite-Morimotoite Garnet from Ambadungar-Saidivasan alkaline carbonatite complex, India: Implication for the role of hydrothermal fluid-induced metasomatism. Minerals 11(7), 756.

Sarkar, S., Giuliani, A., Ghosh, S., Phillips, D., 2021. Petrogenesis of coeval lamproites and kimberlites from the Wajrakarur field, Southern India: New insights from olivine compositions. Lithos 406-407, 106524.

Self, S., Mittal, T., Dole, G., Vanderkluysen, L., 2022. Toward understanding Deccan volcanism. Annual Review of Earth and Planetary Sciences 50, 477-506.

Shaikh, A.M., Tappe, S., Bussweiler, Y., Patel, S.C., Ravi, S., Bolhar, R., Viljoen, F., 2020. Clinopyroxene and Garnet Mantle Cargo in Kimberlites as Probes of Dharwar Craton Architecture and Geotherms, with Implications for Post-1·1 Ga Lithosphere Thinning Events Beneath Southern India. Journal of Petrology 61(9), egaa087.

Shaikh, A.M., Patel, S.C., Bussweiler, Y, Kumar, S.P., Tappe, S., Ravi, S., Mainkar, D., 2019. Olivine trace element compositions in diamondiferous lamproites from India: Proxies for magma origins and the nature of the lithospheric mantle beneath the Bastar and Dharwar cratons, Lithos 324–325, 501-518. https://doi.org/10.1016/j.lithos.2018.11.026

Sheth, H., Vanderkluysen, L., Demonterova, E.I., Ivanov, A.V., Savatenkov, V.M., 2019. Geochemistry and $^{40}Ar/^{39}Ar$ geochronology of the Nandurbar-Dhule mafic dyke swarm: Dyke-sill-flow correlations and stratigraphic development across the Deccan flood basalt province. Geological Journal, 54(1), 157-176.

Sheth,H., Duraiswami, R.A., Ghule, V., Naik, A., Das, T., 2022. Flood basalt structures and textures as guides to cooling histories and palaeoclimates: the Deccan Traps of Saurashtra, western India. Geological Magazine 159(8), 1415–1436.

Sharma, N.M., Phukon, P., Bhattacharyya, P., 2022a. Petrogenetic evolution of Lichi volcanics from Arunachal Himalaya, Northeast India: Insights from geochemical modelling. Geological Journal 57(12), 4955– 4973. https://doi.org/10.1002/gj.4563.

Sharma, A., Pandey, R., Chalapathi Rao, N.V., Sahoo, S., Belyatsky, B., Dhote, P., 2021. Mineralogy and petrology of lamprophyre and dolerite dykes from the end-Cretaceous (~ 66 Ma) Phenaimata alkaline igneous complex, north-western India: evidence for open magma chamber fractionation, mafic recharge, and disaggregation of crystal mush zone in a large igneous province. Mineralogy and Petrology, https://doi.org/10.1007/s00710-021-00770-y.

Sharma, A., Sahoo, S., Chalapathi Rao, N.V., Belyatsky, B., Dhote, P., Lehmann, B., 2022b. Petrology and Nd-Sr isotopic composition of alkaline lamprophyres from the Early to Late Cretaceous Mundwara alkaline complex, NW India: evidence of crystal fractionation, accumulation and corrosion in a complex magma chamber plumbing system. Geological Society London Special Publications 513, 413-442, https://doi.org/10.1144/SP513-2020-175.

Sharma, A., Kumar, A., Pankaj, P., Pandit, D., Chakrabarti, R., Chalapathi Rao, N.V., 2019. Petrology and Sr-Nd isotope systematics of the Ahobil kimberlite (Pipe-16) from the Wajrakarur field, Eastern Dharwar craton, southern India. Geoscience Frontiers 10(3), 1167-1186.

Shellnutt, J.G., Pang, K.N., Qi, L., Bhat, G.M., 2022. Platinum-group element geochemistry of the Panjal Traps: constraints on mantle melting and implications for mineral exploration. Geological Society London Special Publications 518(1), 531-551.

Silpa, A.S., Satish-Kumar, M., 2018. Dyke Swarms in the Dharwar Craton: A Key to Understanding the Late Archean to Early Proterozoic Cratonic Correlations. J Indian Inst Sci 98, 365–378, https://doi.org/10.1007/s41745-018-0090-4.

Singh, S K., Srivastava, R.K., Kumar, S., Samal, A.K., 2021. Geochemical characterization of the Paleoproterozoic (ca. 1.98-1.97) Darguwan-Surajpura mafic sills within the Bijawar basin, North-Central India: Genetic aspects and geodynamic implications. Geochemistry 81(1), 125689.

Singh, T., Upadhyay, D., Patel, A.K., Mishra, B., 2022. High MREE-HREE solubility in a carbonatite-derived hydrothermal fluid: Evidence from fluorite-hosted fluid inclusions in the Amba Dongar carbonatite complex, India. Chemical Geology 613, 121162.

Srivastava, R.K., 2019. Evidence of sub-continental lithospheric mantle sources and open-system crystallization processes from in-situ U Pb ages and Nd–Sr–Hf isotope geochemistry of the cretaceous ultramafic-alkaline-(carbonatite) intrusions from the Shillong Plateau, North-Eastern India. Lithos 330-331, 108-119.

Srivastava, R.K., 2020. Early Cretaceous alkaline/ultra-alkaline silicate and carbonatite magmatism in the Indian Shield – a review: implications for a possible remnant of the Greater Kerguelen Large Igneous Province. Episodes 43(1), 300-311.

Srivastava, R.K., Guarino, V., Melluso, L., 2022. Early Cretaceous ultramafic-alkaline-carbonatite magmatism in the Shillong Plateau-Mikir Hills, northeastern India- a synthesis. Mineralogy and Petrology, https://doi.org/10.1007/s00710-022-00777-z.

Srivastava, R. K., Söderlund, U., Ernst, R. E., Gautam, G. C., 2021. A Ca. 2.25 Ga mafic dyke swarm discovered in the Bastar craton, Central India: Implications for a widespread plume-generated large Igneous Province (LIP) in the Indian shield. Precambrian Research, 360, 106232.

Srivastava, R.K., Singh, S.K., Samal, A.K., 2022a. Geochemistry and geodynamic implications of the mafic magmatic plumbing system of the ca. 1.98–1.97 Ga Jhansi Large Igneous Province in the northern Indian Shield. J Earth Sys Sci 131, 4,https://doi.org/10.1007/s12040-021-01751-7.

Srivastava, R.K., Banerjee, S., Longstaffe, F.J., Bhagat, S., Sinha, D.K., 2022b. Stable isotopic study of carbonatites from the Pakkanadu Alkaline Complex, southern India: Constraints on carbonatite melt evolution and sub-solidus, high temperature fluid-rock interaction. Lithos, 430-431, https://doi.org/10.1016/j.lithos.2022.106863.

Srivastava, R.K., Guarino, V., Melluso, L., 2022c. Early Cretaceous ultramafic-alkaline-carbonatite magmatism in the Shillong Plateau-Mikir Hills, northeastern India -a synthesis. Mineralogy and Petrology, DOI: 10.1007/s00710-022-00777-z.

Srivastava, R.K., Wang, F., Shi, W., Ernst, R.E., 2023. Early Cretaceous mafic dykes from the Chhota Nagpur Gneissic Terrane, eastern India: Evidence of multiple magma pulses for the main stage of the Greater Kerguelen mantle plume. Journal of Asian Earth Sciences, 241, 105464.

Viladkar, S.G., Sorokhitna, N.V., 2021. Evolution of pyrochlore in carbonatites of the Amba Dongar complex, India. Mineralogical Magazine, 85(4), 1-29.

Vijaya Kumar, J., Randive, K., 2022. Platinum group elements in lamprophyre, picrobasalt, gabbro and basalts of the Phenai Mata and nearby areas: implications for Fe–Ni–Cu–PGE mineralization in the Deccan Large Igneous Province. Geological Society London Special Publications 513, 443-474, https://doi.org/10.1144/SP513-2020-265.